frontiers | Research Topics

Innovative 3D models for understanding mechanisms underlying lung diseases: Powerful tools for translational research

Edited by
Janette K. Burgess, Ramon Farre, Rebecca L. Heise and Jane Elizabeth Bourke

Published in
Frontiers in Pharmacology

ISSN 1664-8714
ISBN 978-2-8325-4417-4
DOI 10.3389/978-2-8325-4417-4

About Frontiers

Frontiers is more than just an open access publisher of scholarly articles: it is a pioneering approach to the world of academia, radically improving the way scholarly research is managed. The grand vision of Frontiers is a world where all people have an equal opportunity to seek, share and generate knowledge. Frontiers provides immediate and permanent online open access to all its publications, but this alone is not enough to realize our grand goals.

Frontiers journal series

The Frontiers journal series is a multi-tier and interdisciplinary set of open-access, online journals, promising a paradigm shift from the current review, selection and dissemination processes in academic publishing. All Frontiers journals are driven by researchers for researchers; therefore, they constitute a service to the scholarly community. At the same time, the *Frontiers journal series* operates on a revolutionary invention, the tiered publishing system, initially addressing specific communities of scholars, and gradually climbing up to broader public understanding, thus serving the interests of the lay society, too.

Dedication to quality

Each Frontiers article is a landmark of the highest quality, thanks to genuinely collaborative interactions between authors and review editors, who include some of the world's best academicians. Research must be certified by peers before entering a stream of knowledge that may eventually reach the public - and shape society; therefore, Frontiers only applies the most rigorous and unbiased reviews. Frontiers revolutionizes research publishing by freely delivering the most outstanding research, evaluated with no bias from both the academic and social point of view. By applying the most advanced information technologies, Frontiers is catapulting scholarly publishing into a new generation.

What are Frontiers Research Topics?

Frontiers Research Topics are very popular trademarks of the *Frontiers journals series*: they are collections of at least ten articles, all centered on a particular subject. With their unique mix of varied contributions from Original Research to Review Articles, Frontiers Research Topics unify the most influential researchers, the latest key findings and historical advances in a hot research area.

Find out more on how to host your own Frontiers Research Topic or contribute to one as an author by contacting the Frontiers editorial office: frontiersin.org/about/contact

Innovative 3D models for understanding mechanisms underlying lung diseases: Powerful tools for translational research

Topic editors

Janette K. Burgess – University Medical Center Groningen, Netherlands
Ramon Farre – University of Barcelona, Spain
Rebecca L. Heise – Virginia Commonwealth University, United States
Jane Elizabeth Bourke – Monash University, Australia

Citation

Burgess, J. K., Farre, R., Heise, R. L., Bourke, J. E., eds. (2024). *Innovative 3D models for understanding mechanisms underlying lung diseases: Powerful tools for translational research*. Lausanne: Frontiers Media SA. doi: 10.3389/978-2-8325-4417-4

Table of contents

frontiers | Frontiers in Pharmacology

TYPE Original Research
PUBLISHED 02 September 2022
DOI 10.3389/fphar.2022.945134

OPEN ACCESS

EDITED BY
Narasaiah Kolliputi,
University of South Florida,
United States

REVIEWED BY
Kamal Hany Hussein,
Assiut University, Egypt
Camila Hochman-Mendez,
Texas Heart Institute, United States

*CORRESPONDENCE
Jorge Otero,
jorge.otero@ub.edu

†These authors have contributed equally to this work

SPECIALTY SECTION
This article was submitted to Respiratory Pharmacology,
a section of the journal
Frontiers in Pharmacology

RECEIVED 16 May 2022
ACCEPTED 08 August 2022
PUBLISHED 02 September 2022

CITATION
Marhuenda E, Villarino A, Narciso M, Elowsson L, Almendros I, Westergren-Thorsson G, Farré R, Gavara N and Otero J (2022), Development of a physiomimetic model of acute respiratory distress syndrome by using ECM hydrogels and organ-on-a-chip devices.
Front. Pharmacol. 13:945134.
doi: 10.3389/fphar.2022.945134

Development of a physiomimetic model of acute respiratory distress syndrome by using ECM hydrogels and organ-on-a-chip devices

Esther Marhuenda[1,2†], Alvaro Villarino[1†], Maria Narciso[1,3], Linda Elowsson[4], Isaac Almendros[1,2,5], Gunilla Westergren-Thorsson[4], Ramon Farré[1,2,5], Núria Gavara[1,2,3] and Jorge Otero[1,2,3]*

[1]Unitat de Biofísica i Bioenginyeria, Facultat de Medicina i Ciències de la Salut, University de Barcelona, Barcelona, Spain, [2]CIBER de Enfermedades Respiratorias, Instituto de Salud Carlos III, Madrid, Spain, [3]The Institute for Bioengineering of Catalonia, The Barcelona Institute of Science and Technology, Barcelona, Spain, [4]Lung Biology, Biomedical Center, Department of Medical Science,Lund University, Lund, Sweden, [5]Institut d'Investigacions Biomèdiques August Pi i Sunyer, Barcelona, Spain

Acute Respiratory Distress Syndrome is one of the more common fatal complications in COVID-19, characterized by a highly aberrant inflammatory response. Pre-clinical models to study the effect of cell therapy and anti-inflammatory treatments have not comprehensively reproduced the disease due to its high complexity. This work presents a novel physiomimetic *in vitro* model for Acute Respiratory Distress Syndrome using lung extracellular matrix-derived hydrogels and organ-on-a-chip devices. Monolayres of primary alveolar epithelial cells were cultured on top of decellullarized lung hydrogels containing primary lung mesenchymal stromal cells. Then, cyclic stretch was applied to mimic breathing, and an inflammatory response was induced by using a bacteriotoxin hit. Having simulated the inflamed breathing lung environment, we assessed the effect of an anti-inflammatory drug (i.e., dexamethasone) by studying the secretion of the most relevant inflammatory cytokines. To better identify key players in our model, the impact of the individual factors (cyclic stretch, decellularized lung hydrogel scaffold, and the presence of mesenchymal stromal cells) was studied separately. Results showed that developed model presented a more reduced inflammatory response than traditional models, which is in line with what is expected from the response commonly observed in patients. Further, from the individual analysis of the different stimuli, it was observed that the use of extracellular matrix hydrogels obtained from decellularized lungs had the most significant impact on the change of the inflammatory response. The developed model then opens the door for further *in vitro* studies with a better-adjusted response to the inflammatory hit and more robust results in the test of different drugs or cell therapy.

KEYWORDS

ARDS, lung-on-a-chip, extracellular matrix, hydrogels, mesenchymal stromal cells, alveolar epithelial cells, inflammation

1 Introduction

Acute Respiratory Distress Syndrome (ARDS), commonly caused by bacterial or viral pneumonia (Matthay et al., 2019), is characterized by lung parenchymal damage from increased endothelial and epithelial permeability (non-cardiogenic pulmonary edema) (Staub 1981). ARDS mortality is approximately 25%–40%, and the only treatment is primarily supportive with lung-protective ventilation (Brower et al., 2000). Major efforts in the medical community are focused mainly on the prevention of the injury (Yadav, Thompson, and Gajic 2017) since, although numerous pharmacologic strategies have been successful in animal studies, few trials have shown a clinical benefit in terms of mortality (Ballard-Croft et al., 2012). On the other hand, cell therapies based on the use of mesenchymal stromal cells (MSCs) have started to show some efficacy. However, the mechanisms involved in the process are still to be determined (Laffey and Matthay 2017). Moreover, during the COVID-19 pandemic, ARDS has been reported as a common complication that dramatically increased the mortality of patients (Wu et al., 2020). The aberrant inflammatory response of these patients (known as the cytokine storm) has been correlated with the severity of the disease and it has become one of the main therapeutic targets (Chen et al., 2020). Nevertheless, neither *in vitro* nor *in vivo* available models realistically recreate the ARDS complex pathophysiology (Huppert and Matthay 2017). Therefore, there is an urgent need to develop models with higher physiological relevance to understand the inflammatory processes related to ARDS, the impact of cell therapy (Nonaka et al., 2020), and the use of anti-inflammatory drugs (Trivedi, Verma, and Kumar 2020). Conventional ARDS *in vitro* models mainly involve applying an inflammatory hit (usually by a bacteriotoxin) to a monolayer of pulmonary epithelial or endothelial cells (Cabrera-Benítez et al., 2016). These conventional models do not fully mimic the complex three-dimensional microarchitecture or the extracellular matrix (Burgess et al., 2016) (ECM) stiffness experienced by cells *in vivo*. Moreover, lung cells *in vivo* are subjected to mechanobiological signals such as those induced by the cyclic stretch associated with breathing or mechanical ventilation.

Two different technologies have recently gained popularity for creating physiomimetic models to recreate the ECM (Busch, Lorenzana, and Ryan 2021) and the mechanobiological signals *in vitro*: 3D cell cultures (Habanjar et al., 2021) and organ-on-a-chip devices (Mertz, Ahmed, and Takayama 2018; Benam, Burgess, and Stewart 2021). Indeed, it has been shown that lung ECM can be obtained by decellularizing the native tissues with detergents and enzymes (Nonaka et al., 2014) and then pulverized and reconstituted in the form of hydrogels suitable for 3D cell culture (Pati and Cho 2017). On the other hand, organ-on-a-chip devices (Bassi et al., 2021) try to recreate the physical microenvironment of living organs *in vitro*. In the specific case of a lung-on-a-chip, devices with control over the cyclic stretch and oxygenation have been developed (Campillo et al., 2016; Huh et al., 2013). In the present work, the aim was to merge these two Frontier technologies (3D ECM hydrogels and lung-on-a-chip-devices) to develop an advanced physiomimetic *in vitro* model of ARDS for the study of inflammatory processes and how they are related to MSCs therapies. Using such an advanced model, we have tested the individual contribution of cyclic stretch and lung ECM and the effect of lung-resident MSCs on the secretion of inflammation-related cytokines after bacterial lipopolysaccharide (LPS) challenge, as well as the impact of treatment with an anti-inflammatory drug (dexamethasone).

2 Materials and methods

Unless otherwise specified, all the reagents were obtained from Sigma Aldrich, Missouri, United States .

2.1 Decellularized extracellular matrix hydrogels

Lung hydrogels were developed from porcine lungs by following the protocol described in (Falcones et al., 2021). Five pig lungs were decellularized and the obtained powder was mixed to reduce batch-to-batch variability. Briefly, porcine lungs were decellularized by perfusion through the trachea and the vasculature with 0.1% Triton X-100% and 2% of sodium deoxycholate for 24 h each, and DNase and 1 M NaCl for 1 hour each. Decellularized lungs were afterward frozen at −80°C, freeze-dried (Telstar Lyoquest-55 Plus, Terrassa, Spain), and milled in liquid N_2 (SPEX SamplePrep, New Jersey, United States) to obtain a fine powder. The resulting ECM powder was digested at a concentration of 20 mg/mL in HCl 0.01 M with porcine gastric mucosa pepsin at a 10:1 concentration at room temperature for 16 h. The digested solution was pH-adjusted to 7.4 ± 0.4 by using 0.1 M NaOH and incubated at 37°C for 20 min to produce the hydrogels. Final ECM concentration in the hydrogels ws ~17 mg/mL.

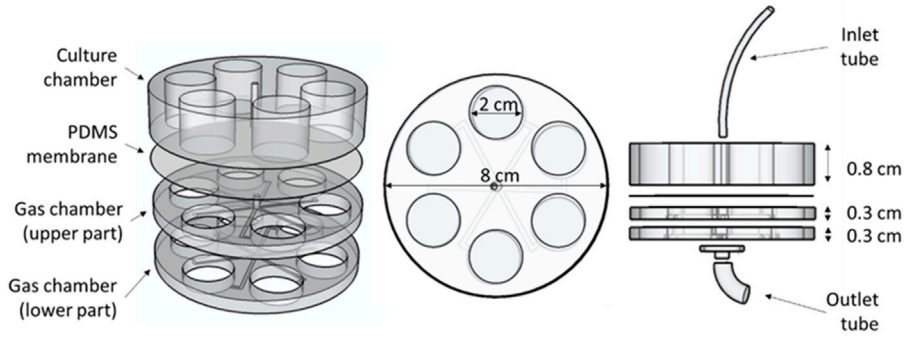

FIGURE 1
Chip design. Dimensions and different parts of the chip can be observed in this 3D representation. The upper part forming the culture chamber and the two lower parts forming the gas chamber can be easily distinguished, separated by the PDMS membrane.

2.2 Lung-on-a-chip devices fabrication

The designed lung-on-a-chip devices were composed of three parts containing six holes, each one located concentrically to form the wells (Figure 1). A video with detailed instructions for fabricating a similar chip is open-source and available in the Supplementary Material of reference (Campillo et al., 2016). The upper part of the device, which was separated from the other two parts by a 380 μm thick gas permeable polydimethylsiloxane (PDMS) membrane (Gel-Pak, Hayward, CA, United States), was the culture chamber (cells and culture medium). The two other parts had channels in their lower part to allow for gas efflux (gas chamber). Gas entered the chip through a small tube inserted in a tiny central hole that perforates the culture chamber and the first part of the gas chamber. The air was distributed through the radial channels of the middle PDMS piece (upper part of the gas chamber) and diffused to the cells through the lower part of the membrane. Gas exited the chip through the radial channels of the lower PDMS piece (lower part of the gas chamber), coming back to the center of the chip, where gas found an exit through the perforated petri dish where the chip was located (Figure 1).

Once the gas had abandoned the chip, it was conducted through a tube to a proportional valve that opened and closed at 0.2 Hz frequency (mimicking the human physiological breathing rate). When the valve closed, the flexible PDMS membrane deflected until reaching a surface strain of up to 10%. The pressure inside the system was alleviated by a leakage that consisted of a small diameter tube (ID = 0.56 mm) (Cole Parmer, Illinois, United States) placed between the outlet of the chip and the proportional valve. The length of the leakage tube was individually adjusted for each fabricated chip to obtain the desired strain for a given pressure.

To fabricate the devices, negative molds of the parts were designed with the Ultimaker Cura software (Ultimaker, Utrecht, Netherlands) and printed with an Ultimaker S5 3D printer (Ultimaker, Utrecht, Netherlands) in polycarbonate material. PDMS prepolymer was mixed in a proportion 10:1 with the curing agent (Sylgard 184 kit, Dow Corning, MI) and poured into the previously printed molds. The resulting mixture was degassed in a bell jar vacuum desiccator (Kartell Labware, Noviglio, Italy) for 45 min and then placed in an oven (Selecta, Barcelona, Spain) for 2 h at 65°C. PDMS parts were carefully removed from the molds and the middle and the upper parts were perforated in the center with an awl for further introduction of the inlet tube. The middle and lower parts were bonded together concentrically after activating their surfaces with a hand-held corona (Electro Technic Products, Chicago, IL) at proximity (~5 mm) for 1 minute at the highest voltage. As previously indicated, the PDMS membrane was also treated with the corona and attached to the already formed gas chamber. The upper part (culture chamber) was attached to the PDMS membrane surface using non-polymerized PDMS and then placed in the oven for 60 min at 65°C. In the meantime, a 60 cm^2 petri dish (Techno Plastic Products AG, Trasadingen, Switzerland) was perforated in the center with a driller (1 cm diameter). The PDMS chip was then placed on the perforated petri dish and adhered to by using non-polymerized PDMS. A 1 mm (ID) inlet tube (Cole Parmer, Illinois, United States) was inserted in the central hole and sealed with non-polymerized PDMS. The whole assembled chip was placed in the oven for 60 min at 65°C. Lastly, a polycarbonate 3D-printed funnel-like piece was attached with glue to the lower part of the petri dish to connect the outlet tube.

The PDMS membranes of the devices fabricated for 3D cell culture were treated for proper adhesion of the hydrogels. Briefly, PDMS membranes were activated by introducing the chips in a plasma cleaner (PDC-002, Harrick Scientific Products Inc. Pleasantville, NY) for 2 min at maximum voltage and then introduced in the culture hood under the UV light for 10 min to sterilize the surface. APTES 10% was added for 1 h and 5 mM genipin (Challenge Bio Products Co., Taiwan) for 45 min. After each reagent, 3 PBS 1X washes of 5 min each were made. Finally, the chip was left to dry overnight.

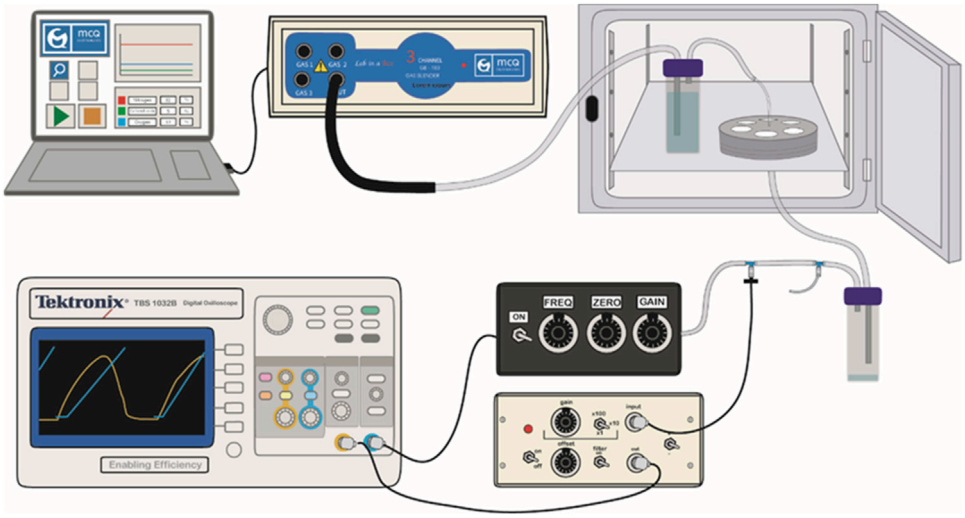

FIGURE 2
Experimental setup. The drawing shows how the air path from the gas blender, controlled by the software, to the valve, through the chip and the two water traps to initially humidify and finally de-humidify the gas. Cyclic stretch-generating pressure is measured along the experiment with the pressure sensor.

2.3 Experimental setup and devices calibration and characterization

2.3.1 Experimental setup

To support the specific gas mixture to the cultured cells, servo-controlled gas blenders (McQ, Virginia, United States) controlled by the Software Gas Mixture Creator (McQ, Virginia, United States) were employed. Previously humidified air went inside the chip through the inlet tube and then it was distributed through (Figure 2) the channels to reach the PDMS membranes where the cells were cultured. Then, the gas abandoned the chip through the outlet tube. After removing the humidity of the air, the conducting tube was connected to a valve for stretch amplitude and frequency control by using an incorporated pressure sensor (176PC14HD2, Honeywell, New Jersey, United States).

2.3.2 Measurement of oxygen diffusion through 3D hydrogels

All the measurements were acquired inside a cell incubator at 100% humidity and 37°C. Before the measurements, chips were ventilated with 100% N_2 for 30 min to displace the existing O_2 in the hydrogel. An optical fiber oxygen sensor (Pyroscience, Aachen, Germany) was calibrated following the manufacturer's instructions and attached to a specifically designed holder that allowed for micrometric-resolution vertical positioning. Measurements were performed with the sensor tip introduced 300 µm in the hydrogel. The gas mixture was changed to room air (20% O_2 and 80% N_2) to measure the oxygen diffusion time through the hydrogel. Measurements were repeated for different distances (100 µm steps) (Colom et al., 2014), and the diffusion time constant τ was calculated.

2.3.3 Membrane and hydrogels strain calibration and characterization

The membrane deformation was calculated by modeling it as a spherical cup shape, where linear strain varies slightly across the membrane, but circumferential strain decreases parabolically to zero at the clamped edge (Campillo et al., 2016). The membrane experiences an equibiaxial linear strain (ε) that can be calculated as follows: the vertical deflection of the spherical cap (h) was calculated by the difference in height assessed with phase-contrast imaging using a confocal microscope with a motorized × 10 objective. At the same time, the radius (r) was known from chip design. The strain of the membrane was calibrated for different gas pressures by using Eq. 1:

$$\epsilon = \frac{2}{3}\left(\frac{h}{r}\right)^2 \quad (1)$$

To assess that the stretch of the membrane was transmitted to the cells through the hydrogels, the latter were coated with 2 µm-diameter fluorescent carboxylated beads (Invitrogen, Oregon, United States). Epifluorescence images were taken at different pressures with a 10X objective. The displacement of the beads was computed by ImageJ as described in (Campillo et al., 2016).

2.4 Cells isolation and culture protocols

Primary lung mesenchymal stromal cells (LMSCs) and type 2 alveolar epithelial cells (ATIIs) were isolated from 180–250 g male Sprague-Dawley rats by following protocols described in (da Silva Meirelles, Chagastelles, and Nardi 2006) and (Guillamat-Prats et al., 2020) respectively, which were approved by the Ethical Committee for Animal Research of the University of Barcelona (Number 154/19, 02/10/2019).

For LMSCs extraction, rats were anesthetized with 1 g/kg urethane and euthanized by exsanguination through abdominal aorta excision. Lungs were perfused with 50 mL of PBS 1X through the right ventricle of the beating heart after cutting the left atrium. Lungs were excised *en bloc* with the heart. Lungs were sectioned into small pieces and digested in 10 mL of 250 U/mL collagenase (Gibco, Massachusetts, United States) solution prepared in DMEM with 10% HEPES for 1 h at 37°C under agitation. The resulting solution was filtered by a 250 µm mesh and then centrifuged at 400 g for 10 min (Rotina 380R, Hettich, Tuttlingen, Germany). The obtained pellet was resuspended in red blood cell lysis buffer (RBC) (BioLegend, San Diego, CA, United States) and was incubated at 4°C for 7 min. After that time, the reaction was stopped by adding PBS 1 × . Finally, cells were centrifuged at 350 g for 5 min and cultured in T-75 flasks for expansion. LMSCs up to passage seven were used for the experiments.

For ATIIs extraction, lungs were perfused with saline through the pulmonary artery and were resected *en bloc*. Five bronchioalveolar lavages were performed with 10 mL of PBS 1X to remove alveolar macrophages. Then, the lungs were digested with 50 mL of 0.25% trypsin through the airways for 30 min. Lungs were cut into small pieces, digested in a 100 units/mL DNase, and filtered through meshes of 100 µm and 40 µm of pore size. The filtered suspension was centrifuged through a percoll (GE HealthCare, Illinois, United States) gradient at 500 g for 20 min. The band containing the ATIIs was recovered and digested by DNase (20 units/mL). The solution was centrifuged for 15 min at 500 g. Then, the pellet was resuspended in DCCM-1 (Biological Industries, Kibbutz Beit Haemek, Israel) medium and cultured for 1 h. After that time, the medium containing ATII non-adherent cells was recovered and centrifuged for 10 min at 800 g. Cells were counted, seeded in the lung-on-a-chip devices and cultured in supplemented DCCM-1 medium (1% penicillin, streptomycin and amphotericin, 1% glutamine, and 10% FBS).

2.5 Acute respiratory distress syndrome-on-a-chip model

For the 3D culture, 3×10^5 cells/mL of LMSC were resuspended in 500 µL of lung ECM pregel before gellification. Then, hydrogels were formed by placing the chips in the incubator for 20 min before adding 500 µl of supplemented DCCM-1. ATII cells were then cultured at a density of 10^6 cells/well. All the experiments were performed at physiological oxygen levels (13%).

A description of the experimental groups is shown in Figure 3: three groups were cultured in each device (co-culture of ATIIs and L-MSCs in 3D hydrogels, ATIIs cultured on top of hydrogels, and ATII cultured over the membrane). Half of the devices were subjected to cyclic stretch, and half of them to an LPS inflammatory hit (L2630 from *Escherichia Coli,* 1 µg/mL). Groups with co-cultures and cyclic stretch are referred to as "advanced physiomimetic model" (AM) while 2D cultures of ATIIs will be referred to as "traditional model" (TM). Cells were cultured under stretch for a total of 72 h (static conditions were maintained for the stretch controls groups), and the LPS hit was applied for 16 h. At the end of the experiment, the supernatants were collected for subsequent analysis. In the experiments involving the effect of an anti-inflammatory drug, 100 nM of dexamethasone were added for 32 h. Duplicates of six different samples were employed for these experiments ($n = 6$).

2.6 Multiplex ELISA analysis

ProcartaPlex Multiplex Immunoassays of the collected supernatants were performed according to the manufacturer's instructions (ThermoFisher, Massachusetts, United States) for the following cytokines: macrophage inflammatory protein-2 (MIP-2), interleukins 1-beta, 6, and 10 (IL-1β, IL-6, IL-10), gamma interferon (INF-γ), alpha tumor necrosis factor (TNF-α), and vascular endothelial growth factor (VEGF). Data were acquired with Magpix (Luminex, Texas, United States) and processed using the ProcartaPlex Analysis App Software (ThermoFisher, Massachusetts, United States).

2.7 Immunohistochemistry

Cells were fixed with 4% paraformaldehyde for 30 min for the immunofluorescence experiments. Primary antibodies were incubated overnight, and secondary antibodies were incubated for 2 h at 37°C. Nuclei were stained with Hoechst 33,342 (ThermoFisher, Massachusetts, United States). To avoid unspecific binding, especially in the hydrogels, a blocking buffer consisting of 2% BSA (ThermoFisher, Massachusetts, United States) diluted in PBS 1X (Gibco, Massachusetts, United States) was employed for 40 min. After the primary antibody incubation, three washes of 5 min under orbital agitation were made. The primary antibodies used were rabbit anti-EpCAM and mouse anti-Vimentin; the secondary

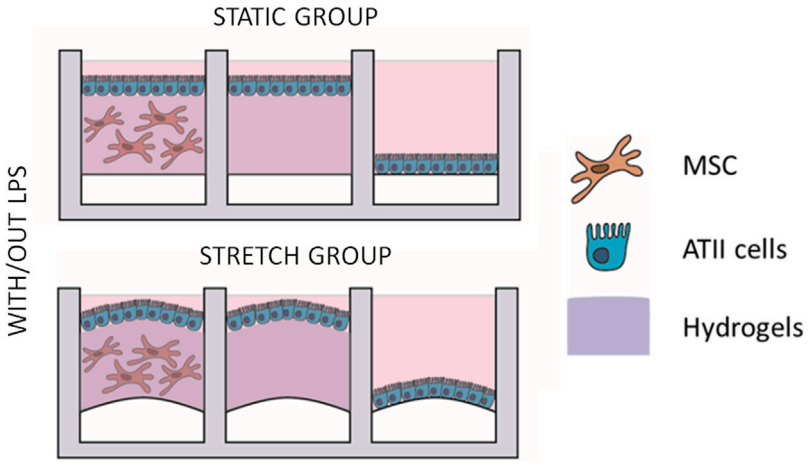

FIGURE 3
Four different experimental groups were designed. In every chip, three different cultures were performed: ATII-LMSC cocultured with/out 3D-cultured LMSC and an ATII monolayer on the hydrogels; ATII single culture monolayer on the hydrogel; and single culture ATII monolayer on the PDMS membrane. In every run of experiments, four chips were used, each of which was subjected to different conditions: static group, static group with an LPS hit, cyclic stretch group, and cyclic stretch group with an LPS hit.

antibodies were goat anti-rabbit cy5 and goat anti-mouse Alexa Fluor 488. All antibodies were purchased from Abcam (Cambridge, United Kingdom). Images were taken with Nikon Confocal Eclipse Ti using a 20X Plan Fluor Multi-immersion objective (0.75 NA). Samples were excited at 488 nm and acquired at 515 nm for Vimentin images, and excited at 543.5 nm and acquired at 605 nm for EpCAM staining. Nuclear images were obtained at 450 nm when illuminating the sample at 408 nm.

2.8 Statistical analysis

Data are expressed as mean ± SE. Statistical analysis was performed with Prism software (GraphPad Software, California, United States). Differences in cytokine expression were studied using Student's *t*-test, except in those cases where they did not follow a normal distribution, where a Mann-Whitney test was performed instead. The normal distribution of the samples was calculated by using a Kolmogorov-Smirnov test. Differences were considered significant for p-values < 0.05.

3 Results

3.1 Lung-on-a-chip device characterization

Three-dimensional images of the ATIIs monolayer on top of the ECM hydrogels with LMSCs cultured inside (Advanced model if stretched) are shown in Figure 4A. The efficient oxygen diffusion through the hydrogel when changing from 0% O_2 to 20% O_2 is shown in Figure 4B, where measurements were taken at different depths inside the hydrogel and compared with those acquired without hydrogel (culture medium) to study whether O_2 was able to diffuse through the whole thickness. Measurements obtained with the fiber optic oxygen sensor showed that the time constant τ for the non-hydrogel measurement (just diffusion in the PDMS membrane) was ≈10 s, increasing by 40% for 300–200 µm depths and by 80% for the 100 µm depth. This indicates that the lung-derived hydrogels present a coefficient of diffusion for O_2 that is quite similar to that of water, indicating these hydrogels are compatible with the three-dimensional culture and the precise control of oxygen partial pressure (Farré et al., 2018). Figure 4C shows the measured strain experienced by the PDMS membrane with the actual strain measured at the surface of the hydrogels calculated by the displacement of the attached fluorescent microbeads. It was observed that the strain applied to the flexible membrane was transmitted to the attached hydrogel 3D structures following a linear relationship with the applied pressure.

3.3 Response of the advanced physiomimetic model to the inflammatory hit

The advanced model was subjected to an LPS endotoxin hit, and the release of inflammatory mediators was studied. LMSCs were cultured three-dimensionally while ATII were

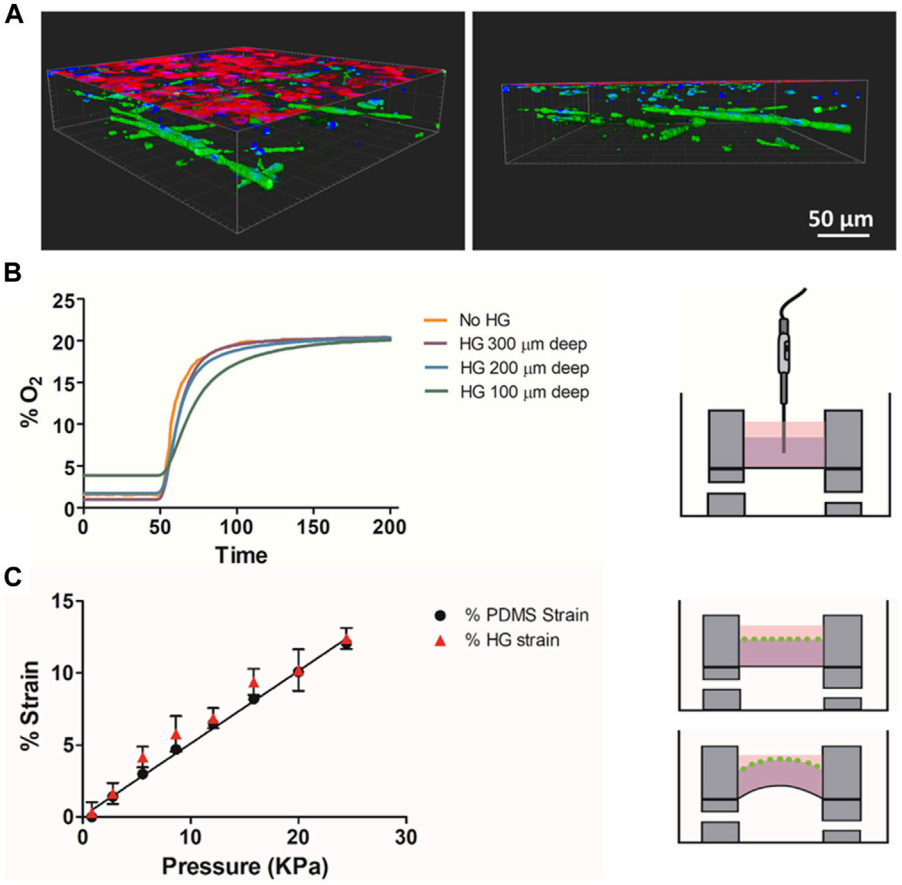

FIGURE 4
(A) Confocal images of the alveolar monolayer on top of the ECM hydrogels with LMSCs cultured inside. Alveolar cells (red) are stained for EpCAM and MSCs (green) are stained for vimentin **(B)** Oxygen diffusion measurements at different depths of the hydrogel and liquid medium (No HG). **(C)** Measured deformation of the membrane and the attached hydrogel at different pressures.

cultured on the top of the hydrogel, forming a monolayer, and cyclic stretch was applied. ELISA results on the secretion of cytokines for the advanced model developed when LPS endotoxin was added to the cultures are shown in Figure 5. The inflammatory hit produced a statistically significant increase in the secretion of inflammation-related cytokines IL-10 (8-fold; $p = 0.003$), IL-6 (2-fold; $p = 0.02$), IL-1β (10-fold; $p = 0.0081$) and TNF-α (3.5-fold; $p = 0.0023$) while no statistical difference was found in the secretion of VEGF, MIP-2α and IFN-γ.

Differences in the inflammatory response of the advanced model compared to the traditional 2D culture model are shown in Figure 6. Results are expressed as the ratio of the cytokines secreted with and without LPS within each group (TM or AM) to compare how both models are responsive. For all the measured cytokines, the response of the advanced model to the inflammatory hit was lower than in the traditional model; statistically significant differences were found for IL-10 (4-fold-fold; $p = 0.015$), IL-6 (29.5-fold-fold $p = 0.024$), MIP-2α (2.4-fold $p = 0.0022$), and TNF-α (6.5-fold-fold; $p = 0.0014$).

3.3 Effects of the 3D culture of mesenchymal stromal cells in hydrogels and cyclic stretch

To study the effect of cyclic stretch alone in the physiomimetic model, four different groups were compared (with and without CS, each of which with and without LPS). Results in Figure 7 show the ratio of the amount of cytokines secreted with and without LPS either in the presence or absence of cyclic stretch. Cyclic stretch showed no impact on the response of the advanced model to the inflammatory hit (Figure 7). However, when studying the effect of CS in the absence of LPS, a statistically significant increase in the secretion of

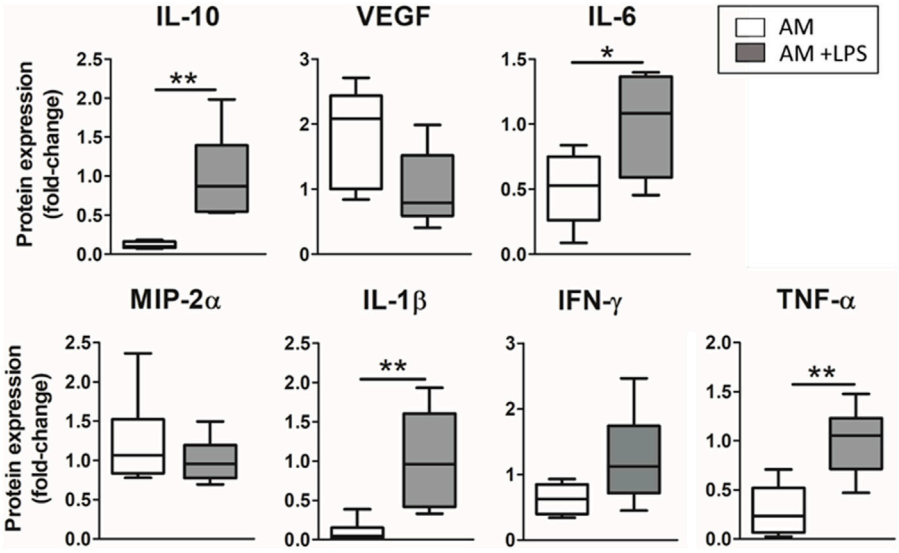

FIGURE 5
Response to LPS endotoxin of the advanced model (3D cultured LMSC in lung hydrogel with ATII cultured on top, subjected to cyclic stretch–Advanced Model).

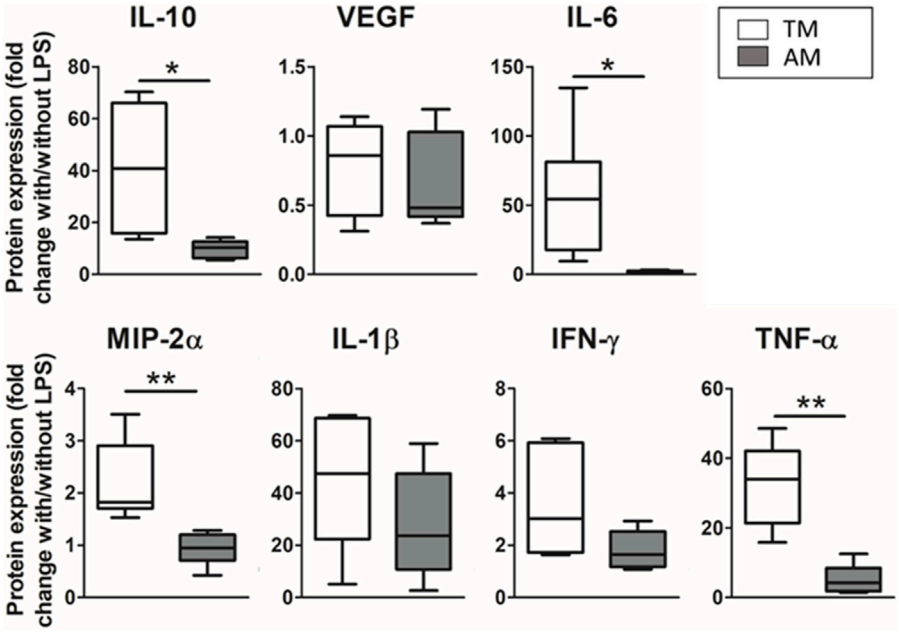

FIGURE 6
Different magnitude response of the advanced model (ATII cultured on hydrogels with 3D-cultured LMSC inside) compared to a traditional 2D culture model (ATII cell cultured on PDMS). Results were expressed as the ratio of cytokines expressed with/out the LPS hit, for either the traditional model or the advanced model.

VEGF and a decrease in the secretion of IFN-γ (2-fold $p = 0.046$; 2-fold/0.55-fold, $p = 0.02$ respectively, data not shown) was observed when cyclic stretch was applied.

The contribution of the lung hydrogel and the embedded LMSCs after application of the LPS hit was studied in three groups, as shown in Figure 8: 1) ATII on PDMS under cyclic

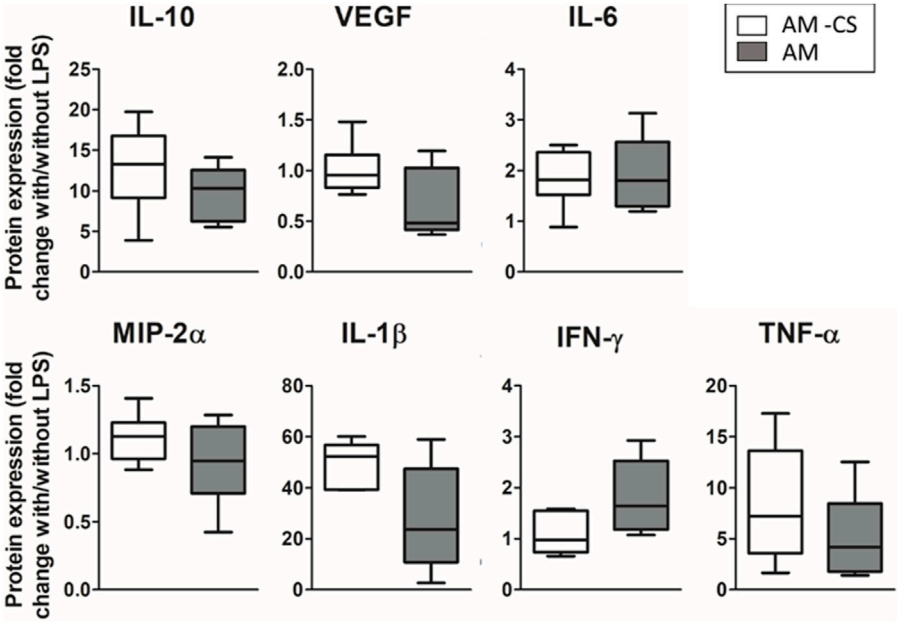

FIGURE 7
Effect of cyclic stretch. No statistical difference was observed in the secretion of inflammatory cytokines.

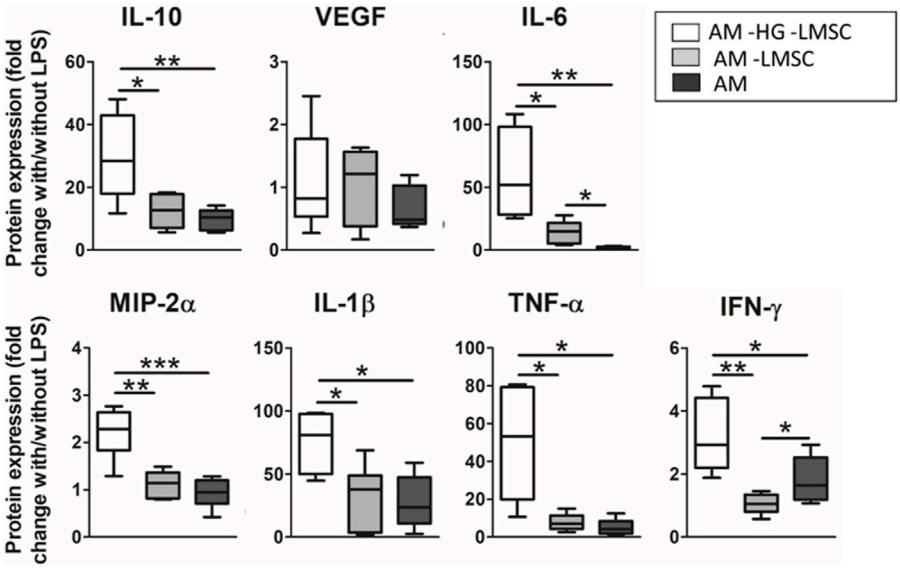

FIGURE 8
Effect of LMSC and hydrogel on the secretion of cytokines. Three groups were studied: ATII on PDMS with cyclic stretch (AM-HG-LMSC), ATII on hydrogel with cyclic stretch (AM-LMSC), and ATII on hydrogel with 3D LMSC cultured inside in the presence of cyclic stretch (AM).

stretch (AM–HG–LMSCs), 2) ATII on hydrogel under cyclic stretch (AM–LMSCs), and 3) ATII-LMSCs coculture in hydrogel subjected to cyclic stretch (AM). The effect of hydrogel significantly attenuated the secretion of all the cytokines but VEGF in response to the LPS endotoxin, showing inflammatory-suppressive properties. On the other hand, the presence of LMSCs significantly over-attenuated the secretion of IL-6 (7-fold; $p = 0.0098$) and promoted IFN-ɣ secretion (1.7-fold $p = 0.032$).

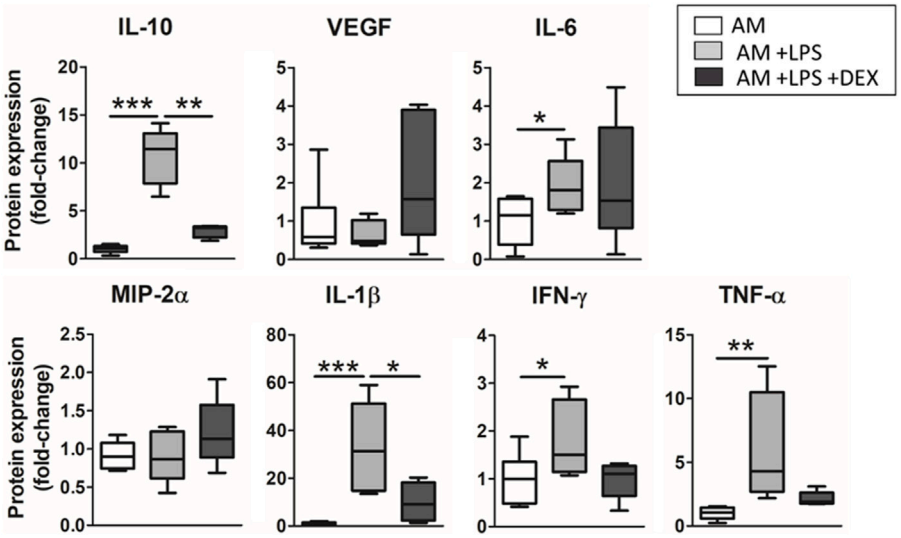

FIGURE 9
Anti-inflammatory effects of dexamethasone were studied in the advanced model. There was observed a general trend in recovering the expression levels observed before the inflammatory hit, which were statistically significant in the case of IL-10 and IL-1β.

3.4 Response to dexamethasone

Results on the secretion of cytokines when dexamethasone was added to the advanced model are shown in Figure 9. The treatment induced a trend to recover the levels of cytokine expression observed before the inflammatory hit in TNF-α and IFN-ɣ, and a significant decrease in the secretion of IL-10 (3.7-fold decrease, $p = 0.0014$) and IL-1β (3.2-fold decrease $p = 0.0407$).

4 Discussion

Experimental *in vitro* models of severe respiratory diseases such as ARDS are important to better understand the basic pathophysiologic mechanisms involved and the potential effects of drug treatments. However, the conventional model based on cells cultured on a plate is an extreme simplification of the microenvironment experienced by cells *in vivo* and it has shown several limitations when trying to mimic *in vivo* results. Therefore, there is an urgent need for improved models that are more realistic in reproducing the cells' physical, chemical, and biological conditions in the lung. The work presented herein shows the feasibility of developing a physiomimetic model for *in vitro* ARDS studies by combining organ-on-a-chip technologies and ECM-derived hydrogels for 3D cell culture. Specifically, the response of the developed model to an endotoxin-mediated inflammatory hit showed marked differences compared to the traditional plastic-based 2D models, the latter apparently overestimating the cytokine response. In this context, the advanced model (3D architecture with biophysical stimuli) described herein is a novel contribution to setting more physiomimetic approaches for studying the mechanisms of ARDS and potential treatments.

The developed model overcomes previous limitations of *in vitro* studies on ARDS by recreating a physiomimetic environment and by using epithelial and stromal cells in co-culture. Device molds were fast prototyped by 3D printing; hence the dimensions of the devices can be easily modified depending on the requirements of each study. The developed chips were compatible with optical microscopy, which eased the calibration of the membrane stretch as a function of the applied pressure. This aspect opens the door for future studies incorporating real-time imaging of the cultured cells in the experiments. We incorporated 3D cultures into the lung-on-a-chip devices developed by attaching cell-laden ECM hydrogels to the PDMS stretchable membrane previously treated with APTES and genipin. No detachment of the hydrogels from the membranes was observed during the experiments. Still, there was an open question for lung-derived ECM hydrogels for organ-on-a-chip devices regarding oxygen diffusivity and stretch transmission from the device to the 3D scaffold (Otero et al., 2021). Oxygen was expected to diffuse quickly in the hydrogels as they are composed mainly of water, and results obtained in the experiments conducted here confirmed that hypothesis. The diffusion of oxygen has been shown to highly impact cell response (Marhuenda et al., 2019); thus, results obtained in our experiments demonstrate the suitability of their use for three-dimensional culturing. Regarding the transmission of the stretch from the membrane to the hydrogel, we observed that it was correctly experienced by the 3D hydrogel by

measuring distances between beads, a method adapted from 2D cultures stretch calibration (Trepat et al., 2004). Nevertheless, it should be noted that changing the geometries and the mechanical properties of the hydrogels could modify this stretch transmission, especially if the hydrogels were softer (as they usually are when using lower ECM powder concentrations in their preparation) (Pouliot et al., 2016; de Hilster et al., 2020; Martinez-Garcia et al., 2021). In our case, the results showed that in the physiomimetic model, the 3D co-cultures were oxygenated and stretched similarly as in traditional 2D models. In this way, the analysis of the contribution of the 3D microarchitecture can be more robustly analyzed from the conducted experiments (Nonaka et al., 2016).

The present study was carried out with freshly isolated rat alveolar cells and primary rat lung mesenchymal stromal cells. The use of primary cells is highly advantageous compared to previous works where cancer cell lines or immortalized ATIIs that have lost some of their typical characteristics were employed (Chen et al., 2019; Abate et al., 2010; Willis et al., 2005). The possibility of using primary ATIIs was eased by the employment of lung-derived hydrogels, which are more suitable substrates for cell culture than culture plates, allowing alveolar cells not only to form monolayers but also to maintain the secretion of surfactant B and C proteins for longer times (Esther Marhuenda et al., 2022), which is of high importance when studying ARDS (Wang S et al., 2021). The results obtained using primary alveolar cells are expected to be more easily translational than those using A549 cells (Chen et al., 2019), which are usually used as a surrogate of ATIIs in *in vitro* studies. Also, all the experiments shown herein were performed at physiological oxygen concentrations (13%) (Wild et al., 2005; Brahimi-Horn and Pouysségur 2007), avoiding that cells were subjected to the typical hyperoxic conditions in traditional culture settings (≈20% oxygen), which can induce the secretion of reactive oxygen species (Stuart et al., 2018) thereby potentially altering the inflammatory response to LPS challenge and to drug treatment. For the sake of experimental simplicity and similarly as most published *in vitro* research on ARDS, this study aimed at designing and testing an advanced physiomimetic model has been carried out using animal samples (rat cells and porcine ECM). However, the model can be exactly reproduced by employing cells and ECM from human lungs, thereby avoiding any effect owing to interspecies differences (Mercer and Crapo 1990; Mercer, Russell, and Crapo 1994).

Results on the inflammatory response of the developed model to a classic inflammatory hit (i.e., LPS) modeling ARDS were in line with what has been observed in previous *in vitro* and *in vivo* studies (Huh et al., 2018; Voiriot et al., 2017; Li et al., 2020; Cabrera-Benítez et al., 2016; Peñuelas et al., 2013). As expected, the inflammatory response observed in the advanced model was attenuated, indicating that the presence of LMSCs and the incorporation of different biophysical stimuli play a protective role in response to an endotoxin hit. The overresponse observed in traditional models can then be a result of culturing cells on petri dishes, which have very different physical properties and biochemical environment than the model developed herein. Interestingly, the fact that our model is less sensitive to the LPS hit could ease the development of future studies with different endotoxin doses aiming to model different degrees of disease severity.

By separately studying the contribution of the different stimuli, very interesting data were obtained regarding the decreased responsiveness to the inflammatory challenge. No significant differences were observed in the secretion of cytokines by the effect of cyclic stretch alone. This could be because the impact of cyclic stretch in a physiomimetic model is moderated and shielded by the other factors present in the advanced model. The anti-inflammatory effect of cyclic stretch has been previously reported (Fang et al., 2018) in a much more responsive model, which was also observed in our control experiments in 2D, and also reported to impact on cell fate in alveolar and mesenchymal cells (Heise et al., 2011). On the other hand, culturing cells in lung ECM-derived hydrogels was the factor of major importance in attenuating the inflammatory response in the developed model. Culturing cells using a substrate with lung parenchyma-like stiffness (Falcones et al., 2021) and a more physiomimetic and complex biochemical composition seem to offer primary alveolar cells and lung mesenchymal stromal cells a protective environment that attenuated the inflammatory response. It should be noted that which components of the ECM present in the hydrogels are playing a major role in this alteration of the inflammatory response is still an open question. Indeed, depending on the ECM decellularization and digestion (Pouliot et al., 2020) protocols, the final composition of the hydrogels may vary. Recent mass spectrometry studies on porcine-derived ECM hydrogels composition (Kim et al., 2022) showed a high number of ECM proteins present in the hydrogels but a high variability between individuals. However, it has been shown that the decellularization protocol presented herein preserves at least partially elastin, collagen and GAGs (Pouliot et al., 2016), and that type I collagen in the lung is mostly preserved by the digestion time used (Pouliot et al., 2020). Finally, the LMSCs played an important role in the inflammatory context due to the cytokine secretion and the interaction with the epithelial monolayer. As previously reported (Chen et al., 2019), the presence of LMSCs in the model altered the inflammatory response, but, interestingly, the results showed that the effect of lung hydrogel itself has a much greater impact than the presence of LMSCs.

The main limitation in correlating the cytokine expression from results obtained *in vitro* and *in vivo*, is the fact that most *in vitro* cultures are performed under quite unrealistic conditions (attending to the complex physiological biochemical and biophysical environment) and more importantly, to the interactions of different cell types (Li et al., 2020; Cabrera-Benítez et al., 2016). The expression of IL-10, IL-8 (its murine counterpart is MIP-2α), and IL-6 have a high clinical significance in ARDS patients, as high values of these cytokines are clearly related to the severity of the disease. IL-6 has particular interest due to the link between its increase and a fatal prognosis, being related to increased lung compliance, the altered levels of Pa o_2/Fi o_2, and the need for mechanical ventilation (Stukas et al., 2020; Wang J et al., 2021). Nowadays, the lack of a gold-standard treatment for ARDS patients is a matter of concern. Glucocorticoids such as dexamethasone are often used to improve ARDS patients' outcomes, but there is still controversy about its benefits in all patients, mainly owing to the heterogeneity in the population receiving the treatment. For example, only severe cases of disease caused by COVID benefited from short-term low-dose treatment (Sterne et al., 2020; van Paassen et al., 2020). In addition, it is broadly accepted that MSCs present immunomodulatory properties, and as such, they have been proposed as a therapy for ARDS (Guillamat-Prats et al., 2020; Liu et al., 2020). However, little is known about how the presence of dexamethasone can modify these immunomodulatory properties. Results presented herein, although limited, suggest that the effect of drugs such as dexamethasone should be better studied *in vitro* by using physiomimetic models like the ones developed in the present work. Studies with dexamethasone-treated epithelial cells in much more responsive 2D models showed a decrease in the proinflammatory cytokines (Chen et al., 2021; Patil et al., 2018), but the results presented in this work are the first ones conducted in a 3D model with more physiological responsiveness to the LPS hit. Regarding MSCs, results are more controversial: while some *in vitro* studies have shown a decrease in cytokines and chemokines secreted by cytokine-stimulated LMSCs under dexamethasone effects (Wallace et al., 2001; Kim, Cheng, and Kim 1999), *in vivo* studies point that dexamethasone could be abrogating the anti-inflammatory effect of MSC (Chen et al., 2014; Wang et al., 2018). This impairment of the LMSC anti-inflammatory properties by dexamethasone could explain why a drastic decrease in the proinflammatory cytokines was not observed in the developed model: while dexamethasone was decreasing the secretion of proinflammatory cytokines by epithelial cells, it could be impairing the anti-inflammatory properties of LMSCs. Therefore, the levels of cytokines measured in the advanced model may be the result of a balance, showing a scenario much more similar to what is occurring *in vivo*, which was the major aim of the developed physiomimetic model for ARDS. The results obtained here were more aligned with some *in vivo* studies performed in rats, where LPS showed an increase in cytokine expression while the treatment with dexamethasone decreased these levels but not completely recover the levels before the LPS hit (Qin and Qiu 2019; Li, Whiteman, and Moore 2009).

In conclusion, this work suggests that the developed model of ARDS-on-a-chip responds to an LPS challenge and partially recovers the secretion of cytokines after anti-inflammatory drug treatment. Thus, this novel model opens the door for further *in vitro* research on developing different therapeutic strategies for ARDS treatment. Although it is impossible that any *in vitro* model fully mimics the inflammatory process occurring in the lungs during ARDS, the advanced model describes a step forward. Lung-on-a-chip devices based on PDMS membranes aimed at analyzing the effects of physical parameters such as stretch on cells have been developed during the last decade. The setting presented herein corresponds to what is known as second generation of lung-on-a-chips (Zamprogno et al., 2021). The main concept is to culture the cells in a physiological matrix instead on functionalized PDMS. In the present work, we did not use a combination of ECM proteins but a biomaterial exclusively made from native ECM components, being therefore a step forward the previous settings. Specifically, our approach allows for studying how alveolar epithelial cells respond to an inflammatory stimulus and how the resident lung mesenchymal stromal cells can play a role in it when cells are in their native ECM and subjected to realistic cyclic stretch. Moreover, it is a versatile model facilitating that different cell types could be included to further study crosstalk mechanisms among the other players involved in the inflammatory process of ARDS. Interestingly, the possibilities in tuning the model makes it suitable for expanding its use to study in detail respiratory diseases other than ARDS, including applications in high-throughput drug testing for new treatment developments.

Data availability statement

Data supporting the findings of this study are available from the corresponding author upon reasonable request.

Ethics statement

The animal study was reviewed and approved by Ethical Committee for Animal Research of the University of Barcelona.

Author contributions

Conceptualization, EM, NG, RF, and JO; Formal analysis, EM, AV, GW-T, RF, NG, IA, and JO; Funding acquisition, RF, IA, NG, and JO; Investigation, EM, AV, NG, IA, and JO.; Methodology, EM, AV, MN, LE, NG, RF, IA, and JO; Project administration, RF, IA, NG, and JO; Resources, NG, RF, IA, and JO; Software, EM, MN, and NG; Supervision, RF, NG, and JO; Writing of original draft, EM and JO. All authors have read and agreed to the published version of the manuscript.

Funding

This research was funded by the Spanish Ministry of Science, Innovation and Universities, grants numbers SAF 2017-85574-R, DPI 2017-83721-P, PID2019-108958RB-I00/ AEI/ 10.13039/501100011033, and PGC 2018-097323-A-I00, and by European Union's Horizon 2020, Marie Sklodowska-Curie, Q13 Grant 821772.

Acknowledgments

The authors thank Miguel A. Rodríguez from the Unit of Biophysics and Bioengineering for his excellent technical assistance.

Conflict of interest

The authors declare that the research was conducted in the absence of any commercial or financial relationships that could be construed as a potential conflict of interest.

Publisher's note

All claims expressed in this article are solely those of the authors and do not necessarily represent those of their affiliated organizations, or those of the publisher, the editors and the reviewers. Any product that may be evaluated in this article, or claim that may be made by its manufacturer, is not guaranteed or endorsed by the publisher.

References

Abate, W., Alghaithy, A. A., Parton, J., Jones, K. P., and Jackson, S. K. (2010). Surfactant lipids regulate LPS-induced interleukin-8 production in A549 lung epithelial cells by inhibiting translocation of TLR4 into lipid raft domains. *J. Lipid Res.* 51 (2), 334–344. doi:10.1194/jlr.M000513

Ballard-Croft, C., Wang, D., Sumpter, L. R., Zhou, X., and Zwischenberger, J. B. (2012). Large-animal models of acute respiratory distress syndrome. *Ann. Thorac. Surg.* 93 (4), 1331–1339. doi:10.1016/j.athoracsur.2011.06.107

Bassi, G., Grimaudo, M. A., Panseri, S., and Montesi, M. (2021). Advanced multi-dimensional cellular models as emerging reality to reproduce *in vitro* the human body complexity. *Int. J. Mol. Sci.* 22 (3), 1195. doi:10.3390/ijms22031195

Benam, K. H., Burgess, J. K., and Stewart, A. G. (2021). Editorial: Accelerated translation using microphysiological organoid and microfluidic chip models. *Front. Pharmacol.* 12, 827172. doi:10.3389/fphar.2021.827172

Brahimi-Horn, M. C., and Pouysségur, J. (2007). Oxygen, a source of life and stress. *FEBS Lett.* 581 (19), 3582–3591. doi:10.1016/j.febslet.2007.06.018

Brower, R. G., Matthay, M. A., Morris, A., Schoenfeld, D., Thompson, B. T., Wheeler, A., et al. (2000). Acute Respiratory Distress Syndrome NetworkVentilation with lower tidal volumes as compared with traditional tidal volumes for acute lung injury and the acute respiratory distress syndrome. *N. Engl. J. Med.* 342 (18), 1301–1308. doi:10.1056/NEJM200005043421801

Burgess, J. K., Mauad, T., Tjin, G., Karlsson, J. C., and Westergren-Thorsson, G. (2016). The extracellular matrix - the under-recognized element in lung disease? *J. Pathol.* 240 (4), 397–409. doi:10.1002/path.4808

Busch, S. M., Lorenzana, Z., and Ryan, A. L. (2021). Implications for extracellular matrix interactions with human lung basal stem cells in lung development, disease, and airway modeling. *Front. Pharmacol.* 12, 645858. doi:10.3389/fphar.2021.645858

Cabrera-Benítez, N. E., Pérez-Roth, E., Ramos-Nuez, Á., Sologuren, I., Padrón, J. M., Slutsky, A. S., et al. (2016). Inhibition of endotoxin-induced airway epithelial cell injury by a novel family of pyrrol derivates. *Lab. Invest.* 96 (6), 632–640. doi:10.1038/labinvest.2016.46

Campillo, N., Jorba, I., Schaedel, L., Casals, B., Gozal, D., Farré, R., et al. (2016). A novel chip for cyclic stretch and intermittent hypoxia cell exposures mimicking obstructive sleep apnea. *Front. Physiol.* 7, 319. doi:10.3389/fphys.2016.00319

Chen, L. D., Zhang, Z. Y., Wei, X. J., Cai, Y. Q., Yao, W. Z., Wang, M. H., et al. (2020). Association between cytokine profiles and lung injury in COVID-19 pneumonia. *Respir. Res.* 21 (1), 201. doi:10.1186/s12931-020-01465-2

Chen, X., Gan, Y., Li, W., Su, J., Zhang, Y., Huang, Y., et al. (2014). The interaction between mesenchymal stem cells and steroids during inflammation. *Cell Death Dis.* 5, e1009. doi:10.1038/cddis.2013.537

Chen, X. X., Tang, L., Han, Z. H., Wang, W. J., and Meng, J. G. (2019). Coculture with bone marrow-derived mesenchymal stem cells attenuates inflammation and apoptosis in lipopolysaccharide-stimulated alveolar epithelial cells via enhanced secretion of keratinocyte growth factor and angiopoietin-1 modulating the Toll-like receptor-4 signal pathway. *Mol. Med. Rep.* 19 (3), 1891–1902. doi:10.3892/mmr.2019.9836

Chen, Y., Zhang, C., Xiao, C. X., Li, X. D., Hu, Z. L., He, S. D., et al. (2021). Dexamethasone can attenuate the pulmonary inflammatory response via regulation of the lncH19/miR-324-3p cascade. *J. Inflamm.* 18 (1), 1. doi:10.1186/s12950-020-00266-0

Colom, A., Galgoczy, R., Almendros, I., Xaubet, A., Farré, R., and Alcaraz, J. (2014). Oxygen diffusion and consumption in extracellular matrix gels: Implications for designing three-dimensional cultures. *J. Biomed. Mat. Res. A* 102 (8), 2776–2784. doi:10.1002/jbm.a.34946

da Silva Meirelles, L., Chagastelles, P. C., and Nardi, N. B. (2006). Mesenchymal stem cells reside in virtually all post-natal organs and tissues. *J. Cell Sci.* 119 (11), 2204–2213. doi:10.1242/jcs.02932

de Hilster, R. H. J., Sharma, P. K., Jonker, M. R., White, E. S., Gercama, E. A., Roobeek, M., et al. (2020). Human lung extracellular matrix hydrogels resemble the stiffness and viscoelasticity of native lung tissue. *Am. J. Physiol. Lung Cell. Mol. Physiol.* 318 (4), L698–L704. doi:10.1152/ajplung.00451.2019

Falcones, B., Sanz-Fraile, H., Marhuenda, E., Mendizábal, I., Cabrera-Aguilera, I., Malandain, N., et al. (2021). Bioprintable lung extracellular matrix hydrogel scaffolds for 3D culture of mesenchymal stromal cells. *Polym. (Basel)* 13 (14), 2350. doi:10.3390/polym13142350

Fang, X. Z., Ge, Y. L., Li, M., Huang, T. F., Yang, Z., and Gao, J. (2018). Preconditioning of physiological cyclic stretch inhibits the inflammatory response induced by pathologically mechanical stretch in alveolar epithelial cells. *Exp. Ther. Med.* 15 (2), 2172–2176. doi:10.3892/etm.2017.5611

Farré, R., Almendros, I., Montserrat, J. M., Gozal, D., and Navajas, D. (2018). Gas partial pressure in cultured cells: Patho-physiological importance and methodological approaches. *Front. Physiol.* 9, 1803. doi:10.3389/fphys.2018.01803

Guillamat-Prats, R., Camprubí-Rimblas, M., Puig, F., Herrero, R., Tantinyà, N., Serrano-Mollar, A., et al. (2020). Alveolar type II cells or mesenchymal stem cells: Comparison of two different cell therapies for the treatment of acute lung injury in rats. *Cells* 9 (8), E1816. doi:10.3390/cells9081816

Habanjar, O., Diab-Assaf, M., Caldefie-Chezet, F., and Delort, L. (2021). 3D cell culture systems: Tumor application, advantages, and disadvantages. *Int. J. Mol. Sci.* 22 (22), 12200. doi:10.3390/ijms222212200

Heise, R. L., Stober, V., Cheluvaraju, C., Hollingsworth, J. W., and Garantziotis, S. (2011). Mechanical stretch induces epithelial-mesenchymal transition in alveolar epithelia via hyaluronan activation of innate immunity. *J. Biol. Chem.* 286 (20), 17435–17444. doi:10.1074/jbc.M110.137273

Huh, D., Kim, H. J., Fraser, J. P., Shea, D. E., Khan, M., Bahinski, A., et al. (2013). Microfabrication of human organs-on-chips. *Nat. Protoc.* 8 (11), 2135–2157. doi:10.1038/nprot.2013.137

Huh, J. W., Kim, W. Y., Park, Y. Y., Lim, C. M., Koh, Y., Kim, M. J., et al. (2018). Anti-inflammatory role of mesenchymal stem cells in an acute lung injury mouse model. *Acute Crit. Care* 33 (3), 154–161. doi:10.4266/acc.2018.00619

Huppert, L. A., and Matthay, M. A. (2017). Alveolar fluid clearance in pathologically relevant conditions: *In vitro* and *in vivo* models of acute respiratory distress syndrome. *Front. Immunol.* 8, 371. doi:10.3389/fimmu.2017.00371

Kim, C. H., Cheng, S. L., and Kim, G. S. (1999). Effects of dexamethasone on proliferation, activity, and cytokine secretion of normal human bone marrow stromal cells: Possible mechanisms of glucocorticoid-induced bone loss. *J. Endocrinol.* 162 (3), 371–379. doi:10.1677/joe.0.1620371

Kim, S., Min, S., Choi, Y. S., Jo, S. H., Jung, J. H., Han, K., et al. (2022). Tissue extracellular matrix hydrogels as alternatives to Matrigel for culturing gastrointestinal organoids. *Nat. Commun.* 13 (1), 1692. doi:10.1038/s41467-022-29279-4

Laffey, J. G., and Matthay, M. A. (2017). Fifty years of research in ARDS. Cell-Based therapy for acute respiratory distress syndrome. Biology and potential therapeutic value. *Am. J. Respir. Crit. Care Med.* 196 (3), 266–273. doi:10.1164/rccm.201701-0107CP

Li, J., Qin, Y., Chen, Y., Zhao, P., Liu, X., Dong, H., et al. (2020). Mechanisms of the lipopolysaccharide-induced inflammatory response in alveolar epithelial cell/macrophage co-culture. *Exp. Ther. Med.* 20 (5), 76. doi:10.3892/etm.2020.920410.3892/etm.2020.9204

Li, L., Whiteman, M., and Philip, K. M. (2009). Dexamethasone inhibits lipopolysaccharide-induced hydrogen sulphide biosynthesis in intact cells and in an animal model of endotoxic shock. *J. Cell. Mol. Med.* 13 (8), 2684–2692. doi:10.1111/j.1582-4934.2008.00610.x

Liu, S., Peng, D., Qiu, H., Yang, K., Fu, Z., and Zou, L. (2020). Mesenchymal stem cells as a potential therapy for COVID-19. *Stem Cell Res. Ther.* 11 (1), 169. doi:10.1186/s13287-020-01678-8

Marhuenda, E., Campillo, N., Gabasa, M., Martínez-García, M. A., Campos-Rodríguez, F., Gozal, D., et al. (2019). Effects of sustained and intermittent hypoxia on human lung cancer cells. *Am. J. Respir. Cell Mol. Biol.* 61 (4), 540–544. doi:10.1165/rcmb.2018-0412LE

Marhuenda, E., Villarino, A., Narciso, M. L., Camprubí-Rimblas, M., Farré, R., Gavara, N., et al. (2022). Lung extracellular matrix hydrogels enhance preservation of type II phenotype in primary alveolar epithelial cells. *Int. J. Mol. Sci.* 23 (9), 4888. doi:10.3390/ijms23094888

Martinez-Garcia, F. D., de Hilster, R. H. J., Sharma, P. K., Borghuis, T., Hylkema, M. N., Burgess, J. K., et al. (2021). Architecture and composition dictate viscoelastic properties of organ-derived extracellular matrix hydrogels. *Polym. (Basel)* 13 (18), 3113. doi:10.3390/polym13183113

Matthay, M. A., Zemans, R. L., Zimmerman, G. A., Arabi, Y. M., Beitler, J. R., Mercat, A., et al. (2019). Acute respiratory distress syndrome. *Nat. Rev. Dis. Prim.* 5 (1), 18. doi:10.1038/s41572-019-0069-0

Mercer, R. R., and Crapo, J. D. (1990). Spatial distribution of collagen and elastin fibers in the lungs. *J. Appl. Physiol.* 69 (2), 756–765. doi:10.1152/jappl.1990.69.2.756

Mercer, R. R., Russell, M. L., and Crapo, J. D. (1994). Alveolar septal structure in different species. *J. Appl. Physiol.* 77 (3), 1060–1066. doi:10.1152/jappl.1994.77.3.1060

Mertz, D. R., Ahmed, T., and Takayama, S. (2018). Engineering cell heterogeneity into organs-on-a-chip. *Lab. Chip* 18 (16), 2378–2395. doi:10.1039/c8lc00413g

Nonaka, P. N., Falcones, B., Farre, R., Artigas, A., Almendros, I., and Navajas, D. (2020). Biophysically preconditioning mesenchymal stem cells improves treatment of ventilator-induced lung injury. *Arch. Bronconeumol.* 56 (3), 179–181. doi:10.1016/j.arbres.2019.08.014

Nonaka, P. N., Uriarte, J. J., Campillo, N., Melo, E., Navajas, D., Farré, R., et al. (2014). Mechanical properties of mouse lungs along organ decellularization by sodium dodecyl sulfate. *Respir. Physiol. Neurobiol.* 200, 1–5. doi:10.1016/j.resp.2014.04.008

Nonaka, P. N., Uriarte, J. J., Campillo, N., Oliveira, V. R., Navajas, D., and Farré, R. (2016). Lung bioengineering: Physical stimuli and stem/progenitor cell biology interplay towards biofabricating a functional organ. *Respir. Res.* 17 (1), 161. doi:10.1186/s12931-016-0477-6

Otero, J., Ulldemolins, A., Farré, R., and Almendros, I. (2021). Oxygen biosensors and control in 3D physiomimetic experimental models. *Antioxidants (Basel)* 10 (8), 1165. doi:10.3390/antiox10081165

Pati, F., and Cho, D. W. (2017). Bioprinting of 3D tissue models using decellularized extracellular matrix bioink. *Methods Mol. Biol.* 1612, 381–390. doi:10.1007/978-1-4939-7021-6_27

Patil, R. H., Naveen Kumar, M., Kiran Kumar, K. M., Nagesh, R., Kavya, K., Babu, R. L., et al. (2018). Dexamethasone inhibits inflammatory response via down regulation of AP-1 transcription factor in human lung epithelial cells. *Gene* 645, 85–94. doi:10.1016/j.gene.2017.12.024

Peñuelas, O., Melo, E., Sánchez, C., Sánchez, I., Quinn, K., Ferruelo, A., et al. (2013). Antioxidant effect of human adult adipose-derived stromal stem cells in alveolar epithelial cells undergoing stretch. *Respir. Physiol. Neurobiol.* 188 (1), 1–8. doi:10.1016/j.resp.2013.04.007

Pouliot, R. A., Link, P. A., Mikhaiel, N. S., Schneck, M. B., Valentine, M. S., Kamga Gninzeko, F. J., et al. (2016). Development and characterization of a naturally derived lung extracellular matrix hydrogel. *J. Biomed. Mat. Res. A* 104 (8), 1922–1935. doi:10.1002/jbm.a.35726

Pouliot, R. A., Young, B. M., Link, P. A., Park, H. E., Kahn, A. R., Shankar, K., et al. (2020). Porcine lung-derived extracellular matrix hydrogel properties are dependent on pepsin digestion time. *Tissue Eng. Part C Methods* 26 (6), 332–346. doi:10.1089/ten.TEC.2020.0042

Qin, M., and Qiu, Z. (2019). Changes in TNF-α, IL-6, IL-10 and VEGF in rats with ARDS and the effects of dexamethasone. *Exp. Ther. Med.* 17 (1), 383–387. doi:10.3892/etm.2018.692610.3892/etm.2018.6926

Staub, N. C. (1981). Pulmonary edema due to increased microvascular permeability. *Annu. Rev. Med.* 32, 291–312. doi:10.1146/annurev.me.32.020181.001451

Sterne, J. A. C., Murthy, S., Diaz, J. V., Slutsky, A. S., Villar, J., Angus, D. C., et al. (2020). WHO rapid evidence appraisal for COVID-19 therapies (react) working GroupAssociation between administration of systemic corticosteroids and mortality among critically ill patients with COVID-19: A meta-analysis. *JAMA* 324 (13), 1330–1341. doi:10.1001/jama.2020.17023

Stuart, J. A., Fonseca, J., Moradi, F., Cunningham, C., Seliman, B., Worsfold, C. R., et al. (2018). How supraphysiological oxygen levels in standard cell culture affect oxygen-consuming reactions. *Oxid. Med. Cell. Longev.* 2018, 8238459. doi:10.1155/2018/8238459

Stukas, S., Hoiland, R. L., Cooper, J., Thiara, S., Griesdale, D. E., Thomas, A. D., et al. (2020). The association of inflammatory cytokines in the pulmonary pathophysiology of respiratory failure in critically ill patients with coronavirus disease 2019. *Crit. Care Explor.* 2 (9), e0203. doi:10.1097/CCE.0000000000000203

Trepat, X., Grabulosa, M., Puig, F., Maksym, G. N., Navajas, D., and Farré, R. (2004). Viscoelasticity of human alveolar epithelial cells subjected to stretch. *Am. J. Physiol. Lung Cell. Mol. Physiol.* 287 (5), L1025–L1034. doi:10.1152/ajplung.00077.2004

Trivedi, N., Verma, A., and Kumar, D. (2020). Possible treatment and strategies for COVID-19: Review and assessment. *Eur. Rev. Med. Pharmacol. Sci.* 24 (23), 12593–12608. doi:10.26355/eurrev_202012_24057

van Paassen, J., Vos, J. S., Hoekstra, E. M., Neumann, K. M. I., Boot, P. C., and Arbous, S. M. (2020). Corticosteroid use in COVID-19 patients: A systematic review and meta-analysis on clinical outcomes. *Crit. Care* 24 (1), 696. doi:10.1186/s13054-020-03400-9

Voiriot, G., Razazi, K., Amsellem, V., Tran Van Nhieu, J., Abid, S., Adnot, S., et al. (2017). Interleukin-6 displays lung anti-inflammatory properties and exerts protective hemodynamic effects in a double-hit murine acute lung injury. *Respir. Res.* 18 (1), 64. doi:10.1186/s12931-017-0553-6

Wallace, S. R., Oken, M. M., Lunetta, K. L., Panoskaltsis-Mortari, A., and Masellis, A. M. (2001). Abnormalities of bone marrow mesenchymal cells in multiple myeloma patients. *Cancer* 91 (7), 1219–1230. doi:10.1002/1097-0142(20010401)91:7<1219:aid-cncr1122>3.0.co;2-1

Wang, D., Sun, Y. Q., Gao, W. X., Fan, X. L., Shi, J. B., and Fu, Q. L. (2018). An *in vitro* and *in vivo* study of the effect of dexamethasone on immunoinhibitory function of induced pluripotent stem cell-derived mesenchymal stem cells. *Cell Transpl.* 27 (9), 1340–1351. doi:10.1177/0963689718780194

Wang, J., Yang, X., Li, Y., Huang, J. A., Jiang, J., and Su, N. (2021). Specific cytokines in the inflammatory cytokine storm of patients with COVID-19-associated acute respiratory distress syndrome and extrapulmonary multiple-organ dysfunction. *Virol. J.* 18 (1), 117. doi:10.1186/s12985-021-01588-y

Wang, S., Li, Z., Wang, X., Zhang, S., Gao, P., and Shi, Z. (2021). The role of pulmonary surfactants in the treatment of acute respiratory distress

syndrome in COVID-19. *Front. Pharmacol.* 12, 698905. doi:10.3389/fphar.2021.698905

Wild, J. M., Fichele, S., Woodhouse, N., Paley, M. N., Kasuboski, L., and van Beek, E. J. (2005). 3D volume-localized pO2 measurement in the human lung with 3He MRI. *Magn. Reson. Med.* 53 (5), 1055–1064. doi:10.1002/mrm.20423

Willis, B. C., Liebler, J. M., Luby-Phelps, K., Nicholson, A. G., Crandall, E. D., du Bois, R. M., et al. (2005). Induction of epithelial-mesenchymal transition in alveolar epithelial cells by transforming growth factor-beta1: Potential role in idiopathic pulmonary fibrosis. *Am. J. Pathol.* 166 (5), 1321–1332. doi:10.1016/s0002-9440(10)62351-6

Wu, C., Chen, X., Cai, Y., Xia, J., Zhou, X., Xu, S., et al. (2020). Risk factors associated with acute respiratory distress syndrome and death in patients with coronavirus disease 2019 pneumonia in wuhan, China. *JAMA Intern. Med.* 180 (7), 934–943. doi:10.1001/jamainternmed.2020.0994

Yadav, H., Thompson, B. T., and Gajic, O. (2017). Fifty years of research in ARDS. Is acute respiratory distress syndrome a preventable disease? *Am. J. Respir. Crit. Care Med.* 195 (6), 725–736. doi:10.1164/rccm.201609-1767CI

Zamprogno, P., Wüthrich, S., Achenbach, S., Thoma, G., Stucki, J. D., Hobi, N., et al. (2021). Second-generation lung-on-a-chip with an array of stretchable alveoli made with a biological membrane. *Commun. Biol.* 4 (1), 168. doi:10.1038/s42003-021-01695-0

frontiers | Frontiers in Pharmacology

TYPE Original Research
PUBLISHED 11 October 2022
DOI 10.3389/fphar.2022.1021317

OPEN ACCESS

EDITED BY
Rebecca L. Heise,
Virginia Commonwealth University,
United States

REVIEWED BY
Reinoud Gosens,
University of Groningen, Netherlands
Chantal Donovan,
University of Technology Sydney,
Australia

*CORRESPONDENCE
Markus Weckmann,
Markus.Weckmann@uksh.de

†These authors share first authorship

‡These authors have contributed equally to this work

SPECIALTY SECTION
This article was submitted to Respiratory Pharmacology,
a section of the journal
Frontiers in Pharmacology

RECEIVED 17 August 2022
ACCEPTED 21 September 2022
PUBLISHED 11 October 2022

CITATION
Lemmel S, Weckmann M, Wohlers A, Jirmo AC, Grychtol R, Ricklefs I, Nissen G, Bachmann A, Singh S, Caicedo J, Bahmer T, Hansen G, Von Mutius E, Rabe KF, Fuchs O, Dittrich A-M, Schaub B, Happle C, Carpenter AE, Kopp MV, Becker T and the ALLIANCE Study Group as part of the German Centre for Lung Research (DZL) (2022), In vitro neutrophil migration is associated with inhaled corticosteroid treatment and serum cytokines in pediatric asthma.
Front. Pharmacol. 13:1021317.
doi: 10.3389/fphar.2022.1021317

In vitro neutrophil migration is associated with inhaled corticosteroid treatment and serum cytokines in pediatric asthma

Solveig Lemmel[1†], Markus Weckmann[1,2,3*‡], Anna Wohlers[1], Adan Chari Jirmo[4], Ruth Grychtol[4], Isabell Ricklefs[1,3], Gyde Nissen[1,3], Anna Bachmann[1], Shantanu Singh[5], Juan Caicedo[5], Thomas Bahmer[6,7], Gesine Hansen[3], Erika Von Mutius[8], Klaus F. Rabe[6], Oliver Fuchs[1,8,9], Anna-Maria Dittrich[4], Bianca Schaub[8], Christine Happle[4], Anne E. Carpenter[5], Matthias Volkmar Kopp[1,3,9], Tim Becker[1,5,10] and the ALLIANCE Study Group as part of the German Centre for Lung Research (DZL)

[1]Department of Paediatric Pneumology and Allergology, University Children's Hospital, Lübeck, Schleswig-Holstein, Germany, [2]Priority Research Area Chronic Lung Diseases Leibniz Lung Research Center Borstel, Epigenetics of Chronic Lung Disease, Großhansdorf, Germany, [3]Airway Research Center North, Member of the German Center of Lung Research (DZL), Lübeck, Germany, [4]Department of Pediatric Pneumology, Allergology and Neonatology, Hannover Medical School, Biomedical Research in Endstage and Obstructive Lung Disease Hannover (BREATH), Member of the German Center of Lung Research (DZL), Hannover, Germany, [5]Imaging Platform, Broad Institute of MIT and Harvard, Cambridge, CA, United States, [6]Department of Pneumology, LungenClinic Grosshansdorf, Airway Research Center North (ARCN), Member of the German Center for Lung Research (DZL), Grosshansdorf, Germany, [7]University Hospital Schleswig-Holstein Campus Kiel, Department for Internal Medicine I, Airway Research Center North (ARCN), German Center for Lung Research (DZL), Kiel, Germany, [8]University Children's Hospital, Ludwig Maximilian's University, German Research Center for Environmental Health (CPC-M), Member of the German Center of Lung Research (DZL), Munich, Germany, [9]Department of Paediatric Respiratory Medicine, Inselspital, University Children's Hospital of Bern, University of Bern, Bern, Switzerland, [10]IAV GmbH, Gifhorn, Germany

Background: Different asthma phenotypes are driven by molecular endotypes. A Th1-high phenotype is linked to severe, therapy-refractory asthma, subclinical infections and neutrophil inflammation. Previously, we found neutrophil granulocytes (NGs) from asthmatics exhibit decreased chemotaxis towards leukotriene B4 (LTB_4), a chemoattractant involved in inflammation response. We hypothesized that this pattern is driven by asthma in general and aggravated in a Th1-high phenotype.

Methods: NGs from asthmatic nd healthy children were stimulated with 10 nM LTB_4/100 nM N-formylmethionine-leucyl-phenylalanine and neutrophil migration was documented following our prior SiMA (simplified migration assay) workflow, capturing morphologic and dynamic parameters from single-cell tracking in the images. Demographic, clinical and serum cytokine data were determined in the ALLIANCE cohort.

Results: A reduced chemotactic response towards LTB_4 was confirmed in asthmatic donors regardless of inhaled corticosteroid (ICS) treatment. By contrast, only NGs from ICS-treated asthmatic children migrate similarly to controls with the exception of Th1-high donors, whose NGs presented a reduced and less directed migration towards the chemokines. ICS-treated and Th1-high asthmatic donors present an altered surface receptor profile, which partly correlates with migration.

Conclusions: Neutrophil migration *in vitro* may be affected by ICS-therapy or a Th1-high phenotype. This may be explained by alteration of receptor expression and could be used as a tool to monitor asthma treatment.

KEYWORDS

neutrophil granulocytes, migration, LTB4, fMLP, high-content image analysis, single-cell analysis

Introduction

Asthma is the most frequent chronic disease in children and highly prevalent in adults. Currently, about 300 million people are affected with a projected number of 400 million patients in 2025 (Croisant, 2014; Network, 2018). The diagnosis "asthma" is an umbrella term rather than a specific diagnosis with many possible causes and different phenotypic expressions (Kuruvilla et al., 2019), (Agache and Akdis, 2016). To clarify the situation, the terms asthma phenotype and asthma endotype have been coined: while an asthma phenotype is defined as a disease subtype associated with characteristic events, demographics, severity and therapy response, a specific asthma endotype is associated with characteristic pathophysiological mechanisms such as cellular and cytokine profiles (expression of Th1, Th2, Th9, Th17 at the mRNA and protein level) (Network, 2018; GINA Global Initiative for Asthma, 2019).

The most common endotype in children is the atopic/Th2 asthma subtype, characterized by high levels of Interleukin (IL-) 4, IL-5, or IL-13 and blood eosinophils, eosinophilic airway inflammation, and elevated exhaled nitrogen monoxide. This endotype is associated with early-onset allergic asthma, the most frequent phenotype amongst pediatric asthma patients. Early-onset allergic asthma includes all courses of the disease - from mild to severe (Boonpiyathad et al., 2019; Kuruvilla et al., 2019). Other endotypes may be Th2-low or mixed or characterized by Th1-related inflammation (definded by cytokines, such as IL-2 and interferon (IFN) ɣ), which is typical in patients with sputum neutrophilia, in smokers, or in older patients (Kuruvilla et al., 2019). But also in children with allergic and non-allergic severe asthma, Th1 signatures or mixed Th1/Th2 signatures have been described which are strongly associated with recent airway infections (Wisniewski et al., 2018).

In this context, little is known about the function and diagnostic relevance of neutrophil granulocytes (NGs). NGs are part of the innate immune system and represent the first line of defense against viral or bacterial airway infections, but also play a pivotal role in pathological lung tissue inflammation and airway damage in asthma (Pignatti et al., 2005). Chemotaxis towards pathogen-associated-molecular-patterns (PAMP) is mediated by a plethora of molecules including IL-8, leukotriene B4 (LTB_4) and bacterial-derived peptide N-formylmethionine-leucyl-phenylalanine (fMLP) (de Oliveira et al., 2016). NGs from asthma patients have been shown to display reduced chemotactic speed towards fMLP compared to healthy donors (Sackmann et al., 2014). To assess neutrophil movement continuously during the migratory process on single cell level, we previously developed a simplified migration assay (SiMA) and found that NGs of asthmatic children were less responsive to an LTB_4 gradient than those of healthy controls (Weckmann et al., 2017). In the current study, we aim to elucidate whether reduced NGs chemotaxis in response to LTB_4 and fMLP was associated with features of Th1 inflammation with or without ICS therapy in children with asthma.

Materials and methods

Study population

From November 2017 to March 2019, blood samples from $n = 75$ asthmatic children and $n = 13$ healthy controls of the pediatric arm of the ALLIANCE cohort of the German Center for Lung Research [DZL, (Fuchs et al., 2018) clinicaltrials.gov (KIRA: NCT02496468)] were collected (all patients were 6 years or older). All in- and exclusion criteria are available in (Fuchs et al., 2018). Informed consent of all participants and/or their legal guardians was obtained, and ethical approval

for all presented experiments was provided by the local ethics committee (Vote 12-215; 18.12.2012; ethics committee of the University of Lübeck).

Patients with asthma and healthy controls were invited yearly for a broad medical check-up (Fuchs et al., 2018). Besides acquisition of biomateriales (e.g., blood, stool, urine), study workups included lung function measurement, including spirometry, assessment of exhaled nitrogen monoxide (NO), whole-body plethysmography and multiple-breath washout. Interviews were used to record current medication, allergies and chronic diseases. General patient-relevant information (e.g., age, weight, height, gender and medication) was obtained at every visit.

A summary of the demographic parameters of asthmatic and healthy participants of this study is presented in Supplementary Table SA1.

Clinical and demographical data

Continuous treatment with inhaled glucocorticoids (ICS) was inquired by questionnaire and categorized into healthy control, no, low, medium or high dose ICS treatment according to the GINA guidelines (GINA Global Initiative for Asthma, 2019). Medication that was taken on demand was assessed by questionnaire as well. Daily ICS doses were compared as fluticasone equivalent. To compensate for the resulting small numbers in some categories, the following classification was used:

- Control population (healthy, no asthma medication per definition, $n = 13$)
- Athmatics with no controller treatment ($n = 31$)
- Asthmatics taking low dose ICS controller treatment (<200ug fluticasone equivalent for children <12 years and <250 µg for children 12 years and older) $n = 29$ or low dose ICS treatment on demand ($n = 5$) and no additional controller medication
- Asthmatics taking moderate to high ICS dosis (containing asthmatics with a medium ($n = 4$; 200–400 µg fluticasone equivalent for children <12 years and 250–500 µg for children 12 years and older per day) and high ($n = 6$; <12 years = >400 µg/>12 years = >500 µg fluticasone equivalent per day) dose ICS treatment)

Cell culture

Isolation of neutrophil granulocytes was performed after venous blood sampling, using ficoll density centrifugation and erythrocyte lysis as described in a Simplified Migration Assay for Analyzing Neutrophil Migration (SiMA). In addition to the SiMA-protocol, samples were stored a maximum of 12 h at 8°C between density centrifugation and lysis of erythrocytes. The final pellet was resuspended in 100 µl sterile human AB serum and stored at 8°C for 2 h, too. A cell count was performed using a Neubauer counting chamber (Marienfeld-Superior, Lauda Königshofen, Germany).

Migration assay

Neutrophil migration was analyzed on a single cell level using the microfluidic migration assay, known as SiMA-workflow (Weckmann et al., 2017). Therefore, isolated NGs were mixed with 70µg/ml Fibronectin (FN; Sigma-Aldrich, St. Louis, Missouri, United States). Migratory behavior was observed towards the chemoattractants LTB_4, (3.37 ng/ml; Abcam, Cambridge, England), IL8 (100 ng/ml; BD Biosciences, Franklin Lakes, New Jersey, United States) and fMLP (43.76 ng/ml; Abcam, Cambridge, England), utilizing µ-slides Chemotaxis 3D (IBIDI, Martinsried, Germany). Pictures were taken every 10 s for at least 30 min in a climate controlled room with a temperature of 20°C using the CytoSMART 2 System (CytoSMART, Einthoven, Netherlands). Image size was 1280 × 720 pixels with a pixel resolution of 0.96 µm per pixel stored in JPEG format.

Prior to analysis a quality check was performed excluding those experiments with a visible sidewards flow (cells with lateral trajectory, therefore skewing the gradient direction and prohibiting the establishment of chemotactic gradient), a too low cell number or pre-activated cells. This included cells that became stationary and did not migrate at all.

This quality control resulted in a different subset of migration experiments for each chemokine, compare Figure 2. To comprehensively assess proband specific NGs chemotaxis, at least 30 min of migration of at least $n = 25$ NGs were recorded. Supplementary Table SA3 gives an overview of the available experiments.

Atopy

The atopy status was determined by questionnaire, being defined as the occurrence of allergic comorbidities or allergic sensitization with symptoms.

Cytokine measurement

To measure blood cytokine levels, a bead ELISA Bio-Plex-Pro Human Cytokine 27-plex Assay was performed and measured with a Bio-Plex MAGPIX Multiplex Reader (both: BioRad, Hercules, United States), according to the manufacturer's specifications.

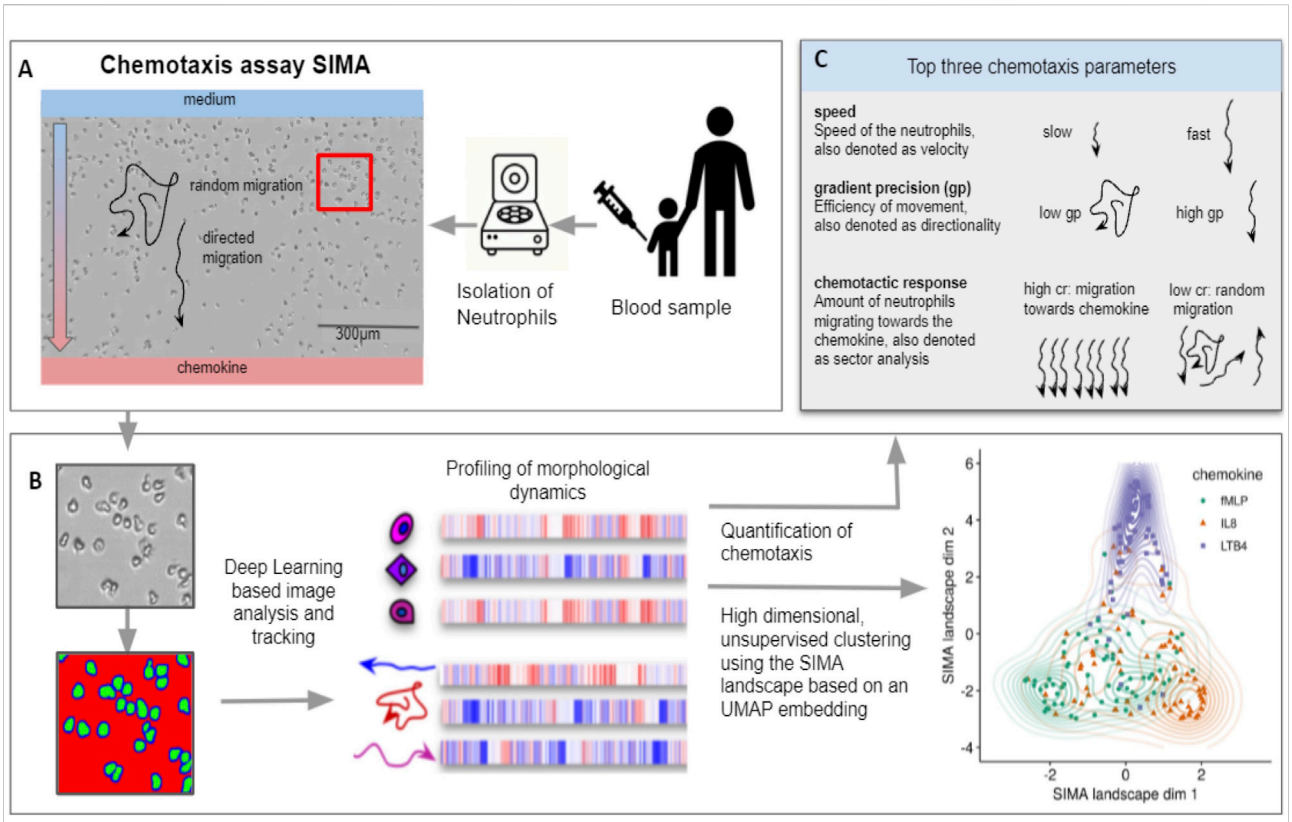

FIGURE 1
Pipeline of the SiMA chemotaxis analysis. **(A)** Neutrophils are isolated from a blood sample and chemotaxis is induced using a SiMA assay. For each patient, the migration towards IL8, fMLP and LTB_4 is recorded using time lapse microscopy. **(B)** A Deep Learning based image segmentation (UNet model) is used to identify and track neutrophil granulocytes. For each experiment, single-cell and single-trajectory profiles are created using CellProfiler and MigrationmineR, describing each neutrophil with a total of 25 features (after feature selection). These features are aggregated on an experiment level and used for quantification of chemotaxis. **(C)** The most telling and interpretable migration parameters are speed, chemotactic response and the gradient precision. A multidimensional analysis is performed using the complete feature set, which is projected into a two dimensional SiMA landscape using the UMAP algorithm for dimension reduction.

Chipcytometry based neutrophil granulocytes phenotyping

Chip cytometry was performed as previously described (Hennig et al., 2009; Jirmo et al., 2020a; Jirmo et al., 2020b). Briefly, approximately 2 × 105 isolated granulocytes were loaded and fixed on cell-adhesive microfluidic-chips according to company instructions (ZellSafe Chips, Zellkraftwerk GmbH, Leipzig, Germany). Neutrophils loaded on ZellSafe chips were then subsequently exposed to an iterative staining/bleaching cycle using ZellScannerONE (Zellkraftwerk GmbH, Leipzig, Germany). Phycoerythrin (PE) conjugated antibodies targeting BLT1, FPR1, CD62L, CD184, CD11b and CD16 (for specific clones, company and dilution details see Supplementary Table SA4) were used to characterize NGs. Data acquisition and analysis of fluorescence intensities was accomplished using the ZellExplorer App (Zellkraftwerk GmbH, Leipzig, Germany).

Data analysis

Profiling of morphological dynamics Cell tracking data was processed in R following best practices and pipelines adapted from high throughput image analysis using the cytominer R package[1].

Image processing and cell tracking

To analyze NGs movement over time, neutrophils were identified by deep learning-based image segmentation. In detail, a three-class UNet (Ronneberger et al., 2015) was implemented[2] and trained using 20 randomly chosen,

1 https://github.com/cytomining/cytominer
2 https://github.com/cells2numbers/unet4neutrophils

manually labeled images. The UNet model predicts the probabilities for background, boundary of the NGs and foreground (NGs), compare Figure 1. The first 15 min of each 30-minute-long experiment were not evaluated as the gradient is not yet stable during this time. As a result, the cells were tracked and processed in a time window of 15 min length from 15 to 30 min after the experiment was started/the gradient was established.

Images and predictions were loaded into CellProfiler and cells were segmented, tracked over time and morphological information was extracted on single cell level. Morphological description parameters included texture, area, shape and intensity features as described by Becker et al. (Rapoport et al., 2011), Becker et al. (2018). To find a good set of morphological features, a selection was made to remove highly correlated features in single cell measurements (if two features had a pearson correlation >0.85, the one with the overall higher correlation was removed).

Next, dynamic features like speed, directionality and chemotactic response were extracted for each cell, which were denoted as trajectories, using the migrationmineR package[3]. For a short explanation of each parameter please see Figure 1.

To remove NGs that had not been tracked correctly, cells with a track length less than 50% of the observation time were removed. For the remaining trajectories, mean profiles were calculated describing the morphological dynamics of each experiment. These profiles were created by calculating the mean values of all dynamic and morphological features. The complete set included n = 25 features and is Supplementary Table SA5.

The data set was analyzed and four variables (gender, age, season and batch) were controlled for in a linear model. The corrected data set was normalized with respect to all experiments, i.e., the mean value of all features was set to 0 and the standard deviation to 1. The values for cytokine levels were log transformed, corrected for the variables age, gender, date of measurement and normalized with mean 0 and standard deviation 1.

Positive values describe a value larger than the mean of this feature across all experiments and across the chemokines IL8, fMLP, LTB_4. Negative values describe a reduced value compared to the mean. For example for speed, a negative value does not imply a movement in reversed direction but a reduced speed that is lower than the mean speed of all neutrophils.

3 https://github.com/cells2numbers/migrationminer

Cluster analysis

All presented cluster analyses were performed as unsupervised clustering based on a "Uniform Manifold Approximation and Projection"-dimension reduction (McInnes et al., 2018). This clustering, using the extracted dynamic and morphologic migration parameters, conserves global connections and therefore allows to detect differences and similarities between single measurements. In the following, these global connections are displayed in the form of the SiMA landscape.

Statistical analysis

Statistical analysis was performed using the statistical software R (v.3.6) and confirmed using JMP (JMP®, Version 14, SAS Institute Inc., Cary, NC, 1989-2019). Throughout the paper we use the following levels of significance: $^{*}p < 0.05$, $^{**}p < 0.01$, $^{***}p < 0.001$.

Results

Asthma reduces the chemotactic response of neutrophils

We ran migration experiments for a total of n = 75 asthmatic and n = 13 healthy donors using our live cell assay (Weckmann et al., 2017). The groups do not show significant differences in demographic or clinical variables except for exhaled NO and percentage of children with allergic symptoms, which was significantly elevated in the asthmatic donor population ($p < 0.05$) (Table 1).

We found that migratory *speed* was not altered between patients and controls for either LTB_4 (n asthma/control 45/8) nor fMLP (n asthma/control 55/10) (Figure 2A). However, the chemotactic response of NGs measured as the *percentage* of cells migrating towards the chemokine from asthmatic donors was significantly reduced towards LTB_4 only (Figure 2B).

On average, 73% (z-value: 0.625 standard deviations from global mean) of NGs from healthy individuals migrated towards LTB_4. In contrast, neutrophils from asthmatic donors only showed a directed migration towards the chemoattractant in 51% (z-value of 0.042) of trajectories. Interestingly, this was opposite to the migratory behavior towards fMLP. In addition to LTB_4 and fMLP, IL8 was used as a chemoattractant. None of the effects described above occurred during IL8 induced chemotaxis (data not shown).

TABLE 1 The asthmatic and healthy donor populations are very similar with no significant differences in demographic parameters, but asthma patients show a significantly increased exhaled NO and reported atopy ($p < 0.05$).

	Asthma ($n = 75$)	Control ($n = 13$)	Significance
Gender (male)	45 (60%)	5 (38.5%)	n.s.
Age	12.6 (±3.9)	13.1 (±3.4)	n.s.
BMI (body mass index)	21.6 (±6.5)	19.9 (±3.4)	n.s.
Reported Atopy	51 (68%)	3 (23.1%)	$p = 0.0031$
FEV1	104 (±13.3)	106.6 (±13.4)	n.s.
Exhaled NO	17.1 (±18.5)	9.8 (±11.3)	$p = 0.0334$
Eosinophils (%)	4.7 (±3.3)	3.5 (±3)	n.s.
Controlled asthma	36 (55.4%)		

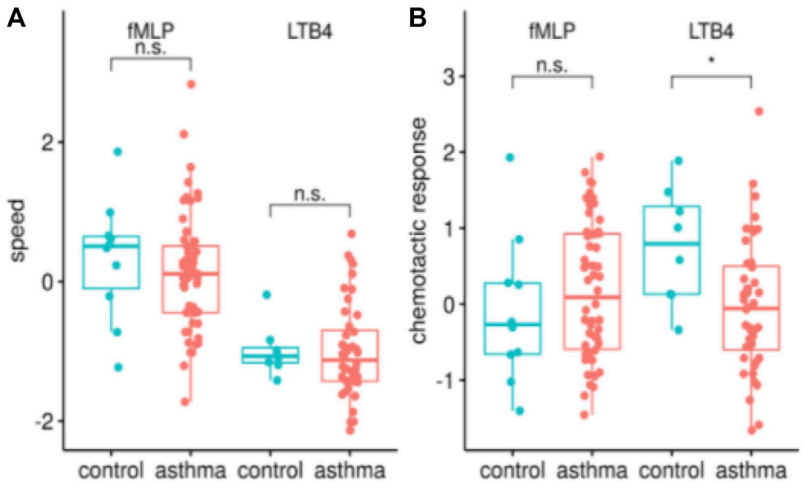

FIGURE 2
Asthma patients have a reduced chemotactic response towards LTB4, in terms of percentage of NGs moving as opposed to average speed. The analysis of the SiMA chemotaxis assays is characterized using the two most telling migration parameters, speed [z-value, in **(A)**] and chemotactic response [z-value, in **(B)**] for all migrations towards fMLP and LTB4. The distribution is shown for healthy controls ($n = 10/8$ fMLP/LTB4) and asthma patients ($n = 55/45$ for fMLP/LTB4). Migration parameters show a significantly reduced chemotactic response of asthma patients towards LTB_4 ($p < 0.05$).

Neutrophils of inhaled corticosteroid-treated asthmatic patients migrate similarly to healthy controls

Next, we investigated how neutrophil migration compares *in vitro* in asthmatic patients with and without inhaled corticosteroid (ICS) treatment. Therefore, we analysed migratory behavior of asthmatic donors with reported ICS treatment (LTB_4: $n = 26$; fMLP: $n = 34$) and those without ICS treatment (LTB_4: $n = 19$; fMLP: $n = 2$); demographic and clinical parameters are presented in Supplementary Table SA1. There were no significant differences between age, gender, BMI or atopy between patients with and without ICS treatment. Unexpectedly, the speed towards LTB_4 was significantly decreased in the group of ICS-treated asthmatics compared to untreated asthmatics (Figure 3A, $p < 0.05$). Still, neither the chemotactic response towards LTB_4 nor migration parameters towards fMLP were significantly altered (Figures 3A,B). We explored this finding using additional information about each patient's daily dose of ICS treatment; neither migration speed nor chemotactic response was linked to the daily dose of ICS treatment. A third parameter called gradient precision, which reports on the directionality of movement, showed a trend to increase in fMLP attracted NGs from ICS naive patients as compared to those with ICS treatment, but this did not reach significance (Figure 3B lower panel).

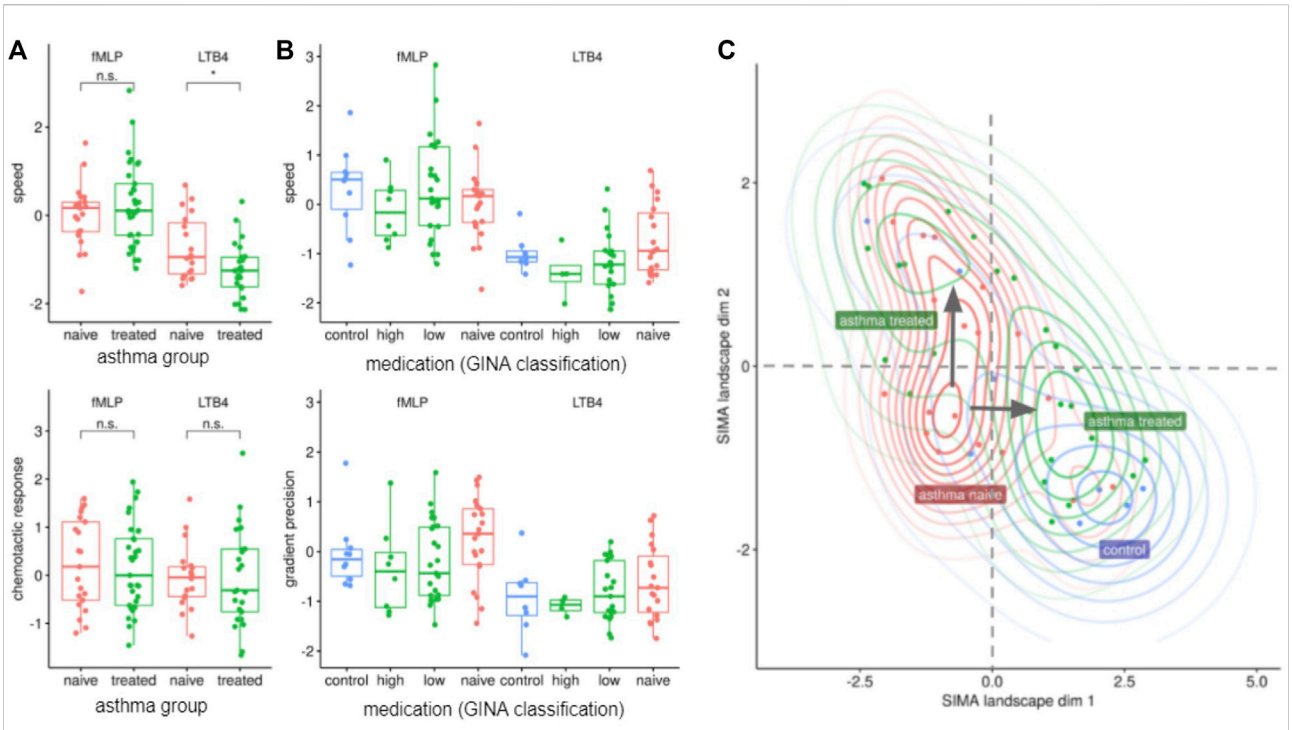

FIGURE 3
ICS-treated donors' NGs show decreased speed of chemotaxis towards LTB4, but few other changes. **(A)** ICS treatment has a significant effect on the migration towards LTB_4, reducing the speed (z-value) of neutrophils (p-value < 0.05, t-test), n = 26/19 for treated/naive). **(B)** Neutrophil migration parameters (z-values) grouped by ICS treatment doses. A patient specific dose was calculated as fluticasone equivalent based on the reported medication. The classes "control", "high", "low", "naive" were defined according to GINA classifications and modified in two ways (to compensate for small n): First, class "low" includes patients with low daily doses and patients treated "as required". Second, medium and high ICS dose were combined as "high". **(C)** The SiMA landscape projects dynamic and morphological features into a two-dimensional embedding using the UMAP dimension reduction, which preserves similarities and distances between feature profiles from each patient. Asthma patients (red cluster lower left corner) and healthy controls (blue cluster lower right corner) have distinct migration profiles. When treated with inhaled corticosteroids (ICS), the profiles of Asthma patients form two main clusters: while most patients are located close to healthy controls (green cluster lower right corner), some patients show a pattern that is relatively distinct but close to a subset of from untreated asthma patients (green cluster upper left corner). Patients in this second cluster have increased vital capacity, decreased residual lung volume and a decreased total lung capacity. None of the determined cytokine profiles Th1, Th2, Th9 or Th17 are elevated in this cluster.

Unsupervised clustering based on migratory and morphological parameters identified four different clusters of patients: 1. a control cluster, 2. a cluster containing untreated asthmatics, 3. a cluster containing treated asthmatics and a 4th cluster containing a different subset of treated asthmatics (Figure 3C, see Materials and Methods for details).

The separability of control and ICS-untreated (ICS-naive) patients nicely confirmed our prior feature-specific analysis. This analysis also showed that *in vivo* ICS treatment resulted in asthmatics (asthmatics treated, cluster AT1, Figure 3C) being located in close proximity to healthy controls.

However, some treated asthmatics (cluster AT2) were located even further away from healthy control donors than the ICS naive group did. No significant differences between patients in cluster AT1 and AT2 were found, whether in lung function results or other clinical parameters (Supplementary Table SA1). In both groups of ICS-treated asthmatics, significantly less asthma control was reported as compared to ICS-naive asthmatics (naive: 84.6% vs. AT1: 34.4% vs. AT2: 37.5%, p < 0.01), indicating that the ICS-treated asthmatics include patients with higher disease severity.

Neutrophils of Th1-high asthmatics show a reduced and randomized migration

The effects between ICS naïve and treated patients for the dynamic parameters were largely insignificant, hence we did not choose to adjust for them. In a next, we investigated asthma phenotypes based on a Th1 serum cytokine signature. Asthmatics with elevated levels of both cytokines IL-2 and IFNɣ (above the 75% quantile, Figure 4A), were defined to be "Th1-high" (n = 7) (Table 2). Asthmatic donors were labeled "Th1-low" (n = 30), if none of the cytokines were elevated. The remaining intermediate asthmatic donors (n = 38) were omitted from this analysis. No control donor

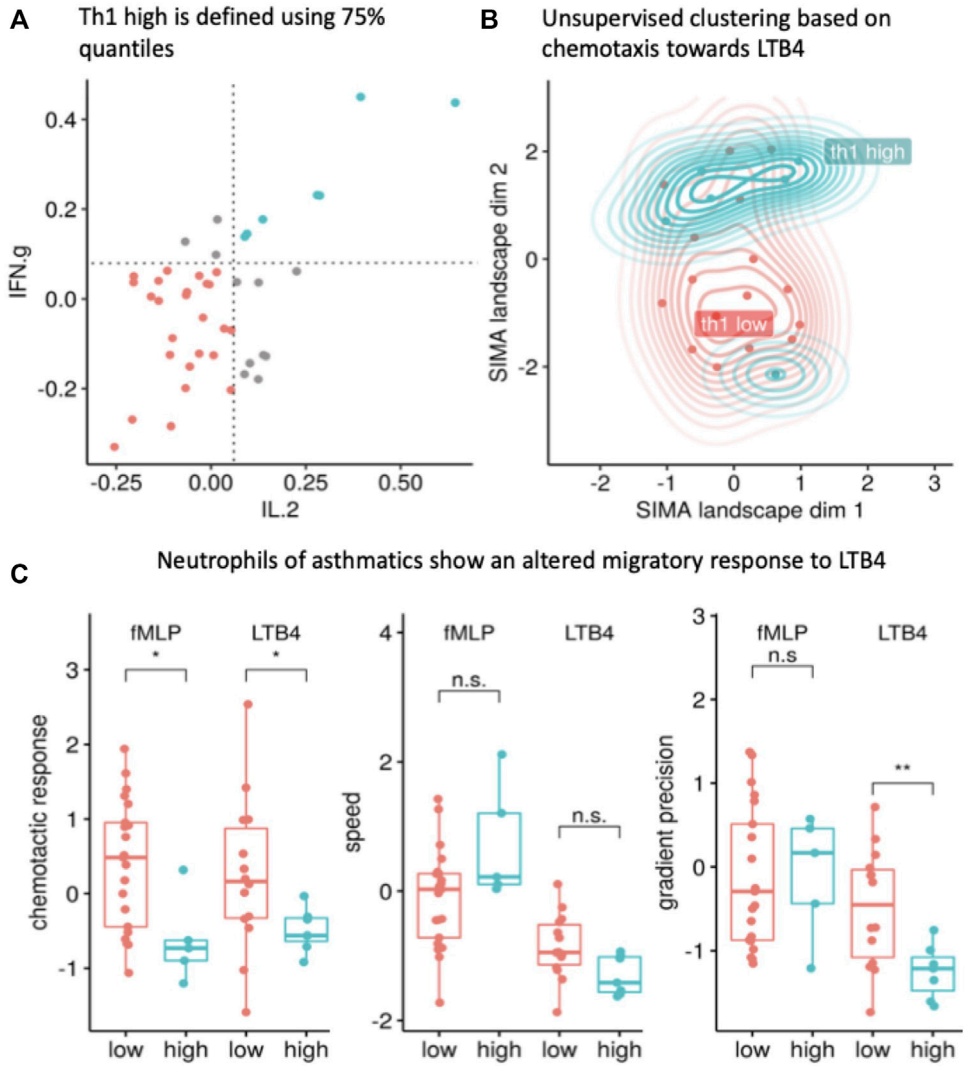

FIGURE 4
The Th1-high asthma phenotype (blue) corresponds to a unique chemotaxis pattern. **(A)** The Th1-high phenotype (marked in blue) is defined as a patient with interleukin 2 (IL2) and interferon gamma (IFNγ) levels above the >75% quantile (quantiles are shown as dotted line; each dot represents one patient and only patients with valid readouts for IL2 and IFNγ were included; Th1-low donors are presented in red). **(B)** The morphological dynamics are projected into the SiMA landscape and show a cluster of Th1-high asthma patients. The 2D embedding was calculated using a UMAP projection of all morphological and dynamic features based on chemotaxis experiments towards LTB_4 with IL2 and IFNγ measurements (n = 20 with 13 Th1-low and 7 Th1-high). **(C)** The migratory response (z-value) of Th1-high NGs in a LTB_4 gradient shows a significant difference compared to neutrophils isolated from Th1-low donors (reduced chemotactic response (z-value), $p < 0.01$, t-test) and reduced gradient precision (z-value, $p < 0.01$, t-test). The migration towards fMLP shows a similar effect for the chemotactic response (z-value, $p < 0.05$, t-test).

presented with a Th1-high cytokine profile; these were also ignored in this analysis.

Th1-high asthmatics displayed a significantly ($p < 0.0003$) lower BMI than Th1-low donors but there were no other significant differences in the demographic data (Table 2). The majority of Th1-high donors were non-atopic and treated more often with ICS as compared to Th1-low donors. When examining the measured cytokine levels in both groups, Th1-high asthmatics presented significantly elevated levels of IL1β, IL6, TNFα and G-CSF (Table 2). Th1-high patients showed a trend towards less controlled asthma, however due to the small numbers, significance was not reached (Table 2). Of note, out of the seven Th1-high patients, three were classified as Th2-high patients (Supplementary Table SA2).

Again, we performed unsupervised UMAP clustering based on morphologic and dynamic migration parameters (Figure 4B). Here, two different clusters were detectable. While Th1-low donors were associated in one loose cluster, a second, very

TABLE 2 Demographics of the Th1-high/low donor population. The Th1-high phenotype is characterised by significantly increased interleukin 6 (IL6), IL1b, TNFa and G-CSF level (**$p < 0.01$, ***$p < 0.001$), and a significant difference in BMI but no other patient demographics.

	Th1-low ($n = 30$)	Th1-high ($n = 7$)	p-value
Gender (male)	16 (53%)	4 (57%)	n.s.
Age	12 (±3.9)	10.6 (±3.9)	n.s.
BMI	20.9 (±5.4)	16.7 (±1)	$p = 0.0003$
ICS treatment (%)	20 (67%)	5 (71%)	n.s.
Reported atopy (%)	21 (70%)	3 (43%)	n.s.
Exh. NO	22.1 (±23.1)	15.6 (±17.3)	n.s.
Tiffaneau Index	98.9 (±8.4)	105.4 (±9.1)	n.s.
Eosinophils (%)	5.2 (±3.7)	5.4 (±2.9)	n.s.
IL-6	−0.032 (±0.153)	0.248 (±0.174)	$p = 0.0041$
IL1β	−0.049 (±0.126)	0.229 (±0.264)	$p = 0.0314$
TNFα	−0.017 (±0.122)	0.3 (±0.169)	$p = 0.0018$
G-CSF	−0.0527 (±0.125)	0.186 (±0.214)	$p = 0.0387$
Controlled asthma	15 (58%)	3 (43%)	n.s.

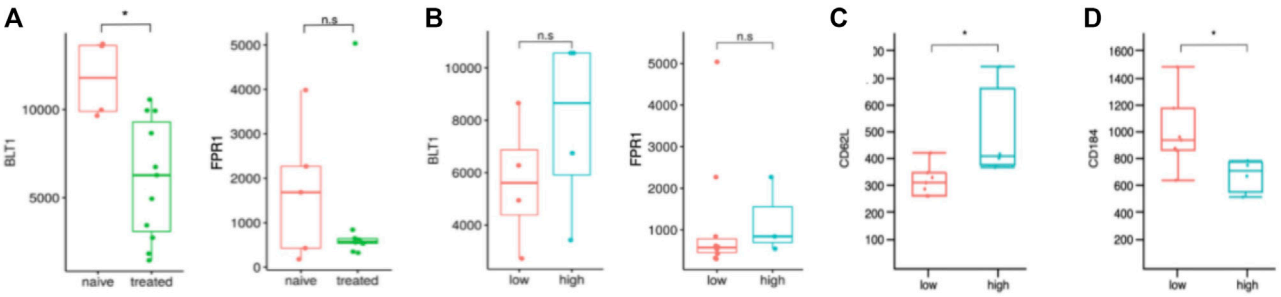

FIGURE 5
Surface receptor expressions of asthmatic patients could explain the altered migration behavior. **(A)** Comparison of BLT1 and FPR1 expression on neutrophils of corticosteroid naive and treated patients. Fluorescence units arbitrary on y-axis; BLT1: $n = 4$ naive and $n = 10$ treated. FPR1: $n = 5$ naive and $n = 7$ treated. n.s. not significant, *$p < 0.05$, Wilcoxon. **(B)** Comparison of BLT1 and FPR1 expression on neutrophils of patients with Th1 high and low profiles. No significant difference was detected. Fluorescence units arbitrary on y-axis; BLT1: $n = 4$ low and $n = 4$ high. FPR1: $n = 8$ low and $n = 3$ high. n.s., not significant. Comparison of CD62L **(C)** and CD184 **(D)** expression on neutrophils of patients with Th1 high and low profiles. Fluorescence units arbitrary on y-axis; CD62L: $n = 4$ high and $n = 8$ low. CD184: $n = 4$ high and $n = 7$ low. *$p < 0.05$, Wilcoxon.

dense cluster containing almost all Th1-high donors was obvious. The only exception was one outlier with a markedly elevated level of exhaled NO (exh. NO > 90ppb) and overall, very dissimilar migration patterns as compared to the rest of the Th1 cluster. This outlier was removed from further analysis.

In a comparison based on specific migratory parameters, Th1-high donors were characterized by significantly reduced chemotactic responses (percent of cells) towards LTB_4 and fMLP (Figure 4C left panel, $p < 0.05$). Speed did not differ significantly in any chemotactic condition Figure 4C panel in the middle). Additionally, gradient precision towards LTB_4 also was significantly reduced, indicating that compared to Th1-low donors, fewer neutrophils from Th1-high donors migrated towards the stimulus while also being slower and less directed (Figure 4C, right panel).

Some asthmatic subpopulations present altered surface expression of receptors, which partially correlates with migratory behavior

Next, we were interested in the cause of the altered migratory behavior. Therefore, we analyzed the expression level of the chemokine receptors for LTB_4 (BLT1; $n = 14$) and fMLP (FPR1; $n = 12$) for a subgroup of our patients. We observed

significantly less BLT1 on neutrophils of patients treated with ICS as compared to untreated asthmatics (Figure 5A, left panel, $p < 0.05$).

We did not detect a changed expression of FPR1 between treated and untreated asthmatics (Figure 5A, right panel). This fits our observation that the migratory speed of neutrophils attracted to fMLP is similar between both groups (Figure 4C).

Furthermore, we examined Th1-high vs. Th1-low asthma patients but did not detect a significant difference in receptor expression between these groups, neither in BLT1 nor FPR1 expression (Figure 5B, left and right panel). Nevertheless, neutrophils of Th1-high patients expressed significantly more CD62L ($p < 0.05$, L-selectin, Figure 5C) and less CD184 ($p < 0.05$, CXCR4, Figure 5D).

Discussion

We present here the comprehensive migration analysis on single cell level of NGs from asthmatic children and healthy controls thus far. NGs from children with asthma display impaired *in vitro* chemotactic responses towards LTB_4. However, ICS treatment largely had no significant effects on dynamic migration parameters. A less directed and reduced chemotactic response towards LTB_4 was observed in Th1-high asthmatic children.

Previously, we reported a reduced *in vitro* chemotaxis of NGs towards LTB_4 for asthmatic patients (Weckmann et al., 2017). Here, we confirm this phenomenon in a larger cohort and show a reduced percentage of directed trajectories when stimulated by LTB_4 (73.4% vs. 51.68%) but not for fMLP or IL8. The latter did not show any difference between disease status, treatment or phenotype (data not shown). The migration effect is preserved, confirming that peripheral neutrophils from asthmatic children respond less to LTB_4 than healthy controls.

We did not replicate the observation by Sackman and colleagues that asthmatic neutrophils migrate slower in an fMLP gradient, regardless of ICS treatment (Sackmann et al., 2014). Several differences (fibronectin vs. p-selectin coating; density gradient centrifugation vs. blood drop) between the two microfluidic platforms exist, which may account for the lack of comparability.

In order to identify the asthmatic phenotype associated with this migratory behavior we investigated the difference between ICS-treated and non-treated children. We previously described a reversal of the chemotactic response *in vitro* when NGs were incubated with prednisolone. However, in this study we analyzed the *in vitro* chemotaxis of NGs from ICS treated asthmatic children compared to untreated children and healthy controls. We found a reduced migration speed (LTB_4) in the cohort of ICS-treated children, while we could not detect a significant change of the chemotactic response (either fMLP or LTB_4) or gradient precision even after stratifying for ICS dosage. (Weckmann et al., 2017) An unsupervised analysis using the high dimensional morphologic and dynamic features from our tracking data, revealed a 2-dimensional SiMA landscape, in which ICS-treated asthmatics and control patients showed a similar chemotaxis pattern. The only exception is a small fraction of ICS-treated patients (cluster AT2 in Figure 4C), very far from healthy controls and from the majority of the treated patients as well. We found no significant difference in clinical of demographical data defining this cluster. Further research is warranted to better understand the patients in this special migratory cluster and the relevance of the altered neutrophil migration.

Next, we used the serum cytokine levels to define immunological "endotypes" to characterize their migration pattern. We identified patients with elevated Th1 cytokines (IL-2 and IFNγ) whose NGs are characterized by a below average chemotactic response towards LTB_4. Further, the SiMA landscape projection clearly separated the Th1-high and Th1-low patients into two clusters. We did not find significant differences in chemotactic responses in Th2, Th9 or Th17 (Supplementary Figure SA1).

In order to identify underlying causes for the altered migratory behavior, we analysed NGs surface receptor expression in our asthma patients. We found less BLT1 protein expressed on the surface of neutrophils from ICS-treated asthmatic patients that migrate slower towards LTB_4. Qasaimeh et al. subjected NGs to different levels of IL-8 gradients and found that at about 90% of the maximal IL-8 concentrations, the chemotactic speed reduced significantly (Qasaimeh et al., 2018). The authors suggested a saturation of the IL-8 receptor to be causative for this behavior. Lower BLT1 levels in our assay would result in earlier termination of migration due to receptor saturation in our gradient and an overall reduced migratory speed. IL-8 and LTB_4 belong to so-called "intermediate chemokines" and migration response is distinct as compared to end-target chemoattractants such as fMLP (reviewed in (Sadik et al., 2011)). Petrie Aronin et al. showed that whilst intermediate chemokines require an ever-increasing concentration to stably recruit neutrophils, for end-target chemoattractants a stable gradient suffices (Petrie Aronin et al., 2017). In particular, the authors argue that in devices like the ones used in our study (3D Ibidi slide) the gradient is not fully established in the initial phase, so intermediate chemokine concentration follows an ever-increasing pattern until a steady-state level is achieved. Any migration measurements under these conditions would eliminate differences between IL-8/LTB_4 and fMLP.

In our analysis, we only used images starting from 15min into the migration experiment until the end (after 30 min). Also, we did not see any of the LTB_4 migration effects to occur in IL-8 recruited neutrophils, which suggests that the effect of LTB_4 is chemokine-specific at least in direct comparison with IL-8. However, levels of chemokine receptor expression (FPR1 and

BLT1) did not explain the difference in the chemotactic response. This may point towards an alternative hypothesis, in which NGs are primed by the existing milieu and therefore respond differently to chemotactic cues. This may unfold in two distinct scenarios:

A. Peripheral neutrophils exposed to chemokines in serum are desensitized and less responsive towards those (and other) chemokines. It is known that CXCR1 ligation leads to a reduced BLT1-induced chemotaxis (Tarlowe et al., 2003). In our Th1-high patients IL-8 is significantly increased in serum, but no difference in migration speed or chemotactic response towards IL-8 is observed (data not shown). In addition, we did not see a decrease of BLT1 in neutrophils from Th1-high patients.
B. Alternately, the neutrophil population is primed or distinctly different in its composition. In our study, the reduced chemotactic response of peripheral neutrophils from Th1 high asthmatics was associated with decreased CD184 (CXCR4) levels. Numbers of CXCR4 high neutrophils are significantly reduced in peripheral blood and the bone marrow after intraperitoneal injection of LPS in mice. Recently, Uhl et al. showed that elevated CXCR4 expression is found on "aged" neutrophils, which are more likely to respond to LPS injection in mice and lead to increased levels of CXCR4 high neutrophils in liver, kidney and lung (Uhl et al., 2016). Furthermore, approximately 50% of all NGs in the lung belonged to the CXCR4 high ("aged") phenotype. This is supported by earlier work from Yamada et al. Yamada et al. (2011) who identified CXCR4 expression to be increased on extravascular NGs after endotoxin-induced lung injury. Nasal LPS installation led to a significant increase of neutrophil influx in their mouse model characterized by higher CXCR4 expression on neutrophils. Blocking CXCR4 or CXCL12 (the only known ligand for CXCR4) resulted in a significant decrease in neutrophil influx in LPS induced lung injury. CXCL12 has been reported to be increased in serum and broncho-alveolar lavage in asthmatics and is produced by the airway epithelium during asthma exacerbation (Daubeuf et al., 2013; Wang et al., 2015). This may suggest that in asthmatic patients with a Th1-high signature more "aged" neutrophils are recruited as a consequence of a recent infection or lack of resolution of inflammation, whilst "younger" NGs are found in circulation. These younger neutrophils may respond differently to LTB_4. Further experiments with CXCR4 high/low neutrophils and LTB_4 induced chemotaxis may help to unravel this intricate relationship.

Evidence for a complex interplay of recent infections and Th1 "endotype" characteristics in asthmatic children is presented by Wisniewski and colleagues. In their study, current or recent viral or bacterial infection were associated with persistently increased Th1 cytokines and Th1 lymphocytes in broncho-alveolar lavage fluid (BALF) (Wisniewski et al., 2018). Additionally, Grunwell et al. demonstrated that BALF from severe, neutrophil high, asthmatic children stimulated peripheral neutrophils to increase CD62L (L-selectin expression) and become more pro-inflammatory (Grunwell et al., 2019). Interestingly, we found CD62L to be significantly increased in our Th1-high asthma NGs population. On the other hand, a lack of proresolving mediators such as lipoxin A4 (LXA_4), may result in differentially primed neutrophils. LXA_4 was decreased in peripheral blood, sputum and BALF of severe asthma patients (Ricklefs et al., 2017). LXA_4 correlated inversely with the number of airway neutrophils especially in severe asthma patients (Ricklefs et al., 2017). Th1-high asthma is more prevalent in the group of severe asthma patients. Whether unresolved inflammation or recent infections remains to be elucidated but may support an endotype-related priming environment supportive of our alternative hypothesis (see hypothesis B in previous paragraph).

Our study has several limitations. First, the overall number of individuals in our migration cohort is relatively small. This poses problems especially when smaller subgroups are investigated and compared. Although we see an ICS dose-associated difference in NGs migration speed, we lack statistical power to confirm this difference. In a future study, a double-blinded, randomized, placebo-controlled cross-over design could help to disentangle possible dose relationships of ICS on *ex vivo* neutrophil migration. Furthermore, overall numbers of patients in our SiMA landscape analysis of ICS use are too small. We also did not succeed in recruiting sufficient numbers of healthy controls in our second batch for our cytochip analysis to compare BLT1, CXCR4, CD62L and FRP1 expressions from asthmatics and controls. As we observe the strongest loss of chemotactic response in Th1-high vs. -low asthma patients, the lack of a direct comparison to controls is however less critical. In addition, although the overall effect of reduced chemotactic response appears to be preserved, the actual percentages differ from our previous results. In our initial setup we used a single video-microscope setup (EVOS) as compared to a multiple video-microscope array (CytoSmart) in our current study. This increased our throughput and data generation at the expense of exact replication of our previous results. Furthermore, in this study we continuously recruited over several years as compared to a single season in our previous study. As it is known that cytokine levels differ significantly in between seasons this might influence comparability (Weckmann et al., 2021). Another limitation is that despite the elevated levels of Th1 cytokines, we did not investigate severe childhood asthmatics. Lung function was relatively normal in our asthmatic children and even our Th1-high patients did not show a pronounced reduction of FEV1% or the Tiffeneau index. This is in contrast to the studies by Grunwell and Wisniewski, which analysed more severe childhood asthma cases. Therefore, one needs to be careful to extrapolate our

results to more severe asthma without further experiments in such individuals.

Taken together, this study identifies neutrophil migration to be associated with asthma therapy (ICS) and related to a "Th1" endotype in asthma. NGs isolated from peripheral blood retained their priming or programming as such, which enabled clustering and identification of subtypes of patients by morphologic and dynamic migratory parameters. This suggests that the underlying asthma endotype/theratype has direct consequences for granulocyte effector functions. Analysis of neutrophil migration with the SiMA protocol paired with neutrophil receptor analysis may be a valuable strategy to monitor effective treatment in children with asthma.

ALLIANCE Study Group

Mustafa Abdo, LungenClinic Grosshansdorf GmbH, Grosshansdorf, Germany, and Airway Research Center North (ARCN), Germany; German Center for Lung Research (DZL), **Miguel Alcazar**, University of Cologne, Faculty of Medicine and University Hospital Cologne, Translational Experimental Pediatrics - Experimental Pulmonology, Department of Pediatric and Adolescent Medicine, Germany, University of Cologne, Faculty of Medicine and University Hospital Cologne, Center for Molecular Medicine Cologne (CMMC), Germany, Excellence Cluster on Stress Responses in Aging-associated Diseases (CECAD), University of Cologne, Faculty of Medicine and University Hospital Cologne Cologne, Germany, and Institute for Lung Health, University of Giessen and Marburg Lung Centre (UGMLC), Member of the German Centre for Lung Research (DZL), Gießen, Germany, **Thomas Bahmer**, LungenClinic Grosshansdorf GmbH, Grosshansdorf, Germany, and Airway Research Center North (ARCN), Germany; German Center for Lung Research (DZL), **Mira Berbig**, Department of Paediatric Allergology, Dr von Hauner Children's Hospital, Ludwig Maximilians University, Munich, Germany, and Comprehensive Pneumology Center, Munich (CPC-M), Germany; German Center for Lung Research (DZL), Heike Biller, LungenClinic Grosshansdorf GmbH, Grosshansdorf, Germany, and Airway Research Center North (ARCN), Germany; German Center for Lung Research (DZL), **Xenia Bovermann**, University Children's Hospital, Luebeck, Germany, and Airway Research Center North (ARCN), Germany; German Center for Lung Research (DZL), **Folke Brinkmann**, Department of Paediatric Pneumology, Allergology and Neonatology, Hannover Medical School, Hannover, Germany, and Biomedical Research in Endstage and Obstructive Lung Disease Hannover (BREATH), Germany; German Center for Lung Research (DZL), and Department of Paediatric Pneumology, University Children's Hospital, Ruhr-University Bochum, Bochum, Germany, **Mifflin-Rae Calveron**, Hannover Medical School, Hannover, Germany, and Biomedical Research in Endstage and Obstructive Lung Disease Hannover (BREATH), Germany; German Center for Lung Research (DZL), **Adan Chari Jirmo**, Department of Paediatric Pneumology, Allergology and Neonatology, Hannover Medical School, Hannover, Germany, and Biomedical Research in Endstage and Obstructive Lung Disease Hannover (BREATH), Germany; German Center for Lung Research (DZL), **David S. DeLuca**, Hannover Medical School, Hannover, Germany, and Biomedical Research in Endstage and Obstructive Lung Disease Hannover (BREATH), Germany; German Center for Lung Research (DZL), **Gesa Diekmann**, University Children's Hospital, Luebeck, Germany, and Airway Research Center North (ARCN), Germany; German Center for Lung Research (DZL), **Anna-Maria Dittrich**, Department of Paediatric Pneumology, Allergology and Neonatology, Hannover Medical School, Hannover, Germany, and Biomedical Research in Endstage and Obstructive Lung Disease Hannover (BREATH), Germany; German Center for Lung Research (DZL), **Christian Dopfer**, Department of Paediatric Pneumology, Allergology and Neonatology, Hannover Medical School, Hannover, Germany, and Biomedical Research in Endstage and Obstructive Lung Disease Hannover (BREATH), Germany; German Center for Lung Research (DZL), **Markus Ege**, Department of Paediatric Allergology, Dr von Hauner Children's Hospital, Ludwig Maximilians University, Munich, Germany, and Comprehensive Pneumology Center, Munich (CPC-M), Germany; German Center for Lung Research (DZL), **Svenja Foth**, University Children's Hospital Marburg, University of Marburg, Germany, and University of Giessen Marburg Lung Center (UGMLC); Member of the German Center for Lung Research, **Oliver Fuchs**, Department of Paediatric Allergology, Dr von Hauner Children's Hospital, Ludwig Maximilians University, Munich, Germany, and Comprehensive Pneumology Center, Munich (CPC-M), Germany; German Center for Lung Research (DZL), and Department of Paediatric Respiratory Medicine, Inselspital, University Children's Hospital of Bern, University of Bern, Bern, Switzerland, **Svenja Gaedcke**, Hannover Medical School, Hannover, Germany, and Biomedical Research in Endstage and Obstructive Lung Disease Hannover (BREATH), Germany; German Center for Lung Research (DZL), **Karoline I. Gaede**, Research Center Borstel—Medical Clinic, Borstel, Germany, and Airway Research Center North (ARCN), Germany; German Center for Lung Research (DZL), **Ruth Grychtol**, Department of Paediatric Pneumology, Allergology and Neonatology, Hannover Medical School, Hannover, Germany, and Biomedical Research in Endstage and Obstructive Lung Disease Hannover (BREATH), Germany; German Center for Lung Research (DZL), **Anika Habener**, Department of Paediatric Pneumology, Allergology and Neonatology, Hannover Medical School, Hannover, Germany, and Biomedical Research in Endstage and Obstructive Lung Disease Hannover (BREATH), Germany; German Center for Lung Research (DZL), **Gesine Hansen**, Department of Paediatric Pneumology, Allergology and Neonatology, Hannover Medical School, Hannover,

Germany, and Biomedical Research in Endstage and Obstructive Lung Disease Hannover (BREATH), Germany; German Center for Lung Research (DZL), **Christine Happle**, Department of Paediatric Pneumology, Allergology and Neonatology, Hannover Medical School, Hannover, Germany, and Biomedical Research in Endstage and Obstructive Lung Disease Hannover (BREATH), Germany; German Center for Lung Research (DZL), **Christian Herzmann**, Research Center Borstel – Medical Clinic, Borstel, Germany, and Airway Research Center North (ARCN), Germany; German Center for Lung Research (DZL), **Alexander Hose**, Department of Paediatric Allergology, Dr von Hauner Children's Hospital, Ludwig Maximilians University, Munich, Germany, and Comprehensive Pneumology Center, Munich (CPC-M), Germany; German Center for Lung Research (DZL), **Sabina Illi**, Institut für Asthma- und Allergieprävention (IAP), Helmholtz Zentrum Munich, Deutsches Forschungszentrum für Gesundheit und Umwelt (GmbH), Munich, Germany, **Anne-Marie Kirsten**, Pulmonary Research Institute at LungenClinic Grosshansdorf, Grosshansdorf, Germany, and Airway Research Center North (ARCN), Germany; German Center for Lung Research (DZL), **Naschla Kohistani-Greif**, Department of Paediatric Allergology, Dr von Hauner Children's Hospital, Ludwig Maximilians University, Munich, Germany, and Comprehensive Pneumology Center, Munich (CPC-M), Germany; German Center for Lung Research (DZL), **Inke R. König**, Institute for Medical Biometry and Statistics, University Luebeck, University Medical Centre Schleswig-Holstein, Campus Luebeck, Germany, and Airway Research Center North (ARCN), Germany; German Center for Lung Research (DZL), **Silke Van Koningsbruggen-Rietschel**, University of Cologne, Faculty of Medicine and University Hospital Cologne, Department of Pediatrics, Cologne, Germany, **Matthias V. Kopp**, University Children's Hospital, Luebeck, Germany, and Airway Research Center North (ARCN), Germany; German Center for Lung Research (DZL), **Johanna Kurz**, Department of Paediatric Allergology, Dr von Hauner Children's Hospital, Ludwig Maximilians University, Munich, Germany, and Comprehensive Pneumology Center, Munich (CPC-M), Germany; German Center for Lung Research (DZL), and Department of Paediatric Respiratory Medicine, Inselspital, University Children's Hospital of Bern, University of Bern, Bern, Switzerland, **Katja Landgraf-Rauf**, Department of Paediatric Allergology, Dr von Hauner Children's Hospital, Ludwig Maximilians University, Munich, Germany, and Comprehensive Pneumology Center, Munich (CPC-M), Germany; German Center for Lung Research (DZL), **Kristina Laubhahn**, Department of Paediatric Allergology, Dr von Hauner Children's Hospital, Ludwig Maximilians University, Munich, Germany, and Comprehensive Pneumology Center, Munich (CPC-M), Germany; German Center for Lung Research (DZL), **Lena Liboschik**, University Children's Hospital, Luebeck, Germany, and Airway Research Center North (ARCN), Germany; German Center for Lung Research (DZL), **Claudia Liebl**, Department of Paediatric Allergology, Dr von Hauner Children's Hospital, Ludwig Maximilians University, Munich, Germany, and Comprehensive Pneumology Center, Munich (CPC-M), Germany; German Center for Lung Research (DZL), **Berrit Liselotte Husstedt**, University Children's Hospital, Luebeck, Germany, and Airway Research Center North (ARCN), Germany; German Center for Lung Research (DZL), **Bin Liu**, Hannover Medical School, Hannover, Germany, and Biomedical Research in Endstage and Obstructive Lung Disease Hannover (BREATH), Germany; German Center for Lung Research (DZL), **Nicole Maison**, Department of Paediatric Allergology, Dr von Hauner Children's Hospital, Ludwig Maximilians University, Munich, Germany, and Comprehensive Pneumology Center, Munich (CPC-M), Germany; German Center for Lung Research (DZL), and Institut für Asthma- und Allergieprävention (IAP), Helmholtz Zentrum Munich, Deutsches Forschungszentrum für Gesundheit und Umwelt (GmbH), Munich, Germany, **Aydin Malik**, Department of Paediatric Pneumology, Allergology and Neonatology, Hannover Medical School, Hannover, Germany, and Biomedical Research in Endstage and Obstructive Lung Disease Hannover (BREATH), Germany; German Center for Lung Research (DZL), **Carola Marzi**, Institut für Asthma- und Allergieprävention (IAP), Helmholtz Zentrum Munich, Deutsches Forschungszentrum für Gesundheit und Umwelt (GmbH), Munich, Germany, **Meike Meyer**, University of Cologne, Faculty of Medicine and University Hospital Cologne, Department of Pediatrics, Cologne, Germany, **Erika Von Mutius**, Department of Paediatric Allergology, Dr von Hauner Children's Hospital, Ludwig Maximilians University, Munich, Germany, and Comprehensive Pneumology Center, Munich (CPC-M), Germany; German Center for Lung Research (DZL), and Institut für Asthma- und Allergieprävention (IAP), Helmholtz Zentrum Munich, Deutsches Forschungszentrum für Gesundheit und Umwelt (GmbH), Munich, Germany, **Gyde Nissen**, University Children's Hospital, Luebeck, Germany, and Airway Research Center North (ARCN), Germany; German Center for Lung Research (DZL), **Catharina Nitsche**, University Children's Hospital, Luebeck, Germany, and Airway Research Center North (ARCN), Germany; German Center for Lung Research (DZL), **Frauke Pedersen**, LungenClinic Grosshansdorf GmbH, Grosshansdorf, Germany, and Airway Research Center North (ARCN), Germany; German Center for Lung Research (DZL), **Mareike Price**, Department of Paediatric Pneumology, Allergology and Neonatology, Hannover Medical School, Hannover, Germany, and Biomedical Research in Endstage and Obstructive Lung Disease Hannover (BREATH), Germany; German Center for Lung Research (DZL), **Klaus F. Rabe**, LungenClinic Grosshansdorf GmbH, Grosshansdorf, Germany, and Airway Research Center North (ARCN), Germany; German Center for Lung Research (DZL), **Harald Renz**, Institute of Laboratory Medicine and Pathobiochemistry, Molecular Diagnostics, University of Marburg, Germany, and University

of Gießen, Marburg Lung Center (UGMLC); German Center for Lung Research (DZL), **Isabell Ricklefs**, University Children's Hospital, Luebeck, Germany, and Airway Research Center North (ARCN), Germany; German Center for Lung Research (DZL), **Ernst Rietschel**, University of Cologne, Faculty of Medicine and University Hospital Cologne, Department of Pediatrics, Cologne, Germany, **Barbara Roesler**, Department of Paediatric Allergology, Dr von Hauner Children's Hospital, Ludwig Maximilians University, Munich, Germany, and Comprehensive Pneumology Center, Munich (CPC-M), Germany; German Center for Lung Research (DZL), **Bianca Schaub**, Department of Paediatric Allergology, Dr von Hauner Children's Hospital, Ludwig Maximilians University, Munich, Germany, and Comprehensive Pneumology Center, Munich (CPC-M), Germany; German Center for Lung Research (DZL), **Christina Schauberger**, Department of Paediatric Allergology, Dr von Hauner Children's Hospital, Ludwig Maximilians University, Munich, Germany, and Comprehensive Pneumology Center, Munich (CPC-M), Germany; German Center for Lung Research (DZL), **Tom Schildberg**, University of Cologne, Faculty of Medicine and University Hospital Cologne, Department of Pediatrics, Cologne, Germany, **Carsten Schmidt-Weber**, Center of Allergy and Environment (ZAUM), Technical University of Munich and Helmholtz Center Munich, German Research Center for Environmental Health, Munich, Germany; German Center for Lung Research (DZL), Munich, Germany, **Nicolaus Schwerk**, Department of Paediatric Pneumology, Allergology and Neonatology, Hannover Medical School, Hannover, Germany, and Biomedical Research in Endstage and Obstructive Lung Disease Hannover (BREATH), Germany; German Center for Lung Research (DZL), **Chrysanthi Skevaki**, Institute of Laboratory Medicine and Pathobiochemistry, Molecular Diagnostics, University of Marburg, Germany, and University of Gießen, Marburg Lung Center (UGMLC); German Center for Lung Research (DZL), **Alena Steinmetz**, University Children's Hospital, Luebeck, Germany, and Airway Research Center North (ARCN), Germany; German Center for Lung Research (DZL), **Laila Sultansei**, University Children's Hospital, Luebeck, Germany, and Airway Research Center North (ARCN), Germany; German Center for Lung Research (DZL), **Marlen Szewczyk**, LungenClinic Grosshansdorf GmbH, Grosshansdorf, Germany, and Airway Research Center North (ARCN), Germany; German Center for Lung Research (DZL), **Dominik Thiele**, Institute for Medical Biometry and Statistics, University Luebeck, University Medical Centre Schleswig-Holstein, Campus Luebeck, Germany, and Airway Research Center North (ARCN), Germany; German Center for Lung Research (DZL), **Vera Veith**, LungenClinic Grosshansdorf GmbH, Grosshansdorf, Germany, and Airway Research Center North (ARCN), Germany; German Center for Lung Research (DZL), **Gesche Voigt**, University Children's Hospital, Luebeck, Germany, and Airway Research Center North (ARCN), Germany; German Center for Lung Research (DZL), **Benjamin Waschki**, LungenClinic Grosshansdorf GmbH, Grosshansdorf, Germany, and Airway Research Center North (ARCN), Germany; German Center for Lung Research (DZL), **Henrik Watz**, Pulmonary Research Institute at LungenClinic Grosshansdorf, Grosshansdorf, Germany, and Airway Research Center North (ARCN), Germany; German Center for Lung Research (DZL), **Stefanie Weber**, University Children's Hospital Marburg, University of Marburg, Germany, and University of Giessen Marburg Lung Center (UGMLC); Member of the German Center for Lung Research, **Markus Weckmann**, University Children's Hospital, Luebeck, Germany, and Airway Research Center North (ARCN), Germany; German Center for Lung Research (DZL), **Nils Welchering**, Department of Paediatric Allergology, Dr von Hauner Children's Hospital, Ludwig Maximilians University, Munich, Germany, and Comprehensive Pneumology Center, Munich (CPC-M), Germany; German Center for Lung Research (DZL), **Esther Zeitlmann**, Department of Paediatric Allergology, Dr von Hauner Children's Hospital, Ludwig Maximilians University, Munich, Germany, and Comprehensive Pneumology Center, Munich (CPC-M), Germany; German Center for Lung Research (DZL), **Ulrich Zissler**, Center of Allergy and Environment (ZAUM), Technical University of Munich and Helmholtz Center Munich, German Research Center for Environmental Health, Munich, Germany; German Center for Lung Research (DZL), Munich, Germany

Data availability statement

The raw data supporting the conclusions of this article will be made available by the authors, without undue reservation.

Ethics statement

The studies involving human participants were reviewed and approved by Ethics committee of the University of Lübeck, Lübeck, Germany (Vote 12-215; 18.12.2012). Written informed consent to participate in this study was provided by the participants' legal guardian/next of kin.

Author contributions

Conceptualization, TB and MW; methodology, TB and MW; software, TB, SS, JC, AC and SL; validation, TB and SL; formal analysis, SL, TB, AW, MW, RG, AJ; data curation, TB and SL; writing—original draft preparation, TB, SL, MW; writing—review and editing, TB, SL, MW, GN, IR, and AC; visualization: TB, SL; supervision, AC, SS, MK; project administration, MW; funding acquisition, TB, SL, MW, OF, TB, A-MD, BS, CH, KR, EV, GH, MK. designed the ALLIANCE cohort recruitment scheme, recruited participants,

collected specimens and edited the manuscript. All authors have read and agreed to the published version of the manuscript.

Funding

MW was funded by grants from the German Federal Ministry of Education and Research (BMBF, 82DZL001A6) and a Junior Research cluster grant from the University of Luebeck (JC01-2016). BMBF (82DZL001A6) financed all direct costs of the ALLIANCE cohort. TB was funded by DFG Research Fellowship 5728. SL was funded by the IGRK/IRTG 1911 "Immune Regulation of Inflammation in Allergy and Infection". AC and SS were funded by the U.S. National Institutes of Health (R35 GM122547 to AC).

Acknowledgments

The authors would like to thank the ALLIANCE study participants, their parents and caretakers for their ongoing support. Furthermore, the authors would like to thank Nadine Weissheimer, Detlev Schult-Badusche and Elvira Ehlers-Jeske (Division of Pediatric Pneumology and Allergology, University Childrens Hospital, Lübeck, Germany).

Conflict of interest

Author TB was employed by IAV GmbH.

The remaining authors declare that the research was conducted in the absence of any commercial or financial relationships that could be construed as a potential conflict of interest.

Publisher's note

All claims expressed in this article are solely those of the authors and do not necessarily represent those of their affiliated organizations, or those of the publisher, the editors and the reviewers. Any product that may be evaluated in this article, or claim that may be made by its manufacturer, is not guaranteed or endorsed by the publisher.

Supplementary material

The Supplementary Material for this article can be found online at: https://www.frontiersin.org/articles/10.3389/fphar.2022.1021317/full#supplementary-material

References

Agache, I., and Akdis, C. A. (2016). Endotypes of allergic diseases and asthma: An important step in building blocks for the future of precision medicine. *Allergol. Int.* 65, 243–252. doi:10.1016/j.alit.2016.04.011

Becker, T., Caicedo, J. C., Singh, S., Weckmann, M., and Carpenter, A. (2018). "Combining morphological and migration profiles of *in vitro* time-lapse data," in Proceedings of the 2018 15th IEEE International Symposium on Biomedical Imaging (ISBI), Washington DC, USA, 04-07 Apr. 2018 (IEEE).

Boonpiyathad, T., Sözener, Z. C., Satitsuksanoa, P., and Akdis, C. A. (2019). Immunologic mechanisms in asthma. *Semin. Immunol.* 46, 101333. doi:10.1016/j.smim.2019.101333

Croisant, S. (2014). Epidemiology of asthma: Prevalence and burden of disease. *Adv. Exp. Med. Biol.* 795, 17–29. doi:10.1007/978-1-4614-8603-9_2

Daubeuf, F., Hachet-Haas, M., Gizzi, P., Gasparik, V., Bonnet, D., Utard, V., et al. (2013). An antedrug of the CXCL12 neutraligand blocks experimental allergic asthma without systemic effect in mice. *J. Biol. Chem.* 288, 11865–11876. doi:10.1074/jbc.M112.449348

de Oliveira, S., Rosowski, E. E., and Huttenlocher, A. (2016). Neutrophil migration in infection and wound repair: Going forward in reverse. *Nat. Rev. Immunol.* 16, 378–391. doi:10.1038/nri.2016.49

Fuchs, O., Bahmer, T., Weckmann, M., Dittrich, A.-M., Schaub, B., Rösler, B., et al. (2018). The all age asthma cohort (ALLIANCE) - from early beginnings to chronic disease: A longitudinal cohort study. *BMC Pulm. Med.* 18, 140. doi:10.1186/s12890-018-0705-6

GINA Global Initiative for Asthma. 2019, Global strategy for asthma management and prevention Available online: www.ginasthma.org (accessed 2019).

Grunwell, J. R., Stephenson, S. T., Tirouvanziam, R., Brown, L. A. S., Brown, M. R., and Fitzpatrick, A. M. (2019). Children with neutrophil-predominant severe asthma have proinflammatory neutrophils with enhanced survival and impaired clearance. *J. Allergy Clin. Immunol. Pract.* 7, 516–525. doi:10.1016/j.jaip.2018.08.024

Hennig, C., Adams, N., and Hansen, G. (2009). A versatile platform for comprehensive chip-based explorative cytometry. *Cytom. A* 75, 362–370. doi:10.1002/cyto.a.20668

Jirmo, A. C., Busse, M., Happle, C., Skuljec, J., Dalüge, K., Habener, A., et al. (2020). IL-17 regulates DC migration to the peribronchial LNs and allergen presentation in experimental allergic asthma. *Eur. J. Immunol.* 50, 1019–1033. doi:10.1002/eji.201948409

Jirmo, A. C., Rossdam, C., Grychtol, R., Happle, C., Gerardy-Schahn, R., Buettner, F. F. R., et al. (2020). Differential expression patterns of glycosphingolipids and C-type lectin receptors on immune cells in absence of functional regulatory T cells. *Immun. Inflamm. Dis.* 8, 512–522. doi:10.1002/iid3.334

Kuruvilla, M. E., Lee, F. E.-H., and Lee, G. B. (2019). Understanding asthma phenotypes, endotypes, and mechanisms of disease. *Clin. Rev. Allergy Immunol.* 56, 219–233. doi:10.1007/s12016-018-8712-1

McInnes, L., Healy, J., Saul, N., and Großberger, L. (2018). UMAP: Uniform Manifold approximation and projection. *J. Open Source Softw.* 3, 861. doi:10.21105/joss.00861

Network, G. A. (2018). *The global asthma report 2018*. Auckland, New Zealand: Global Asthma Network.

Petrie Aronin, C. E., Zhao, Y. M., Yoon, J. S., Morgan, N. Y., Prüstel, T., Germain, R. N., et al. (2017). Migrating myeloid cells sense temporal dynamics of chemoattractant concentrations. *Immunity* 47, 862–874. doi:10.1016/j.immuni.2017.10.020

Pignatti, P., Moscato, G., Casarini, S., Delmastro, M., Poppa, M., Brunetti, G., et al. (2005). Downmodulation of CXCL8/IL-8 receptors on neutrophils after recruitment in the airways. *J. Allergy Clin. Immunol.* 115, 88–94. doi:10.1016/j.jaci.2004.08.048

Qasaimeh, M. A., Pyzik, M., Astolfi, M., Vidal, S. M., and Juncker, D. (2018). Neutrophil chemotaxis in moving gradients. *Adv. Biosys.* 2, 1700243. doi:10.1002/adbi.201700243

Rapoport, D. H., Becker, T., Mamlouk, A. M., Schicktanz, S., and Kruse, C. (2011). A novel validation algorithm allows for automated cell tracking and the extraction of biologically meaningful parameters. *PLoS One* 6, e27315. doi:10.1371/journal.pone.0027315

Ricklefs, I., Barkas, I., Duvall, M. G., Cernadas, M., Grossman, N. L., Israel, E., et al. (2017). ALX receptor ligands define a biochemical endotype for severe asthma. *JCI Insight* 2, 93534. doi:10.1172/jci.insight.93534

Ronneberger, O., Fischer, P., and Brox, T. (2015). "U-Net: Convolutional networks for biomedical image segmentation," in Proceedings of the Medical Image Computing and Computer-Assisted Intervention – MICCAI 2015, October 05–09, 2015, Munich, Germany (Springer International Publishing), 234–241.

Sackmann, E. K.-H., Berthier, E., Schwantes, E. A., Fichtinger, P. S., Evans, M. D., Dziadzio, L. L., et al. (2014). Characterizing asthma from a drop of blood using neutrophil chemotaxis. *Proc. Natl. Acad. Sci. U. S. A.* 111, 5813–5818. doi:10.1073/pnas.1324043111

Sadik, C. D., Kim, N. D., and Luster, A. D. (2011). Neutrophils cascading their way to inflammation. *Trends Immunol.* 32, 452–460. doi:10.1016/j.it.2011.06.008

Tarlowe, M. H., Kannan, K. B., Itagaki, K., Adams, J. M., Livingston, D. H., and Hauser, C. J. (2003). Inflammatory chemoreceptor cross-talk suppresses leukotriene B4 receptor 1-mediated neutrophil calcium mobilization and chemotaxis after trauma. *J. Immunol.* 171, 2066–2073. doi:10.4049/jimmunol.171.4.2066

Uhl, B., Vadlau, Y., Zuchtriegel, G., Nekolla, K., Sharaf, K., Gaertner, F., et al. (2016). Aged neutrophils contribute to the first line of defense in the acute inflammatory response. *Blood* 128, 2327–2337. doi:10.1182/blood-2016-05-718999

Wang, C.-H., Punde, T. H., Huang, C.-D., Chou, P.-C., Huang, T.-T., Wu, W.-H., et al. (2015). Fibrocyte trafficking in patients with chronic obstructive asthma and during an acute asthma exacerbation. *J. Allergy Clin. Immunol.* 135, 1154–1162.e1-5. doi:10.1016/j.jaci.2014.09.011

Weckmann, M., Becker, T., Nissen, G., Pech, M., and Kopp, M. V. SiM. A. (2017). SiMA: A simplified migration assay for analyzing neutrophil migration. *Cytom. A* 91, 675–685. doi:10.1002/cyto.a.23114

Weckmann, M., Thiele, D., Liboschik, L., Bahmer, T., Pech, M., Dittrich, A.-M., et al. (2021). Cytokine levels in children and adults with wheezing and asthma show specific patterns of variability over time. *Clin. Exp. Immunol.* 204, 152–164. doi:10.1111/cei.13550

Wisniewski, J. A., Muehling, L. M., Eccles, J. D., Capaldo, B. J., Agrawal, R., Shirley, D.-A., et al. (2018). TH1 signatures are present in the lower airways of children with severe asthma, regardless of allergic status. *J. Allergy Clin. Immunol.* 141, 2048–2060. doi:10.1016/j.jaci.2017.08.020

Yamada, M., Kubo, H., Kobayashi, S., Ishizawa, K., He, M., Suzuki, T., et al. (2011). The increase in surface CXCR4 expression on lung extravascular neutrophils and its effects on neutrophils during endotoxin-induced lung injury. *Cell. Mol. Immunol.* 8, 305–314. doi:10.1038/cmi.2011.8

frontiers | Frontiers in Pharmacology

TYPE Original Research
PUBLISHED 28 October 2022
DOI 10.3389/fphar.2022.991072

OPEN ACCESS

EDITED BY
Jane Elizabeth Bourke,
Monash University, Australia

REVIEWED BY
Rebecca L. Heise,
Virginia Commonwealth University, United States
Gert Folkerts,
Utrecht University, Netherlands
Steven S. An,
The State University of New Jersey, United States

*CORRESPONDENCE
R. Gosens,
r.gosens@rug.nl
A. M. Dolga,
a.m.dolga@rug.nl

SPECIALTY SECTION
This article was submitted to Respiratory Pharmacology, a section of the journal Frontiers in Pharmacology

RECEIVED 11 July 2022
ACCEPTED 12 October 2022
PUBLISHED 28 October 2022

CITATION
Goldsteen PA, Sabogal Guaqueta AM, Mulder PPMFA, Bos IST, Eggens M, Van der Koog L, Soeiro JT, Halayko AJ, Mathwig K, Kistemaker LEM, Verpoorte EMJ, Dolga AM and Gosens R (2022), Differentiation and on axon-guidance chip culture of human pluripotent stem cell-derived peripheral cholinergic neurons for airway neurobiology studies. *Front. Pharmacol.* 13:991072. doi: 10.3389/fphar.2022.991072

Differentiation and on axon-guidance chip culture of human pluripotent stem cell-derived peripheral cholinergic neurons for airway neurobiology studies

P. A. Goldsteen[1,2], A. M. Sabogal Guaqueta[1], P. P. M. F. A. Mulder[3], I. S. T. Bos[1,2], M. Eggens[1], L. Van der Koog[1,2], J. T. Soeiro[1], A. J. Halayko[4], K. Mathwig[3], L. E. M. Kistemaker[1,2,5], E. M. J. Verpoorte[3], A. M. Dolga[1,2]* and R. Gosens[1,2]*

[1]Department of Molecular Pharmacology, University of Groningen, Groningen, Netherlands, [2]GRIAC, Groningen Research Institute for Asthma and COPD, University of Groningen, Groningen, Netherlands, [3]Department of Pharmaceutical Analysis, University of Groningen, Groningen, Netherlands, [4]Department of Physiology and Pathophysiology, University of Manitoba, Winnipeg, MB, Canada, [5]Aquilo BV, Groningen, Netherlands

Airway cholinergic nerves play a key role in airway physiology and disease. In asthma and other diseases of the respiratory tract, airway cholinergic neurons undergo plasticity and contribute to airway hyperresponsiveness and mucus secretion. We currently lack human *in vitro* models for airway cholinergic neurons. Here, we aimed to develop a human *in vitro* model for peripheral cholinergic neurons using human pluripotent stem cell (hPSC) technology. hPSCs were differentiated towards vagal neural crest precursors and subsequently directed towards functional airway cholinergic neurons using the neurotrophin brain-derived neurotrophic factor (BDNF). Cholinergic neurons were characterized by ChAT and VAChT expression, and responded to chemical stimulation with changes in Ca^{2+} mobilization. To culture these cells, allowing axonal separation from the neuronal cell bodies, a two-compartment PDMS microfluidic chip was subsequently fabricated. The two compartments were connected *via* microchannels to enable axonal outgrowth. On-chip cell culture did not compromise phenotypical characteristics of the cells compared to standard culture plates. When the hPSC-derived peripheral cholinergic neurons were cultured in the chip, axonal outgrowth was visible, while the somal bodies of the neurons were confined to their compartment. Neurons formed contacts with airway smooth muscle cells cultured in the axonal compartment. The microfluidic chip developed in this study represents a human *in vitro* platform to model neuro-effector interactions in the airways that may be used for mechanistic studies into neuroplasticity in asthma and other lung diseases.

KEYWORDS
neuron, asthma, organ-on-chip, cholinergic, stem cell

Introduction

The lungs are innervated through a dense network of afferent and efferent nerves, which are arranged along the vagus nerve (van der Velden and Hulsmann, 1999). Among the efferent nerves, the parasympathetic neurons are most dominant in controlling several effector functions, including: airway smooth muscle (ASM) tone and mucus secretion (Kistemaker and Prakash, 2019). As is the case for all neurons, the airway nervous system is subjected to changes over time in response to intrinsic and extrinsic stimuli, known as neuronal plasticty (Nockher and Renz, 2006; Cramer et al., 2011). Severe or prolonged stimuli can cause permanent changes to the neurons, manifested as altered neurite length or innervation, lowered firing threshold, or even phenotype switching (Vasina et al., 2006; Undem and Taylor-Clark, 2014). Asthma patients have an increased innervation of both the sensory and the autonomic cholinergic nervous system (Drake et al., 2018; Dragunas et al., 2020). In asthma, neuroplasticity of the cholinergic nervous system is a newly discovered phenomenon (Dragunas et al., 2020). However, we do not yet fully understand the underlying mechanisms.

Conventional models, such as animal models or patient biopsies, can only provide limited information about mechanisms underlying neuroplasticity (Goldsteen et al., 2020). Patient biopsies provide much information on the final stages of neuronal remodeling. Animal models can be favored over biopsies for mechanistic studies as they take into account full physiological complexity, and the nervous system is well integrated into the organs and connected to the central nervous system. However, the problem with animal models is that the translation to the human situation is poor (Pound and Bracken, 2014; Leenaars et al., 2019). Human pluripotent stem cells (hPSCs) can aid in the development of a human disease model to study the process of neuronal plasticity *in vitro* (Goldsteen et al., 2020). Developing a human *in vitro* model to understand neuroplasticity in asthma has mostly been hampered by a lack of protocols for robust differentiation from hPSCs to that of airway cholinergic neurons.

Airway cholinergic neurons and enteric neurons originate from a vagal neural crest cell (NCC) precursor before developing into different directions (Aven and Ai, 2013; Hutchins et al., 2018). The differentiation of NCCs towards the peripheral neurons is dependent on neurotrophic factor (NTF) signaling. NTFs regulate neurogenesis, neuronal differentiation, neuronal survival, nerve conduction, and neuronal plasticity (Huang and Reichardt, 2001; Aven and Ai, 2013). Brain-derived neurotrophic factor (BDNF) is the predominant NTF in the lungs (Ricci et al., 2004), opposed to glial cell-derived neurotrophic factor (GDNF) in the enteric system (Fattahi et al., 2016; Barber et al., 2019). Secreted NTFs act as essential chemo-attractants for NCCs. For example, airway smooth muscle secretes BDNF in the lungs and guides airway neurons towards the muscle during development (Radzikinas et al., 2011).

Peripheral nervous system (PNS) neurons should be cultured and arranged correctly to anatomically reconstruct neuro-effector interactions *in vitro*. Several devices have been designed to study this axonal communication. The Campenot chamber is a Teflon-based culture chamber to separate neurites from cell bodies, used as the first compartmentalized culture technique to study the local effects of growth factors on neurite outgrowth (Campenot, 1977). As a follow-up, microfabrication techniques have been expanded into tailoring suitable devices for PNS-effector interactions (Goldsteen et al., 2020). Next-generation compartmentalized cell culture vessels were created from polydimethylsiloxane (PDMS), a biocompatible and versatile polymer that is easy to use and fabricate microfluidic chips even in submicron dimensions (Mata et al., 2005). PDMS chambers have been widely integrated into organ-on-a-chip devices, including compartmentalized axon-guidance chips (Taylor et al., 2005). This design has been adapted many times and is highly suitable for integrating PNS neurons and their target organs (Taylor et al., 2003; Takayama and Kida, 2016; Neto et al., 2014; Goldsteen et al., 2020).

In this study, we established a robust protocol for cholinergic neuron differentiation for studies on neuro-effector communication in the respiratory tract. Using dual SMAD inhibition and Wnt activation, $p75^{+}$-$HNK1^{+}$ NCC precursors were generated. Subsequently, vagal NCCs were guided into mature and functional peripheral cholinergic neurons using BDNF. To establish a platform on which these cells can be co-cultured with effector cells, we created a PDMS chip, consisting of two culture compartments, a somal and an axonal compartment, connected with tapered microchannels. In the somal compartment, we cultured neuronal cell bodies, whereas the axonal compartment displayed axonal outgrowth of the neurons and cell contact with airway smooth muscle cells. Cell morphology and function were evaluated on both regular plastic cell culture plates and the microfluidic chips, comparing microscopic observations, mRNA expression, immunofluorescence staining, and live-cell calcium imaging. We thus provide technical feasibility data for this culture system as a suitable device for PNS neuronal culture.

Materials and methods

H9WA09 cell culturing

H9WA09 cells were obtained from the European Institute for the Biology of Ageing (ERIBA) at the University of Groningen.

H9WA09 cells were cultured on Matrigel hESC-qualified (Corning, 354277) pre-coated 6-well plates in mTeSR1 medium (STEMCELL technologies, 85850). The cells were incubated at 5% CO_2 and 37°C. Once the cells grew confluent, the H9WA09 cells were passaged using ReLeSR (STEMCELL technologies, 05872). The pluripotency of the H9WA09 cells was tested regularly by staining for the pluripotency-marker OCT4. In addition, the cells were examined regularly for the presence of *mycoplasma*.

Differentiating H9WA09 cells towards a neuronal cell fate

For differentiation of H9WA09 cells into airway cholinergic neurons, several stages were passed (Supplementary Table S1). Vagal NCC induction was started when pluripotent stem cells were 40–60% confluent. Pluripotent stem cells were first differentiated into vagal NCCs in 12 days. Two types of media were used: KSR medium (KnockOut DMEM (Thermo Fisher, 10829018) and 15% KnockOut Serum Replacement (Thermo Fisher, 10828028)) and N2 medium (DMEM HEPES (Thermo Fisher, 12320032), 1% Penicillin-Streptomycin (Thermo Fisher, 15070063), and 10 µg/mL N2 supplement (Thermo Fisher, A1370701)). The manufacturer supplies N2 supplement as 100x, but double the amount was used in this protocol. KSR and N2 medium were freshly supplemented with 10 µM SB431542 (STEMCELL Technologies, Vancouver, Canada, 72234), 1 µM LDN193189 (STEMCELL Technologies, Vancouver, Canada, 72147), 3 µM CHIR99021 (STEMCELL Technologies, Vancouver, Canada, 72054), and 1 µM retinoic acid. The medium was changed every other day, medium composition according to Supplementary Table S2.

Next, the vagal NCCs were cultured in the form of floating spheroids for 4 days. The cells were washed with EDTA (0.5 mM) twice, followed by 10 min incubation at 37°C. After aspirating the EDTA, vagal precursor (VP) spheroid medium was added, consisting of Neurobasal Medium (Thermo Fisher, 21103049) supplemented with 10 µL/mL N2 supplement, 20 µL/ml B27 supplement (Thermo Fisher, 17504044), 10 µL/ml Glutamax (Thermo Fisher, 35050061), and 10 µL/ml MEM Nonessential Amino Acids). Prior to medium change, 10 ng/ml FGF2 (Thermo Fisher, PHG6015) and 3 µM CHIR99021 (STEMCELL Technologies, 72054) was freshly added. The cells were mechanically detached in VP spheroid medium using a serological pipette before transfer to a 6-well plate pre-coated with anti-adherence solution (STEMCELL Technologies, 07010). Detached cells from five wells of a 6-well plate were added divided over six wells of a 6-well plate. On day 14, the medium was refreshed.

After spheroid formation, the vagal cells undergo airway cholinergic neuron induction and airway cholinergic neuron maturation. On day 16 of the protocol, the VP spheroid medium was aspirated, and the spheroids were dissociated using EDTA (0.5 mM; wash twice, followed by 10 min incubation, 37°C). The cell suspension was carefully transferred to a tube and centrifuged (290 g, 1 min, RT). The supernatant was aspirated, and the cell pellet was resuspended in airway neuron (AN) medium (Neurobasal medium supplemented with 10 µg/mL N2 supplement, 20 µL/ml B27 supplement, 10 µg/ml Glutamax, and 10 µg/ml MEM Nonessential Amino Acids). 10 ng/ml BDNF (Peprotech, 450-02) and 100 µM freshly prepared L-Ascorbic Acid (Sigma-Aldrich, A5960) were added before medium change. Dissociated spheroids were plated onto culture plates pre-coated with 15 µg/ml Poly-L-Ornithine (PLO, Sigma-Aldrich, P4538), 2 µg/ml fibronectin (FB, Thermo Fisher, 33016015), and 2 µg/ml laminin (LM, R&D systems, 3400-010-02).

In the first stage of airway cholinergic neuron induction (day 16–30), the medium was changed three times per week, changing ¾ of the total volume. In the second stage (day 30–40), the medium was changed twice per week the medium volume was 1.5 times increased. In addition, from day 35 onwards, AN medium was supplemented with 2 µg/ml FB and 2 µg/ml LM. In the final stage of airway cholinergic neuron maturation (day 40–50), the medium was changed once per week. Cells were stimulated with 10 nM dexamethasone, or with the cytokines IL-4 (10 ng/ml, Peprotech, 200-04), IL-13 (3 ng/ml, Peprotech, 200-13), and IL-33 (10 ng/ml, Peprotech, 200-33). PCR analysis and immunofluorescence (IF) staining were performed on different time points: day 25, 35, and day 50. Additionally, fluorescence-activated cell sorting (FACS) was performed on day 50.

Gene expression analysis RT-qPCR

mRNA was isolated using NucleoSpin RNA XS kit (740902.50, Macherey-Nagel, Dueren, Germany) according to the manufacturer's protocol. The yield and purity of the isolated RNA were measured using the NanoDrop 1000 spectrophotometer and further processed for RT-qPCR or RNA sequencing.

For RT-qPCR, cDNA was synthesized using Reverse Transcription System (A3500, Promega, Leiden, Netherlands) according to the manufacturer's protocol. The qRT-PCR reactions were completed using SYBR Green. A list of the qPCR forward primers and reverse primers used is provided in Supplementary Table S4. The program for RT-qPCR reactions started with polymerase activation at 95°C for 10 min, 45 cycles of PCR cycling, which included denaturation at 95°C for 30 s, annealing for 30 s at 59°C, and extension at 72°C for 30 s, and incubation at 72°C for 5 min. Melting curves were obtained consecutively: 15 s at 95°C, 15 s at 55°C, and 15 s at 95°C. Analysis of the gene expression was performed with Quantstudio Real-Time PCR software v1.2.

RNA for sequencing was sent to GenomeScan BV (Leiden, Netherlands), and raw counts were provided together with a quality report. Genes with at least one count per million (CPM) were considered expressed and included for further analysis. Non-expressed genes were removed. Normalized expression levels of several neuronal and non-neuronal markers was compared. Normalized counts can be found in Supplementary Table S3 and on GEO using accession number GSE211478.

Immunofluorescence staining of cultures

Cells were fixed in 4% paraformaldehyde (PFA, Sigma-Aldrich, 97H0752) and permeabilized using 0.3% Triton X (Sigma-Aldrich, 101371900) for 5 min, RT. The cells were blocked for 1 h with blocking buffer, consisting of Cyto-TBS + 2% bovine serum albumin (Sigma Aldrich, 1002695029) and directly after incubated with a primary antibody overnight at 4°C. See Supplementary Table S5 for used antibodies and dilutions. The next day, the cells were incubated with a secondary antibody for 2 h in the dark, RT. Optionally, cells were counterstained for 45 min using 1 unit/assay Alexa Fluor 488 Phalloidin (Thermo Fisher, A12379). Mounting medium with DAPI (Abcam, ab104139) was used. Samples were imaged using a TissueFAXS (TissueGnostics) or a Zeiss LSM 780 (Zeiss, Germany) microscope and analyzed using Fiji (http://fiji.sc/).

Live cell CA^{2+} imaging using Fluo-4 AM

Live-cell imaging to show mature neuronal response to potassium chloride (KCl) or metacholine (MCh) was performed using Fluo-4-AM (Invitrogen™, F14217). Cells were incubated with Fluo-4-AM in HBSS-Ca^{2+} (45 min, RT, dark) and maintained at RT in the dark until data acquisition. Data were acquired using the Zeiss LSM 780 microscope. 3-10 neurons were identified for data acquisition. Cells were excited with 488-nm light (for Fluo-4-AM) and red-nm light (for 7-ADD cell death marker). Images were collected by taking an image every 100 msec for 3 min. After 30 s, the cells were challenged by adding 60 mM KCl or 100 µM MCh. To ensure that KCl enters the somal compartment within seconds, a volume of 10% of the chip volume was added (20 µl KCl solution into 200 µl HBSS). An increase in intensity was measured to quantify the neuronal response. A supplementary video is provided to demonstrate the calcium response (Supplementary Video S1).

Spontaneous firing of neurons

A Maestro Pro (Axion Biosystems) multi-electrode array (MEA) system was used to measure the spontaneous firing of neurons (Trombetta-Lima et al., 2021). We coated CytoView MEA 48 plates (Axion Biosystems, M768-tMEA-48W) containing sixteen embedded electrodes per well with PO/LM/FN. The coating solution was aspirated, and the wells were left to dry for 30 min. Dissociated NCC spheroids (day 16) were seeded in high-concentration LM (10 µM/ml) drops (5 µl/drop) into the center of the MEA well. The cells were incubated (60 min, 37 °C) before adding AN medium. Repeated recordings were made every 10 days for 15 min. The MEA plate was inserted into the MEA Maestro (37C, 5% CO_2) for spike detection. Axion AxIS Software recorded raw voltage data and detected spikes for rate analysis.

Chip fabrication

The axon-guidance chip master was fabricated from PDMS using photo–and soft lithography according to Peyrin et al., 2011. We used an additional PDMS-PFPE molding step to increase the viability of the cells cultured in the chip. The replica molding technique was partly derived from Jellali et al., 2016 (Peyrin et al., 2011; Jellali et al., 2016). For producing the master mold, SU-8 2002 (micro resist technology GmbH, Berlin, Germany) was spin-coated onto a 10 mm glass wafer at 845 rpm for 30 s to reach a height of 3 µm. The coated wafer was soft-baked at 95 °C for 2 min. Then, the wafer was covered with the first chrome mask (Delta mask, Enschede, Netherlands) and exposed to a collimated light source with a wavelength of 365 nm (model 30; OAI, San Jose, CA, United States) with a dose of 60 mJ/cm^2. The first photomask was designed to fabricate 140-180 tapered microchannels with a width of 15 µm, decreasing towards 3 µm, and with a length of 450 µm (layout Editor CleWin version 3.0.11, Hengelo, Netherlands). Then the exposed wafer was post-baked at 95 °C for 2 min and developed with the SU-8 developer (micro resist technology GmbH). Prior to the second layer, the wafer was treated with oxygen plasma at 310–320 mTorr for 20 s and spin-coated with SU-8 50 (micro resist technology GmbH) at 2000 rpm for 30 s to reach a height of 50 µm. Next, the wafer was incubated for 30 min at room temperature and soft-baked by increasing the temperature to 65 °C at a rate of 1°C/min, followed by 6 min at 65 °C, and then increasing to 95°C at a rate of 1°C/min, and incubated for another 20 min at 95°C. The wafer was gradually cooled down to room temperature before being exposed to UV light with a dose of 200 mJ/cm^2 through the second chrome photomask. This photomask was designed to fabricate the two main compartments of the chip. The wafer was post-baked by increasing the temperature to 65 °C with 1 °C/min, incubated for 1 min at 65 °C, increasing to 95°C with 1°C, and incubated for 5 min at 95°C. After cooling down to room temperature, the wafer was developed with the SU-8 developer, followed by a hard bake step for 20 min at 150°C. The master was incubated with 10 µL Trichloro (1H,1H,2H, 2H-perfluorooctyl)silane

(Sigma Aldrich, Zwijndrecht, Netherlands) for 1 h in a desiccator to remove PDMS more easily from the SU-8 masters. A mixture of the PDMS-prepolymer and curing agent (10:1 weight ratio; Sylgard®184, Mavon B.V. Alphen aan de Rijn, Netherlands) was cast to the master to achieve a thickness of 3 mm. Then, PDMS was cured on a hotplate at 70 °C for 70 min. After curing, the PDMS slab was cut in shape, and 8 mm holes were made using a biopsy punch (Kai, D-care BV, Houten, Netherlands) to create reservoirs that hold culture media in the respective compartments (Peyrin et al., 2011).

To fabricate perfluoropolyether (PFPE) molds, the PDMS chip was bonded to a PDMS box (50 × 50 × 7 mm; LxWxH). A mixture of Fluorolink MD 700 (Acota Ltd., Shropshire, UK) and 2% photoinitiator 2-Hydroxy-2-methylpropiophenone (Sigma Aldrich, Zwijndrecht, Netherlands) was poured into the box and exposed to N_2 for 20 min to remove oxygen (Vitale et al., 2012). The mixture was cured at 5–7 J/cm^2 in a blue wave LED flood-curing system (Dymax Europe GmbH, Wiesbaden, Germany), depending on the amount of the mixture. Then the PFPE mold was removed from the PDMS chip (Jellali et al., 2016).

Each PFPE mold was filled with 1.5 g of PDMS mixture to create chips with a thickness of 2–3 mm. PDMS was cured in an oven at 70°C for 1.5 h. PDMS chips were removed from the molds using a spatula. Chips were cut, and a puncher was used to open the reservoirs if necessary. The PDMS chamber was sealed with a 24 × 50 mm coverslip (Menzel Gläser) using oxygen plasma at 310–320 mTorr for 20 s and filled with water immediately. The chips were sterilized by incubating with 70% ethanol for 5 min at room temperature and washed 3 times with UP water. The chips are kept in a Petridish with moist filter paper to avoid evaporation of fluids.

Culturing and differentiating SH-SY5Y cells

Neuron-like SH-SY5Y cells were cultured in DMEM: F12 supplemented with 10% heat-inactivated FBS, L-glutamine (2 mM), penicillin (100 U/mL), and streptomycin (100 µg/ml) (Life Technologies, #15070-063). Once the cells grew confluent, the SH-SY5Y cells were passaged using trypsin. The cells were incubated at 5% CO_2 and 37°C. The cells were tested frequently for the presence of *mycoplasma*. For differentiation, SH-SY5Y cells were cultured in DMEM (DMEM; Life Technologies, United Kingdom, #42340-025) containing 1% heat-inactivated FBS, L-glutamine (2 mM), penicillin (100 U/mL), and streptomycin (100 µg/ml), freshly supplemented with 10 µM all-trans retinoic acid (r.a. cat. R2625, Sigma-Aldrich).

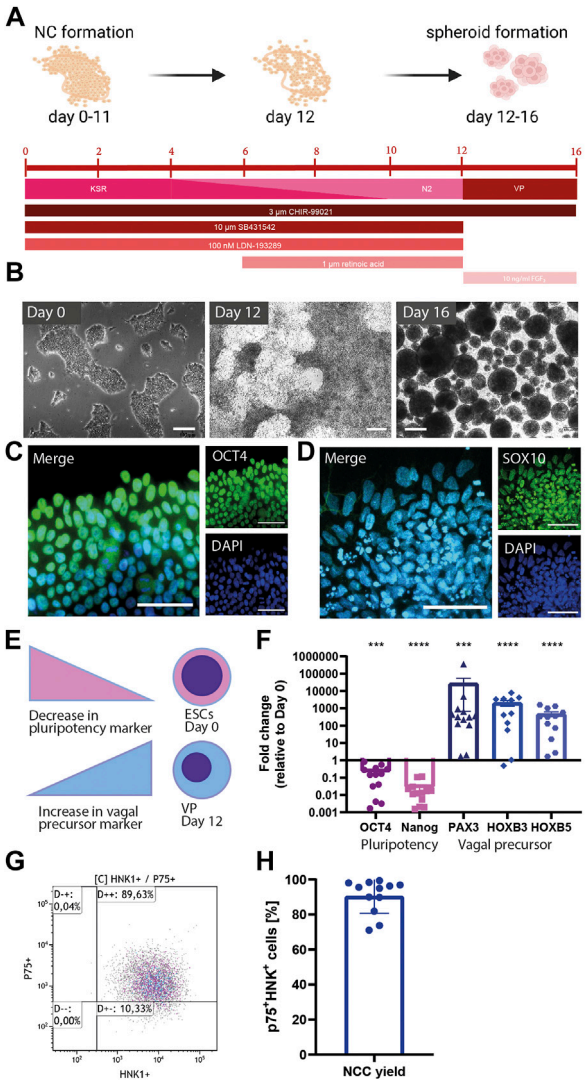

FIGURE 1
Derivation of vagal NCCs from hPSCs. **(A)** Schematic overview of vagal NCC induction from hPSCs. H9WA09 cells were directed into a vagal NCC faith using dual SMAD inhibition, and early WNT activation, r. a. Was added to direct NCCs from a cranial into a more distal phenotype. Knock-out serum replacer medium (KSR) was gradually replaced by N2 medium. Vagal NCCs were cultured in spheroids for 4 days to complete maturation. Created with BioRender.com. **(B)** Bright images of the differentiating cells over time. Scale bar = 200 µm. **(C)** OCT4 expression of Day 0 pluripotent cells. Scale bar = 50 µm. **(D)** SOX10 expression of Day 16 vagal NCC spheroids. Scale bar = 50 µm. **(E,F)** Gene expression of several markers for pluripotency, NCC, and vagal NCC. After 12 days, a decrease in the pluripotency genes OCT4 and Nanog was observed. The NCC marker PAX3 was upregulated, in combination with the vagal NCC markers HOXB3 and HOXB5 (N = 13) **(G,H).** FACS analysis showed that 90.48% (±2.83%) of the vagal NCCs were p75+-HNK1+ double positive. (N = 12) A paired *t*-test was performed to calculate statistical significance between means. ***$p < 0.001$; ****$p < 0.0001$ compared to day 0.

Culturing ASM cells

Immortalized human ASM were cultured in DMEM supplemented with 10% Fetal Bovine Serum (FBS), 2.2% Penicillin-Streptomycin, and 0.6% Amphotericin B. Once the cells grew confluent, the ASM cells were passaged using trypsin. The cells were incubated at 5% CO_2 and 37 °C. The cells were tested frequently for the presence of *mycoplasma*.

Statistical analysis

The data are presented as mean ± standard error of the mean (SEM). Statistical differences between distinct conditions were calculated using a two-way ANOVA or mixed effect analysis followed by either a Dunnett's test or a Tukey's multiple comparisons test to calculate significant differences comparing three or more variables. A paired *t*-test was performed comparing two variables. Statistical analyses were performed in GraphPad Prism (version 9.3.0), and performed tests are specified in the figure legends.

Results

Derivation of vagal NCCs from hPSCs

During embryonic development, airway cholinergic neurons originate from vagal NCCs. H9WA09 cells were directed into vagal NCCs using dual SMAD inhibition and early WNT activation using chemically defined conditions (Figure 1A) (Barber et al., 2019). To induce dual SMAD inhibition, SB431542 and LDN193189 were used as a BMP/TGF-β pathway inhibitor and a BMP pathway inhibitor, respectively. Later during the NCC differentiation, CHIR99021 was added for temporal WNT activation. A monolayer of pluripotent H9WA09 colonies differentiated into vagal NCCs in 12 days (Figure 1B). Following vagal NCC induction, cells were cultured as spheroids for 4 days in order to further mature the NCC phenotype (Figure 1B, right panel). On day 0, colonies were positive for OCT4, a marker for pluripotency (Figure 1C), while after 16 days of differentiation, cells showed decreased OCT4 expression and shifted to $SOX10^+$ NCCs (Figure 1D). The NCC stem cell marker Nestin was detected in day 16 spheroids (Supplementary Figure S1A).

To confirm the vagal NCC identity of the acquired cells, we performed a gene expression analysis of NCC (*PAX3*) and vagal NCC (*HOXB3*, *HOXB5*) markers. Firstly, *PAX3* is reported to be one of the earliest markers of NCC induction (Monsoro-Burq, 2015). In addition, vagal NCCs express *HOXB3* and *HOXB5* during embryogenesis (Chan et al., 2005; Kam and Lui, 2015). After 12 days of differentiation, vagal NCCs displayed lower expression of pluripotency genes (*OCT4*, $p < 0.001$; *NANOG*, $p < 0.0001$) and higher expression of NCC genes (*PAX3*, $p < 0.001$; *HOXB3*, $p < 0.0001$; *HOXB5*, $p < 0.0001$) compared to day 0 (Figures 1E,F). On day 12, the normalized expression of OCT4 and NANOG was significantly downregulated compared to day 0 (Figure 1F). Comparison of these relative gene expressions between samples collected during differentiation revealed a population transition from pluripotent stem cells to vagal NCCs. *PAX3* is involved in NCC development; *PAX6*, on the other hand, is an important early marker for neural tube formation and subsequent central nervous system differentiation (Monsoro-Burq, 2015). The obtained NCCs showed a high expression of *PAX3*, whereas *PAX6* was completely absent (Supplementary Figure S1B).

The efficiency of the differentiation protocol was analyzed by determining the yield of NCCs using FACS. HNK1 and p75 are both surface markers that are highly abundant on the surface of migratory NCCs (Betters et al., 2010). Figure 1G shows a representative FACS analysis at day 12 of differentiation. Induction of H9WA09 cells towards a NCC fate was highly efficient, with 90.48% (±2.83%) of total cells being double positive for p75 and HNK1 (Figure 1H). Together, these data indicate that vagal NCCs (displaying HOXB3 and HOXB5) were induced with high efficiency.

Neuronal differentiation from vagal NCCs

To differentiate vagal NCC precursors further into mature peripheral cholinergic neurons suitable for studies in to airway neuronal plasticity, we plated day-16-spheroids on FB/LM-coated surfaces and used BDNF as a main neurotrophic factor in the media in view of its prominent role in guiding neuronal development in the lung *in utero* (Figure 2A). A neuronal network was formed gradually and increased every day, with the first axonal outgrowth already visible after 24 h (Figure 2B, left panel; Figure 2C). At day 25 of differentiation, a neuronal network was clearly visible, which further expanded and became denser over time. β-3-tubulin staining confirmed the overall neuronal network formation (Figures 2C–E).

To track the development of cholinergic neurons during differentiation, we compared the gene expression between samples collected at several time points during the differentiation protocol. *In utero*, vagal NCCs express PHOX2B and ASCL1 after their inclusion in the foregut (Hao and Young, 2009). Accordingly, differentiated cells showed a relative increase in gene expression of *PHOX2B*, and *ASCL1*, with a peak at day 35 for *ASCL1* (Figures 2F,G). The expression of both the *TUBB3* and *UCHL1* confirmed that neurons were abundantly present and that their marker gene expression increased from day 16 to day 50 (Figures 2H,I). Expression of peripherin (*PRPH*), a cytoskeletal protein found in peripheral neurons, also increased towards day 50 and confirmed a peripheral neuronal phenotype (Figure 2J). Vesicular

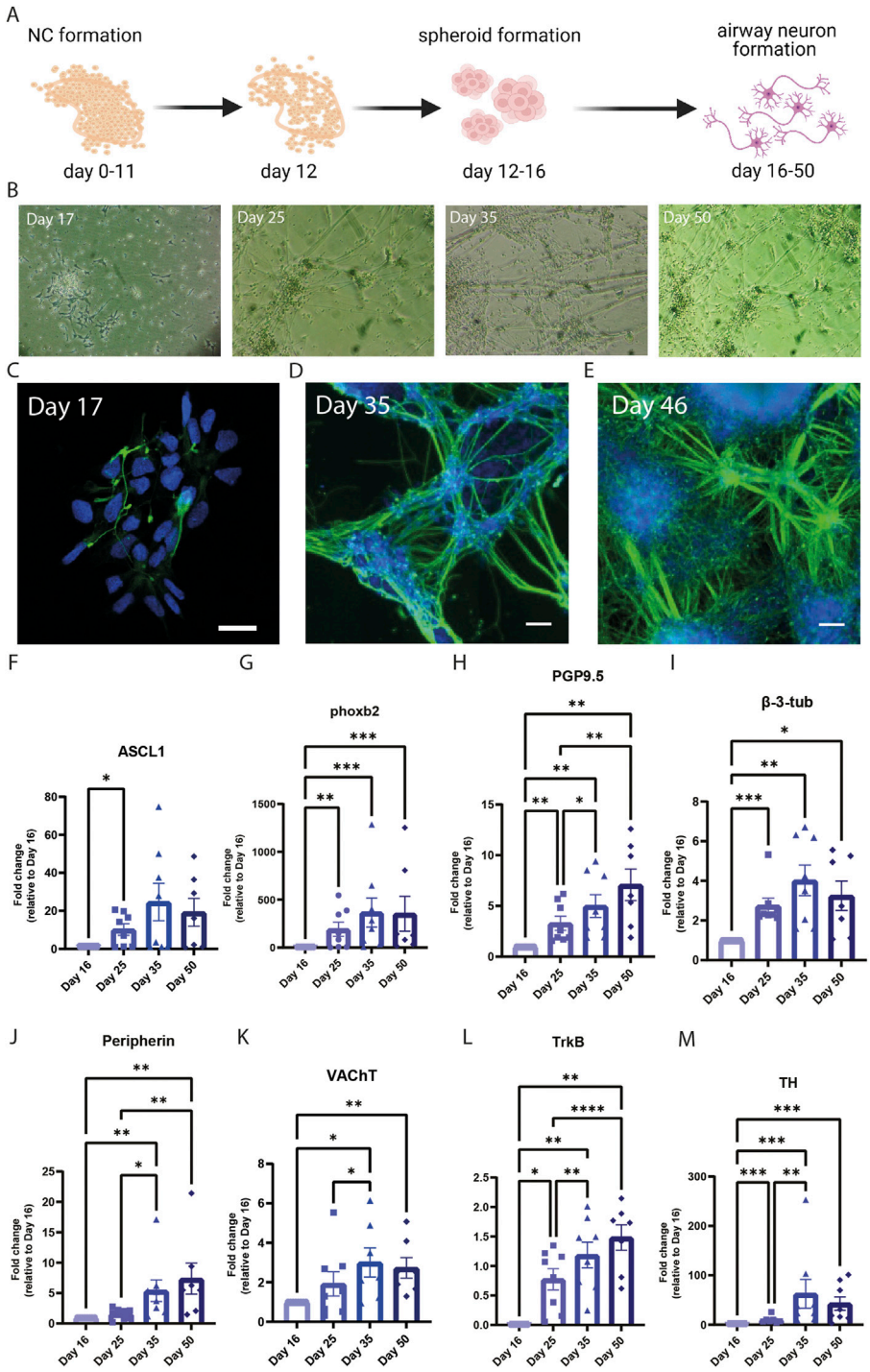

FIGURE 2
Differentiation of peripheral cholinergic neurons. **(A)** Schematic overview of hPSC differentiation into peripheral cholinergic neurons. Created with BioRender.com. **(B)** Brightfield images of the differentiating cells over time. **(C–E)** Immunofluorescence images of differentiating cells over time, showing the development of β-3-tubulin expression. Over time a greater neuronal network is being formed. Day 17, scale bar = 20 μm. Day 35 and day 46, scale bar = 100 μm. **(F–L)** Gene expression of airway cholinergic neuronal development over time. Gene expression was examined at different time points: Day 16, day 25, day 35, and day 50. ASCL1 **(F)** and phoxb2 **(G)** are essential for neuronal development and increased over the course of day 50. The pan-neuronal markers PGP9.5 **(H)** and β-3-tubulin **(I)** indicate the formation of neurons, in combination with peripherin **(J)** they indicate the development of peripheral neurons. VAChT **(K)**, indicating the formation of cholinergic neurons, was higher expressed over the course of 50 days. TH **(L)** showed a peak at day 35 before declining in expression towards day 50. TrkB **(M)** increased in expression over the course of 50 days (N = 8) A mixed-effect analysis followed by Tukey's multiple comparisons test was performed to calculate statistical significance between means. *$p < 0.05$; **$p < 0.01$; ***$p < 0.001$; ****$p < 0.0001$, compared to day 16.

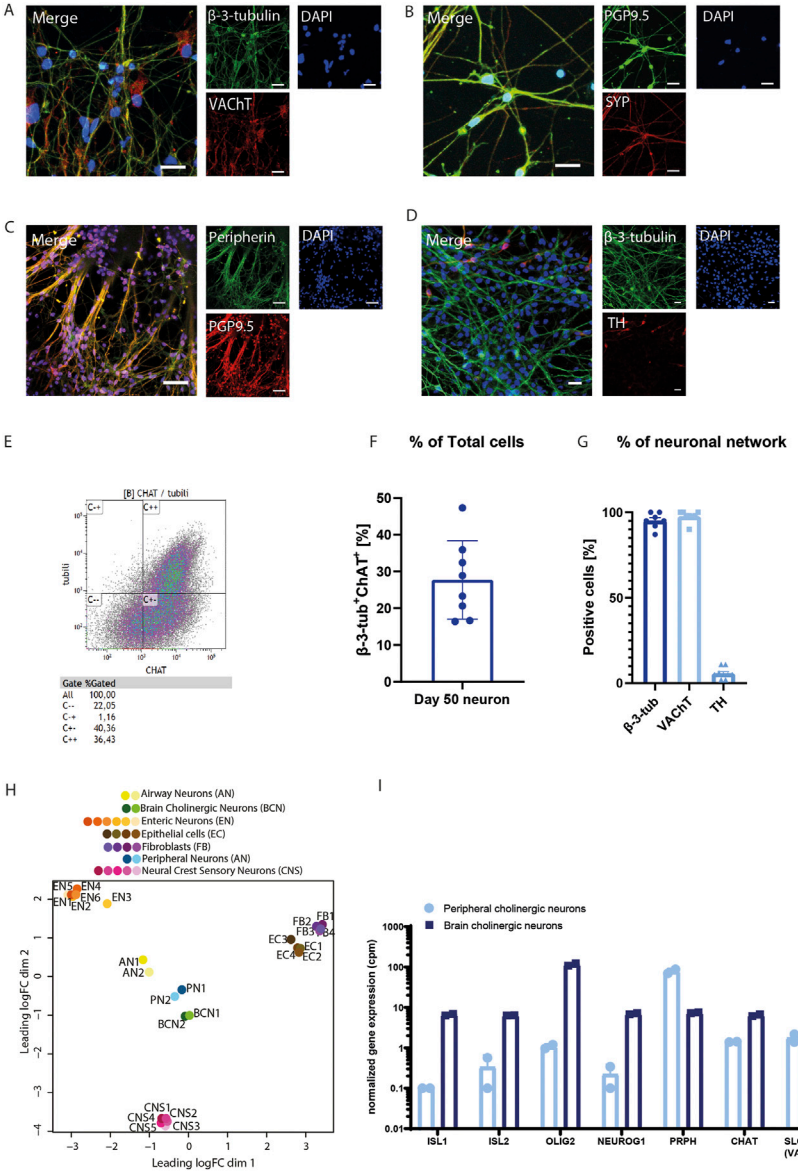

FIGURE 3
Peripheral cholinergic neurons **(A–D)**. Immunofluorescence images characterizing neurons. β-3-tubulin or PGP9.5 were used as a pan-neuronal marker. The neurons show the presence of VAChT **(A)** after 50 days of differentiation, in addition to SYP **(B)** and peripherin **(C)**. A smaller proportion of the neurons show TH$^+$ after 50 days. **(E–G)** FACS analysis demonstrated that 27.7% (±3.8%) of the neurons are β-3-tubulin$^+$-ChAT$^+$, indicative of cholinergic neurons. A representative FACS analysis plot is shown in E, panel F shows the quantification (n = 8). **(G)** Quantification of IF staining of β-3-tubulin (n = 6), VAChT (n = 8), and TH (n = 8) showed that the majority of sprouting cells expressed β-3-tubulin and VAChT, whilst TH was only sparsely present. **(H)** PCA analysis of RNAseq data showed that hPSC-derived airway neurons were distinct from airway epithelial cells or fibroblasts, but showed more overlap with hPSC-derived peripheral neurons or brain cholinergic neurons. **(I)** Despite similarities with brain cholinergic neurons in the PCA analysis, peripheral cholinergic neurons showed a distinct expression of central and peripheral markers with the central markers ISL1, ISL2, OLIG2 and NEUROG1 being enriched in brain cholinergic neurons and the peripheral marker PRPH being enriched in peripheral cholinergic neurons. Figures were presented as mean ± SEM.

acetylcholine transporter (VAChT, *SLC18A3*) expression confirmed the cholinergic phenotype of the neurons (Figure 2K).

Both VAChT (*SLC18A3*) and TrkB (*NTRK2*) increased over the course of 50 days, indicating neuronal formation and maturation (Figures 2K–M). Tyrosine hydroxylase (*TH*) is a marker for sympathetic neurons; however, it is also a precursor for cholinergic neurons during development (Weihe et al., 2006). Consistent with this contention, *TH* peaked in expression at day 35 of differentiation and declined afterward (Figure 2L). Our data implies that the cells matured over time

into peripheral cholinergic neurons as *TH* expression decreased (Figure 2L), and the expression of *PRPH* and *SLC18A3* increased.

Further identification of neuronal identity revealed that after 50 days, most of the generated airway neurons were VAChT$^+$ (Figure 3A), indicating a cholinergic phenotype. Neurons matured gradually into airway cholinergic neurons after 35 days of differentiation. On day 35, neurons stained positive for β-3-tubulin, while VAChT expression was sparse (Supplementary Figure S2A). Other important markers of the neuronal network include the presence of synaptophysin (SYP) and peripherin (Figures 3B,C). We observed TH expression using IF staining, but found that only a minor proportion of the generated neurons was TH$^+$ (Figures 3D,G), in contrast to abundant VAChT expression (Figures 3A,E–G). TH$^+$ neurons were not overlapping with VAChT$^+$ neurons (Supplementary Figure S2B). Most of the neurons appeared Peripherin$^+$ at day 50, indicating that the obtained neurons are PNS neurons, not central nervous system neurons (Figure 3C). Also, part of the neurons expressed SYP, indicating the presence of synapses. In autonomic neurons, synapses are distributed over the length of the axons, rather than having a synapse formed at the extremity end of the axons, which was also observed here (Figure 3B).

Airway cholinergic neurons use ACh as their primary neurotransmitter, which is produced by the presence of the ACh synthesizing enzyme ChAT. While direct assessment of ACh release by these cells is not possible due to insufficient sensitivity of such assays, FACS analysis further confirmed the final cholinergic phenotype of day 50 of neuronal differentiation and maturation. After 50 days of differentiation, 27.6% (SEM ±4.5%) of the totalcell population was β-3-tubulin$^+$-ChAT$^+$ (Figures 3E–G). Of importance, this is a percentage of total cells, including cells from the vagal spheroid as well as the cells that sprouted from the spheroids into neuronal networks. When the proportion of β-3-tubulin$^+$ cells was analyzed for ChAT expression, 80.0% (SEM ±6.5%) were ChAT$^+$ cells. Zooming in on the sprouted neuronal network only (excluding the vagal spheroids), quantification of the IF staining of these cells showed that 95.1% (SEM ±4.6%) of the sprouted cells were β-3-tubulin$^+$ and 97.6% (SEM ±3.3%) of the cells were VAChT$^+$ (Figure 3G), supporting the conclusion that the majority of the neurons sprouted from the vagal spheroids are cholinergic.

RNA sequencing analysis of two samples at day 50 of differentiation provided further support of the identity of the peripheral cholinergic neurons. Neuronal markers were abundantly present and in higher numbers than other neural crest derivatives like glial cells, mesenchymal cells, melanocytes, or endocrine cells. The pan-neuronal markers *NEFM* and *UCHL1* showed the highest read counts compared to other cell types (Supplementary Figures S3A-C). Mature peripheral cholinergic neurons display the autonomic ganglia-specific nicotinic and muscarinic ACh receptors: *CHRNA3*, *CHRNB4*, *CHRM2*, *CHRM3*, and *CHRM4* (Coulson and Fryer, 2003; Hollenhorst and Krasteva-Christ, 2021). These ACh receptors, especially the nicotinic receptor 3 (*CHRNA3*) and muscarinic receptor 3 (*CHRM3*), were present in the generated neurons. In addition, the glutamate receptor *VGLUT2* was abundantly expressed on day 50 neuronal differentiation, as well as the vesicular monoamine transporter *VMAT2I* (Supplementary Table S3).

We performed a comparison to determine the resemblance of the generated neurons with other cells types through principal component analysis (PCA). PCA is a statistical technique to summarize the information from extensive databases to improve interpretability while keeping as much information as possible (Jolliffe and Cadima, 2016). We compared the RNAseq profile of the obtained neurons with previously published datasets using hPSC-derived peripheral neurons (Lyoo et al., 2022), hPSC-derived neural crest sensory neurons (Nickolls et al., 2020), human-induced brain cholinergic neurons (from fetal fibroblasts) (Liu et al., 2013), human enteric neurons (May-Zhang et al., 2021), human epithelial cells, and human fibroblasts. Interestingly, the gene expression pattern from generated neurons most closely resembles that of hPSC-derived peripheral neurons and brain cholinergic neurons. On the other hand, enteric neurons, fibroblasts, epithelial cells, and neural crest sensory neurons remained quite distinct from the generated airway neurons with the current protocol (Figure 3H). While the peripheral cholinergic neurons showed expected similarities in gene expression to CNS cholinergic neurons, important differences exist between these subtypes that mark their different developmental origins. Crucially, the peripheral cholinergic neurons were negative in expression or showed limited expression of the neural tube markers *ISL1*, *ISL2*, *OLIG2* and *NEUROG2*, which were expressed in abundance by CNS cholinergic neurons (Figure 3I). In contrast, the peripheral cholinergic neurons were enriched in *PRPH* and in the vagal marker PAX3 (Figure 3I and Supplementary Figure S1).

Next, we investigated whether the generated neurons were functional using a multi-electrode array (MEA). Recordings of a MEA enable the measurement of neurons' spontaneous firing to validate neuronal maturation. Over the course of day 25 through day 73, neurons became more spontaneously active (Supplementary Figure S4).

Generation of a two-compartment microfluidic chip allowing directional axonal outgrowth and separate cell culture

PNS neurons extend their axons into peripheral tissues, and communicate with a diversity of target cells. Therefore, we designed and fabricated an *in vitro* cell culture device that mimics axonal communication (Taylor et al., 2005; Peyrin et al., 2011). Using PDMS, we fabricated a culture chamber

with two separate compartments connected by microchannels, as outlined in Supplementary Figure S5 and Supplementary Figure S6.

The device ensured a separate culture of different cell types in their culture medium: hydrostatic pressure prevented the mixing between the media from the somal and the axonal compartment. (Supplementary Video S2, demonstrated with food coloring).

A microfluidic neuron culture chip design is commercially available (Xona Microfluidics®) and consists of two main compartments, connected by an array of 3 µm by 3 µm microchannels that allow axonal communication between these chambers without mixing Soma (Supplementary Figure S6B, left panel). In initial experiments using SH-SY5Y cells, however, the channels were found too small for our purpose, and we could not guide axons into the axonal compartment. Altering the design to a bigger microchannel of 10 µm by 10 µm (Supplementary Figure S6B, center panel) resulted in axonal outgrowth; however, it also resulted in somal bodies moving into the axonal compartment. With this knowledge, we next developed a third design, inspired by Peyrin et al., which encompassed arrays of rectangular microchannels of decreasing width (Supplementary Figure S6B, right panel) (Peyrin et al., 2011). The resulting microfluidic chip also comprised two distinct cell culture chambers as the somal and axonal compartments. The compartments were connected by a series of 450 µm long, 3 µm high, asymmetrical microchannels starting at 15 µm entrance allowing optimal neuronal collection, followed by the narrow 3 µm tapering of the microchannels to promote unidirectional growth of axons and to ensure the confinement of SH-SY5Y cell bodies to the somal compartment (Supplementary Figure S6A).

hPSC-derived cholinergic neuron differentiation and characterization on a chip

Airway neurons were differentiated from hPSCs following the above described protocol (Figures 4A,B). The vagal NCCs were derived in six wells-plates in 16 days, and VP spheroids were plated into PLO/LM/FB coated chips for the remainder of the 50-day-differentiation period (Figure 4C). After 6 days of on-chip differentiation (day 22 of the hPSC-differentiation protocol), axons typically start to extend into the axonal compartment (Figures 4C,D). Over time, as the network of airway neurons expands, the extension of axons into the axonal compartment increases tremendously (Figures 4E,F). On-chip staining of hPSC-derived airway neurons confirmed the presence of vesicular acetylcholine transporter (VAChT), an important marker for airway cholinergic neurons (Figure 4G). In addition, the airway cholinergic neurons are peripherin^{+} (Figure 4H). A Ca^{2+} response to KCl in live cells was used to demonstrate the functionality of hPSC-derived airway cholinergic neurons. Imaging using conventional culture was compared to on-chip imaging of the generated neurons directly in the chip (Figures 6I–N). Using direct on-chip imaging, one can choose to image either the mix of somal bodies and axons in the somal compartment, or to visualize only axons in the axonal compartment. KCl was always added directly onto the somal bodies or into the somal compartment, where KCl stimulated the cells within seconds. Traces of Ca^{2+} were followed using FLUO-4 AM and quantified (Figures 4J,L,N). Imaging of somal bodies of cells cultured in a six wells-plate (Figures 4I,J, Supplementary Video S3) showed a similar Ca^{2+} response to KCl compared to somal bodies cultured on-chip and imaged in the somal compartment (Figures 4K–L, Supplementary Video S4). The Ca^{2+} response of axons measured in the axonal compartment was clearly present, even though cells were stimulated in the somal compartment. The Ca^{2+} response extended all the way into the axonal compartment (Figures 4M,N, Supplementary Video S5).

The axon-guidance chip is biocompatible and does not differ from conventional cell culture systems

ASM bundles in the lung are densely innervated, making ASM cells an interesting cell type to implement in co-cultures with neurons. To implement two co-culturing capabilities of the chip, neuronal-like SH-SY5Y cells and ASM cells were initially cultured in the chip simultaneously, in the somal and axonal compartment, respectively (Figure 5A). We investigated if an on-chip culture of cells would compromise their morphology and functionality compared to culture in plastic 6-well plates (6WP) and explored the advantages of on-chip culture. First, cell morphology did not differ between on-chip culture and 6WP culture for both the SH-SY5Y cells and the ASM cells (Figure 5B). The SH-SY5Y cells did not extend long neurites into the axonal compartment, as their neurites remain relatively short after differentiation. Still, the SH-SY5Y cells proved a suitable cell type to validate and optimize chip characteristics. An advantage of mounting the PDMS chip to a microscopic glass coverslip is that the coverslip allows on-chip staining and imaging. On-chip IF staining showed the confinement of both cells to their compartment (Figure 5C).

Comparing gene expression of the smooth muscle markers ACTA2 (α-sm-actin) and CHRM3 (M_3 receptor) of ASM cells both on-chip and in 6WPs showed no difference in expression between culture vessels (Figures 5D,E). Comparing ACTA2 expression of cells from either the somal compartment or the axonal compartment showed that ACTA2 mRNA was mainly expressed in the axonal compartment, in which ASM cells were cultured (Figure 5F). Similarly, the neuronal marker TUBB3 (β-3-tubulin) was mainly

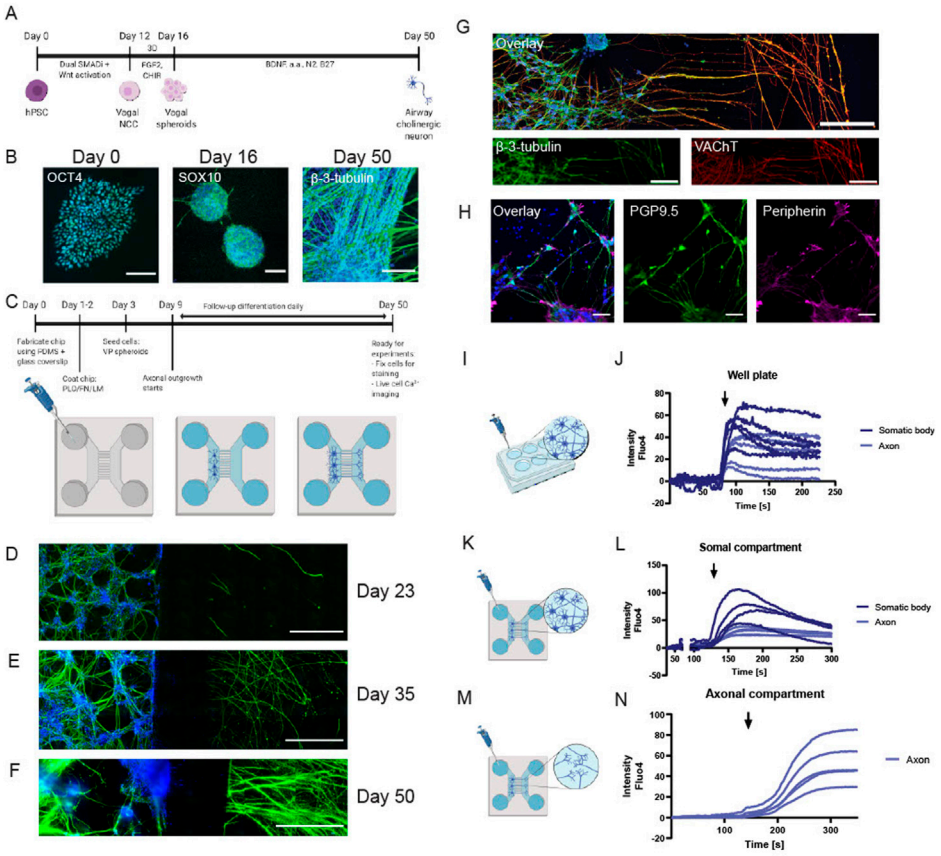

FIGURE 4
hPSC-derived peripheral cholinergic neurons on a chip. **(A)** Timeline of differentiation of peripheral neurons from hPSCs via vagal NCCs. In 50 days, peripheral cholinergic neurons were generated in the presence of BDNF. **(B)** If images of different stages of differentiation of hPSCs. Left: OCT4$^+$ hPSC colony at day 0 of differentiation. Scalebar = 200 µm. Middle: SOX10$^+$ vagal NCC spheroids at day 16 of differentiation. Scalebar = 200 µm. Right: β-3-tubulin$^+$ airway neurons at day 50 of differentiation. Scalebar = 50 µm. **(C)** Schematic overview of the timeline of stemcell seeding into the chips after fabrication; the chips were first coated with PLO/LM/FB, after which vagal NCC spheroids were dissociated and seeded into the chip. The medium was changed 2-3 times per week. Axons started to grow out of the microchannels into the axonal compartment after 6 days. Neurons were cultured into the chip up to day 50. **(D–F)**: IF images of β-3-tubilin$^+$ neurons showing increased axonal outgrowth over time. Scalebar = 500 µm **(D)**. At day 23 of differentiation (7 days on chip) some axonal outgrowth was visible, which increased towards day 35 **(E)** and day 50 **(F)**. **(G,H)** IF images of peripheral neurons showing the majority of neurons was VACHT$^+$ (G, scalebar = 200 µm) and peripherin$^+$ (H, scalebar = 50 µm). **(I–N)**. Schematic overview of Ca^{2+} imaging of hPSC-derived neurons cultured in six wells-plates or on-chip, plus traces of Ca^{2+} response of the generated neurons. KCl (60 mM) was added to the neurons or to a medium reservoir of the somal compartment. The time point of adding KCl is indicated with a black arrow. I-J. KCl stimulation and Ca^{2+} response of generated neurons cultured in a six wells-plate. **(K–L)** KCl stimulation and Ca^{2+} response of generated neurons cultured on-chip, neurons and axons were imaged in the somal compartment. **(M,N)** KCl stimulation and Ca^{2+} response of generated neurons cultured on-chip, axons were imaged in the axonal compartment. Shown are five representative traces for each experimental design, taken from n = 5 differentiations, each performed in 1-3 separate chips. Created with BioRender.com.

expressed in the somal compartment when comparing its gene expression of mRNA isolated from either the somal or the axonal compartment (Figure 5G).

Using the glass coverslip, live-cell fluorescent imaging using FLUO-4 AM could be performed directly on-chip as well. Stimulating ASM cells with 10 µM of methacholine (MCh), a muscarinic receptor agonist, showed similar responses in ASM cultured on coverslips on a 6WP compared to on-chip culture (Figures 5H,I). Collectively, this indicates that the chips can harbor and grow cells preserving phenotypic and functional features compared to conventional methods, with the advantage of direct on-chip imaging techniques and mRNA isolation of individual cell types after co-culture.

Next, ASM cells were added to the chips together with the hPSC-derived airway cholinergic neurons to complement the device for neuro-effector interactions. Airway neurons were first differentiated in the somal compartment for 2 weeks. After confirming that axon bundles passed through the microchannels on day 45, ASM cells were added to the axonal compartment (Figure 6A). The chip allows the addition of cell culture media optimal for each cell type; thus, both cells were cultured in their respective culture

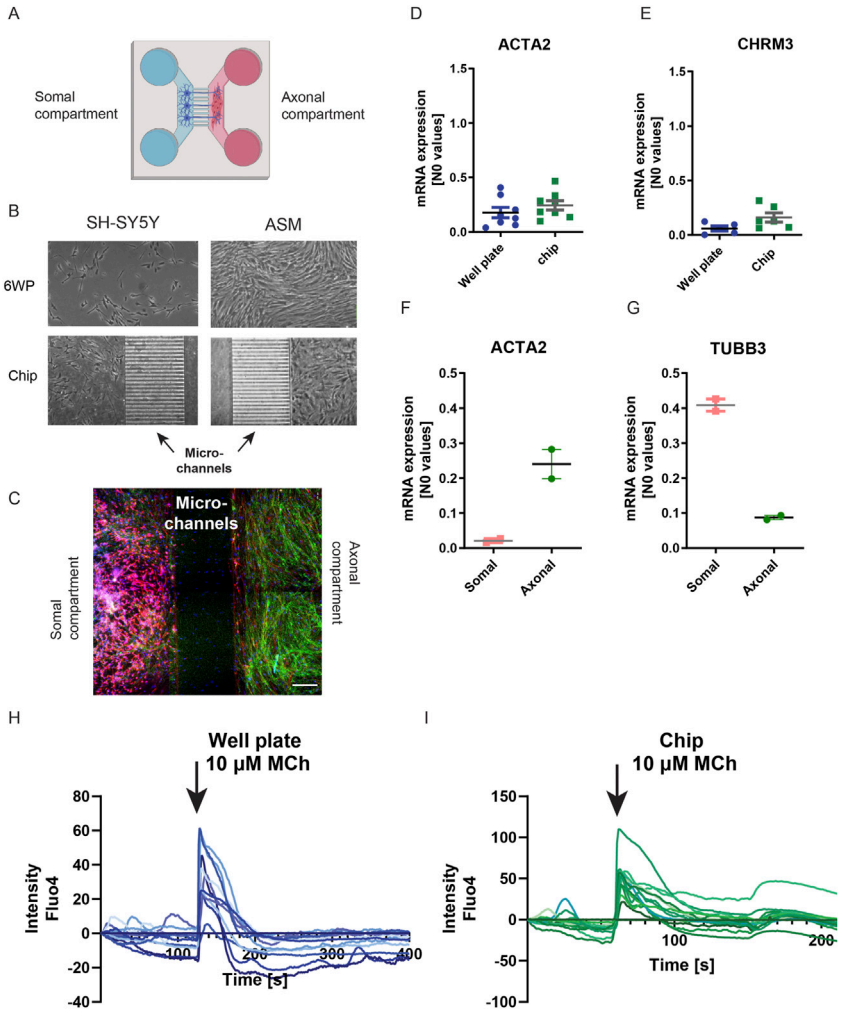

FIGURE 5
Comparing cell culture on-chip and in conventional cell culture. **(A)** Schematic overview of co-culture of neurons and ASM cells in the chip. In the left main compartment (blue) of the chip, neurons were seeded and in the right main compartment (red) ASM cells were seeded. Axons connected the two main compartments by growing for the neuronal to the axonal compartment. To compare, cells were cultured in a 6WP. Created with BioRender.com. **(B)** Left Brightfield images of neuronal-like SH-SYSY cells cultured both in a 6WP and in a chip. Right: Brightfield images of ASM cells cultured both in a 6WP and in a chip. Both SH-SY5Y and ASM cells had a similar morphology independent of the culture vessel. **(C)** IF image of an ASM-neuronal co-culture on-chip showed that both cell types are confined to their own compartment. Red: β-3-tubulin; green: Phalloidin. Scalebar = 200 µm. **(D,E)** mRNA expression of ASM cells cultured both in the chip and in a 6WP. The expression of ACTA2 and the CHRM3 receptor are similar for both culture vessels. F-G mRNA expression of cells isolated from individual channels. **(F)** ACTA2 expression of cells from either the somal compartment or the axonal compartment showed that ACTA2 was mainly expressed in the axonal compartment. **(G)** TUBB3 expression of cells isolated from either the somal or the axonal compartment showed that TUBB3 was mainly expressed in the somal compartment. **(H,I)** Live cell Ca^{2+} imaging using Fluo-4. MCh (10 µM) stimulation of ASM showed a similar trace for ASM both cultured in a 6WP or on-chip. The time point of adding MCh is indicated with a black arrow. Shown are individual traces of 10 regions of interest taken from n = 6 chips.

media as mentioned in the materials and methods. After co-culturing the generated neurons with ASM cells, we found the expression of synaptophysin (SYP), a marker for presynaptic vesicles (Figure 6B), after co-culturing the generated neurons with ASM. Indeed, the neuronal bundles innervated the ASM cells in the axonal compartment (Figures 6B–D). Staining of β-3-tubulin revealed that axons integrated with and innervated the ASM cells (Figure 6D, white arrows).

Discussion

Here, we established a cell culture protocol for the differentiation of peripheral cholinergic neurons suitable for studies on airway neuroplasticity along with a compartmentalized microfluidic device for the study of neuro-effector interactions in the lungs. We demonstrate the differentiation of peripheral cholinergic neurons *via* a vagal

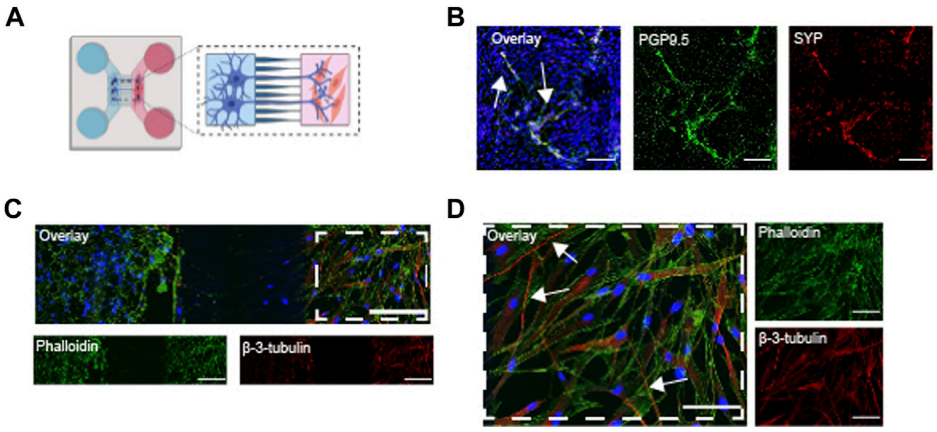

FIGURE 6
Co-cultures of hPSC-derived airway neurons and ASM cells on a chip **(A)** Schematic overview of the stem cell and ASM cell seeding into the chips after fabrication; Vagal NCCs were seeded and cultured in PLO/LM/FB coated chips up to day 45. The medium was changed 2-3 times per week. At day 45, ASM cells were seeded in the axonal compartment. Both cells were co-cultured for 5 days, up to day 50. **(B)** IF image of co-culture showing the expression of PGP9.5 and SYP in generated neurons. Scalebar = 50 μm. **(C)** IF image ASM cells and hPSC derived neurons. Phalloidin captured the actin-rich ASM cells and also the neurons (green). β-3-tubilin$^+$ neurons innervate ASM in the axonal compartment (red). Scalebar = 200 μm. **(D)** Close-up of IF image of co-culture. White arrows indicate some innervating neurons (red). Scalebar = 100 μm. Created with BioRender.com.

NCC precursor. The cholinergic phenotype, mainly present in the airways, was confirmed in our cultures by ChAT and VAChT expression. We improved the translational value of the model by creating an organ-on-chip model suitable for studying neuro-effector interactions. A PDMS chip was fabricated and successfully implemented. The PNS-on-chip model could serve as a useful experimental platform for monitoring neuro-effector interactions in various cell types and for investigating the effectiveness or safety of drugs.

The induction of the vagal precursors was highly efficient, with a >90% yield of HNK$^+$-p75$^+$ cells. This high efficiency is in accordance with vagal NCC induction for enteric neuronal development, showing a similar yield for NCC induction (Barber et al., 2019). The subsequent differentiation of vagal NCC into peripheral cholinergic neurons showed the formation of a neuronal network that kept increasing gradually, reflected both in protein and in gene expression. Protein expression analysis revealed that most neurons displayed a cholinergic phenotype. IF staining showed the utmost part of neurons to be VAChT$^+$, while only a minor part was TH$^+$. In addition, FACS analysis revealed ChAT expression in the majority of β-3-tubulin$^+$ cells. Comparing the generated neurons with other cells using a PCA affirmed that the characterization mainly overlaps with peripheral and brain cholinergic neuronal samples. Although the cholinergic phenotype is similar to central nervous system (CNS) cholinergic neurons, as expected, the developmental origin of these neuronal subtypes is completely distinct. CNS neurons are derived from the neural tube, not the neural crest and in line with this, the peripheral cholinergic neurons were derived from an essentially pure vagal precursor population at day 12, positive for PAX3 and negative for the neural tube marker PAX6. The enrichment of *PRPH* and lack of/limited expression of the CNS markers *ISL1*, *ISL2*, *OLIG2* and *NEUROG1* confirms this peripheral neuronal identity and clearly distinguishes these neurons from CNS cholinergic neurons. Similarly, RNAseq analysis showed that neurons were the predominant cell type in our samples. VAChT expression confirms maturation of the cholinergic neurons over time: at day 35, VAChT is hardly present, while at day 50, VAChT is present in the majority of neurons.

Following the changes in gene expression, the neuronal differentiation follows a developmental maturation as observed *in vivo*. TH is considered a marker for sympathetic neurons. However, it is also a precursor for airway cholinergic neurons during development (Weihe et al., 2006). TH is expressed transiently during development: in neurons and neuroendocrine cells, TH is expressed in cells that in adulthood no longer express TH or only at very low levels (Weihe et al., 2006). The peak expression of *TH* observed at day 35 of differentiation could be explained by a transient TH expression. The obtained neurons still express *TH* after 50 days of differentiation, directing towards an incomplete neuronal maturation. However, IF staining showed a minor proportion of cells were TH$^+$, which could be the transient expression or a small population of sympathetic neurons. In addition, gene expression for sensory neuronal markers was detected, indicating that although the cholinergic nerve population is highly enriched, minor populations of other neurons are present as well.

In the development of the chip, we passed through several optimization steps. The designed device was based on an

improved version of the commercially available XonaChip, incorporating a funnel-shaped structure of the microchannels to improve axonal in- and outgrowth. Moreover, the microchannel dimensions (3 μm × 3 μm at the exit of the channels) ensure that cell bodies cannot travel from the somal compartment into the axonal compartment or *vice versa*.

The design of the chip incorporates several advantages over conventional cell culture techniques and other versions of microfluidic chips. First, microfluidic chips use less medium compared to conventional culture plates. In the case of hPSC culture, medium can be costly. A range of analyses, such as staining or gene expression analysis, was simplified or improved using the chip. In the current design, we could perform an IF staining on-chip directly: instead of making the chip completely out of PDMS, we added a glass coverslip at the bottom of the system, allowing on-chip imaging. Direct on-chip imaging makes cell characterization using IF staining or live-cell imaging to test functionality a very accessible process. In addition, this chip design is easy implementable in other labs. Many chips rely on the use of flow pumps. Flow rate pumps have the disadvantage of taking up much space in cell culture incubators (Perdigones, 2021). Such static chips can easily be cultured with many at a time: a significant advantage to scaling experiments up. The design was based on hydrostatic pressure to seed cells and to supply medium and nutrients (Taylor et al., 2005). Some cell types, like endothelial cells, rely on flow for proper differentiation (Kim et al., 2013). Neurons, on the other hand, thrive in static conditions for their differentiation (Wang et al., 2017). In our experiments, the system without flow pumps was not only convenient for culture but also encompassed better experimental outcomes.

As we observed, many of the seeded vagal NCCs in the chip differentiated into neurons with long neurites. The axons extended through the 450 μm long microchannels and formed dense bundles in the axonal compartment, allowing to learn more about the axonal communication between the cholinergic nervous system and the lungs. The bundles stained positive for VAChT and peripherin, confirming the formation of cholinergic neurons from the PNS, which are predominant in the lungs. Here, the neurite bundles gave a clear view of Ca^{2+} traces after KCl stimulation of the somal bodies independently. The outgrowth of bundles into the neurite compartment could already be used as a platform to understand neuronal outgrowth and development and to measure the response of axons after neuronal stimulation adequately. Many drugs have been developed in the central nervous system that target neuroplasticity, whereas drugs targeting the PNS are lacking (Goldsteen et al., 2020). Visualizing the neuronal network aids in developing PNS neuroplasticity models and subsequent drug development and testing.

A next challenge for an on-chip *in vitro* model would be this indirect activation of effector cells. Innervation of the airways during development relies on guidance from ASM (Aven and Ai, 2013), making ASM a logical cell type to implement in co-cultures with neurons. To implement patient-specific neuro-effector cultures, one could also differentiate smooth muscle cells from hPSCs. However, among the many differentiation protocols that are available for smooth muscle cells, none is able to generate tissue-specific smooth muscle cells (Goldsteen et al., 2021). We valued the inherent properties that ASM cells have to aid the differentiation into airway neurons specifically, hence our choice for immortalized human ASM cells. Still, now that the first step for an airway nervous system on a chip is established, other cell types can be used to co-culture with airway cholinergic neurons. Nevertheless, for each chosen effector cell used for the on-chip neuro-effector interactions applies: especially the individual mRNA isolation from each cell type might, for the first time, enable *in vitro* experiments to determine the contribution of each cell type to the onset of neuroplasticity.

The use of stem cell-derived sources of differentiated human cells has its advantages as these primary cells are often difficult to obtain. However, important limitations to this approach need to be acknowledged and our work is no exception. hPSC derived cells often maintain a relatively immature phenotype in comparison to primary cells. When comparing electrophysiological properties of hPSC-derived neurons and primary neurons using MEA recordings, our hPSC-derived neurons were found to have relatively limited spontaneous firing activity. Furthermore, while co-cultures in the chip can be established, it remains to be confirmed that such co-cultures adequately recapitulate the neuro-effector junction *in situ*. These are challenges on the horizon that are worthwhile resolving. Until that time, the hPSC derived neurons are likely most suitable for neurodevelopmental, neuronal differentiation and neuroplasticity related questions.

Conclusion

In conclusion, we have demonstrated the ability to differentiate hPSCs into peripheral cholinergic neurons suitable for studies on airway neuroplasticity in asthma *via* a vagal precursor using chemically defined media. We have implemented these neurons on a two-compartment axon guidance chip for the study of airway neurobiology and established that phenotypic and functional characteristics of the cells are preserved in the microfluidic chip. The organ-on-chip device can provide a valuable tool as a human *in vitro* model that aids in the discovery of important neuro-effector mechanisms. In addition, understanding the pathophysiological mechanism of airway neuronal plasticity and the interaction of airway cholinergic neurons with effector cells might contribute to our understanding of neuro-effector interactions in asthma.

Data availability statement

The datasets presented in this study can be found in online repositories. The names of the repository/repositories and accession number(s) can be found below: https://www.ncbi.nlm.nih.gov/geo; GSE211478.

Author contributions

PG, KM, LK, AD, and RG conceived the study. PG, AD, and RG designed the experiments. PG, AS, PM, IB, ME, LV, and JS performed the experiments and analyzed the data. AJH provided the airway smooth muscle cells for the study. PG, PM, and EV manufactured the chip. PG drafted the first version of the manuscript. All authors interpreted the data, contributed to manuscript revision, read, and approved the submitted version.

Funding

The work was financially supported by the More Knowledge with Fewer Animals (Meer Kennis met Minder Dieren) programme of ZonMW (grant number 114021505) with co-financing from Stichting Proefdiervrij, Aquilo BV, Boehringer Ingelheim and Longfonds. AH is supported by the Canada Research Chairs Program.

Acknowledgments

We would like to thank Floris Foijer (ERIBA, Groningen, the Netherlands) for the cells he kindly provided, and we thank Valentina Pegoretti (University of Groningen, Groningen, the Netherlands) and Peter Oomen (University of Groningen, Groningen, Netherlands) for the initial support on the design of the microfluidic chips, and Marina Trombetta Lima (University of Groningen, Groningen, Netherlands) for her technical assistance.

Conflict of interest

LK is employed by the company Aquilo BV.

The remaining authors declare that the research was conducted in the absence of any commercial or financial relationships that could be construed as a potential conflict of interest.

Publisher's note

All claims expressed in this article are solely those of the authors and do not necessarily represent those of their affiliated organizations, or those of the publisher, the editors and the reviewers. Any product that may be evaluated in this article, or claim that may be made by its manufacturer, is not guaranteed or endorsed by the publisher.

Supplementary material

The Supplementary Material for this article can be found online at: https://www.frontiersin.org/articles/10.3389/fphar.2022.991072/full#supplementary-material

References

Aven, L., and Ai, X. (2013). Mechanisms of respiratory innervation during embryonic development. *Organogenesis* 9, 194–198. doi:10.4161/org.24842

Barber, K., Studer, L., and Fattahi, F. (2019). Derivation of enteric neuron lineages from human pluripotent stem cells. *Nat. Protoc.* 14, 1261–1279. doi:10.1038/s41596-019-0141-y

Betters, E., Liu, Y., Kjaeldgaard, A., Sundström, E., and García-Castro, M. I. (2010). Analysis of early human neural crest development. *Dev. Biol.* 344, 578–592. doi:10.1016/j.ydbio.2010.05.012

Campenot, R. B. (1977). Local control of neurite development by nerve growth factor. *Proc. Natl. Acad. Sci. U. S. A.* 74, 4516–4519. doi:10.1073/pnas.74.10.4516

Chan, K. K., Chen, Y. S., Yau, T. O., Fu, M., Lui, V. C. H., Tam, P. K. H., et al. (2005). Hoxb3 vagal neural crest-specific enhancer element for controlling enteric nervous system development. *Dev. Dyn.* 233, 473–483. doi:10.1002/dvdy.20347

Coulson, F. R., and Fryer, A. D. (2003). Muscarinic acetylcholine receptors and airway diseases. *Pharmacol. Ther.* 98, 59–69. doi:10.1016/s0163-7258(03)00004-4

Cramer, S. C., Sur, M., Dobkin, B. H., O'Brien, C., Sanger, T. D., Trojanowski, J. Q., et al. (2011). Harnessing neuroplasticity for clinical applications. *Brain* 134, 1591–1609. doi:10.1093/brain/awr039

Dragunas, G., Woest, M. E., Nijboer, S., Bos, S. T., van Asselt, J., de Groot, A. P., et al. (2020). Cholinergic neuroplasticity in asthma driven by TrkB signaling. *FASEB J.* 34, 7703–7717. doi:10.1096/fj.202000170R

Drake, M. G., Scott, G. D., Blum, E. D., Lebold, K. M., Nie, Z., Lee, J. J., et al. (2018). Eosinophils increase airway sensory nerve density in mice and in human asthma. *Sci. Transl. Med.* 10, eaar8477. doi:10.1126/scitranslmed.aar8477

Fattahi, F., Steinbeck, J. A., Kriks, S., Tchieu, J., Zimmer, B., Kishinevsky, S., et al. (2016). Deriving human ENS lineages for cell therapy and drug discovery in Hirschsprung disease. *Nature* 531, 105–109. doi:10.1038/nature16951

Goldsteen, P. A., Dolga, A. M., and Gosens, R. (2020). Advanced modeling of peripheral neuro-effector communication and -plasticity. *Physiology* 35, 348–357. doi:10.1152/physiol.00010.2020

Goldsteen, P. A., Yoseif, C., Dolga, A. M., and Gosens, R. (2021). Human pluripotent stem cells for the modelling and treatment of respiratory diseases. *Eur. Respir. Rev.* 30, 210042. doi:10.1183/16000617.0042-2021

Hao, M. M., and Young, H. M. (2009). Development of enteric neuron diversity. *J. Cell. Mol. Med.* 13, 1193–1210. doi:10.1111/j.1582-4934.2009.00813.x

Hollenhorst, M. I., and Krasteva-Christ, G. (2021). Nicotinic acetylcholine receptors in the respiratory tract. *Molecules* 26, 6097. doi:10.3390/molecules26206097

Huang, E. J., and Reichardt, L. F. (2001). Neurotrophins: Roles in neuronal development and function. *Annu. Rev. Neurosci.* 24, 677–736. doi:10.1146/annurev.neuro.24.1.677

Hutchins, E. J., Kunttas, E., Piacentino, M. L., Howard, A. G. A., Bronner, M. E., and Uribe, R. A. (2018). Migration and diversification of the vagal neural crest. *Dev. Biol.* 444, S98–S109. doi:10.1016/j.ydbio.2018.07.004

Jellali, R., Bricks, T., Jacques, S., Fleury, M. J., Paullier, P., Merlier, F., et al. (2016). Long-term human primary hepatocyte cultures in a microfluidic liver biochip show maintenance of mRNA levels and higher drug metabolism compared with Petri cultures. *Biopharm. Drug Dispos.* 37, 264–275. doi:10.1002/bdd.2010

Jolliffe, I. T., and Cadima, J. (2016). Principal component analysis: A review and recent developments. *Philos. Trans. A Math. Phys. Eng. Sci.* 374, 20150202. doi:10.1098/rsta.2015.0202

Kam, M. K. M., and Lui, V. C. H. (2015). Roles of Hoxb5 in the development of vagal and trunk neural crest cells. *Dev. Growth Differ.* 57, 158–168. doi:10.1111/dgd.12199

Kim, S., Lee, H., Chung, M., and Jeon, N. L. (2013). Engineering of functional, perfusable 3D microvascular networks on a chip. *Lab. Chip* 13, 1489–1500. doi:10.1039/c3lc41320a

Kistemaker, L. E. M., and Prakash, Y. S. (2019). Airway innervation and plasticity in asthma. *Physiology* 34, 283–298. doi:10.1152/physiol.00050.2018

Leenaars, C. H. C., Kouwenaar, C., Stafleu, F. R., Bleich, A., Ritskes-Hoitinga, M., De Vries, R. B. M., et al. (2019). Animal to human translation: A systematic scoping review of reported concordance rates. *J. Transl. Med.* 17, 223. doi:10.1186/s12967-019-1976-2

Liu, M.-L., Zang, T., Zou, Y., Chang, J. C., Gibson, J. R., Huber, K. M., et al. (2013). Small molecules enable neurogenin 2 to efficiently convert human fibroblasts into cholinergic neurons. *Nat. Commun.* 4, 2183. doi:10.1038/ncomms3183

Lyoo, K.-S., Kim, H. M., Lee, B., Kim, S. J., and Song, D. (2022). Direct neuronal infection of SARS-CoV-2 reveals cellular and molecular pathology of chemosensory impairment of COVID-19 patients. *Emerg. Microbes Infect.* 11, 406–411. doi:10.1080/22221751.2021.2024095

Mata, A., Fleischman, A. J., and Roy, S. (2005). Characterization of polydimethylsiloxane (PDMS) properties for biomedical micro/nanosystems. *Biomed. Microdevices* 7, 281–293. doi:10.1007/s10544-005-6070-2

May-Zhang, A. A., Tycksen, E., Southard-Smith, A. N., Deal, K. K., Benthal, J. T., Buehler, D. P., et al. (2021). Combinatorial transcriptional profiling of mouse and human enteric neurons identifies shared and disparate subtypes *in situ*. *Gastroenterology* 160, 755e26–770.e26. doi:10.1053/j.gastro.2020.09.032

Monsoro-Burq, A. H. (2015). PAX transcription factors in neural crest development. *Semin. Cell Dev. Biol.* 44, 87–96. doi:10.1016/j.semcdb.2015.09.015

Neto, E., Alves, C. J., Sousa, D. M., Alencastre, I. S., Lourenco, A. H., Leitao, L., et al. (2014). Sensory neurons and osteoblasts: Close partners in a microfluidic platform. *Integr. Biol.* 6, 586–595. doi:10.1039/c4ib00035h

Nickolls, A. R., Lee, M. M., Espinoza, D. F., Szczot, M., Lam, R. M., Wang, Q., et al. (2020). Transcriptional programming of human mechanosensory neuron subtypes from pluripotent stem cells. *Cell Rep.* 30, 932e7–946. doi:10.1016/j.celrep.2019.12.062

Nockher, W. A., and Renz, H. (2006). Neurotrophins in allergic diseases: From neuronal growth factors to intercellular signaling molecules. *J. Allergy Clin. Immunol.* 117, 583–589. doi:10.1016/j.jaci.2005.11.049

Perdigones, F. (2021). Lab-on-PCB and flow driving: A critical review. *Micromachines* 12, 175. doi:10.3390/mi12020175

Peyrin, J.-M., Deleglise, B., Saias, L., Vignes, M., Gougis, P., Magnifico, S., et al. (2011). Axon diodes for the reconstruction of oriented neuronal networks in microfluidic chambers. *Lab. Chip* 11, 3663–3673. doi:10.1039/c1lc20014c

Pound, P., and Bracken, M. B. (2014). Is animal research sufficiently evidence based to be a cornerstone of biomedical research? *BMJ Br. Med. J.* 348, g3387. doi:10.1136/bmj.g3387

Radzikinas, K., Aven, L., Jiang, Z., Tran, T., Paez-Cortez, J., Boppidi, K., et al. (2011). A shh/miR-206/BDNF cascade coordinates innervation and formation of airway smooth muscle. *J. Neurosci.* 31, 15407–15415. LP – 15415. doi:10.1523/JNEUROSCI.2745-11.2011

Ricci, A., Felici, L., Mariotta, S., Mannino, F., Schmid, G., Terzano, C., et al. (2004). Neurotrophin and neurotrophin receptor protein expression in the human lung. *Am. J. Respir. Cell Mol. Biol.* 30, 12–19. doi:10.1165/rcmb.2002-0110OC

Taylor, A. M., Blurton-Jones, M., Rhee, S. W., Cribbs, D. H., Cotman, C. W., and Jeon, N. L. (2005). A microfluidic culture platform for CNS axonal injury, regeneration and transport. *Nat. Methods* 2, 599–605. doi:10.1038/nmeth777

Taylor, A. M., Rhee, S. W., Tu, C. H., Cribbs, D. H., Cotman, C. W., and Jeon, N. L. (2003). Microfluidic multicompartment device for neuroscience research. *Langmuir* 19, 1551–1556. doi:10.1021/la026417v

Undem, B. J., and Taylor-Clark, T. (2014). Mechanisms underlying the neuronal-based symptoms of allergy. *J. Allergy Clin. Immunol.* 133, 1521–1534. doi:10.1016/j.jaci.2013.11.027

van der Velden, V. H., and Hulsmann, A. R. (1999). Autonomic innervation of human airways: Structure, function, and pathophysiology in asthma. *Neuroimmunomodulation* 6, 145–159. doi:10.1159/000026376

Vasina, V., Barbara, G., Talamonti, L., Stanghellini, V., Corinaldesi, R., Tonini, M., et al. (2006). Enteric neuroplasticity evoked by inflammation. *Auton. Neurosci.* 126–127, 264–272. doi:10.1016/j.autneu.2006.02.025

Vitale, A., Quaglio, M., Cocuzza, M., Pirri, C. F., and Bongiovanni, R. (2012). Photopolymerization of a perfluoropolyether oligomer and photolithographic processes for the fabrication of microfluidic devices. *Eur. Polym. J.* 48, 1118–1126. doi:10.1016/j.eurpolymj.2012.03.016

Wang, Y., Ma, J., Li, N., Wang, L., Shen, L., Sun, Y., et al. (2017). Microfluidic engineering of neural stem cell niches for fate determination. *Biomicrofluidics* 11, 014106. doi:10.1063/1.4974902

Weihe, E., Depboylu, C., Schütz, B., Schäfer, M. K.-H., and Eiden, L. E. (2006). Three types of tyrosine hydroxylase-positive CNS neurons distinguished by dopa decarboxylase and VMAT2 co-expression. *Cell. Mol. Neurobiol.* 26, 659–678. doi:10.1007/s10571-006-9053-9

Takayama, Y., and Kida, Y. S. (2016). *In Vitro* Reconstruction of Neuronal Networks Derived from Human iPS Cells Using Microfabricated Devices. *PLoS One* 11, e0148559. doi:10.1371/journal.pone.0148559

Trombetta-Lima, M., Sabogal-Guáqueta, A. M., and Dolga, A. M. (2021). Mitochondrial dysfunction in neurodegenerative diseases: A focus on iPSC-derived neuronal models. *Cell Calcium* 94, 102362. doi:10.1016/j.ceca.2021.102362

frontiers | Frontiers in Pharmacology

TYPE Original Research
PUBLISHED 03 November 2022
DOI 10.3389/fphar.2022.989169

OPEN ACCESS

EDITED BY
Ramaswamy Krishnan,
Beth Israel Deaconess Medical Center,
Harvard Medical School, United States

REVIEWED BY
Erzsébet Bartolák-Suki,
Boston University, United States
Matthew Lech,
Pfizer, United States

*CORRESPONDENCE
Janette K. Burgess,
j.k.burgess@umcg.nl

SPECIALTY SECTION
This article was submitted to Respiratory Pharmacology, a section of the journal Frontiers in Pharmacology

RECEIVED 08 July 2022
ACCEPTED 24 October 2022
PUBLISHED 03 November 2022

CITATION
Blokland KEC, Nizamoglu M, Habibie H, Borghuis T, Schuliga M, Melgert BN, Knight DA, Brandsma C-A, Pouwels SD and Burgess JK (2022), Substrate stiffness engineered to replicate disease conditions influence senescence and fibrotic responses in primary lung fibroblasts.
Front. Pharmacol. 13:989169.
doi: 10.3389/fphar.2022.989169

Substrate stiffness engineered to replicate disease conditions influence senescence and fibrotic responses in primary lung fibroblasts

Kaj E. C. Blokland[1,2,3,4], Mehmet Nizamoglu[1,2], Habibie Habibie[2,5,6], Theo Borghuis[1,2], Michael Schuliga[3], Barbro N. Melgert[1,2,5], Darryl A. Knight[3,4,7], Corry-Anke Brandsma[1,2], Simon D. Pouwels[1,2,8] and Janette K. Burgess[1,2]*

[1]University of Groningen, University Medical Center Groningen, Department of Pathology and Medical Biology, Groningen, Netherlands, [2]University of Groningen, University Medical Center Groningen, Groningen Research Institute for Asthma and COPD, Groningen, Netherlands, [3]University of Newcastle, School of Biomedical Sciences and Pharmacy, Callaghan, NSW, Australia, [4]National Health and Medical Research Council Centre of Research Excellence in Pulmonary Fibrosis, Sydney, NSW, Australia, [5]University of Groningen, Department of Molecular Pharmacology, Groningen Research Institute of Pharmacy, Groningen, Netherlands, [6]Hasanuddin University, Faculty of Pharmacy, Makassar, Indonesia, [7]Providence Health Care Research Institute, Vancouver, BC, Canada, [8]University of Groningen, University Medical Center Groningen, Department of Pulmonology, Groningen, Netherlands

In fibrosis remodelling of ECM leads to changes in composition and stiffness. Such changes can have a major impact on cell functions including proliferation, secretory profile and differentiation. Several studies have reported that fibrosis is characterised by increased senescence and accumulating evidence suggests that changes to the ECM including altered composition and increased stiffness may contribute to premature cellular senescence. This study investigated if increased stiffness could modulate markers of senescence and/or fibrosis in primary human lung fibroblasts. Using hydrogels representing stiffnesses that fall within healthy and fibrotic ranges, we cultured primary fibroblasts from non-diseased lung tissue on top of these hydrogels for up to 7 days before assessing senescence and fibrosis markers. Fibroblasts cultured on stiffer (±15 kPa) hydrogels showed higher Yes-associated protein-1 (YAP) nuclear translocation compared to soft hydrogels. When looking at senescence-associated proteins we also found higher secretion of receptor activator of nuclear factor kappa-B ligand (RANKL) but no change in transforming growth factor-β1 (TGF-β1) or connective tissue growth factor (CTGF) expression and higher decorin protein deposition on stiffer matrices. With respect to genes associated with fibrosis, fibroblasts on stiffer hydrogels compared to soft had higher expression of smooth muscle alpha (α)-2 actin (*ACTA2*), *collagen (COL) 1A1* and *fibulin-1* (Fbln1) and higher Fbln1 protein deposition after 7 days. Our results show that exposure of lung fibroblasts to fibrotic stiffness activates genes and secreted factors that are part of fibrotic

responses and part of the Senescence-associated secretory phenotype (SASP). This overlap may contribute to the creation of a feedback loop whereby fibroblasts create a perpetuating cycle reinforcing progression of a fibrotic response.

KEYWORDS

cellular senescence, stiffness, GelMA hydrogels, fibrosis, SASP

1 Introduction

The extracellular matrix (ECM) is a complex structure composed of various proteins, proteoglycans and other biological factors that are secreted and/or modified by cells embedded within this microenvironment (Bonnans et al., 2014). Our understanding of ECM has greatly advanced in the last decade, particularly with respect to its role in providing essential biochemical and biomechanical cues that regulate cellular functions (Hansen et al., 2015; Zhou et al., 2018). During normal tissue homeostasis, fibroblasts that reside in the ECM are maintained in a quiescent state; meaning they do not proliferate but secrete, sustain, and remodel the ECM. The biomechanical cues provided by the three-dimensional ECM, that provides the microenvironment in which these cells reside, regulate cellular processes such as adhesion, migration, proliferation, and differentiation (Liu et al., 2010; Huang et al., 2012). Using specific receptors, including integrins, fibroblasts are able to sense and respond to changes in the ECM (Sapir and Tzlil, 2017). The mechanical forces that are generated in response to changes in the ECM local environment generate signals within the cell that rapidly propagate and activate signalling pathways (Tschumperlin et al., 2018).

The remodelling of ECM during fibrosis leads to a change in composition, structural organisation, increased crosslinking, and ultimately increased stiffness. The stiffness of healthy tissue does not exceed 5 kPa while in fibrotic tissue, the stiffness can be up to 30 times stiffer. The range of fibrotic stiffness varies depending on location and it has been reported that locally tissue can be as stiff as 20–100 kPa while the average stiffness is approximately 17 kPa (Foucher et al., 2006; Liu et al., 2010; Booth et al., 2012; Hinz, 2012; Petzold et al., 2019; de Hilster et al., 2020; Leong et al., 2021). These changes greatly influence the biochemical and biomechanical properties of the ECM, leading to alterations in cellular response such as migration and proliferation (Blokland et al., 2020a). Tissue damage that leads to disruption of mechanical homeostasis drives mechano-activation of quiescent fibroblasts into myofibroblasts, which is a feature of tissue wound repair (Humphrey et al., 2014). After successful wound repair myofibroblasts are cleared from the tissue *via* apoptosis to prevent excessive ECM production and contraction (Li and Wang, 2011). Myofibroblasts are characterised by expression of contractile proteins such as α-smooth muscle actin (αSMA) and their ability to contract tissue. During repair they play a key role in remodelling the injured tissue and are responsible for excessive ECM deposition in fibrotic diseases such as idiopathic pulmonary fibrosis (IPF). Furthermore, as a direct effect of increased matrix stiffness, fibroblasts will produce and secrete transforming growth factor (TGF)-β1, a key fibrogenic mediator (Piersma et al., 2015a; Piersma et al., 2015b). The increased stiffness and secretion of cytokines reinforce the activation which results in myofibroblast activation and progression of fibrosis creating a perpetuating feedback loop (Yan et al., 2018).

Cells that undergo (premature) cellular senescence show marked changes in morphology, phenotype, and metabolism. Most notably, irreversible cell-cycle arrest and apoptosis resistance are defining features of cellular senescence. Senescent cells remain metabolically active and acquire a dynamic pro-inflammatory secretory profile known as the Senescence-Associated Secretory Phenotype (SASP) (Coppe et al., 2010). The SASP is comprised of differently secreted pro-inflammatory and pro-fibrotic cytokines which impact on neighbouring cells and the local microenvironment (Blokland et al., 2020b). To which degree altered ECM contributes to fibrosis progression is not yet fully understood, specifically in relation to cellular senescence. Evidence is emerging that increased tissue stiffness might contribute to cellular senescence. Recently it was described that stiffness could lead to increase ROS productions which is linked to cellular senescence *via* activation of STAT3 (Waters et al., 2019; Wang et al., 2021). In addition, pathological stiffness leads to upregulation of TGF-β1, lysyl oxidase (LOX) and downregulation of micro-RNA-29 together with increased deposition of matricellular proteins they could potentially regulate cell-cycle arrest, apoptosis, and production of cytokines through the SASP (Blokland et al., 2020a). Increased ECM stiffness may drive excessive ECM production creating a perpetuating feedback loop in favour of disease progression. We hypothesised that the increased stiffness of fibrotic ECM detrimentally influences fibroblast function to perpetuate disease progression in fibrosis. Here we aimed to investigate whether adjusting the stiffness of *in vitro* produced methacrylated-gelatine (GelMA) hydrogels resembling the stiffness of healthy and fibrotic tissues could

modulate cellular senescence, the SASP or the fibrotic response in primary human lung fibroblasts.

2 Materials and methods

2.1 Methacrylated-gelatine synthesis

Gelatine was functionalised as described before with small modifications to the original protocol (Shirahama et al., 2016). Ten grams medical grade 262 Bloom Type A gelatine (Gelita, Ter Apelkanaal, the Netherlands) was added to 1 L 0.25 M carbonate-bicarbonate (CB, Sigma-Aldrich, Zwijndrecht, the Netherlands) buffer pH 9.0 and allowed to dissolve at 50°C for 60 min. Heating was turned off and then 563 µL methacrylic anhydride (MAA; Sigma-Aldrich, CCID: 12974) was added dropwise in three steps. Ten minutes after each step the pH was measured and corrected using a 3 M NaOH (Sigma-Aldrich, CCID: 14798) solution to maintain pH 9.0. The gelatine-MAA solution was allowed to react overnight at room temperature (RT) while stirring. The next day the GelMA solution was dialysed using dialysis with molecular weight cut-off of 12–14 kDa (Sigma-Aldrich) for up to 5 days against deionised water pH 9.0. After dialysis, GelMA solution was aliquoted in 50 ml tubes, frozen with liquid nitrogen and lyophilised on a Labconco Freezone 2.5 L benchtop freeze-dryer (Labconco, Kansas City, MO, United States). Samples were considered dry when weights of the tubes were stable. Three batches were produced, lyophilised, re-dissolved into one large batch and then lyophilised again to minimise batch-to-batch variation.

2.2 Trinitrobenzenesulfonic acid assay

The degree of modification of GelMA was measured using a Trinitrobenzenesulfonic acid (TNBS) colorimetric assay (Ravichandran et al., 2016). Two mg of dry GelMA and gelatine were dissolved in 1 ml of 4% w/v sodium bicarbonate solution (Sigma-Aldrich) and 1 ml of 0.5% w/v TNBS solution (Sigma-Aldrich, CCID:11045) followed by incubation at 40°C with mild shaking for 2 h. Afterwards, the solution was transferred to a 7.5 ml glass bottle and 3 ml 6N HCL solution (Sigma-Aldrich, CCID: 313) was added to stop the reaction. Unreacted TNBS was extracted twice with diethyl ether (Sigma-Aldrich, CCID: 3283) by removing the upper phase. Absorbance (346 nm) of samples was measured using a Benchmark plus UV-VIS spectrophotometer (Bio-Rad Technologies). A blank sample was generated as described above but without the addition of GelMA or gelatine and was subtracted from each measurement. The degree of functionalisation (%DoF) was calculated using the formula:

$$[\ (\text{AbsGelatine} - \text{AbsGelMA})\ /\ \text{AbsGelatine}\ ] \times 100\%$$

2.3 Fabrication of GelMA hydrogels

GelMA samples were dissolved at 5 and 8% w/v in PBS containing 1% w/v filter sterilised lithium phenyl-2,4,6-trimethylbenzoylphosphinate (LAP; TCI Europe, Zwijndrecht, Belgium, CCID: 68384915), and kept in the dark at 37 °C prior to usage. To assemble the gels, 400 µl of 5 or 8% GelMA solution was added per well of a 24-well plate (Corning, New York, United States) and irradiated using a Unic nail dryer (MEANAIL© Paris, France) equipped with a UV/VIS (405 nm) LED lamp for 4 min at 20 mW/cm^2. After irradiation, gels were allowed to swell overnight in low glucose Dulbecco's Modified Eagle Medium (DMEM) (Lonza, Geleen, the Netherlands) supplemented with 10% foetal bovine serum (FBS) (Sigma-Aldrich), 100U/mL penicillin and 100 µg/ml streptomycin (Gibco, Breda, the Netherlands), and 1% GlutaMAX (Gibco) prior to use in experiments. This media was referred to as complete growth media.

2.4 Mechanical testing with low load compression testing

Mechanical properties of the GelMA hydrogels were measured using Low Load Compression Testing (LLCT) as previously described (de Hilster et al., 2020). LLCT analyses were performed on three different locations (2.5 mm apart) of each hydrogel with a 20% fixed strain rate. The stress and strain values for each measurement were determined using formulas (i) and (ii), respectively. Young's modulus (E, i.e., stiffness) values were calculated from the slope of the linear region of the Stress-Strain graph, using formula (iii). After the peak value, the viscoelastic relaxation measurement was performed for 5 s, and the relaxation percentage was measured according to the formula (iv).

$$Stress = \frac{Load\ x\ g}{Area} \quad \text{(i)}$$

$$Strain = \frac{Deformation}{Thickness} \quad \text{(ii)}$$

$$E(t) = \frac{Stress}{Strain} \quad \text{(iii)}$$

$$Relaxation\ (t) = \frac{E(t_0) - E(t)}{E(t_0)} \quad \text{(iv)}$$

2.5 Human lung tissue

The study protocol was consistent with the Research Code of the University Medical Centre Groningen (https://www.umcg.nl/SiteCollectionDocuments/English/Researchcode/umcg-research-code-2018-en.pdf) and national ethical and professional guidelines ("Human tissue and medical research: code of conduct

TABLE 1 Characteristics of fibroblast donors.

Donor #	Sex	Age	Smoking history	Pack years	FEV1/FVC
1	F	49	Current	33	82.3
2	F	50	Never	0	77.9
3	F	47	Current	30	73.9
4	F	51	Current	70	78.3
5	F	49	Ex	35	77.7
6	F	46	Ex	32	81.5
7	M	69	Current	20	70.0

F = female, M = male and Ex = former smoker.

for responsible use (2011)", https://www.coreon.org/wp-content/uploads/2020/04/coreon-code-of-conduct-english.pdf). Lung fibroblasts and lung tissues used in this study were derived from leftover lung material after lung surgery and transplant procedures. This material was not subject to the Medical Research Human Subjects Act in the Netherlands, and, therefore, an ethics waiver was provided by the Medical Ethical Committee of the University Medical Center Groningen (UMCG). All samples and clinical information were deidentified before experiments were performed. Fibroblasts were isolated from macroscopically and histologically normal tissue as described before (Noordhoek et al., 2005).

Table 1 shows the characteristics of fibroblast donors used in this study: comprising 6 female and 1 male donors, 4 current smokers, 2 ex-smoker and 1 never smoker. The average age of the donors was 51.6 ± 7.87 years, all of which had normal lung capacity as demonstrated by a forced expiratory volume in 1 s/forced vital capacity (FEV1/FVC) that was above 70%.

2.6 Cell culture

Primary LFs were cultured in complete growth media and used between passage 3 to 5 (Blokland et al., 2020b). LFs were routinely checked for *mycoplasma* infection using a PCR assay, and only used when certified negative (Uphoff and Drexler, 2002). To improve attachment of fibroblasts, hydrogels were coated with a 5% w/v Bovine Serum Albumin (BSA) solution (Sigma-Aldrich) in low glucose DMEM for 24 h prior to cell seeding. Twenty thousand LFs/gel were seeded on top of soft and stiff GelMA hydrogels in complete growth media. After 24 h, the media was replaced with fresh complete growth media, and cells were allowed to grow for another 6 days after which supernatant, RNA, hydrogels for live/dead stain and immunofluorescent staining were harvested. Supernatants were collected, pooled, and centrifuged for 5 min at 300 x g to remove debris and dead cells after which the cell-free supernatants were stored at -80 °C. Hydrogels in RNA lysis buffer (Machery-Nagel, Düren, Germany) were stored at −80°C until RNA isolation. Hydrogels for immunofluorescent imaging were fixed in 2% paraformaldehyde (PFA; Sigma-Aldrich) and 0.2% glutaraldehyde in PBS for 30 min. The hydrogels were then washed three times in PBS and stored in PBS supplemented with 1% Pen/Strep at 4°C until analyses.

2.7 Live and dead cell assays

Cell viability after 1 and 7 days was examined using Calcein AM (Thermo Scientific, Breda, the Netherlands, CCID: 390986) for live cells and propidium iodide (PI; Sigma-Aldrich, CCID: 104981) for dead cells. Briefly, GelMA hydrogels were washed and incubated with Hank's Balanced Salt Solution (HBSS; Gibco) containing magnesium and calcium for 20 min at 37°C. A working solution was prepared containing 5 μM Calcein AM and 2 μM PI in HBSS, which was added to the GelMA hydrogels before they were incubated for 20 min in the dark. Images were captured using a EVOS Cell Imaging System (Thermo Scientific). ImageJ was used to create an overlay of both GFP and Texas Red channels without modifications (Schneider et al., 2012). Morphological analysis was performed using CellProfiler software (Broad Institute, MIT, Cambridge MA) (Stirling et al., 2021).

2.8 Gene expression analysis

Total RNA from GelMA hydrogels was isolated using a Nucleospin RNA isolation kit (Machery-Nagel). Media was removed and lysis buffer in a 1:3.3 sample-to-buffer ratio was added to each well before incubation for 15 min on ice, after which the samples (gel and lysis buffer) were stored at -80 °C. Samples were thawed on ice and mixed thoroughly before the lysis buffer was transferred to a new Eppendorf tube without the GelMA hydrogel. RNA isolation was performed according to the manufacturer's instructions. Total RNA was quantified using the Qubit HS RNA assay kit (Thermo Scientific)

TABLE 2 Primers and probes with designated exon boundaries.

Gene	Number	Exon boundary
18S	Hs99999901_s1	1-1
CDKN2A	Hs00923894_m1	2-3
CDKN1A	Hs00355782_m1	2-3
P53	Hs01034249_m1	10-11
IL-6	Hs00174131_m1	4-5
CXCL8	Hs00174103_m1	1-2
DCN	Hs00370385_m1	7-8
ACTA2	Hs00426835_g1	2-3
COL1A1	Hs00164004_m1	1-2
FN1	Hs01549976_m1	8-9
FBLN1	Hs00242545_m1	13-14
FBLN1C	Hs00242546_m1	14-15
LOX	Hs00942483_m1	5-6
TGF-β1	Hs00998133_m1	6-7
CTGF	Hs00170014_m1	4-5

18S ribosomal RNA, 18S, Cyclin-dependent kinase inhibitor 2A = CDKN2A, Interleukin 6 = IL-6, Chemokine ligand 8 = CXCL8, Decorin = DCN, Actin alpha 2 = ACTA2, Collagen 1α1 = COL1A1, Fibronectin = FN1, Fibulin-1 = FBLN1, Lysyl oxidase = LOX, Transforming growth factor β1 = TGF-β1, Connective tissue growth factor = CTGF.

according to the manufacturer's instructions. RNA was reversed transcribed into cDNA using the ReverseAid First Strand cDNA Synthesis Kit (Thermo Scientific). DNA was amplified using GoTaq Probe qPCR Master Mix (Promega, Leiden, the Netherlands) and TaqMan Gene Expression Assay (Thermo Scientific) on a ViiA7 Real-Time PCR System (Applied Biosystems, Breda, the Netherlands) with the relevant predeveloped primers listed in table 2 (Thermo Scientific).

2.9 Immunofluorescence

For immunofluorescence cells were washed twice with PBS and fixed with 2% PFA/0.2% glutaraldehyde (Sigma-Aldrich) in PBS for 20 min at room temperature. Fixed cells were permeabilized with 0.5% Triton X-100 in PBS for 10 min and incubated with 2.2% bovine serum albumin (BSA) for 30 min. Next cells were incubated with primary antibodies for 16 h: rabbit polyclonal to YAP (GeneTex Cat# GTX129151, 0.3 μg/ml, RRID:AB_2885910), mouse monoclonal to P16 (Abcam Cat# ab54210, 2.5 μg/ml, RRID:AB_881819), rabbit polyclonal to Decorin (Proteintech Cat# 14667-1-AP, 0.9 μg/ml, RRID:AB_2090265) 14667-1-AP; ThermoFisher), rabbit polyclonal to fibulin-1 (Thermo Fisher Scientific Cat# PA5-103841, 3.33 μg/ml, RRID: AB_2853174) in PBS +0.1% Triton X-100 and 2.2% BSA. After three washes with PBS containing 0.5% Tween-20 samples were incubated with fluorescent labelled secondary antibodies containing 4′,6-diamidino-2-phenylindole (DAPI; Roche Cat# 10236276001, 1.0 μg/ml) for 30 min. Actin was visualized by incubating with TRITC labelled-Phalloidin (Sigma-Aldrich Cat# P1951, 100nM, RRID:AB_2315148) in PBS for 30 min. Slides were mounted in Citifluor (Agar Scientific, Stansted, United Kingdom). Fluorescent photomicrographs were acquired using a SP8 scanning confocal microscope equipped with photomultiplier tubes (PMTs) (Leica Microsystems, Amsterdam, Netherlands) and a HC PL APO CS2 63x/1.4 oil immersion objective at room temperature. Fluorescent images were loaded in ImageJ and subsequently split into the separate channels. The DAPI channel was used to count the number of nuclei and determine the nucleic area. This was done using the particle Analyzer with particles size set at 50—Infinity. Then, a mask was made of the nuclear area. In the YAP channel total positive area was measured and by using the nuclear mask also the nuclear area was determined. The nuclear fraction was calculated as follows: total nuclear YAP was divided by total YAP to calculate the ratio between total and nuclear YAP. Matrix ECM patterns were analysed using The Workflow Of Matrix BioLogy Informatics (TWOMBLI) as described before (Wershof et al., 2021).

2.10 Enzyme linked immunosorbent assay

Secreted IL-6 (DY205), CXCL8 (DY208), DCN (DY143), TGF-β1 (DY240), Osteoprotegerin (OPG; DY805), receptor activator of nuclear factor kappa-B ligand (RANKL; DY626) and Connective Tissue Growth Factor (CTGF) (DY9190-05) were measured using Human DuoSet Enzyme linked immunosorbent assay (ELISA) kits (R&D Systems, Abingdon, United Kingdom) according to the manufacturer's instructions. Total RANKL was calculated by measuring free RANKL and in complex with OPG using an in house developed OPG/RANKL complex sandwich ELISA by using a human capture RANKL antibody (part of cat#DY626, R&D Systems) and a human detection OPG antibody (part of cat#DY805, R&D Systems) (Mogi and Kondo, 2010). Total OPG was calculated by measuring free OPG and bound OPG. To normalise ELISA data, cell numbers from ten fields of DAPI positive cells per donor on soft (±5 kPa) and stiff (±15 kPa) GelMA hydrogels were counted, and the total number of cells calculated for the overall GelMA hydrogel surface (1.9 cm^2) area.

2.11 Statistical analyses

Statistical analyses were performed using IBM SPSS Statistics for windows version 25 (IBM Corp., Armonk,

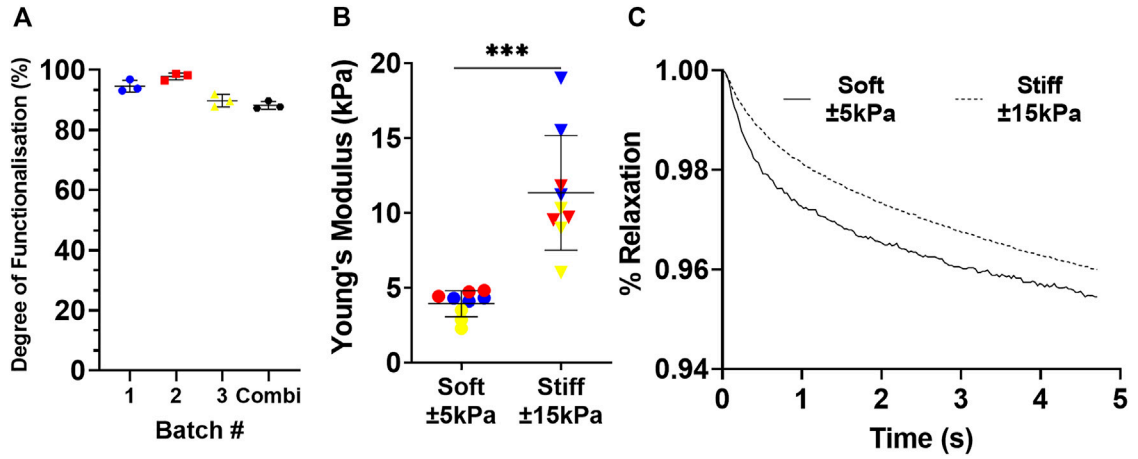

FIGURE 1
Mechanical properties of GelMA hydrogels. **(A)** Three different batches of GelMA were produced and the methacrylation efficiency was measured to demonstrate minimal variety before being combined into one large batch. Each dot represents a technical replicate of a batch. Data expressed as mean ± SD. Rheological properties were characterised by the Young's modulus of 3 different series **(B)**; blue, red and yellow) produced from three GelMA hydrogel solutions used in this study and the relaxation **(C)** over a period of 5 s. $n = 3$ with each dot representing a technical replicate of a unique sample. Data is expressed as mean ± SD in panel A–B, and mean in panel C ($n = 3$). Data were considered significant at $p < 0.05$.

N.Y., United States) and evaluated using Wilcoxon matched pair signed rank test for comparison between soft GelMA hydrogels and stiff GelMA hydrogels. Data were considered statistically significant at $p < 0.05$ unless stated otherwise. D'Agostino test was used to examine normality of the data and when necessary, log transformation applied. Correlations were assessed by calculating a Pearson correlation coefficient.

3 Results

3.1 Mechanical properties of GelMA hydrogels

Three different GelMA batches were produced and the methacrylation consistency was tested to determine if they could be combined into one large batch. The three different GelMA batches prepared for this study had a methacrylation efficiency of 94.58 ± 1.98%, 97.84 ± 1.14% and 89.77 ± 2.04% respectively (Figure 1A). The combined batch had a methacrylation efficiency of 88.22 ± 1.32%. Next, the Young's modulus was measured across a range of different percentage GelMA hydrogels of up to 10% GelMA (data not shown) to select the hydrogel composition with the stiffness that best mimicked healthy (±5 kPa) and fibrotic (±15 kPa) lung tissue. A hydrogel made of 5% wt/v GelMA resembled healthy tissue with Young's modulus of 3.94 kPa ±0.87 kPa whereas 8% wt% hydrogels most resembled stiff tissue with a Young's modulus of 11.34 kPa ±3.82 kPa (Figure 1B). To further characterise these hydrogels, relaxation was measured to see if the percentage of GelMA has an impact on relaxation. After initial compression of 20%, the dissipation of force was followed for a duration of 5 s (Figure 1C). The relaxation values were 4.54 ± 1.60% for 5% (soft) and 4.00 ± 0.32% for 8% (stiff) GelMA hydrogels.

3.2 Morphological differences of fibroblasts on soft and stiff GelMA hydrogels

To characterise responses of fibroblasts to their environment, fibroblasts were cultured on soft (±5 kPa) and stiff (±15 kPa) hydrogels and their morphology was observed after 1 and 7 days of culture. Fibroblasts seeded on both soft and stiff hydrogels exhibited a similar morphology after 24 h of culture (Figures 2A,B). After 7 days of culture, fibroblast morphology was also similar on both soft and stiff hydrogels (Figures 2A,B day 7). After observing a round morphology in some donors after 24 h a live/dead stain was performed to rule out apoptosis, which revealed live cells with no dead cells evident after 1 or 7 days of culture on either hydrogel (Figures 2C,D). Total fibroblast cell number after 7 days of culture was higher on stiffer hydrogels compared to soft hydrogels (Figure 2E) which is in concordance with literature in response to a stiff matrix. Morphology analysis using CellProfiler did not demonstrate major differences between fibroblast on day 1 or 7 and between soft and stiff hydrogels (Supplementary Figure S1).

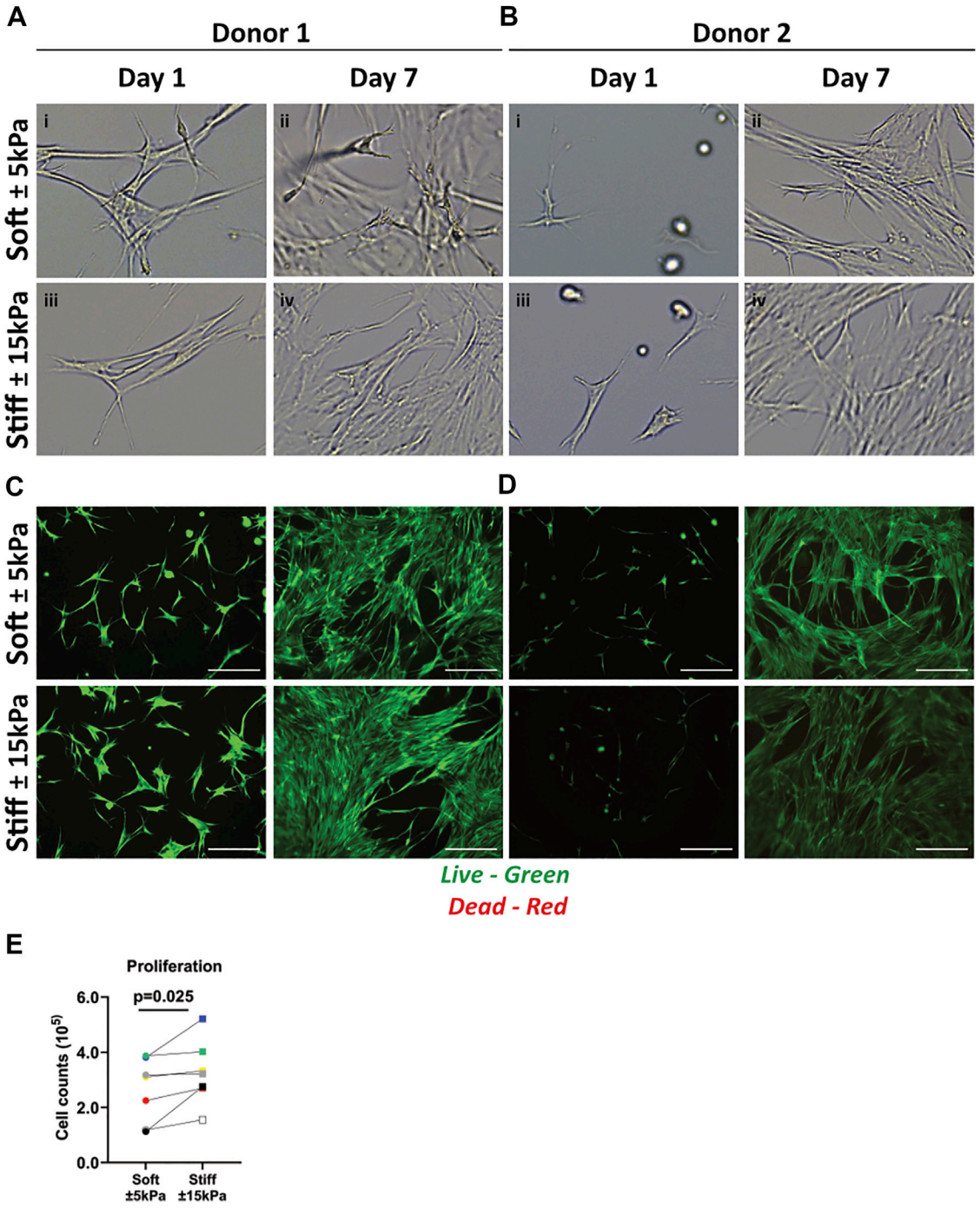

FIGURE 2
Primary human lung fibroblast morphology, live/dead staining and proliferation on soft (3.94 ± 0.87 kPa) and stiff (11.34 ± 3.82 kPa) GelMA hydrogels. **(A–B)** Representative brightfield microscopy images of cells 24 h post seeding and after 7 days of culture on top of soft and stiff hydrogels (digital magnification). Letters i-iv show areas of interest with different morphologies between donors. **(C,D)** Live (green) and dead (red) stain of two donors at day 1 and 7 of culture. **(E)** Total cell numbers on soft (3.94 ± 0.87 kPa) and stiff (11.34 ± 3.82 kPa) hydrogels after 7 days of cell culture. Images are representative of responses seen in 7 unique donors. (n = 7) Scale bar = 250 μm. Each donor has a different unique colour (blue, red, yellow, green, black, white, and grey).

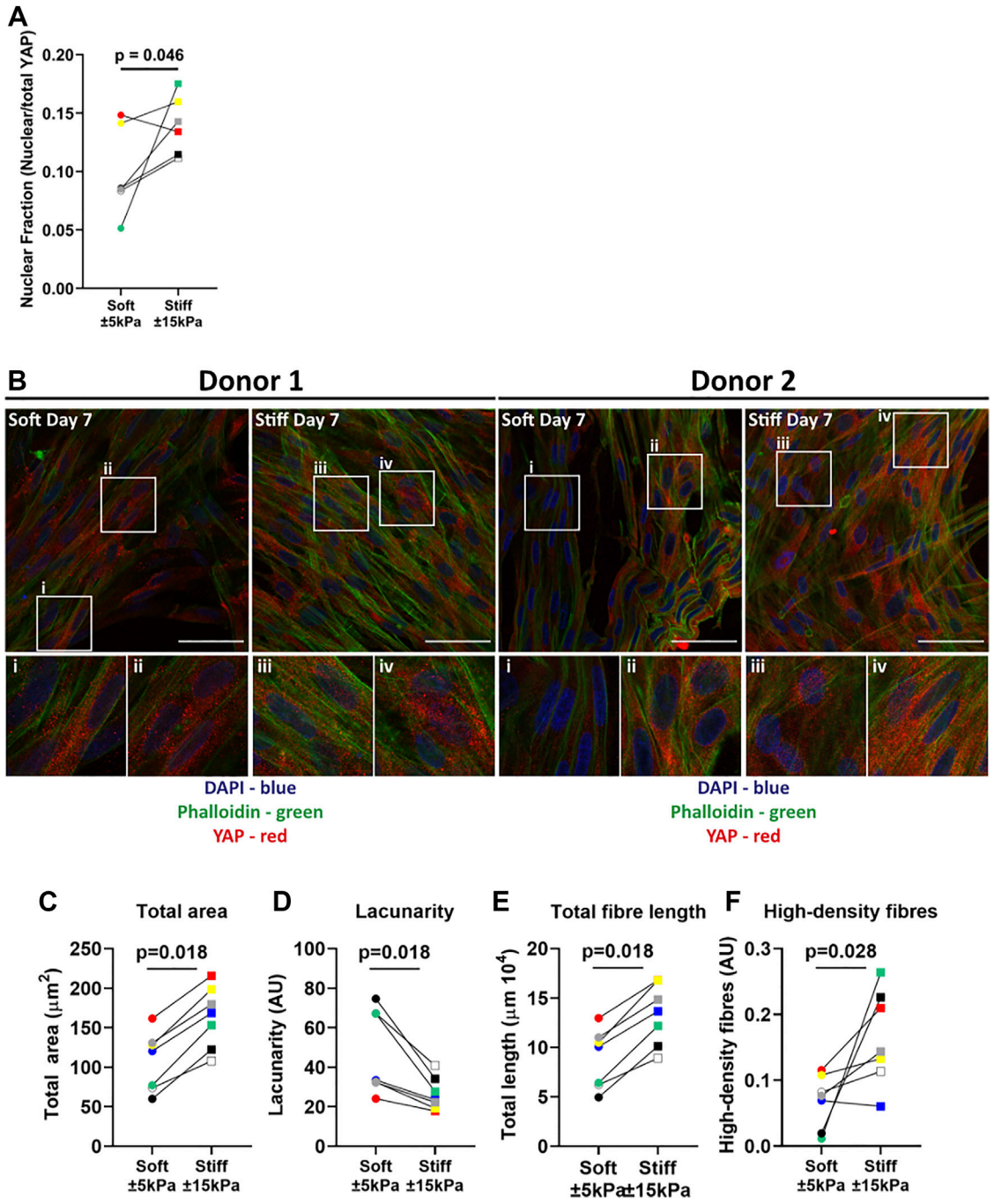

FIGURE 3
YAP translocation and F-actin stress fibre formation in primary human lung fibroblasts on soft (3.94 ± 0.87 kPa) and stiff (11.34 ± 3.82 kPa) hydrogels. Hydrogels after 7 days of culture were fixed and fibroblasts were stained for YAP and F-actin. **(A)** Quantification of YAP nuclear fraction **(B)** representative fluorescent images of DAPI (Blue), YAP (Red) and F-actin (green). i-iv) White boxes show the region of interest that is magnified. TWOMBLI analyses of phalloidin stained fibroblasts showing total area **(C)**, lacunarity **(D)**, fibre length **(E)** and high-density fibre networks **(F)** (calculated using the high-density matrix algorithm). Images are representative of responses seen in 7 unique donors. (n = 6–7) Scale bar = 50 μm. Each donor has a different unique colour (blue, red, yellow, green, black, white, and grey).

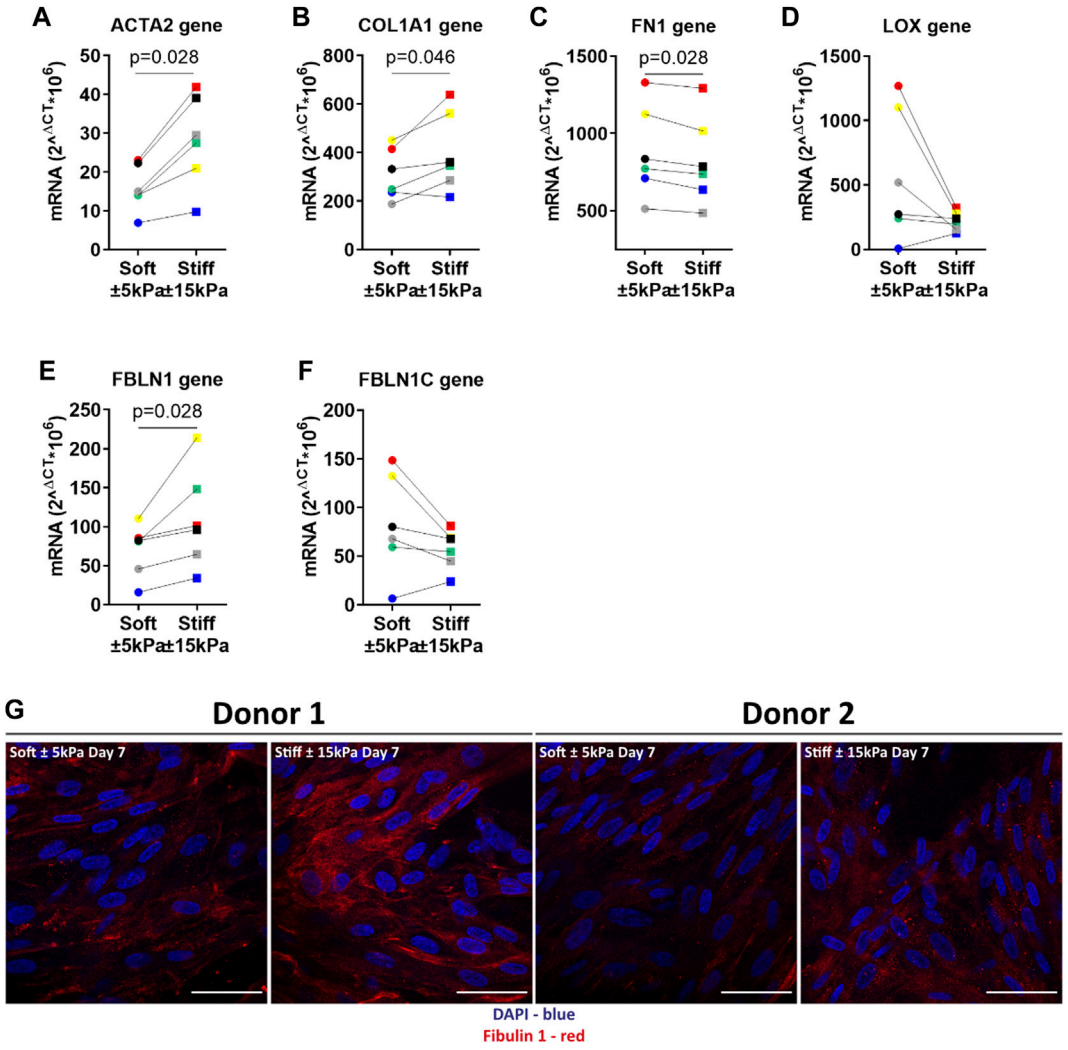

FIGURE 4
Primary human lung fibroblast markers of cellular senescence in response to surface stiffness. **(A–C)** Gene expression of the cell-cycle inhibitors *p21*$^{Waf1/Cip1}$ *and p16*^{Ink4a}, *p53* and known SASP factors *IL-6* and *CXCL8* after 7 days of culture, data were normalised against 18S and expressed as $2^{-\Delta CT}$ x 10^6. **(D-G)** Levels of SASP cytokine production in supernatant, data were normalised to cell numbers and are expressed as pg/mL per 10^5 cells. Differences between soft (3.94 ± 0.87 kPa) and stiff (11.34 ± 3.82 kPa) hydrogels were analysed by a Wilcoxon matched pairs signed rank test (n = 6) and $p < 0.05$ was considered significant. Each donor has a different unique colour (blue, red, yellow, green, black, and grey).

3.3 Increased total yes-associated protein-1 content and organised F-actin formation in fibroblasts on stiffer matrices

Next, the mechanosensory response of fibroblasts to their environment was examined using a dual stain for Yes-associated protein 1 (YAP) nuclear translocation and F-actin fibre formation. The YAP nuclear fraction was higher on stiff hydrogels compared to soft hydrogels (Figure 3A). Figure 3B shows the nuclear translocation of YAP on soft and stiff hydrogels on day 7. F-actin cytoskeleton arrangement in fibroblasts on soft hydrogels was composed of both diffuse and organised F-actin fibres, while fibroblasts on stiffer hydrogels display bundled organised F-actin fibres (Figure 3B), indicative of their responsiveness to the substrate stiffness. To quantify the differences in ECM patterns between soft and stiff hydrogels we measured several parameters using the TWOMBLI plugin. Figure 3C demonstrates that there is a clear increase in total area of F-actin fibres in fibroblasts cultured on stiff hydrogels. This is supported by the reduction in space between the fibres (Figure 3D) as well as the increase in F-actin fibre length (Figure 3E). Lasty, we measured a strong increase in the high-density fibre network, which confirms areas with increased tight f-actin bundles formed in response to stiffness (Figure 3F).

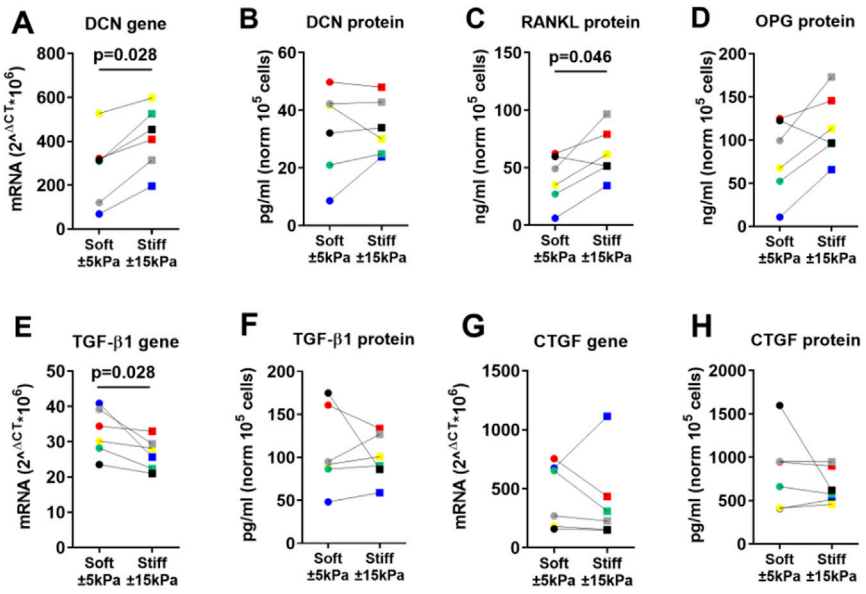

I

		IL-6	CXCL8	TGF-β1	CTGF	OPG	RANKL	DCN
OPG	Pearson r	0.84600	0.85900	0.81500	0.62800		0.98600	0.48008
	p value	5.26E-04	3.40E-04	1.25E-03	2.88E-02		4.75E-09	1.14E-01
RANKL	Pearson r	0.82900	0.84500	0.78400	0.57061	0.98600		0.40576
	p value	8.64E-04	5.45E-04	2.55E-03	5.27E-02	4.75E-09		1.91E-01

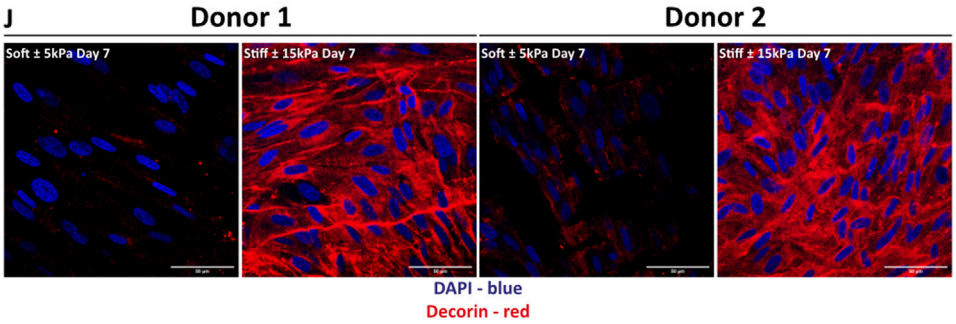

FIGURE 5
Stiffness induced a secretory phenotype in Primary human lung fibroblasts cultured on stiff matrices. **(A,B)** DCN gene expression and secreted protein were measured after 7 days of culture on soft (3.94 ± 0.87 kPa) and stiff (11.34 ± 3.82 kPa) hydrogels. **(C–H)** Levels of secreted factors RANKL, OPG, CTGF and TGF-β1 including TGF-β1 and CTGF gene expression after 7 days of culture on soft and stiff hydrogels. I) Correlation was calculated between OPG, RANKL and all other secreted factors. Panel J shows a fluorescent staining for DCN, DAPI was used for identification of cell nuclei. Illustrated photographs are representative images of in total 7 unique donors. Gene expression data were normalised against 18S and expressed as $2^{-\Delta CT}$ x 10^6. Secreted matrix proteins and cytokines were normalised to cell counts and expressed as pg/ml or ng/ml 10^5 cells. Differences between soft and stiff hydrogels were analysed by a Wilcoxon matched pairs signed rank test. Correlation was calculated using Pearson correlation coefficient. (n = 6) Scale bar = 50 μm. Each donor has a different unique colour (blue, red, yellow, green, black, and grey).

3.4 Higher matrix stiffness does not contribute to cellular senescence in fibroblasts

After confirming that fibroblasts respond to their environment, we explored our hypothesis that increased stiffness may contribute to the senescent state. Therefore, several biomarkers for senescence were analysed in fibroblasts grown on soft and stiff hydrogels mimicking healthy and diseased tissue stiffnesses. Gene expression analysis of early-stage marker *p21*$^{Waf1/Cip1}$ did not demonstrate a difference while late-stage senescence marker *p16*^{Ink4a} demonstrated a trend ($p = 0.075$) towards an increase between soft and stiff hydrogels (Figures 4B,C). Interestingly, *p53* demonstrated a trend towards a decrease in fibroblasts on stiff hydrogels (Figure 4C). To further characterise cellular senescence, both gene expression and secretion of the well characterised SASP factors IL-6 and CXCL8 were measured (Figures

4D–G). Gene expression of *IL-6* was significantly higher on stiffer hydrogels (Figure 4D). However, the secretion of IL-6 did not change between soft and stiff hydrogels. Both CXCL8 gene and protein expression did not exemplify a difference between soft and stiff hydrogels after 7 days of culture (Figures 4F,G).

3.5 Higher matrix stiffness induces a secretory phenotype in primary fibroblasts

Our data indicated that there was no greater activation of the cell-cycle inhibitors $p16^{Ink4a}$ and $p21^{Waf1/Cip1}$ on stiffer hydrogels compared to softer hydrogels, but rather an increase in proliferation. To further characterise the activation of a secretory phenotype we measured several factors that have been reported to be part of the senescent phenotype and/or to be part of a fibrotic response (Verrecchia and Mauviel, 2007; Coppe et al., 2010; Zhang et al., 2018; Faget et al., 2019). Gene expression and secreted protein levels of the proteoglycan DCN were higher on stiff compared to soft hydrogels (Figure 5A). Next, RANKL was measured as it was recently shown to be secreted by senescent fibroblasts in COPD (Woldhuis et al., 2020a). RANKL secretion was significantly higher at day 7 on stiffer hydrogels while its decoy receptor OPG showed a trend towards an increase at day 7 on stiffer hydrogels (Figures 5C,D). Additionally, TGF-β1 gene expression and protein secretion were measured. TGF-β1 gene expression demonstrated a significant decrease on stiff hydrogels compared to soft hydrogels (Figures 5E,F) while there was no change in protein secretion (Figure 5G). Finally, CTGF gene expression and secretion were measured, which demonstrated no difference for secretion between soft and stiffer hydrogels at day 7 while gene expression demonstrated a trend towards a decrease (Figures 5G,H). To explore if the OPG-RANKL axis serves as a mechanism that potentially could have an effect on both fibrosis and senescence, we explored the correlation between OPG-RANKL and other secreted factors (Figure 5I). Correlations for both OPG and RANKL were observed with IL-6, CXCL8 and TGF-β1. CTGF was correlated with OPG but not RANKL, and no correlations were observed with DCN. Additionally, we stained the cells on the surfaces of the hydrogels for DCN protein levels. Figure 5J shows the DCN stain on both soft and stiffer hydrogels after 7 days in culture. DCN displayed a strong visual increase on the stiffer hydrogels in comparison to the soft hydrogels.

3.6 Matrix stiffness activates a profibrotic response in primary fibroblasts

To further characterise the fibrotic response of fibroblasts on stiffer hydrogels we measured several fibrosis-associated genes. Previous studies have reported that higher expression of these genes is associated with persistent fibroblast activation and higher ECM deposition in fibrosis. Lung fibroblasts on stiffer hydrogels exhibited higher α-SMA and COL1α1 expression after 7 days of culture compared to soft hydrogels (Figures 6A,B). The expression of FN1 was significantly lower after 7 days on stiffer hydrogels (Figure 6C). Interestingly, LOX gene expression was lower in cells grown on stiff hydrogels compared to soft hydrogels (Figure 6D). Fibulin-1 gene expression was higher after 7 days on stiffer hydrogels (Figure 6E). However, FBLN1C gene expression was not different between cells grown on soft or stiffer hydrogels (Figure 6F). The final characterisation was an immunofluorescent staining for deposited FBLN1 on both soft and stiffer hydrogels at day 7. We visualised a higher deposition of FBLN1 on stiffer hydrogels in comparison to soft hydrogels (Figure 6G).

4 Discussion

During fibrotic disease, the ECM undergoes tremendous change that influence the composition and stiffness of the tissue. These changes have a substantial effect on cell function, and it has been reported that fibrotic ECM is able to create a profibrotic positive feedback loop (Parker et al., 2014). In the present study we created hydrogels reflecting the approximate median pathological stiffness measured in fibrotic diseases and examined the impact on cellular responses of lung fibroblasts focusing on markers of senescence, including the SASP and fibrosis. Pathological stiffness did not affect $p16^{Ink4a}$,$p21^{Waf1/Cip1}$ or *p53*, the main markers of senescence, instead it resulted in higher expression of genes/proteins associated with the SASP and fibrosis such as *IL-6*, *ACTA2, COL1A1*, *FBLN1* and *DCN* compared to soft matrix. However, some markers including IL-6, OPG and RANKL are identified to be both expressed/secreted during cellular senescence and different stages of fibrosis. Collectively, the data presented in this study suggest that exposure of fibroblasts to a surface within the range of pathological stiffness modulates gene expression and secreted factors that are both involved in cellular senescence and the fibrotic response in fibroblasts.

Methacrylated-gelatine gels are well characterised hydrogels that support growth of a large variety of cells, that are biodegradable, that allow cell adhesions through Arg-Gly-Asp (RGD) sequences and allow for precise tuning of mechanical properties. Precise tuning of the degree of functionalisation, gelatine concentration and number of crosslinks results in high reproducibility and controllability of biophysiochemical properties (Schuurman et al., 2013; Zhu et al., 2019; Tabatabaei et al., 2020). These characteristics made these hydrogels ideal for our study. In this study we generated two hydrogels with a different Young's modulus while the initial stress relaxation behaviour did not significantly change. This was not unexpected as both hydrogels were almost equal in their constituent biomaterials, reflecting the difference in

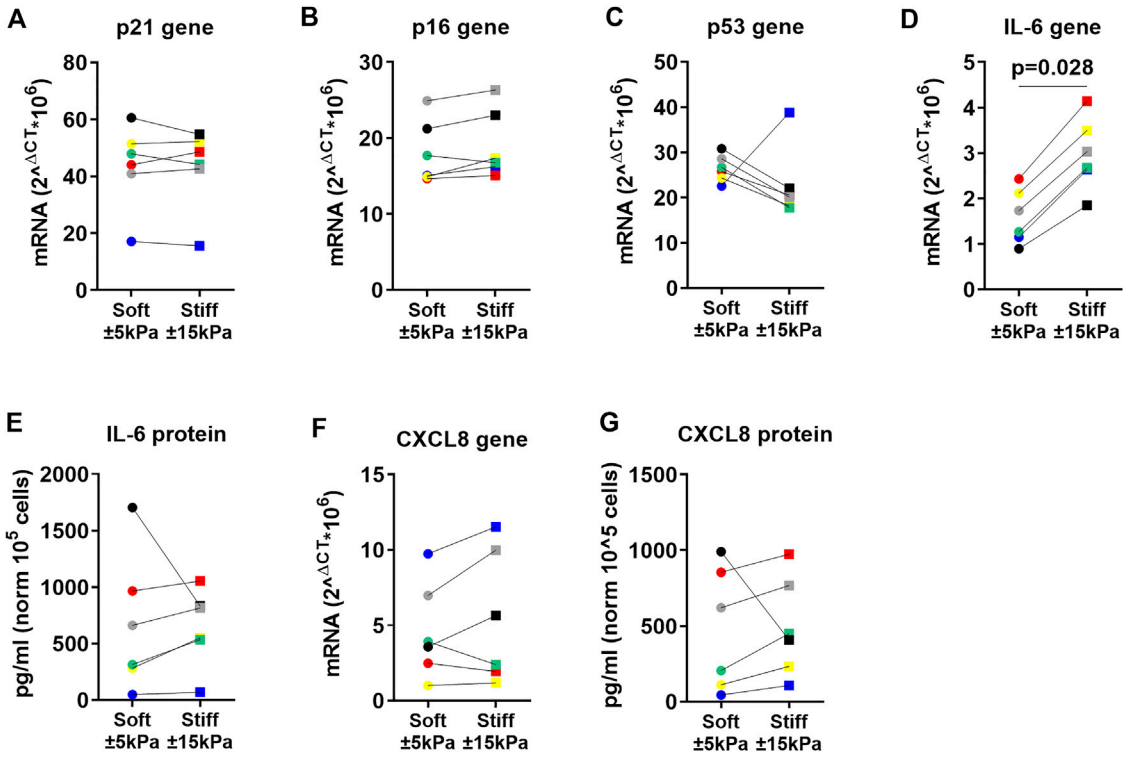

FIGURE 6
Primary human lung fibroblasts exhibit an activated and profibrotic phenotype on stiff (11.34 ± 3.82 kPa) compared to soft (3.94 ± 0.87 kPa) hydrogels. To characterise the fibrotic response of fibroblasts on hydrogels, gene expression levels for fibroblast activation α-SMA and matrix proteins COL1α1, FN1, LOX, FBLN1 and FBLN1C were measured at day 7 **(A–F)**. Finally, deposited FBLN1 (Red) was stained using fluorescent labelled antibodies and DAPI for identification of cell nuclei in panel **(G)**. Illustrated photographs are representative images of in total 7 donors. Differences between soft and stiff hydrogels were analysed by a Wilcoxon matched pairs signed rank test (n = 6). Scale = 50 μm. Each donor has a different unique colour (blue, red, yellow, green, black, and grey).

percentage of GelMA used. This observation authenticates that the responses of the fibroblasts measured herein could be contributed to the differences in Young's modulus only. However, more focus is directed towards the effect of stress relaxation and how it may influence cell behaviour (Chaudhuri et al., 2015; Chaudhuri et al., 2020). Tests on tissues such as liver, skin, muscle, and breast reveal that these organs dissipate stress ranging from milliseconds to hundreds of seconds (McKinnon et al., 2014; Chaudhuri et al., 2016). Changes in viscoelastic properties have been associated with disease progression including cancer. Substrate stiffness has a robust effect on cell function and regulates cell viability, proliferation, migration, differentiation, and cell-matrix adhesion (Huang et al., 2012). Higher proliferation, contractility and activation of fibroblasts are all reported as responses to a stiffer environment (Balestrini et al., 2012; Asano et al., 2017; Sun et al., 2018). In this regard, the proliferation and high viability of fibroblasts grown on both soft and stiffer hydrogels observed in this study were comparable to observations from previous investigations (Solon et al., 2007; Asano et al., 2017; Ruiz-Zapata et al., 2020). Furthermore, the morphology of fibroblasts on soft gels was comparable to fibroblasts on stiffer gels. This is in contrast to some literature where it is shown that there is little spread of cells on soft stiffness (Solon et al., 2007). However, the stiffness representing a soft matrix is often much lower than used in this study and is more in the range of 0.5 kPa In addition, culture times were also different which potentially contributes to the morphology as fibroblasts produce matrix of their own which facilitates attachment. Furthermore, differences in gel composition may also contribute to this effect, for example polyacrylamide has no RGD sequences as are present in GelMA due to its biological origin, and this may impact on the ability of the fibroblasts to attach and spread on the gel surface.

In response to mechanical cues such as stiffness, fibroblasts organise their actin fibres and translocate YAP into the nucleus leading to cellular activation and transcription of genes in many cell types (Dupont et al.,

2011; Raghunathan et al., 2013; Liu et al., 2015). The data in this study showed that total YAP content in fibroblasts is higher on stiffer compared to soft hydrogels and that organised bundled F-actin fibres are formed, which is indicative of the cells responding to the mechanical environment. However, there was an apparent lack of nuclear staining for YAP at day 7 in the fibroblasts on either hydrogel, particularly in regions of higher cell density. This may be explained by the fact that YAP becomes less mechanosensitive and remains in the cytoplasm as a response to cell-cell interactions (Das et al., 2016; Totaro et al., 2017). Furthermore, while increased nuclear translocation is well documented in response to a stiffer environment, the increase in total YAP is not yet clarified. In fact, stimulation with TGF-β1 demonstrated a reduction in YAP mRNA expression in the first 24 h while protein levels did not change (Piersma et al., 2015b). Moreover, the formation of organised bundled actin may also contribute to this effect by altering the shape of the nuclear envelope which potentially changes the environment for transcription and thus impacting on fibroblast function (Zhao et al., 2007). Little is known about the interplay between an altered ECM and cellular senescence, therefore after confirming that, in our model, fibroblast respond to their substrate, we investigated what the contribution was of increased stiffness on cellular senescence and the SASP. The results from the present study provided evidence that there was an increase of proliferation and modulation of some markers of senescence in response to pathological stiffness at day 7. Higher cell proliferation and migration, as reflected in our study, has been widely documented as a result of increased matrix stiffness and is part of an important response to injury in wound repair (Reinke and Sorg, 2012; Wickert et al., 2016). Interestingly, we also observed an increase in *IL-6* gene expression and a trend towards an increase in CXCL8 protein secretion in the stiffer environment. Both pro-inflammatory cytokines are involved in wound repair and are identified as part of the SASP, which plays an important role in fibrosis (Coppe et al., 2010; Schafer et al., 2017). Furthermore, there is evidence suggesting that the SASP can be activated independently of cell-cycle inhibitors $p16^{Ink4a}$ and $p21^{Waf1/Cip1}$ in cellular senescence (Coppe et al., 2011; Wang et al., 2017). Activation of the SASP might be an early indicator of senescence and precedes the irreversible cell-cycle arrest of premature cellular senescence.

Activation of a secretory phenotype is beneficial for tissue repair, but it can also be detrimental and contribute to disease progression in fibrosis (Pratsinis et al., 2019). Our results showed activation of a secretory phenotype in response to increased surface stiffness, including a strong correlation of RANKL and OPG with other secreted factors, but not DCN. All of these factors have been recognised to be part of the SASP and/or to be part of the fibrotic response. DCN is recognised for its role in many different biological processes and recently DCN has been found negatively correlated with $p16^{Ink4a}$ in senescence in COPD (Woldhuis et al., 2020b). Our results suggest, in the context of fibrosis, that DCN deposition is in response to stiffer hydrogels, further supporting the important role DCN plays in fibrosis (Westergren-Thorsson et al., 2004; Zhang et al., 2018). CTGF is an important mediator in tissue remodelling and has been associated with senescence, fibrosis and cancer (Riser et al., 2015; Jun and Lau, 2017). CTGF can be regulated *via* its main inducer TGF-β1 or can be negatively regulated by DCN and OPG (Vial et al., 2011; Aoyama et al., 2015). Given the fact that, in our study, TGF-β1 secretion was unaltered and an increase in DCN secretion was observed, it was not surprising that no change in CTGF secretion was found in response to increasing stiffness. CTGF has also been reported to be downstream of YAP, and we reported there was more YAP retention in the cytoplasm potentially contributing to less upregulation in response to the stiffer environment (Davis and Foster, 2018; Shome et al., 2020). In addition, there was downregulation of CTGF gene expression in response to stiffer hydrogels confirming the findings that protein secretion was unaltered. The RANKL-OPG system is essential for bone metabolism, where OPG acts as a decoy receptor for RANKL, regulating development and activity of osteoclasts. OPG is currently used as a biomarker for liver fibrosis (Coppe et al., 2010; Adhyatmika et al., 2020), while RANKL was recently identified to be part of the SASP in senescent COPD fibroblasts (Woldhuis et al., 2020a). In IPF the exact role of OPG is not fully understood but evidence suggests it may play a role in active fibrosis and associates with disease progression (Wang et al., 2019; Habibie et al., 2020). Our correlation analysis between RANKL, OPG and other secreted factors demonstrated a strong correlation. These factors, such as TGF-β1 and CTGF, are part of both the SASP and fibrotic response. It might be possible that RANKL as a SASP and OPG as a fibrotic-associated marker create a regulatory pathway between the senescent and fibrotic response in stiff lung tissues. Moreover, CTGF has been identified to bind to OPG and might be a potential fourth factor in the RANK-RANKL-OPG system, potentially contributing to the regulatory mechanism as well (Lipson et al., 2012; Aoyama et al., 2015; Jun and Lau, 2017; Kim et al., 2020). This mechanism might also contribute to the fact that we did not measure any difference in protein secretion, despite lower mRNA levels. Taken together these data suggest that the RANKL-OPG-CTGF system may contribute to secreted factor regulation, increased ECM deposition and potentially contribute to the progression/perpetuation of fibrosis in response to a stiffer tissue environment as central regulator.

Fibroblasts can be activated in response to increased stiffness leading to higher expression of α-SMA and matrix proteins, which is part of a normal wound repair response after injury. Our

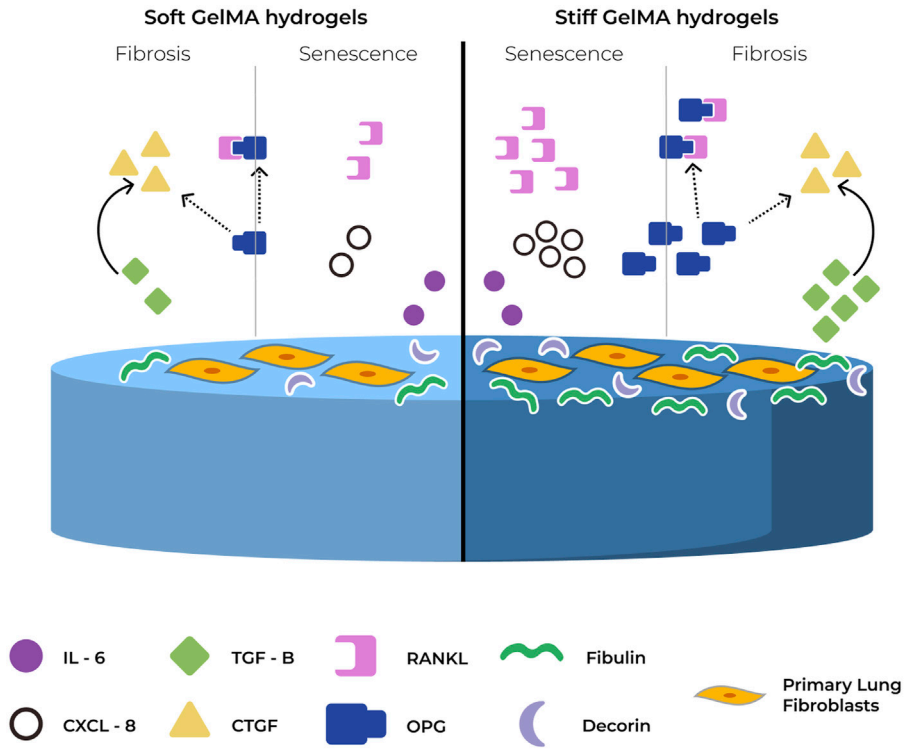

FIGURE 7
Summary of proposed mechanism for OPG in senescence and fibrosis. In response to stiffness, Primary human lung fibroblasts show increased proliferation, higher deposition of ECM proteins and higher secretion of SASP and fibrosis related cytokines. OPG is proposed to act as a regulatory mechanism between senescence and fibrosis by binding to RANKL and CTGF, and potentially inhibiting their function.

results indicate that in response to stiffer hydrogels fibroblasts show upregulation of several fibrosis associated genes including *ACTA2* and *COL1A1*. Increase in *FBLN1* expression and deposition on stiffer hydrogels was expected and is in line with what has been reported in literature (Paapstel et al., 2016; YasminMaskari et al., 2018). However, the lack of response of *FBLN1C* gene expression was unexpected as *FBLN1C* has been reported to be implicated in fibrosis and lung injury (Ge et al., 2015; Liu et al., 2019). However, it has been reported that TGF-β1, which is unaltered in our study, downregulates *FBLN1* gene expression and promotes FBLN1 deposition in airway smooth muscle cells (Chen et al., 2013). This could indicate that FBLN1/C regulation might be cell-type and disease specific. Interestingly, FN1 which is associated with FBLN1 was decreased on stiffer hydrogels after 7 days. This was in contrast with literature where FN1 was shown to be an important mediator of early wound repair, collagen fibril formation and fibrosis (Valiente-Alandi et al., 2018). Additionally, Zhou and others demonstrated that FN1 expression increased when primary lung fibroblasts were cultured for up to 48 h on stiff matrixes (Zhou et al., 2020). However, it is possible that FN1 peaked early in the time-course of our experiment, especially given its role in the initial phase of wound repair and had subsequently decreased at the time we measured it. Finally, *LOX* gene expression demonstrated a fine regulation by stiffer hydrogels regardless of gene expression on soft hydrogels. LOX is implicated in fibrosis and its role is disease specific (Huang et al., 2019; Nguyen et al., 2021). For example, in renal and liver fibrosis increased LOX expression leads to ECM production and progression of fibrosis (Ikenaga et al., 2017). In IPF, LOX gene expression did not change between healthy and IPF. However, on protein level it was reported that LOX deposition was decreased in IPF tissue (Tjin et al., 2017). Therefore, it would be appropriate to determine enzyme activity as gene and protein expression do not always correlate.

The experimental strategy used in this study was designed to measure the impact of stiffness on the senescent phenotype in fibroblasts after 7 days in culture. While there was modulation of some markers of cellular senescence, other studies investigating senescence induce this by stimulating the cells with paraquat or hydrogen peroxide (Waters et al., 2019; Woldhuis et al., 2020b). It is possible that the early senescence marker $p21^{Waf1/Cip1}$ reached its highest expression before we assessed the expression at day 7, while still being too early to detect high levels of $p16^{Ink4a}$. In several of our datasets there appear to be data points driving the lack of statistical

difference, however, these are not attributed to a single donor but rather represent different donors in each dataset. This variability can be attributed to the biological heterogeneity of the primary lung fibroblasts used in this study. Cell numbers at the start of the study were optimised for measuring senescence readouts. This made the assessment of YAP translocation challenging as the density of fibroblasts on day 7 were higher than optimal for this readout. In addition, YAP translocation is a swift process as cytoplasmic/nuclear levels can be stable within 1 day after changing the stiffness (Zhang et al., 2021). This could have implications for measuring YAP translocation as the regulatory effect may have been partially diminished demonstrating a weaker effect.

In conclusion, we have established that the culture of human lung fibroblasts on matrices that mimic pathological stiffness within the range of fibrotic tissues for up to 7 days leads to activation of genes and secretion of matrix proteins and cytokines that are part of the fibrotic response, with overlap of SASP factors (Figure 7). Our data suggest that there may be an overlap between cellular senescence/SASP and the fibrotic response, indicating that the fibroblasts may acquire a pre-senescent and/or activated phenotype. The modulation of cell function in response to pathological stiffness may ultimately lead to the creation of a negative feedback loop in which pre-senescent and/or activated fibroblasts reinforce each other causing a perpetuating cycle driving aberrant ECM accumulation and progression of a fibrotic response.

Data availability statement

The raw data supporting the conclusions of this article will be made available by the authors, without undue reservation.

Ethics statement

Ethical review and approval was not required for the study on human participants in accordance with the local legislation and institutional requirements. Written informed consent for participation was not required for this study in accordance with the national legislation and the institutional requirements.

Author contributions

KB, MN, MS, DK, CB, SP, and JB conceived and designed research; KB and MN performed experiments; KB, MN, HH, and TB analysed data; KB, MN, HH, MS, BM, DK, CB, SP, and JB interpreted results; KB and MN prepared figures; KB, MN, HH, and TB writing–original draft; KB, MN, HH, TB, MS, BM, DK, CB, SP, and JB Writing–review and editing. All authors have read and agreed to the final version of the manuscript. All authors have access to the raw data and BM, CB, SP, and JB can verify the raw data in this study.

Funding

KB was supported by De Cock—Hadders Foundation research grant 2020-48, and the UMCG Abel Tasman Scholarship. JB was supported by a Rosalind Franklin Fellowship (co-funded by the University of Groningen and European Union), and the Nederlandse Organisatie voor Wetenschappelijk Onderzoek (NWO) Aspasia-premie subsidienummer 015.013.010.

Acknowledgments

The authors thank M.R. Jonker, L. Apperloo and G.J. Teitsma for their technical assistance in this study.

Publisher's note

Supplementary material

The Supplementary Material for this article can be found online at: https://www.frontiersin.org/articles/10.3389/fphar.2022.989169/full#supplementary-material.

References

Adhyatmika, A., Beljaars, L., Putri, K. S. S., Habibie, H., Boorsma, C. E., Reker-Smit, C., et al. (2020). Osteoprotegerin is more than a possible serum marker in liver fibrosis: A study into its function in human and murine liver. *Pharmaceutics* 12 (5), 471. doi:10.3390/pharmaceutics12050471

Aoyama, E., Kubota, S., Khattab, H. M., Nishida, T., and Takigawa, M. (2015). CCN2 enhances RANKL-induced osteoclast differentiation via direct binding to RANK and OPG. *Bone* 73, 242–248. doi:10.1016/j.bone.2014.12.058

Asano, S., Ito, S., Takahashi, K., Furuya, K., Kondo, M., Sokabe, M., et al. (2017). Matrix stiffness regulates migration of human lung fibroblasts. *Physiol. Rep.* 5 (9), e13281. doi:10.14814/phy2.13281

Balestrini, J. L., Chaudhry, S., Sarrazy, V., Koehler, A., and Hinz, B. (2012). The mechanical memory of lung myofibroblasts. *Integr. Biol.* 4 (4), 410–421. doi:10.1039/c2ib00149g

Blokland, K. E. C., Pouwels, S. D., Schuliga, M., Knight, D. A., and Burgess, J. K. (2020). Regulation of cellular senescence by extracellular matrix during chronic fibrotic diseases. *Clin. Sci.* 134 (20), 2681–2706. doi:10.1042/CS20190893

Blokland, K. E. C., Waters, D. W., Schuliga, M., Read, J., Pouwels, S. D., Grainge, C. L., et al. (2020). Senescence of IPF lung fibroblasts disrupt alveolar epithelial cell proliferation and promote migration in wound healing. *Pharmaceutics* 12 (4), E389. doi:10.3390/pharmaceutics12040389

Bonnans, C., Chou, J., and Werb, Z. (2014). Remodelling the extracellular matrix in development and disease. *Nat. Rev. Mol. Cell Biol.* 15 (12), 786–801. doi:10.1038/nrm3904

Booth, A. J., Hadley, R., Cornett, A. M., Dreffs, A. A., Matthes, S. A., Tsui, J. L., et al. (2012). Acellular normal and fibrotic human lung matrices as a culture system for *in vitro* investigation. *Am. J. Respir. Crit. Care Med.* 186 (9), 866–876. doi:10.1164/rccm.201204-0754OC

Chaudhuri, O., Cooper-White, J., Janmey, P. A., Mooney, D. J., and Shenoy, V. B. (2020). Effects of extracellular matrix viscoelasticity on cellular behaviour. *Nature* 584 (7822), 535–546. doi:10.1038/s41586-020-2612-2

Chaudhuri, O., Gu, L., Darnell, M., Klumpers, D., Bencherif, S. A., Weaver, J. C., et al. (2015). Substrate stress relaxation regulates cell spreading. *Nat. Commun.* 6 (1), 6364. doi:10.1038/ncomms7365

Chaudhuri, O., Gu, L., Klumpers, D., Darnell, M., Bencherif, S. A., Weaver, J. C., et al. (2016). Hydrogels with tunable stress relaxation regulate stem cell fate and activity. *Nat. Mat.* 15 (3), 326–334. doi:10.1038/nmat4489

Chen, L., Ge, Q., Black, J. L., Deng, L., Burgess, J. K., and Oliver, B. G. (2013). Differential regulation of extracellular matrix and soluble fibulin-1 levels by TGF-β1 in airway smooth muscle cells. *PLoS One* 8 (6), e65544. doi:10.1371/journal.pone.0065544

Coppe, J. P., Desprez, P. Y., Krtolica, A., and Campisi, J. (2010). The senescence-associated secretory phenotype: The dark side of tumor suppression. *Annu. Rev. Pathol.* 5 (1), 99–118. doi:10.1146/annurev-pathol-121808-102144

Coppe, J. P., Rodier, F., Patil, C. K., Freund, A., Desprez, P. Y., and Campisi, J. (2011). Tumor suppressor and aging biomarker p16(INK4a) induces cellular senescence without the associated inflammatory secretory phenotype. *J. Biol. Chem.* 286 (42), 36396–36403. doi:10.1074/jbc.M111.257071

Das, A., Fischer, R. S., Pan, D., and Waterman, C. M. (2016). YAP nuclear localization in the absence of cell-cell contact is mediated by a filamentous actin-dependent, myosin II- and phospho-YAP-independent pathway during extracellular matrix mechanosensing. *J. Biol. Chem.* 291 (12), 6096–6110. doi:10.1074/jbc.M115.708313

Davis, J. T., and Foster, W. J. (2018). Substrate stiffness influences the time dependence of CTGF protein expression in muller cells. *Int. Physiol. J.* 1 (1), 1. doi:10.14302/issn.2578-8590.ipj-17-1910

de Hilster, R. H. J., Sharma, P. K., Jonker, M. R., White, E. S., Gercama, E. A., Roobeek, M., et al. (2020). Human lung extracellular matrix hydrogels resemble the stiffness and viscoelasticity of native lung tissue. *Am. J. Physiol. Lung Cell. Mol. Physiol.* 318 (4), L698–L704. doi:10.1152/ajplung.00451.2019

Dupont, S., Morsut, L., Aragona, M., Enzo, E., Giulitti, S., Cordenonsi, M., et al. (2011). Role of YAP/TAZ in mechanotransduction. *Nature* 474 (7350), 179–183. doi:10.1038/nature10137

Faget, D. V., Ren, Q., and Stewart, S. A. (2019). Unmasking senescence: Context-dependent effects of SASP in cancer. *Nat. Rev. Cancer* 19 (8), 439–453. doi:10.1038/s41568-019-0156-2

Foucher, J., ChantEloup, E., Vergniol, J., Castera, L., Le Bail, B., Adhoute, X., et al. (2006). Diagnosis of cirrhosis by transient elastography (FibroScan): A prospective study. *Gut* 55 (3), 403–408. doi:10.1136/gut.2005.069153

Ge, Q., Chen, L., Jaffar, J., Argraves, W. S., Twal, W. O., Hansbro, P., et al. (2015). Fibulin1C peptide induces cell attachment and extracellular matrix deposition in lung fibroblasts. *Sci. Rep.* 5 (1), 9496. doi:10.1038/srep09496

Habibie, H., Putri, K. S. S., Boorsma, C. E., Brass, D. M., Heukels, P., Wijsenbeek, M., et al. (2020). Osteoprotegerin is elevated in pulmonary fibrosis and associates with IPF progression. *bioRxiv*. doi:10.1101/2020.12.02.408062

Hansen, N. U., Genovese, F., Leeming, D. J., and Karsdal, M. A. (2015). The importance of extracellular matrix for cell function and *in vivo* likeness. *Exp. Mol. Pathol.* 98 (2), 286–294. doi:10.1016/j.yexmp.2015.01.006

Hinz, B. (2012). Mechanical aspects of lung fibrosis: A spotlight on the myofibroblast. *Proc. Am. Thorac. Soc.* 9 (3), 137–147. doi:10.1513/pats.201202-017AW

Huang, M., Liu, Z., Baugh, L., Defuria, J., Maione, A., Smith, A., et al. (2019). Lysyl oxidase enzymes mediate TGF-β1-induced fibrotic phenotypes in human skin-like tissues. *Lab. Invest.* 99 (4), 514–527. doi:10.1038/s41374-018-0159-8

Huang, X., Yang, N., Fiore, V. F., Barker, T. H., Sun, Y., Morris, S. W., et al. (2012). Matrix stiffness-induced myofibroblast differentiation is mediated by intrinsic mechanotransduction. *Am. J. Respir. Cell Mol. Biol.* 47 (3), 340–348. doi:10.1165/rcmb.2012-0050OC

Humphrey, J. D., Dufresne, E. R., and Schwartz, M. A. (2014). Mechanotransduction and extracellular matrix homeostasis. *Nat. Rev. Mol. Cell Biol.* 15 (12), 802–812. doi:10.1038/nrm3896

Ikenaga, N., Peng, Z. W., Vaid, K. A., Liu, S. B., Yoshida, S., Sverdlov, D. Y., et al. (2017). Selective targeting of lysyl oxidase-like 2 (LOXL2) suppresses hepatic fibrosis progression and accelerates its reversal. *Gut* 66 (9), 1697–1708. doi:10.1136/gutjnl-2016-312473

Jun, J. I., and Lau, L. F. (2017). CCN2 induces cellular senescence in fibroblasts. *J. Cell Commun. Signal.* 11 (1), 15–23. doi:10.1007/s12079-016-0359-1

Kim, B., Kim, H., Jung, S., Moon, A., Noh, D. Y., Lee, Z. H., et al. (2020). A CTGF-RUNX2-RANKL Axis in breast and prostate cancer cells promotes tumor progression in bone. *J. Bone Min. Res.* 35 (1), 155–166. doi:10.1002/jbmr.3869

Leong, S. S., Wong, J. H. D., Md Shah, M. N., Vijayananthan, A., Jalalonmuhali, M., Chow, T. K., et al. (2021). Shear wave elastography accurately detects chronic changes in renal histopathology. *Nephrology* 26 (1), 38–45. doi:10.1111/nep.13805

Li, B., and Wang, J. H. (2011). Fibroblasts and myofibroblasts in wound healing: Force generation and measurement. *J. Tissue Viability* 20 (4), 108–120. doi:10.1016/j.jtv.2009.11.004

Lipson, K. E., Wong, C., Teng, Y., and Spong, S. (2012). CTGF is a central mediator of tissue remodeling and fibrosis and its inhibition can reverse the process of fibrosis. *Fibrogenes. Tissue Repair* 5 (1), S24. doi:10.1186/1755-1536-5-S1-S24

Liu, F., Lagares, D., Choi, K. M., Stopfer, L., Marinkovic, A., Vrbanac, V., et al. (2015). Mechanosignaling through YAP and TAZ drives fibroblast activation and fibrosis. *Am. J. Physiol. Lung Cell. Mol. Physiol.* 308 (4), L344–L357. doi:10.1152/ajplung.00300.2014

Liu, F., Mih, J. D., Shea, B. S., Kho, A. T., Sharif, A. S., Tager, A. M., et al. (2010). Feedback amplification of fibrosis through matrix stiffening and COX-2 suppression. *J. Cell Biol.* 190 (4), 693–706. doi:10.1083/jcb.201004082

Liu, G., Cooley, M. A., Jarnicki, A. G., Borghuis, T., Nair, P. M., Tjin, G., et al. (2019). Fibulin-1c regulates transforming growth factor-beta activation in pulmonary tissue fibrosis. *JCI Insight* 5 (16), 124529. doi:10.1172/jci.insight.124529

McKinnon, D. D., Domaille, D. W., Cha, J. N., and Anseth, K. S. (2014). Biophysically defined and cytocompatible covalently adaptable networks as viscoelastic 3D cell culture systems. *Adv. Mat.* 26 (6), 865–872. doi:10.1002/adma.201303680

Mogi, M., and Kondo, A. (2010). ELISA for RANKL-OPG complex in mouse sera. *J. Immunoass. Immunochem.* 31 (2), 103–110. doi:10.1080/15321811003617305

Nguyen, X. X., Nishimoto, T., Takihara, T., Mlakar, L., Bradshaw, A. D., and Feghali-Bostwick, C. (2021). Lysyl oxidase directly contributes to extracellular matrix production and fibrosis in systemic sclerosis. *Am. J. Physiol. Lung Cell. Mol. Physiol.* 320 (1), L29–L40. doi:10.1152/ajplung.00173.2020

Noordhoek, J. A., Postma, D. S., Chong, L. L., Menkema, L., Kauffman, H. F., Timens, W., et al. (2005). Different modulation of decorin production by lung fibroblasts from patients with mild and severe emphysema. *COPD* 2 (1), 17–25. doi:10.1081/copd-200050678

Paapstel, K., Zilmer, M., Eha, J., Tootsi, K., Piir, A., and Kals, J. (2016). Association between fibulin-1 and aortic augmentation index in male patients with peripheral arterial disease. *Eur. J. Vasc. Endovasc. Surg.* 51 (1), 76–82. doi:10.1016/j.ejvs.2015.09.004

Parker, M. W., Rossi, D., Peterson, M., Smith, K., Sikstrom, K., White, E. S., et al. (2014). Fibrotic extracellular matrix activates a profibrotic positive feedback loop. *J. Clin. Invest.* 124 (4), 1622–1635. doi:10.1172/JCI71386

Petzold, G., Hofer, J., Ellenrieder, V., Neesse, A., and Kunsch, S. (2019). Liver stiffness measured by 2-dimensional shear wave elastography: Prospective evaluation of healthy volunteers and patients with liver cirrhosis. *J. Ultrasound Med.* 38 (7), 1769–1777. doi:10.1002/jum.14866

Piersma, B., Bank, R. A., and Boersema, M. (2015). Signaling in fibrosis: TGF-beta, WNT, and YAP/TAZ converge. *Front. Med.* 2, 59. doi:10.3389/fmed.2015.00059

Piersma, B., de Rond, S., Werker, P. M., Boo, S., Hinz, B., van Beuge, M. M., et al. (2015). YAP1 is a driver of myofibroblast differentiation in normal and diseased fibroblasts. *Am. J. Pathol.* 185 (12), 3326–3337. doi:10.1016/j.ajpath.2015.08.011

Pratsinis, H., Mavrogonatou, E., and Kletsas, D. (2019). Scarless wound healing: From development to senescence. *Adv. Drug Deliv. Rev.* 146, 325–343. doi:10.1016/j.addr.2018.04.011

Raghunathan, V. K., Morgan, J. T., Dreier, B., Reilly, C. M., Thomasy, S. M., Wood, J. A., et al. (2013). Role of substratum stiffness in modulating genes associated with extracellular matrix and mechanotransducers YAP and TAZ. *Invest. Ophthalmol. Vis. Sci.* 54 (1), 378–386. doi:10.1167/iovs.12-11007

Ravichandran, R., Islam, M. M., Alarcon, E. I., Samanta, A., Wang, S., Lundstrom, P., et al. (2016). Functionalised type-I collagen as a hydrogel building block for bio-orthogonal tissue engineering applications. *J. Mat. Chem. B* 4 (2), 318–326. doi:10.1039/c5tb02035b

Reinke, J. M., and Sorg, H. (2012). Wound repair and regeneration. *Eur. Surg. Res.* 49 (1), 35–43. doi:10.1159/000339613

Riser, B. L., Barnes, J. L., and Varani, J. (2015). Balanced regulation of the CCN family of matricellular proteins: A novel approach to the prevention and treatment of fibrosis and cancer. *J. Cell Commun. Signal.* 9 (4), 327–339. doi:10.1007/s12079-015-0309-3

Ruiz-Zapata, A. M., Heinz, A., Kerkhof, M. H., van de Westerlo-van Rijt, C., Schmelzer, C. E. H., Stoop, R., et al. (2020). Extracellular matrix stiffness and composition regulate the myofibroblast differentiation of vaginal fibroblasts. *Int. J. Mol. Sci.* 21 (13), E4762. doi:10.3390/ijms21134762

Sapir, L., and Tzlil, S. (2017). Talking over the extracellular matrix: How do cells communicate mechanically? *Semin. Cell Dev. Biol.* 71, 99–105. doi:10.1016/j.semcdb.2017.06.010

Schafer, M. J., White, T. A., Iijima, K., Haak, A. J., Ligresti, G., Atkinson, E. J., et al. (2017). Cellular senescence mediates fibrotic pulmonary disease. *Nat. Commun.* 8, 14532. doi:10.1038/ncomms14532

Schneider, C. A., Rasband, W. S., and Eliceiri, K. W. (2012). NIH image to ImageJ: 25 years of image analysis. *Nat. Methods* 9 (7), 671–675. doi:10.1038/nmeth.2089

Schuurman, W., Levett, P. A., Pot, M. W., van Weeren, P. R., Dhert, W. J., Hutmacher, D. W., et al. (2013). Gelatin-methacrylamide hydrogels as potential biomaterials for fabrication of tissue-engineered cartilage constructs. *Macromol. Biosci.* 13 (5), 551–561. doi:10.1002/mabi.201200471

Shirahama, H., Lee, B. H., Tan, L. P., and Cho, N. J. (2016). Precise tuning of facile one-pot gelatin methacryloyl (GelMA) Synthesis. *Sci. Rep.* 6, 31036. doi:10.1038/srep31036

Shome, D., von Woedtke, T., Riedel, K., and Masur, K. (2020). The HIPPO transducer YAP and its targets CTGF and Cyr61 drive a paracrine signalling in cold atmospheric plasma-mediated wound healing. *Oxid. Med. Cell. Longev.* 2020, 4910280. doi:10.1155/2020/4910280

Solon, J., Levental, I., Sengupta, K., Georges, P. C., and Janmey, P. A. (2007). Fibroblast adaptation and stiffness matching to soft elastic substrates. *Biophys. J.* 93 (12), 4453–4461. doi:10.1529/biophysj.106.101386

Stirling, D. R., Swain-Bowden, M. J., Lucas, A. M., Carpenter, A. E., Cimini, B. A., and Goodman, A. (2021). CellProfiler 4: Improvements in speed, utility and usability. *BMC Bioinforma.* 22 (1), 433. doi:10.1186/s12859-021-04344-9

Sun, M., Chi, G., Li, P., Lv, S., Xu, J., Xu, Z., et al. (2018). Effects of matrix stiffness on the morphology, adhesion, proliferation and osteogenic differentiation of mesenchymal stem cells. *Int. J. Med. Sci.* 15 (3), 257–268. doi:10.7150/ijms.21620

Tabatabaei, F., Moharamzadeh, K., and Tayebi, L. (2020). Fibroblast encapsulation in gelatin methacryloyl (GelMA) versus collagen hydrogel as substrates for oral mucosa tissue engineering. *J. Oral Biol. Craniofac. Res.* 10 (4), 573–577. doi:10.1016/j.jobcr.2020.08.015

Tjin, G., White, E. S., Faiz, A., Sicard, D., Tschumperlin, D. J., Mahar, A., et al. (2017). Correction: Lysyl oxidases regulate fibrillar collagen remodelling in idiopathic pulmonary fibrosis (doi: 10.1242/dmm.030114). *Dis. Model. Mech.* 10 (12), 1545. doi:10.1242/dmm.033191)

Totaro, A., Castellan, M., Battilana, G., Zanconato, F., Azzolin, L., Giulitti, S., et al. (2017). YAP/TAZ link cell mechanics to Notch signalling to control epidermal stem cell fate. *Nat. Commun.* 8 (1), 15206. doi:10.1038/ncomms15206

Tschumperlin, D. J., Ligresti, G., Hilscher, M. B., and Shah, V. H. (2018). Mechanosensing and fibrosis. *J. Clin. Invest.* 128 (1), 74–84. doi:10.1172/JCI93561

Uphoff, C. C., and Drexler, H. G. (2002). Detection of mycoplasma in leukemia-lymphoma cell lines using polymerase chain reaction. *Leukemia* 16 (2), 289–293. doi:10.1038/sj.leu.2402365

Valiente-Alandi, I., Potter, S. J., Salvador, A. M., Schafer, A. E., Schips, T., Carrillo-Salinas, F., et al. (2018). Inhibiting Fibronectin attenuates fibrosis and improves cardiac function in a model of heart failure. *Circulation* 138 (12), 1236–1252. doi:10.1161/CIRCULATIONAHA.118.034609

Verrecchia, F., and Mauviel, A. (2007). Transforming growth factor-beta and fibrosis. *World J. Gastroenterol.* 13 (22), 3056–3062. doi:10.3748/wjg.v13.i22.3056

Vial, C., Gutierrez, J., Santander, C., Cabrera, D., and Brandan, E. (2011). Decorin interacts with connective tissue growth factor (CTGF)/CCN2 by LRR12 inhibiting its biological activity. *J. Biol. Chem.* 286 (27), 24242–24252. doi:10.1074/jbc.M110.189365

Wang, B., Ke, W., Wang, K., Li, G., Ma, L., Lu, S., et al. (2021). Mechanosensitive ion channel Piezo1 activated by matrix stiffness regulates oxidative stress-induced senescence and apoptosis in human intervertebral disc degeneration. *Oxid. Med. Cell. Longev.* 2021, 8884922. doi:10.1155/2021/8884922

Wang, R., Yu, Z., Sunchu, B., Shoaf, J., Dang, I., Zhao, S., et al. (2017). Rapamycin inhibits the secretory phenotype of senescent cells by a Nrf2-independent mechanism. *Aging Cell* 16 (3), 564–574. doi:10.1111/acel.12587

Wang, Y., Michiels, T., Setroikromo, R., van Merkerk, R., Cool, R. H., and Quax, W. J. (2019). Creation of RANKL mutants with low affinity for decoy receptor OPG and their potential anti-fibrosis activity. *FEBS J.* 286 (18), 3582–3593. doi:10.1111/febs.14925

Waters, D. W., Blokland, K. E. C., Pathinayake, P. S., Wei, L., Schuliga, M., Jaffar, J., et al. (2019). STAT3 regulates the onset of oxidant-induced senescence in lung fibroblasts. *Am. J. Respir. Cell Mol. Biol.* 61 (1), 61–73. doi:10.1165/rcmb.2018-0328OC

Wershof, E., Park, D., Barry, D. J., Jenkins, R. P., Rullan, A., Wilkins, A., et al. (2021). A Fiji macro for quantifying pattern in extracellular matrix. *Life Sci. Alliance* 4 (3), e202000880. doi:10.26508/lsa.202000880

Westergren-Thorsson, G., Sime, P., Jordana, M., Gauldie, J., Sarnstrand, B., and Malmstrom, A. (2004). Lung fibroblast clones from normal and fibrotic subjects differ in hyaluronan and decorin production and rate of proliferation. *Int. J. Biochem. Cell Biol.* 36 (8), 1573–1584. doi:10.1016/j.biocel.2004.01.009

Wickert, L. E., Pomerenke, S., Mitchell, I., Masters, K. S., and Kreeger, P. K. (2016). Hierarchy of cellular decisions in collective behavior: Implications for wound healing. *Sci. Rep.* 6 (1), 20139. doi:10.1038/srep20139

Woldhuis, R. R., de Vries, M., Timens, W., van den Berge, M., Demaria, M., Oliver, B. G. G., et al. (2020). Link between increased cellular senescence and extracellular matrix changes in COPD. *Am. J. Physiol. Lung Cell. Mol. Physiol.* 319 (1), L48–L60. doi:10.1152/ajplung.00028.2020

Woldhuis, R. R., Heijink, I. H., van den Berge, M., Timens, W., Oliver, B. G. G., de Vries, M., et al. (2020). COPD-derived fibroblasts secrete higher levels of senescence-associated secretory phenotype proteins. *Thorax* 76, 508–511. thoraxjnl-2020. doi:10.1136/thoraxjnl-2020-215114

Yan, X., Xiong, X., and Chen, Y. G. (2018). Feedback regulation of TGF-beta signaling. *Acta Biochim. Biophys. Sin.* 50 (1), 37–50. doi:10.1093/abbs/gmx129

YasminMaskari, R. A., McEniery, C. M., Cleary, S. E., Li, Y., Siew, K., et al. (2018). The matrix proteins aggrecan and fibulin-1 play a key role in determining aortic stiffness. *Sci. Rep.* 8 (1), 8550. doi:10.1038/s41598-018-25851-5

Zhang, C., Zhu, H., Ren, X., Gao, B., Cheng, B., Liu, S., et al. (2021). Mechanics-driven nuclear localization of YAP can be reversed by N-cadherin ligation in mesenchymal stem cells. *Nat. Commun.* 12 (1), 6229. doi:10.1038/s41467-021-26454-x

Zhang, W., Ge, Y., Cheng, Q., Zhang, Q., Fang, L., and Zheng, J. (2018). Decorin is a pivotal effector in the extracellular matrix and tumour microenvironment. *Oncotarget* 9 (4), 5480–5491. doi:10.18632/oncotarget.23869

Zhao, B., Wei, X., Li, W., Udan, R. S., Yang, Q., Kim, J., et al. (2007). Inactivation of YAP oncoprotein by the Hippo pathway is involved in cell contact inhibition and tissue growth control. *Genes Dev.* 21 (21), 2747–2761. doi:10.1101/gad.1602907

Zhou, Y., Horowitz, J. C., Naba, A., Ambalavanan, N., Atabai, K., Balestrini, J., et al. (2018). Extracellular matrix in lung development, homeostasis and disease. *Matrix Biol.* 73, 77–104. doi:10.1016/j.matbio.2018.03.005

Zhou, Z., Qu, J., He, L., Zhu, Y., Yang, S. Z., Zhang, F., et al. (2020). Stiff matrix instigates type I collagen biogenesis by mammalian cleavage factor I complex-mediated alternative polyadenylation. *JCI Insight* 5 (3), 133972. doi:10.1172/jci.insight.133972

Zhu, M., Wang, Y., Ferracci, G., Zheng, J., Cho, N-J., and Lee, B. H. (2019). Gelatin methacryloyl and its hydrogels with an exceptional degre of controllability and batch-to-batch consistency. *Sci. Rep.* 9 (1), 6863. doi:10.1038/s41598-019-42186-x

frontiers | Frontiers in Pharmacology

TYPE Review
PUBLISHED 03 November 2022
DOI 10.3389/fphar.2022.995051

OPEN ACCESS

EDITED BY
Isaac Kirubakaran Sundar,
University of Kansas Medical Center,
United States

REVIEWED BY
Ranu Surolia,
University of Alabama at Birmingham,
United States
Niki Ubags,
Service de Pneumologie, Centre
Hospitalier Universitaire Vaudois,
Switzerland
Claude Jourdan Le Saux,
School of Medicine, United States

*CORRESPONDENCE
Mugdha M. Joglekar,
m.m.joglekar@umcg.nl
Janette K. Burgess,
j.k.burgess@umcg.nl

†These authors have contributed equally to this work and share first authorship

SPECIALTY SECTION
This article was submitted
to Respiratory Pharmacology,
a section of the journal
Frontiers in Pharmacology

RECEIVED 15 July 2022
ACCEPTED 19 October 2022
PUBLISHED 03 November 2022

CITATION
Joglekar MM, Nizamoglu M, Fan Y, Nemani SSP, Weckmann M, Pouwels SD, Heijink IH, Melgert BN, Pillay J and Burgess JK (2022), Highway to heal: Influence of altered extracellular matrix on infiltrating immune cells during acute and chronic lung diseases.
Front. Pharmacol. 13:995051.
doi: 10.3389/fphar.2022.995051

Highway to *heal*: Influence of altered extracellular matrix on infiltrating immune cells during acute and chronic lung diseases

Mugdha M. Joglekar[1,2*†], Mehmet Nizamoglu[1,2†], YiWen Fan[1,2], Sai Sneha Priya Nemani[3,4], Markus Weckmann[3,4], Simon D. Pouwels[1,2,5], Irene H. Heijink[1,2,5], Barbro N. Melgert[2,6], Janesh Pillay[2,7] and Janette K. Burgess[1,2,8*]

[1]University of Groningen, University Medical Center Groningen, Department of Pathology and Medical Biology, Groningen, Netherlands, [2]University of Groningen, University Medical Center Groningen, Groningen Research Institute for Asthma and COPD (GRIAC), Groningen, Netherlands, [3]Department of Paediatric Pneumology &Allergology, University Children's Hospital, Schleswig-Holstein, Campus Lübeck, Germany, [4]Epigenetics of Chronic Lung Disease, Priority Research Area Chronic Lung Diseases; Leibniz Lung Research Center Borstel; Airway Research Center North (ARCN), Member of the German Center for Lung Research (DZL), Germany, [5]University of Groningen, University Medical Center Groningen, Department of Pulmonology, Groningen, Netherlands, [6] University of Groningen, Department of Molecular Pharmacology, Groningen Research Institute for Pharmacy, Groningen, Netherlands, [7]University of Groningen, University Medical Center Groningen, Department of Critical Care, Groningen, Netherlands, [8]University of Groningen, University Medical Center Groningen, W.J. Kolff Institute for Biomedical Engineering and Materials Science-FB41, Groningen, Netherlands

Environmental insults including respiratory infections, in combination with genetic predisposition, may lead to lung diseases such as chronic obstructive pulmonary disease, lung fibrosis, asthma, and acute respiratory distress syndrome. Common characteristics of these diseases are infiltration and activation of inflammatory cells and abnormal extracellular matrix (ECM) turnover, leading to tissue damage and impairments in lung function. The ECM provides three-dimensional (3D) architectural support to the lung and crucial biochemical and biophysical cues to the cells, directing cellular processes. As immune cells travel to reach any site of injury, they encounter the composition and various mechanical features of the ECM. Emerging evidence demonstrates the crucial role played by the local environment in recruiting immune cells and their function in lung diseases. Moreover, recent developments in the field have elucidated considerable differences in responses of immune cells in two-dimensional versus 3D modeling systems. Examining the effect of individual parameters of the ECM to study their effect independently and collectively in a 3D microenvironment will help in better understanding disease pathobiology. In this article, we discuss the importance of investigating cellular migration and recent advances in this field. Moreover, we summarize changes in the ECM in lung diseases and the potential impacts on infiltrating immune cell migration in these diseases. There has been compelling progress in this field that encourages further developments, such as advanced *in vitro* 3D modeling using native ECM-based models, patient-derived materials, and bioprinting. We conclude with an overview of these state-of-the-art methodologies, followed by a

discussion on developing novel and innovative models and the practical challenges envisaged in implementing and utilizing these systems.

KEYWORDS

extracellular matrix, migration, infiltrating immune cells, *in vitro* models, lung diseases, three-dimensional

1. Introduction

1.1 ECM as the highway for infiltrating immune cells

Cellular migration has a fundamental role in directing development, tissue homeostasis, and disease progression (Morales et al., 2021; Yamada et al., 2022). Cells have different modes of migration–singular, amoeboid or mesenchymal, or collective fashion depending on the local tissue microenvironment and activated signaling pathways (van Helvert et al., 2018; Yamada and Sixt, 2019). The extracellular matrix (ECM) of the lung is a dynamic structural network which consists of proteins, glycosaminoglycans, and glycoproteins (Burgstaller et al., 2017). It provides structural support during important mechanical events of breathing. It is also an important bioactive component of the cellular microenvironment as it provides cues that regulate cellular processes (Theocharis et al., 2016; Yamada and Sixt, 2019). Local molecular composition (including growth factors and cytokines) and biomechanical properties (elasticity, stiffness, and compression forces) of the ECM can govern migration of (infiltrating) immune cells (van Helvert et al., 2018; Yamada and Sixt, 2019; Morales et al., 2021). Other factors that influence cellular migration include confinement of cells, ECM crosslinking and remodeling, and ECM geometry such as topology, fiber alignment, and porosity (van Helvert et al., 2018; Yamada and Sixt, 2019; Morales et al., 2021; Burgess and Harmsen, 2022). Further, ECM fragments resultant from remodeling can promote or inhibit cellular migration (Gu et al., 2018; Nissen et al., 2018; Sharma et al., 2018; de Castro Bras and Frangogiannis, 2020).

The lung is a unique organ exposed to exogenous environmental insults and infectious agents and consequently has highly regulated immune and damage repair responses. Severe or repetitive insults can cause micro-injuries leading to acute and chronic lung diseases (Labaki and Han, 2020). Chronic lung diseases are in general incurable and often have high hospitalization rates. Additionally, some patients are at risk of disease exacerbations that accelerate disease progression. Moreover, insight into the pathobiology of each of the lung diseases is still limited (Labaki and Han, 2020). Therefore, understanding the immunopathology of each of these diseases is essential for developing effective clinical management and new treatment approaches. Chronic obstructive pulmonary disease (COPD), lung fibrosis, asthma, and acute respiratory distress syndrome (ARDS) are all characterized by abnormal ECM turnover and chronic inflammatory responses in varying degrees, which lead to tissue damage (Ito et al., 2019; Burgess and Harmsen, 2022).

Investigating cell-ECM interactions as a contributing factor to the disease progression has been emerging in the last decade (McMahon et al., 2021; Burgess and Harmsen, 2022). Upon injury, the process of tissue repair is initiated, during which recruited immune cells migrate through ECM to reach the target location. Inflammation and resolution of wound healing processes are regulated by contribution of (infiltrating) immune cells (Volk et al., 2013; Manon-Jensen et al., 2016; Wang et al., 2022). It is likely that their migration, in these lung diseases, through aberrant ECM will affect the function of the infiltrating immune cells.

Conventional immune cell migration studies using standard two-dimensional (2D) cell assessment systems have provided conceptual advances (Puttur et al., 2019). Such studies have revealed a specialized mode of migration (repetitive protrusion, adhesion and contraction) that cells adopt in 2D microenvironments (Hallmann et al., 2015; Yamada and Sixt, 2019). However, it is now clear that cells implement several different modes of migration in three-dimensional (3D) environments (Hallmann et al., 2015; Yamada and Sixt, 2019). In both 2D and 3D *in vitro* migration assays the role of ECM in regulating these processes has been explored. Several different materials have been used as ECM-mimicking substrates. These include synthetic polymers such as poly (ethylene glycol) (Widener et al., 2021) and natural polymers such as collagen (Li et al., 2018; Surendran et al., 2021). Methodologies including precision cut lung slices (PCLS), organoids, lung-on-chip, whole decellularized lung tissues, and hydrogels have been developed over the past decades to mimic physiological environments *in vitro*, each with their own advantages and challenges (Gkatzis et al., 2018; Liu et al., 2019; Nizamoglu et al., 2022). However, there has been limited implementation of such models for studying immune cell infiltration, thereby providing future opportunities for exploring the dynamics between ECM and infiltrating immune cell migration in the context of lung diseases.

1.2 Flyovers: New discoveries in cellular migration and implications of the ECM highway

As the field moves ahead with innovative models, it is simultaneously important to consider new discoveries in cellular migration and how the inclusion of ECM could add

TABLE 1 Changes in the components of extracellular matrix in lung diseases compared to non-diseased controls (unless otherwise specified). *

ECM proteins	Lung fibrosis	COPD	Asthma	ARDS
Collagen Type I	a) Higher in airways Liu et al. (2021a); b) Higher in fibroblastic foci Herrera et al. (2019)	Lower in inner layer of large and small airways and outer layer of small airways Hogg et al. (2009); Annoni et al. (2012)	a) Higher in small airways Dolhnikoff et al. (2009); b) Higher deposits in reticular basement membrane Hough et al. (2020)	Higher in early and late phase Santos et al. (2006)
Collagen Type III	a) Higher in airways Liu et al. (2021a); b) Higher in fibroblastic foci Herrera et al. (2019)	Relatively higher compared to collagen type I Hogg et al. (2009)	a) Lower in small airways of fatal asthma Dolhnikoff et al. (2009); b) Higher in the airway mucosa Araujo et al. (2008)	Higher in the early phase Santos et al. (2006)
Collagen Type IV	Higher in fibroblastic foci Herrera et al. (2018)	Higher in large airways with epithelial damage Dekkers et al. (2021)	Collagen type IV, alpha 3 deposition is lower in the asthmatic airways Burgess et al. (2010)	Unknown
Collagen Type VI	Higher in fibroblastic foci Herrera et al. (2019)	Higher in airways Abdillahi et al. (2015)	Higher in the alveolar parenchyma of uncontrolled asthmatics Andersson et al. (2018)	Unknown
Other collagens	Collagen type V: higher in fibroblastic foci Herrera et al. (2019)	a) Overall deposition higher in collagen in alveolar walls and small airways walls Eurlings et al. (2014); b) Lower total collagen Hogg et al. (2009)	Collagen type V: higher in airways Liu et al. (2021b)	Unknown
Elastin	Higher in fibrotic areas Burgess et al. (2016)	Lower in alveolar and small airways walls Eurlings et al. (2014)	a) Lower in subepithelium Reddel et al. (2012); b) Higher in submucosa Reddel et al. (2012)	a) Degraded in the early phase Santos et al. (2006); b) Deposited in the late phase Santos et al. (2006)
Fibronectin	Higher in fibroblastic foci Herrera et al. (2019)	Higher in inner and outer layer of small airways, no difference in parenchyma Annoni et al. (2012)	Higher in the outer area of the small airways Dolhnikoff et al. (2009)	Higher in both early and late phase of ARDS Morales et al. (2011); Ito et al. (2019)
Laminin	Unknown	β2: higher in large airways with epithelial damage Dekkers et al. (2021)	α2,3,5 chains: higher epithelial basement membrane expression; α4,5 chains: lower in ASM BM expression Dekkers et al. (2021)	Unknown
Glycosaminoglycans, glycoproteins and proteoglycans	Hyaluronic acid: higher expression in IPF lungs Herrera et al. (2019); Versican: higher expression in fibroblastic foci Herrera et al. (2019); Tenascin-C: higher expression in fibroblastic foci Burgess et al. (2016)	Hyaluronic acid: higher in alveolar and small airway walls Eurlings et al. (2014); Versican: lower in distal parenchyma Annoni et al. (2012); Decorin, biglycan, and lumican: No differences Annoni et al. (2012), lower in peribronchiolar area in severe emphysema van Straaten et al. (1999); Tenascin-C: higher in subepithelial area of large airways and inner layer of small airways Annoni et al. (2012)	Hyaluronic acid: higher in peri-bronchioles and perivascular regions in the lung Lauer et al. (2015); Decorin, lumican, and versican: higher in the subepithelial layer of the airway wall in atopic asthmatics Hough et al. (2020); Biglycan, versican and decorin: higher percentage areas in both central airways and alveolar parenchyma of non-controlled asthma Weitoft et al. (2014)	Versican: higher in small airway walls of patients with fatal ARDS Morales et al. (2011), higher in thickened alveolar walls Bensadoun et al. (1996)

*only the most frequently investigated ECM components are included. Soluble ECM fragments reported in fluids including bronchoalveolar lavage and sputum are beyond the scope of this table.

to this knowledge. Cells produce and leave behind retraction fibers during migration that support the formation of vesicle-like structures called migrasomes (Tavano and Heisenberg, 2019; Fan et al., 2022). Cancer cells more frequently migrated along residual retraction fibers in microfluidic channels compared to channels without these fibers (Lee et al., 2021). Neutrophils have been shown to leave cytoplasmic trails containing chemokines for T cells upon viral infection, which may very well consist of migrasomes (Lim et al., 2015). The involvement of the ECM was highlighted through the discovery that the generation of these extracellular vesicles was being triggered by the interaction of cells with fibronectin fibers (Wu et al., 2017; Lee et al., 2021). In concert, migratory trajectories of chemotaxing neutrophils have previously been shown dependent on collagen concentration

(Francois et al., 2021). Thus, migrasomes in combination with trails, could increase efficiency of directional migration. The effect of healthy and diseased ECM on the cellular source of migrasomes and trails could begin to explain the continual recruitment of immune cells. Whether a diseased ECM highway provides additional road bumps in the formation of migrasomes and migratory trails remains unexplored. Altogether, these studies highlight the role of the ECM in not just the regulation of the migratory behavior of first responders, but also the recruitment of subsequent immune cells or secondary responses such as adaptive immunity. A study using *Drosophila* embryos demonstrated weakened cell-ECM connections during cellular division that facilitated macrophage infiltration (Akhmanova et al., 2022). Although it may sound counter intuitive, the (increased rate of) division of cells might act as an "exit" from the ECM highway. A similar phenomenon occurring in diseases associated with hyperproliferation of stromal cells such as asthma and fibrotic lung diseases may be possible but it is unexplored to date. These new insights mentioned above on how infiltrating immune cells interact with ECM and the (resident or recruited) cells can also be further expanded in the context of the influence of ECM using *in vitro* models.

In this review, we highlight the importance of interactions between the "highway" ECM and infiltrating cells in the pathogenesis of various lung diseases. We review emerging technologies for *in vitro* modeling that better represent physiological characteristics. Some challenges that exist for implementing these models to study ECM-immune cell interactions during their migration into lung tissue will also be discussed.

2. A hazardous highway: Altered ECM in lung diseases and effects on infiltrating immune cells

Knowledge of how ECM relates to cellular migration has been the focus of recent studies illustrating that the ECM acts as a highway for the migrating/infiltrating immune cells. Biochemical and biomechanical properties of ECM influence the migratory behavior of cells, including immune cells. The importance of available adhesion ligands was established when fibroblasts were able to migrate along stiffness gradients (durotaxis) on fibronectin-coated substrates, whereas this ability was lost on substrates coated with laminin (Hartman et al., 2017). Increased fiber alignment promoted cell migration and directionality of migration (Wang et al., 2018). The inability of aged fibroblasts to produce a hyaluronan and proteoglycan cross-linking proteinresulted in the formation of a more aligned matrix that promoted metastasis while inhibiting T cell migration (Kaur et al., 2019). Accelerated ageing is a distinctive feature of some chronic lung diseases such as COPD (Brandsma et al., 2017) and idiopathic pulmonary fibrosis (IPF) (Chilosi et al., 2013; Selman and Pardo, 2021), making the above observation relevant to the field of lung research. In addition to being a reservoir for growth factors and cytokines, other factors of the ECM discussed here collectively influence the migratory behavior of infiltrating immune cells. As the composition of the ECM has been the main focus of many studies so far, most knowledge is on the influence of different ECM components on cell migration. A summary of the changes in composition of lung ECM during lung diseases can be found in Table 1. It is evident from this table that different studies have different conclusions. The diversity in these observations could be attributed to disease heterogeneity, variation in study population, and disease phenotypes. Nevertheless, the table can serve as a guide while developing *in vitro* models within the realms of current knowledge. A simple assumption would be that altered composition of ECM triggers changes in the mesenchymal mode of migration due to the alterations in the number of binding domains available for integrins (Yamada and Sixt, 2019). The following subsections will discuss how infiltrating immune cells participate in lung diseases and what is the role of ECM in influencing these migration patterns in the context of lung fibrosis, COPD, asthma, and ARDS.

2.1 Lung fibrosis

ECM in lung parenchyma during lung fibrosis is substantially altered from healthy lungs. This has been illustrated both in terms of amounts and/or ratios of ECM components and with respect to the 3D organization of the ECM network (Burgess et al., 2016; Burgstaller et al., 2017; Burgess and Harmsen, 2022; Nizamoglu and Burgess, 2022). Along with altered biochemical composition (Table 1), altered mechanical environment with increased stiffness, decreased viscoelastic relaxation, as well as disorganized fibers and abnormal topography are well-documented changes in ECM in lung fibrosis (Booth et al., 2012; Tjin et al., 2017; de Hilster et al., 2020).

The involvement of circulating immune cells in lung fibrosis is well recognized: among these cells are monocytes and neutrophils (Ishikawa et al., 2021). While the details of recruitment and involvement of these cells are outside scope of this review, these processes can take place through both soluble mediators (Huang et al., 2020; van Geffen et al., 2021) and mechanical factors (Du et al., 2022). Higher counts of monocytes in blood were associated with faster disease progression in interstitial lung diseases (Kim et al., 2022). In mice, monocytes arriving in fibrotic lung tissue transform to macrophages to repopulate lung tissue and remain in the tissue with higher profibrotic activity compared to tissue-resident macrophages (Misharin et al., 2017). Monocytes and neutrophils were found in higher numbers in bronchoalveolar lavage (BAL) fluid of IPF patients (Kinder et al., 2008).

Neutrophils were also increased during acute exacerbations of lung fibrosis (Lee et al., 2012). Due to their dynamic nature, both monocytes/macrophages and neutrophils are readily instructed by their microenvironment (Nissen et al., 2018; Vasse et al., 2018; Vasse et al., 2021).

The altered (fibrotic) microenvironment influences infiltrating immune cells in several different ways. In a study, fibroblasts cultured for different durations resulted in varying degrees of fiber organization in collagen matrices (Pakshir et al., 2019). These alterations in fiber organization, however, were unable to influence macrophage migration speed in 3D (Pakshir et al., 2019). On the other hand, neutrophil migration speed but not the directionality, was lower in denser 3D collagen networks (Francois et al., 2021). When fiber crosslinking was applied, increased crosslinking of 2D fibrin surfaces promoted macrophage migration. However, the fiber crosslinking also changed other mechanical parameters, such as stiffness. This unintended change might have also influenced the migrational behavior of the infiltrating immune cells (Hsieh et al., 2019). The influence of ECM crosslinking on migration of neutrophils has yet to be described. Similarly, the influence of altered stress relaxation, another important property of altered microenvironment in fibrotic lung ECM, on infiltrating immune cells has not been examined. New insights for lung fibrosis research can be drawn from a recent study illustrating minimal migration of cancer cells on 2D surfaces which lack stress relaxation, but robust migration of the same cells on the surfaces with high stress relaxation capacity (Adebowale et al., 2021). In addition to the changes in the ECM organization, released ECM fragments can also alter the migratory behavior of the lung resident cells (Nizamoglu and Burgess, 2022). Although there are recent studies focusing on these fragments (Burgess and Harmsen, 2022), their potential influence on migratory behavior and function of infiltrating immune cells remains unknown.

2.2 Chronic obstructive pulmonary disease

COPD is characterized by excessive ECM remodeling and ECM deposition around the small airways, while the alveolar region is characterized by ECM disruption and tissue destruction (Burgess et al., 2016; Brandsma et al., 2020). Inflammatory responses are central to COPD and understanding the immunopathology is particularly important as current treatments are ineffective in mitigating disease progression and lung tissue damage. In the context of migration in COPD, neutrophils, monocytes, and T cells to an extent, and have received most attention. These cells, and associated secreted factors, have been reported elevated in patients' sputum, blood, and BAL, and often correlate with the progression of COPD (Hogg et al., 2004; Vargas-Rojas et al., 2011). In addition, neutrophils and macrophages from patients with COPD display impaired effector functions such as efferocytosis and phagocytosis (Taylor et al., 2010; Tan et al., 2017; Dicker et al., 2018; Belchamber et al., 2019), likely extending to a variation in normal migratory behavior of infiltrating immune cells. This has been previously demonstrated with respect to chemotactic cytokines (Sapey et al., 2011; Costa et al., 2016).

While studies exploring the influence of the ECM and ECM fragments on immune cell migration in COPD are limited, sputum has often been investigated as a chemotactic agent. $CD14^+$ monocytes from healthy individuals not only migrated more than $CD14^+$ monocytes from patients with COPD, but also more towards COPD sputum compared to normal sputum (Ravi et al., 2017). Similarly, neutrophils from patients with COPD migrated more towards COPD sputum compared to normal sputum, although T cells from these patients did not show the same trend (Wu et al., 2015). These studies did not identify specific sputum factors responsible for the induction of immune migratory responses. Thus, there can be multiple constituents of the sputum that can have chemotactic effects on cells including ECM fragments (Nissen et al., 2018). Indeed, alterations in sputum composition between health and disease have been demonstrated (Titz et al., 2015; Moon et al., 2018), also with respect to differential levels of ECM fragments that can alter cellular migration in patients with COPD. For example, fragments of production or degradation of collagen (Schumann et al., 2018), elastin (Ronnow et al., 2019), and fibrinogen (Manon-Jensen et al., 2019) have also been detected in sputum and serum/plasma in patients with COPD and are proposed as biomarkers of disease progression. Proline-glycine-proline (PGP), a matrikine derived from collagen, is elevated in sputum of patients with COPD and is a potent chemoattractant for neutrophils (Gaggar et al., 2008; O'Reilly et al., 2013; Patel et al., 2018). However, the role of abnormal ECM in recruitment and regulation of migratory behavior of immune cells remains unexplored.

Secreted pro-inflammatory factors such as cytokines and proteases perpetuate immune responses and remodel ECM (Ni and Dong, 2018; Brightling and Greening, 2019). In COPD, higher neutrophil elastase activity was associated with emphysematous tissue destruction (Walton et al., 2016), and lower trans-endothelial T cell migration (Rao et al., 2004). Consequently, biomechanical properties of lung tissue of patients with COPD are altered, such as loss of elasticity, increased stiffness around small airways, and decreased stiffness in the emphysematous regions (Burgess and Harmsen, 2022). These changes are bound to alter the characteristics of cellular migration.

2.3 Asthma

Asthma is characterized by hallmark features such as airway inflammation and remodelling. Airway remodeling, a feature of

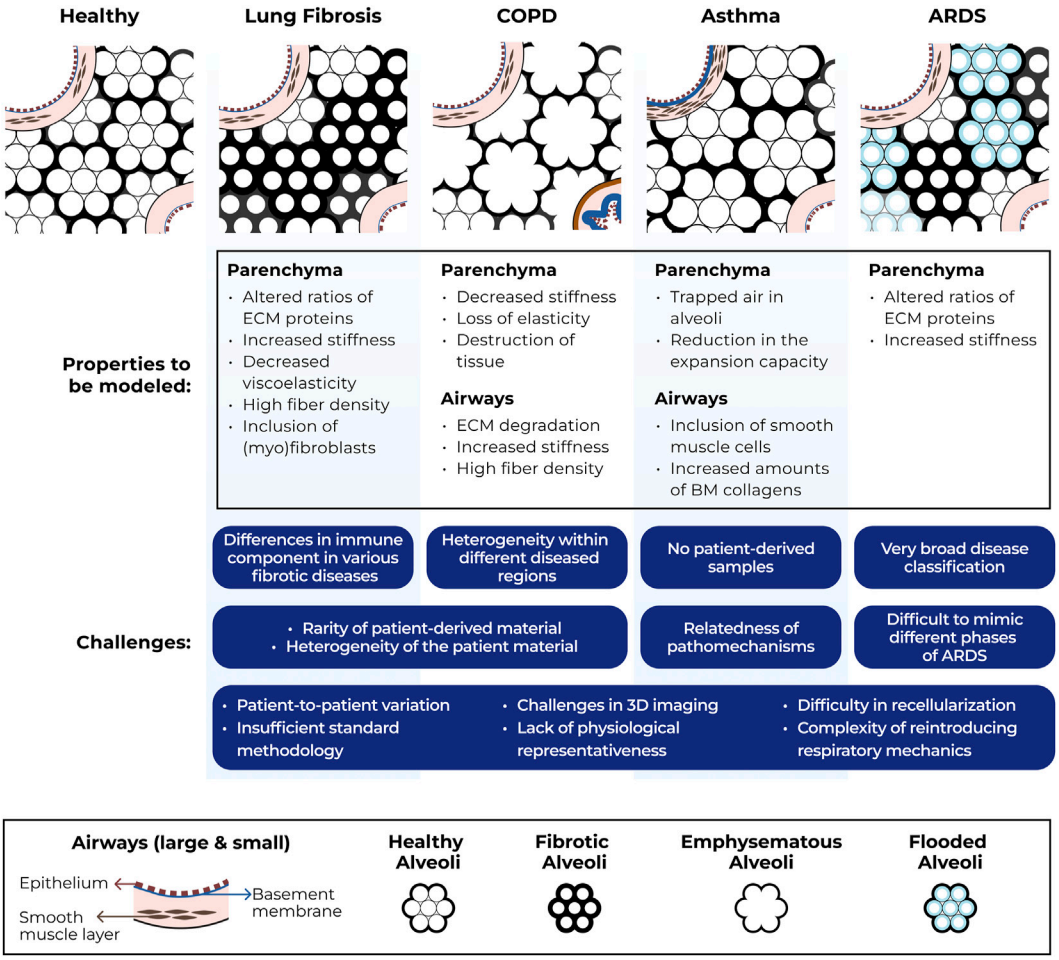

FIGURE 1
Schematic representation of structural ECM changes in lung diseases, ideal properties for modeling immune cell migration through ECM in these disease conditions and challenges associated with generating such models. COPD = chronic obstructive pulmonary disease, ARDS = acute respiratory distress syndrome, ECM = extracellular matrix, BM = basement membrane, 3D = three-dimensional.

asthma—but also seen in COPD, refers to the structural and ECM changes in both small and large airways (Hough et al., 2020). The profile of ECM is altered in the asthmatic airways with less deposition of collagen type IV, elastin, and more deposition of collagen type I, fibronectin, laminin, periostin, versican, decorin, and lumican (Burgess et al., 2010; Hough et al., 2020; Dekkers et al., 2021). Recently, also fibrillar collagen was shown to be fragmented and disorganized in the lamina propria of large and small airways from patients with asthma (Mostaco-Guidolin et al., 2019). Several factors have been identified in asthma that led to abnormal turnover of ECM components such as epigenetic modifications, recurrent viral infections and excess fibrolysis (Pech et al., 2018; Nemani et al., 2021; Weckmann et al., 2021; Ronnow et al., 2022).

Several immune cells, including neutrophils, eosinophils, monocytes, macrophages, and mast cells, among others, are considered to play an important role in airway remodeling in asthma (Holgate et al., 2015; Helfrich et al., 2019). Alveolar macrophages, mast cells, eosinophils, and neutrophils were shown to degrade ECM by releasing matrix metalloproteinase (MMP)−9 (Hough et al., 2020). MMP-driven degradation of collagen released biologically active fragments in asthma such as the pro-neutrophilic matrikine PGP (Patel and Snelgrove, 2018). Another significant matrikine in asthma is tumstatin, a non-collagenous domain of collagen type IV α3 which was shown to be significantly reduced in airways from patients with asthma (Burgess et al., 2010). Interestingly, when mice were treated with tumstatin the inflammatory cell counts in the lungs were reduced (Burgess et al., 2010).

It was recently suggested that migration of tissue eosinophils in ECM - likely occurs *via* periostin interactions which were particularly higher in T2-high asthmaand correlated with

recruitment of eosinophils to the airway (Johansson, 2017; Burgess et al., 2020). Another study reported the chemotaxis of neutrophils was reduced on tumstatin-induced asthmatic airway smooth muscle cell-derived ECM (Harkness et al., 2017). Using a human airway-on-chip, transmigration of immune cells to the epithelial lumen from the vascular microchannel during a viral infection was analyzed. Greatest neutrophil adhesion at the surface of the microvascular endothelium was observed in presence of IL-13 stimulation (to mimic T-helper cell type 2 asthmatic phenotype) rapidly followed by neutrophil trans-endothelial migration through a combination of migratory events (Nawroth et al., 2020).

2.4 Acute respiratory distress syndrome

In ARDS, changes in pulmonary ECM are a direct consequence of the inflammatory injury and subsequent repair responses (Tomashefski, 2000; Ito et al., 2019). The changes in ECM can be divided in distinct ARDS phases, with ECM destruction and alveolar and capillary damage predominating in the early phase, which transitions to a fibroproliferative repair phase later. However, the phases are not strictly separated as early fibroblast activation and matrix deposition are also present (Meduri et al., 1998; Boyd et al., 2020).

Early recruitment of neutrophils and monocytes, following lung injury results in ECM degradation, predominantly through the production of MMPs (Torii et al., 1997; Davey et al., 2011). Fragments generated from degradation of ECM play a role in amplifying recruitment of inflammatory cells. The matrikines PGP and its acetylated form induce neutrophil chemotactic activity and migration (Biesalski, 2007; Pierpaoli et al., 2011; Sava et al., 2015; Misiura and Miltyk, 2019; Palmieri et al., 2019). This effect was dose dependent (van Houwelingen et al., 2008) and occurred through C-X-C motif chemokine receptor two interaction on leukocytes (Weathington et al., 2006; Braber et al., 2011; Kim et al., 2011; Hahn et al., 2015; Sharma et al., 2018; Robison et al., 2021). Additionally, the matricellular protein cellular communication network factor 1 (CCN1) was found in high concentrations in BAL fluid of patients with ARDS, while mice overexpressing CCN1 spontaneously developed ARDS coinciding with neutrophil influx (Grazioli et al., 2015; Morrell et al., 2020). The direct effect of CCN1 on cell migration is not straightforward, as it appeared to increase chemokinesis by interaction with αMβ2 integrins. However, prolonged presence of CCN1 inhibited cell migration and played a role in neutrophil clearance through efferocytosis (Lobel et al., 2012; Jun et al., 2015). Fibronectin deposition in the acute phase of ARDS facilitated neutrophil migration partly by higher expression and redistribution of intracellular adhesion molecule-1 (ICAM-1) in endothelial cells (Sava et al., 2015). In a model of *S. aureus* induced skin infection, hyaluronic acid deposition was increased in ARDS and the failure to digest this ECM increased neutrophil influx (Hällgren et al., 1989; Dokoshi et al., 2020).

Less is known about the exact ECM changes in the fibroproliferative phase of ARDS. Synthesis of collagen types I and III was present, but unlike lung fibrosis; at this stage no information on the crosslinking states of these collagens exists. Interestingly, commonalities including similar ECM composition and distribution between IPF and ARDS have been recognized (Raghu et al., 1985). In patients with ARDS, epithelial lining fluid levels of C-terminal propeptide (marker of collagen type I synthesis) were increased, while degradation products of collagen type I/II were reduced compared to individuals at risk of ARDS/ALI (Armstrong et al., 1999). BAL measurement of N-terminal peptide of alveolar procollagen type III, a precursor of collagen type III, has been validated as a diagnostic tool to indicate fibroproliferation in ARDS patients as well as to identify patients who can benefit from corticosteroid treatment (Forel et al., 2015; Hamon et al., 2019). Serological and BAL levels of hyaluronic acid were found associated with ARDS severity and organ failure (Esposito et al., 2017). Recently, lung tissue obtained from patients with coronavirus disease (COVID-19) induced ARDS, stained positively for hyaluronic acid which was associated with the degree of alveolar damage (Hellman et al., 2020). An *in vitro* chemotaxis model recently showed that collagen type III had an inhibitory effect on neutrophil migration regarding track length, direction, and targeting (Kraus et al., 2021). However, it is still unknown whether these mechanisms are active in ARDS.

3 *In vitro* modeling

To further strengthen understanding of interactions between infiltrating immune cells and ECM in the context of migration, development of innovative *in vitro* models is key. Some of the ideal properties for *in vitro* modeling of immune cell migration in different types of lung diseases are illustrated in Figure 1.

Moving towards *in vitro* models for studying ECM influences on immune cell migration, ECM-derived *in vitro* models are emerging as a novel methodology. ECM-derived systems have been established using single proteins or by decellularization of native lung tissue. These models recapitulate the biochemical and mechanical properties of native ECM more closely than 2D models in which cells are cultured on plastic with unrepresentative polarity. To facilitate the investigation of altered biomechanics separately or in combination with altered composition of lung ECM, development of novel methodologies and ECM-mimicking biomaterials is warranted. This includes but is not limited to: changing pore size or fiber density without changing ECM-composition or altering mechanical properties without changing fiber density. In a recent study from our group, we demonstrated the possibility of modulating stromal mechanical properties without altering

composition (Nizamoglu et al., 2022). Another study implemented macromolecular crowding to induce changes in the collagen fibril networks, without significantly changing the bulk stiffness (Ranamukhaarachchi et al., 2019).

In addition to native ECM-based models, patient-derived materials are an important source of cells that are essential for establishing *in vivo* representative models. Involving multiple cell types (such as epithelial cells or fibroblasts) adds to the physiological relevance of a model and these cell-cell interactions can provide invaluable information about disease-driving mechanisms. Effects of cell-cell interactions on immune cell migration has been demonstrated for many types of immune cells, such as between peripheral blood-derived monocytes and leukocytes (Costa et al., 2016), between fibroblasts and macrophages (Ford et al., 2019), and between epithelial spheroids and neutrophils (Surendran et al., 2021). Investigating the influence of these cell-cell interactions on (infiltrating) cell migration within the context of diseased ECM could bring new perspectives to our current understanding of lung disease pathobiology.

3.1 Challenges associated with 3D migration models

Patient-derived material has the highest physiological relevance when used for modeling *in vitro* systems, however, such samples pose various challenges associated with their nature. The availability of human lung tissue for scientific research is rare, except in some specialized clinical centers. Moreover, large volumes of tissue cannot be obtained for every disease; for instance, for asthma and ARDS usually only small bronchial biopsies are available. Furthermore, obtaining true healthy control tissue is an added obstacle. Control "healthy" material is often obtained from lung tissue resected during lobectomies, tumors, or transplantation. The resected tissue is assessed for morphological and anatomical normalcy and although the cells and tissues may appear to be healthy, their microenvironment is possibly altered as a consequence of disease compared to a healthy individual. Patient-to-patient variability creates additional challenges while working with the small(er) sample sizes that are inherent to such models. Modeling chronic diseases should also be accompanied by modeling with appropriate controls, which include important considerations such as matching for age, sex, and smoking history. However, the limitations in the availability of precious patient material also constrains the inclusion of proper controls to perform appropriate comparisons. This challenge of limited availability of donor material also extends to models that utilize human-derived ECM. Another important consideration for ECM-based models is heterogeneity of mechanical properties in different compartments of the available human material. For example, small airways in COPD become stiffer but the parenchyma on the whole appears softer due to enlarged emphysematous regions while the remaining alveolar walls are measured as having stiffness similar to control alveolar walls (Burgess and Harmsen, 2022). There are several well-established protocols to decellularize the lung to obtain either intact scaffolds or solubilized ECM, that is, reconstituted to form hydrogels (Wagner et al., 2013; Gilpin and Wagner, 2018; de Hilster et al., 2020). An unmet challenge for these models, however, is recellularization (Wagner et al., 2013). Current efforts at recellularization are unable to ensure appropriate 3D distribution of cells. Advances in 3D bioprinting technology such as ECM based bioinks reinforced with cells can bolster the development of models with correct spatial distribution of cells (De Santis et al., 2021; Falcones et al., 2021).

Conducting experiments in 3D provides a plethora of information in addition to the physiological relevance. An extra dimension goes hand-in-hand with added challenges for retrieving readouts to generate these data. Visualizing the network of ECM with varying degrees of resolution, is possible using histological staining (Masson Trichrome, Picrosirius Red), immunohistochemistry and/or immunofluorescence staining, scanning electron microscopy, and atomic force microscopy. However, sample processing techniques may limit the extent of visualization and/or introduce artefacts. For example, sectioning the sample for staining procedures limits the information provided to only one plane, the harsh treatments necessary for scanning electron microscopy sample preparation can alter ECM structure. Similarly, fluorescence imaging approaches might be hindered by auto-fluorescence of native ECM. Second harmonics generation and multiphoton microscopy are emerging as prominent high-resolution imaging techniques for visualizing the matrix and overcoming these limitations (Mayorca-Guiliani et al., 2017; Tjin et al., 2017). Fluorescent-labeling of cells or matrix has also allowed deciphering matrix changes and cellular movement in different studies (Fischer et al., 2022). Digital holographic microscopy has been utilized to visualize cell migration in 3D Matrigel matrices (Hellesvik et al., 2020). While each visualization method has advantages and disadvantages (Martinez-Garcia et al., 2022), combination of different techniques for the visualization of migrating cells and the ECM network might be the key for advancing knowledge.

Another important feature of the lung is the presence of oxygen gradient. The alveolar-arterial (A-a) oxygen gradient has been previously used as an indicator of disease severity and outcome in pneumonia and recently in COVID-19 (Singh et al., 2022). Often, acute and chronic lung diseases are also characterized by hypoxemia and hypoxia. Thus, modeling gradients *in vitro* systems, although challenging, is crucial as cells modulate their responses depending on the oxygen levels in their microenvironment (Zenewicz, 2017). Most 3D migration systems are modeled under static conditions, missing the dynamic state of the lung. Inclusion of respiratory mechanics

associated with breathing and blood flow also poses a challenge while modeling these systems. One such event is cyclic deformations which have been mimicked in lung-on-chip models recently (Kumar et al., 2022; Zhu et al., 2022). Including cyclic deformations in the state-of-the-art ECM-based migration models would increase the translational capacity of the models and bring them one step closer to *in vivo*. Similarly, the lack of (interstitial) flow is an important aspect that can add another dimension to these migration models. The effect of interstitial flow was elucidated when tumor-associated interstitial flow promoted tumor-like characteristics in healthy macrophages (Li et al., 2018). Similarly, neutrophils were shown to infiltrate cancer-derived spheroids deeper when a flow was present in the *in vitro* system (Surendran et al., 2021).

Altogether, using innovative 3D *in vitro* models to mimic migration of infiltrating immune cells in lung diseases has been emerging as a new possibility. Developing new systems to represent altered ECM composition, structure, organization and mechanics in each of these lung diseases will help us advance our understanding how the ECM-immune cell interplay influences the migration of these cells.

4 Conclusion: Highway to *heal*

Interactions with the microenvironment critically direct cell behavior, including cell migration. Therefore, it is highly likely that disrupted ECM homeostasis in lung diseases such as lung fibrosis, COPD, asthma and/or ARDS alters the behavior of infiltrating inflammatory cells, similar to how a hazardous highway would hinder the smooth flow of traffic. Advances in methodologies for 3D culture systems and advances in the biomaterials field in the last decade have greatly improved our understanding of how migrating cells interact with their microenvironment with respect to the biochemical and biomechanical properties. Emerging data suggest that the contributions of different ECM properties may differ when assessed individually as compared to when in combinations. Targeting isolated parameters within an altered ECM is one of the important questions upon which future research should focus. Another important aspect that remains unknown is the influence that lung-resident cells, such as epithelial cells, endothelial cells and fibroblasts, have on migration of immune cells. Multicellular *in vitro* models are necessary to investigate whether resident lung cells modulate immune cell migration through abnormal ECM in lung diseases. Developing 3D ECM *in vitro* models helps to further our understanding of the pathobiology of a disease (Tabdanov et al., 2021). Recently, modulating cancer ECM has been shown to have potential for therapeutic targeting as weakening cell-matrix adhesion and reducing fiber rigidity reduced cancer cell invasiveness (Pal et al., 2021). Therefore, it is not unlikely that similar approaches targeting the contribution of altered ECM to immune cell recruitment could be employed as therapeutic strategies against lung diseases.

The lack of techniques to obtain information from these novel models poses a future challenge. Nevertheless, steady progress has led to advances in new qualitative and quantitative methodologies for studying disease mechanisms using 3D models. Newer approaches for better imaging, improved compositional analyses, recellularization, and modeling dynamic conditions are paving the way for improved and innovative models. Incorporation of patient-derived material such as native ECM and cells in research will play an important role in our understanding of disease origin and progression.

In summary, understanding the recruitment of immune cells from peripheral blood during lung diseases and how the diseased ECM alters their behavior is a key factor to deepen our knowledge of these diseases and to start generating hypotheses revolving around targeting these interactions for the development of new treatment strategies.

Author contributions

MMJ, MN, and JKB conceptualized and designed the manuscript. The content was the manuscript was written by MMJ, MN, YF, SSPN, and JP. The figure was prepared by MN. All authors contributed towards editing and reviewing the manuscript. All authors also approved the final version of the manuscript.

Funding

MMJ is funded by the Graduate School of Medical Sciences of the University of Groningen. MN, IHH, BNM, and JKB receive unrestricted research funds from Boehringer Ingelheim. YF acknowledges support from the State Scholarship Fund by the China Scholarship Council (202006230092). SSPN and MW were funded by grants from the German Federal Ministry of Education and Research (BMBF, 82DZL001A6) and MW by a Junior Research cluster grant from the University of Lübeck (JC01-2016). JKB also acknowledges support from the NWO (Aspasia 015.013.010).

Conflict of interest

MN, IHH, BNM, and JKB receive unrestricted research funds from Boehringer Ingelheim.

The remaining authors declare that the research was conducted in the absence of any commercial or financial relationships that could be construed as a potential conflict of interest.

Publisher's note

References

Abdillahi, S. M., Bober, M., Nordin, S., Hallgren, O., Baumgarten, M., Erjefalt, J., et al. (2015). Collagen VI is upregulated in COPD and serves both as an adhesive target and a bactericidal barrier for Moraxella catarrhalis. *J. Innate Immun.* 7 (5), 506–517. doi:10.1159/000381213

Adebowale, K., Gong, Z., Hou, J. C., Wisdom, K. M., Garbett, D., Lee, H. P., et al. (2021). Enhanced substrate stress relaxation promotes filopodia-mediated cell migration. *Nat. Mat.* 20 (9), 1290–1299. doi:10.1038/s41563-021-00981-w

Akhmanova, M., Emtenani, S., Krueger, D., Gyoergy, A., Guarda, M., Vlasov, M., et al. (2022). Cell division in tissues enables macrophage infiltration. *Science* 376 (6591), 394–396. doi:10.1126/science.abj0425

Andersson, C. K., Weitoft, M., Rydell-Tormanen, K., Bjermer, L., Westergren-Thorsson, G., and Erjefalt, J. S. (2018). Uncontrolled asthmatics have increased FceRI(+) and TGF-beta-positive MCTC mast cells and collagen VI in the alveolar parenchyma. *Clin. Exp. Allergy* 48 (3), 266–277. doi:10.1111/cea.13092

Annoni, R., Lancas, T., Yukimatsu Tanigawa, R., de Medeiros Matsushita, M., de Morais Fernezlian, S., Bruno, A., et al. (2012). Extracellular matrix composition in COPD. *Eur. Respir. J.* 40 (6), 1362–1373. doi:10.1183/09031936.00192611

Araujo, B. B., Dolhnikoff, M., Silva, L. F., Elliot, J., Lindeman, J. H., Ferreira, D. S., et al. (2008). Extracellular matrix components and regulators in the airway smooth muscle in asthma. *Eur. Respir. J.* 32 (1), 61–69. doi:10.1183/09031936.00147807

Armstrong, L., Thickett, D. R., Mansell, J. P., Ionescu, M., Hoyle, E., Billinghurst, R. C., et al. (1999). Changes in collagen turnover in early acute respiratory distress syndrome. *Am. J. Respir. Crit. Care Med.* 160 (6), 1910–1915. doi:10.1164/ajrccm.160.6.9811084

Belchamber, K. B. R., Singh, R., Batista, C. M., Whyte, M. K., Dockrell, D. H., Kilty, I., et al. (2019). Defective bacterial phagocytosis is associated with dysfunctional mitochondria in COPD macrophages. *Eur. Respir. J.* 54 (4), 1802244. doi:10.1183/13993003.02244-2018

Bensadoun, E. S., Burke, A. K., Hogg, J. C., and Roberts, C. R. (1996). Proteoglycan deposition in pulmonary fibrosis. *Am. J. Respir. Crit. Care Med.* 154 (6), 1819–1828. doi:10.1164/ajrccm.154.6.8970376

Biesalski, H. K. (2007). Polyphenols and inflammation: Basic interactions. *Curr. Opin. Clin. Nutr. Metab. Care* 10 (6), 724–728. doi:10.1097/MCO.0b013e3282f0cef2

Booth, A. J., Hadley, R., Cornett, A. M., Dreffs, A. A., Matthes, S. A., Tsui, J. L., et al. (2012). Acellular normal and fibrotic human lung matrices as a culture system for *in vitro* investigation. *Am. J. Respir. Crit. Care Med.* 186, 866–876. doi:10.1164/rccm.201204-0754OC

Boyd, D. F., Allen, E. K., Randolph, A. G., Guo, X. J., Weng, Y., Sanders, C. J., et al. (2020). Exuberant fibroblast activity compromises lung function via ADAMTS4. *Nature* 587 (7834), 466–471. doi:10.1038/s41586-020-2877-5

Braber, S., Overbeek, S. A., Koelink, P. J., Henricks, P. A., Zaman, G. J., Garssen, J., et al. (2011). CXCR2 antagonists block the N-Ac-PGP-induced neutrophil influx in the airways of mice, but not the production of the chemokine CXCL1. *Eur. J. Pharmacol.* 668 (3), 443–449. doi:10.1016/j.ejphar.2011.03.025

Brandsma, C.-A., de Vries, M., Costa, R., Woldhuis, R. R., Königshoff, M., and Timens, W. (2017). Lung ageing and COPD: Is there a role for ageing in abnormal tissue repair? *Eur. Respir. Rev.* 26, 170073. doi:10.1183/16000617.0073-2017

Brandsma, C. A., Van den Berge, M., Hackett, T. L., Brusselle, G., and Timens, W. (2020). Recent advances in chronic obstructive pulmonary disease pathogenesis: From disease mechanisms to precision medicine. *J. Pathol.* 250 (5), 624–635. doi:10.1002/path.5364

Brightling, C., and Greening, N. (2019). Airway inflammation in COPD: Progress to precision medicine. *Eur. Respir. J.* 54 (2), 1900651. doi:10.1183/13993003.00651-2019

Burgess, J. K., Boustany, S., Moir, L. M., Weckmann, M., Lau, J. Y., Grafton, K., et al. (2010). Reduction of tumstatin in asthmatic airways contributes to angiogenesis, inflammation, and hyperresponsiveness. *Am. J. Respir. Crit. Care Med.* 181 (2), 106–115. doi:10.1164/rccm.200904-0631OC

Burgess, J. K., and Harmsen, M. C. (2022). Chronic lung diseases: Entangled in extracellular matrix. *Eur. Respir. Rev.* 31 (163), 210202. doi:10.1183/16000617.0202-2021

Burgess, J. K., Jonker, M. R., Berg, M., ten Hacken, N. T. H., Meyer, K. B., van den Berge, M., et al. (2020). Periostin: Contributor to abnormal airway epithelial function in asthma? *Eur. Respir. J.* 57, 2001286. doi:10.1183/13993003.01286-2020

Burgess, J. K., Mauad, T., Tjin, G., Karlsson, J. C., and Westergren-Thorsson, G. (2016). The extracellular matrix - the under-recognized element in lung disease? *J. Pathol.* 240 (4), 397–409. doi:10.1002/path.4808

Burgstaller, G., Oehrle, B., Gerckens, M., White, E. S., Schiller, H. B., and Eickelberg, O. (2017). The instructive extracellular matrix of the lung: Basic composition and alterations in chronic lung disease. *Eur. Respir. J.* 50 (1), 1601805. doi:10.1183/13993003.01805-2016

Chilosi, M., Carloni, A., Rossi, A., and Poletti, V. (2013). Premature lung aging and cellular senescence in the pathogenesis of idiopathic pulmonary fibrosis and COPD/emphysema. *Transl. Res.* 162 (3), 156–173. doi:10.1016/j.trsl.2013.06.004

Costa, C., Traves, S. L., Tudhope, S. J., Fenwick, P. S., Belchamber, K. B. R., Russell, R. E. K., et al. (2016). Enhanced monocyte migration to CXCR3 and CCR5 chemokines in COPD. *Eur. Respir. J.* 47 (4), 1093–1102. doi:10.1183/13993003.01642-2015

Davey, A., McAuley, D. F., and O'Kane, C. M. (2011). Matrix metalloproteinases in acute lung injury: Mediators of injury and drivers of repair. *Eur. Respir. J.* 38 (4), 959–970. doi:10.1183/09031936.00032111

de Castro Bras, L. E., and Frangogiannis, N. G. (2020). Extracellular matrix-derived peptides in tissue remodeling and fibrosis. *Matrix Biol.* 91-92, 176–187. doi:10.1016/j.matbio.2020.04.006

de Hilster, R. H. J., Sharma, P. K., Jonker, M. R., White, E. S., Gercama, E. A., Roobeek, M., et al. (2020). Human lung extracellular matrix hydrogels resemble the stiffness and viscoelasticity of native lung tissue. *Am. J. Physiol. Lung Cell. Mol. Physiol.* 318 (4), L698-L704–L704. doi:10.1152/ajplung.00451.2019

De Santis, M. M., Alsafadi, H. N., Tas, S., Bolukbas, D. A., Prithiviraj, S., Da Silva, I. A. N., et al. (2021). Extracellular-matrix-reinforced bioinks for 3D bioprinting human tissue. *Adv. Mat.* 33 (3), e2005476. doi:10.1002/adma.202005476

Dekkers, B. G. J., Saad, S. I., van Spelde, L. J., and Burgess, J. K. (2021). Basement membranes in obstructive pulmonary diseases. *Matrix Biol. Plus* 12, 100092. doi:10.1016/j.mbplus.2021.100092

Dicker, A. J., Crichton, M. L., Pumphrey, E. G., Cassidy, A. J., Suarez-Cuartin, G., Sibila, O., et al. (2018). Neutrophil extracellular traps are associated with disease severity and microbiota diversity in patients with chronic obstructive pulmonary disease. *J. Allergy Clin. Immunol.* 141 (1), 117–127. doi:10.1016/j.jaci.2017.04.022

Dokoshi, T., Zhang, L. J., Li, F., Nakatsuji, T., Butcher, A., Yoshida, H., et al. (2020). Hyaluronan degradation by cemip regulates host defense against *Staphylococcus aureus* skin infection. *Cell. Rep.* 30 (1), 61–68. e64. doi:10.1016/j.celrep.2019.12.001

Dolhnikoff, M., da Silva, L. F., de Araujo, B. B., Gomes, H. A., Fernezlian, S., Mulder, A., et al. (2009). The outer wall of small airways is a major site of remodeling in fatal asthma. *J. Allergy Clin. Immunol.* 123 (5), 1090–1097. doi:10.1016/j.jaci.2009.02.032

Du, H., Bartleson, J. M., Butenko, S., Alonso, V., Liu, W. F., Winer, D. A., et al. (2022). Tuning immunity through tissue mechanotransduction. *Nat. Rev. Immunol.* doi:10.1038/s41577-022-00761-w

Esposito, A. J., Bhatraju, P. K., Stapleton, R. D., Wurfel, M. M., and Mikacenic, C. (2017). Hyaluronic acid is associated with organ dysfunction in acute respiratory distress syndrome. *Crit. Care* 21 (1), 304. doi:10.1186/s13054-017-1895-7

Eurlings, I. M., Dentener, M. A., Cleutjens, J. P., Peutz, C. J., Rohde, G. G., Wouters, E. F., et al. (2014). Similar matrix alterations in alveolar and small airway walls of COPD patients. *BMC Pulm. Med.* 14 (1), 90. doi:10.1186/1471-2466-14-90

Falcones, B., Sanz-Fraile, H., Marhuenda, E., Mendizabal, I., Cabrera-Aguilera, I., Malandain, N., et al. (2021). Bioprintable lung extracellular matrix hydrogel scaffolds for 3D culture of mesenchymal stromal cells. *Polymers* 13 (14), 2350. doi:10.3390/polym13142350

Fan, C., Shi, X., Zhao, K., Wang, L., Shi, K., Liu, Y. J., et al. (2022). Cell migration orchestrates migrasome formation by shaping retraction fibers. *J. Cell. Biol.* 221 (4), e202109168. doi:10.1083/jcb.202109168

Fischer, A., Wannemacher, J., Christ, S., Koopmans, T., Kadri, S., Zhao, J., et al. (2022). Neutrophils direct preexisting matrix to initiate repair in damaged tissues. *Nat. Immunol.* 23 (4), 518–531. doi:10.1038/s41590-022-01166-6

Ford, A. J., Orbach, S. M., and Rajagopalan, P. (2019). Fibroblasts stimulate macrophage migration in interconnected extracellular matrices through tunnel formation and fiber alignment. *Biomaterials* 209, 88–102. doi:10.1016/j.biomaterials.2019.03.044

Forel, J.-M., Guervilly, C., Hraiech, S., Voillet, F., Thomas, G., Somma, C., et al. (2015). Type III procollagen is a reliable marker of ARDS-associated lung fibroproliferation. *Intensive Care Med.* 41 (1), 1–11. doi:10.1007/s00134-014-3524-0

Francois, J., Kandasamy, A., Yeh, Y. T., Schwartz, A., Ayala, C., Meili, R., et al. (2021). The interplay between matrix deformation and the coordination of turning events governs directed neutrophil migration in 3D matrices. *Sci. Adv.* 7 (29), eabf3882. doi:10.1126/sciadv.abf3882

Gaggar, A., Jackson, P. L., Noerager, B. D., O'Reilly, P. J., Mcquaid, D. B., Rowe, S. M., et al. (2008). A novel proteolytic cascade generates an extracellular matrix-derived chemoattractant in chronic neutrophilic inflammation. *J. Immunol.* 180 (8), 5662–5669. doi:10.4049/jimmunol.180.8.5662

Gilpin, S. E., and Wagner, D. E. (2018). Acellular human lung scaffolds to model lung disease and tissue regeneration. *Eur. Respir. Rev.* 27, 180021. doi:10.1183/16000617.0021-2018

Gkatzis, K., Taghizadeh, S., Huh, D., Stainier, D. Y. R., and Bellusci, S. (2018). Use of three-dimensional organoids and lung-on-a-chip methods to study lung development, regeneration and disease. *Eur. Respir. J.* 52 (5), 1800876. doi:10.1183/13993003.00876-2018

Grazioli, S., Gil, S., An, D., Kajikawa, O., Farnand, A. W., Hanson, J. F., et al. (2015). CYR61 (CCN1) overexpression induces lung injury in mice. *Am. J. Physiol. Lung Cell. Mol. Physiol.* 308 (8), L759–L765. doi:10.1152/ajplung.00190.2014

Gu, B. H., Madison, M. C., Corry, D., and Kheradmand, F. (2018). Matrix remodeling in chronic lung diseases. *Matrix Biol.* 73, 52–63. doi:10.1016/j.matbio.2018.03.012

Hahn, C. S., Scott, D. W., Xu, X., Roda, M. A., Payne, G. A., Wells, J. M., et al. (2015). The matrikine N-alpha-PGP couples extracellular matrix fragmentation to endothelial permeability. *Sci. Adv.* 1 (3), e1500175. doi:10.1126/sciadv.1500175

Hällgren, R., Samuelsson, T., Laurent, T. C., and Modig, J. (1989). Accumulation of hyaluronan (hyaluronic acid) in the lung in adult respiratory distress syndrome. *Am. Rev. Respir. Dis.* 139 (3), 682–687. doi:10.1164/ajrccm/139.3.682

Hallmann, R., Zhang, X., Di Russo, J., Li, L., Song, J., Hannocks, M. J., et al. (2015). The regulation of immune cell trafficking by the extracellular matrix. *Curr. Opin. Cell. Biol.* 36, 54–61. doi:10.1016/j.ceb.2015.06.006

Hamon, A., Scemama, U., Bourenne, J., Daviet, F., Coiffard, B., Persico, N., et al. (2019). Chest CT scan and alveolar procollagen III to predict lung fibroproliferation in acute respiratory distress syndrome. *Ann. Intensive Care* 9 (1), 42. doi:10.1186/s13613-019-0516-9

Harkness, L. M., Weckmann, M., Kopp, M., Becker, T., Ashton, A. W., and Burgess, J. K. (2017). Tumstatin regulates the angiogenic and inflammatory potential of airway smooth muscle extracellular matrix. *J. Cell. Mol. Med.* 21 (12), 3288–3297. doi:10.1111/jcmm.13232

Hartman, C. D., Isenberg, B. C., Chua, S. G., and Wong, J. Y. (2017). Extracellular matrix type modulates cell migration on mechanical gradients. *Exp. Cell. Res.* 359 (2), 361–366. doi:10.1016/j.yexcr.2017.08.018

Helfrich, S., Mindt, B. C., Fritz, J. H., and Duerr, C. U. (2019). Group 2 innate lymphoid cells in respiratory allergic inflammation. *Front. Immunol.* 10, 930. doi:10.3389/fimmu.2019.00930

Hellesvik, M., Oye, H., and Aksnes, H. (2020). Exploiting the potential of commercial digital holographic microscopy by combining it with 3D matrix cell culture assays. *Sci. Rep.* 10 (1), 14680. doi:10.1038/s41598-020-71538-1

Hellman, U., Karlsson, M. G., Engström-Laurent, A., Cajander, S., Dorofte, L., Ahlm, C., et al. (2020). Presence of hyaluronan in lung alveoli in severe Covid-19: An opening for new treatment options? *J. Biol. Chem.* 295 (45), 15418–15422. doi:10.1074/jbc.ac120.015967

Herrera, J., Forster, C., Pengo, T., Montero, A., Swift, J., Schwartz, M. A., et al. (2019). Registration of the extracellular matrix components constituting the fibroblastic focus in idiopathic pulmonary fibrosis. *JCI Insight* 4 (1), 125185. doi:10.1172/jci.insight.125185

Herrera, J., Henke, C. A., and Bitterman, P. B. (2018). Extracellular matrix as a driver of progressive fibrosis. *J. Clin. Investig.* 128 (1), 45–53. doi:10.1172/JCI93557

Hogg, J. C., Chu, F., Utokaparch, S., Woods, R., Elliott, W. M., Buzatu, L., et al. (2004). The nature of small-airway obstruction in chronic obstructive pulmonary disease. *N. Engl. J. Med.* 350 (26), 2645–2653. doi:10.1056/NEJMoa032158

Hogg, J. C., McDonough, J. E., Gosselink, J. V., and Hayashi, S. (2009). What drives the peripheral lung-remodeling process in chronic obstructive pulmonary disease? *Proc. Am. Thorac. Soc.* 6 (8), 668–672. doi:10.1513/pats.200907-079DP

Holgate, S. T., Wenzel, S., Postma, D. S., Weiss, S. T., Renz, H., and Sly, P. D. (2015). Asthma. *Nat. Rev. Dis. Prim.* 1 (1), 15025. doi:10.1038/nrdp.2015.25

Hough, K. P., Curtiss, M. L., Blain, T. J., Liu, R. M., Trevor, J., Deshane, J. S., et al. (2020). Airway remodeling in asthma. *Front. Med.* 7, 191. doi:10.3389/fmed.2020.00191

Hsieh, J. Y., Keating, M. T., Smith, T. D., Meli, V. S., Botvinick, E. L., and Liu, W. F. (2019). Matrix crosslinking enhances macrophage adhesion, migration, and inflammatory activation. *Apl. Bioeng.* 3 (1), 016103. doi:10.1063/1.5067301

Huang, E., Peng, N., Xiao, F., Hu, D., Wang, X., and Lu, L. (2020). The roles of immune cells in the pathogenesis of fibrosis. *Int. J. Mol. Sci.* 21 (15), 5203. doi:10.3390/ijms21155203

Ishikawa, G., Liu, A., and Herzog, E. L. (2021). Evolving perspectives on innate immune mechanisms of IPF. *Front. Mol. Biosci.* 8, 676569. doi:10.3389/fmolb.2021.676569

Ito, J. T., Lourenco, J. D., Righetti, R. F., Tiberio, I., Prado, C. M., and Lopes, F. (2019). Extracellular matrix component remodeling in respiratory diseases: What has been found in clinical and experimental studies? *Cells* 8 (4), 342. doi:10.3390/cells8040342

Johansson, M. W. (2017). Eosinophil activation status in separate compartments and association with asthma. *Front. Med.* 4, 75. doi:10.3389/fmed.2017.00075

Jun, J. I., Kim, K. H., and Lau, L. F. (2015). The matricellular protein CCN1 mediates neutrophil efferocytosis in cutaneous wound healing. *Nat. Commun.* 6 (1), 7386. doi:10.1038/ncomms8386

Kaur, A., Ecker, B. L., Douglass, S. M., Kugel, C. H., Webster, M. R., Almeida, F. V., et al. (2019). Remodeling of the collagen matrix in aging skin promotes melanoma metastasis and affects immune cell motility. *Cancer Discov.* 9 (1), 64–81. doi:10.1158/2159-8290.CD-18-0193

Kim, J. S., Axelsson, G. T., Moll, M., Anderson, M. R., Bernstein, E. J., Putman, R. K., et al. (2022). Associations of monocyte count and other immune cell types with interstitial lung abnormalities. *Am. J. Respir. Crit. Care Med.* 205 (7), 795–805. doi:10.1164/rccm.202108-1967OC

Kim, S. D., Lee, H. Y., Shim, J. W., Kim, H. J., Yoo, Y. H., Park, J. S., et al. (2011). Activation of CXCR2 by extracellular matrix degradation product acetylated Pro-Gly-Pro has therapeutic effects against sepsis. *Am. J. Respir. Crit. Care Med.* 184 (2), 243–251. doi:10.1164/rccm.201101-0004OC

Kinder, B. W., Brown, K. K., Schwarz, M. I., Ix, J. H., Kervitsky, A., and King, T. E., Jr. (2008). Baseline BAL neutrophilia predicts early mortality in idiopathic pulmonary fibrosis. *Chest* 133 (1), 226–232. doi:10.1378/chest.07-1948

Kraus, R. F., Gruber, M. A., and Kieninger, M. (2021). The influence of extracellular tissue on neutrophil function and its possible linkage to inflammatory diseases. *Immun. Inflamm. Dis.* 9 (4), 1237–1251. doi:10.1002/iid3.472

Kumar, V., Madhurakkat Perikamana, S. K., Tata, A., Hoque, J., Gilpin, A., Tata, P. R., et al. (2022). An *in vitro* microfluidic alveolus model to study lung biomechanics. *Front. Bioeng. Biotechnol.* 10, 848699. doi:10.3389/fbioe.2022.848699

Labaki, W. W., and Han, M. K. (2020). Chronic respiratory diseases: A global view. *Lancet. Respir. Med.* 8 (6), 531–533. doi:10.1016/S2213-2600(20)30157-0

Lauer, M. E., Majors, A. K., Comhair, S., Ruple, L. M., Matuska, B., Subramanian, A., et al. (2015). Hyaluronan and its heavy chain modification in asthma severity and experimental asthma exacerbation. *J. Biol. Chem.* 290 (38), 23124–23134. doi:10.1074/jbc.M115.663823

Lee, J. S., Song, J. W., Wolters, P. J., Elicker, B. M., King, T. E., Jr., Kim, D. S., et al. (2012). Bronchoalveolar lavage pepsin in acute exacerbation of idiopathic pulmonary fibrosis. *Eur. Respir. J.* 39 (2), 352–358. doi:10.1183/09031936.00050911

Lee, S. Y., Choi, S. H., Lee, M. S., Kurmashev, A., Lee, H. N., Ko, Y. G., et al. (2021). Retraction fibers produced by fibronectin-integrin α5β1 interaction promote motility of brain tumor cells. *FASEB J.* 35 (10), e21906. doi:10.1096/fj.202100452RR

Li, R., Serrano, J. C., Xing, H., Lee, T. A., Azizgolshani, H., Zaman, M., et al. (2018). Interstitial flow promotes macrophage polarization toward an M2 phenotype. *Mol. Biol. Cell.* 29 (16), 1927–1940. doi:10.1091/mbc.E18-03-0164

Lim, K., Hyun, Y. M., Lambert-Emo, K., Capece, T., Bae, S., Miller, R., et al. (2015). Neutrophil trails guide influenza-specific CD8$^+$ T cells in the airways. *Science* 349 (6252), aaa4352. doi:10.1126/science.aaa4352

Liu, G., Betts, C., Cunoosamy, D. M., Åberg, P. M., Hornberg, J. J., Sivars, K. B., et al. (2019). Use of precision cut lung slices as a translational model for the study of lung biology. *Respir. Res.* 20 (1), 162. doi:10.1186/s12931-019-1131-x

Liu, G., Philp, A. M., Corte, T., Travis, M. A., Schilter, H., Hansbro, N. G., et al. (2021a). Therapeutic targets in lung tissue remodelling and fibrosis. *Pharmacol. Ther.* 225, 107839. doi:10.1016/j.pharmthera.2021.107839

Liu, L., Stephens, B., Bergman, M., May, A., and Chiang, T. (2021b). Role of collagen in airway mechanics. *Bioengineering* 8 (1), 13. doi:10.3390/bioengineering8010013

Lobel, M., Bauer, S., Meisel, C., Eisenreich, A., Kudernatsch, R., Tank, J., et al. (2012). CCN1: A novel inflammation-regulated biphasic immune cell migration modulator. *Cell. Mol. Life Sci.* 69 (18), 3101–3113. doi:10.1007/s00018-012-0981-x

Manon-Jensen, T., Kjeld, N. G., and Karsdal, M. A. (2016). Collagen-mediated hemostasis. *J. Thromb. Haemost.* 14 (3), 438–448. doi:10.1111/jth.13249

Manon-Jensen, T., Langholm, L. L., Ronnow, S. R., Karsdal, M. A., Tal-Singer, R., Vestbo, J., et al. (2019). End-product of fibrinogen is elevated in emphysematous chronic obstructive pulmonary disease and is predictive of mortality in the ECLIPSE cohort. *Respir. Med.* 160, 105814. doi:10.1016/j.rmed.2019.105814

Martinez-Garcia, F. D., Fischer, T., Hayn, A., Mierke, C. T., Burgess, J. K., and Harmsen, M. C. (2022). A beginner's guide to the characterization of hydrogel microarchitecture for cellular applications. *Gels* 8 (9), 535. doi:10.3390/gels8090535

Mayorca-Guiliani, A. E., Madsen, C. D., Cox, T. R., Horton, E. R., Venning, F. A., and Erler, J. T. (2017). ISDoT: *In situ* decellularization of tissues for high-resolution imaging and proteomic analysis of native extracellular matrix. *Nat. Med.* 23 (7), 890–898. doi:10.1038/nm.4352

McMahon, M., Ye, S., Pedrina, J., Dlugolenski, D., and Stambas, J. (2021). Extracellular matrix enzymes and immune cell biology. *Front. Mol. Biosci.* 8, 703868. doi:10.3389/fmolb.2021.703868

Meduri, G. U., Tolley, E. A., Chinn, A., Stentz, F., Postlethwaite, A., and PostlethwAite, A. (1998). Procollagen types I and III aminoterminal propeptide levels during acute respiratory distress syndrome and in response to methylprednisolone treatment. *Am. J. Respir. Crit. Care Med.* 158 (1), 1432–1441. doi:10.1164/ajrccm.158.5.9801107

Misharin, A. V., Morales-Nebreda, L., Reyfman, P. A., Cuda, C. M., Walter, J. M., McQuattie-Pimentel, A. C., et al. (2017). Monocyte-derived alveolar macrophages drive lung fibrosis and persist in the lung over the life span. *J. Exp. Med.* 214 (8), 2387–2404. doi:10.1084/jem.20162152

Misiura, M., and Miltyk, W. (2019). Proline-containing peptides-new insight and implications: A review. *Biofactors* 45 (6), 857–866. doi:10.1002/biof.1554

Moon, J. Y., Leitao Filho, F. S., Shahangian, K., Takiguchi, H., and Sin, D. D. (2018). Blood and sputum protein biomarkers for chronic obstructive pulmonary disease (COPD). *Expert Rev. Proteomics* 15 (11), 923–935. doi:10.1080/14789450.2018.1539670

Morales, M. M., Pires-Neto, R. C., Inforsato, N., Lancas, T., da Silva, L. F., Saldiva, P. H., et al. (2011). Small airway remodeling in acute respiratory distress syndrome: A study in autopsy lung tissue. *Crit. Care* 15 (1), R4. doi:10.1186/cc9401

Morales, X., Cortes-Dominguez, I., and Ortiz-de-Solorzano, C. (2021). Modeling the mechanobiology of cancer cell migration using 3D biomimetic hydrogels. *Gels* 7 (1), 17. doi:10.3390/gels7010017

Morrell, E. D., Grazioli, S., Hung, C., Kajikawa, O., Kosamo, S., Stapleton, R. D., et al. (2020). Alveolar CCN1 is associated with mechanical stretch and acute respiratory distress syndrome severity. *Am. J. Physiol. Lung Cell. Mol. Physiol.* 319 (5), L825-L832–L832. doi:10.1152/ajplung.00073.2020

Mostaco-Guidolin, L. B., Osei, E. T., Ullah, J., Hajimohammadi, S., Fouadi, M., Li, X., et al. (2019). Defective fibrillar collagen organization by fibroblasts contributes to airway remodeling in asthma. *Am. J. Respir. Crit. Care Med.* 200 (4), 431–443. doi:10.1164/rccm.201810-1855OC

Nawroth, J. C., Lucchesi, C., Cheng, D., Shukla, A., Ngyuen, J., Shroff, T., et al. (2020). A microengineered airway lung chip models key features of viral-induced exacerbation of asthma. *Am. J. Respir. Cell. Mol. Biol.* 63 (5), 591–600. doi:10.1165/rcmb.2020-0010MA

Nemani, S. S. P., Vermeulen, C. J., Pech, M., Faiz, A., Oliver, B. G. G., van den Berge, M., et al. (2021). COL4A3 expression in asthmatic epithelium depends on intronic methylation and ZNF263 binding. *ERJ Open Res.* 7 (2), 00802-2020–02020. doi:10.1183/23120541.00802-2020

Ni, L., and Dong, C. (2018). Roles of myeloid and lymphoid cells in the pathogenesis of chronic obstructive pulmonary disease. *Front. Immunol.* 9, 1431. doi:10.3389/fimmu.2018.01431

Nissen, G., Hollaender, H., Tang, F. S. M., Wegmann, M., Lunding, L., Vock, C., et al. (2018). Tumstatin fragment selectively inhibits neutrophil infiltration in experimental asthma exacerbation. *Clin. Exp. Allergy* 48 (11), 1483–1493. doi:10.1111/cea.13236

Nizamoglu, M., and Burgess, J. K. (2022). The multi-faceted extracellular matrix: Unlocking its secrets for understanding the perpetuation of lung fibrosis. *Curr. Tissue Microenviron. Rep.* 2 (4), 53–71. doi:10.1007/s43152-021-00031-2

Nizamoglu, M., de Hilster, R. H. J., Zhao, F., Sharma, P. K., Borghuis, T., Harmsen, M. C., et al. (2022). An *in vitro* model of fibrosis using crosslinked native extracellular matrix-derived hydrogels to modulate biomechanics without changing composition. *Acta Biomater.* 147, 50–62. doi:10.1016/j.actbio.2022.05.031

O'Reilly, P. J., Jackson, P. L., Wells, J. M., Dransfield, M. T., Scanlon, P. D., and Blalock, J. E. (2013). Sputum PGP is reduced by azithromycin treatment in patients with COPD and correlates with exacerbations. *Bmj Open* 3 (12), e004140. doi:10.1136/bmjopen-2013-004140

Pakshir, P., Alizadehgiashi, M., Wong, B., Coelho, N. M., Chen, X., Gong, Z., et al. (2019). Dynamic fibroblast contractions attract remote macrophages in fibrillar collagen matrix. *Nat. Commun.* 10 (1), 1850. doi:10.1038/s41467-019-09709-6

Pal, A., Haliti, P., Dharmadhikari, B., Qi, W., and Patra, P. (2021). Manipulating extracellular matrix organizations and parameters to control local cancer invasion. *IEEE/ACM Trans. Comput. Biol. Bioinform.* 18 (6), 2566–2576. doi:10.1109/TCBB.2020.2989223

Palmieri, B., Vadala, M., and Laurino, C. (2019). Nutrition in wound healing: Investigation of the molecular mechanisms, a narrative review. *J. Wound Care* 28 (10), 683–693. doi:10.12968/jowc.2019.28.10.683

Patel, D. F., Peiro, T., Shoemark, A., Akthar, S., Walker, S. A., Grabiec, A. M., et al. (2018). An extracellular matrix fragment drives epithelial remodeling and airway hyperresponsiveness. *Sci. Transl. Med.* 10 (455), eaaq0693. doi:10.1126/scitranslmed.aaq0693

Patel, D. F., and Snelgrove, R. J. (2018). The multifaceted roles of the matrikine Pro-Gly-Pro in pulmonary health and disease. *Eur. Respir. Rev.* 27 (148), 180017. doi:10.1183/16000617.0017-2018

Pech, M., Weckmann, M., Konig, I. R., Franke, A., Heinsen, F. A., Oliver, B., et al. (2018). Rhinovirus infections change DNA methylation and mRNA expression in children with asthma. *PLoS One* 13 (11), e0205275. doi:10.1371/journal.pone.0205275

Pierpaoli, E., Cirioni, O., Barucca, A., Orlando, F., Silvestri, C., Giacometti, A., et al. (2011). Vitamin E supplementation in old mice induces antimicrobial activity and improves the efficacy of daptomycin in an animal model of wounds infected with methicillin-resistant *Staphylococcus aureus*. *J. Antimicrob. Chemother.* 66 (9), 2184–2185. doi:10.1093/jac/dkr254

Puttur, F., Denney, L., Gregory, L. G., Vuononvirta, J., Oliver, R., Entwistle, L. J., et al. (2019). Pulmonary environmental cues drive group 2 innate lymphoid cell dynamics in mice and humans. *Sci. Immunol.* 4 (36), eaav7638. doi:10.1126/sciimmunol.aav7638

Raghu, G., Striker, L. J., Hudson, L. D., and Striker, G. E. (1985). Extracellular matrix in normal and fibrotic human lungs. *Am. Rev. Respir. Dis.* 131 (2), 281–289. doi:10.1164/arrd.1985.131.2.281

Ranamukhaarachchi, S. K., Modi, R. N., Han, A., Velez, D. O., Kumar, A., Engler, A. J., et al. (2019). Macromolecular crowding tunes 3D collagen architecture and cell morphogenesis. *Biomater. Sci.* 7 (2), 618–633. doi:10.1039/c8bm01188e

Rao, R. M., Betz, T. V., Lamont, D. J., Kim, M. B., Shaw, S. K., Froio, R. M., et al. (2004). Elastase release by transmigrating neutrophils deactivates endothelial-bound SDF-1alpha and attenuates subsequent T lymphocyte transendothelial migration. *J. Exp. Med.* 200 (6), 713–724. doi:10.1084/jem.20040499

Ravi, A. K., Plumb, J., Gaskell, R., Mason, S., Broome, C. S., Booth, G., et al. (2017). COPD monocytes demonstrate impaired migratory ability. *Respir. Res.* 18 (1), 90. doi:10.1186/s12931-017-0569-y

Reddel, C. J., Weiss, A. S., and Burgess, J. K. (2012). Elastin in asthma. *Pulm. Pharmacol. Ther.* 25 (2), 144–153. doi:10.1016/j.pupt.2012.02.001

Robison, S. W., Li, J., Viera, L., Blackburn, J. P., Patel, R. P., Blalock, J. E., et al. (2021). A mechanism for matrikine regulation in acute inflammatory lung injury. *JCI Insight* 6 (7), 140750. doi:10.1172/jci.insight.140750

Ronnow, S. R., Langholm, L. L., Sand, J. M. B., Thorlacius-Ussing, J., Leeming, D. J., Manon-Jensen, T., et al. (2019). Specific elastin degradation products are associated with poor outcome in the ECLIPSE COPD cohort. *Sci. Rep.* 9 (1), 4064. doi:10.1038/s41598-019-40785-2

Ronnow, S. R., Sand, J. M. B., Staunstrup, L. M., Bahmer, T., Wegmann, M., Lunding, L., et al. (2022). A serological biomarker of type I collagen degradation is related to a more severe, high neutrophilic, obese asthma subtype. *Asthma Res. Pract.* 8 (1), 2. doi:10.1186/s40733-022-00084-6

Santos, F. B., Nagato, L. K., Boechem, N. M., Negri, E. M., Guimaraes, A., Capelozzi, V. L., et al. (2006). Time course of lung parenchyma remodeling in pulmonary and extrapulmonary acute lung injury. *J. Appl. Physiol.* 100 (1), 98–106. doi:10.1152/japplphysiol.00395.2005

Sapey, E., Stockley, J. A., Greenwood, H., Ahmad, A., Bayley, D., Lord, J. M., et al. (2011). Behavioral and structural differences in migrating peripheral neutrophils from patients with chronic obstructive pulmonary disease. *Am. J. Respir. Crit. Care Med.* 183 (9), 1176–1186. doi:10.1164/rccm.201008-1285OC

Sava, P., Cook, I. O., Mahal, R. S., and Gonzalez, A. L. (2015). Human microvascular pericyte basement membrane remodeling regulates neutrophil recruitment. *Microcirculation* 22 (1), 54–67. doi:10.1111/micc.12173

Schumann, D. M., Leeming, D., Papakonstantinou, E., Blasi, F., Kostikas, K., Boersma, W., et al. (2018). Collagen degradation and formation are elevated in exacerbated COPD compared with stable disease. *Chest* 154 (4), 798–807. doi:10.1016/j.chest.2018.06.028

Selman, M., and Pardo, A. (2021). Fibroageing: An ageing pathological feature driven by dysregulated extracellular matrix-cell mechanobiology. *Ageing Res. Rev.* 70, 101393. doi:10.1016/j.arr.2021.101393

Sharma, N. S., Lal, C. V., Li, J. D., Lou, X. Y., Viera, L., Abdallah, T., et al. (2018). The neutrophil chemoattractant peptide proline-glycine-proline is associated with acute respiratory distress syndrome. *Am. J. Physiol. Lung Cell. Mol. Physiol.* 315 (5), L653-L661–L661. doi:10.1152/ajplung.00308.2017

Singh, A., Soni, K. D., Singh, Y., Aggarwal, R., Venkateswaran, V., Ashar, M. S., et al. (2022). Alveolar arterial gradient and respiratory index in predicting the outcome of COVID-19 patients; a retrospective cross-sectional study. *Arch. Acad. Emerg. Med.* 10 (1), e28. doi:10.22037/aaem.v10i1.1543

Surendran, V., Rutledge, D., Colmon, R., and Chandrasekaran, A. (2021). A novel tumor-immune microenvironment (TIME)-on-Chip mimics three dimensional neutrophil-tumor dynamics and neutrophil extracellular traps (NETs)-mediated collective tumor invasion. *Biofabrication* 13 (3), 035029. doi:10.1088/1758-5090/abe1cf

Tabdanov, E. A.-O. X., Rodríguez-Merced, N. A.-O., Cartagena-Rivera, A. A.-O., Puram, V. A.-O., Callaway, M. A.-O., Ensminger, E. A.-O., et al. (2021). Engineering T cells to enhance 3D migration through structurally and mechanically complex tumor microenvironments. *Nat. Commun.* 12, 2815–1723. doi:10.1038/s41467-021-22985-5

Tan, D. B. A., Teo, T. H., Setiawan, A. M., Ong, N. E., Zimmermann, M., Price, P., et al. (2017). Increased CTLA-4(+) T cells may contribute to impaired T helper type 1 immune responses in patients with chronic obstructive pulmonary disease. *Immunology* 151 (2), 219–226. doi:10.1111/imm.12725

Tavano, S., and Heisenberg, C. P. (2019). Migrasomes take center stage. *Nat. Cell. Biol.* 21 (8), 918–920. doi:10.1038/s41556-019-0369-3

Taylor, A. E., Finney-Hayward, T. K., Quint, J. K., Thomas, C. M., Tudhope, S. J., Wedzicha, J. A., et al. (2010). Defective macrophage phagocytosis of bacteria in COPD. *Eur. Respir. J.* 35 (5), 1039–1047. doi:10.1183/09031936.00036709

Theocharis, A. D., Skandalis, S. S., Gialeli, C., and Karamanos, N. K. (2016). Extracellular matrix structure. *Adv. Drug Deliv. Rev.* 97, 4–27. doi:10.1016/j.addr.2015.11.001

Titz, B., Sewer, A., Schneider, T., Elamin, A., Martin, F., Dijon, S., et al. (2015). Alterations in the sputum proteome and transcriptome in smokers and early-stage COPD subjects. *J. Proteomics* 128 (1876-7737), 306–320. (Electronic)). doi:10.1016/j.jprot.2015.08.009

Tjin, G., White, E. S., Faiz, A., Sicard, D., Tschumperlin, D. J., Mahar, A., et al. (2017). Lysyl oxidases regulate fibrillar collagen remodelling in idiopathic pulmonary fibrosis. *Dis. Model. Mech.* 10 (11), 1301–1312. doi:10.1242/dmm.030114

Tomashefski, J. F., Jr. (2000). Pulmonary pathology of acute respiratory distress syndrome. *Clin. Chest Med.* 21 (3), 435–466. doi:10.1016/s0272-5231(05)70158-1

Torii, K., Iida, K., Miyazaki, Y., Saga, S., Kondoh, Y., Taniguchi, H., et al. (1997). Higher concentrations of matrix metalloproteinases in bronchoalveolar lavage fluid of patients with adult respiratory distress syndrome. *Am. J. Respir. Crit. Care Med.* 155 (1), 43–46. doi:10.1164/ajrccm.155.1.9001287

van Geffen, C., Deißler, A., Quante, M., Renz, H., Hartl, D., and Kolahian, S. (2021). Regulatory immune cells in idiopathic pulmonary fibrosis: Friends or foes? *Front. Immunol.* 12, 663203. doi:10.3389/fimmu.2021.663203

van Helvert, S., Storm, C., and Friedl, P. (2018). Mechanoreciprocity in cell migration. *Nat. Cell. Biol.* 20 (1), 8–20. doi:10.1038/s41556-017-0012-0

van Houwelingen, A. H., Weathington, N. M., Verweij, V., Blalock, J. E., Nijkamp, F. P., and Folkerts, G. (2008). Induction of lung emphysema is prevented by L-arginine-threonine-arginine. *FASEB J.* 22 (9), 3403–3408. doi:10.1096/fj.07-096230

van Straaten, J. F., Coers, W., Noordhoek, J. A., Huitema, S., Flipsen, J. T., Kauffman, H. F., et al. (1999). Proteoglycan changes in the extracellular matrix of lung tissue from patients with pulmonary emphysema. *Mod. Pathol.* 12 (7), 697–705.

Vargas-Rojas, M. I., Ramirez-Venegas, A., Limon-Camacho, L., Ochoa, L., Hernandez-Zenteno, R., and Sansores, R. H. (2011). Increase of Th17 cells in peripheral blood of patients with chronic obstructive pulmonary disease. *Respir. Med.* 105 (11), 1648–1654. doi:10.1016/j.rmed.2011.05.017

Vasse, G. F., Kühn, P. T., Zhou, Q., Bhusari, S. A., Reker-Smit, C., Melgert, B. N., et al. (2018). Collagen morphology influences macrophage shape and marker expression *in vitro*. *J. Immunol. Regen. Med.* 1, 13–20. doi:10.1016/j.regen.2018.01.002

Vasse, G. F., Nizamoglu, M., Heijink, I. H., Schleputz, M., van Rijn, P., Thomas, M. J., et al. (2021). Macrophage-stroma interactions in fibrosis: Biochemical, biophysical, and cellular perspectives. *J. Pathol.* 254 (4), 344–357. doi:10.1002/path.5632

Volk, S. W., Iqbal, S. A., and Bayat, A. (2013). Interactions of the extracellular matrix and progenitor cells in cutaneous wound healing. *Adv. Wound Care* 2 (6), 261–272. doi:10.1089/wound.2012.0417

Wagner, D. E., Bonvillain, R. W., Jensen, T., Girard, E. D., Bunnell, B. A., Finck, C. M., et al. (2013). Can stem cells be used to generate new lungs? *ex vivo* lung bioengineering with decellularized whole lung scaffolds. *Respirology* 18 (6), 895–911. doi:10.1111/resp.12102

Walton, G. M., Stockley, J. A., Griffiths, D., Sadhra, C. S., Purvis, T., and Sapey, E. (2016). Repurposing treatments to enhance innate immunity. Can statins improve neutrophil functions and clinical outcomes in COPD? *J. Clin. Med.* 5 (10), 89. doi:10.3390/jcm5100089

Wang, W. Y., Pearson, A. T., Kutys, M. L., Choi, C. K., Wozniak, M. A., Baker, B. M., et al. (2018). Extracellular matrix alignment dictates the organization of focal adhesions and directs uniaxial cell migration. *Apl. Bioeng.* 2 (4), 046107. doi:10.1063/1.5052239

Wang, Z., Qi, F., Luo, H., Xu, G., and Wang, D. (2022). Inflammatory microenvironment of skin wounds. *Front. Immunol.* 13, 789274. doi:10.3389/fimmu.2022.789274

Weathington, N. M., van Houwelingen, A. H., Noerager, B. D., Jackson, P. L., Kraneveld, A. D., Galin, F. S., et al. (2006). A novel peptide CXCR ligand derived from extracellular matrix degradation during airway inflammation. *Nat. Med.* 12 (3), 317–323. doi:10.1038/nm1361

Weckmann, M., Bahmer, T., Sand, J. M., Ronnow, S. R., Pech, M., Vermeulen, C., et al. (2021). COL4A3 is degraded in allergic asthma and degradation predicts response to anti-IgE therapy. *Eur. Respir. J.* 58 (6), 2003969. doi:10.1183/13993003.03969-2020

Weitoft, M., Andersson, C., Andersson-Sjoland, A., Tufvesson, E., Bjermer, L., Erjefalt, J., et al. (2014). Controlled and uncontrolled asthma display distinct alveolar tissue matrix compositions. *Respir. Res.* 15 (1), 67. doi:10.1186/1465-9921-15-67

Widener, A. E., Bhatta, M., Angelini, T. E., and Phelps, E. A. (2021). Guest-host interlinked PEG-MAL granular hydrogels as an engineered cellular microenvironment. *Biomater. Sci.* 9 (7), 2480–2493. doi:10.1039/d0bm01499k

Wu, D., Xu, Y., Ding, T., Zu, Y., Yang, C., and Yu, L. (2017). Pairing of integrins with ECM proteins determines migrasome formation. *Cell. Res.* 27 (11), 1397–1400. doi:10.1038/cr.2017.108

Wu, J., Hillier, C., Komenda, P., Lobato de Faria, R., Levin, D., Zhang, M., et al. (2015). A microfluidic platform for evaluating neutrophil chemotaxis induced by sputum from COPD patients. *PLoS One* 10 (5), e0126523. doi:10.1371/journal.pone.0126523

Yamada, K. M., Doyle, A. D., and Lu, J. (2022). Cell-3D matrix interactions: Recent advances and opportunities. *Trends Cell. Biol.* 32, 883–895. doi:10.1016/j.tcb.2022.03.002

Yamada, K. M., and Sixt, M. (2019). Mechanisms of 3D cell migration. *Nat. Rev. Mol. Cell. Biol.* 20 (12), 738–752. doi:10.1038/s41580-019-0172-9

Zenewicz, L. A. (2017). Oxygen levels and immunological studies. *Front. Immunol.* 8, 324. doi:10.3389/fimmu.2017.00324

Zhu, Y., Sun, L., Wang, Y., Cai, L., Zhang, Z., Shang, Y., et al. (2022). A biomimetic human lung-on-a-chip with colorful display of microphysiological breath. *Adv. Mat.* 34 (13), e2108972. doi:10.1002/adma.202108972

frontiers | Frontiers in Pharmacology

TYPE Review
PUBLISHED 12 December 2022
DOI 10.3389/fphar.2022.1033043

OPEN ACCESS

EDITED BY
Rebecca L. Heise,
Virginia Commonwealth University,
United States

REVIEWED BY
Manash K. Paul,
California State University, Los Angeles,
United States
Rahul K. Nelli,
Iowa State University, United States

*CORRESPONDENCE
Mingzhi Luo,
luomingzhi@cczu.edu.cn
Linhong Deng,
dlh@cczu.edu.cn

†These authors have contributed equally to this work

SPECIALTY SECTION
This article was submitted to Respiratory Pharmacology, a section of the journal Frontiers in Pharmacology

RECEIVED 31 August 2022
ACCEPTED 30 November 2022
PUBLISHED 12 December 2022

CITATION
Ni K, Che B, Yang C, Qin Y, Gu R, Wang C, Luo M and Deng L (2022), Emerging toolset of three-dimensional pulmonary cell culture models for simulating lung pathophysiology towards mechanistic elucidation and therapeutic treatment of SARS-COV-2 infection.
Front. Pharmacol. 13:1033043.
doi: 10.3389/fphar.2022.1033043

Emerging toolset of three-dimensional pulmonary cell culture models for simulating lung pathophysiology towards mechanistic elucidation and therapeutic treatment of SARS-COV-2 infection

Kai Ni†, Bo Che†, Chongxin Yang, Youyuan Qin, Rong Gu, Chunhong Wang, Mingzhi Luo* and Linhong Deng*

Changzhou Key Laboratory of Respiratory Medical Engineering, Institute of Biomedical Engineering and Health Sciences, School of Medical and Health Engineering, Changzhou University, Changzhou, Jiangsu, China

The ongoing COVID-19 pandemic caused by severe acute respiratory syndrome coronavirus-2 (SARS-CoV-2) poses a never before seen challenge to human health and the world economy. However, it is difficult to widely use conventional animal and cell culture models in understanding the underlying pathological mechanisms of COVID-19, which in turn hinders the development of relevant therapeutic treatments, including drugs. To overcome this challenge, various three-dimensional (3D) pulmonary cell culture models such as organoids are emerging as an innovative toolset for simulating the pathophysiology occurring in the respiratory system, including bronchial airways, alveoli, capillary network, and pulmonary interstitium, which provide a robust and powerful platform for studying the process and underlying mechanisms of SARS-CoV-2 infection among the potential primary targets in the lung. This review introduces the key features of some of these recently developed tools, including organoid, lung-on-a-chip, and 3D bioprinting, which can recapitulate different structural compartments of the lung and lung function, in particular, accurately resembling the human-relevant pathophysiology of SARS-CoV-2 infection *in vivo*. In addition, the recent progress in developing organoids for alveolar and airway disease modeling and their applications for discovering drugs against SARS-CoV-2 infection are highlighted. These innovative 3D cell culture models together may hold the promise to fully understand the pathogenesis and eventually eradicate the pandemic of COVID-19.

KEYWORDS

COVID-19, lung organoid, lung-on-a-chip, 3D bioprinting, drug discovery

1 Introduction

The world has been facing coronavirus 2019 (COVID-19) pandemic for 3 years, caused by severe acute respiratory syndrome coronavirus 2 (SARS-CoV-2) (Wang C. et al., 2020; Castiello et al., 2022; Luo et al., 2022). Although most COVID-19 patients present mild or moderate symptoms including cough, fever, fatigue, shortness of breath, and pharyngodynia, critically ill patients of COVID-19 always present severe respiratory complications such as pulmonary edema, acute respiratory distress syndrome (ARDS), and even death (Chen et al., 2020; Guan et al., 2020; Huang et al., 2020). Therefore, COVID-19 which has led to such a global health crisis with huge economic and social impact requires urgent and thorough investigations to elucidate its mechanisms of pathogenesis and explore corresponding therapeutic treatments as well as potential post-disease implications.

However, these investigations so far have been limited by the scarcity of suitable models to mimic the pathophysiological processes of SARS-CoV-2 infection that occur during COVID-19 *in vivo*. Conventional models used to experimentally investigate pathophysiology of human diseases include animal-based models (de Oliveira et al., 2021; Lee and Lowen, 2021). Several kinds of animals including mice (Dinnon et al., 2020), hamsters (Tostanoski et al., 2020), ferrets (Cox et al., 2021), and non-human primates (NHPs) (Corbett et al., 2020; Maisonnasse et al., 2020) have been used to study pathogenesis and host responses associated with COVID-19. It is however difficult to use animal models to recapitulate human physiology and at the same time decipher fundamental molecular mechanisms of host-pathogen interactions, viral replication kinetics, and virus tropism. These animal models are also not very suitable for early-stage drug screening since they are time-consuming and often fail to translate to human trials due to the species difference (Knight, 2008; Konar et al., 2016).

Alternatively, two-dimensional (2D) cell culture systems can be used as experimental models in the study of COVID-19, which are both relatively inexpensive and highly efficient (Duval et al., 2017). But increasing evidence suggests that 2D cell culture systems have inherent drawbacks. For example, 2D cell culture cannot correctly mimic the organ's *in vivo* architecture and microenvironments (Elsdale and Bard, 1972; Korff and Augustin, 1999; Ghajar et al., 2008). More specifically, the lung is a complex organ including 23 generations of branching airways, multiple cell types, specified tubular three-dimensional (3D) geometry, and cyclic stretch stimulation, which limit the simulating effect using 2D cell culture (Weibel and Gomez, 1962). A recent report has shown that SARS-CoV-2 infection arises from the proximal airways (containing basal, secretory, and ciliated cells) and induces associated inflammation in distal alveoli (containing type I and type II cells) (Morrisey and Hogan, 2010; Borczuk et al., 2020; Tay et al., 2020), which are largely infeasible to be recapitulated by the traditional 2D cell culture systems.

Fortunately, many novel 3D cell culture toolsets such as organoid, lung-on-a-chip, and 3D bioprinting have been developed during the past decade, which provide new platforms for exploring complex pathophysiology of lung diseases such as COVID-19 (de Melo et al., 2021). These 3D cell culture models are indeed gaining increasing momentum to be the primary choice of experimental methods due to their physiological relevance and operational flexibility as well as high-throughput adaptability (Bircsak et al., 2021). Cells cultured in these 3D models exhibit features close to the complex lung conditions *in vivo*, mimic cell-cell and cell-matrix interactions, and reproduce the morphology and function of the lung (Baker and Chen, 2012). Thus, it is evident that 3D cell culture models are advantageous in the investigation of COVID-19 pathogenesis and the development of therapeutic agents to combat the pandemic disease.

In this review, we first describe the characteristics of SARS-CoV-2 and immuno-inflammatory responses related to the viral infection and pathogenesis of COVID-19, and then summarize the 3D cell culture models including the traditional air-liquid interface (ALI) culture and spheroid, and the emerging organoid, lung-on-a-chip (containing organoplate), and 3D bioprinting which may be suitable *ex vivo* models to mimic various vital lung functions in a cell culture dish. We also highlight the possibility of building new robust models to recapitulate different structural compartments of the lung and lung function, in particular, accurately resembling the pathophysiology of COVID-19 *in vivo*. This information may hopefully help investigators to select and/or develop suitable 3D cell culture models for the pursuit of mechanistic understanding and therapeutic treatment of COVID-19.

2 Characteristics and immuno-inflammatory responses of SARS-CoV-2

SARS-CoV-2 is a virus with a genome of nearly 30 kb, with 11 open reading frames (ORFs) and 27 viral encoding proteins (Lu et al., 2020). Among them, an array of ORFs, i.e., ORF 3, 6, 7a, 7b, 8, and 10 are the accessory proteins, and the main structural viral proteins include spike glycoprotein (S), envelope glycoprotein (E), membrane glycoprotein (M), and nucleocapsid proteins (N) (Zhou P. et al., 2020; Wu et al., 2020). SARS-CoV-2 enters host cells (ciliated, club, alveolar epithelial type 2 (AT2) cells, vascular endothelial cells, and alveolar macrophages) by endocytosis mediated by the interaction of the S proteins with host receptors such as angiotensin-converting enzyme 2 (ACE2). The S proteins on the envelope of SARS-CoV-2 are cleaved into S1 and S2 subunits (Ke et al., 2020). But only S1 consists of the receptor-binding domain (RBD), which directly binds to the peptidase domain (PD) of ACE2 to gain entry into host cells (Yan et al., 2020).

Therefore, the S1 protein/receptor interaction is the critical determinant for the virus to infect host cells. According to various mutation sites in the S protein, six main variants of SARS-CoV-2 viruses have been identified including Alpha, Beta, Gamma, Delta, Lambda, and Omicron. Some variants are more transmissible or easier to escape from immunity than others, which leads to increased transmissibility and a higher viral load in the human body. Garrett and others (Garrett et al., 2022) evaluated asymptomatic carriage in a sub-study of the Sisonke vaccine trial and found that 2.6% of the asymptomatic carriage during the Beta and Delta outbreaks rose to 16% during the Omicron period.

Additionally, some host factors can enable and/or facilitate viral entry. For example, transmembrane protease serine 2 (TMPRSS2) is widely expressed in epithelial cells of the respiratory tract and could activate SARS-CoV-2 in Calu-3 cells (Bugge et al., 2009; Bestle et al., 2020). Furin also plays a critical role in the cleavage activation of SARS-CoV-2 spike proteins (Johnson et al., 2021). Neuropilin-1 (NRP1), which regulates pleiotropic biological processes, facilitates SARS-CoV-2 cell entry and infectivity (Cantuti-Castelvetri et al., 2020; Daly et al., 2020). In brief, these host factors provide an essential mechanism for SARS-CoV-2 infectivity and a scientific basis for targeting infected cells to develop antiviral drugs. Therefore, these host factors' expression levels in 3D cell culture models may be an important indicator for selecting suitable models for SARS-CoV-2 infection study.

Once SARS-CoV-2 infects the host, both innate and adaptive immune systems initiate to counteract the virus infection. The innate immune response provides the first line of defense against SARS-CoV-2 infection in the airways, *via* various mechanisms for rapid sensing and suppressing of the viral infection. For example, the viral infection is detected by endosomal Toll-like receptor 3&7 (TLR3, TLR7), and melanoma differentiation-associated gene 5 (MDA5) of the innate immune cells in the airways (Totura et al., 2015; Zhou et al., 2021). This subsequently triggers the release of a series of pro-inflammatory factors such as tumor necrosis factor-alpha (TNF-α), and interleukin 1&6 (IL-1, IL-6), which together facilitate the early controlling of the viral infection.

On the other hand, the adaptive immune response provides the second line of defense against SARS-CoV-2 infection, which is enabled by a broader and more finely tuned repertoire of recognition mechanisms for viral infection, involving antigen presenting cells (APCs), $CD4^+$ T cells, $CD8^+$ T cells and B cells (Sette and Crotty, 2021). More specifically, following SARS-CoV-2 infection, the APCs present viral particles to $CD8^+$/$CD4^+$ T cells *via* interaction of TCR-MHC I or II, respectively. When exposed to antigens, $CD8^+$ T cells release cytotoxic granules that are critical for clearance of virus-infected cells, and $CD4^+$ T cells polarize towards Th1 and Th2 cells. Then Th1 cells release IFN-γ to eliminate the virus, and Th2 cells activate humoral immunity (such as B cells) to generate antibodies that neutralize SARS-CoV-2 (Toor et al., 2021). Unfortunately, in severe cases of COVID-19 the potential of this mechanism is significantly limited because the number of APCs is largely reduced (Zhou R. et al., 2020; Qin et al., 2021).

It is obvious that a deficiency of the immune responses would give an opportunity for viruses such as SARS-CoV-2 to freely complete their RNA replication process and subsequent release of the genetic materials, and ultimately result in reassembling and release of large amounts viruses (Jiang et al., 2021). However, an excessive immune response may also trigger excessive production of inflammatory cytokines, a phenomenon known as the cytokine storm. For example, in critically ill patients of COVID-19 the expression of inflammatory cytokines including IL-2, IL-6, IL-7, IL-10, IP-10, MCP-1, TNF-α, and IFN-γ has been shown to be excessively elevated, and this kind of cytokine storm is thought as the main cause of multi-organ failure and death in COVID-19 patients (Castelli et al., 2020; Hu et al., 2021; Luo et al., 2022).

3 3D cell culture models to mimic lung in study of SARS-CoV-2 infection

With increasing studies of COVID-19, the importance is acknowledged that different lung regions (airway, alveolus, a thin epithelial-endothelial barrier, and pulmonary interstitium) play different essential roles in the pathogenesis and development of COVID-19. Therefore, 3D cell culture models (ALI culture, spheroid, organoid, organ-on-a-chip including organoplate, and 3D bioprinting) which could mimic different structural compartments of the lung and lung function may be more suitable for studying different physiopathological processes of COVID-19 (Figure 1). In addition, these 3D cell culture models have different advantages in mimicking the physiology and pathology of diseases (Table 1). For example, the ALI approach is primarily used to mimic the epithelial air-liquid interface environment of respiratory tract in the lung. Spheroids are mainly used in study of tumor growth such as in lung cancer. Organoids are self-assembled constructs that can "freely" grow in resemblance to natural development. Organ-on-a-chip has bridged microfluidic technology and living cells, resulting in a dynamic biomimetic device (de Oliveira et al., 2021). 3D bioprinting models can print more complex constructs and mimic complex anatomical structures.

3.1 3D cell culture to mimic ALI of the lung

The respiratory system provides an ALI interface to protect the body from invasion by inhaled pathogens that are commonly encountered in the environments. This interface can not be mimicked by the submerged 2D cell culture models, until the development of 3D ALI culture models (Whitcutt et al., 1988).

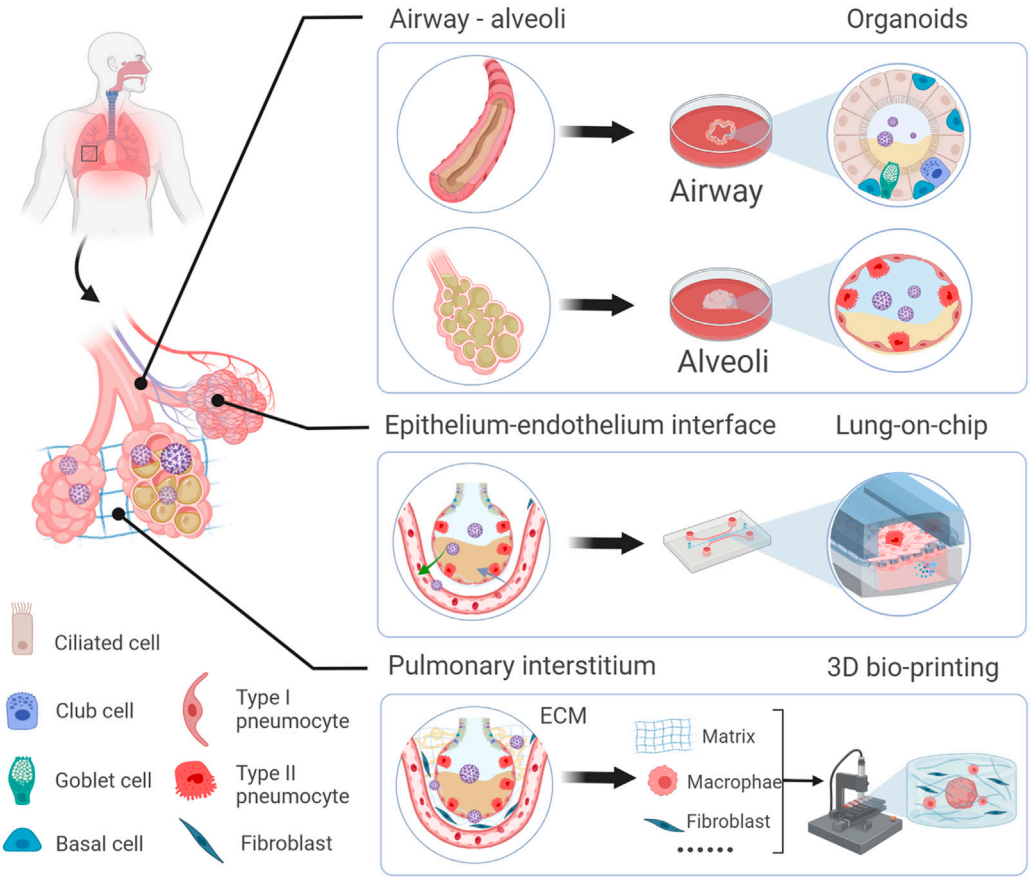

FIGURE 1
Schematic representation of novel 3D models to mimic *in vivo* the physiology and pathophysiology of different lung regions. Different 3D cell culture models (organoid, organ-on-a-chip, and 3D bioprinting) have their own advantages which could mimic the structure and function of different lung regions (airway, alveoli, a thin epithelial-endothelial barrier, and pulmonary interstitium).

3D ALI culture mainly consists of an outer plastic culture dish and an inner porous membrane insert (usually in a 6-well plate format with a pore size of 0.4 μm). Cells are cultured on the insert, and once confluent (often in 2–4 days), the medium is removed from the apical aspect of the insert, forming an ALI. Consequently, this cell culture method has been used to mimic ALI in the lung with different types of airway epithelial cells, including ciliated cells, club cells, goblet cells, and basal cells, to self-assemble into a pseudo-stratified columnar epithelium (Ghio et al., 2013). These functional epithelia provide crucial functions for maintaining airway tissue integrity and homeostasis by secreting inflammatory mediators and antimicrobial peptides (Tam et al., 2011).

By using this traditional 3D cell culture, Mulay et al. (Mulay et al., 2021) discovered that SARS-CoV-2 infected ciliated cells at a significantly higher rate than goblet cells in the proximal airway epithelium. In addition, Mullen and others (Mullen et al., 2021) found in ALI cultures that SARS-CoV-2 infection increased pyruvate carboxylase (PC) and mTORC1 activity and inhibition of mTORC1 could reduce SARS-CoV-2 replication. These studies collectively demonstrate that ALI culture system is an important platform for screening therapeutics targeting airway cells of SARS-CoV-2 and related antivirals for COVID-19.

3.2 Spheroids culture to mimic alveoli of the lung

Spheroids allow cell colonies to self-assemble and form aggregates of 3D microtissues (Ryu et al., 2019). The process of spheroid formation is affected by adhesion and differentiation of cells and various factors, including gradients of nutrients, oxygen, and growth factors in cell culture medium.

Spheroids are mainly used for cancer studies because it shows some characteristics similar to tumor microenvironments such as hypoxia and tumoral cell-to-cell interaction (Nigjeh et al., 2018). But it has also been used as 3D cell cultures for recapitulating the

TABLE 1 Summary of the different *in vitro* models with advantages and disadvantages.

Culture model	Advantages	Disadvantages
Animals	Long-term effects of drugs	Time consuming
	Whole living organism	Limited high-throughput experiment
	Complex heterotypic microenvironment	Prominent differences between animals and human
2D cultures	Simple	Limited ECM production
	Low-cost	High stiffness of surface
	Commercially available	2D flat culture
ALI cell culture	Co-culture with epithelial and stromal cells	Cell-matrix interactions
	Achieve airway complete epithelium	Dynamic physical factors
Spheroids	Maintain intrinsic phenotypic properties	Diffusion gradient and lack of nutrients in the core
	Organotypic model for cancer study	Uniform size
Organoids	Cell-cell and cell-matrix interactions	Establishment can take long
	Follows developmental stages similar to actual organs	No control on cellular arrangement and growth
	Highly relevant morphology and phenotype	Limited in size
Lung-on-chip	Physiologically relevant air and liquid flows	Commonly used material for chips (PDMS) is hydrophobic and can absorb drugs
	Small volumes required	Limited throughput, especially when combined with flow
	Very controlled environment	Requires special equipment and, depending on design, access to special facilities
3D bioprinting	Accurately arranges the cells	Cell viability varies based on cross-linking and the shear stress of passing through the nozzle
	Enhances cell viability, function, migration and self-assembly	Expensive material of limited availability
	Different printing strategies available	Time-consuming, limited throughput

Abbreviations: ECM, extracellular matrix; PDMS, polydimethylsiloxane.

anti-viral drug responses in airway cells. For example, Ebisudani et al. (Ebisudani et al., 2021) established and validated a long-term culture of alveolospheres that could be used as an efficient drug testing platform for the development of therapeutic agents to combat viruses such as SARS-CoV-2.

3.3 Organoids to mimic different regions of the lung

Novel 3D cell culture systems such as organoids have emerged recently with great potential in biomedical research. Organoids are 3D structures derived from stem/progenitor cells in specific biomaterials that can be differentiated to generate 3D structures containing multiple cell types and assembles that resemble the organization and functions of specific tissue/organs. Therefore, the development of stem cell technology has been central to the formation and progression of organoids. For example, Takahashi and Yamanaka (Takahashi and Yamanaka, 2006) demonstrated the creation of pluripotent cells directly from mouse embryonic or adult fibroblasts by introducing four transcription factors. Soon afterward, Sato et al. (Sato et al., 2009) reported the formation of 3D structures of single-sorted $Lgr5^{+}$ stem cells in Matrigel. Ever since, there have been many organoids successfully generated and used in different fields.

Lung organoids can be established from induced pluripotent stem cells (iPSCs) or airway epithelial progenitor cells such as AT2 cells or basal cells under optimal conditions. The processes of different cell sources to generate lung organoids are described in Table 2. iPSCs-derived organoids contain AT1, AT2, and epithelial cells, and recapitulate the structure and function of the alveolus or airway when exposed to suitable induction signals (Takahashi et al., 2007; Leibel et al., 2020).

AT2 cells reside in the alveoli which are characterized by the production of pulmonary surfactant proteins and can behave as alveolar stem cells during repair after injury, repopulating both AT1 and AT2 cells (Diem et al., 2020). Basal cells, characterized by the marker of the transcription factor Trp63, the cytokeratin Krt5, and integrin alpha 6, are one type of proximal airway

TABLE 2 The process of different cell source to generate lung organoids.

Cell source	Medium		Treatment period	Matrigel concentration	Results/Application	Refs
iPSCs	DE	CHIR99021 and Activin A in RPMI1640	Day 1	100% matrigel mixed with LPs (Corning, #354234)	hAWOs contain goblet cells ($MUC5AC^+$), basal cells ($P63^+$), ciliated-like cells ($FOXJ1^+$), and proliferating cells ($CDK1^+TOP2A^+$)/Serve as a platform to perform a high content screen for blocking SARS-CoV-2 infection	Duan et al. (2021)
		Activin A and 2% FBS in RPMI1640	Day 2–3			
	AFE	Dorsomorphin dihydrochloride, SB431542, IWP2	Day 4–5			
	LPs	CHIR99021, human BMP4, all-trans retinoic acid	Day 6–14			
	hAWOs	FGF10, FGF2, dexamethasone, 8-bromo-cAMP, IBMX	D15-			
ESCs	DE	CHIR99021 and Activin A in RPMI1640	Day 1–3	100% Matrigel mixed with AFE (BD Biosciences, #356237)	hAWOs contain basal cells ($P63^+$), ciliated cells (acetylated TUBULIN, a-TUB^+), club cells ($CC10^+$), and goblet cells ($MUC5AC^+$) hALOs contained AT2 cells (SPC^+) and AT1 cells ($PDPN^+$)/Serve as a pathophysiological model to investigate the underlying mechanism of SARS-CoV-2 infection	Pei et al. (2021)
	AFE	Noggin, FGF4, CHIR99021 and SB431542 in Advanced DMEM/F12	Day 3–7			
	VAFE	Human BMP4, all-trans retinoic acid, CHIR and 1% Glutamax in DMEM/F12	Day 8–14			
	LPs	CHIR99021, FGF10, KGF, DAPT	Day 15–21			
	hAWOs	Dexamethasone, 8-Br-cAMP, 3-isobutyl-1-methylxanthine, KGF, B-27 supplement, BSA and 0.1% ITS premix in Ham's F12	Day 22–28			
	hALOs	CHIR99021, SB431542, Dexamethasone, 8-Br-cAMP, 3-isobutyl-1-methylxanthine, KGF, B-27 supplement, BSA and 0.1% ITS premix in Ham's F12	Day 22–28			
HBECs derived from airways tissue	hAWOs	R-Spondin 1, FGF 7, FGF 10, Noggin, A83-01, Y-27632, SB202190, B27 supplement, N-Acetylcysteine, Nicotinamide, GlutaMax and HEPES in Advanced DMEM/F12	Cultured for 21 days	50% growth factor reduced Matrigel mixed with HBECs (Corning)	hAWOs contain basal cells ($KRT5^+$) and goblet cells ($MUC5AC^+$)/Serve as a physiologically relevant airway epithelial model to investigate SARS-CoV-2 therapeutics	Chen et al. (2022)
AT2s derived from primary lung tissue	hALOs	CHIR99021, BIRB796, Y-27632, SB431542, EGF, EGF10, B27 supplement, N-Acetyl-L-cysteine, Heparin, Antibiotic-Antimycotic, GlutaMax and HEPES	Cultured for 10–14 days	50% Matrigel mixed with AT2s (Corning, #354230)	hALOs contained AT2 cells (SFTPC) and AT1 cells (AGER)/Serve as an alveolar epithelium model for understanding human respiratory diseases	Katsura et al. (2020)
Tracheal epithelial cells derived from mouse trachea	AWOs	Insulin, transferrin, cholera toxin, EGF, bovine pituitary extract, 5% FBS and retinoic acid in DMEM/F12	Cultured for 10–14 days	100% growth factor-reduced Matrigel mixed with cells (Corning)	AWOs fused and formed interconnected lumina in a free-floating condition/Serve as ideal modular units for the biofabrication of biomimetic organs	Liu et al. (2021)
HBECs purchased from company	hAWOs	PneumaCult-ALI Maintenance Medium (Stemcell Technologies)	Cultured for 21 days	40% on the bottom, 5% mixed with cells	hAWOs are able to self-organize and mature toward lung tissue-like structures/Serve as a novel tool for studying disease-relevant cellular and molecular function and ectopic transplantation	Tan et al. (2017)

Abbreviations: DE, definitive endoderm; AFE, anterior foregut endoderm; VAFE, ventralized anterior foregut endoderm; LPs, lung progenitors; hAWOs, human airway organoids; hALOs, human alveolar organoids; AT2s, human alveolar epithelial type-2 cells; EGF, epidermal growth factor.

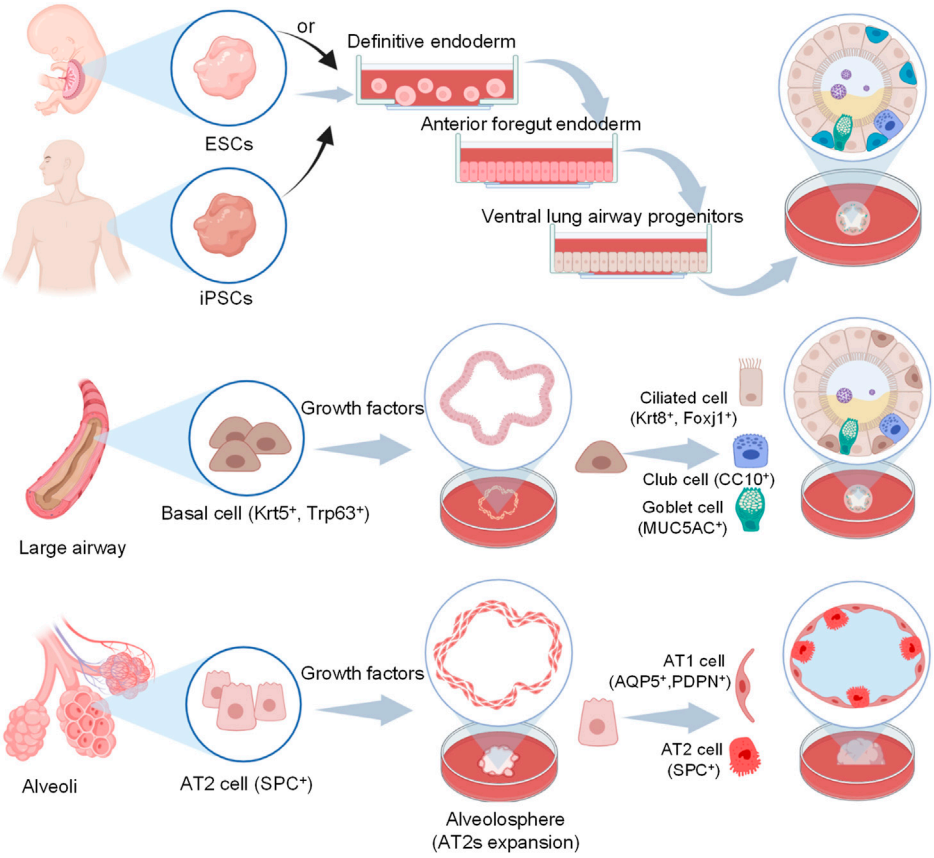

FIGURE 2
Schematic representation of human airway and alveoli organoids developed from different origin cells and cultivation include particular steps. For iPSCs, they first generate definitive endoderm (DE), then anterior foregut endoderm (AFE) and lung progenitors (LPs) with different additives, finally yield lung organoids *via* 3D culture using Matrigel (Barkauskas et al., 2017). For basal cells and AT2 cells, they maintain under suitable conditions and self-organize in a more natural manner with Matrigel.

epithelium (accounting for ~30%), which can differentiate into secretory and ciliated cells (Lambrecht and Hammad, 2012; Barkauskas et al., 2017; Bilodeau et al., 2021). Compared to iPSCs, alveolar or airway organoids based on AT2 cells and basal cells from adults present the physiological dynamic consistent with normal *in vivo* or human patients, especially for COVID-19 (Wang et al., 2021).

Due to the need to mimic the effects in different lung regions, alveolar and airway organoids have been developed to mimic the airway and alveoli, respectively. And a simplified visual description of the main steps to generate lung organoids of different origin cells is in Figure 2.

3.3.1 Alveolar organoids

Though the SARS-CoV-2 virus typically initiates in the proximal airways, severe symptoms of COVID-19 arise from infection and associated inflammation in the distal alveoli, which has strikingly different physiology from that of the proximal airways (Katsura et al., 2020; Mulay et al., 2021). Previous studies have demonstrated that ACE2 is essential for SARS-CoV-2 entry, indicating that AT2 cells with a high expression of ACE2 proteins are significant targets of SARS-CoV-2 infection (Zhao B. et al., 2020). To explore the response of lung cells (particularly AT2 cells) to the SARS-CoV-2 infection, Han and collaborators (Han et al., 2021) developed an alveolar organoid model derived from iPSCs. Similar to what is seen in COVID-19 patients' lung autopsy tissues (Blanco-Melo et al., 2020), their results revealed that robust induction of chemokines (such as rheumatoid arthritis, TNF signaling, and IL-17 signaling) upon SARS-CoV-2 infection. Also, these AT2-derived organoids were able to differentiate into AT1 cells and could facilitate diverse investigations of pulmonary pathogens, including SARS-CoV-2 infection (Salahudeen et al., 2020).

In addition, the expression of ACE2 could be modulated by the activation of different pathways. When treated with particulate matter (PM2.5), Kim et al. (Kim et al., 2020) proved that ACE2 significantly upregulated in alveolar organoids. On the contrary, androgen signaling inhibition

reduced ACE2 expression and protected lung organoids against SARS-CoV-2 infection (Samuel et al., 2020).

3.3.2 Airway organoids

Since the proximal airway regions are the first target of SARS-CoV-2 infection, airway organoids are suitable for exploring the interaction of SARS-CoV-2 with proximal airway cells. To accurately mimic proximal airway physiological conditions during SARS-CoV-2 infection, (Chen et al., 2022) used human airway basal cells to generate airway organoids, in which basal cells differentiate into ciliated cells, goblet cells, and club cells. Furthermore, they compared ALI cultures and airway organoid cultures and acknowledged that the latter expressed high levels of ACE2 and TMPRSS2, which are highly susceptible to SARS-CoV-2 infection and promote inflammatory cytokine responses (Marescotti et al., 2019; Wang J. et al., 2020; Chen et al., 2022).

Furthermore, to observe cellular dynamic changes similar to clinical features in COVID-19 patients, (Xu et al., 2021) developed airway organoids derived from patient biopsy residues. Therefore, these airway organoids can be used to investigate the tissue-specific SARS-CoV-2 infection, host responses, and viral infection inhibitors.

To investigate whether multibasic cleavage site (MBCS) can alter protease usage during entry and which entry pathway is taken by SARS-CoV-2, (Mykytyn et al., 2021) found that SARS-CoV-2 spike MBCS increases infectivity and serine protease usage on human airway organoids based on collagen-coated transwell inserts. In addition, (Kastenhuber et al., 2022) demonstrated that coagulation factors, including factor Xa and thrombin, increase SARS-CoV-2 infection in human lung organoids derived from iPSCs. These data indicate that these hose factors can directly cleave SARS-CoV-2 spike, which is important to promote viral entry into airway epithelia.

Together, these data demonstrate that organoid models could accurately mimic alveolar and airway cellular composition to provide a valuable platform for screening new drugs to identify candidate COVID-19 therapeutics.

3.3.3 Lung organoids

iPSCs-derived lung organoids are indisputably a fast-moving field due to the unique property of unlimited self-renewal capacity (Kolagar et al., 2020; Sharma et al., 2020). To date, the most classical differentiation protocols first generate definitive endoderm (DE), then anterior foregut endoderm (AFE) and lung progenitors (LPs), and finally yield lung organoids using 3D Matrigel. Tiwari et al. (2021) developed human lung organoids derived from iPSCs to investigate viral pathogenesis. iPSCs were differentiated into definitive endoderm, lung progenitor cells, then an epithelial-like structure with surrounding mesenchymal cells (labeled with smooth muscle actin and acetylated tubulin) by day 60, and subsequently a pseudostratified epithelial structure with $P63^+$ basal-like cells, $FOXJ1^+$ ciliated cells, and structural alveolar type 1 & 2 cells.

In addition, 3D cell culture models such as organoids are suitable for further understanding immuno-inflammatory responses associated with SARS-CoV-2 infection, which is crucial for effective control and clearance of the virus. For example, iPSCs-derived lung organoids have been used to determine the early cellular response to SARS-CoV-2 infection, particularly the change in the expression level of inflammatory factors with 48 h infection (Pei et al., 2021). The results of RNA-sequencing analysis show that several inflammatory factors, including IL-6, TNF, CXCL8, CXCL2, CXCL3, CXCL10, CXCL11, and NF-κB were upregulated, which is consistent with the clinically observed phenomenon in COVID-19 patients (Huang et al., 2020; Wilk et al., 2020).

Therefore, iPSCs-derived lung organoids containing the component and structure of proximal airways and distal alveoli, can be used for revealing cell/tissue-specific SARS-CoV-2 Infection and host responses in the whole lung (Dye et al., 2015).

3.4 Lung-on-a-chip models to mimic epithelium-endothelium interface

Although lung organoids are promising tools to elucidate the pathophysiological mechanisms of COVID-19, a significant limitation of them is the absence of vasculature, and could not mimic the interaction of alveoli-capillary networks and related gas exchange in the lung (Barkauskas et al., 2017). The gas exchange process in the human body depends on the direct interaction between a monolayer alveolar epithelia lining the alveoli and a monolayer endothelial cell lining the capillary network, which allows for diffusive gas exchange and prevents plasma fluid entry into the alveoli (Weibel, 2017; Bernard et al., 2020). With growing interest in COVID-19, the importance of crosstalk between alveolar epithelial cells and the capillary network gets more attention. Fortunately, the lung-on-a-chip model could replicate this alveolar-capillary interaction by integrating tissue–tissue interfaces and may be crucial for the systemic understanding of COVID-19.

Organ-on-a-chip is a novel 3D cell culture tool based on the integration of the techniques of bioengineering and microfluidics disciplines (Shrestha et al., 2020). It always consists of upper and lower microchannels separated by a thin, flexible, extracellular matrix (ECM)-coated membrane, which is very suitable for mimicking the alveolar-capillary interface (Huh et al., 2010; Kızılkurtlu et al., 2018). For example, when human alveolar epithelial cells and pulmonary microvascular endothelial cells are cultured on the opposite sides of the membrane and grown to confluence, the upper channel is introduced into the air to create an air-liquid interface. In addition, a computer-controlled vacuum in these chambers can be used to produce cyclic

TABLE 3 List for characteristics and application of current lung-on-a-chip devices.

Devices	Structures and seeding cells	Fabrication materials/ Techniques	Characteristics	Aplication	Refs
Lung-on-a-chip	Two microchannels; the upper: human alveolar epithelial cells and the lower: microvascular endothelial cells	PDMS/soft lithography	Cyclic stretching: computer-controlled two larger, lateral vacuum microchambers to produce cyclic stretching (5 ~ 15%)	Replicates dynamic mechanical distortion of the alveolar-capillary interface caused by breathing movements	Huh et al. (2010)
Lung-on-a-chip	Two microchannels; the upper: Calu-3 lung epithelial cell and the lower: microvascular endothelial cells	PC film/three-dimensional (3D) microfilm forming and ion track technology	The membranes with the shape of hexagonally arrayed hemispherical microwells (inner diameter: 200 μm, depth: 100.6 ± 3.0 μm)	Set the stage for other (micro) anatomically inspired membrane-based lung-on-a-chip models	Baptista et al. (2022)
Alveolar lung-on-a-chip	A three-dimensional porous hydrogel made of gelatin methacryloyl with an inverse opal structure; human alveolar epithelial cells	7% (wt/wt) GelMA/assemble alginate microbeads into a cubic close-packed lattice, infiltrate GelMA, remove alginate microbeads	Possess both the sac-like pores and the interconnecting windows between the sacs, in addition to a stiffness close to the native human lung	Investigates the effects of cigarette smoke and SARS-CoV-2 pseudoviral infection	Huang et al. (2021)
Airway-on-a-chip	Two microchannels; the upper: airway epithelial cells and the lower: airway smooth muscle cells	PMMA/Micromilling	Suspended hydrogels (type I collagen and Matrigel) as a middle layer to allow disassembly for downstream analyses	Significantly advance the understanding of smooth muscle cells–epithelial cells–matrix interactions	Humayun et al. (2018)
Airways-on-Chip	Three individual chips; nasal: RPMI-2650 cells, bronchial: Calu-3 cells, and acinar airways: hAELVi cell	PDMS/microfabrication and 3D printing	Mimics key elements of the respiratory system spanning (i) nasal passages, (ii) the mid-bronchial airway region and (iii) the deep acinar region, distinct with alveolated airways	Serve as a preclinical *in vitro* benchmark underlining regional lung crosstalk for viral infection pathways	Nof et al. (2022)

Abbreviations: PDMS, polydimethylsiloxane; PC, polycarbonate; GelMA, gelatin methacryloyl; SARS-CoV-2, severe acute respiratory syndrome coronavirus 2; PMMA, polymethylmethacrylate.

strain ranging from 5% to 15% to match normal levels of strain to mimic physiopathological breathing movements (Birukov et al., 2003). Therefore, organ-on-a-chip can manipulate not only biochemical factors (such as cytokines, oxygen, and nutrients) but also dynamic physical factors (such as shear stress and cyclic strain), both of which are critical in understanding lung organ-level functions and permit researchers to mimic disease pathogenesis of COVID-19 (Huh et al., 2010; Benam et al., 2016; Novak et al., 2021; Wang et al., 2022).

In addition to dynamic mechanical distortion of the alveolar-capillary interface, there is increasing evidence that the microscale curved surfaces affect the spatiotemporal organization and behaviors of cells (Callens et al., 2020; Jin et al., 2021). To recreate the mainly spherical geometry of the cells' native microenvironment, Baptista et al. (2022) made the membranes the shape of hexagonally arrayed hemispherical microwells by using a combination of 3D microfilm forming and ion track technology. Each microwell has a little bit more than 200 μm maximum inner diameter and an average maximum depth of 100.6 ± 3.0 μm. With integration in microfluidic chips, the microcurved membranes were seeded with Calu-3 lung epithelial cell line and human lung microvascular endothelial cells, respectively. Also, Huang et al. (2021) successfully designed an alveolar lung-on-a-chip platform with the alveoli-like 3D gelatin methacryloyl (GelMA) inverse opal structure. Significantly, this device also provided an air-liquid interface and cyclic strain, which was better able to maintain the functions of human alveolar epithelial cells. A list of characteristics and applications of current lung-on-a-chip devices is given in Table 3. A visual representation of these classifications is found in Figure 3.

Multiple clinical trials have found that microvascular thrombotic and inflammatory processes may be crucial in exacerbating ARDS and increasing lung damage (Ackermann et al., 2020; Jung et al., 2020; Sardu et al., 2020). The vascular damage, and whether it is a direct consequence of endothelial infection or an indirect consequence of immune cells-mediated cytokine storm remain unclear. By using a vascularized lung-on-a-chip model, Thacker et al. (2021) found that infection of alveolar epithelial cells leads to the limited apical release of virions, and viral RNA and proteins are rapidly detected in underlying endothelial cells, which are themselves refractory to apical infection in monocultures. In addition, endothelial cells infected by SARS-CoV-2 lose expression of tight junction markers and adopt a pro-coagulatory phenotype. These results indicate that the dynamics of vascular damage are a direct consequence of endothelial infection independently of a cytokine storm.

To accurately resemble human-relevant responses to viral infection, Zhang M. et al. (2020) also created an alveoli-on-a-chip

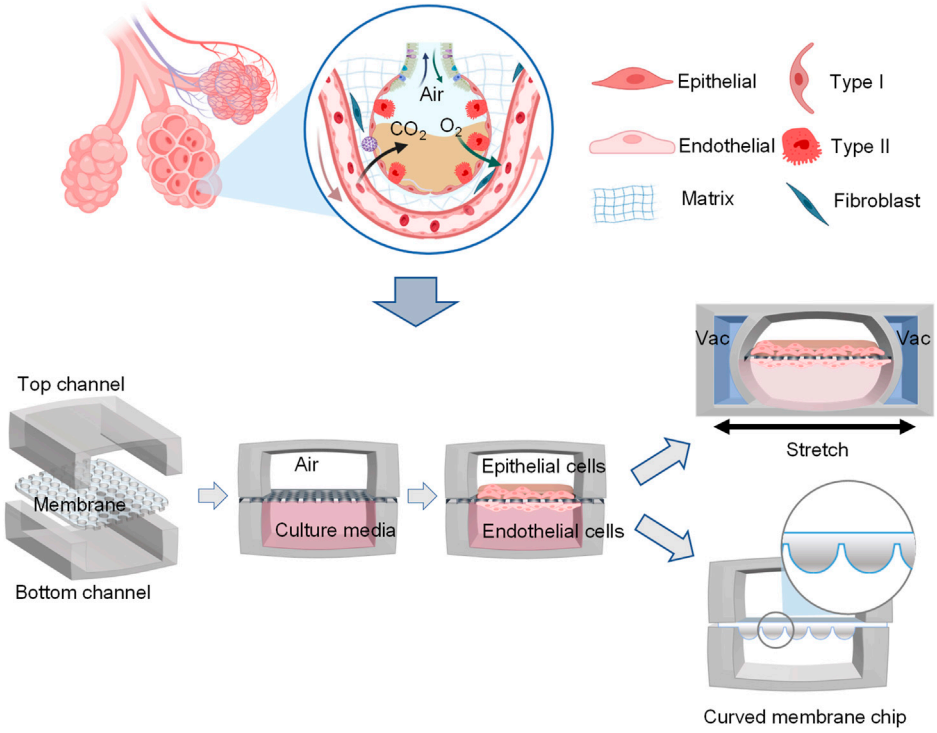

FIGURE 3
Schematic representation of functional lung-on-a-chip based on epithelium-endothelium interface physiology characteristic. During normal inspiration, pressure pulls air into the lungs, resulting in stretching of the alveolar epithelium. For mimicking this phenomenon, pressure-driven stretching by incorporating two larger, lateral microchambers into the device design (Huh et al., 2010). Also, microscale curved surfaces affect the spatiotemporal organization and behaviors of cells. The membrane was given the shape of hexagonally arrayed hemispherical microwells into the device design (Baptista et al., 2022).

consisting of the upper human alveolar epithelium channel, lower microvascular endothelium, and circulating immune cells channel. They found a higher susceptibility to SARS-CoV-2 infection in the epithelium than in endothelium upon SARS-CoV-2 infection. Furthermore, they used RNA-seq analysis of immune responses to SARS-CoV-2 infection in this alveolus chip, and the results suggested the crucial role of immune cells involved in alveolar barrier injury and exacerbated inflammation. These results might explain the pathogenesis of the lung microvascular thrombosis and endotheliitis that existed in severe cases of SARS-CoV-2 infection.

With the advances in microfabrication technology, microfluidics, and tissue engineering (Jin et al., 2021), new approaches to the development of lung-on-a-chip models enable the production of more robust and high-throughput human *in vitro* respiratory tract models. The organoplate is an organ-on-a-chip platform comprising 96 microchambers that can be used for 3D cell culture (Trietsch et al., 2013). These microchambers are incorporated into a standard 384-well microtiter plate that is pipette-operatable and fully compatible with industrial readout and liquid handling equipment. Each microchamber consists of adjacent microchannels separated by phase-guides and four wells are linked together by microfluidic channels (Junaid and Hankemeier, 2021). van Duinen et al. (2017) used such organoplate to assess the vascular barrier function of 96 perfusable blood vessels which have a size-selective permeability with data from *in vivo* studies, and found that cytokines such VEGF and TNFα have dose-dependent effects on the vascular permeability.

In short, these studies show that lung-on-a-chip contributes to the exploration of the intricate cross-talk between vascular networks and alveolar epithelial cells.

3.5 3D bioprinting to mimic pulmonary interstitium

Although organoid and lung-on-a-chip models are suitable for mimicking the 3D structure and function of alveoli and airway as well as the interaction of alveoli and capillary networks, they cannot mimic the heterogenic pulmonary interstitium structures with complex components (consisting of collagen, elastin, fibronectin, glycoproteins, proteoglycans,

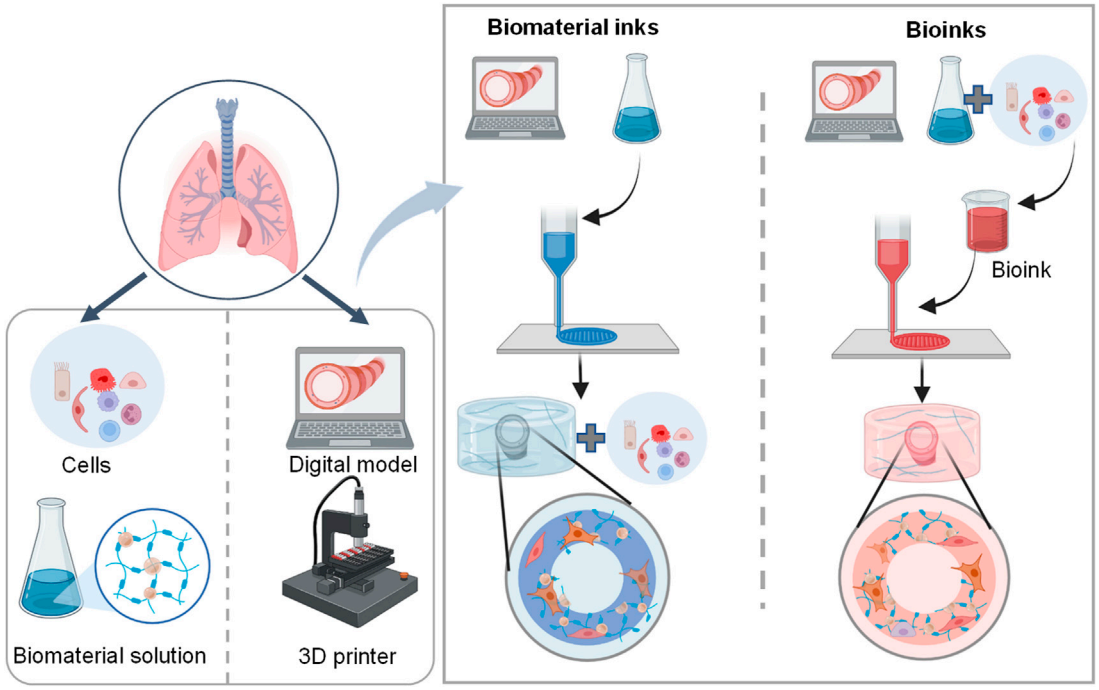

FIGURE 4
Schematic representation of the 3D lung bioprinting process. The general process of 3D bioprinting contains three steps: acquisition of a 3D CAD model, automated deposition of biomaterials (referred to biomaterial inks) or the mixture of cells and biomaterials (referred to bioinks), and maturation of cell-laden constructs to mimic desired tissue constructs (Barreiro Carpio et al., 2021).

60 different kinds of cells) and certain arrangement (airways tree, alveoli network, and the vascular tree), which play an important role in controlling and guiding cellular behaviors to ultimately define tissue architecture (Suki et al., 2011; Barreiro Carpio et al., 2021; Novak et al., 2021).

3D bioprinting, an emerging novel 3D cell culture tool, deposits layer-by-layer cells and biomaterials in an organized and automatized manner (Zhang et al., 2017). Due to the capability of delivering cells and biomaterials with precise control over spatial distributions, it is possible to rapidly recreate engineered constructs with accurate architecture and composition of targeting tissues such as lungs, which are suitable for drug testing and virus infection (Malda et al., 2013; Murphy and Atala, 2014; Matai et al., 2020).

The general process of 3D bioprinting contains three steps: acquisition of a 3D computer-aided design (CAD) model, automated deposition of biomaterials (referred to biomaterial inks) or the mixture of cells and biomaterials (referred to bioinks), and maturation of cell-laden constructs to reinforce the development of desired tissue constructs (Figure 4) (Mironov et al., 2003; Mironov et al., 2008; Zhang et al., 2017; Barreiro Carpio et al., 2021). There are different 3D printing strategies including extrusion-based bioprinting, inkjet/drop-on-demand, laser-assisted, stereolithography, and electronspinning-based bioprinting (Table 4). The most commonly used bioprinting is the extrusion-based technique, due to its ease of handling and low cost. The success of 3D bioprinting chiefly depends on the ability to formulate complex, cell-laden 3D structures. To date, there is no single bioprinting technique that enables the production of all scales and complexities of synthetic tissues and organs (Matai et al., 2020).

To get high mm-sized high-precision scaffolds, Erben and co-workers (Erben et al., 2020) adopted two-photon stereolithography to print 3D cell scaffolds with varying Young's moduli ranging from 7–300 kPa. The dynamics of colonizing primary human lung fibroblast cells are observed by modifying scaffold geometry. Also, Jing et al. (2021) successfully fabricated fibrous scaffolds *via* electrohydrodynamic printing. Based on drop-on-demand inkjet-printing, high-resolution deposition of alveolar cells enables to fabricate a three-layered alveolar barrier model with an unprecedented thickness of ≈10 μm, which better recapitulates the structure, morphologies, and functions of the lung tissue and could reproduce practical tissue-level responses to influenza infection (Kang et al., 2021).

Nowadays, more than 100 types of biomaterials are currently being used as bioinks for 3D bioprinting. The most important features of bioinks are bioactivity, biocompatibility, biodegradability, and mechanical properties which provide mechanical strength, physical

TABLE 4 List of some 3D bioprinting examples of different printing strategies.

Printing strategy	Cells/Bioink	Results	Application	Refs
Inkjet bioprinting	A549, EA.hy926 cells/Matrigel	Print the biofabrication of the human air-blood tissue barrier analogue composed of an endothelial cell, basement membrane and epithelial cell layer	An advanced 3D lung model for high-throughput screening for safety assessment and drug efficacy testing	Horvath et al. (2015)
Drop-on-demand	Human lung epithelial cells, human endothelial cells, and human lung fibroblasts/2.5% PVP	Cultured over a period of 14 days with high survivability rates	Fabricate 3D *in-vitro* alveolar lung models in an automated manner with high repeatability and reliability for studying respiratory diseases caused by infectious pathogens	Ng et al. (2021)
Two-photon stereolithography	phLFs/protein-based resins, such as bovine serum albumin or gelatin methacryloyl	Print up to mm-sized high-precision 3D cell scaffolds at micrometer with varying Young's moduli ranging from 7–300 kPa	Allow for a systematic investigation ofsingle-cell and tissue dynamics in response to defined mechanical and bio-molecular cues	Erben et al. (2020)
Electrohydrodynamic printing	Mouse embryonic fibroblast cells and human non-small cell lung cancer cells/PCL/gliadin inks	The microstructure and the surface nanotopography of the printed scaffolds could be precisely controlled and turned	Provide the potential of cancer cell-seeded scaffolds as 3D *in vitro* tumor models for cancer research and drug screening	Jing et al. (2021)
Laser-assisted bioprinting	AR42J-B-13 rat acinar cell line/ GELMA	Generate 3D pancreatic cell spheroid arrays	Provide a platform for the study of the internal and external factors that contribute to the formation of precursor PDAC lesions and to cancer progression	Hakobyan et al. (2020)

Abbreviations: A549, human alveolar epithelial type II cell line; EA.hy926, endothelial cells; PVP, polyvinylpyrrolidone; phLFs, primary human lung fibroblasts; PCL, poly-ε-caprolactone; GELMA, methacrylated gelatin; PDAC, pancreatic ductal adenocarcinoma.

stability, and biological features (Petersen et al., 2010; O'Brien, 2011; Nichols et al., 2014). Therefore, these bioinks are composed of many types of biocompatible materials from either natural or synthetic materials. Hydrogels such as collagen and GelMA are the most common scaffold to encapsulate cells since they are akin to the native ECM to enable cell differentiation and proper function (Zhao Z. et al., 2020). Studies suggested that some patients with severe COVID-19 develop fibrotic lung disease, an interstitial lung disease characterized by the excessive deposition of ECM proteins in the lung (Bharat et al., 2020; Tale et al., 2020). When the virus binds to the ECM components, it may significantly affect cellular responses to assist its infection in the host (de Melo et al., 2021). A good selection of bioink is of great significance for cell growth and the establishment of disease models. For example, Falcones et al. (2021) successfully designed a new bioink with tunable stiffness based on decellularized porcine lung ECM hydrogels for 3D culturing of lung-resident MSCs. This bioink doesn't need additional chemical or physical crosslinking and improves preconditioning MSCs for therapeutic purposes.

These elements provide a basis for mimicking the heterogenic pulmonary interstitium structures. Horvath et al. (2015) reported the 3D bioprinting of an alveolar barrier by using a micro-extrusion bioprinter. The biofabricated structure was morphologically similar to the native tissue, being highly organized in a thin layer. On the other hand, cells manually mixed to Matrigel formed multi-layered clusters with tick ECM between the epithelial and endothelial cells, which can affect the permeability of biomolecules. Using 3D bioprinting *via* photopolymerizable hydrogels, Grigoryan et al. (2019) successfully designed the most complex alveolar models, which contain elaborate entangled vascular networks from space-filling mathematical topologies and can be used to explore the oxygenation and flow of human red blood cells during tidal ventilation and distension of a proximate airway.

To study the mechanisms of SARS-CoV-2 infection in the lung, the alveolar tissue can be mimicked using a 3D bioprinting model with high repeatability and reliability. Ng et al. (2021) reported the fabrication of human triple-layered alveolar lung models using the drop-on-demand 3D bioprinting. These 3D bioprinted human triple-layered alveolar lung models consisted of human lung epithelial cells, human endothelial cells, and human lung fibroblasts and showed high survivability rates over a long-term period of at least 14 days. This would help to address the demand for highly repeatable and scalable fabrication of 3D *in-vitro* alveolar lung models for studying global respiratory diseases caused by infectious pathogens. Also, in order to clarify virus detection and characterization, Koban et al. (2020) designed easy-to-handle 3D bioprinting platforms based on Wellbrick matrix containing gelatin and collagen additives. This will provide a promising way for the characterization of virus infections due to sensitive monitoring virus-host interactions and replication of different viruses under physiologically relevant conditions.

4 Application of 3D cell culture models in study of COVID-19 treatments

3D cell culture models can provide robust support to simulate SARS-CoV-2 infection, replication, and related immuno-inflammatory responses in humans, which is crucial to understanding the virus's biology and developing antiviral drugs. For example, in addition to investigating viral effects on human pulmonary tissue, lung organoids are very helpful for high-throughput assays to screen therapeutic drugs, such as RNA-seq analyses, proteomics, phosphoproteomics, transcriptomics, and molecular docking analysis (Elbadawi and Efferth, 2020; Hekman et al., 2020). Moreover, organoids derived from patient lung tissue may lead to a promising resource of potentially effective drugs for treating and managing the disease (Xu et al., 2021). This process from the organoid establishment to drug testing is concise so that the organoid models will be a valuable platform for screening patient-specific drugs (Zhou et al., 2018; Sachs et al., 2019). Apart from organoid, a spheroid culture system for human alveolus was established and this platform has been used for accurate pre-clinical testing of candidate drugs for the treatment of COVID-19 (Ebisudani et al., 2021).

ACE2 is the canonical entry receptor used by SARS-CoV-2 yet is expressed in only a small fraction of airway epithelial cells, predominantly AT2 (Zhao B. et al., 2020). For example, by using hESC-derived cardiac and lung organoids, 1,443 FDA-approved drugs were used to search for modulators of ACE2 levels and identified that inhibitors of 5 alpha reductases, which inhibit androgen signaling, can reduce ACE2 levels in the target cells and thereby decrease SARS-CoV-2 infectivity (Samuel et al., 2020).

However, ACE2 alone cannot explain the multi-organ tropism of SARS-CoV-2, and some analyses of patients with COVID-19 revealed many virus-positive cells without ACE2 expression (Chua et al., 2020; Hikmet et al., 2020; Ren et al., 2021). This evidence indicates other receptors involved in SARS-CoV-2 host interactions. By using lung organoids that provide more physiological conditions, KREMEN1/ASGR1 and Tetraspanin 8 (TSPAN8) were identified as alternative functional receptors of SARS-CoV-2 (Hysenaj et al., 2021; Gu et al., 2022). Adult human stem cell-derived alveolosphere has been developed to provide long-term expansion and differentiation of human alveolar type 2 cells/pneumocytes, which express ACE2 and TMPRSS2. These organoids respond to SARS-CoV-2 infection with upregulation of IFN and downregulation of surfactant, and low-dose IFN blocks SARS-CoV-2 replication, which mimics the features of COVID-19 lungs (Katsura et al., 2020). These newly discovered host receptors play essential roles in ACE2-independent virus entry and potential therapeutic targets for COVID-19.

COVID-19 patients who are hospitalized frequently manifest lymphopenia, which suggests suppression of cellular immune responses (Zhang J. J. et al., 2020; Wang D. et al., 2020). 3D models mimicking the lung structure and function have great advantages to investigate airway immune responses to viral infection. For example, Nelli et al. (2016) developed an ALI culture system that closely mimics the natural airway epithelium to characterize the innate immune response of feline herpesvirus-1 (FHV-1). In addition, Purwada et al. (2015) described a B cell follicle organoid to control the rate of immune reaction through tunable design parameters. The next major development may be organoids of the thymus and lymph node because the thymus and bone marrow are the central immune organs for development, differentiation, and maturation of human immune cells.

COVID-19 patients in severe cases may also develop complications such as hypercoagulopathy, systemic endotheliitis, and even multi-organ failure, which are concomitant with a sustained release of inflammatory factors caused by an excessive inflammatory response. Such phenomenon of elevated levels of inflammatory factors has been detected in organoid models following SARS-CoV-2 infection (Mills et al., 2021; Pei et al., 2021). SARS-CoV-2 is also likely to enter vascular endothelial cells through infected airway epithelial cells, which may lead to endothelial dysfunction (Harrison et al., 2020). More recently, Hashimoto et al. (2022) used a lung-on-a-chip model consisting of two microchannels to mimic the interactions between epithelial, endothelial, and immune cells, and they demonstrated in this model that Claudin-5 is a key factor in disrupting vascular endothelial cadherin-mediated adherent junctions.

In clinical trials different strategies have been adopted to deal with an excessive inflammatory response. They either boost the early type I or III interferon responses in order to help patient get rid of the virus before it causes hyper-inflammation, or suppress immune response by inhibiting specific pro-inflammatory pathways such as IL-6. However, it is still in question how to balance the immune status so that the viral replication can be effectively suppressed without cytokine storm to cause organ failure. Correct use of 3D models may help better understand this question and thus accelerate optimization of the immune therapeutic approach for SARS-CoV-2 infection.

Furthermore, 3D lung models serve as a powerful platform for drug screening and safety assays against SARS-CoV-2, targeting host cells factors (ACE2, TMPRSS2, ACAT and HIF1α) and the virus itself (Tiwari et al., 2021; Kastenhuber et al., 2022). By combining iPSCs-derived lung organoids and high-throughput screening techniques from United States Food and Drug Administration (FDA)-approved drugs, GW6471 has been identified to block SARS-CoV-2 infection (Duan et al., 2021) and imatinib, mycophenolic acid (MPA), and quinacrine dihydrochloride (QNHC) have been identified to block SARS-CoV-2 entry (Han et al., 2021). Combining iPSCs-derived lung organoids with differentiated AT2 cells and a connectivity mapping approach, atorvastatin was predicted to be the most

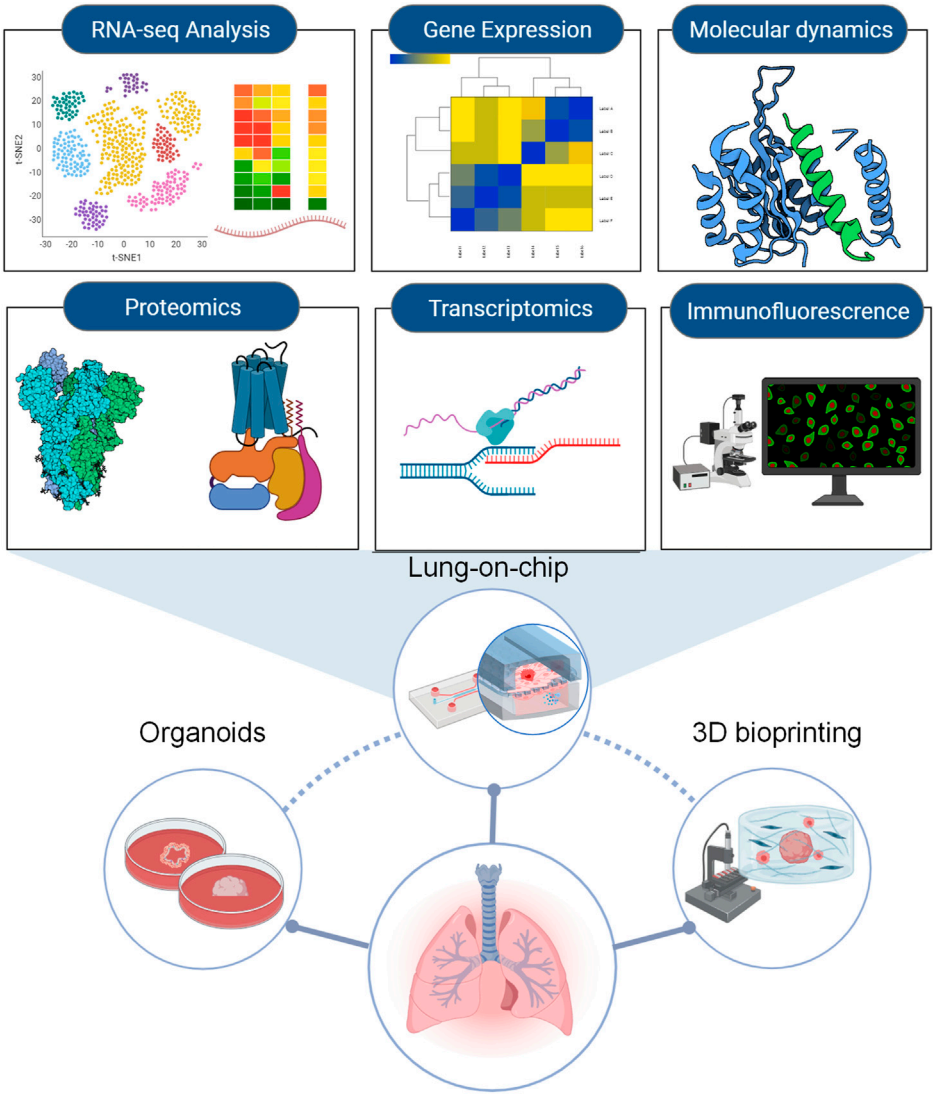

FIGURE 5
An overview of assays for screening agents to combat SARS-CoV-2 with 3D models.

promising candidate from 20,000 small compounds for blocking SARS-CoV-2 (Duarte et al., 2021).

Remdesivir has been recently recognized as a promising antiviral drug against many RNA viruses (e.g., SARS, MERS-CoV), including SARS-CoV-2 (Wang M. et al., 2020). By using an air-liquid interface model, remdesivir has been reported to decrease the colony-forming efficiency (CFE) of club cells, but promote the growth of club organoids (Wang J. et al., 2020). Also, by using an alveolar chip, remdesivir has been proven to inhibit viral replication and alleviate the disruption of the alveolar-capillary barrier (Zhang M. et al., 2020).

A systematic example of 3D cell culture models with some fast-track approaches used in screening drugs against COVID-19 is listed in Figure 5. A summary of the aforementioned drugs suitable for COVID-19 treatment can be seen in Table 5.

5 Future direction and perspectives

Since the complexity of SARS-CoV-2 infection and the pathogenesis of COVID-19 and the timeliness for high-throughput of drug screening for therapeutic treatment, the use of 3D cell culture toolsets provides increasing similarity to the *in vivo* pathophysiology and may give us valuable insights and more reliable tools for drug development and testing in the treatments of COVID-19 (Ravi et al., 2015).

TABLE 5 Drugs against SARS-CoV-2 discovered/tested by human lung organoids.

Names	Combined with screening/Sources of drugs	Objective targets	Mechanism	Concentration	Cells for construct organoids	Refs
Antiandrogenic drugs	A Selleckchem small molecule library	ACE2	Reduce ACE2 expression	1 μM, 2 μM or 5 μM	hESCs	Samuel et al. (2020)
25HC	A natural product	ACAT	Block membrane fusion	5 μM	iPSCs	Wang et al. (2020e)
GW6471	Agonists and antagonists and FDA-approved drugs	HIF1α	Inhibit the HIF1a-glycolysis axis	EC50 = 2.1 μM	hESCs	Duan et al. (2021)
Atorvastatin	A connectivity mapping approach in combination with chemoinformatic analyses		Bind to SARS-CoV-2's main protease and RNA-dependent RNA polymerase	IC50 values of 31.65 μM	hESCs	Duarte et al. (2021)
K-874A	VHH-cDNA display	SARS-CoV-2 S1 proteins	Block the virus membrane from fusing with the host cell membrane	IC50 values of 5.74 ± 2.6 μg/ml	Normal lung tissues	Haga et al. (2021)
Ciclesonide, nelfinavir, and camostat	FDA-approved drugs, bioactives kinase inhibitors, and natural products				iPSCs	Ko et al. (2021)
Lead E24	Medicinal chemistry and rational drug design strategies	SARS-CoV-2 main protease	Bind SARS-CoV-2 M^{pro} and inhibit proteolytic activity	EC50 values of 844 nM	iPSCs	Huff et al. (2022)
DPP4 peptide; Ab15033-7		DPP4 receptor; Spike protein		DPP4 peptide (200 μg) or Ab15033-7 (200 ng/ml)	iPSCs	Spitalieri et al. (2022)

Abbreviations: SARS-CoV-2, Severe Acute Respiratory Syndrome-CoronaVirus-2; ACAT, activating acyl-CoA, cholesterol acyltransferase; DPP4, dipeptidyl peptidase-4; 25HC, 25-hydrocholesterol; BALF, bronchoalveolar lavage fluid; ACE2, angiotensinconverting enzyme 2; FDA, US food and drug administration; HIF1a, hypoxia-inducible factor 1 subunit alpha; iPSCs, induced pluripotent stem cells; AT2s, alveolar epithelial type-2 cells; ESCs, embryonic stem cells.

Recent advances in organoids have enabled the modeling of SARS-CoV-2 infection using human airway epithelial and alveolar cells. These culture models, however, lack airway smooth muscle cells (ASMCs). ASMCs are known to switch between contractile and proliferative phenotypes in response to various physical and chemical cues, which play essential roles in lung development and respiratory diseases (Kim et al., 2015). Therefore, organoids containing ASMCs may better recapitulate the airway structure and function *in vivo*, and if co-cultured with immune cells, could be used to reveal more detailed mechanisms of the COVID-19-associated immunology.

Appropriate culture media should also be developed for efficient generation and maintenance of lung organoids. Such media should contain not only basal medium, but also a variety of growth factors and small-molecules. For example, TGF-β has an anti-inflammatory effect on cell response induced by influenza H1N1 virus (BustosRivera-Bahena et al., 2021). TGF-β also inhibits cell proliferation and promotes apoptosis and differentiation. So far, effect of TGF-β in the culture medium on efficiency of organoid formation has been evaluated (Shi and Massague, 2003), and evaluation may be required of other signaling pathways such as Wnt/β regarding their effects on organoid culture medium.

Lung-on-a-chip is always restricted to mimic the alveolar-capillary barrier and cannot be used to resemble the airway tubular structure. In addition, lung-on-a-chip is typically limited by the number of cells as compared to that *in vivo*, which may lead to altered cellular function such as the metabolic rate. Such issues need to be addressed in the development of next-generation lung-on-a-chip systems.

3D bioprinting airway or alveoli is always expensive, which leads that it is almost impossible to set up high-throughput approaches for drug screening using these 3D cell culture models. In addition, despite the extensive use of 3D cell culture models in basic research, their translational biomedical application is restricted since the lack of robust, reproducible, and scalable methods of production in compliance with current pharmaceutical standards. The reproducibility, accuracy, and scalability of the methodologies proposed still need to be improved (Vives and Batlle-Morera, 2020). Therefore, easy-to-use, rapid, and low-cost strategies in the fabrication of 3D cell culture models

with more complex cytoarchitecture and a more physiological microenvironment still need to develop.

Despite of their potential, 3D models still entail considerable technical problems that may compromise their application, which include but are not limited to sample collection, high-quality imaging, and cost of substrate materials such as Matrigel. For example, it is technically challenging to directly collect samples from Matrigel-based 3D models such as organoids or 3D bioprinting because direct sample collection would disrupt the integrity of Matrigel and thus the structure of the 3D model, leading to inaccurate results. It is also difficult to obtain high-quality imaging of these 3D cultures by using traditional imaging techniques such as paraffin embedding and tissue slicing (Rios and Clevers, 2018). Although non-invasive microscopy methods such as multi-photon and light-sheet microscopy can be used to visualize cellular details of 3D cultures, the thick sample can cause light scattering because of mismatched refractive indices. To reduce scattering within the sample, various optical clearing methods have been developed. For example, Dekkers et al. (2019) successfully designed a simple optical clearing method utilizing a homemade fructose-glycerol clearing agent to improve the light penetration through fixed organoids, whereas Boothe et al. (2017) used another agent named Iodixanol for the same purpose.

3D models commonly use Matrigel (Corning) or Cultrex BME (Trevigen) as substrate materials. These materials are too expensive to be used in large-scale studies such as high-throughput screening, regenerative medicine and diagnostics (Curvello et al., 2020). This high cost may be reduced by replacing Matrigel/Cultrex BME with an alternative in the 3D models. For example, gels made of decellularized porcine small intestine mucosa/submucosa were used to generate human gastric organoids (Giobbe et al., 2019). Recently, a novel engineered plant-based nanocellulose hydrogel was developed to provide the required microenvironment for small intestinal organoid growth and budding (Curvello et al., 2020).

Materials properties and fluid dynamics are also important issues to consider in developing 3D cultures. For example, Matrigel needs to be mixed with agarose to achieve proper mechanical properties for long time maintenance of a tubular organoid structure (Güney et al., 2021). In order to provide the low shear environment suitable for iPSCs differentiation, organoids can be cultured in spinner flasks, which can be further combined with microfluidic design to achieve both chemical and mechanical stimulation in tunable fashions.

Last but not least, each of the 3D models has its own advantages and disadvantages, and it may be feasible to combine some of these models as a novel platform with enhanced functionality. For example, although lung organoids always automatedly generate target tissue structure and function, they lack typical epithelium-endothelium tissue interfaces *in vivo* and are time-consuming to fabricate. On the other hand, the advantage of 3D bioprinting is the possibility to precisely define the composition and arrangement of a culture which can be realized rapidly. Combining the organoid and 3D bioprinting techniques may establish a new cell culture model to reflect the near-physiological cross-talk among airway and vascular vessels after SARS-CoV-2 infection. Advances in bioink preparation including the incorporation of bioactive matrices, and induced pluripotent stem cells, and suitable induction factors may open up broad applications for 3D cell culture models in disease diagnostics, and regenerative medicine.

6 Conclusion

The COVID-19 pandemic has resulted in global health and economic burden, but the underlying pathogenesis and therapeutic treatments remain to be further explored. Novel 3D cell culture models representing the lung structure and function in a dish that is in good agreement with reports from animal models and clinical disease are undoubtedly a valuable toolset for these studies, which may provide a promising alternative for animal models and 2D cell culture models. This review of the strategies to fabricate useful 3D pulmonary cell culture models including organoids, lab-on-a-chip, and bioprinting, although by no means comprehensive, indeed provide new insights for understanding how SARS-CoV-2 infects human lung cells, which is essential for elaborating the virus-induced human responses and helping further development of novel therapeutics and prophylactics for COVID-19.

Author contributions

ML and LD conceived and designed the study. KN and BC wrote the manuscript. CY, YQ, RG, CW collected some data for this manuscript. ML and LD edited and revised the manuscript. All authors read and approved the final version of the manuscript.

Funding

This work was supported by NSF of China (Nos.12072048, 12272063, and 31670950), the Key Program of NSF of China (No.11532003), the science and technology innovation leading plan of high tech industry in Hunan Province (2020SK2018), and the International Science and Technology Cooperation Project of Changzhou (CZ20180017).

Conflict of interest

The authors declare that the research was conducted in the absence of any commercial or financial relationships that could be construed as a potential conflict of interest.

Publisher's note

References

Ackermann, M., Verleden, S. E., Kuehnel, M., Haverich, A., Welte, T., Laenger, F., et al. (2020). Pulmonary vascular endothelialitis, thrombosis, and angiogenesis in covid-19. *N. Engl. J. Med.* 383 (2), 120–128. doi:10.1056/NEJMoa2015432

Baker, B. M., and Chen, C. S. (2012). Deconstructing the third dimension: How 3D culture microenvironments alter cellular cues. *J. Cell Sci.* 125, 3015–3024. doi:10.1242/jcs.079509

Baptista, D., Moreira Teixeira, L., Barata, D., Tahmasebi Birgani, Z., King, J., van Riet, S., et al. (2022). 3D lung-on-chip model based on biomimetically microcurved culture membranes. *ACS Biomater. Sci. Eng.* 8 (6), 2684–2699. doi:10.1021/acsbiomaterials.1c01463

Barkauskas, C. E., Chung, M. I., Fioret, B., Gao, X., Katsura, H., and Hogan, B. L. (2017). Lung organoids: Current uses and future promise. *Development* 144 (6), 986–997. doi:10.1242/dev.140103

Barreiro Carpio, M., Dabaghi, M., Ungureanu, J., Kolb, M. R., Hirota, J. A., and Moran-Mirabal, J. M. (2021). 3D bioprinting strategies, challenges, and opportunities to model the lung tissue microenvironment and its function. *Front. Bioeng. Biotechnol.* 9, 773511. doi:10.3389/fbioe.2021.773511

Benam, K. H., Villenave, R., Lucchesi, C., Varone, A., Hubeau, C., Lee, H.-H., et al. (2016). Small airway-on-a-chip enables analysis of human lung inflammation and drug responses *in vitro*. *Nat. Methods* 13 (2), 151–157. doi:10.1038/nmeth.3697

Bernard, I., Limonta, D., Mahal, L. K., and Hobman, T. C. (2020). Endothelium infection and dysregulation by SARS-CoV-2: Evidence and caveats in COVID-19. *Viruses* 13 (1), 29. doi:10.3390/v13010029

Bestle, D., Heindl, M. R., Limburg, H., Van Lam van, T., Pilgram, O., Moulton, H., et al. (2020). TMPRSS2 and furin are both essential for proteolytic activation of SARS-CoV-2 in human airway cells. *Life Sci. Alliance* 3 (9), e202000786. doi:10.26508/lsa.202000786

Bharat, A., Querrey, M., Markov, N. S., Kim, S., Kurihara, C., Garza-Castillon, R., et al. (2020). Lung transplantation for patients with severe COVID-19. *Sci. Transl. Med.* 12 (574), eabe4282. doi:10.1126/scitranslmed.abe4282

Bilodeau, C., Shojaie, S., Goltsis, O., Wang, J., Luo, D., Ackerley, C., et al. (2021). TP63 basal cells are indispensable during endoderm differentiation into proximal airway cells on acellular lung scaffolds. *NPJ Regen. Med.* 6 (1), 12. doi:10.1038/s41536-021-00124-4

Bircsak, K. M., DeBiasio, R., Miedel, M., Alsebahi, A., Reddinger, R., Saleh, A., et al. (2021). A 3D microfluidic liver model for high throughput compound toxicity screening in the OrganoPlate®. *Toxicology* 450, 1879–3185. doi:10.1016/j.tox.2020.152667

Birukov, K. G., Jacobson, J. R., Flores, A. A., Ye, S. Q., Birukova, A. A., Verin, A. D., et al. (2003). Magnitude-dependent regulation of pulmonary endothelial cell barrier function by cyclic stretch. *Am. J. Physiol. Lung Cell. Mol. Physiol.* 285 (4), L785–L797. doi:10.1152/ajplung.00336.2002

Blanco-Melo, D., Nilsson-Payant, B. E., Liu, W. C., Uhl, S., Hoagland, D., Møller, R., et al. (2020). Imbalanced host response to SARS-CoV-2 drives development of COVID-19. *Cell* 181 (5), 1036–1045. doi:10.1016/j.cell.2020.04.026

Boothe, T., Hilbert, L., Heide, M., Berninger, L., Huttner, W. B., Zaburdaev, V., et al. (2017). A tunable refractive index matching medium for live imaging cells, tissues and model organisms. *Elife* 6, e27240. doi:10.7554/eLife.27240

Borczuk, A. C., Salvatore, S. P., Seshan, S. V., Patel, S. S., Bussel, J. B., Mostyka, M., et al. (2020). COVID-19 pulmonary pathology: A multi-institutional autopsy cohort from Italy and New York city. *Mod. Pathol.* 33 (11), 2156–2168. doi:10.1038/s41379-020-00661-1

Bugge, T. H., Antalis, T. M., and Wu, Q. (2009). Type II transmembrane serine proteases. *J. Biol. Chem.* 284 (35), 23177–23181. doi:10.1074/jbc.R109.021006

BustosRivera-Bahena, G., Lopez-Guerrero, D. V., Marquez-Bandala, A. H., Esquivel-Guadarrama, F. R., and Montiel-Hernandez, J. L. (2021). TGF-β1 signaling inhibit the *in vitro* apoptotic, infection and stimulatory cell response induced by influenza H1N1 virus infection on A549 cells. *Virus Res.* 297, 198337. doi:10.1016/j.virusres.2021.198337

Callens, S. J. P., Uyttendaele, R. J. C., Fratila-Apachitei, L. E., and Zadpoor, A. A. (2020). Substrate curvature as a cue to guide spatiotemporal cell and tissue organization. *Biomaterials* 232, 119739. doi:10.1016/j.biomaterials.2019.119739

Cantuti-Castelvetri, L., Ojha, R., Pedro, L. D., Djannatian, M., Franz, J., Kuivanen, S., et al. (2020). Neuropilin-1 facilitates SARS-CoV-2 cell entry and infectivity. *Science* 370 (6518), 856–860. doi:10.1126/science.abd2985

Castelli, V., Cimini, A., and Ferri, C. (2020). Cytokine storm in COVID-19: "When you come out of the storm, you won't Be the same person who walked in. *Front. Immunol.* 11, 2132. doi:10.3389/fimmu.2020.02132

Castiello, T., Georgiopoulos, G., Finocchiaro, G., Claudia, M., Gianatti, A., Delialis, D., et al. (2022). COVID-19 and myocarditis: A systematic review and overview of current challenges. *Heart fail. Rev.* 27 (1), 251–261. doi:10.1007/s10741-021-10087-9

Chen, N., Zhou, M., Dong, X., Qu, J., Gong, F., Han, Y., et al. (2020). Epidemiological and clinical characteristics of 99 cases of 2019 novel coronavirus pneumonia in wuhan, China: A descriptive study. *Lancet* 395 (10223), 507–513. doi:10.1016/S0140-6736(20)30211-7

Chen, Q., Langenbach, S., Li, M., Xia, Y. C., Gao, X., Gartner, M. J., et al. (2022). ACE2 expression in organotypic human airway epithelial cultures and airway biopsies. *Front. Pharmacol.* 13, 813087. doi:10.3389/fphar.2022.813087

Chua, R. L., Lukassen, S., Trump, S., Hennig, B. P., Wendisch, D., Pott, F., et al. (2020). COVID-19 severity correlates with airway epithelium-immune cell interactions identified by single-cell analysis. *Nat. Biotechnol.* 38 (8), 970–979. doi:10.1038/s41587-020-0602-4

Corbett, K. S., Flynn, B., Foulds, K. E., Francica, J. R., Boyoglu-Barnum, S., Werner, A. P., et al. (2020). Evaluation of the mRNA-1273 vaccine against SARS-CoV-2 in nonhuman primates. *N. Engl. J. Med.* 383 (16), 1544–1555. doi:10.1056/NEJMoa2024671

Cox, R. M., Wolf, J. D., and Plemper, R. K. (2021). Therapeutically administered ribonucleoside analogue MK-4482/EIDD-2801 blocks SARS-CoV-2 transmission in ferrets. *Nat. Microbiol.* 6 (1), 11–18. doi:10.1038/s41564-020-00835-2

Curvello, R., Kerr, G., Micati, D. J., Chan, W. H., Raghuwanshi, V. S., Rosenbluh, J., et al. (2020). Engineered plant-based nanocellulose hydrogel for small intestinal organoid growth. *Adv. Sci.* 8 (1), 2002135. doi:10.1002/advs.202002135

Daly, J. L., Simonetti, B., Klein, K., Chen, K. E., Williamson, M. K., Antón-Plágaro, C., et al. (2020). Neuropilin-1 is a host factor for SARS-CoV-2 infection. *Science* 370 (6518), 861–865. doi:10.1126/science.abd3072

de Melo, B. A. G., Benincasa, J. C., Cruz, E. M., Maricato, J. T., and Porcionatto, M. A. (2021). 3D culture models to study SARS-CoV-2 infectivity and antiviral candidates: From spheroids to bioprinting. *Biomed. J.* 44 (1), 31–42. doi:10.1016/j.bj.2020.11.009

de Oliveira, M., De Sibio, M. T., Costa, F. A. S., and Sakalem, M. E. (2021). Airway and alveoli organoids as valuable research tools in COVID-19. *ACS Biomater. Sci. Eng.* 7 (8), 3487–3502. doi:10.1021/acsbiomaterials.1c00306

Dekkers, J. F., Alieva, M., Wellens, L. M., Ariese, H. C. R., Jamieson, P. R., Vonk, A. M., et al. (2019). High-resolution 3D imaging of fixed and cleared organoids. *Nat. Protoc.* 14 (6), 1756–1771. doi:10.1038/s41596-019-0160-8

Diem, K., Fauler, M., Fois, G., Hellmann, A., Winokurow, N., Schumacher, S., et al. (2020). Mechanical stretch activates piezo1 in caveolae of alveolar type I cells to trigger ATP release and paracrine stimulation of surfactant secretion from alveolar type II cells. *FASEB J.* 34 (9), 12785–12804. doi:10.1096/fj.202000613RRR

Dinnon, K. H., 3rd, Leist, S. R., Schäfer, A., Edwards, C. E., Martinez, D. R., Montgomery, S. A., et al. (2020). A mouse-adapted model of SARS-CoV-2 to test COVID-19 countermeasures. *Nature* 586 (7830), 560–566. doi:10.1038/s41586-020-2708-8

Duan, X., Tang, X., Nair, M. S., Zhang, T., Qiu, Y., Zhang, W., et al. (2021). An airway organoid-based screen identifies a role for the HIF1α-glycolysis axis in SARS-CoV-2 infection. *Cell Rep.* 37 (6), 109920. doi:10.1016/j.celrep.2021.109920

Duarte, R. R. R., Copertino, D. C., Jr., Iñiguez, L. P., Marston, J. L., Bram, Y., Han, Y., et al. (2021). Identifying FDA-approved drugs with multimodal properties against COVID-19 using a data-driven approach and a lung organoid model of SARS-CoV-2 entry. *Mol. Med.* 27 (1), 105. doi:10.1186/s10020-021-00356-6

Duval, K., Grover, H., Han, L. H., Mou, Y., Pegoraro, A. F., Fredberg, J., et al. (2017). Modeling physiological events in 2D vs. 3D cell culture. *Physiol. (Bethesda)* 32 (4), 266–277. doi:10.1152/physiol.00036.2016

Dye, B. R., Hill, D. R., Ferguson, M. A., Tsai, Y. H., Nagy, M. S., Dyal, R., et al. (2015). *In vitro* generation of human pluripotent stem cell derived lung organoids. *Elife* 4, e05098. doi:10.7554/eLife.05098

Ebisudani, T., Sugimoto, S., Haga, K., Mitsuishi, A., Takai-Todaka, R., Fujii, M., et al. (2021). Direct derivation of human alveolospheres for SARS-CoV-2 infection modeling and drug screening. *Cell Rep.* 35 (10), 109218. doi:10.1016/j.celrep.2021.109218

Elbadawi, M., and Efferth, T. (2020). Organoids of human airways to study infectivity and cytopathy of SARS-CoV-2. *Lancet. Respir. Med.* 8 (7), e55–e56. doi:10.1016/S2213-2600(20)30238-1

Elsdale, T., and Bard, J. (1972). Collagen substrata for studies on cell behavior. *J. Cell Biol.* 54 (3), 626–637. doi:10.1083/jcb.54.3.626

Erben, A., Horning, M., Hartmann, B., Becke, T., Eisler, S. A., Southan, A., et al. (2020). Precision 3D-printed cell scaffolds mimicking native tissue composition and mechanics. *Adv. Healthc. Mat.* 9 (24), e2000918. doi:10.1002/adhm.202000918

Falcones, B., Sanz-Fraile, H., Marhuenda, E., Mendizabal, I., Cabrera-Aguilera, I., Malandain, N., et al. (2021). Bioprintable lung extracellular matrix hydrogel scaffolds for 3D culture of mesenchymal stromal cells. *Polym. (Basel)* 13 (14), 2350. doi:10.3390/polym13142350

Garrett, N., Tapley, A., Andriesen, J., Seocharan, I., Fisher, L. H., Bunts, L., et al. (2022). High rate of asymptomatic carriage associated with variant strain Omicron. medRxiv., 2021.2012.2021.12.20.21268130.2021.12.20.21268130. doi: doi:10.1101/2021.12.20.21268130

Ghajar, C. M., Chen, X., Harris, J. W., Suresh, V., Hughes, C. C., Jeon, N. L., et al. (2008). The effect of matrix density on the regulation of 3-D capillary morphogenesis. *Biophys. J.* 94 (5), 1930–1941. doi:10.1529/biophysj.107.120774

Ghio, A. J., Dailey, L. A., Soukup, J. M., Stonehuerner, J., Richards, J. H., and Devlin, R. B. (2013). Growth of human bronchial epithelial cells at an air-liquid interface alters the response to particle exposure. *Part. Fibre Toxicol.* 10, 25. doi:10.1186/1743-8977-10-25

Giobbe, G. G., Crowley, C., Luni, C., Campinoti, S., Khedr, M., Kretzschmar, K., et al. (2019). Extracellular matrix hydrogel derived from decellularized tissues enables endodermal organoid culture. *Nat. Commun.* 10 (1), 5658. doi:10.1038/s41467-019-13605-4

Grigoryan, B., Paulsen, S. J., Corbett, D. C., Sazer, D. W., Fortin, C. L., Zaita, A. J., et al. (2019). Multivascular networks and functional intravascular topologies within biocompatible hydrogels. *Science* 364 (6439), 458–464. doi:10.1126/science.aav9750

Gu, Y., Cao, J., Zhang, X., Gao, H., Wang, Y., Wang, J., et al. (2022). Receptome profiling identifies KREMEN1 and ASGR1 as alternative functional receptors of SARS-CoV-2. *Cell Res.* 32 (1), 24–37. doi:10.1038/s41422-021-00595-6

Guan, W. J., Ni, Z. Y., Hu, Y., Liang, W. H., Ou, C. Q., He, J. X., et al. (2020). Clinical characteristics of coronavirus disease 2019 in China. *N. Engl. J. Med.* 382 (18), 1708–1720. doi:10.1056/NEJMoa2002032

Güney, T. G., Herranz, A. M., Mumby, S., Dunlop, I. E., and Adcock, I. M. (2021). Epithelial-stromal cell interactions and extracellular matrix mechanics drive the formation of airway-mimetic tubular morphology in lung organoids. *iScience* 24 (9), 103061. doi:10.1016/j.isci.2021.103061

Haga, K., Takai-Todaka, R., Matsumura, Y., Song, C., Takano, T., Tojo, T., et al. (2021). Nasal delivery of single-domain antibody improves symptoms of SARS-CoV-2 infection in an animal model. *PLoS Pathog.* 17 (10), e1009542. doi:10.1371/journal.ppat.1009542

Hakobyan, D., Medina, C., Dusserre, N., Stachowicz, M. L., Handschin, C., Fricain, J. C., et al. (2020). Laser-assisted 3D bioprinting of exocrine pancreas spheroid models for cancer initiation study. *Biofabrication* 12 (3), 035001. doi:10.1088/1758-5090/ab7cb8

Han, Y., Duan, X., Yang, L., Nilsson-Payant, B. E., Wang, P., Duan, F., et al. (2021). Identification of SARS-CoV-2 inhibitors using lung and colonic organoids. *Nature* 589 (7841), 270–275. doi:10.1038/s41586-020-2901-9

Harrison, A. G., Lin, T., and Wang, P. (2020). Mechanisms of SARS-CoV-2 transmission and pathogenesis. *Trends Immunol.* 41 (12), 1100–1115. doi:10.1016/j.it.2020.10.004

Hashimoto, R., Takahashi, J., Shirakura, K., Funatsu, R., Kosugi, K., Deguchi, S., et al. (2022). SARS-CoV-2 disrupts respiratory vascular barriers by suppressing Claudin-5 expression. *Sci. Adv.* 8 (38), eabo6783. doi:10.1126/sciadv.abo6783

Hekman, R. M., Hume, A. J., Goel, R. K., Abo, K. M., Huang, J., Blum, B. C., et al. (2020). Actionable cytopathogenic host responses of human alveolar type 2 cells to SARS-CoV-2. *Mol. Cell* 80 (6), 1104–1122.e9. doi:10.1016/j.molcel.2020.11.028

Hikmet, F., Mear, L., Edvinsson, A., Micke, P., Uhlen, M., and Lindskog, C. (2020). The protein expression profile of ACE2 in human tissues. *Mol. Syst. Biol.* 16 (7), e9610. doi:10.15252/msb.20209610

Horvath, L., Umehara, Y., Jud, C., Blank, F., Petri-Fink, A., and Rothen-Rutishauser, B. (2015). Engineering an *in vitro* air-blood barrier by 3D bioprinting. *Sci. Rep.* 5, 7974. doi:10.1038/srep07974

Hu, B., Huang, S., and Yin, L. (2021). The cytokine storm and COVID-19. *J. Med. Virol.* 93 (1), 250–256. doi:10.1002/jmv.26232

Huang, C., Wang, Y., Li, X., Ren, L., Zhao, J., Hu, Y., et al. (2020). Clinical features of patients infected with 2019 novel coronavirus in Wuhan, China. *Lancet* 395 (10223), 497–506. doi:10.1016/s0140-6736(20)30183-5

Huang, D., Liu, T., Liao, J., Maharjan, S., Xie, X., Perez, M., et al. (2021). Reversed-engineered human alveolar lung-on-a-chip model. *Proc. Natl. Acad. Sci. U. S. A.* 118 (19), e2016146118. doi:10.1073/pnas.2016146118

Huff, S., Kummetha, I. R., Tiwari, S. K., Huante, M. B., Clark, A. E., Wang, S., et al. (2022). Discovery and mechanism of SARS-CoV-2 main protease inhibitors. *J. Med. Chem.* 65 (4), 2866–2879. doi:10.1021/acs.jmedchem.1c00566

Huh, D., Matthews, B. D., Mammoto, A., Montoya-Zavala, M., Hsin, H. Y., and Ingber, D. E. (2010). Reconstituting organ-level lung functions on a chip. *Science* 328 (5986), 1662–1668. doi:10.1126/science.1188302

Humayun, M., Chow, C. W., and Young, E. W. K. (2018). Microfluidic lung airway-on-a-chip with arrayable suspended gels for studying epithelial and smooth muscle cell interactions. *Lab. Chip* 18 (9), 1298–1309. doi:10.1039/c7lc01357d

Hysenaj, L., Little, S., Kulhanek, K., Gbenedio, O. M., Rodriguez, L., Shen, A., et al. (2021). SARS-CoV-2 infection studies in lung organoids identify TSPAN8 as novel mediator. bioRxiv., 2021.2006.2001.2021.06.01.446640. doi: doi:10.1101/2021.06.01.446640

Jiang, Y., Wu, Q., Song, P., and You, C. (2021). The variation of SARS-CoV-2 and advanced research on current vaccines. *Front. Med.* 8, 806641. doi:10.3389/fmed.2021.806641

Jin, Y., Liu, L., Yu, P., Lin, F., Shi, X., Guo, J., et al. (2021). Emergent differential organization of airway smooth muscle cells on concave and convex tubular surface. *Front. Mol. Biosci.* 8, 717771. doi:10.3389/fmolb.2021.717771

Jing, L., Wang, X., Leng, B., Zhan, N., Liu, H., Wang, S., et al. (2021). Engineered nanotopography on the microfibers of 3D-printed PCL scaffolds to modulate cellular responses and establish an *in vitro* tumor model. *ACS Appl. Bio Mat.* 4 (2), 1381–1394. doi:10.1021/acsabm.0c01243

Johnson, B. A., Xie, X., Bailey, A. L., Kalveram, B., Lokugamage, K. G., Muruato, A., et al. (2021). Loss of furin cleavage site attenuates SARS-CoV-2 pathogenesis. *Nature* 591 (7849), 293–299. doi:10.1038/s41586-021-03237-4

Junaid, A., and Hankemeier, T. (2021). OrganoPlate micro-fluidic microvessel culture and analysis. *Bio. Protoc.* 11 (13), e4070. doi:10.21769/BioProtoc.4070

Jung, F., Kruger-Genge, A., Franke, R. P., Hufert, F., and Kupper, J. H. (2020). COVID-19 and the endothelium. *Clin. Hemorheol. Microcirc.* 75 (1), 7–11. doi:10.3233/CH-209007

Kang, D., Park, J. A., Kim, W., Kim, S., Lee, H. R., Kim, W. J., et al. (2021). All-inkjet-printed 3D alveolar barrier model with physiologically relevant microarchitecture. *Adv. Sci.* 8 (10), 2004990. doi:10.1002/advs.202004990

Kastenhuber, E. R., Mercadante, M., Nilsson-Payant, B., Johnson, J. L., Jaimes, J. A., Muecksch, F., et al. (2022). Coagulation factors directly cleave SARS-CoV-2 spike and enhance viral entry. *Elife* 11, e77444. doi:10.7554/eLife.77444

Katsura, H., Sontake, V., Tata, A., Kobayashi, Y., Edwards, C. E., Heaton, B. E., et al. (2020). Human lung stem cell-based alveolospheres provide insights into SARS-CoV-2-mediated interferon responses and pneumocyte dysfunction. *Cell Stem Cell* 27 (6), 890–904. doi:10.1016/j.stem.2020.10.005

Ke, Z., Oton, J., Qu, K., Cortese, M., Zila, V., McKeane, L., et al. (2020). Structures and distributions of SARS-CoV-2 spike proteins on intact virions. *Nature* 588 (7838), 498–502. doi:10.1038/s41586-020-2665-2

Kim, H. Y., Pang, M. F., Varner, V. D., Kojima, L., Miller, E., Radisky, D. C., et al. (2015). Localized smooth muscle differentiation is essential for epithelial bifurcation during branching morphogenesis of the mammalian lung. *Dev. Cell* 34 (6), 719–726. doi:10.1016/j.devcel.2015.08.012

Kim, J.-H., Kim, J., Kim, W. J., Choi, Y. H., Yang, S.-R., and Hong, S.-H. (2020). Diesel particulate matter 2.5 induces epithelial-to-mesenchymal transition and upregulation of SARS-CoV-2 receptor during human pluripotent stem cell-derived alveolar organoid development. *Int. J. Environ. Res. Public Health* 17 (22), 8410. doi:10.3390/ijerph17228410

Kızılkurtlu, A. A., Polat, T., Aydın, G. B., and Akpek, A. (2018). Lung on a chip for drug screening and design. *Curr. Pharm. Des.* 24 (45), 5386–5396. doi:10.2174/1381612825666190208122204

Knight, A. (2008). Systematic reviews of animal experiments demonstrate poor contributions toward human healthcare. *Rev. Recent Clin. Trials* 3 (2), 89–96. doi:10.2174/157488708784223844

Ko, M., Chang, S. Y., Byun, S. Y., Ianevski, A., Choi, I., Pham, H., et al. (2021). Screening of FDA-approved drugs using a MERS-CoV clinical isolate from South Korea identifies potential therapeutic options for COVID-19. *Viruses* 13 (4), 651. doi:10.3390/v13040651

Koban, R., Lam, T., Schwarz, F., Kloke, L., Bürge, S., Ellerbrok, H., et al. (2020). Simplified bioprinting-based 3D cell culture infection models for virus detection. *Viruses* 12 (11), 1298. doi:10.3390/v12111298

Kolagar, T. A., Farzaneh, M., Nikkar, N., and Khoshnam, S. E. (2020). Human pluripotent stem cells in neurodegenerative diseases: Potentials, advances and limitations. *Curr. Stem Cell Res. Ther.* 15 (2), 102–110. doi:10.2174/1574888x14666190823142911

Konar, D., Devarasetty, M., Yildiz, D. V., Atala, A., and Murphy, S. V. (2016). Lung-on-A-chip technologies for disease modeling and drug development. *Biomed. Eng. Comput. Biol.* 7, 17–27. doi:10.4137/BECB.S34252

Korff, T., and Augustin, H. G. (1999). Tensional forces in fibrillar extracellular matrices control directional capillary sprouting. *J. Cell Sci.* 112, 3249–3258. doi:10.1242/jcs.112.19.3249

Lambrecht, B. N., and Hammad, H. (2012). The airway epithelium in asthma. *Nat. Med.* 18 (5), 684–692. doi:10.1038/nm.2737

Lee, C. Y., and Lowen, A. C. (2021). Animal models for SARS-CoV-2. *Curr. Opin. Virol.* 48, 73–81. doi:10.1016/j.coviro.2021.03.009

Leibel, S. L., McVicar, R. N., Winquist, A. M., Niles, W. D., and Snyder, E. Y. (2020). Generation of complete multi-cell type lung organoids from human embryonic and patient-specific induced pluripotent stem cells for infectious disease modeling and therapeutics validation. *Curr. Protoc. Stem Cell Biol.* 54 (1), e118. doi:10.1002/cpsc.118

Liu, Y., Dabrowska, C., Mavousian, A., Strauss, B., Meng, F., Mazzaglia, C., et al. (2021). Bio-assembling macro-scale, lumenized airway tubes of defined shape via multi-organoid patterning and fusion. *Adv. Sci.* 8 (9), 2003332. doi:10.1002/advs.202003332

Lu, R., Zhao, X., Li, J., Niu, P., Yang, B., Wu, H., et al. (2020). Genomic characterisation and epidemiology of 2019 novel coronavirus: Implications for virus origins and receptor binding. *Lancet* 395 (10224), 565–574. doi:10.1016/S0140-6736(20)30251-8

Luo, M., Ni, K., Sun, Y., Guo, J., Wen, K., and Deng, L. (2022). Toward an optimized strategy of using various airway mucus clearance techniques to treat critically ill COVID-19 patients. *Biocell* 46 (4), 855–871. doi:10.32604/biocell.2022.017520

Maisonnasse, P., Guedj, J., Contreras, V., Behillil, S., Solas, C., Marlin, R., et al. (2020). Hydroxychloroquine use against SARS-CoV-2 infection in non-human primates. *Nature* 585 (7826), 584–587. doi:10.1038/s41586-020-2558-4

Malda, J., Visser, J., Melchels, F. P., Jungst, T., Hennink, W. E., Dhert, W. J., et al. (2013). 25th anniversary article: Engineering hydrogels for biofabrication. *Adv. Mat.* 25 (36), 5011–5028. doi:10.1002/adma.201302042

Marescotti, D., Serchi, T., Luettich, K., Xiang, Y., Moschini, E., Talikka, M., et al. (2019). How complex should an *in vitro* model be? Evaluation of complex 3D alveolar model with transcriptomic data and computational biological network models. *ALTEX* 36 (3), 388–402. doi:10.14573/altex.1811221

Matai, I., Kaur, G., Seyedsalehi, A., McClinton, A., and Laurencin, C. T. (2020). Progress in 3D bioprinting technology for tissue/organ regenerative engineering. *Biomaterials* 226, 119536. doi:10.1016/j.biomaterials.2019.119536

Mills, R. J., Humphrey, S. J., Fortuna, P. R. J., Lor, M., Foster, S. R., Quaife-Ryan, G. A., et al. (2021). BET inhibition blocks inflammation-induced cardiac dysfunction and SARS-CoV-2 infection. *Cell* 184 (8), 2167–2182.e22. doi:10.1016/j.cell.2021.03.026

Mironov, V., Boland, T., Trusk, T., Forgacs, G., and Markwald, R. R. (2003). Organ printing: Computer-aided jet-based 3D tissue engineering. *Trends Biotechnol.* 21 (4), 157–161. doi:10.1016/S0167-7799(03)00033-7

Mironov, V., Kasyanov, V., Drake, C., and Markwald, R. R. (2008). Organ printing: Promises and challenges. *Regen. Med.* 3 (1), 93–103. doi:10.2217/17460751.3.1.93

Morrisey, E. E., and Hogan, B. L. (2010). Preparing for the first breath: Genetic and cellular mechanisms in lung development. *Dev. Cell* 18 (1), 8–23. doi:10.1016/j.devcel.2009.12.010

Mulay, A., Konda, B., Garcia, G., Jr., Yao, C., Beil, S., Villalba, J. M., et al. (2021). SARS-CoV-2 infection of primary human lung epithelium for COVID-19 modeling and drug discovery. *Cell Rep.* 35 (5), 109055. doi:10.1016/j.celrep.2021.109055

Mullen, P. J., Garcia, G., Jr., Purkayastha, A., Matulionis, N., Schmid, E. W., Momcilovic, M., et al. (2021). SARS-CoV-2 infection rewires host cell metabolism and is potentially susceptible to mTORC1 inhibition. *Nat. Commun.* 12 (1), 1876. doi:10.1038/s41467-021-22166-4

Murphy, S. V., and Atala, A. (2014). 3D bioprinting of tissues and organs. *Nat. Biotechnol.* 32 (8), 773–785. doi:10.1038/nbt.2958

Mykytyn, A. Z., Breugem, T. I., Riesebosch, S., Schipper, D., van den Doel, P. B., Rottier, R. J., et al. (2021). SARS-CoV-2 entry into human airway organoids is serine protease-mediated and facilitated by the multibasic cleavage site. *Elife* 10, e64508. doi:10.7554/eLife.64508

Nelli, R. K., Maes, R., Kiupel, M., and Hussey, G. S. (2016). Use of a feline respiratory epithelial cell culture system grown at the air-liquid interface to characterize the innate immune response following feline herpesvirus 1 infection. *Virus Res.* 214, 39–48. doi:10.1016/j.virusres.2016.01.006

Ng, W. L., Ayi, T. C., Liu, Y. C., Sing, S. L., Yeong, W. Y., and Tan, B. H. (2021). Fabrication and characterization of 3D bioprinted triple-layered human alveolar lung models. *Int. J. Bioprint.* 7 (2), 332. doi:10.18063/ijb.v7i2.332

Nichols, J. E., Niles, J. A., Vega, S. P., Argueta, L. B., Eastaway, A., and Cortiella, J. (2014). Modeling the lung: Design and development of tissue engineered macro- and micro-physiologic lung models for research use. *Exp. Biol. Med.* 239 (9), 1135–1169. doi:10.1177/1535370214536679

Nigjeh, S. E., Yeap, S. K., Nordin, N., Kamalideghan, B., Ky, H., and Rosli, R. (2018). Citral induced apoptosis in MDA-MB-231 spheroid cells. *BMC Complement. Altern. Med.* 18 (1), 56. doi:10.1186/s12906-018-2115-y

Nof, E., Zidan, H., Artzy-Schnirman, A., Mouhadeb, O., Beckerman, M., Bhardwaj, S., et al. (2022). Human multi-compartment airways-on-chip platform for emulating respiratory airborne transmission: From nose to pulmonary acini. *Front. Physiol.* 13, 853317. doi:10.3389/fphys.2022.853317

Novak, C., Ballinger, M. N., and Ghadiali, S. (2021). Mechanobiology of pulmonary diseases: A review of engineering tools to understand lung mechanotransduction. *J. Biomech. Eng.* 143 (11), 110801. doi:10.1115/1.4051118

O'Brien, F. J. (2011). Biomaterials & scaffolds for tissue engineering. *Mater. Today* 14(3), 88–95. doi: Doi doi:10.1016/S1369-7021(11)70058-X

Pei, R., Feng, J., Zhang, Y., Sun, H., Li, L., Yang, X., et al. (2021). Host metabolism dysregulation and cell tropism identification in human airway and alveolar organoids upon SARS-CoV-2 infection. *Protein Cell* 12 (9), 717–733. doi:10.1007/s13238-020-00811-w

Petersen, T. H., Calle, E. A., Zhao, L., Lee, E. J., Gui, L., Raredon, M. B., et al. (2010). Tissue-engineered lungs for *in vivo* implantation. *Science* 329 (5991), 538–541. doi:10.1126/science.1189345

Purwada, A., Jaiswal, M. K., Ahn, H., Nojima, T., Kitamura, D., Gaharwar, A. K., et al. (2015). *Ex vivo* engineered immune organoids for controlled germinal center reactions. *Biomaterials* 63, 24–34. doi:10.1016/j.biomaterials.2015.06.002

Qin, S., Jiang, Y., Wei, X., Liu, X., Guan, J., Chen, Y., et al. (2021). Dynamic changes in monocytes subsets in COVID-19 patients. *Hum. Immunol.* 82 (3), 170–176. doi:10.1016/j.humimm.2020.12.010

Ravi, M., Paramesh, V., Kaviya, S. R., Anuradha, E., and Solomon, F. D. (2015). 3D cell culture systems: Advantages and applications. *J. Cell. Physiol.* 230 (1), 16–26. doi:10.1002/jcp.24683

Ren, X., Wen, W., Fan, X., Hou, W., Su, B., Cai, P., et al. (2021). COVID-19 immune features revealed by a large-scale single-cell transcriptome atlas. *Cell* 184 (7), 1895–1913.e19. doi:10.1016/j.cell.2021.01.053

Rios, A. C., and Clevers, H. (2018). Imaging organoids: A bright future ahead. *Nat. Methods* 15 (1), 24–26. doi:10.1038/nmeth.4537

Ryu, N. E., Lee, S. H., and Park, H. (2019). Spheroid culture system methods and applications for mesenchymal stem cells. *Cells* 8 (12), 1620. doi:10.3390/cells8121620

Sachs, N., Papaspyropoulos, A., Zomer-van Ommen, D. D., Heo, I., Bottinger, L., Klay, D., et al. (2019). Long-term expanding human airway organoids for disease modeling. *EMBO J.* 38 (4), e100300. doi:10.15252/embj.2018100300

Salahudeen, A. A., Choi, S. S., Rustagi, A., Zhu, J., van Unen, V., de la, O. S., et al. (2020). Progenitor identification and SARS-CoV-2 infection in human distal lung organoids. *Nature* 588 (7839), 670–675. doi:10.1038/s41586-020-3014-1

Samuel, R. M., Majd, H., Richter, M. N., Ghazizadeh, Z., Zekavat, S. M., Navickas, A., et al. (2020). Androgen signaling regulates SARS-CoV-2 receptor levels and is associated with severe COVID-19 symptoms in men. *Cell Stem Cell* 27 (6), 876–889. doi:10.1016/j.stem.2020.11.009

Sardu, C., Gambardella, J., Morelli, M. B., Wang, X., Marfella, R., and Santulli, G. (2020). Hypertension, thrombosis, kidney failure, and diabetes: Is COVID-19 an endothelial disease? A comprehensive evaluation of clinical and basic evidence. *J. Clin. Med.* 9 (5), 1417. doi:10.3390/jcm9051417

Sato, T., Vries, R. G., Snippert, H. J., van de Wetering, M., Barker, N., Stange, D. E., et al. (2009). Single Lgr5 stem cells build crypt-villus structures *in vitro* without a mesenchymal niche. *Nature* 459 (7244), 262–265. doi:10.1038/nature07935

Sette, A., and Crotty, S. (2021). Adaptive immunity to SARS-CoV-2 and COVID-19. *Cell* 184 (4), 861–880. doi:10.1016/j.cell.2021.01.007

Sharma, A., Sances, S., Workman, M. J., and Svendsen, C. N. (2020). Multi-lineage human iPSC-derived platforms for disease modeling and drug discovery. *Cell Stem Cell* 26 (3), 309–329. doi:10.1016/j.stem.2020.02.011

Shi, Y., and Massague, J. (2003). Mechanisms of TGF-beta signaling from cell membrane to the nucleus. *Cell* 113 (6), 685–700. doi:10.1016/s0092-8674(03)00432-x

Shrestha, J., Razavi Bazaz, S., Aboulkheyr Es, H., Yaghobian Azari, D., Thierry, B., Ebrahimi Warkiani, M., et al. (2020). Lung-on-a-chip: The future of respiratory disease models and pharmacological studies. *Crit. Rev. Biotechnol.* 40 (2), 213–230. doi:10.1080/07388551.2019.1710458

Spitalieri, P., Centofanti, F., Murdocca, M., Scioli, M. G., Latini, A., Di Cesare, S., et al. (2022). Two different therapeutic approaches for SARS-CoV-2 in hiPSCs-derived lung organoids. *Cells* 11 (7), 1235. doi:10.3390/cells11071235

Suki, B., Stamenovic, D., and Hubmayr, R. (2011). Lung parenchymal mechanics. *Compr. Physiol.* 1 (3), 1317–1351. doi:10.1002/cphy.c100033

Takahashi, K., Tanabe, K., Ohnuki, M., Narita, M., Ichisaka, T., Tomoda, K., et al. (2007). Induction of pluripotent stem cells from adult human fibroblasts by defined factors. *Cell* 131 (5), 861–872. doi:10.1016/j.cell.2007.11.019

Takahashi, K., and Yamanaka, S. (2006). Induction of pluripotent stem cells from mouse embryonic and adult fibroblast cultures by defined factors. *Cell* 126 (4), 663–676. doi:10.1016/j.cell.2006.07.024

Tale, S., Ghosh, S., Meitei, S. P., Kolli, M., Garbhapu, A. K., and Pudi, S. (2020). Post-COVID-19 pneumonia pulmonary fibrosis. *QJM Mon. J. Assoc. Physicians* 113 (11), 837–838. doi:10.1093/qjmed/hcaa255

Tam, A., Wadsworth, S., Dorscheid, D., Man, S. F., and Sin, D. D. (2011). The airway epithelium: More than just a structural barrier. *Ther. Adv. Respir. Dis.* 5 (4), 255–273. doi:10.1177/1753465810396539

Tan, Q., Choi, K. M., Sicard, D., and Tschumperlin, D. J. (2017). Human airway organoid engineering as a step toward lung regeneration and disease modeling. *Biomaterials* 113, 118–132. doi:10.1016/j.biomaterials.2016.10.046

Tay, M. Z., Poh, C. M., Rénia, L., MacAry, P. A., and Ng, L. F. P. (2020). The trinity of COVID-19: Immunity, inflammation and intervention. *Nat. Rev. Immunol.* 20 (6), 363–374. doi:10.1038/s41577-020-0311-8

Thacker, V. V., Sharma, K., Dhar, N., Mancini, G. F., Sordet-Dessimoz, J., and McKinney, J. D. (2021). Rapid endotheliitis and vascular damage characterize SARS-CoV-2 infection in a human lung-on-chip model. *EMBO Rep.* 22 (6), e52744. doi:10.15252/embr.202152744

Tiwari, S. K., Wang, S., Smith, D., Carlin, A. F., and Rana, T. M. (2021). Revealing tissue-specific SARS-CoV-2 infection and host responses using human stem cell-derived lung and cerebral organoids. *Stem Cell Rep.* 16 (3), 437–445. doi:10.1016/j.stemcr.2021.02.005

Toor, S. M., Saleh, R., Sasidharan Nair, V., Taha, R. Z., and Elkord, E. (2021). T-cell responses and therapies against SARS-CoV-2 infection. *Immunology* 162 (1), 30–43. doi:10.1111/imm.13262

Tostanoski, L. H., Wegmann, F., Martinot, A. J., Loos, C., McMahan, K., Mercado, N. B., et al. (2020). Ad26 vaccine protects against SARS-CoV-2 severe clinical disease in hamsters. *Nat. Med.* 26 (11), 1694–1700. doi:10.1038/s41591-020-1070-6

Totura, A. L., Whitmore, A., Agnihothram, S., Schafer, A., Katze, M. G., Heise, M. T., et al. (2015). Toll-like receptor 3 signaling via TRIF contributes to a protective innate immune response to severe acute respiratory syndrome coronavirus infection. *mBio* 6 (3), e00638–e00615. doi:10.1128/mBio.00638-15

Trietsch, S. J., Israels, G. D., Joore, J., Hankemeier, T., and Vulto, P. (2013). Microfluidic titer plate for stratified 3D cell culture. *Lab. Chip* 13 (18), 3548–3554. doi:10.1039/c3lc50210d

van Duinen, V., van den Heuvel, A., Trietsch, S. J., Lanz, H. L., van Gils, J. M., van Zonneveld, A. J., et al. (2017). 96 perfusable blood vessels to study vascular permeability *in vitro*. *Sci. Rep.* 7 (1), 18071. doi:10.1038/s41598-017-14716-y

Vives, J., and Batlle-Morera, L. (2020). The challenge of developing human 3D organoids into medicines. *Stem Cell Res. Ther.* 11 (1), 72. doi:10.1186/s13287-020-1586-1

Wang, C., Horby, P. W., Hayden, F. G., and Gao, G. F. (2020a). A novel coronavirus outbreak of global health concern. *Lancet* 395 (10223), 470–473. doi:10.1016/s0140-6736(20)30185-9

Wang, D., Hu, B., Hu, C., Zhu, F., Liu, X., Zhang, J., et al. (2020b). Clinical characteristics of 138 hospitalized patients with 2019 novel coronavirus-infected pneumonia in wuhan, China. *JAMA* 323 (11), 1061–1069. doi:10.1001/jama.2020.1585

Wang, J., Li, X., Wang, A., Zhao, F., Wu, Q., Li, L., et al. (2020c). Organoid technology demonstrates effects of potential drugs for COVID-19 on the lung regeneration. *Cell Prolif.* 53 (12), e12928. doi:10.1111/cpr.12928

Wang, M., Cao, R., Zhang, L., Yang, X., Liu, J., Xu, M., et al. (2020d). Remdesivir and chloroquine effectively inhibit the recently emerged novel coronavirus (2019-nCoV) *in vitro*. *Cell Res.* 30 (3), 269–271. doi:10.1038/s41422-020-0282-0

Wang, S., Li, W., Hui, H., Tiwari, S. K., Zhang, Q., Croker, B. A., et al. (2020e). Cholesterol 25-Hydroxylase inhibits SARS-CoV-2 and other coronaviruses by depleting membrane cholesterol. *EMBO J.* 39 (21), e106057. doi:10.15252/embj.2020106057

Wang, T., Zhang, N., Fan, S., Zhao, L., Song, W., Gong, Y., et al. (2021). Establishment of human distal lung organoids for SARS-CoV-2 infection. *Cell Discov.* 7 (1), 108. doi:10.1038/s41421-021-00346-2

Wang, Y., Wang, P., and Qin, J. (2022). Human organoids and organs-on-chips for addressing COVID-19 challenges. *Adv. Sci.* 9 (10), e2105187. doi:10.1002/advs.202105187

Weibel, E. R., and Gomez, D. M. (1962). Architecture of the human lung. Use of quantitative methods establishes fundamental relations between size and number of lung structures. *Science* 137 (3530), 577–585. doi:10.1126/science.137.3530.577

Weibel, E. R. (2017). Lung morphometry: The link between structure and function. *Cell Tissue Res.* 367 (3), 413–426. doi:10.1007/s00441-016-2541-4

Whitcutt, M. J., Adler, K. B., and Wu, R. (1988). A biphasic chamber system for maintaining polarity of differentiation of cultured respiratory tract epithelial cells. *Vitro Cell. Dev. Biol.* 24 (5), 420–428. doi:10.1007/BF02628493

Wilk, A. J., Rustagi, A., Zhao, N. Q., Roque, J., Martinez-Colon, G. J., McKechnie, J. L., et al. (2020). A single-cell atlas of the peripheral immune response in patients with severe COVID-19. *Nat. Med.* 26 (7), 1070–1076. doi:10.1038/s41591-020-0944-y

Wu, F., Zhao, S., Yu, B., Chen, Y.-M., Wang, W., Song, Z.-G., et al. (2020). A new coronavirus associated with human respiratory disease in China. *Nature* 579 (7798), 265–269. doi:10.1038/s41586-020-2008-3

Xu, G., Li, Y., Zhang, S., Peng, H., Wang, Y., Li, D., et al. (2021). SARS-CoV-2 promotes RIPK1 activation to facilitate viral propagation. *Cell Res.* 31 (12), 1230–1243. doi:10.1038/s41422-021-00578-7

Yan, R., Zhang, Y., Li, Y., Xia, L., Guo, Y., and Zhou, Q. (2020). Structural basis for the recognition of SARS-CoV-2 by full-length human ACE2. *Science* 367 (6485), 1444–1448. doi:10.1126/science.abb2762

Zhang, J. J., Dong, X., Cao, Y. Y., Yuan, Y. D., Yang, Y. B., Yan, Y. Q., et al. (2020a). Clinical characteristics of 140 patients infected with SARS-CoV-2 in Wuhan, China. *Allergy* 75 (7), 1730–1741. doi:10.1111/all.14238

Zhang, M., Wang, P., Luo, R., Wang, Y., Li, Z., Guo, Y., et al. (2020b). Biomimetic human disease model of SARS-CoV-2 induced lung injury and immune responses on organ chip system. *Adv. Sci.* 8 (3), 2002928. doi:10.1002/advs.202002928

Zhang, Y. S., Yue, K., Aleman, J., Moghaddam, K. M., Bakht, S. M., Yang, J., et al. (2017). 3D bioprinting for tissue and organ fabrication. *Ann. Biomed. Eng.* 45 (1), 148–163. doi:10.1007/s10439-016-1612-8

Zhao, B., Ni, C., Gao, R., Wang, Y., Yang, L., Wei, J., et al. (2020a). Recapitulation of SARS-CoV-2 infection and cholangiocyte damage with human liver ductal organoids. *Protein Cell* 11 (10), 771–775. doi:10.1007/s13238-020-00718-6

Zhao, Z., Vizetto-Duarte, C., Moay, Z. K., Setyawati, M. I., Rakshit, M., Kathawala, M. H., et al. (2020b). Composite hydrogels in three-dimensional *in vitro* models. *Front. Bioeng. Biotechnol.* 8, 611. doi:10.3389/fbioe.2020.00611

Zhou, J., Li, C., Sachs, N., Chiu, M. C., Wong, B. H., Chu, H., et al. (2018). Differentiated human airway organoids to assess infectivity of emerging influenza virus. *Proc. Natl. Acad. Sci. U. S. A.* 115 (26), 6822–6827. doi:10.1073/pnas.1806308115

Zhou, P., Yang, X.-L., Wang, X.-G., Hu, B., Zhang, L., Zhang, W., et al. (2020a). A pneumonia outbreak associated with a new coronavirus of probable bat origin. *Nature* 579 (7798), 270–273. doi:10.1038/s41586-020-2012-7

Zhou, R., To, K. K., Wong, Y. C., Liu, L., Zhou, B., Li, X., et al. (2020b). Acute SARS-CoV-2 infection impairs dendritic cell and T cell responses. *Immunity* 53 (4), 864–877. doi:10.1016/j.immuni.2020.07.026

Zhou, Z., Zhang, X., Lei, X., Xiao, X., Jiao, T., Ma, R., et al. (2021). Sensing of cytoplasmic chromatin by cGAS activates innate immune response in SARS-CoV-2 infection. *Signal Transduct. Target. Ther.* 6 (1), 382. doi:10.1038/s41392-021-00800-3

Glossary

2D Two-dimensional
3D Three-dimensional
ACE2 Angiotensin-converting enzyme 2
AFE Anterior foregut endoderm
ALI Air liquid interface
APCs Antigen presenting cells
ARDS Acute respiratory distress syndrome
ASMCs Airway smooth muscle cells
AT2 Alveolar epithelial type 2
CAD Computer-aided design
CFE Colony-forming efficiency
COVID-19 Coronavirus disease 2019
DE Definitive endoderm
ECM Extracellular matrix
ESCs Embryonic stem cells
FDA Food and Drug Administration
FHV-1 Feline herpesvirus-1
GelMA Gelatin methacryloyl
IL Interleukin
iPSCs Induced pluripotent stem cells
LPs Lung progenitors
MDA5 Melanoma differentiation-associated gene 5
MBCS Multibasic cleavage site
MPA Mycophenolic acid
NHPs Non-human primates
NRP1 Neuropilin-1
ORFs Open reading frames
PC Pyruvate carboxylase
PD Peptidase domain
PM2.5 Fine particulate matter
QNHC Quinacrine dihydrochloride
RBD Receptor-binding domain
SARS-CoV-2 Severe acute respiratory syndrome coronavirus-2
TLR3 Toll-like receptor 3
TLR7 Toll-like receptor 7
TMPRSS2 Transmembrane protease serine 2
TNF-a Tumor necrosis factor alpha
TSPAN8 Tetraspanin 8

frontiers | Frontiers in Pharmacology

TYPE Original Research
PUBLISHED 12 January 2023
DOI 10.3389/fphar.2022.1081345

OPEN ACCESS

EDITED BY
Haiyang Tang,
University of Arizona, United States

REVIEWED BY
Raoua Ben Messaoud,
INSERM U1042 Laboratoire Hypoxie et Physiopathologies cardiovasculaires et respiratoires (HP2), France
Ramaswamy Krishnan,
Beth Israel Deaconess Medical Center and Harvard Medical School, United States

*CORRESPONDENCE
Ramon Farré,
rfarre@ub.edu

SPECIALTY SECTION
This article was submitted to Respiratory Pharmacology, a section of the journal Frontiers in Pharmacology

RECEIVED 27 October 2022
ACCEPTED 28 December 2022
PUBLISHED 12 January 2023

CITATION
Jurado A, Ulldemolins A, Lluís H, Gasull X, Gavara N, Sunyer R, Otero J, Gozal D, Almendros I and Farré R (2023), Fast cycling of intermittent hypoxia in a physiomimetic 3D environment: A novel tool for the study of the parenchymal effects of sleep apnea. *Front. Pharmacol.* 13:1081345. doi: 10.3389/fphar.2022.1081345

Fast cycling of intermittent hypoxia in a physiomimetic 3D environment: A novel tool for the study of the parenchymal effects of sleep apnea

Alicia Jurado[1], Anna Ulldemolins[1], Helena Lluís[2,3], Xavier Gasull[2,3], Núria Gavara[1,4], Raimon Sunyer[1,4], Jorge Otero[1,4,5], David Gozal[6], Isaac Almendros[1,3,5] and Ramon Farré[1,3,5]*

[1]Unitat de Biofísica i Bioenginyeria, Facultat de Medicina i Ciències de la Salut, Universitat de Barcelona, Barcelona, Spain, [2]Neurophysiology Laboratory, Department of Biomedicine, School of Medicine, Institute of Neurosciences, University of Barcelona, Barcelona, Spain, [3]Institut Investigacions Biomèdiques August Pi Sunyer, Barcelona, Spain, [4]The Institute for Bioengineering of Catalonia (IBEC), The Barcelona Institute of Science and Technology (BIST), Barcelona, Spain, [5]CIBER de Enfermedades Respiratorias, Madrid, Spain, [6]Department of Child Health, The University of Missouri School of Medicine, Columbia, KY, United States

Background: Patients with obstructive sleep apnea (OSA) experience recurrent hypoxemic events with a frequency sometimes exceeding 60 events/h. These episodic events induce downstream transient hypoxia in the parenchymal tissue of all organs, thereby eliciting the pathological consequences of OSA. Whereas experimental models currently apply intermittent hypoxia to cells conventionally cultured in 2D plates, there is no well-characterized setting that will subject cells to well-controlled intermittent hypoxia in a 3D environment and enable the study of the effects of OSA on the cells of interest while preserving the underlying tissue environment.

Aim: To design and characterize an experimental approach that exposes cells to high-frequency intermittent hypoxia mimicking OSA in 3D (hydrogels or tissue slices).

Methods: Hydrogels made from lung extracellular matrix (L-ECM) or brain tissue slices (300–800-µm thickness) were placed on a well whose bottom consisted of a permeable silicone membrane. The chamber beneath the membrane was subjected to a square wave of hypoxic/normoxic air. The oxygen concentration at different depths within the hydrogel/tissue slice was measured with an oxygen microsensor.

Results: 3D-seeded cells could be subjected to well-controlled and realistic intermittent hypoxia patterns mimicking 60 apneas/h when cultured in L-ECM hydrogels ≈500 µm-thick or *ex-vivo* in brain slices 300–500 µm-thick.

Conclusion: This novel approach will facilitate the investigation of the effects of intermittent hypoxia simulating OSA in 3D-residing cells within the parenchyma of different tissues/organs.

KEYWORDS

obstructive sleep apnea, hypoxia, cell culture, hydrogels, tissue slice, 3D culture, oxygen diffusion, disease model

1 Introduction

Obstructive sleep apnea (OSA) is a very prevalent respiratory disorder affecting patients of all ages, from children to the elderly (Benjafield et al., 2019). Patients suffering from OSA exhibit an abnormally increased collapsibility of the upper airway during sleep and thereby experience recurrent events of upper airway obstruction, usually terminated by an arousal. In more severe instances, these patients can sustain more than one obstructive event per minute of sleep. In addition to the consequences directly caused by the disruption of sleep architecture (diurnal somnolence, fatigue, increased traffic and labor accidents, poor quality of life, cognitive deficits, and depression), patients with OSA are also at increased risk of both morbidity and mortality from cardiovascular, metabolic, neurocognitive and malignant diseases (Sánchez-de-la-Torre et al., 2013; Gileles-Hillel et al., 2016; Gozal et al., 2020; Brockmann and Gozal, 2022). These adverse outcomes are primarily caused by the recurrent events of hypoxemia induced by the upper airway obstructions (i.e., apneas and hypopneas). Indeed, during these events, the absence/reduction of pulmonary alveolar ventilation results in transient reductions in the partial pressure of O_2 in arterial blood, which is clinically assessed by non-invasively measuring arterial oxygen saturation (SaO_2) by pulse oximetry (Figure 1A) (Farré et al., 1998). The recurrently hypoxic blood leaving the lungs enters the systemic capillaries that perfuse all the patient tissues and organs (Almendros et al., 2011; Reinke et al., 2011; Torres et al., 2014; Moreno-Indias et al., 2015), and this reduced O_2 tension then diffuses into the surrounding extra capillary space, thereby subjecting parenchymal cells to intermittent hypoxia of varying degrees (Figure 1B). It has been well established that this

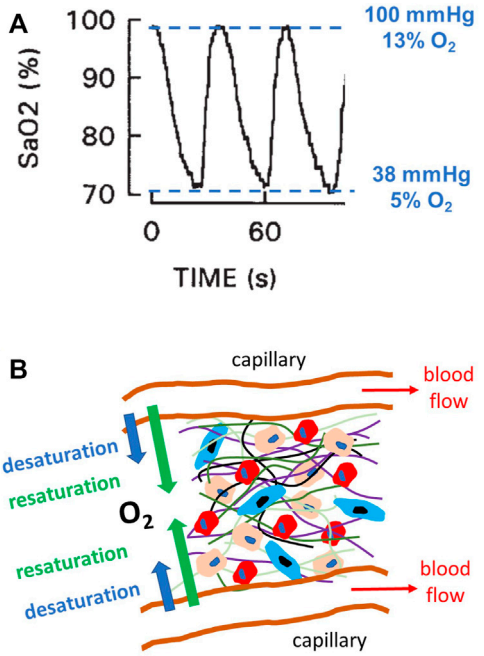

FIGURE 1
Intermittent hypoxia in obstructive sleep apnea (OSA). **(A)** Example of a recording of arterial oxygen saturation (SaO_2) measured by pulse oximetry in a patient with severe OSA, showing the fast and marked hypoxemic events characterizing this disease. The figure also indicates the values of O_2 partial pressure, and thus O_2 percentage (for 760 mmHg atmospheric pressure), corresponding to the maximum and minimum levels of SaO_2. Modified from Reference (Farré et al., 1998) and reproduced with permission. **(B)** Diagram representing a section of the parenchymal cells in any organ/tissue where different cell types (represented by different sizes and colors) reside within an extracellular matrix (different fibers represented by different color lines). This 3D environment is perfused by O_2 from the arterial blood circulating through systemic capillaries. Given the intermittent hypoxemia, the magnitude of O_2 diffusion through the capillary wall cycles (desaturation and resaturation), and cells are subjected to intermittent hypoxia caused by hypoxemic events **(A)**.

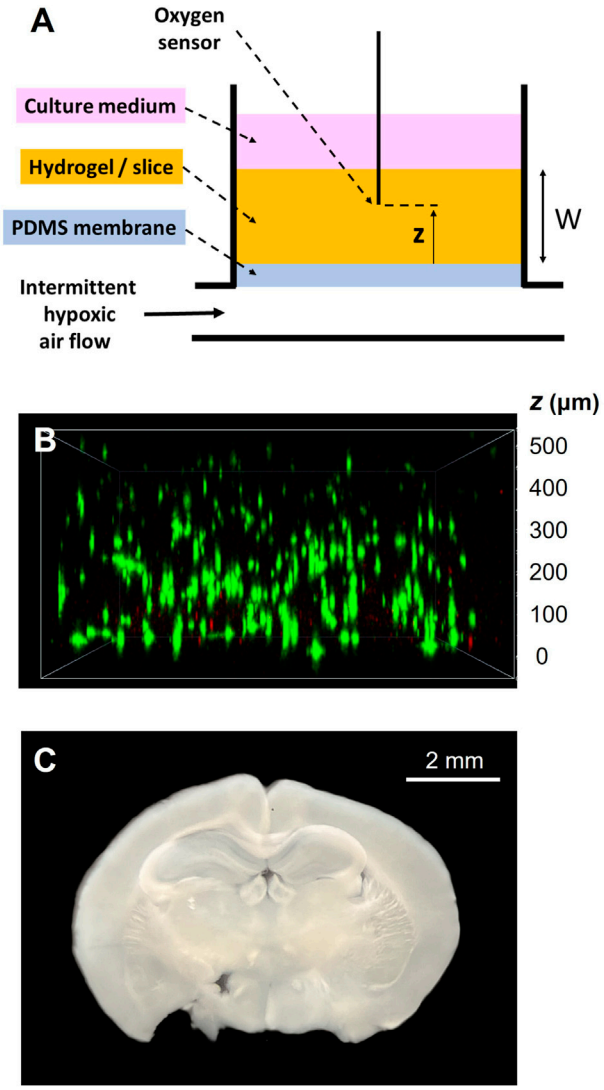

FIGURE 2
(A) Experimental setting for applying intermittent hypoxia to 3D-cultured cells. A culture well has a bottom consisting of a polydimethylsiloxane (PDMS) membrane. The compartment beneath the membrane is circulated with intermittent hypoxic air. The cells to be subjected to intermittent hypoxia are cultured within a 3D hydrogel or tissue slice of width W placed on the membrane. Only to characterize the setting, a thin fast-response O_2 sensor probe is used to measure O_2 concentration at different positions (*z*) across the sample. **(B)** Example of the achieved distribution of lung mesenchymal stromal cells within a lung ECM hydrogel (20 mg/mL) along the sample thickness, with green and red colors indicating live and dead cells respectively (Live/Dead viability kit; Invitrogen). Reproduced from Reference (Falcones et al., 2021) under Creative Commons Attribution (CC BY) license. **(C)** Example of a mouse brain slice to be subjected to intermittent hypoxia.

noxious challenge triggers cascades of oxidative stress, inflammation, and immune and hormonal deregulations, which ultimately result in the increased end-organ and systemic adverse consequences of OSA (Sánchez-de-la-Torre et al., 2013; Gileles-Hillel et al., 2016; Gozal et al., 2020; Brockmann and Gozal, 2022).

Given that intermittent hypoxia is a major driver of the OSA-induced increase in morbidity and mortality, considerable experimental research efforts have been devoted to investigating how different types of cultured cells respond to these hypoxic cycles (Farré et al., 2018). However, a particular challenge in precisely achieving this research aim is to ensure that the cultured cells of interest are *de facto* subjected to the high-frequency events of hypoxia (up to 60 cycles per hour) characterizing OSA. Indeed, given the relatively slow process of O_2 diffusion in water or other liquids, using the conventional procedure based on cyclically modifying the O_2 partial pressure in the air on top of the culture medium is sub-optimal to achieve adequate fast changes of O_2 partial pressure at the cell culture level (Allen et al., 2001). Fortunately, optimized experimental settings based on culturing cells on a thin O_2-permeable membrane have been described to ensure that the cultured cells experience the desirable fast OSA-mimicking intermittent hypoxia events (Campillo et al., 2016; Minoves et al., 2017). However, these improved settings were designed and tested in cells cultured in 2D set-ups. Whereas such geometry is suitable for cells naturally living in monolayers (e.g., epithelial and endothelial cells), it is suboptimal when investigating the effects of intermittent hypoxia in most parenchymal (or tumor) cell types that naturally reside and evolve in a 3D environment within an extracellular matrix (ECM). To date, it has been a common approach to use 2D culture plates to investigate the biology of cells that naturally live *in vivo* in 3D microenvironments. However, there is solid emerging evidence that 2D and 3D cell microenvironments differently modulate essential cell functions (Duval et al., 2017; Jensen and Teng, 2020; Kusuma et al., 2022). Therefore, optimal study of parenchymal cell biology requires realistic simulation and replication of the native 3D configuration by culturing cells inside hydrogels or using *ex-vivo* precision-cut tissue slices (Tibbitt and Anseth, 2009; Caliari and Burdick, 2016; Dewyse et al., 2021). Accordingly, the present study aimed to devise and characterize a procedure for applying physiomimetic intermittent hypoxia to cells in a 3D microenvironment.

2 Materials and methods

The experimental setting devised to apply intermittent hypoxia to cells in a 3D environment is schematically shown in Figure 2A. It is based on a previously described well with a bottom consisting of a membrane of O_2-permeable polydimethylsiloxane (PDMS) (Campillo et al., 2016). A flow of intermittently hypoxic air at a frequency characterizing severe OSA (e.g., 60 apneas/h: 30 s of normoxic gas (i.e., air) and 30 s of hypoxic gas (i.e., target FiO2 of interest) circulates through the compartment beneath the membrane. The 3D scaffold (thickness W) containing the cells subjected to intermittent hypoxia (hydrogel made of natural ECM or precision-cut tissue slices) is placed on the PDMS membrane. A micrometric fast-response O2 sensor is only used to characterize the setting to measure O_2 inside the 3D sample at different distances from the membrane (*z*, Figure 2A).

2.1 Well fabrication

As described in detail elsewhere (Campillo et al., 2016), the PDMS wells were assembled from 2 different parts: the upper one, composed of 6 wells constituting the culture chamber, and the bottom part with also 6 wells which comprised the gas chamber. Both parts were separated by a 165 μm thick gas-permeable PDMS membrane (Gel-Pak, Hayward, CA, United States). Each part of the setting was fabricated with a 1:10 mixture of curing agent and pre-polymer (Sylgard 184 kit, Dow Corning) using negative molds designed with the Ultimaker Cura software (Ultimaker, Utrecht, Netherlands) and printed with an Ultimaker S5 3D printer (Ultimaker, Utrecht, Netherlands) in polycarbonate material. In the center of the chip, an inlet tube connected to a servo-controlled gas blender (McQ, Virginia, United States) which was controlled by the Software Gas Mixture Creator (McQ, Virginia, United States) to provide the pre-defined specific gas mixture into the gas chamber. For the correct adhesion of the hydrogels, PDMS membranes were activated by placing the chips in a plasma cleaner (PDC-002, Harrick Scientific Products Inc. Pleasantville, NY) at maximum voltage for 1 min 90 s. Next, membranes were incubated with APTES 10% for 60 min and 5 mM genipin (Challenge Bio Products Co., Taiwan) for 45 min. Following each incubation, 2 washes of PBS 1X for 5 min were done. Lastly, the device was allowed to dry overnight.

2.2 Cell culture

Primary Rat Bone Marrow-derived Mesenchymal Stem Cells (rBMMSCs) acquired from Merck (SCR027) were used. Cells were expanded and cultured in MEM-α medium (Gibco) supplemented with 10% FBS and 1% Penicillin/Streptomycin, which was replaced every 48–72 h. At 80–90% of confluency, cells were trypsinized with TripLE express trypsin (Gibco) for 5 min and counted for hydrogel seeding. All experiments were performed with rBMMSCs at passage 4.

2.3 Hydrogel preparation

Porcine lungs were purchased in a local slaughterhouse and decellularized as previously reported (Falcones et al., 2021) based on a protocol previously described (Pouliot et al., 2016). In brief, pig lungs were perfused *via* the trachea and the vasculature with .1% Triton X-100 and 2% sodium deoxycholate for 24 h at 4°C. Afterwards, another perfusion with 1 M NaCl and DNase solution for 1 h was performed (4°C). Then, decellularized tissue was cut in small pieces and frozen at −80°C, lyophilized (Telstar Lyoquest55 Plus, Terrassa, Spain) and cryomilled (6,755, SPEX, Metuchen, NJ, United States) resulting in a fine powder. The lung ECM powder obtained was digested at 20 mg/mL concentration with pepsin from porcine gastric mucosa in .01 M HCl solution (1:10 concentration) under constant agitation at room temperature for 16 h. Then, the pH solution was adjusted to 7.4 (±.2) by adding 0.1 M NaOH and 10X PBS. The resulting pre-gel was stored frozen at −80°C for subsequent use. For preparing acellular hydrogels, lung ECM pre-gel at a concentration of 20 mg/mL was pipetted into the well and left to gellify at 37°C for 20 min followed by the addition of 1 mL of 1X PBS. This procedural approach allowed consistent and reproducible fabrication of hydrogel layers that were very uniform and of accurate

thickness. For instance, when targeting a 500 µm-thick gel made of lung ECM, the achieved thickness measured by microscopy in 4 different random sites of the hydrogel surface in 4 different wells was 512 µm, with intra-sample and inter-sample variances of 1.7% and 1.6%, respectively. In the case of cell-laden hydrogels, rat bone marrow mesenchymal stem cells at two different concentrations (3×10^5 cells/mL and 4.5×10^5 cells/mL) were mixed with the lung ECM pre-gel. Then, the chip was placed at 37°C for 20 min to allow gelation prior to the addition of 1 mL of supplemented MEM-α medium. Cells were allowed to settle for 24 h in the incubator (20% O_2, 5% CO_2, 37°C) before starting the experiments.

2.4 Preparation of precision-cut mouse brain slices

Brain slices were obtained from 6-week-old C57BL/6J mice housed at the animal facility of the Medical School of the University of Barcelona. Mice were decapitated after being deeply anesthetized with inhaled isoflurane, the brain was immediately extracted with dissection tools and placed into the ice-cold artificial cerebrospinal fluid (aCSF) denominated as aCSF1 to reflect its use during brain tissue sectioning. Of note, the harvested brain was placed in aCSF1 within less than 1 min after sacrificing the animal. The aCSF1 used for slicing contained the following (in mM): 25 Sucrose, 2.5 Glucose, 125 NaCl, 2.5 KCl, 1.25 NaH_2PO_4, 26 $NaHCO_3$, 5.9 $MgCl_2$, adjusted to pH 7.3, osmolarity 320 mOsmol/kg, and bubbled with carbogen (95% O_2, 5% CO_2). The brain was glued to the cutting chamber of the slicer with cyanoacrylate glue in the proper orientation to prepare coronal cortico-hippocampal slices. Thick slices (300 and 500 µm) from the brain were prepared using a vibrating microtome (Leica VT1000 S), with a cutting blade vibrating at a 60 Hz frequency and moving at .125 mm/s forward speed. The slices were incubated in aCSF solution designed for recovery (aCSF2) at 34°C for 30 min, consisting of (in mM): 20 Glucose, 125 NaCl, 2.5 KCl, 1.25 NaH_2PO_4, 26 $NaHCO_3$, 2 $CaCl_2$, 1 $MgCl_2$, adjusted to pH 7.4, osmolarity 310 mOsmol/kg, and continuously bubbled with carbogen. Afterward, slices were transferred with a glass Pasteur pipette to the measurement well, filled with aCSF2 and oxygenated with carbogen, in a thermostatic chamber at 37°C. The slice was held down by a nylon mesh attached to a platinum U-wire, which provided mechanical stability during the experiment. Animal care and procedures were approved and conducted following the CEEA-UB (Ethical Committee for Animal Research) from the University of Barcelona following European (2010/63/UE) and Spanish (RD 53/2013) regulations about the use and care of experimental animals.

2.5 Measurement of O_2 concentration within the 3D sample

An optical fiber oxygen microsensor (OXR50, Pyroscience, Aachen, Germany) with a ≈40 µm sharp tip and a typical response time for 90% signal change <2 s was calibrated following the manufacturer's instructions and attached to a specifically designed holder that allowed for micrometric-resolution vertical positioning. The signal from the oxygen sensor was recorded by an oxygen meter (FireStingO2; PyroScience) and digitally stored for subsequent analysis. This meter also carried out automatic temperature compensation by using the reference signal from a shielded submersible temperature sensor (TSUB36; PyroScience) placed into the culture well. Measurements were performed with the sensor tip introduced inside the sample (Figure 2A), at room temperature (23°C) in the case of acellular hydrogels and 37°C in cell-seeded hydrogels or tissue slices.

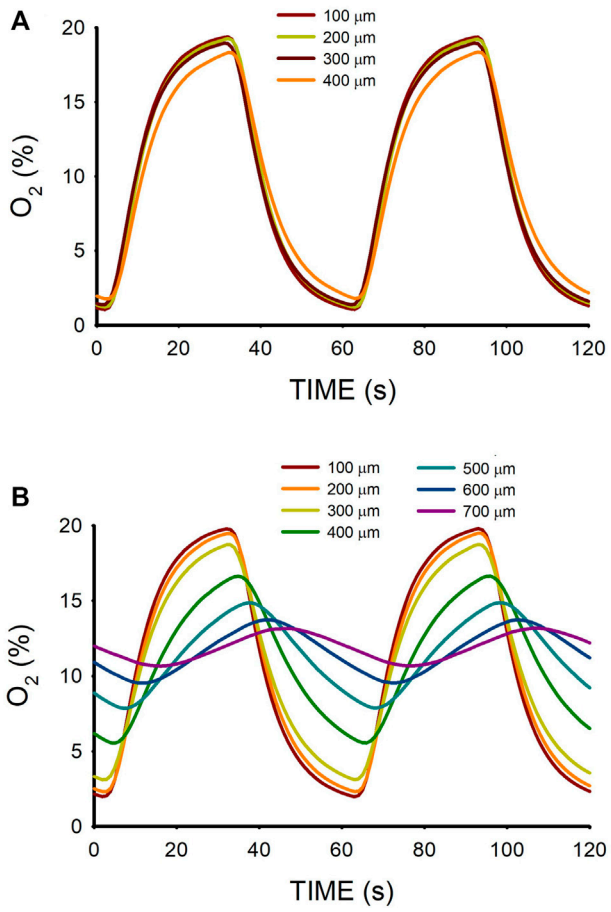

FIGURE 3
(A) Oxygen concentration measured at different positions (*z*; Figure 2A) within a lung extracellular matrix hydrogel of thickness W = 500 µm when the intermittent air circulating beneath the membrane was 20% O_2 for 30 s 0% O_2 for 30 s. **(B)** Same for hydrogel thickness W = 800 µm.

3 Results

The time course of O_2 concentration measured at different distances from the membrane (Figure 2A) in a W = 500-µm lung ECM hydrogel when subjected to intermittent hypoxia (20% O_2-0% O_2) at a rate of 60 events/h is shown in Figure 3A. For z = 100 µm, the maximum O_2 concentration was virtually 20%, but the minimum was slightly greater than 0% O_2 because of the slight drop in O_2 concentration caused by diffusion across the PDMS membrane. As expected, increases in z decreased the amplitude of O_2 concentration swings. However, the amplitude of O_2 cycles was still considerable, even close to the top of the hydrogel (z = 400 µm). In contrast, when the thickness of the hydrogel was

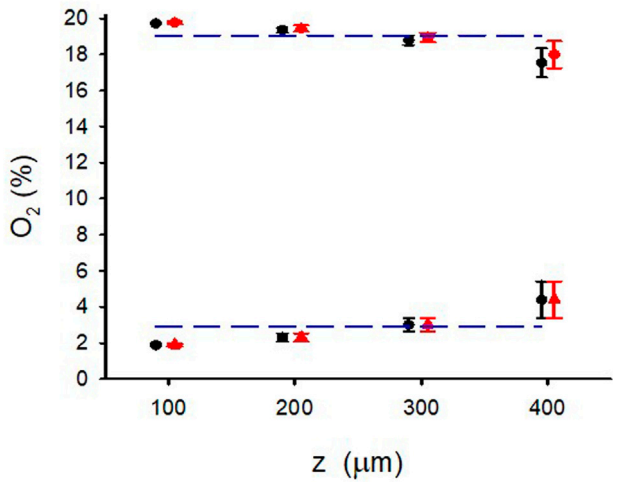

FIGURE 4
Maximum and minimum of O_2 for different positions (*z*) in the W = 500 µm lung extracellular matrix hydrogel when the intermittent air circulating beneath the membrane was 20% O_2 for 30 s 0% O_2 for 30 s. O_2 concentration was measured in 4 different random areas (data show the mean ± SD in each area) of two different hydrogel samples (red and blue symbols). Lines correspond to the mean corresponding to all values of *z*.

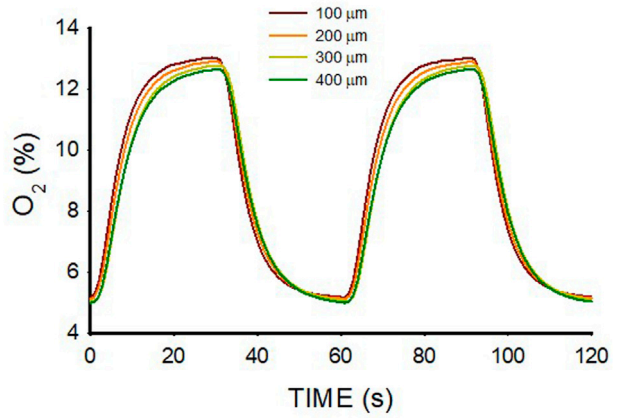

FIGURE 5
Oxygen concentration measured at different positions (*z*; Figure 2A) within a lung extracellular matrix hydrogel of thickness W = 500 µm when the intermittent air circulating beneath the membrane was 15% O_2 for 30 s and 5% O_2 for 30 s.

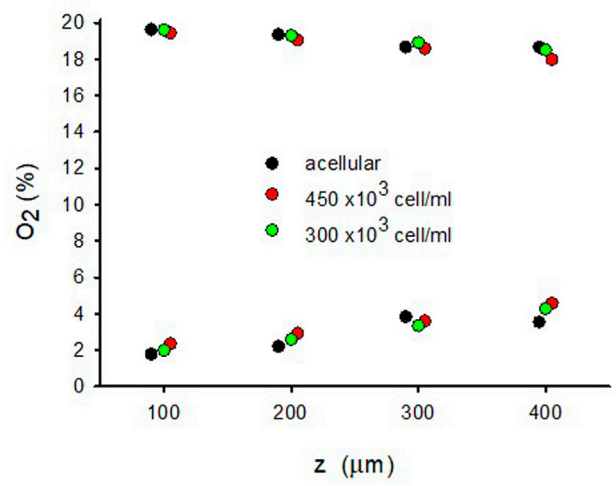

FIGURE 6
Maximum and minimum of O_2 for different positions (*z*) in the W = 500 µm lung extracellular matrix hydrogel when the intermittent air circulating beneath the membrane was 20% O_2 for 30 s 0% O_2 for 30 s in an acellular hydrogel and when the hydrogel was seeded with two different concentrations of MSC.

800 µm, the amplitudes of O_2 oscillations were considerably reduced as *z* increased (Figure 3B), with a maximum of 13.1% O_2 and a minimum of 10.7% O_2 for z = 700 µm.

Figure 4 shows the excellent reproducibility observed (mean ± SD) of the maximum and minimum data shown in Figure 3A when the O_2 measurements were carried out in 4 different random areas of two different W = 500-µm hydrogel samples. This figure also reflects that, despite the slight decrease in maximum and increase in minimum observed when *z* increased, the variance of minimum and maximum O_2 concentrations across the hydrogel section was lower than 2% O_2 around the corresponding mean value.

The range of O_2 oscillations within the sample was readily modulated by modifying the O_2 concentration of the gas circulating beneath the membrane. For instance, as shown in Figure 5, lower amplitude of intermittent hypoxic gas (15% O_2–5% O_2 in the gas beneath the membrane) subjected the hydrogel to oxygenation values close to the ones in the arterial blood perfusing tissues in patients with severe OSA (Figure 1A). The maximum and minimum values were similar over the hydrogel section (*z* from 100 to 400 µm), with maxima and minima ranging within .5% O_2 and .2% O_2, respectively.

3D culturing MSCs in the hydrogel did not significantly change the O_2 diffusion across the sample as compared with the acellular hydrogel (Figure 3). Figure 6 shows the small differences in maxima and minima of O_2 concentration observed in W = 500-µm lung ECM hydrogels in three cases: acellular and seeded with MSCs at two concentrations (300 and 450 × 10^3 cells/mL).

Figure 7 shows the O_2 concentration recordings in mouse brain slices for 500-µm and 300-µm thicknesses. This figure further illustrates that changing the gas concentration flowing beneath the membrane (in this case 95%/50% O_2) allowed modulation of the maximum and minimum of oxygenation in the sample. For W = 500-µm, O_2 profiles were less homogeneous across the sample as compared with acellular (Figure 3) or MSC-cultured hydrogels (Figure 6). Indeed, the maximum - minimum of O_2 were 80.8%–42.0% for z = 100 µm and 66.3%–34.0% for z = 400 µm (Figure 7A). In contrast, the intermittent hypoxia experienced across 300-µm mouse brain slices was nearly homogeneous, with maximum - minimum of O_2 of 90.5%–49.0% for *z* = 50 µm and 82.3%—44.3% for *z* = 250 µm (Figure 7B).

4 Discussion

This study provides initial and compelling experimental evidence that it is possible to apply well-controlled fast intermittent hypoxia

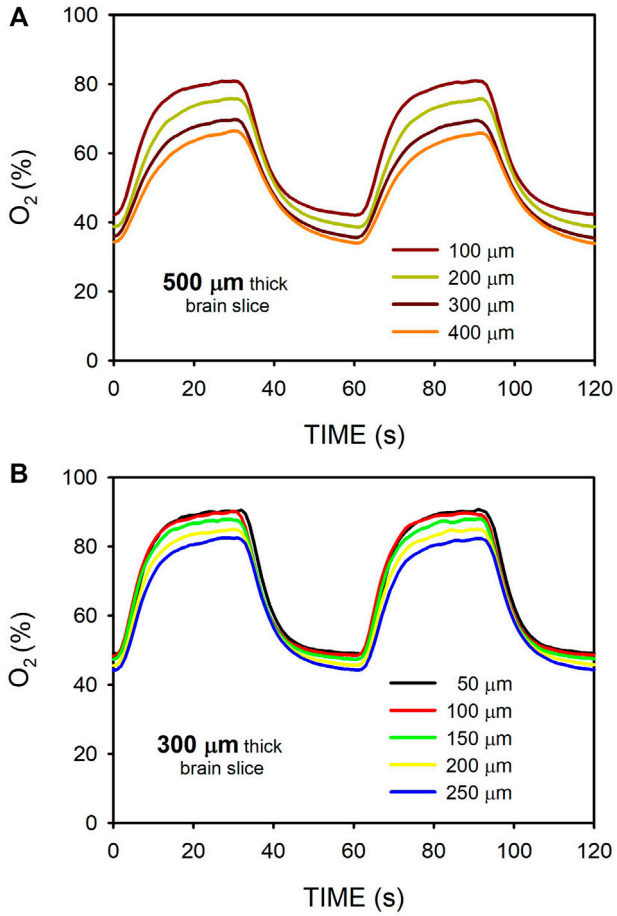

FIGURE 7
Oxygen concentration measured at different positions (Figure 2A) within mouse brain slices when the intermittent air circulating beneath the membrane was 95% O_2 for 30 s and 50% O_2 for 30 s. **(A)** O_2 measured at the hippocampus of a 500-µm thick slice. **(B)** Same as in **(A)** for a slice thickness of 300-µm.

cycling to cultured cells in 3D environments mimicking severe sleep apnea, either when using an ECM hydrogel or when cells are maintained *ex vivo* in tissue slices.

In addition to its robust and reliable performance, one advantage of the experimental setting employed and tested in this study is its simplicity. Indeed, it is based on the fast diffusion of O_2 through a thin membrane of PDMS, a material with a coefficient of diffusion for O_2 ($D \approx 3.5 \times 10^{-5}$ cm^2/s) slightly higher than that of water ($\approx 2.5 \times 10^{-5}$ cm^2/s) (Farré et al., 2018). Thus, the 3D diffusion time ($\Delta t = L^2/6{\cdot}D$) for O_2 corresponding to a membrane with a thickness L = 100–200 µm is .5–2 s, a time much shorter than the periods of intermittent hypoxia in severe OSA (60 apneas/h). In this study, we used a commercially available PDMS membrane that was not particularly thin (165 µm). Therefore, employing thinner membranes (≤100 µm) as the ones also used in the bottom of cell culture wells (Campillo et al., 2016) could further fasten the transmission of O_2 concentration changes to the 3D sample. Interestingly, as it does not require the use of complex microfluidic tools, this experimental setting can be easily employed by any cell biology laboratory: PDMS bottom wells are already commercially available or can be easily homemade (Campillo et al., 2016; Campillo et al., 2019). The other component required is a flow of intermittent hypoxic-normoxic gas beneath the membrane. It is of note that using a relatively expensive blender like the one employed in this work is not necessary. Indeed, the required square wave of O_2 concentration can be achieved in a much easier and cheaper way by simply connecting the inlet of the well to two conventional sources of gas. For instance, compressed gas bottles (with a low-pressure regulator) can be alternatively connected to the well by a simple on-off timer (either by two low-cost perfusion pumps or a 3-way controllable valve).

The O_2 microsensor was employed to characterize the specific levels and dynamics of hypoxia applied to the different 3D materials (hydrogels or tissue slices) and thicknesses. Therefore, once a given setting is defined, carrying out repeated and systematic experiments to study cell behavior should not require continued O_2 measurements across all experiments. However, using the sensor is advisable when designing a specific experiment given that different hydrogels/tissues, and mainly their thickness, modify O_2 transmission across the sample. It should be mentioned that an O_2 microsensor device similar to the one employed in this study (or one based on Clark micro-electrode (Almendros et al., 2011) is not expensive (Otero et al., 2021). It is also worth noting that although we focused only on the application of intermittent hypoxia, the setting could easily be used for also applying intermittent hypercapnia which parallels intermittent hypoxia in OSA and is another challenge to normal cell response. Alternatively, both intermittent hypoxia and hypercapnia could be also implemented easily by a pre-mixed gas source, thereby reproducibly simulating naturally occurring events in patients with OSA (Imamura et al., 2019; Tripathi et al., 2019). However, we did not test intermittent hypercapnia because there is no available CO_2 sensor with the size and time resolutions required for this application. Nevertheless, it can be anticipated that the setting would also work for intermittent hypercapnia, taking into account that the coefficients of diffusion for CO_2 in PDMS (2.2×10^{-5} cm^2/s) and water (2.1×10^{-5} cm^2/s) are only slightly lower than for O_2 (Hou et al., 2010; Kanehashi et al., 2012).

The results obtained in W = 500-µm hydrogels (Figure 3; Figure 5) show that O_2 diffusion through the 3D scaffold was sufficiently fast to allow high-frequency intermittent hypoxia requiring 30-s for raising and decreasing times in O_2 concentration across the 3D sample. Interestingly, ≈500 µm is a commonly used thickness for the research of 3D cell-seeded samples (De Hilster et al., 2020; Falcones et al., 2021; Marhuenda et al., 2022). The suitability of this thickness for optimal application of 60 hypoxic events/h was expected taking into account that the O_2 coefficient of diffusion D in this type of hydrogel is slightly lower than that of water. Indeed, data from O_2 diffusion studies in similar hydrogels (alginate, agarose, collagen, dense fibrin, reconstituted basement membrane (rBM/Matrigel)) indicate that D ranges around 75% of D in water (Ehsan and George, 2013; Colom et al., 2014). Also, it has been shown that in alginate and agarose hydrogels, the diffusion of small molecular weight species such as O_2 is not significantly affected by the characteristics of the matrix (Li et al., 1996). Hence, assuming $D = 1.87 \times 10^{-5}$ cm^2/s (75% of D in water), the diffusion time would be $\Delta t = 22$ s which fits with the apparent time-constant of the quasi-exponential variation pattern of O_2 concentration changes (Figure 3). However, it is remarkable that the diffusion rate and, thus, the amplitude of the high-frequency intermittent hypoxia cycles achieved largely depends on W, as illustrated by comparing the results of O_2 cycling across two hydrogels that only differed in thickness. Whereas for W = 500 µm the

transmission of O_2 cycling was very satisfactory (Figure 3A), in the case of W = 800 μm the attenuation of O_2 cycles amplitude was so apparent (Figure 3B) that no application of uniform intermittent hypoxia could be ensured for cells residing across the hydrogel. This considerable difference in results when comparing 500 μm and 800 μm thicknesses is not surprising given the quadratic dependence of the diffusion time Δt on L ($\Delta t = L^2/6{\cdot}D$). Indeed, Δt would be 57 s for L = 800 μm (as compared with 22 s for L = 500 μm), a time similar to the period of oscillation for 60 events/h.

Theoretically, the coefficient of diffusion D is not the only factor affecting the rate of O_2 concentration change in cell-containing 3D scaffolds. Indeed, the rate of decreasing concentration $C(z,t)$ depends on the coefficient of diffusion D according to the second Fick law and also on the cellular O_2 consumption rate per unit volume of the material. Assuming that cellular O_2 consumption follows the Michaelis-Menten kinetics:

$$\frac{\partial C(z,t)}{\partial t} = D\frac{\partial^2 C(z,t)}{\partial z^2} - \frac{\rho_{cell} \cdot sOCR \cdot C(z,t)}{K_m + C(z,t)} \quad (1)$$

where ρ_{cell} is cell density, sOCR is the maximum rate of O_2 consumption per single cell, and K_m is the half-maximum rate of O_2 concentration (Magliaro et al., 2019). When considering Eq. 1 in the case of O_2 unidirectionally flowing through a membrane-like hydrogel with thickness W, the rate of O_2 consumption (V'_{con}) per unit area within the volume can be estimated as

$$V'_{con} = \frac{\rho_{cell} \cdot sOCR \cdot C_{mean} \cdot W}{(K_m + C_{mean})} \quad (2)$$

where C_{mean} is the average O_2 concentration across the construct. The diffusion flow (V'_{dif}) across the membrane-like hydrogel is

$$V'_{dif} = \frac{D \cdot \Delta C}{W} = \frac{D \cdot \alpha \cdot \Delta P}{W} \quad (3)$$

where ΔC is the difference in O_2 concentration across the construct, α is the solubility of O_2 in the material (assuming that of water $\alpha = 1.1 \times 10^{-6}$ mol/(cm^3 · atm)) and ΔP is the difference of O_2 partial pressure across the membrane-like hydrogel. Therefore, the ratio between consumed and diffused O_2 flows is

$$\frac{V'_{con}}{V'_{dif}} = \frac{\rho_{cell} \cdot sOCR \cdot C_{mean} \cdot W^2}{D \cdot \alpha \cdot \Delta P \cdot (K_m + C_{mean})} \quad (4)$$

Given the quadratic dependence of this ratio on W, the role played by O_2 consumption is decreased as the hydrogel thickness is reduced. Indeed, assuming W = 500 μm, ΔP = 152 mmHg (corresponding to a difference from 20% O_2 to 0% O_2), and taking the parameters ($D = 1.2 \times 10^{-5}$ cm^2/s, sOCR = 1.22×10^{-16} mol/(cell·s), and $K_m = 4.1 \times 10^{-6}$ mol/cm^3) reported (Magliaro et al., 2019) for a collagen hydrogel seeded with hepatocytes with a cell concentration $\rho_{cell} = 500 \times 10^3$ cell/cm^3, Eq. 4 results in a ratio V'_{con}/V'_{dif} = .015, indicating that, in this case, the consumption of O_2 can be neglected when compared with O_2 diffusion. This conclusion remains valid when using the parameters measured for a cell concentration one order of magnitude higher (5×10^6 cell/cm^3) (Magliaro et al., 2019) or when considering cell types other than hepatocytes since, together with neurons, hepatocytes are the highest O_2-consuming cells (McMurtrey, 2016). The fact that oxygen consumption is not relevant for applying O_2 cycling in thin hydrogel samples is reflected by the results in Figure 6 showing virtually no differences between acellular and cell-seeded hydrogels.

The systematic O_2 concentration measurements carried out in hydrogels have been complemented with preliminary data obtained when applying intermittent hypoxia to tissue slices. Figure 7 provides a proof-of-concept measurement in brain mouse slices having a thickness (300 and 500 μm) typical in studies using precision-cut tissue slices (Majorova et al., 2021). These results clearly suggest that, as in hydrogels, fast intermittent hypoxia can be applied to *ex vivo* tissue samples. We observed that for the same sample thickness of W = 500 μm O_2 diffusion across the brain slices was slightly slower than across the hydrogels (Figures 3, 7), resulting in a less homogeneous distribution of intermittent hypoxia as z varied. Based on the two components in Eq. 1, two potential reasons may account for this observed difference. On the one hand, the diffusion coefficient for O_2 in body tissues could be lower than in most usual hydrogels, as suggested by the few data available providing measured values of D for O_2 in native tissues (MacDougall and McCabe, 1967). On the other hand, owing to higher cell density (ρ_{cell}), the Eq. 1 component corresponding to the rate of O_2 consumption by cells could be greater in native tissues than in artificial hydrogels. Regarding this particular point, it is interesting to note that when considering specific O_2 consumption per cell (sOCR), brain tissue is most challenging for O_2 transfer given the very high metabolic rate of its cellular components (McMurtrey, 2016). Although requiring further systematic analysis to characterize reproducibility in different types of *ex vivo* slices, the results obtained in brain samples suggest that similar or even better results could be obtained in 300–500 μm tissue slices from different organs (e.g., lung, liver, kidney, heart, pancreas, spinal cord or tumors (Wang et al., 2015; Stribos et al., 2016; Wu et al., 2019; Dewyse et al., 2021; Dimou et al., 2022)) particularly affected by end-organ OSA morbidity (Sánchez-de-la-Torre et al., 2013; Gileles-Hillel et al., 2016; Gozal et al., 2020; Brockmann and Gozal, 2022).

In conclusion, we have characterized an experimental approach, based on existing and easily available tools, that allows for controlled and precise application of high-frequency intermittent hypoxia both to 3D cell culture scaffolds such as ECM hydrogels as well as to precision-cut tissue slices. This approach, which is an advance on previous models investigating continuous hypoxia (Svanström et al., 2021), opens the door for the study of the specific noxious effects of intermittent hypoxia in the 3D-residing cells of the organs and tissues of patients with OSA under physiomimetic conditions.

Data availability statement

The raw data supporting the conclusion of this article will be made available by the author, without undue reservation.

Ethics statement

The animal study was reviewed and approved by Ethical Committee for Animal Research of the University of Barcelona.

Author contributions

AJ performed the measurements and data processing, and contributed to drafting the manuscript. AU and HL provided

experimental support. XG, NG, RS, JO, DG, and IA contributed to planning the experiments, to data interpretation and to scientific discussion. RF conceived and supervised the study and drafted the manuscript. All authors have agreed with the published version of the article and agree to be accountable for the content of the work.

Funding

This work was partially supported by the Spanish Ministry of Science and Innovation (PID 2020-113910RB-I00-AEI/10.13039/501100011033, PID 2020-11608RB-I00, PID 2019-108958RB-I00/AEI/10.13039/501100011033, PID 2020-119305RB-I00, MCIN/AEI/10.13039/501100011033).

Conflict of interest

The authors declare that the research was conducted in the absence of any commercial or financial relationships that could be construed as a potential conflict of interest.

Publisher's note

All claims expressed in this article are solely those of the authors and do not necessarily represent those of their affiliated organizations, or those of the publisher, the editors and the reviewers. Any product that may be evaluated in this article, or claim that may be made by its manufacturer, is not guaranteed or endorsed by the publisher.

References

Allen, C. B., Schneider, B. K., and White, C. W. (2001). Limitations to oxygen diffusion and equilibration in *in vitro* cell exposure systems in hyperoxia and hypoxia. *Am. J. Physiol. Lung Cell Mol. Physiol.* 281, L1021–L1027. doi:10.1152/ajplung.2001.281.4.L1021

Almendros, I., Farré, R., Planas, A. M., Torres, M., Bonsignore, M. R., Navajas, D., et al. (2011). Tissue oxygenation in brain, muscle, and fat in a rat model of sleep apnea: Differential effect of obstructive apneas and intermittent hypoxia. *Sleep* 34, 1127–1133. doi:10.5665/SLEEP.1176

Benjafield, A. V., Ayas, N. T., Eastwood, P. R., Heinzer, R., Ip, M. S. M., Morrell, M. J., et al. (2019). Estimation of the global prevalence and burden of obstructive sleep apnoea: A literature-based analysis. *Lancet Respir. Med.* 7 (8), 687–698. doi:10.1016/S2213-2600(19)30198-5

Brockmann, P. E., and Gozal, D. (2022). Neurocognitive consequences in children with sleep disordered breathing: Who is at risk? *Child. (Basel)* 9 (9), 1278. doi:10.3390/children9091278

Caliari, S. R., and Burdick, J. A. (2016). A practical guide to hydrogels for cell culture. *Nat. Methods* 13 (5), 405–414. doi:10.1038/nmeth.3839

Campillo, N., Falcones, B., Otero, J., Colina, R., Gozal, D., Navajas, D., et al. (2019). Differential oxygenation in tumor microenvironment modulates macrophage and cancer cell crosstalk: Novel experimental setting and proof of concept. *Front. Oncol.* 9, 43. doi:10.3389/fonc.2019.00043

Campillo, N., Jorba, I., Schaedel, L., Casals, B., Gozal, D., Farré, R., et al. (2016). A novel chip for cyclic stretch and intermittent hypoxia cell exposures mimicking obstructive sleep apnea. *Front. Physiol.* 7, 319. doi:10.3389/fphys.2016.00319

Colom, A., Galgoczy, R., Almendros, I., Xaubet, A., Farré, R., and Alcaraz, J. (2014). Oxygen diffusion and consumption in extracellular matrix gels: Implications for designing three-dimensional cultures. *J. Biomed. Mater Res. A* 102 (8), 2776–2784. doi:10.1002/jbm.a.34946

De Hilster, R. H. J., Sharma, P. K., Jonker, M. R., White, E. S., Gercama, E. A., Roobeek, M., et al. (2020). Human lung extracellular matrix hydrogels resemble the stiffness and viscoelasticity of native lung tissue. *Am. J. Physiol. Lung Cell Mol. Physiol.* 318 (4), L698–L704. doi:10.1152/ajplung.00451.2019

Dewyse, L., Reynaert, H., and van Grunsven, L. A. (2021). Best practices and progress in precision-cut liver slice cultures. *Int. J. Mol. Sci.* 22 (13), 7137. doi:10.3390/ijms22137137

Dimou, P., Trivedi, S., Liousia, M., D'Souza, R. R., and Klampatsa, A. (2022). Precision-cut tumor slices (PCTS) as an *ex vivo* model in immunotherapy research. *Antibodies (Basel)* 11 (2), 26. doi:10.3390/antib11020026

Duval, K., Grover, H., Han, L. H., Mou, Y., Pegoraro, A. F., Fredberg, J., et al. (2017). Modeling physiological events in 2D vs. 3D cell culture. *Physiol. (Bethesda)* 32 (4), 266–277. doi:10.1152/physiol.00036.2016

Ehsan, S. M., and George, S. C. (2013). Nonsteady state oxygen transport in engineered tissue: Implications for design. *Tissue Eng. Part A* 19 (11-12), 1433–1442. doi:10.1089/ten.TEA.2012.0587

Falcones, B., Sanz-Fraile, H., Marhuenda, E., Mendizábal, I., Cabrera-Aguilera, I., Malandain, N., et al. (2021). Bioprintable lung extracellular matrix hydrogel scaffolds for 3D culture of mesenchymal stromal cells. *Polym. (Basel)* 13 (14), 2350. doi:10.3390/polym13142350

Farré, R., Almendros, I., Montserrat, J. M., Gozal, D., and Navajas, D. (2018). Gas partial pressure in cultured cells: Patho-physiological importance and methodological approaches. *Front. Physiol.* 9, 1803. doi:10.3389/fphys.2018.01803

Farré, R., Montserrat, J. M., Ballester, E., Hernández, L., Rotger, M., and Navajas, D. (1998). Importance of the pulse oximeter averaging time when measuring oxygen desaturation in sleep apnea. *Sleep* 21 (4), 386–390. doi:10.1093/sleep/21.4.386

Gileles-Hillel, A., Kheirandish-Gozal, L., and Gozal, D. (2016). Biological plausibility linking sleep apnoea and metabolic dysfunction. *Nat. Rev. Endocrinol.* 12 (5), 290–298. doi:10.1038/nrendo.2016.22

Gozal, D., Almendros, I., Phipps, A. I., Campos-Rodriguez, F., Martínez-García, M. A., and Farré, R. (2020). Sleep apnoea adverse effects on cancer: True, false, or too many confounders? *Int. J. Mol. Sci.* 21 (22), 8779. PMID: 33233617; PMCID: PMC7699730. doi:10.3390/ijms21228779

Hou, C., Gheorghiu, S., Huxley, V. H., and Pfeifer, P. (2010). Reverse engineering of oxygen transport in the lung: Adaptation to changing demands and resources through space-filling networks. *PLoS Comput. Biol.* 6 (8), e1000902. doi:10.1371/journal.pcbi.1000902

Imamura, T., Xue, J., Poulsen, O., Zhou, D., Karin, M., and Haddad, G. G. (2019). Intermittent hypoxia and hypercapnia induces inhibitor of nuclear factor-κB kinase subunit β-dependent atherosclerosis in pulmonary arteries. *Am. J. Physiol. Regul. Integr. Comp. Physiol.* 317 (6), R763–R769. doi:10.1152/ajpregu.00056.2019

Jensen, C., and Teng, Y. (2020). Is it time to start transitioning from 2D to 3D cell culture? *Front. Mol. Biosci.* 7, 33. doi:10.3389/fmolb.2020.00033

Kanehashi, S., Sato, T., Sato, S., and Nagai, K. (2012). Microstructure and gas diffusivity of poly(dimethylsiloxane) dense membrane using molecular dynamics (MD) simulation. *Trans. Mater. Res. Soc. Jpn.* 37, 439–442. doi:10.14723/tmrsj.37.439

Kusuma, G. D., Li, A., Zhu, D., McDonald, H., Inocencio, I. M., Chambers, D. C., et al. (2022). Effect of 2D and 3D culture microenvironments on mesenchymal stem cell-derived extracellular vesicles potencies. *Front. Cell Dev. Biol.* 10, 819726. doi:10.3389/fcell.2022.819726

Li, R. H., Altreuter, D. H., and Gentile, F. T. (1996). Transport characterization of hydrogel matrices for cell encapsulation. *Biotechnol. Bioeng.* 50 (4), 365–373. doi:10.1002/(SICI)1097-0290(19960520)50:4<365::AID-BIT3>3.0.CO;2-J

MacDougall, J. D., and McCabe, M. (1967). Diffusion coefficient of oxygen through tissues. *Nature* 215 (5106), 1173–1174. doi:10.1038/2151173a0

Magliaro, C., Mattei, G., Iacoangeli, F., Corti, A., Piemonte, V., and Ahluwalia, A. (2019). Oxygen consumption characteristics in 3D constructs depend on cell density. *Front. Bioeng. Biotechnol.* 7, 251. doi:10.3389/fbioe.2019.00251

Majorova, D., Atkins, E., Martineau, H., Vokral, I., Oosterhuis, D., Olinga, P., et al. (2021). Use of precision-cut tissue slices as a translational model to study host-pathogen interaction. *Front. Vet. Sci.* 8, 686088. doi:10.3389/fvets.2021.686088

Marhuenda, E., Villarino, A., Narciso, M., Elowsson, L., Almendros, I., Westergren-Thorsson, G., et al. (2022). Development of a physiomimetic model of acute respiratory distress syndrome by using ECM hydrogels and organ-ona-chip devices. *Front. Pharmacol.* 13, 945134. doi:10.3389/fphar.2022.945134

McMurtrey, R. J. (2016). Analytic models of oxygen and nutrient diffusion, metabolism dynamics, and architecture optimization in three-dimensional tissue constructs with applications and insights in cerebral organoids. *Tissue Eng. Part C Methods* 22 (3), 221–249. doi:10.1089/ten.TEC.2015.0375

Minoves, M., Morand, J., Perriot, F., Chatard, M., Gonthier, B., Lemarié, E., et al. (2017). An innovative intermittent hypoxia model for cell cultures allowing fast Po2 oscillations with minimal gas consumption. *Am. J. Physiol. Cell Physiol.* 313, C460–C468. doi:10.1152/ajpcell.00098.2017

Moreno-Indias, I., Torres, M., Montserrat, J. M., Sanchez-Alcoholado, L., Cardona, F., Tinahones, F. J., et al. (2015). Intermittent hypoxia alters gut microbiota diversity in a mouse model of sleep apnoea. *Eur. Respir. J.* 45, 1055–1065. doi:10.1183/09031936.00184314

Otero, J., Ulldemolins, A., Farré, R., and Almendros, I. (2021). Oxygen biosensors and control in 3D physiomimetic experimental models. *Antioxidants (Basel)* 10 (8), 1165. doi:10.3390/antiox10081165

Pouliot, R. A., Link, P. A., Mikhaiel, N. S., Schneck, M. B., Valentine, M. S., Kamga Gninzeko, F. J., et al. (2016). Development and characterization of a naturally derived lung extracellular matrix hydrogel. *J. Biomed. Mater Res. A* 104 (8), 1922–1935. doi:10.1002/jbm.a.35726

Reinke, C., Bevans-Fonti, S., Drager, L. F., Shin, M. K., and Polotsky, V. Y. (2011). Effects of different acute hypoxic regimens on tissue oxygen profiles and metabolic outcomes. *J. Appl. Physiol.* 111, 881–890. doi:10.1152/japplphysiol.00492.2011

Sánchez-de-la-Torre, M., Campos-Rodriguez, F., and Barbé, F. (2013). Obstructive sleep apnoea and cardiovascular disease. *Lancet Respir. Med.* 1 (1), 61–72. doi:10.1016/S2213-2600(12)70051-6

Stribos, E. G., Hillebrands, J. L., Olinga, P., and Mutsaers, H. A. (2016). Renal fibrosis in precision-cut kidney slices. *Eur. J. Pharmacol.* 790, 57–61. doi:10.1016/j.ejphar.2016.06.057

Svanström, A., Rosendahl, J., Salerno, S., Jonasson, E., Håkansson, J., Ståhlberg, A., et al. (2021). The effect of hypoxic and normoxic culturing conditions in different breast cancer 3D model systems. *Front. Bioeng. Biotechnol.* 9, 711977. doi:10.3389/fbioe.2021.711977

Tibbitt, M. W., and Anseth, K. S. (2009). Hydrogels as extracellular matrix mimics for 3D cell culture. *Biotechnol. Bioeng.* 103 (4), 655–663. doi:10.1002/bit.22361

Torres, M., Laguna-Barraza, R., Dalmases, M., Calle, A., Pericuesta, E., Montserrat, J. M., et al. (2014). Male fertility is reduced by chronic intermittent hypoxia mimicking sleep apnea in mice. *Sleep* 37, 1757–1765. doi:10.5665/sleep.4166

Tripathi, A., Xu, Z. Z., Xue, J., Poulsen, O., Gonzalez, A., Humphrey, G., et al. (2019). Intermittent hypoxia and hypercapnia reproducibly change the gut microbiome and metabolome across rodent model systems. *mSystems* 4 (2), e00588–19. doi:10.1128/mSystems.00058-19

Wang, K., Lee, P., Mirams, G. R., Sarathchandra, P., Borg, T. K., Gavaghan, D. J., et al. (2015). Cardiac tissue slices: Preparation, handling, and successful optical mapping. *Am. J. Physiol. Heart Circ. Physiol.* 308 (9), H1112–H1125. doi:10.1152/ajpheart.00556.2014

Wu, X., van Dijk, E. M., Bos, I. S. T., Kistemaker, L. E. M., and Gosens, R. (2019). Mouse lung tissue slice culture. *Methods Mol. Biol.* 1940, 297–311. doi:10.1007/978-1-4939-9086-3_21

frontiers | Frontiers in Pharmacology

TYPE Mini Review
PUBLISHED 13 January 2023
DOI 10.3389/fphar.2022.1083017

OPEN ACCESS

EDITED BY
Rebecca L. Heise,
Virginia Commonwealth University,
United States

REVIEWED BY
Nikhil Tanaji Awatade,
The University of Newcastle, Australia
Chelsea M. Magin,
University of Colorado Denver,
United States

*CORRESPONDENCE
Robert E. Hynds,
rob.hynds@ucl.ac.uk

†These authors have contributed equally to this work and share first authorship

SPECIALTY SECTION
This article was submitted to Respiratory Pharmacology, a section of the journal Frontiers in Pharmacology

RECEIVED 28 October 2022
ACCEPTED 28 December 2022
PUBLISHED 13 January 2023

CITATION
Hughes T, Dijkstra KK, Rawlins EL and Hynds RE (2023), Open questions in human lung organoid research.
Front. Pharmacol. 13:1083017.
doi: 10.3389/fphar.2022.1083017

Open questions in human lung organoid research

Tessa Hughes[1†], Krijn K. Dijkstra[2,3†], Emma L. Rawlins[1] and Robert E. Hynds[4,5,3*]

[1]Wellcome Trust/CRUK Gurdon Institute and Department Physiology, Development and Neuroscience, University of Cambridge, Cambridge, United Kingdom, [2]Department of Molecular Oncology and Immunology, The Netherlands Cancer Institute, Amsterdam, Netherlands, [3]Cancer Evolution and Genome Instability Laboratory, The Francis Crick Institute, London, United Kingdom, [4]Epithelial Cell Biology in ENT Research (EpiCENTR) Group, Developmental Biology and Cancer Department, Great Ormond Street UCL Institute of Child Health, University College London, London, United Kingdom, [5]CRUK Lung Cancer Centre of Excellence, UCL Cancer Institute, University College London, London, United Kingdom

Organoids have become a prominent model system in pulmonary research. The ability to establish organoid cultures directly from patient tissue has expanded the repertoire of physiologically relevant preclinical model systems. In addition to their derivation from adult lung stem/progenitor cells, lung organoids can be derived from fetal tissue or induced pluripotent stem cells to fill a critical gap in modelling pulmonary development *in vitro*. Recent years have seen important progress in the characterisation and refinement of organoid culture systems. Here, we address several open questions in the field, including how closely organoids recapitulate the tissue of origin, how well organoids recapitulate patient cohorts, and how well organoids capture diversity within a patient. We advocate deeper characterisation of models using single cell technologies, generation of more diverse organoid biobanks and further standardisation of culture media.

KEYWORDS

lung stem cells, respiratory biology, 3D cell culture, in vitro models, epithelial cells

1 Introduction

Organoid cultures are *in vitro* models derived from stem/progenitor cells, and involve the generation of a heterocellular structure that is reminiscent of the tissue of origin in a three-dimensional cell culture environment (Barkauskas et al., 2017; Liberti and Morrisey, 2021; Sen et al., 2022). In the human respiratory system, nasal (Liu et al., 2020; Rodenburg et al., 2022), tracheobronchial (Rock et al., 2009; Sachs et al., 2019), small airway (Basil et al., 2022) and alveolar (Katsura et al., 2020; Salahudeen et al., 2020; Youk et al., 2020) epithelial organoid models have all been generated from post-natal tissue-resident stem cells. Additionally, organoid cultures derived from developing lung epithelia have been described (Nikolić et al., 2017; Miller et al., 2018), and the stepwise differentiation of pluripotent stem cells has been used to derive mature lung organoids and those resembling developmental intermediates (Jacob et al., 2017; Hawkins et al., 2021; Hein et al., 2022). In addition to providing a platform to study lung stem cell biology, organoids present a platform to investigate respiratory diseases, including developmental disorders such as bronchopulmonary dysplasia (Riccetti et al., 2022), genetic disorders such as cystic fibrosis (Sachs et al., 2019) and ciliary dyskinesias (van der Vaart et al., 2021a), chronic respiratory diseases such as chronic obstructive pulmonary disease (COPD) (Ng-Blichfeldt et al., 2018) and lung cancers (Sachs et al., 2019).

Recent, comprehensive reviews are available on advances in methods to derive lung organoids, and the potential uses of organoids in basic research and translational medicine (Evans and Lee, 2020; van der Vaart et al., 2021b; Liberti and Morrisey, 2021; Sen et al., 2022).

While lung organoids can also be derived from mouse lung epithelia, offering an opportunity to address some research questions *in vitro* and reduce the use of animals used in model species research, we will focus on pertinent open questions within the human lung organoid field with relevance across developmental, post-natal stem cell and cancer studies.

2 How closely do lung organoids recapitulate their tissue of origin?

To increase the likelihood of relevant findings, it is crucial that organoids mimic the tissue of interest as closely as possible. To this end, the development of multiple organoids to capture the diversity of cells within developing lungs, adult homeostatic lungs and tumours has been ongoing. It is important to note that in developmental studies, organoids are typically derived from progenitor cells that are capable of differentiation into different tissue types (e.g., airway and alveolar), while adult lung organoids are typically region-specific with less plasticity.

Developmental studies currently tend to favour the use of induced pluripotent stem cells (iPSCs) due to issues of scalability, availability and the fact that iPSCs represent a better-defined starting population than those available from foetal tissue. Customised media have been developed to expand specific cellular subpopulations from iPSCs; in the airways, basal cells and secretory progenitor cells have all been induced from iPSCs (McCauley et al., 2017; McCauley et al., 2018; Hawkins et al., 2021) and, when cultured at an air-liquid interface, goblet cells and ciliated cells have also been generated from iPSCs (Firth et al., 2014; McCauley et al., 2017). For alveolar modelling, iPSCs and human embryonic stem cells (hESCs) have been used to derive AT2 cells (Jacob et al., 2017; 2019; Tamò et al., 2018; Hurley et al., 2020), which can exhibit relevant morphological characteristics, such as lamellar bodies and microvilli. However, although some iPSC-derived AT2 organoids are stable in long-term culture, there are reported stability issues with cells reverting to non-lung fates.

At the histological level, airway and lung cancer organoids can resemble their *in vivo* tissue of origin remarkably well, despite the absence of stroma *in vitro* (Kim et al., 2019; Sachs et al., 2019; Li et al., 2020). Airway organoids contain all of the major airway epithelial cell types, with basal cells, mucosecretory cells and ciliated cells present (Rock et al., 2009; Sachs et al., 2019), although the consistency with which they contain rare populations such as neuroendocrine cells, ionocytes and tuft cells is unclear. Removing extracellular matrix cues can generate organoids with cilia on their outer surface, which has clear advantages for studies of motile cilia (Wijesekara et al., 2022). Media composition appears to be vital in the selection of airway vs. alveolar cells from adult lung tissue, as studies using distal lung resection tissue for organoid generation have led to airway organoid formation but an absence of alveolar organoids (Sachs et al., 2019), in contrast to earlier mouse lung organoid studies in which both organoid types were observed within the same cultures (Lee et al., 2014). The resemblance of alveolar organoids to the alveolus is more limited given the dependence of this tissue on precise architecture. Alveolar organoids typically consist of proliferative AT2-like cells but lack AT1-like cells, though cells resembling AT1 cells can be induced by 2D culture (Youk et al., 2020), suspension culture (Salahudeen et al., 2020) or using inductive culture media (Katsura et al., 2020; Konishi et al., 2022).

Although progenitor differentiation to mature adult cell types is a common goal, the lack of complete lineage characterisation hinders our ability to fully distinguish these differentiated cell types. At present, many iPSC studies accomplish progenitor specification but are not able to fully substantiate claims of mature cells. Marker protein expression remains the most common means to identify differentiated cell types within organoids, which is not in itself sufficient to demonstrate full maturity or functionality. Additional confusion arises when mouse markers are extrapolated to human lung cell types as, particularly in the developing lung, numerous distinct cell types can share marker expression (Miller et al., 2020; He et al., 2022) and marker expression can be transient (McCauley et al., 2018). To overcome this, recent studies have combined marker expression data with spatial information, transcriptomic analysis and organelle characterisation (Dye et al., 2015; Miller et al., 2019; 2020; Sachs et al., 2019; Hurley et al., 2020; Hein et al., 2022). The derivation of organoids that capture the intermediary stages of lung development has also been explored. Bud tip progenitors can be derived from iPSCs, which in turn have the potential to differentiate into all lung epithelial cell types (Hein et al., 2022). iPSCs were also used to culture a progenitor population enriched in basal cells that were reminiscent of those from foetal lungs (Ngan et al., 2021).

The increase in single-cell and bulk RNA sequencing studies of human lung is allowing greater benchmarking of organoid systems and comparisons of iPSC and embryonic tissue-derived cells (Ngan et al., 2021; Alysandratos et al., 2022; He et al., 2022; Murthy et al., 2022). Although cell culture often produces less robust and less mature differentiated cells, iPSC-derived organoids frequently produce more immature cell types than hESC-derived organoids, citing the need for additional validation in these studies, such as through lineage tracing or trajectory analysis (Hurley et al., 2020; Hawkins et al., 2021). In protocols that highlight stepwise differentiation and intermediary stages, the order of differentiation should be carefully analysed, such as by visualising differentiating structures, ensuring proximal-distal cell patterning has been conserved, and/or by matching with corresponding *in vivo* sequencing data. This level of detail allows for a sequence of key developmental milestones and transitional states to be uncovered, and potentially better recapitulation of human foetal lung development (He et al., 2022). A major limitation across lung organoid studies is the lack of direct comparison to the *in vivo* tissue, and as yet, the field has not created a standardised protocol for definitively assessing cell maturity and identity. Additionally, there is a large amount of variation between iPSC lines, with some unable to generate mature lung cells.

In contrast to developmental and adult lung organoid studies, the resemblance of cancer organoids to their tumours of origin has been most extensively studied at the genomic level. There is a relatively high concordance (± 80%) of single nucleotide variants (SNVs) and copy number alterations (CNAs). Although whole exome sequencing has been performed in some studies (Kim et al., 2019; 2021; Shi et al., 2020; Hu et al., 2021), others have investigated a limited set of cancer driver genes (Sachs et al., 2019; Chen et al., 2020; Li et al., 2020). Since targeted approaches tend to target clonal mutations (those that are found in every cancer cell), they identify mutations that are less susceptible to loss during organoid culture. Whether lung cancer organoids recapitulate the full spectrum of (subclonal) cancer mutations is not yet clear; while on average the genetic

concordance between organoids and tumour tissue is high, for some samples the concordance is considerably lower (Kim et al., 2019; Shi et al., 2020), which most likely reflects the selective outgrowth of minor tumour subclones in those organoid cultures.

The extent to which lung cancer organoids diverge from tumour tissues at the phenotypic level is much less clear. Since organoid culture systems were originally developed to expand epithelial stem cells (Sato et al., 2009), it is unclear if lung cancer organoids can reflect tumour cells with different degrees of differentiation. Organoids established from distinct histological subtypes retain characteristic features, such as a cystic morphology for organoids from acinar adenocarcinoma, and a solid morphology for organoids from the solid subtype (Li et al., 2020). This suggests that tumour histology is at least in part shaped by tumour-intrinsic factors and independent of the tumour microenvironment (TME). The few reports of transcriptomic comparisons of lung cancer organoids and primary tissue are limited to overall concordance rates, which is (as expected) lower than genomic similarity, partially due to the absence of TME pathways (Shi et al., 2020; Hu et al., 2021). The absence of the TME might have profound effects on organoid phenotype and drug responses, as has been shown for pancreatic adenocarcinoma organoids (Raghavan et al., 2021). A more thorough transcriptomic and proteomic comparison of organoids and tumour tissues is needed to identify where divergence occurs. While organoids can converge upon culture specific transcriptional states, these can be modified by adding "missing" paracrine signals from the TME to the media (Raghavan et al., 2021). Alternatively, the TME can be partly reconstituted by adding back cell types of interest, such as lymphocytes or fibroblasts (reviewed in (Fiorini et al., 2020)).

The majority of lung organoid cultures are currently performed as mono (epithelial) cultures, although investigations of epithelial-fibroblast (Tan et al., 2019) or epithelial-macrophage (Iakobachvili et al., 2022) interactions have been possible. Epithelial-mesenchymal organoids have been developed from both embryonic cell lines and iPSCs, which contained basal cells, immature ciliated cells, smooth muscle and myofibroblasts (Dye et al., 2015). Additionally, iPSC differentiation generated organoids that contained bronchi-like structures surrounded by mesenchyme, and cells expressing alveolar markers (Miller et al., 2019). Multi-organ systems have also begun to be developed; iPSCs can be differentiated into cardiac and lung epithelial lineages to establish cardio-pulmonary micro-tissues (Ng et al., 2022).

While we advocate a better phenotypic characterisation of lung organoids to investigate their resemblance to lung tissue, it must be emphasised that organoids will always remain a reductionist model. The generalisation or translational relevance of results obtained in this culture system is best validated using orthogonal model systems (e.g., mouse models, 2D primary cultures, precision-cut lung slices) or datasets (including publicly available omics datasets). Moreover, it is not possible to reproduce the complete *in vivo* complexity of epithelial-stromal or epithelial-immune interactions, nor systemic variables such as nutrient availability, mechanical forces and circadian rhythms.

3 How well do organoid cultures represent patient cohorts?

A second important aspect of organoid modelling is the extent to which it is possible to capture the biology of the target population. Primary human bronchial epithelial cell cultures can show wide inter-patient variability in differentiation potential and response to stimulation, and so studying sufficient numbers of patient cultures is crucial, particularly when studying phenomena that are likely to vary with biological characteristics of the donor, such as age and/or sex (Peretz et al., 2016; Maughan et al., 2022). At present, organoid studies typically investigate cells isolated from small numbers of human donors and these cultures are rarely common between investigations from independent laboratories, due to limitations around access to human material, restrictions imposed by ethical approvals, and administrative and practical difficulties in sharing tissue or cultures within and between countries.

Organoids have been derived from patients across a wide range of respiratory diseases, including pulmonary fibrosis (Surolia et al., 2019), primary ciliary dyskinesia (van der Vaart et al., 2021a) and cystic fibrosis (Sachs et al., 2019). An extensive organoid collection from 664 cystic fibrosis patients has been reported (Geurts et al., 2020) meaning that models are now available for a wide range of causative mutations; however, these are rectal rather than lung organoids, since airway organoid forskolin-induced swelling is highly variable and limited to well-differentiated organoids. However, in chronic respiratory diseases the use of patient-derived organoids has been limited, likely due to a combination of the difficulty in obtaining material from patients with COPD and pulmonary fibrosis, the invasive nature of procedures to obtain samples, and the intrinsic lower potential of cells from these patients to generate organoid cultures (Ghosh et al., 2018). The extent to which organoid collections capture the diversity within patient cohorts will be disease-specific and depend on factors such as the opportunity to obtain research biopsies (clinically, but also geographically), the stage at which disease is most commonly diagnosed, and/or the diversity of disease phenotypes. iPSC technology might help to improve the range of chronic respiratory disease organoid models available, although pluripotent cell derived-organoids can have immature phenotypes, resembling fetal, rather than adult, transcriptional profiles. Indeed, a recent study of non-alcoholic fatty liver disease pooled iPSC-derived progenitors cells from 24 genotyped donors and derived mixed donor organoid cultures, before inducing a disease-relevant phenotype to investigate phenotype-genotype interactions (Kimura et al., 2022), suggesting that in the future lung organoid models may also have a role in identifying risk factors in addition to studying disease pathogenesis.

To date, lung cancer research has benefited most from organoid-based disease modelling. As many hundreds of organoid lines have been developed by multiple laboratories worldwide, it is possible to assess the extent to which they reflect non-small cell lung cancer (NSCLC) patient cohorts. Surprisingly, organoid establishment rates are similar for lung squamous cell carcinomas or adenocarcinomas (Kim et al., 2019; Shi et al., 2020; Hu et al., 2021), despite their distinct cells of origin, divergent driver gene landscapes, and the use of one medium composition across histological subtypes. Organoids for diverse histological subtypes (e.g., acinar, lepidic, or solid adenocarcinomas) (Kim et al., 2019; Li et al., 2020) have been reported, although a systematic comparison of organoid establishment across subtypes is lacking. It is likely that current approaches are biased towards establishing organoids from certain tumour phenotypes and/or genotypes. Moreover, each of these

TABLE 1

How closely do lung organoids recapitulate their tissue of origin?	
Challenges	Potential Solutions
• In developmental studies, assessment of cell maturity and identity relies too heavily on expression of markers, which can have low specificity • Adult lung and cancer organoids lack data to determine to what extent they diverge phenotypically from their tissue of origin	• Combining marker expression data with spatial information, transcriptomic analysis and organelle characterisation • Proteomic and transcriptomic characterisation of organoids and tissue of origin at the single cell level • Systematic identification of the influence of how medium composition and co-culture with non-epithelial (e.g. immune cells) influence organoid phenotype
How well do organoid cultures represent patient cohorts?	
Challenges	Potential Solutions
• Success rates in lung cancer organoid establishment differ widely between laboratories • There is poor representation of pre-invasive disease in organoid cancer models • Most chronic pulmonary diseases have limited model availability	• Systematic comparison of different lung cancer organoid derivation protocols • Identification of transcriptional or genomic features associated with successful lung cancer organoid establishment through collaborative efforts • Disease modelling using genetic engineering of stem cell derived or non-diseased lung organoids
To what extent does an organoid capture diversity within a patient?	
Challenges	Potential Solutions
• Intra-patient (spatial) heterogeneity is not considered in the establishment chronic pulmonary disease organoids • There is potential loss of intratumour heterogeneity in lung cancer organoids	• More detailed reporting on biopsy location when establishing organoids for chronic pulmonary disease • Multi-region organoid establishment combined with high coverage sequencing to detect sub-clonal mutations

studies differ in patient cohorts, the tissue digestion protocol used, medium formulation, and criteria of what is considered a successful culture, making it challenging to determine important contributors to successful cultures and resulting in organoid establishment rates of between 15% and 80% (Ma et al., 2022). The field would benefit from standardisation, including systematic comparisons of different protocols. Given the heterogeneity of lung cancer there may not be a "one size fits" medium formulation, and the choice of medium could be guided by driver gene status or features of the tumour TME (Fujii et al., 2016). Larger studies should explore any transcriptional or genomic features that are associated with culture success. Given the heterogeneity of lung cancer, this will likely be best achieved through large-scale collaborative efforts.

To date, most studies have generated lung cancer organoids from surgical resections of primary tumours. To our knowledge, no organoid models have been generated from pre-invasive disease, but pre-cancer organoids would be particularly valuable to study events in early tumourigenesis. Since most lung cancer patients die from metastatic disease, representing these in organoid collections would be valuable. One study established organoids from malignant effusions from patients with advanced lung cancer with a high success rate (Kim et al., 2021), suggesting that establishment rates from metastatic disease could be higher than for early stage disease. Organoid establishment from extrapulmonary metastases can also avoid contamination with normal airway organoids (Sachs et al., 2019; Dijkstra et al., 2020).

An alternative approach to deriving organoids from lung disease patient cohorts, is to use the available model systems to investigate specific hypotheses related to the disease process. In this regard, pluripotent cell-derived organoids have proved useful pulmonary fibrosis models. Introducing Hermansky-Pudlak syndrome (HPS) mutations associated with interstitial pneumonia using CRISPR-Cas9 promotes fibrotic changes in ES-derived lung organoids (Strikoudis et al., 2019) or iPSCs from patients (Korogi et al., 2019), while treatment of iPSC-derived AT2 organoids with bleomycin also promotes fibrotic changes (Suezawa et al., 2021). Moreover, early disease models can be generated by recapitulating aspects of disease development in lung organoids. For example, insights into pulmonary fibrosis have arisen from treating cells with TGFb (Ng-Blichfeldt et al., 2019). These approaches, akin to the sequential introduction of cancer driver mutations into normal organoid cultures to study early events in tumourigenesis (Dost et al., 2020), have the potential to reveal new insights compared to organoids from established disease.

4 To what extent does an organoid culture capture diversity within a patient?

Intra-patient heterogeneity likely represents an understudied source of variation in lung organoid research. At present, authors typically report the diagnosis of the patient from whom organoids were derived and the tissue of origin. However, airway epithelial cell phenotype is known to vary in the proximal-distal axis within normal lungs with cells from the upper airways having distinct transcriptomic profiles (Deprez et al., 2020; Hou et al., 2020), innate immune defences (Mihaylova et al., 2018), and susceptibility to infection (Hou et al., 2020), compared to those from the lower airways. As an example, organoid origins (proximal versus distal, as well as pluripotent versus adult) might partially explain the divergent cell types that have been seen to be infected with SARS-CoV-2 in lung organoid studies (Han et al., 2022). Moreover, patients with chronic respiratory diseases might display additional heterogeneity, particularly as IPF distal airway epithelial cells respond differently in cell culture to proximal epithelial cells from the same patient (Stancil et al., 2021). Since pulmonary fibrosis is characterised by upper lobe emphysema and lower

lobe fibrosis, the environment that cells experience even within the same lung varies and might influence their subsequent behaviour. As such, the precise location of a biopsy is likely to be consequential for experimental reproducibility.

Lung cancers are genetically and phenotypically heterogeneous, but the extent to which this is maintained in lung cancer organoid cultures is so far poorly characterised. Given the variable establishment rates of lung cancer organoids, bottlenecks are expected that restrict heterogeneity *in vitro*. Indeed, one study reported a low correlation of variant allele frequencies (VAFs) between organoids and original tumours in approximately half of the samples analysed (Kim et al., 2019). Evidence for selective subclonal outgrowth has also been observed in bladder (Lee et al., 2018) and colorectal cancer organoids (van de Wetering et al., 2015). This could be due to sampling bias, selective clonal outgrowth, or tumour evolution driven by ongoing genetic instability. While the genetic landscape of organoids is relatively stable during long-term culture (Kim et al., 2019), there is evidence for ongoing genetic instability and clonal selection from single cell sequencing and barcoding studies (Bolhaqueiro et al., 2019; Karlsson et al., 2022; Kester et al., 2022). The establishment of organoids from separate tumour regions, possibly combined with the generation of clonal organoid lines at early passage, could prevent the loss of minor subclones (Fujii et al., 2016; Roerink et al., 2018). Evaluating the extent to which genetic heterogeneity is preserved requires sequencing organoids and tumour tissues at sufficient coverage to detect subclonal mutations.

5 Conclusion

Lung organoids provide a cell culture platform to study lung development, stem/progenitor cell biology and disease pathogenesis. Several open questions remain, however, concerning their ability to recapitulate the tissue of origin and *in vivo* processes, the ability of organoid collections to accurately reflect population level inter-individual variability and intra-patient heterogeneity (Table 1). We advocate for deeper characterisation of organoids alongside the tissue of origin, for the generation of more diverse organoid biobanks and for greater standardisation of culture media and conditions between laboratories.

Author contributions

TH, KD, and RH planned and wrote the draft manuscript. ER reviewed and edited the manuscript.

Funding

TH is supported by funding from the Biotechnology and Biological Sciences Research Council Doctoral Training Partnership at the University of Cambridge, under award No. 2114230. KD was supported by funding from the European Union's Horizon 2020 research and innovation programme under the Marie Skłodowska-Curie grant agreement No. 101024529. ER is supported by the Medical Research Council (MR/P009581/1). RH is an NIHR Great Ormond Street Hospital Biomedical Research Centre Collaborative Catalyst Fellow and receives additional research funding from the CRUK Lung Cancer Centre of Excellence, GOSH Charity and DEBRA International. The views expressed are those of the author(s) and not necessarily those of the NHS, the NIHR or the Department of Health. This work was supported by the Francis Crick Institute which receives its core funding from Cancer Research UK (CC2041), the UK Medical Research Council (CC2041), and the Wellcome Trust (CC2041).

Conflict of interest

KD provides consultancy services to Achilles Therapeutics.

The remaining authors declare that the research was conducted in the absence of any commercial or financial relationships that could be construed as a potential conflict of interest.

Publisher's note

References

Alysandratos, K.-D., de Alba Rivas, C. G., Yao, C., Pessina, P., Villacorta-Martin, C., Huang, J., et al. (2022). Impact of cell culture on the transcriptomic programs of primary and iPSC-derived human alveolar type 2 cells. bioRxiv. doi:10.1101/2022.02.08.479591

Barkauskas, C. E., Chung, M.-I., Fioret, B., Gao, X., Katsura, H., and Hogan, B. L. M. (2017). Lung organoids: Current uses and future promise. *Development* 144, 986–997. doi:10.1242/dev.140103

Basil, M. C., Cardenas-Diaz, F. L., Kathiriya, J. J., Morley, M. P., Carl, J., Brumwell, A. N., et al. (2022). Human distal airways contain a multipotent secretory cell that can regenerate alveoli. *Nature* 604, 120–126. doi:10.1038/s41586-022-04552-0

Bolhaqueiro, A. C. F., Ponsioen, B., Bakker, B., Klaasen, S. J., Kucukkose, E., van Jaarsveld, R. H., et al. (2019). Ongoing chromosomal instability and karyotype evolution in human colorectal cancer organoids. *Nat. Genet.* 51, 824–834. doi:10.1038/s41588-019-0399-6

Chen, J.-H., Chu, X.-P., Zhang, J.-T., Nie, Q., Tang, W.-F., Su, J., et al. (2020). Genomic characteristics and drug screening among organoids derived from non-small cell lung cancer patients. *Thorac. Cancer* 11, 2279–2290. doi:10.1111/1759-7714.13542

Deprez, M., Zaragosi, L.-E., Truchi, M., Becavin, C., Ruiz García, S., Arguel, M.-J., et al. (2020). A single-cell atlas of the human healthy airways. *Am. J. Respir. Crit. Care Med.* 202, 1636–1645. doi:10.1164/rccm.201911-2199OC

Dijkstra, K. K., Monkhorst, K., Schipper, L. J., Hartemink, K. J., Smit, E. F., Kaing, S., et al. (2020). Challenges in establishing pure lung cancer organoids limit their utility for personalized medicine. *Cell Rep.* 31, 107588. doi:10.1016/j.celrep.2020.107588

Dost, A. F. M., Moye, A. L., Vedaie, M., Tran, L. M., Fung, E., Heinze, D., et al. (2020). Organoids model transcriptional hallmarks of oncogenic KRAS activation in lung epithelial progenitor cells. *Cell Stem Cell* 27, 663–678. e8. doi:10.1016/j.stem.2020.07.022

Dye, B. R., Hill, D. R., Ferguson, M. A. H., Tsai, Y.-H., Nagy, M. S., Dyal, R., et al. (2015). *In vitro* generation of human pluripotent stem cell derived lung organoids. *Elife* 4, e05098. doi:10.7554/eLife.05098

Evans, K. V., and Lee, J.-H. (2020). Alveolar wars: The rise of *in vitro* models to understand human lung alveolar maintenance, regeneration, and disease. *Stem Cells Transl. Med.* 9, 867–881. doi:10.1002/sctm.19-0433

Fiorini, E., Veghini, L., and Corbo, V. (2020). Modeling cell communication in cancer with organoids: Making the complex simple. *Front. Cell Dev. Biol.* 8, 166. doi:10.3389/fcell.2020.00166

Firth, A. L., Dargitz, C. T., Qualls, S. J., Menon, T., Wright, R., Singer, O., et al. (2014). Generation of multiciliated cells in functional airway epithelia from human induced pluripotent stem cells. *Proc. Natl. Acad. Sci. U. S. A.* 111, E1723–E1730. doi:10.1073/pnas.1403470111

Fujii, M., Shimokawa, M., Date, S., Takano, A., Matano, M., Nanki, K., et al. (2016). A colorectal tumor organoid library demonstrates progressive loss of niche factor requirements during tumorigenesis. *Cell Stem Cell* 18, 827–838. doi:10.1016/j.stem.2016.04.003

Geurts, M. H., de Poel, E., Amatngalim, G. D., Oka, R., Meijers, F. M., Kruisselbrink, E., et al. (2020). CRISPR-based adenine editors correct nonsense mutations in a cystic fibrosis organoid biobank. *Cell Stem Cell* 26, 503–510. e7. doi:10.1016/j.stem.2020.01.019

Ghosh, M., Miller, Y. E., Nakachi, I., Kwon, J. B., Barón, A. E., Brantley, A. E., et al. (2018). Exhaustion of airway basal progenitor cells in early and established chronic obstructive pulmonary disease. *Am. J. Respir. Crit. Care Med.* 197, 885–896. doi:10.1164/rccm.201704-0667OC

Han, Y., Yang, L., Lacko, L. A., and Chen, S. (2022). Human organoid models to study SARS-CoV-2 infection. *Nat. Methods* 19, 418–428. doi:10.1038/s41592-022-01453-y

Hawkins, F. J., Suzuki, S., Beermann, M. L., Barillà, C., Wang, R., Villacorta-Martin, C., et al. 2021). Derivation of airway basal stem cells from human pluripotent stem cells. *Cell Stem Cell* 28, 79–95.e8. e8. doi:10.1016/j.stem.2020.09.017

He, P., Lim, K., Sun, D., Pett, J. P., Jeng, Q., Polanski, K., et al. (2022). A human fetal lung cell atlas uncovers proximal-distal gradients of differentiation and key regulators of epithelial fates. bioRxiv, doi:10.1101/2022.01.11.474933

Hein, R. F. C., Conchola, A. S., Fine, A. S., Xiao, Z., Frum, T., Brastrom, L. K., et al. (2022). Stable iPSC-derived NKX2-1+ lung bud tip progenitor organoids give rise to airway and alveolar cell types. *Development* 149, dev200693. doi:10.1242/dev.200693

Hou, Y. J., Okuda, K., Edwards, C. E., Martinez, D. R., Asakura, T., Dinnon, K. H., 3rd, et al. (2020). SARS-CoV-2 reverse genetics reveals a variable infection gradient in the respiratory tract. *Cell* 182, 429–446. e14. doi:10.1016/j.cell.2020.05.042

Hu, Y., Sui, X., Song, F., Li, Y., Li, K., Chen, Z., et al. (2021). Lung cancer organoids analyzed on microwell arrays predict drug responses of patients within a week. *Nat. Commun.* 12, 2581. doi:10.1038/s41467-021-22676-1

Hurley, K., Ding, J., Villacorta-Martin, C., Herriges, M. J., Jacob, A., Vedaie, M., et al. (2020). Reconstructed single-cell fate trajectories define lineage plasticity windows during differentiation of human PSC-derived distal lung progenitors. *Cell Stem Cell* 26, 593–608. e8. doi:10.1016/j.stem.2019.12.009

Iakobachvili, N., Leon-Icaza, S. A., Knoops, K., Sachs, N., Mazères, S., Simeone, R., et al. (2022). Mycobacteria-host interactions in human bronchiolar airway organoids. *Mol. Microbiol.* 117, 682–692. doi:10.1111/mmi.14824

Jacob, A., Morley, M., Hawkins, F., McCauley, K. B., Jean, J. C., Heins, H., et al. (2017). Differentiation of human pluripotent stem cells into functional lung alveolar epithelial cells. *Cell Stem Cell* 21, 472–488. e10. doi:10.1016/j.stem.2017.08.014

Jacob, A., Vedaie, M., Roberts, D. A., Thomas, D. C., Villacorta-Martin, C., Alysandratos, K.-D., et al. (2019). Derivation of self-renewing lung alveolar epithelial type II cells from human pluripotent stem cells. *Nat. Protoc.* 14, 3303–3332. doi:10.1038/s41596-019-0220-0

Karlsson, K., Przybilla, M., Xu, H., Kotler, E., Karagyozova, K., Sockell, A., et al. (2022). Experimental evolution in *TP53* deficient human gastric organoids recapitulates tumorigenesis. bioRxiv. doi:10.1101/2022.04.09.487529

Katsura, H., Sontake, V., Tata, A., Kobayashi, Y., Edwards, C. E., Heaton, B. E., et al. (2020). Human lung stem cell-based alveolospheres provide insights into SARS-CoV-2-mediated interferon responses and pneumocyte dysfunction. *Cell Stem Cell* 27, 890–904. e8. doi:10.1016/j.stem.2020.10.005

Kester, L., de Barbanson, B., Lyubimova, A., Chen, L.-T., van der Schrier, V., Alemany, A., et al. (2022). Integration of multiple lineage measurements from the same cell reconstructs parallel tumor evolution. *Cell Genomics* 2, 100096. doi:10.1016/j.xgen.2022.100096

Kim, M., Mun, H., Sung, C. O., Cho, E. J., Jeon, H.-J., Chun, S.-M., et al. (2019). Patient-derived lung cancer organoids as *in vitro* cancer models for therapeutic screening. *Nat. Commun.* 10, 3991. doi:10.1038/s41467-019-11867-6

Kim, S.-Y., Kim, S.-M., Lim, S., Lee, J. Y., Choi, S.-J., Yang, S.-D., et al. (2021). Modeling clinical responses to targeted therapies by patient-derived organoids of advanced lung adenocarcinoma. *Clin. Cancer Res.* 27, 4397–4409. doi:10.1158/1078-0432.CCR-20-5026

Kimura, M., Iguchi, T., Iwasawa, K., Dunn, A., Thompson, W. L., Yoneyama, Y., et al. (2022). En masse organoid phenotyping informs metabolic-associated genetic susceptibility to NASH. *Cell* 185, 4216–4232.e16. doi:10.1016/j.cell.2022.09.031

Konishi, S., Tata, A., and Tata, P. R. (2022). Defined conditions for long-term expansion of murine and human alveolar epithelial stem cells in three-dimensional cultures. *Star. Protoc.* 3, 101447. doi:10.1016/j.xpro.2022.101447

Korogi, Y., Gotoh, S., Ikeo, S., Yamamoto, Y., Sone, N., Tamai, K., et al. (2019). *In vitro* disease modeling of hermansky-pudlak syndrome type 2 using human induced pluripotent stem cell-derived alveolar organoids. *Stem Cell Rep.* 13, 235. doi:10.1016/j.stemcr.2019.05.022

Lee, J.-H., Bhang, D. H., Beede, A., Huang, T. L., Stripp, B. R., Bloch, K. D., et al. (2014). Lung stem cell differentiation in mice directed by endothelial cells via a BMP4-NFATc1-thrombospondin-1 axis. *Cell* 156, 440–455. doi:10.1016/j.cell.2013.12.039

Lee, S. H., Hu, W., Matulay, J. T., Silva, M. V., Owczarek, T. B., Kim, K., et al. (2018). Tumor evolution and drug response in patient-derived organoid models of bladder cancer. *Cell* 173, 515–528. e17. doi:10.1016/j.cell.2018.03.017

Li, Z., Qian, Y., Li, W., Liu, L., Yu, L., Liu, X., et al. (2020). Human lung adenocarcinoma-derived organoid models for drug screening. *iScience* 23, 101411. doi:10.1016/j.isci.2020.101411

Liberti, D. C., and Morrisey, E. E. (2021). Organoid models: Assessing lung cell fate decisions and disease responses. *Trends Mol. Med.* 27, 1159–1174. doi:10.1016/j.molmed.2021.09.008

Liu, Z., Anderson, J. D., Deng, L., Mackay, S., Bailey, J., Kersh, L., et al. (2020). Human nasal epithelial organoids for therapeutic development in cystic fibrosis. *Genes* 11, 603. doi:10.3390/genes11060603

Ma, H.-C., Zhu, Y.-J., Zhou, R., Yu, Y.-Y., Xiao, Z.-Z., and Zhang, H.-B. (2022). Lung cancer organoids, a promising model still with long way to go. *Crit. Rev. Oncol. Hematol.* 171, 103610. doi:10.1016/j.critrevonc.2022.103610

Maughan, E. F., Hynds, R. E., Pennycuick, A., Nigro, E., Gowers, K. H. C., Denais, C., et al. (2022). Cell-intrinsic differences between human airway epithelial cells from children and adults. *iScience* 25, 105409. doi:10.1016/j.isci.2022.105409

McCauley, K. B., Alysandratos, K.-D., Jacob, A., Hawkins, F., Caballero, I. S., Vedaie, M., et al. (2018). Single-cell transcriptomic profiling of pluripotent stem cell-derived SCGB3A2+ airway epithelium. *Stem Cell Rep.* 10, 1579–1595. doi:10.1016/j.stemcr.2018.03.013

McCauley, K. B., Hawkins, F., Serra, M., Thomas, D. C., Jacob, A., and Kotton, D. N. (2017). Efficient derivation of functional human airway epithelium from pluripotent stem cells via temporal regulation of wnt signaling. *Cell Stem Cell* 20, 844–857. e6. doi:10.1016/j.stem.2017.03.001

Mihaylova, V. T., Kong, Y., Fedorova, O., Sharma, L., Dela Cruz, C. S., Pyle, A. M., et al. (2018). Regional differences in airway epithelial cells reveal tradeoff between defense against oxidative stress and defense against rhinovirus. *Cell Rep.* 24, 3000–3007. e3. doi:10.1016/j.celrep.2018.08.033

Miller, A. J., Dye, B. R., Ferrer-Torres, D., Hill, D. R., Overeem, A. W., Shea, L. D., et al. (2019). Generation of lung organoids from human pluripotent stem cells *in vitro*. *Nat. Protoc.* 14, 518–540. doi:10.1038/s41596-018-0104-8

Miller, A. J., Hill, D. R., Nagy, M. S., Aoki, Y., Dye, B. R., Chin, A. M., et al. (2018). *In vitro* induction and *in vivo* engraftment of lung bud tip progenitor cells derived from human pluripotent stem cells. *Stem Cell Rep.* 10, 101–119. doi:10.1016/j.stemcr.2017.11.012

Miller, A. J., Yu, Q., Czerwinski, M., Tsai, Y.-H., Conway, R. F., Wu, A., et al. (2020). *In vitro* and *in vivo* development of the human airway at single-cell resolution. *Dev. Cell* 53, 117–128. doi:10.1016/j.devcel.2020.01.033

Murthy, P. K. L., Sontake, V., Tata, A., Kobayashi, Y., Macadlo, L., Okuda, K., et al. (2022). Human distal lung maps and lineage hierarchies reveal a bipotent progenitor. *Nature* 604, 111–119. doi:10.1038/s41586-022-04541-3

Ng-Blichfeldt, J.-P., de Jong, T., Kortekaas, R. K., Wu, X., Lindner, M., Guryev, V., et al. (2019). TGF-β activation impairs fibroblast ability to support adult lung epithelial progenitor cell organoid formation. *Am. J. Physiol. Lung Cell. Mol. Physiol.* 317, L14–L28. doi:10.1152/ajplung.00400.2018

Ng-Blichfeldt, J.-P., Schrik, A., Kortekaas, R. K., Noordhoek, J. A., Heijink, I. H., Hiemstra, P. S., et al. (2018). Retinoic acid signaling balances adult distal lung epithelial progenitor cell growth and differentiation. *EBioMedicine* 36, 461–474. doi:10.1016/j.ebiom.2018.09.002

Ng, W. H., Johnston, E. K., Tan, J. J., Bliley, J. M., Feinberg, A. W., Stolz, D. B., et al. (2022). Recapitulating human cardio-pulmonary co-development using simultaneous multilineage differentiation of pluripotent stem cells. *Elife* 11. doi:10.7554/eLife.67872

Ngan, S. Y., Quach, H., Dierolf, J., Laselva, O., Lee, J.-A., Huang, E., et al. (2021). Modeling lung cell development using human pluripotent stem cells. bioRxiv. doi:10.1101/2021.07.16.452691

Nikolić, M. Z., Caritg, O., Jeng, Q., Johnson, J.-A., Sun, D., Howell, K. J., et al. (2017). Human embryonic lung epithelial tips are multipotent progenitors that can be expanded *in vitro* as long-term self-renewing organoids. *Elife* 6, e26575. doi:10.7554/eLife.26575

Peretz, J., Pekosz, A., Lane, A. P., and Klein, S. L. (2016). Estrogenic compounds reduce influenza A virus replication in primary human nasal epithelial cells derived from female, but not male, donors. *Am. J. Physiol. Lung Cell. Mol. Physiol.* 310, L415–L425. doi:10.1152/ajplung.00398.2015

Raghavan, S., Winter, P. S., Navia, A. W., Williams, H. L., DenAdel, A., Lowder, K. E., et al. (2021). Microenvironment drives cell state, plasticity, and drug response in pancreatic cancer. *Cell* 184, 6119–6137.e26. e26. doi:10.1016/j.cell.2021.11.017

Riccetti, M. R., Ushakumary, M. G., Waltamath, M., Green, J., Snowball, J., Dautel, S. E., et al. (2022). Maladaptive functional changes in alveolar fibroblasts due to perinatal hyperoxia impair epithelial differentiation. *JCI Insight* 7, e152404. doi:10.1172/jci.insight.152404

Rock, J. R., Onaitis, M. W., Rawlins, E. L., Lu, Y., Clark, C. P., Xue, Y., et al. (2009). Basal cells as stem cells of the mouse trachea and human airway epithelium. *Proc. Natl. Acad. Sci. U. S. A.* 106, 12771–12775. doi:10.1073/pnas.0906850106

Rodenburg, L. W., Delpiano, L., Railean, V., Centeio, R., Pinto, M. C., Smits, S. M. A., et al. (2022). Drug repurposing for cystic fibrosis: Identification of drugs that induce CFTR-independent fluid secretion in nasal organoids. *Int. J. Mol. Sci.* 23, 12657. doi:10.3390/ijms232012657

Roerink, S. F., Sasaki, N., Lee-Six, H., Young, M. D., Alexandrov, L. B., Behjati, S., et al. (2018). Intra-tumour diversification in colorectal cancer at the single-cell level. *Nature* 556, 457–462. doi:10.1038/s41586-018-0024-3

Sachs, N., Papaspyropoulos, A., Zomer-van Ommen, D. D., Heo, I., Böttinger, L., Klay, D., et al. (2019). Long-term expanding human airway organoids for disease modeling. *EMBO J.* 38, e100300. doi:10.15252/embj.2018100300

Salahudeen, A. A., Choi, S. S., Rustagi, A., Zhu, J., van Unen, V., de la O, S. M., et al. (2020). Progenitor identification and SARS-CoV-2 infection in human distal lung organoids. *Nature* 588, 670–675. doi:10.1038/s41586-020-3014-1

Sato, T., Vries, R. G., Snippert, H. J., van de Wetering, M., Barker, N., Stange, D. E., et al. (2009). Single Lgr5 stem cells build crypt-villus structures *in vitro* without a mesenchymal niche. *Nature* 459, 262–265. doi:10.1038/nature07935

Sen, C., Freund, D., and Gomperts, B. N. (2022). Three-dimensional models of the lung: Past, present and future: A mini review. *Biochem. Soc. Trans.* 50, 1045–1056. doi:10.1042/BST20190569

Shi, R., Radulovich, N., Ng, C., Liu, N., Notsuda, H., Cabanero, M., et al. (2020). Organoid cultures as preclinical models of non-small cell lung cancer. *Clin. Cancer Res.* 26, 1162–1174. doi:10.1158/1078-0432.CCR-19-1376

Stancil, I. T., Michalski, J. E., Davis-Hall, D., Chu, H. W., Park, J.-A., Magin, C. M., et al. (2021). Pulmonary fibrosis distal airway epithelia are dynamically and structurally dysfunctional. *Nat. Commun.* 12, 4566. doi:10.1038/s41467-021-24853-8

Strikoudis, A., Cieślak, A., Loffredo, L., Chen, Y.-W., Patel, N., Saqi, A., et al. (2019). Modeling of fibrotic lung disease using 3D organoids derived from human pluripotent stem cells. *Cell Rep.* 27, 3709–3723. e5. doi:10.1016/j.celrep.2019.05.077

Suezawa, T., Kanagaki, S., Moriguchi, K., Masui, A., Nakao, K., Toyomoto, M., et al. (2021). Disease modeling of pulmonary fibrosis using human pluripotent stem cell-derived alveolar organoids. *Stem Cell Rep.* 16, 2973–2987. doi:10.1016/j.stemcr.2021.10.015

Surolia, R., Li, F. J., Wang, Z., Li, H., Dsouza, K., Thomas, V., et al. (2019). Vimentin intermediate filament assembly regulates fibroblast invasion in fibrogenic lung injury. *JCI Insight* 4, e123253. doi:10.1172/jci.insight.123253

Tamò, L., Hibaoui, Y., Kallol, S., Alves, M. P., Albrecht, C., Hostettler, K. E., et al. (2018). Generation of an alveolar epithelial type II cell line from induced pluripotent stem cells. *Am. J. Physiol. Lung Cell. Mol. Physiol.* 315, L921–L932. doi:10.1152/ajplung.00357.2017

Tan, Q., Ma, X. Y., Liu, W., Meridew, J. A., Jones, D. L., Haak, A. J., et al. (2019). Nascent lung organoids reveal epithelium- and bone morphogenetic protein-mediated suppression of fibroblast activation. *Am. J. Respir. Cell Mol. Biol.* 61, 607–619. doi:10.1165/rcmb.2018-0390OC

van de Wetering, M., Francies, H. E., Francis, J. M., Bounova, G., Iorio, F., Pronk, A., et al. (2015). Prospective derivation of a living organoid biobank of colorectal cancer patients. *Cell* 161, 933–945. doi:10.1016/j.cell.2015.03.053

van der Vaart, J., Böttinger, L., Geurts, M. H., van de Wetering, W. J., Knoops, K., Sachs, N., et al. (2021a). Modelling of primary ciliary dyskinesia using patient-derived airway organoids. *EMBO Rep.* 22, e52058. doi:10.15252/embr.202052058

van der Vaart, J., Lamers, M. M., Haagmans, B. L., and Clevers, H. (2021b). Advancing lung organoids for COVID-19 research. *Dis. Model. Mech.* 14, dmm049060. doi:10.1242/dmm.049060

Wijesekara, P., Yadav, P., Perkins, L. A., Stolz, D. B., Franks, J. M., Watkins, S. C., et al. (2022). Engineering rotating apical-out airway organoid for assessing respiratory cilia motility. *iScience* 25, 104730. doi:10.1016/j.isci.2022.104730

Youk, J., Kim, T., Evans, K. V., Jeong, Y.-I., Hur, Y., Hong, S. P., et al. (2020). Three-dimensional human alveolar stem cell culture models reveal infection response to SARS-CoV-2. *Cell Stem Cell* 27, 905–919. e10. doi:10.1016/j.stem.2020.10.004

frontiers | Frontiers in Pharmacology

TYPE Review
PUBLISHED 13 February 2023
DOI 10.3389/fphar.2023.1130074

OPEN ACCESS

EDITED BY
Janette K. Burgess,
University Medical Center Groningen, Netherlands

REVIEWED BY
Ramon Farre,
University of Barcelona, Spain
Jane Elizabeth Bourke,
Monash University, Australia

*CORRESPONDENCE
Daniel J. Weiss,
dweiss@uvm.edu

SPECIALTY SECTION
This article was submitted to Respiratory Pharmacology, a section of the journal Frontiers in Pharmacology

RECEIVED 22 December 2022
ACCEPTED 23 January 2023
PUBLISHED 13 February 2023

CITATION
Weiss DJ (2023), What is the need and why is it time for innovative models for understanding lung repair and regeneration?
Front. Pharmacol. 14:1130074.
doi: 10.3389/fphar.2023.1130074

What is the need and why is it time for innovative models for understanding lung repair and regeneration?

Daniel J. Weiss*

University of Vermont, Burlington, VT, United States

Advances in tissue engineering continue at a rapid pace and have provided novel methodologies and insights into normal cell and tissue homeostasis, disease pathogenesis, and new potential therapeutic strategies. The evolution of new techniques has particularly invigorated the field and span a range from novel organ and organoid technologies to increasingly sophisticated imaging modalities. This is particularly relevant for the field of lung biology and diseases as many lung diseases, including chronic obstructive pulmonary disease (COPD) and idiopathic fibrosis (IPF), among others, remain incurable with significant morbidity and mortality. Advances in lung regenerative medicine and engineering also offer new potential avenues for critical illnesses such as the acute respiratory distress syndrome (ARDS) which also continue to have significant morbidity and mortality. In this review, an overview of lung regenerative medicine with focus on current status of both structural and functional repair will be presented. This will serve as a platform for surveying innovative models and techniques for study, highlighting the need and timeliness for these approaches.

KEYWORDS

lung, cell therapy, bioengineering, lung disease, stem cells

Overview of lung regenerative medicine

As lung diseases and critical illnesses have diverse pathophysiologies and manifestations, multiple potential regenerative medicine-based therapeutic approaches are being investigated. For functional repair, ARDS and sepsis/septic shock offer paradigms for disease entities marked by acute high intensity inflammation and associated injuries. A range of pharmacologic agents including monoclonal antibodies, corticosteroids, non-steroidal anti-inflammatory agents have only modestly improved morbidity and mortality if at all and current strategies are primarily focused on supportive care (Matthay et al., 2019a). Acknowledging that some ARDS survivors develop long term fibrotic changes, focus for new therapeutics is on novel approaches that can counter inflammation. This includes consideration for patients with respiratory failure and ARDS in the setting of SARS CoV2 infection.

Cell-based therapies: Functional repair

One new promising approach centers on cell-based therapies, predominantly utilizing mesenchymal stromal cells (MSCs) (Walter et al., 2014). MSCs are multipotent progenitor cells with the potential to secrete a spectrum of biologic mediators, such as anti-inflammatory cytokines, angiogenic factors, anti-bacterial peptides, and extracellular vesicles (EVs) (reviewed

in 3). Originally isolated from bone marrow, MSCs can be isolated from a wide range of tissues including adipose, placental, cord blood, and from the lung itself (Walter et al., 2014). The general approach is to isolate MSCs from the source tissue and expand in culture for subsequent investigation and potential therapeutic effects. Following systemic administration, MSCs primarily lodge in the pulmonary capillary system, through as yet poorly understood interactions with the endothelium. They do not engraft and are cleared by a range of host immune mechanisms over 1–2 days, although available data suggests that they may persist for up to 3–4 days in the setting of lung inflammation (Allers et al., 2004; Armitage et al., 2018). MSCs express a range of danger and molecular pathogen cell surface receptors, including the Toll-Like receptors and a growing body of literature demonstrates that while in the pulmonary capillary bed, the MSCs respond to specific inflammatory environments by releasing different portfolios of mediators (Romieu-Mourez et al., 2009; Waterman et al., 2010; Kusuma et al., 2017; Abreu et al., 2019; Islam et al., 2019; Enes et al., 2021; Galipeau et al., 2021). The MSCs also constitutively express low levels of cell surface antigens such as human leukocyte antigens (HLA) DR and co-stimulatory molecules such as CD40 (Galipeau and Sensébé, 2018). This has allowed a range of investigations in which allogeneic MSCs have been administered by systemic (intravenous) administration in a wide range of disease models and clinical investigations. However, HLA and co-stimulatory molecules can be upregulated in response to inflammatory signals, notably interferon gamma (IFNγ) (Krampera et al., 2006; Polchert et al., 2008). Accordingly increasing evidence suggests that host responses to the allogeneic MSCs, including MSCs undergoing apoptotic or necrotic changes following administration, may be driving potential therapeutic effects (Galleu et al., 2017; Weiss et al., 2019).

There have been a large number of investigations of both systemic and direct airway administration of MSCs in a wide range of pre-clinical models of lung diseases and critical illnesses. These have been predominantly in rodents but also include large animal models such as sheep and also in explanted human lungs (Ikonomou et al., 2022; Ting et al., 2022). In virtually every case, MSC administration has ameliorated acute, and in some cases chronic, inflammation and injury in models of acute endotoxin and bacterial lung injury, allergic airways inflammation/asthma, bronchopulmonary dysplasia (BPD), COPD, pulmonary hypertension, and sepsis/septic shock (Ikonomou et al., 2022; Ting et al., 2022). The data is less clear for chronic diseases such as pulmonary fibrosis, in part as the available pre-clinical models, for example bleomycin administration in rodents, do not fully replicate human disease. MSC administration during the acute inflammatory phase resulting shortly after bleomycin administration is decreased with subsequent decrease in resulting fibrosis, however, it is less clear as to whether MSCs have benefit in models of established fibrosis. The mechanisms by which the MSCs act in each of these models are not yet fully elucidated and available evidence suggests different mechanisms in the different disease models, consonant with growing appreciation that MSCs will behave differently in varying injuries. Pre-conditioning MSCs, for example by exposure to hypoxia or to different mixtures of cytokines can alter subsequent MSC actions consonant with the observations that MSC behaviors are dictated by the inflammatory environment they encounter (Romieu-Mourez et al., 2009; Waterman et al., 2010; Kusuma et al., 2017; Abreu et al., 2019; Islam et al., 2019; Enes et al., 2021; Galipeau et al., 2021). Further, a growing experience demonstrates that EVs derived from MSCs can mimic many of the beneficial effects of the MSCs themselves (Zhu et al., 2014; Cruz et al., 2015a; Mahida et al., 2020). The mechanisms by which the EVs act are still being elucidated and postulated mechanisms include actions of miRNAs, proteins such as anti-inflammatory cytokines, mitochondria, and lipids contained in the EVs (Abreu et al., 2021).

Nonetheless, these pre-clinical data have provided a platform for a growing number of clinical investigations of MSCs and also MSC-derived EVs in a range of pulmonary diseases and critical illnesses including but not limited to ARDS, asthma, BPD, COPD, IPF, and others [reviewed in (Matthay et al., 2019b; Ting et al., 2022)]. This includes a large number of clinical investigations of MSCs in patients with SARS-CoV2 (COVID-19)-relatedd ARDS in the setting of the COVID-19 pandemic (Dilogo et al., 2021; Lanzoni et al., 2021; Monsel et al., 2022). The majority of these investigations for which published data is available have been phase 1 safety trials and have uniformly demonstrated no acute infusional toxicities and no attributable subsequent serious adverse events. A smaller but growing number of phase 2 efficacy trials have demonstrated efficacy in some cases but not in others. The most extensive experience to date is in investigations of systemic MSC administration in patients with either non-COVID or COVID19-related ARDS with recent meta-analyses of COVID-19 related-ARDS demonstrating significant benefits of MSC administration (Khoury et al., 2020; Qu et al., 2020; Zhu et al., 2021; Kirkham et al., 2022; Lu et al., 2022). Intensive deliberation about the varying outcomes in these trials has highlighted ongoing issues with investigations of MSC administration not just in patients with respiratory diseases or critical illnesses but in a wider range of conditions. These include lack of concordance or clear guidelines as to which source of MSCs may be most effective in any given indication, dose and dosing strategy, and whether freshly thawed (from frozen stocks) or continuously cultured MSCs may be more effective (Francois et al., 2012; Cruz et al., 2015b). These considerations also include growing appreciation that the patient phenotype is critically important in identifying patients more likely to respond to MSCs administration (Matthay et al., 2020). This is in the setting of growing appreciation of different inflammatory phenotypes for patients with ARDS, COPD, and other conditions. For example, a recent trial of systemic administration of bone marrow-derived MSCs in patients with COVID19-related ARDS and respiratory failure requiring mechanical ventilation demonstrated no benefit in survival or other ICU outcome measures across the entire study population (Bowdish et al., 2022). However, a pre-specified subgroup analysis demonstrated significant and substantial improvement in mortality in patients under age 65 (Ting et al., 2022). In a parallel example, systemic administration of allogeneic bone marrow-derived MSCs in COPD patients did result in improvements on lung function (Weiss et al., 2013) but a post-hoc subgroup analysis, in which patients were stratified by entry levels of a circulating inflammatory mediator, C-reactive protein, associated with worse overall clinical outcomes, demonstrated statistically significant and clinically meaningful improvements in lung functions in treated patients compared to controls (Weiss et al., 2021). In a third example, the presence of *Aspergillus* in bronchoalveolar lavage samples from cystic fibrosis (CF) patients resulted in rapid MSC death, through actions of fungal gliotoxin on mitochondrial function (Abreu et al., 2020). As such, in the setting of a recent proof of concept safety trial of systemic bone marrow-derived MSC administration in CF patients, arguably patients

with known Aspergillus lung infections, not uncommon in CF, should be excluded from subsequent efficacy investigations.

These observations and experience to date highlight both the promise and challenges of MSC-based cell therapies in lung regenerative medicine. This includes the still as yet unclear roles of endogenous lung MSCs in normal homeostasis and disease pathophysiology (Matthay et al., 2020; Bowdish et al., 2022; Kruk et al., 2021a; Kruk et al., 2021b). Further, MSCs are not the only cells being utilized in this context. Endothelial progenitor cells (EPCs) derived from both bone marrow as well as circulating sources have demonstrated efficacy in pre-clinical models of pulmonary hypertension and are currently under clinical investigation in pulmonary hypertension patients (Nagaya et al., 2003; Zhao et al., 2005; Foster et al., 2014; Suen et al., 2016). These are based on paracrine actions of the EPCs in part to stimulate angiogenesis and also include data on EPCs genetically engineered to produce angiogenic growth factors. The same considerations with respect to MSC therapeutics, source of origin, dose, dosing, etc, apply to EPCs and any other cell type being utilized for paracrine functional effects.

Cell-based therapies: Structural repair

A landmark paper was published in 2002 in which bone marrow-derived cells appeared to structurally engraft as airway epithelial cells (Krause et al., 2001). This stimulated large-scale investigations of utilizing cell engraftment to repair damaged lung epithelium, notably in the context of cystic fibrosis. However, it was subsequently determined that technical and other errors provided misleading results and that engraftment of bone marrow-derived cells as structural lung cells was a rare occurrence of unlikely physiologic or clinical significance (Krause et al., 2001; Loi et al., 2006; Kotton et al., 2005).

However, the concept of engraftment has been re-invigorated with increasing appreciation of the different populations of endogenous lung progenitor cells, both in the airway and alveolar epithelium, as well as advances in deriving lung epithelial cells from induced pluripotent-derived cells (iPSCs). Increasing data demonstrates that these cells can structurally and potentially functional engraft in pre-clinical models. One important caveat for these studies to date is that injury to the airway or alveolar epithelium is a predicate for engraftment. One simplistic explanation is that the damage provides "room" and allows the engrafting cells to integrate into previously intact cell monolayers. How this might translate into clinical practice is unclear at present but this is an exciting area of research.

Lung support and assist devices: Functional repair

Regenerative medicine and engineering also incorporates developing devices that can augment or replace failing organs. This is well evidenced by examples of hemodialysis for chronic renal failure and left ventricular assist devices for heart failure. Such devices can also be utilized as bridges until organ transplantation or to improve quality of life in patients who do not qualify for organ transplants.

This is an area of necessary growth in respiratory medicine. Mechanical ventilators and other non-invasive ventilation approaches are powerful and well-established tools. However, for intractable respiratory failure, there are limited options. Extra-corporeal membrane oxygenation (ECMO) is an established tool for use in both neonatal and adult patients with intractable respiratory failure and has had increasing utilization in adult patients, particularly in the setting of the COVID-19 pandemic. However, ECMO is a complex approach requiring specialized centers and highly trained support personnel and is currently limited to relatively few tertiary care centers. Further ECMO can be complicated by clotting and bleeding in the circuitry as well as by infection. ECMO is also limited to short term use in intensive care settings; there are no current available device options for long term use in ambulatory patients on lung transplant waiting lists or who will not qualify for transplantation (Johnson et al., 2022).

There are several devices undergoing development and investigation by both academic and commercial entities (Syed et al., 2021). This includes a novel respiratory assist device based on decellularized bird lungs (Wrenn et al., 2018). However, there is much room for innovation and advancement.

Ex Vivo generation of gas exchange tissues: Structural and functional repair

While lung transplantation is available and increasingly successful for patients with end-stage lung diseases, there remains a significant shortage of suitable donor organs. Lung transplantation is also complicated by still unacceptably high rates of both acute and chronic rejection. Accordingly, extensive effort has taken place over the past approximate 15 years to develop functional gas exchange tissue that can be implanted to replace defective lungs. This has led to development of a number of novel technical approaches that will be overviewed here.

Lung de- and recellularization

Organ de- and recellularization has been widely investigated in a number of different tissues as a means to develop functional tissue *ex vivo* (Crapo et al., 2011). The overall goal is to utilize the native 3-dimensional (3D) extracellular matrix (ECM) as a scaffold for re-populating with organ-specific cells to develop functional organs and tissues. A variety of approaches are utilized to remove native cells and cellular debris including chemical, for example ionic and non-ionic detergents, and physical, for example multiple freeze thaws (reviewed in 51). With respect to lung, several seminal papers were published in 2010, based on an original report in 1986, that detailed detergent-based decellularization of rodent lungs and subsequent initial attempts at recellularization and implantation into rodent models (Lwebuga-Mukasa et al., 1986; Ott et al., 2010; Petersen et al., 2010; Price et al., 2010). Another report from that time investigated multiple freeze thaws as a model for decellularization (Cortiella et al., 2010). These proof-of concept studies provided a platform for a large number of subsequent studies through which significant progress has been made including ability to engraft multiple cell types and maintain viability for up to several weeks (Daly et al., 2012; Wallis et al., 2012; Bonenfant et al., 2013; Sokocevic et al., 2013; Wagner et al., 2014a; Wagner et al., 2014b).

However, significant challenges remain including the ability to fully repopulate and cover the entire ECM surface area and the question of having the proper cells in the proper location,

i.e., alveolar in alveoli, airway in airways, etc. Significant parallel issues have been developing sources of cells to use in re-population strategies with increasing focus on utilizing lung endogenous progenitor cells and/or IPSC-derived cells as stem or progenitor populations with the goal of having these expand to large numbers and appropriately differentiate. One particular potential advantage of using lung progenitor or iPSC-derived cells is that they can be obtained from the eventual transplant recipient thus resulting in autologous tissue for use in transplantation. The working hypothesis here is that immune epitopes on the ECM that could potentially trigger rejection will either be removed during the decellularization process or covered by the seeded autologous cells. While an attractive hypothesis, direct studies addressing this have yet to be performed.

Efforts towards optimizing recellularization further depend in large part on environmental cues such as ECM composition and stiffness (Melo et al., 2014). Mechanical forces, i.e., cyclic mechanical stretch ("breathing") for directing differentiation into airway or alveolar cells, or shear forces (vascular blood flow) for directing differentiation into pulmonary vascular endothelial cells, are increasingly being incorporated into re-population schemes. The development of novel bioreactor technology has also progressed enabling incorporation of mechanical forces but significant challenges remain in keeping the re-populating tissues alive for the weeks-months that may be required for full recellularization. Although the primary goal of functional *ex vivo* lung tissue is to provide gas exchange, immune regulatory actions of the lungs are also important functions. However, re-populating decellularized scaffolds with immune and inflammatory cells, such as macrophages, in addition to epithelial, vascular endothelial, and stromal cells, remains less well explored.

Thus, despite significant progress, a truly functional *ex vivo* organ capable of gas exchange as well as other immune regulating functions of the lung has not yet been developed. Further, even if this becomes technically achievable, there may still be not enough donor human lungs available to provide decellualrized scaffolds for use. Currently lungs are predominantly from those donor lungs that do not reach standards for use in transplantation or alternatively from autopsy. This has led to investigation of xenogeneic sources, primarily from pig lungs, as potential scaffolds for re-population with human lung cells (Platz et al., 2016; Gasek et al., 2021). As discussed previously, other postulated uses of other sources of lungs for decellularization include using decellularized bird lungs repopulated with human lung cells as artificial gas exchange (Wrenn et al., 2018). Further, even though there remains significant room for innovation and improvement in lung de- and recellularization approaches, decellularized organs have proven to be valuable experimental tools to study diseased ECM and cell-ECM interactions. For example, decellularized lungs from patients with COPD or IPF have provided significant insight into disease pathogenesis and the role of the ECM and disordered cell-matrix interactions in disease processes (Booth et al., 2012; Wagner et al., 2014b; Ahrman et al., 2018; Hoffman et al., 2023).

Organoid and hydrogel approaches: Structural and functional repair

Three-dimensional cultures of cells in a supporting matrix has been an exploding field over the past few years. In contrast to standard two-dimensional (2D) tissue culture, 3D culturing proves a platform for 3D tissue formation and growth, in many cases resulting in miniature versions of the target organ or tissue (Saldin et al., 2017; Giobbe et al., 2019). These organoid culture approaches have provided a wealth of new information and studies including those for primary lung, lung progenitor cell, and iPSC-derived lung cells (Pouliot et al., 2016; De Hilster et al., 2020; Petrou et al., 2020; Pouliot et al., 2020; Nizamoglu et al., 2022; Marhuenda et al., 2022b; Saleh et al., 2022). These have also offered more sophisticated technologies with which to study interactions between different cell types co-seeded into the matrices as well as the influence of the 3D environmental niche as the 3D matrices can be produced with tunable stiffness and can also undergo cyclic mechanical strain (Pouliot et al., 2016; De Hilster et al., 2020; Petrou et al., 2020; Pouliot et al., 2020; Nizamoglu et al., 2022; Marhuenda et al., 2022b; Saleh et al., 2022).

Organoid culture approaches also offer a powerful opportunity to study the influence of the surrounding ECM composition on cell behaviors. However, to date, most organoid culture work, including those utilizing lung cells, have primarily utilized Matrigel™, a non-relevant ECM derived from cancerous mouse tissue typically utilized for stem and cancer cell proliferation, and thus, an insufficient ECM to replicate the *in situ* human lung environment (Petrou et al., 2020). However, recent studies have highlighted the potential role of physiologically relevant ECM on type 2 alveolar epithelial cells (AT2) differentiation (Alysandratos et al., 2022; Nizamoglu et al., 2022; Sucre et al., 2022). As such, several groups have recently been decellularized lungs for hydrogel formation and cell culture (Hughes et al., 2010; Pouliot et al., 2016; De Hilster et al., 2020; Petrou et al., 2020; Pouliot et al., 2020; Uhl et al., 2020; Alysandratos et al., 2022; Nizamoglu et al., 2022; Marhuenda et al., 2022b; Saleh et al., 2022; Sucre et al., 2022). Used in place of Matrigel™, the hydrogels are a unique culture model that provide a native and thus more relevant matrix. The lung-derived hydrogels can be produced not just from the entire lung but from airway, vascular, and alveolar-enriched regions obtained by dissection of decellularized lungs (Hoffman et al., 2023), this providing an opportunity to investigate regional differences in cell-matrix interactions. Further, hydrogels can be produced from decellularized diseased lungs providing additional novel model investigative systems (Petrou et al., 2020; Uhl et al., 2020; Saleh et al., 2022; Hoffman et al., 2023). These are powerful investigative tools that will provide novel information that in part can be utilized to improve recellularization schemes for decellularized lungs.

3D bioprinting: Structural repair

3D bioprinting has an increasingly important role in replacing damaged or diseased structural tissues with successful clinical applications in fields such as orthopedics and cosmetic repair. With respect to respiratory tissues, 3D-bioprinted tracheas and large airways have a growing potential clinical role (Ke et al., 2019; Mahfouzia et al., 2021; Park et al., 2021; Huo et al., 2022). However, there are a number of challenges including choice of matrix material to be used in the bioprinting process as well as effective vascularization and epithelialization of the bioprinted structure (Galliger et al., 2019; De Santis et al., 2021; Falcones et al., 2021). For use in congenital tracheal or airway defects, another consideration is whether the 3D-bioprinted structure will grow as the neonatal or infant recipient grows. While there is good progress to date, challenges in 3D bioprinting tissues that might

participate in gas exchange result from several considerations mostly relating to the complex anatomic and physiologic lung structure-function relationship (Berg et al., 2021; Kang et al., 2021). Increasing sophistication of 3D bioprinting approaches, for example including use of techniques such as freeform reversible embedding of suspended hydrogels (FRESH) and incorporation of stereolithography along with advances in printer programming have allowed for ever more fine resolution of distal airways and potentially alveolar structures on a nano and micrometer scale (Sun et al., 2021). An exciting proof of concept study demonstrated that a 3D bioprinted vascular network on a micron scale, produced utilizing stereolithography and a light sensitive hydrogel that allowed for cell embedding could function in gas exchange (Grigoryan et al., 2019).

Other considerations include the bioink utilized in the printing process (Galliger et al., 2019; De Santis et al., 2021; Falcones et al., 2021). Will it mimic the native ECM composition, stiffness, and deformability (stretchability)? Of necessity, these will need to be varied during the bioprinting process in order to mimic the native lung structure. Similarly, the cells incorporated into the bioprinting process will need to be appropriately located in the relevant anatomic compartment and region. Alternative approaches include seeding cells into pre-printed scaffolds but the same challenges arise as for re-populating decellularized whole lung scaffolds. Can the distal bioprinted lung be effectively ventilated and undergo according cyclic mechanical strain? These are all substantial bioengineering challenges and there as yet no effective 3D-printed lungs. One alternative approach is to 3D-bioprint matrices that can be utilized in lung assist devices for gas exchange (Kang et al., 2021). These could be utilized for example in devices such as ECMO and obviate the need to fully mimic the lung anatomy.

Other investigative tools to study structural and functional repair

A number of powerful tools have developed and are still in evolution. While not geared towards eventual direct *in vivo* use, these have provided platforms that underlie other attempts at structural and functional repair.

Lung-on-a-Chip

Organ-on-a-chip model systems have developed for a number of organs and tissues. The first descriptions of lung-on-a-chip models highlights the general approach: cells are grown on either one or both sides of a biomimetic semi-permeable membrane in a small enclosed chamber. A general approach is to have epithelial cells on one side and vascular endothelial cells on the other (Huh et al., 2010; Huh et al., 2013). Microfluidic chambers on both compartments allow for gas and/or fluid flow and the biomimetic membranes can also undergo cyclic mechanical stretch (Zamprogno et al., 2021). Further innovative approaches have included incorporating lung stem and progenitor cells as well as primary lung epithelial and endothelial cells cultured on the membranes (Nawroth et al., 2019). These are powerful systems with which to study cell behaviors, cell-cell interactions, cell-matrix interactions, and the effects of environmental, such as tobacco smoke exposure, and physical forces on cell behaviors (Huh et al., 2012; Benam et al., 2016; Nawroth et al., 2020; Plebani et al., 2020; Bai et al., 2022). These, along with organoid model systems, are also powerful tools for evaluating drug effects and also for evaluating inflammatory and immune responses as both immune cells as well as infectious agents can be added to the culture systems (Huh et al., 2012; Benam et al., 2016; Nawroth et al., 2020; Plebani et al., 2020; Bai et al., 2022; Marhuenda et al., 2022a).

Precision cut lung slices (PCLS)

Culturing thin sections of lung tissue has been an approach used for many years, primarily to assess actions of pharmacologic agents on airway smooth muscle contraction and relaxation [reviewed in (Alsafadi et al., 2020)]. However, one longstanding problem has been the viability of the cultures as cells, particularly those in more central and less well perfused regions of the cultures die within relatively short time periods. Another issue has been uniformity of the tissue slices. However, recent improvements in techniques for both producing and maintaining uniform slices have led to increased utility of this methodology for studying a range of biologic processes (Bailey et al., 2020; Stegmayr et al., 2021; Stegmayr and Wagner, 2021; Rosmark et al., 2022). As with lung-on-a-chip technologies, PCLS approaches offer strong models for studying cell behaviors, particularly in response to pharmacologic interventions or as short-term disease models. Continued improvements in technologies are necessary and desirable to further increase the utility of these approaches.

Imaging and analytical techniques

Powerful advances in imaging and visualization techniques have provided further insights into processes involved in lung repair and regeneration [reviewed in (Ikonomou et al., 2020; Ikonomou et al., 2022)]. This includes both new techniques for cell and tissue labeling including multicolor multicomponent labeling of single cells that allows for detailed dynamic monitoring of cell behaviors *in situ* utilizing conventional fluoresence or confocal microscopy [reviewed in (Ikonomou et al., 2020; Ikonomou et al., 2022)]. In parallel a range of sophisticated imaging modalities have developed which allow for greater spatial and cellular resolution. One example of a relatively simple yet effective technique is termed inflation ie, infusion of fluorescently labelled antibodies in tissues of intact organs (Alsafadi et al., 2022). As indicated by the title, a continuous inflation-based infusion of antibodies provides opportunity to study 3-dimensional distribution of the cells or proteins of interest as compared to traditional immunostaining of mounted histologic sections.

Light sheet fluorescence microscopy is a technique that utilizes a plane of light to optically section and view tissues with subcellular resolution, essentially functioning as a non-destructive microtome [reviewed in (Santi, 2011)]. As tissues are exposed to only a thin plane of light, photobleaching and phototoxicity is minimized compared to other imaging modalities. Other techniques including live cell single particle imaging and multimodal imaging are also powerful tools (Ikonomou et al., 2020; Ikonomou et al., 2022).

In parallel with imaging, increasing advances in "omics" technologies, including *in situ* genomics and proteomics, along with advances in machine learning, single cell RNA sequencing and development of multi-omics atlases including gene and protein lung maps, are all tools that will help advance lung regenerative medicine and engineering (Pothen et al., 2016; Jorba et al., 2019; Marklein et al., 2019; Andreu et al., 2021).

Summary

Techniques and approaches developed to study lung regenerative medicine and engineering offer promise to both better understand normal homeostasis and disease pathophysiologies as well as to devise new therapeutics. However, there remain multiple challenges and thus opportunities for up-and-coming lung biologists, biomedical engineers, and pulmonary and critical care physicians. The dictum that "today's science fiction is tomorrow's science" is particularly appropriate in this rapidly moving field.

Author contributions

The author confirms being the sole contributor of this work and has approved it for publication.

Conflict of interest

The author declares that the research was conducted in the absence of any commercial or financial relationships that could be construed as a potential conflict of interest.

Publisher's note

References

Abreu, S. C., Enes, S. R., Dearbron, J., Goodwin, M., Coffey, A., Borg, Z. D., et al. (2019). Lung inflammatory environments differentially alter mesenchymal stromal cell behavior. *Am. J. Physiol. Lung Cell Mol. Physiol.* 317 (6), L823–L831. doi:10.1152/ajplung.00263.2019

Abreu, S. C., Hampton, T. H., Hoffman, E., Dearborn, J., Ashare, A., Singh Sidhu, K., et al. (2020). Differential effects of the cystic fibrosis lung inflammatory environment on mesenchymal stromal cells. *Am. J. Physiology - Lung Cell. Mol. Physiology* 319 (6), L908–L925. doi:10.1152/ajplung.00218.2020

Abreu, S. C., Lopes-Pacheco, M., Weiss, D. J., and Rocco, P. R. M. (2021). Mesenchymal stromal cell-derived extracellular vesicles in lung diseases: Current status and perspectives. *Front. Cell & Dev. Biol.* 9, 600711. doi:10.3389/fcell.2021.600711

Ahrman, E., Hallgren, O., Malmstrom, L., Hedstrom, U., Malmstrom, A., Bjermer, L., et al. (2018). Quantitative proteomic characterization of the lung extracellular matrix in chronic obstructive pulmonary disease and idiopathic pulmonary fibrosis. *J. Proteomics* 189, 23–33. doi:10.1016/j.jprot.2018.02.027

Allers, C., Sierralta, W. D., Neubauer, S., Rivera, F., Minguell, J. J., and Conget, P. A. (2004). Dynamic of distribution of human bone marrow-derived mesenchymal stem cells after transplantation into adult unconditioned mice. *Transplantation* 78 (4), 503–508. doi:10.1097/01.tp.0000128334.93343.b3

Alsafadi, H. N., Uhl, F. E., Pineda, R. H., Bailey, K. E., Rojas, M., Wagner, D. E., et al. (2020). Applications and approaches for three-dimensional precision-cut lung slices. Disease modeling and drug discovery. *Am. J. Respir. Cell & Mol. Biol.* 62 (6), 681–691. doi:10.1165/rcmb.2019-0276TR

Alsafadi, H. N., Tamargo, I., Neves da Silva, I. A., Rehnberb, E., Wagner, D., and Stegmayr, J. (2022). inFLATION: INfusion of fluorescent labelled antibodies in tissue of intact OrgaNs. 17th Annual Meeting of the European Society for Molecular Imaging, Mar 15 - 18, 2022, Greece

Alysandratos, K.-D., Garcia, C., Rivas, A., Yao, C., Pessina, P., Villacorta-Martin, C., et al. (2022). Impact of cell culture on the transcriptomic programs of primary and iPSC-derived human alveolar type 2 cells. *BioRxiv*, 2022. doi:10.1101/2022.02.08.479591

Andreu, I., Falcones, B., Hurst, S., Chahare, N., Quiroga, X., Le Roux, A. L., et al. (2021). The force loading rate drives cell mechanosensing through both reinforcement and cytoskeletal softening. *Nat. Commun.* 12 (1), 4229. doi:10.1038/s41467-021-24383-3

Armitage, J., Tan, D. B. A., Troedson, R., Young, P., Lam, K. V., Shaw, K., et al. (2018). Mesenchymal stromal cell infusion modulates systemic immunological responses in stable COPD patients: a phase I pilot study. *Eur. Respir. J.* 51 (3), 1702369. doi:10.1183/13993003.02369-2017

Bai, H., Si, L., Jiang, A., Belgur, C., Zhai, Y., Plebani, R., et al. (2022). Mechanical control of innate immune responses against viral infection revealed in a human lung alveolus chip. *Nat. Commun.* 13 (1), 1928. doi:10.1038/s41467-022-29562-4

Bailey, K. E., Pino, C., Lennon, M. L., Lyons, A., Jacot, J. G., Lammers, S. R., et al. (2020). Embedding of precision-cut lung slices in engineered hydrogel biomaterials supports extended *ex vivo* culture. *Am. J. Respir. Cell & Mol. Biol.* 62 (1), 14–22. doi:10.1165/rcmb.2019-0232MA

Benam, K. H., Novak, R., Nawroth, J., Hirano-Kobayashi, M., Ferrante, T. C., Choe, Y., et al. (2016). Matched-comparative modeling of normal and diseased human airway responses using a microengineered breathing lung chip. *Cell Syst.* 3 (5), 456–466. doi:10.1016/j.cels.2016.10.003

Berg, J., Weber, Z., Fechler-Bitteti, M., Hocke, A. C., Hippenstiel, S., Elomaa, L., et al. (2021). Bioprinted multi-cell type lung model for the study of viral inhibitors. *Viruses* 13 (8), 1590. doi:10.3390/v13081590

Bonenfant, N., Sokocevic, D., Wagner, D. E., Borg, Z. D., Lathrop, M., Lam, Y. W., et al. (2013). The effects of storage and sterilization on de-cellularized and Re-cellularized whole lung. *Biomaterials* 34 (13), 3231–3245. doi:10.1016/j.biomaterials.2013.01.031

Booth, A. J., Hadley, R., Cornett, A. M., Dreffs, A. A., Matthes, S. A., Tsui, J. L., et al. (2012). Acellular normal and fibrotic human lung matrices as a culture system for *in vitro* investigation. *Am. J. Respir. Crit. Care Med.* 186 (9), 866–876. doi:10.1164/rccm.201204-0754OC

Bowdish, M. E., Barkauskas, C. E., Overbey, J. R., Gottlieb, R. L., Osman, K., Duggal, A., et al. (2022). A randomized trial of mesenchymal stromal cells for moderate to severe ARDS from COVID-19. *Am. J. Respir. Crit. Care Med.* doi:10.1164/rccm.202201-0157OC

Cortiella, J., Niles, J., Cantu, A., Brettler, A., Pham, A., Vargas, G., et al. (2010). Influence of acellular natural lung matrix on murine embryonic stem cell differentiation and tissue formation. *Tissue Eng. Part A* 16 (8), 2565–2580. doi:10.1089/ten.tea.2009.0730

Crapo, P. M., Gilbert, T. W., and Badylak, S. F. (2011). An overview of tissue and whole organ decellularization processes. *Biomaterials* 32 (12), 3233–3243. doi:10.1016/j.biomaterials.2011.01.057

Cruz, F. F., Borg, Z. D., Goodwin, M., Sokocevic, D., Wagner, D. E., Coffey, A., et al. (2015). Systemic administration of human bone marrow-derived mesenchymal stromal cell extracellular vesicles ameliorates Aspergillus hyphal extract-induced allergic airway inflammation in immunocompetent mice. *Stem Cells Transl. Med.* 4 (11), 1302–1316. doi:10.5966/sctm.2014-0280

Cruz, F. F., Borg, Z. D., Goodwin, M., Sokocevic, D., Wagner, D., McKenna, D. H., et al. (2015). Freshly thawed and continuously cultured human bone marrow-derived mesenchymal stromal cells comparably ameliorate allergic airways inflammation in immunocompetent mice. *Stem Cells Transl. Med.* 4 (6), 615–624. doi:10.5966/sctm.2014-0268

Daly, A. B., Wallis, J. M., Borg, Z. D., Bonvillain, R. W., Deng, B., Ballif, B. A., et al. (2012). Initial binding and recellularization of decellularized mouse lung scaffolds with bone marrow-derived mesenchymal stromal cells. *Bone Marrow-Derived Mesenchymal Stromal Cells Tissue Eng. Part A* 18 (1-2), 1–16. doi:10.1089/ten.TEA.2011.0301

De Hilster, R. H. J., Sharma, P. K., Jonker, M. R., White, E. S., Gercama, E. A., Roobeek, M., et al. (2020). Human lung extracellular matrix hydrogels resemble the stiffness and viscoelasticity of native lung tissue. *Am. J. Physiol. - Lung Cell. Mol. Physiol.* 318, L698–L704. doi:10.1152/ajplung.00451.2019

De Santis, M. M., Alsafadi, H. N., Tas, S., Bolukbas, D. A., Prithiviraj, S., Da Silva, I. A. N., et al. (2021). Extracellular-matrix-reinforced bioinks for 3D bioprinting human tissue. *Adv. Mater.* 33 (3), e2005476. doi:10.1002/adma.202005476

Dilogo, I. H., Aditianingsih, D., Sugiarto, A., Burhan, E., Damayanti, T., Sitompul, P. A., et al. (2021). Umbilical cord mesenchymal stromal cells as critical COVID-19 adjuvant therapy: A randomized controlled trial. *Stem Cells Transl. Med.* 10 (9), 1279–1287. doi:10.1002/sctm.21-0046

Enes, S. R., Hampton, T. H., Barua, J., McKenna, D. H., dos Santos, C. C., Amiel, E., et al. (2021). Healthy versus inflamed lung environments differentially effect MSCs. *Eur. Respir. J.* 58 (4), 2004149. doi:10.1183/13993003.04149-2020

Falcones, B., Sanz, H., Marhuenda, E., Mendizabal, I., Cabrera, I., Malandain, N., et al. (2021). Bioprintable lung extracellular matrix hydrogel scaffolds for 3D culture of mesenchymal stromal cells. *Polymers* 13, 2350. doi:10.3390/polym13142350

Foster, W. S., Suen, C. M., and Stewart, D. J. (2014). Regenerative cell and tissue-based therapies for pulmonary arterial hypertension. *Can. J. Cardiol.* 30 (11), 1350–1360. doi:10.1016/j.cjca.2014.08.022

Francois, M., Copland, I. B., Yuan, S., Romieu-Mourez, R., Waller, E. K., and Galipeau, J. (2012). Cryopreserved mesenchymal stromal cells display impaired immunosuppressive properties as a result of heat-shock response and impaired interferon-gamma licensing. *Cytotherapy* 14 (2), 147–152. doi:10.3109/14653249.2011.623691

Galipeau, J., and Sensébé, L. (2018). Mesenchymal stromal cells: Clinical challenges and therapeutic opportunities. *Cell Stem Cell* 22 (6), 824–833. doi:10.1016/j.stem.2018.05.004

Galipeau, J., Krampera, M., Leblanc, K., Nolta, J. A., Phinney, D. G., Shi, Y., et al. (2021). Mesenchymal stromal cell variables influencing clinical potency: The impact of viability, fitness, route of administration and host predisposition. *Cytotherapy* 23 (5), 368–372. doi:10.1016/j.jcyt.2020.11.007

Galleu, A., Riffo-Vasquez, Y., Trento, C., Lomas, C., Dolcetti, L., Cheung, T. S., et al. (2017). Apoptosis in mesenchymal stromal cells induces *in vivo* recipient-mediated immunomodulation. *Sci. Transl. Med.* 9 (416), eaam7828. doi:10.1126/scitranslmed.aam7828

Galliger, Z., Vogt, C. D., and Panoskaltsis-Mortari, A. (2019). 3D bioprinting for lungs and hollow organs. *Transl. Res. J. Laboratory Clin. Med.* 211, 19–34. doi:10.1016/j.trsl.2019.05.001

Gasek, N., Dearborn, J., Enes, S. R., Pouliot, R., Louie, J., Phillips, Z., et al. (2021). Comparative immunogenicity of decellularized wild type and alpha 1,3 galactosyltransferase knockout pig lungs. *Biomaterials* 276, 121029. doi:10.1016/j.biomaterials.2021.121029

Giobbe, G. G., Crowley, C., Luni, C., Campinoti, S., Khedr, M., Kretzschmar, K., et al. (2019). Extracellular matrix hydrogel derived from decellularized tissues enables endodermal organoid culture. *Nat. Commun.* 10, 5658. doi:10.1038/s41467-019-13605-4

Grigoryan, B., Paulsen, S. J., Corbett, D. C., Sazer, D. W., Fortin, C. L., Zaita, A. J., et al. (2019). Multivascular networks and functional intravascular topologies within biocompatible hydrogels. *Science* 364 (6439), 458–464. doi:10.1126/science.aav9750

Hoffman, E. T., Uhl, F. E., Asarian, L., Deng, B., Becker, C., Uriarte, J. J., et al. (2023). Regional and disease specific human lung extracellular matrix composition. *Biomaterials* 293, 121960. in press 2023. doi:10.1016/j.biomaterials.2022.121960

Hughes, C. S., Postovit, L. M., and Lajoie, G. A. (2010). Matrigel: A complex protein mixture required for optimal growth of cell culture. *Proteomics* 10, 1886–1890. doi:10.1002/pmic.200900758

Huh, D., Matthews, B. D., Mammoto, A., Montoya-Zavala, M., Hsin, H. Y., and Ingber, D. E. (2010). Reconstituting organ-level lung functions on a chip. *Science* 328 (5986), 1662–1668. doi:10.1126/science.1188302

Huh, D., Leslie, D. C., Matthews, B. D., Fraser, J. P., Jurek, S., Hamilton, G. A., et al. (2012). A human disease model of drug toxicity-induced pulmonary edema in a lung-on-a-chip microdevice. *Sci. Transl. Med.* 4 (159), 159ra147. doi:10.1126/scitranslmed.3004249

Huh, D., Kim, H. J., Fraser, J. P., Shea, D. E., Khan, M., Bahinski, A., et al. (2013). Microfabrication of human organs-on-chips. *Nat. Protoc.* 8 (11), 2135–2157. doi:10.1038/nprot.2013.137

Huo, Y., Xu, Y., Wu, X., Gao, E., Zhan, A., Chen, Y., et al. (2022). Functional trachea reconstruction using 3D-bioprinted native-like tissue architecture based on designable tissue-specific bioinks. *Adv. Sci.* 9 (29), e2202181. doi:10.1002/advs.202202181

Ikonomou, L., Wagner, D. E., Gilpin, S. E., Weiss, D. J., and Ryan, A. L. (2020). Technological advances in study of lung regenerative medicine: Perspective from the 2019 Vermont lung stem cell conference. *Cytotherapy* 22 (10), 519–520. doi:10.1016/j.jcyt.2020.04.001

Ikonomou, L., Magnusson, M., Dries, R., Herzog, E., Hynds, R., BorokPark, Z. J-A., et al. (2022). Stem cells, cell therapies, and bioengineering in lung biology and disease 2021. *Am. J. Physiology - Lung Cell. Mol. Physiology* 323 (3), L341–L354. doi:10.1152/ajplung.00113.2022

Islam, D., Huang, Y., Fanelli, V., Delsedime, L., Wu, S., Khang, J., et al. (2019). Identification and modulation of microenvironment is crucial for effective mesenchymal stromal cell therapy in acute lung injury. *Am. J. Respir. Crit. Care Med.* 199 (10), 1214–1224. doi:10.1164/rccm.201802-0356OC

Johnson, B., Dobkin, S. L., and Josephson, M. (2022). Extracorporeal membrane oxygenation as a bridge to transplant in neonates with fatal pulmonary conditions: A review. *Paediatr. Respir. Rev.* 44, 31–39. doi:10.1016/j.prrv.2022.11.001

Jorba, I., Beltran, G., Falcones, B., Suki, B., Farre, R., Garcia-Aznar, J. M., et al. (2019). Nonlinear elasticity of the lung extracellular microenvironment is regulated by macroscale tissue strain. *Acta Biomater.* 92, 265–276. doi:10.1016/j.actbio.2019.05.023

Kang, D., Park, J. A., Kim, W., Kim, S., Lee, H. R., Kim, W. J., et al. (2021). All-inkjet-printed 3D alveolar barrier model with physiologically relevant microarchitecture. *Adv. Sci.* 8 (10), 2004990. doi:10.1002/advs.202004990

Ke, D., Yi, H., Est-Witte, S., George, S., Kengla, C., Lee, S. J., et al. (2019). Bioprinted trachea constructs with patient-matched design, mechanical and biological properties. *Biofabrication* 12 (1), 015022. doi:10.1088/1758-5090/ab5354

Khoury, M., Cuenca, J., Cruz, F. F., Figueroa, F. E., Rocco, P. R. M., and Weiss, D. J. (2020). Current status of cell-based therapies for respiratory virus infections. *Eur. Respir. J.* 55 (6), 2000858. doi:10.1183/13993003.00858-2020

Kirkham, A. M., Bailey, A. J. M., Monaghan, M., Shorr, R., Lalu, M. M., Fergusson, D. A., et al. (2022). Updated living systematic review and meta-analysis of controlled trials of mesenchymal stromal cells to treat COVID-19: A framework for accelerated synthesis of trial evidence for rapid approval – FASTER approval. *Stem Cells Transl. Med.* 11, 675–687. in press. doi:10.1093/stcltm/szac038

Kotton, D. N., Fabian, A. J., and Mulligan, R. C. (2005). Failure of bone marrow to reconstitute lung epithelium. *Am. J. Respir. Cell & Mol. Biol.* 33 (4), 328–334. doi:10.1165/rcmb.2005-0175RC

Krampera, M., Cosmi, L., Angeli, R., Pasini, A., Liotta, F., Andreini, A., et al. (2006). Role for interferon-gamma in the immunomodulatory activity of human bone marrow mesenchymal stem cells. *Stem Cells* 24 (2), 386–398. doi:10.1634/stemcells.2005-0008

Krause, D. S., Theise, N. D., Collector, M. I., Henegariu, O., Hwang, S., Gardner, R., et al. (2001). Multi-organ, multi-lineage engraftment by a single bone marrow-derived stem cell. *Cell* 105 (3), 369–377. doi:10.1016/s0092-8674(01)00328-2

Kruk, D. M. L. W., Wisman, M., Bruin, H. G., Lodewijk, M. E., Hof, D. J., Borghuis, T., et al. (2021a). Abnormalities in reparative function of lung-derived mesenchymal stromal cells in emphysema. *Am. J. Physiology - Lung Cell. Mol. Physiology* 320 (5), L832–L844. doi:10.1152/ajplung.00147.2020

Kruk, D. M. L. W., Wisman, M., Noordhoek, J. A., Nizamoglu, M., Jonker, M. R., de Bruin, H. G., et al. (2021b). Paracrine regulation of alveolar epithelial damage and repair responses by human lung-resident mesenchymal stromal cells. *Cells* 10 (11), 2860. doi:10.3390/cells10112860

Kusuma, G. D., Carthew, J., Lim, R., and Frith, J. E. (2017). Effect of the microenvironment on mesenchymal stem cell paracrine signaling: Opportunities to engineer the therapeutic effect. *Stem Cells Dev.* 26 (9), 617–631. doi:10.1089/scd.2016.0349

Lanzoni, G., Linetsky, E., Correa, D., Messinger Cayetano, S., Alvarez, R. A., Kouroupis, D., et al. (2021). Umbilical cord mesenchymal stem cells for COVID-19 acute respiratory distress syndrome: A double-blind, phase 1/2a, randomized controlled trial. *Stem Cells Transl. Med.* 10, 660–673. doi:10.1002/sctm.20-0472

Loi, R., Beckett, T., Goncz, K. K., Suratt, B. T., and Weiss, D. J. (2006). Limited restoration of cystic fibrosis lung epithelium *in vivo* with adult bone marrow-derived cells. *Am. J. Resp. Crit. Care Med.* 173, 171–179. doi:10.1164/rccm.200502-309OC

Lu, K., Geng, S. T., Tang, S., Yang, H., Xiong, W., Xu, F., et al. (2022). Clinical efficacy and mechanism of mesenchymal stromal cells in treatment of COVID-19. *Stem Cell Res. Ther.* 13, 61–15. doi:10.1186/s13287-022-02743-0

Lwebuga-Mukasa, J. S., Ingbar, D. H., and Madri, J. A. (1986). Repopulation of a human alveolar matrix by adult rat type II pneumocytes *in vitro*. A novel system for type II pneumocyte culture. *Exptl Lung Res.* 162 (2), 423–435. doi:10.1016/0014-4827(86)90347-2

Mahfouzia, S. H., Tali, S. H. S., and Amoabediny, G. (2021). 3D bioprinting for lung and tracheal tissue engineering: Criteria, advances, challenges, and future directions. *Bioprinting* 21, e00124. doi:10.1016/j.bprint.2020.e00124

Mahida, R. Y., Matsumoto, S., and Matthay, M. A. (2020). Extracellular vesicles: A new frontier for research in acute respiratory distress syndrome. *Am. J. Respir. Cell & Mol. Biol.* 63 (1), 15–24. doi:10.1165/rcmb.2019-0447TR

Marhuenda, E., Villarino, A., Narciso, M., Elowsson, L., Almendros, I., Westergren-Thorsson, G., et al. (2022a). Development of a physiomimetic model of acute respiratory distress syndrome by using ECM hydrogels and organ-on-a-chip devices. *Front. Pharmacol.* 13, 945134. doi:10.3389/fphar.2022.945134

Marhuenda, E., Villarino, A., Narciso, M. L., Camprubi-Rimblas, M., Farre, R., Gavara, N., et al. (2022b). Lung extracellular matrix hydrogels enhance preservation of type II phenotype in primary alveolar epithelial cells. *Int. J. Mol. Sci.* 23 (9), 4888. doi:10.3390/ijms23094888

Marklein, R. A., Klinker, M. W., Drake, K. A., Polikowsky, H. G., Lessey-Morillon, E. C., and Bauer, S. R. (2019). Morphological profiling using machine learning reveals emergent subpopulations of interferon-gamma-stimulated mesenchymal stromal cells that predict immunosuppression. *Cytotherapy* 21 (1), 17–31. doi:10.1016/j.jcyt.2018.10.008

Matthay, M. A., Zemans, R. L., Zimmerman, G. A., Arabi, Y. M., Beitler, J. R., Mercat, A., et al. (2019). Acute respiratory distress syndrome. *Nat. Rev. Dis. Prim.* 5 (1), 18. doi:10.1038/s41572-019-0069-0

Matthay, M. A., Calfee, C. S., Zhuo, H., Thompson, B. T., Wilson, J. G., Levitt, J. E., et al. (2019). Treatment with allogeneic mesenchymal stromal cells for moderate to severe acute respiratory distress syndrome (START study): A randomised phase 2a safety trial. *Lancet Respir. Med.* 7 (2), 154–162. doi:10.1016/S2213-2600(18)30418-1

Matthay, M. A., Arabi, Y. M., Siegel, E. R., Ware, L. B., Bos, L. D. J., Sinha, P., et al. (2020). Phenotypes and personalized medicine in the acute respiratory distress syndrome. *Intensive Care Med.* 46 (12), 2136–2152. doi:10.1007/s00134-020-06296-9

Melo, E., Garreta, E., Luque, T., Cortiella, J., Nichols, J., Navajas, D., et al. (2014). Effects of the decellularization method on the local stiffness of acellular lungs. *Tissue Eng. - Part C. Methods* 20 (5), 412–422. doi:10.1089/ten.TEC.2013.0325

Monsel, A., Hauw-Berlemont, C., Mebarki, M., Heming, N., Mayaux, J., Nguekap Tchoumba, O., et al. (2022). Treatment of COVID-19-associated ARDS with

mesenchymal stromal cells: A multicenter randomized double-blind trial. *Crit. Care* 26, 48. doi:10.1186/s13054-022-03930-4

Nagaya, N., Kangawa, K., Kanda, M., Uematsu, M., Horio, T., Fukuyama, N., et al. (2003). Hybrid cell-gene therapy for pulmonary hypertension based on phagocytosing action of endothelial progenitor cells. *Circulation* 108, 889–895. doi:10.1161/01.CIR.0000079161.56080.22

Nawroth, J. C., Barrile, R., Conegliano, D., van Riet, S., Hiemstra, P. S., and Villenave, R. (2019). Stem cell-based Lung-on-Chips: The best of both worlds? *Adv. Drug Deliv. Rev.* 140, 12–32. doi:10.1016/j.addr.2018.07.005

Nawroth, J. C., Lucchesi, C., Cheng, D., Shukla, A., Ngyuen, J., Shroff, T., et al. (2020). A microengineered airway lung chip models key features of viral-induced exacerbation of asthma. *Am. J. Respir. Cell & Mol. Biol.* 63 (5), 591–600. doi:10.1165/rcmb.2020-0010MA

Nizamoglu, M., de Hilster, R. H. J., Zhao, F., Sharma, P. K., Borghuis, T., Harmsen, M. C., et al. (2022). An *in vitro* model of fibrosis using crosslinked native extracellular matrix-derived hydrogels to modulate biomechanics without changing composition. *Acta Biomater.* 147, 50–62. doi:10.1016/j.actbio.2022.05.031

Ott, H. C., Clippinger, B., Conrad, C., Schuetz, C., Pomerantseva, I., Ikonomou, L., et al. (2010). Regeneration and orthotopic transplantation of a bioartificial lung. *Nat. Med.* 16, 927–933. doi:10.1038/nm.2193

Park, J. H., Ahn, M., Park, S. H., Kim, H., Bae, M., Park, W., et al. (2021). 3D bioprinting of a trachea-mimetic cellular construct of a clinically relevant size. *Biomaterials* 279, 121246. doi:10.1016/j.biomaterials.2021.121246

Petersen, T. H., Calle, E. A., Zhao, L., Lee, E. J., Gui, L., Raredon, M. B., et al. (2010). Tissue-engineered lungs for *in vivo* implantation. *Science* 329, 538–541. doi:10.1126/science.1189345

Petrou, C. L., D'Ovidio, T. J., Bolukbas, D. A., Tas, S., Brown, R. D., Allawzi, A., et al. (2020). Clickable decellularized extracellular matrix as a new tool for building hybrid-hydrogels to model chronic fibrotic diseases *in vitro*. *J. Mater. Chem. B* 8 (31), 6814–6826. doi:10.1039/d0tb00613k

Platz, J., Bonenfant, N. R., Uhl, F. E., Coffey, A. L., McKnight, T., Parsons, C., et al. (2016). Comparative decellularization and recellularization of wild-type and alpha 1,3 galactosyltransferase knockout pig lungs: A model for *ex vivo* xenogeneic lung bioengineering and transplantation. *Tissue Eng. Part C Methods* 22 (8), 725–739. doi:10.1089/ten.TEC.2016.0109

Plebani, R., Potla, R., Soong, M., Bai, H., Izadifar, Z., Jiang, A., et al. (2020). Modeling pulmonary cystic fibrosis in a human lung airway-on-a-chip. *J. Cyst. Fibros.* 21 (4), 606–615. doi:10.1016/j.jcf.2021.10.004

Polchert, D., Sobinsky, J., Douglas, G., Kidd, M., Moadsiri, A., Reina, E., et al. (2008). IFN-gamma activation of mesenchymal stem cells for treatment and prevention of graft versus host disease. *Eur. J. Immunol.* 38 (6), 1745–1755. doi:10.1002/eji.200738129

Pothen, J. J., Rajendran, V., Wagner, D., Weiss, D. J., Smith, B. J., Ma, B., et al. (2016). A computational model of cellular engraftment on lung scaffolds. *Biores Open Access* 5 (1), 308–319. doi:10.1089/biores.2016.0031

Pouliot, R. A., Link, P. A., Mikhaiel, N. S., Schneck, M. B., Valentine, M. S., Kamga Gninzeko, F. J., et al. (2016). Development and characterization of a naturally derived lung extracellular matrix hydrogel. *J. Biomed. Mat. Res. - Part A.* 104, 1922–1935. doi:10.1002/jbm.a.35726

Pouliot, R. A., Young, B. M., Link, P. A., Park, H. E., Kahn, A. R., Shankar, K., et al. (2020). Porcine lung-derived extracellular matrix hydrogel properties are dependent on pepsin digestion time. *Tissue Eng. - Part C. Methods* 26 (6), 332–346. doi:10.1089/ten.TEC.2020.0042

Price, A. P., England, K. A., Matson, A. M., Blazar, B. R., and Panoskaltsis-Mortari, A. (2010). Development of a decellularized lung bioreactor system for bioengineering the lung: The matrix reloaded. *Tissue Eng. Part A* 16, 2581–2591. doi:10.1089/ten.TEA.2009.0659

Qu, W., Wang, Z., Hare, J. M., Bu, G., Mallea, J. M., Pascual, J. M., et al. (2020). Cell-based therapy to reduce mortality from COVID-19: Systematic review and meta-analysis of human studies on acute respiratory distress syndrome. *Stem Cells Transl. Med.* 9, 1007–1022. doi:10.1002/sctm.20-0146

Romieu-Mourez, R., Francois, M., Boivin, M. N., Bouchentouf, M., Spaner, D. E., and Galipeau, J. (2009). Cytokine modulation of TLR expression and activation in mesenchymal stromal cells leads to a proinflammatory phenotype. *J. Immunol.* 182 (12), 7963–7973. doi:10.4049/jimmunol.0803864

Rosmark, O., Ibanez-Fonseca, A., Thorsson, J., Dellgren, G., Hallgren, O., Larsson Callerfelt, A. K., et al. (2022). A tunable physiomimetic stretch system evaluated with precision cut lung slices and recellularized human lung scaffolds. *Front. Bioeng. Biotechnol.* 10, 995460. doi:10.3389/fbioe.2022.995460

Saldin, L. T., Cramer, M. C., Velankar, S. S., White, L. J., and Badylak, S. F. (2017). Extracellular matrix hydrogels from decellularized tissues: Structure and function. *Acta Biomater.* 49, 1–15. doi:10.1016/j.actbio.2016.11.068

Saleh, K. S., Hewawasam, R., Serbedzija, P., Blomberg, R., Noreldeen, S. E., Edelman, B., et al. (2022). Engineering hybrid-hydrogels comprised of healthy or diseased decellularized extracellular matrix to study pulmonary fibrosis. *Cell. Mol. Bioeng.* 15 (5), 505–519. doi:10.1007/s12195-022-00726-y

Santi, P. A. (2011). Light sheet fluorescence microscopy: A review. *J. Histochem Cytochem* 59 (2), 129–138. doi:10.1369/0022155410394857

Sokocevic, D., Bonenfant, N., Wagner, D. E., Borg, Z. D., Lathrop, M., Lam, Y. W., et al. (2013). The effect of age and emphysematous and fibrotic injury on the Re-cellularization of de-cellularized lungs. *Biomaterials* 34 (13), 3256–3269. doi:10.1016/j.biomaterials.2013.01.028

Stegmayr, J., and Wagner, D. E. (2021). The dawn of the omics era in human precision-cut lung slices. *Eur. Respir. J.* 58 (1), 2100203. doi:10.1183/13993003.00203-2021

Stegmayr, J., Alsafadi, H. N., Langwinski, W., Niroomand, A., Lindstedt, S., Leigh, N. D., et al. (2021). Isolation of high-yield and -quality RNA from human precision-cut lung slices for RNA-sequencing and computational integration with larger patient cohorts. *Am. J. Physiology - Lung Cell. Mol. Physiology* 320 (2), L232–L240. doi:10.1152/ajplung.00401.2020

Sucre, J. M. S., Bock, F., Negretti, N. M., Benjamin, J. T., Gulleman, P. M., Dong, X., et al. (2022). β1 integrin regulates alveolar epithelial cell differentiation following injury, BioRxiv.

Suen, C. M., Zhai, A., Lalu, M. M., Welsh, C., Levac, B. M., Fergusson, D., et al. (2016). Efficacy and safety of regenerative cell therapy for pulmonary arterial hypertension in animal models: A preclinical systematic review protocol. *Syst. Rev.* 5, 89. doi:10.1186/s13643-016-0265-x

Sun, W., Schaffer, S., Dai, K., Yao, L., Feinberg, A., and Webster-Wood, V. (2021). 3D printing hydrogel-based soft and biohybrid actuators: A mini-review on fabrication techniques, applications, and challenges. *Front. Robotics AI* 8, 673533. doi:10.3389/frobt.2021.673533

Syed, A., Kerdi, S., and Qamar, A. (2021). Bioengineering progress in lung assist devices. *Bioengineering Basel* 8, 89. doi:10.3390/bioengineering8070089

Ting, A. E., Baker, E. K., Champagne, J., Desai, T. J., dos Santos, C. C., Heijink, I. H., et al. (2022). Proceedings of the ISCT scientific signature series symposium, "Advances in cell and gene therapies for lung diseases and critical illnesses": International Society for Cell & Gene Therapy, Burlington VT, US, July 16, 2021. *Cytotherapy* 24 (8), 774–788. doi:10.1016/j.jcyt.2021.11.007

Uhl, F. E., Zhang, F., Pouliot, R. A., Uriarte, J. J., Rolandsson Enes, S., Han, X., et al. (2020). Functional role of glycosaminoglycans in decellularized lung extracellular matrix. *Acta Biomater.* 102, 231–246. doi:10.1016/j.actbio.2019.11.029

Wagner, D. E., Bonenfant, N. R., Sokocevic, D., DeSarno, M., Borg, Z., Parsons, C., et al. (2014). Three-dimensional scaffolds of acellular human and porcine lungs for high throughput studies of lung disease and regeneration. *Biomaterials* 35 (9), 2664–2679. doi:10.1016/j.biomaterials.2013.11.078

Wagner, D. E., Bonenfant, N. R., Parsons, C., Sokocevic, D., Borg, Z. S., Lathrop, M., et al. (2014). Comparative decellularization and recellularization of normal versus emphysematous human lungs. *Biomaterials* 35 (10), 3281–3297. doi:10.1016/j.biomaterials.2013.12.103

Wallis, J. M., Borg, Z. D., Daly, A. B., Deng, B., Ballif, B. A., Allen, G. B., et al. (2012). Comparative assessment of detergent-based protocols for mouse lung de-cellularization and Re-cellularization. *Tissue Eng. Part C* 18 (6), 420–432. doi:10.1089/ten.tec.2011.0567

Walter, J., Ware, L. B., and Matthay, M. A. (2014). Mesenchymal stem cells: Mechanisms of potential therapeutic benefit in ARDS and sepsis. *Lancet Respir. Med.* 2 (12), 1016–1026. doi:10.1016/S2213-2600(14)70217-6

Waterman, R. S., Tomchuck, S. L., Henkle, S. L., and Betancourt, A. M. (2010). A new mesenchymal stem cell (MSC) paradigm: Polarization into a pro-inflammatory MSC1 or an immunosuppressive MSC2 phenotype. *PLoS One* 5 (4), e10088. doi:10.1371/journal.pone.0010088

Weiss, D. J., Casaburi, R., Flannery, R., LeRoux-Williams, M., and Tashkin, D. P. (2013). A placebo-controlled, randomized trial of mesenchymal stem cells in COPD. *Chest* 143 (6), 1590–1598. doi:10.1378/chest.12-2094

Weiss, D. J., English, K., Krasnodembskaya, A., Isaza-Correa, J. M., Hawthorne, I. J., and Mahon, B. P. (2019). The necrobiology of mesenchymal stromal cells affects therapeutic efficacy. *Front. Immunol.* 10, 1228. doi:10.3389/fimmu.2019.01228

Weiss, D. J., Segal, K., Casaburi, R., Hayes, J., and Tashkin, D. (2021). Effect of mesenchymal stromal cell infusions on lung function in COPD patients with high CRP levels. *Respir. Res.* 22 (1), 142. doi:10.1186/s12931-021-01734-8

Wrenn, S. M., Griswold, E. D., Uhl, F. E., Uriarte, J. J., Park, H. E., Coffey, A. L., et al. (2018). Avian lungs: A novel scaffold for lung bioengineering. *PLoS One* 13 (6), e0198956. doi:10.1371/journal.pone.0198956

Zamprogno, P., Wuthrich, S., Achenbach, S., Thoma, G., Stucki, J. D., Hobi, N., et al. (2021). Second-generation lung-on-a-chip with an array of stretchable alveoli made with a biological membrane. *Commun. Biol.* 4 (1), 168. doi:10.1038/s42003-021-01695-0

Zhao, Y. D., Courtman, D. W., Deng, Y., Kugathasan, L., Zhang, Q., and Stewart, D. J. (2005). Rescue of monocrotaline-induced pulmonary arterial hypertension using bone marrow-derived endothelial-like progenitor cells: Efficacy of combined cell and eNOS gene therapy in established disease. *Circ. Res.* 96, 442–450. doi:10.1161/01.RES.0000157672.70560.7b

Zhu, Y. G., Feng, X. M., Abbott, J., Fang, X. H., Hao, Q., Monsel, A., et al. (2014). Human mesenchymal stem cell microvesicles for treatment of *Escherichia coli* endotoxin-induced acute lung injury in mice. *Stem Cells* 32 (1), 116–125. doi:10.1002/stem.1504

Zhu, R., Yan, T., Feng, Y., Liu, Y., Cao, H., Peng, G., et al. (2021). Mesenchymal stem cell treatment improves outcome of COVID-19 patients via multiple immunomodulatory mechanisms. *Cell Res.* 31 (12), 1244–1262. doi:10.1038/s41422-021-00573-y

frontiers | Frontiers in Pharmacology

TYPE Original Research
PUBLISHED 06 March 2023
DOI 10.3389/fphar.2023.1114739

OPEN ACCESS

EDITED BY
Ramon Farre,
University of Barcelona, Spain

REVIEWED BY
Jesus Perez-Gil,
Complutense University of Madrid, Spain
Josue Sznitman,
Technion Israel Institute of Technology, Israel

*CORRESPONDENCE
Arunima Sengupta,
arunima.sengupta@unibe.ch

†These authors have contributed equally to this work

SPECIALTY SECTION
This article was submitted to Respiratory Pharmacology, a section of the journal Frontiers in Pharmacology

RECEIVED 02 December 2022
ACCEPTED 07 February 2023
PUBLISHED 06 March 2023

CITATION
Sengupta A, Dorn A, Jamshidi M, Schwob M, Hassan W, De Maddalena LL, Hugi A, Stucki AO, Dorn P, Marti TM, Wisser O, Stucki JD, Krebs T, Hobi N and Guenat OT (2023), A multiplex inhalation platform to model *in situ* like aerosol delivery in a breathing lung-on-chip. *Front. Pharmacol.* 14:1114739. doi: 10.3389/fphar.2023.1114739

A multiplex inhalation platform to model *in situ* like aerosol delivery in a breathing lung-on-chip

Arunima Sengupta[1]*, Aurélien Dorn[1,2], Mohammad Jamshidi[1], Magali Schwob[1], Widad Hassan[1], Lea Lara De Maddalena[2], Andreas Hugi[2], Andreas O. Stucki[1], Patrick Dorn[3,4], Thomas M. Marti[3,4], Oliver Wisser[5], Janick D. Stucki[2], Tobias Krebs[5], Nina Hobi[2†] and Olivier T. Guenat[1,3,6†]

[1]Organs-on-Chip Technologies, ARTORG Center for Biomedical Engineering, University of Bern, Bern, Switzerland, [2]AlveoliX AG, Swiss Organs-on-Chip Innovation, Bern, Switzerland, [3]Department of General Thoracic Surgery, Inselspital, Bern University Hospital, Bern, Switzerland, [4]Department for BioMedical Research, University of Bern, Bern, Switzerland, [5]VITROCELL Systems GmbH, Waldkirch, Germany, [6]Department of Pulmonary Medicine, Inselspital, Bern University Hospital, Bern, Switzerland

Prolonged exposure to environmental respirable toxicants can lead to the development and worsening of severe respiratory diseases such as asthma, chronic obstructive pulmonary disease (COPD) and fibrosis. The limited number of FDA-approved inhaled drugs for these serious lung conditions has led to a shift from *in vivo* towards the use of alternative *in vitro* human-relevant models to better predict the toxicity of inhaled particles in preclinical research. While there are several inhalation exposure models for the upper airways, the fragile and dynamic nature of the alveolar microenvironment has limited the development of reproducible exposure models for the distal lung. Here, we present a mechanistic approach using a new generation of exposure systems, the Cloud α AX12. This novel *in vitro* inhalation tool consists of a cloud-based exposure chamber (VITROCELL) that integrates the breathing ^{AX}Lung-on-chip system (AlveoliX). The ultrathin and porous membrane of the AX12 plate was used to create a complex multicellular model that enables key physiological culture conditions: the air-liquid interface (ALI) and the three-dimensional cyclic stretch (CS). Human-relevant cellular models were established for a) the distal alveolar-capillary interface using primary cell-derived immortalized alveolar epithelial cells (^{AX}iAECs), macrophages (THP-1) and endothelial (HLMVEC) cells, and b) the upper-airways using Calu3 cells. Primary human alveolar epithelial cells (^{AX}hAEpCs) were used to validate the toxicity results obtained from the immortalized cell lines. To mimic *in vivo* relevant aerosol exposures with the Cloud α AX12, three different models were established using: a) titanium dioxide (TiO2) and zinc oxide nanoparticles b) polyhexamethylene guanidine a toxic chemical and c) an anti-inflammatory inhaled corticosteroid, fluticasone propionate (FL). Our results

Abbreviations: COPD, Chronic obstructive pulmonary disease; ALI, air-liquid interface; CS, cyclic stretch; NPs, nanoparticles; TiO2, titanium dioxide; ZnO, zinc oxide; PHMG, polyhexamethylene guanidine; FL, fluticasone propionate; 3D, three-dimensional; ECs, endothelial cells; AMs, alveolar macrophages; AT1, alveolar type 1 cells; AT2, alveolar type 2 cells; AXhAEpC, Primary human alveolar epithelial cells; AXiAECs, primary cell-derived immortalized alveolar epithelial cell line; d-THP1, differentiated THP-1 cells; TER, transepithelial barrier; tri-cell culture, triple-cell culture; ECM, extracellular matrix; QCM, quartz crystal microbalance; OR, Output Rate; SBL, suspension base liquid; h, hours; mins, minutes; PMA, phorbol 12-myristate 13-acetate; LDH, Lactate Dehydrogenase; ROS, reactive oxygen species; fc, fold change; EMT, epithelial-mesenchymal transition.

suggest an important synergistic effect on the air-blood barrier sensitivity, cytotoxicity and inflammation, when air-liquid interface and cyclic stretch culture conditions are combined. To the best of our knowledge, this is the first time that an *in vitro* inhalation exposure system for the distal lung has been described with a breathing lung-on-chip technology. The Cloud α AX12 model thus represents a state-of-the-art pre-clinical tool to study inhalation toxicity risks, drug safety and efficacy.

KEYWORDS

lung-on-chip, inhalation therapeutics, nanoparticles, aerosolized drug delivery, cyclic stretch, air-liquid interface, COPD, toxicity assessments

Introduction

Inhalation is a major route of airborne toxicant exposure, in which the lung epithelial barrier serves as the main portal of entry into the systemic circuit for the human body. This may lead to progressive and perpetual inflammation of the epithelium leading to development of chronic respiratory conditions such as asthma, COPD, ARDS and interstitial lung diseases (ILD) (Baumgartner et al., 2000; Sokol et al., 2013; Assad et al., 2018; Zhao et al., 2019; Peng et al., 2020; Shima et al., 2022). Inhaled toxicants are ubiquitous across the globe and come from a variety of sources ranging from organic pollution to industrial chemicals and consumer-related products (Adeola, 2021; Naidu et al., 2021). Therefore, it is crucial to understand the harmful effects of these inhaled substances, especially in the lungs, being the primary point of contact. Inhaled toxicants are known to trigger microinjuries which lead to epithelial barrier damage (Carlier et al., 2021), activation of alveolar macrophages (AMs) (Hamilton et al., 2008; Kuroda et al., 2016) and differentiation and translocation of the circulating monocytes into the alveolar space (van Eeden et al., 2001; Bliss et al., 2018).

To assess the impact of inhaled substances, human exposure data are still considered as the "gold standard" to identify and understand potential risk factors. However, controlled human exposure and epidemiologic studies for respirable substances are generally very costly, of long duration and when suspected to be toxic, non-ethical (London et al., 2010). Therefore, toxicity tests have mainly been carried out in animals, typically rats to fill this knowledge gap. . Inhalation testing using animals is still a regulatory requirement in most jurisdictions including Canada, the United States of America (United States of America), and the European Union (E.U.) for substances such as chemicals, plant production products or pharmaceuticals (Stucki et al., 2022). However, due to scientific and ethical concerns, and to adhere to the 3R principles (Ehrhardt & Kim, 2008) to reduce, refine and replace the use of animals in science, regulations worldwide are being amended and new approaches are being developed.

For example, the Senate of Canada passed the "Bill S-5" in June 2022 (Bill S-5.44-1, 2022), an act to amend the Canadian Environmental Protection Act to strengthen the importance of alternatives to animal testing. The FDA Modernization Act 2.0 was signed into U.S. law by President Biden in December 2022, amending and deleting wording from 1938 in the Food, Drugs, and Cosmetics Act that required all drugs to be tested on animals before conducting clinical trials (Animal Wellness Action, 2022). In addition, the U.S. Food and Drug Administration (FDA) has also set out new proposals for its New Alternative Methods Programs in June 2022 (Nuwer, 2022). In November 2022, the European Commission and European Chemicals Agency announced its commitment to modernize alternative non-animal *in vitro* testing strategies and to develop a roadmap to phase-out animal testing (EPAA, 2022). Furthermore, international efforts are going on to develop robust and efficient processes to establish scientific confidence in new approaches and to facilitate the timely uptake into regulatory application of alternatives to animal testing (van der Zalm et al., 2022).

Several alternative *in vitro* approaches for inhalation toxicity testing have been developed in the past years (Clippinger et al., 2018; Singh et al., 2021). Until a few years ago, most inhalation testing with these approaches were typically performed by exposing the cells or tissues to the substance by pipetting (Ramanarayanan et al., 2022; OECD case no. 367). However, previous studies have demonstrated that nebulization of chemicals and drugs to mimic realistic aerosol exposure has resulted in faster (about 12 folds higher) uptake of inhaled compounds (Lenz et al., 2014). Also, observations made by comparing transepithelial barrier (TER) measurements, oxidative stress and cytotoxic effects of nebulized compounds in air-liquid interface (ALI) correlated better with *in vivo* readouts (Fizeşan et al., 2018; Stewart et al., 2012; H; Wang H. et al., 2018) compared to submerged cells where the compound is instilled. Moreover, submerged cell cultures lack proper physiological representation because aerosols generally sediment on the air-filled bronchial and alveolar epithelium (Fröhlich et al., 2013). The polarity of the epithelial cells and the presence of mucus or surfactant (SP) on the cell layer also plays a vital role in simulating the *in situ* environment of the epithelium which is only achieved through ALI culture conditions (Hobi et al., 2012; Schleh et al., 2013; Lock et al., 2018). Furthermore, multicellular co-culture models contribute to make particle translocation models more predictable and realistic (Rothen-Rutishauser et al., 2005). In particular, alveolar epithelial cells covering the distal airspace act as a gateway keeper for the systemic circulation of inhaled particles. Hence, a complex mixture of AT1 and AT2 cells is required to accurately model the alveoli *in vitro* (Sanches-Zuttion et al., 2022). In addition, immune cells like macrophages play a vital role for triggering a proper inflammatory cascade in response to infection (Artzy-Schnirman et al., 2021) as well as nebulized toxicants (Ji et al., 2018) in the alveoli.

Although ALI cell cultures capture the complicated nature of the lung epithelium with a high degree of precision, yet the slow

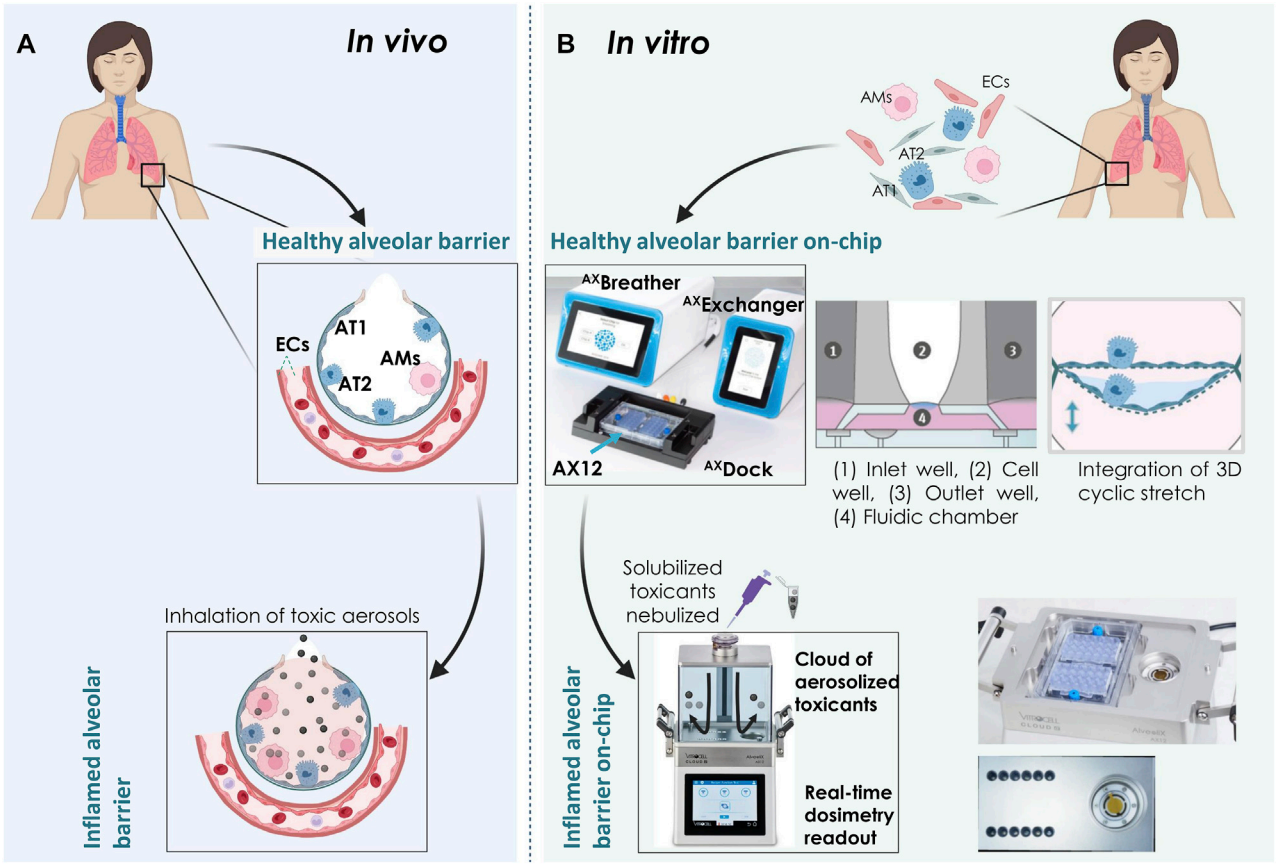

FIGURE 1
Overview of the Cloud α AX12 platform **(A)** An illustration showing the alveolar barrier *in situ*. The alveolar epithelial cells are situated on a thin basement membrane and are in close contact with the endothelial cells (ECs) on the basal side. The alveolar epithelium is comprised of squamous and thin alveolar type 1 (AT1) and cuboidal alveolar type 2 (AT2) cells along with resident alveolar macrophages (AMs). Inhaled toxic particles are represented as black and grey spheres. Inhalation of such airborne toxic particles result in lung inflammation, toxicity and progression to COPD. **(B)** Schematic representation of the ^{AX}Lung-on-chip (including ^{AX}Breather, ^{AX}Exchanger, ^{AX}Dock platform and the lung-on-chip consumable AX12) and Cloud α AX12 platform to model healthy and inflamed alveolar barrier *in vitro*. Primary and immortalized cells isolated from human sources were used in the model. Inflammation on-chip was mimicked using nebulized compounds with the Cloud α AX12. *Created with BioRender.com.*

development of inhalation therapy reflects the lack of efficient aerosol delivery systems compatible with medium to high throughput biomimetic technologies. Rats and mice have been popularly used as surrogate animals so far for lung inhalation *in vivo* (Kolanjiyil et al., 2019; S. Y; Lee et al., 2008; Lewis et al., 2013) and *ex vivo* (Hess et al., 2016; Cidem et al., 2020) studies. The lungs with its exclusive functionality provide a unique opportunity to target it directly *via* inhalation therapy and thus reduce systemic side-effects. However, the small number of approved inhaled drugs and in general the very high attrition rate of respiratory drugs (Barnes et al., 2015) shows the difficulty of developing such drugs as well as the lack of standardized predictive pre-clinical models. One of the major limitations for developing inhalation exposure system is the substantially higher amount (30 folds) of expensive testing drug requirement (where 10 mg/kg in oral = 1.7 g v/s approximately 50 g for inhalation) in efficacy studies (Resources, Charles River 2022). Moreover, until now, the pharma companies were not so much invested in inhaled therapy, therefore the lack of interest and demand has substantially affected the growth of preclinical tools for studying inhaled medicines. As of today, "inhaled therapeutics" have gained considerable momentum, hence current research trends focus on the development of advanced *in vitro* (Abaci & Shuler, 203315) and *in silico* platforms (Antonio et al., 2016; Walenga et al., 2019) to address the limitations with animal models. These advanced *in vitro* models are able to provide reliable tools that combine human-relevant inhalation exposure systems including particle diffusion and sedimentation kinetics with *in-vivo*-like features of the lung epithelium barrier, macrophage-assisted clearance, multicellular communication and differentiation (He et al., 2022).

Earlier, traditional cell exposure devices used ultrasonic or jet nebulizers (Schreier et al., 1998; Bur et al., 2009; Cooney & Hickey, 2011) which required longer experimental duration, complicated handling and most importantly had poor aerosol-to-cell ratio. However, modern cloud-based exposure solutions employ vibrating mesh nebulizers that have overcome these limitations and are efficiently delivering aerosols to cells in ALI cultures (Lenz et al., 2014). Several research groups have successfully utilized commercially available systems like Vitrocell-CLOUD 6 and 12 (VITROCELL Systems GmbH) to predict the fate of

TABLE 1 Choice of environment-related substances used in the study.

Proof-of-concept models	Type of agents	
(a) Toxicity induced by NPs	Nanoparticles (NPs)	TiO2 ZnO TiO2+ZnO
(b) Inflammation induced by inhaled toxic chemicals	Chemical	PHMG
(c) Anti-inflammation treatment	Corticosteroid	Fluticasone (FL)

aerosolized nanoparticles on transwell ALI cell cultures (Leibrock et al., 2019; Ding et al., 2020; Leroux et al., 2022). These systems have also been used to develop screening platforms for inhaled protein formulations (Röhm et al., 2017) and profile toxic aerosolized biocidal agents like Carbendazim (Tollstadius et al., 2019). Although these advanced transwell ALI exposure models can be well used for upper airways, they are not suited to model the dynamic microenvironment of the distal alveolar space where cyclic stretch plays an imminent role in alveolar cell differentiation and lung disease progression (Desai et al., 2008; Wu et al., 2018; Sehlmeyer et al., 2020). Exposing lung cells to ALI culture conditions along with physiological levels of cyclic stretch has been recently established to affect particle uptake (Doryab et al., 2021), maintain alveolar characteristics (Sengupta et al., 2022) and contribute to lung inflammation (Wu et al., 2013). However, due to the lack of proper exposure systems, the relevance and importance for including cyclic stretch (CS) with ALI culture conditions has not been studied in depth for inhalation studies.

With the rapid advances in microfluidics, lung-on-chip platforms offer the possibility of integrating biologically relevant cell microenvironment including a soft extracellular matrix (ECM) substrate, bio-relevant breathing motions and flow conditions (Huh et al., 2010; Stucki et al., 2015; Stucki et al., 2018; Zamprogno et al., 2021). Recently an airway-on-chip model with an integrated bronchial tree was utilized to successfully predict *in situ* deposition outcomes for inhaled airborne particles (about 2 µm in size) in the upper respiratory tract. The authors reported significant increase in cytotoxicity along with reduced expression of the tight junction protein, Zonula Occludens 1 (ZO-1) after exposure to the streamed aerosol particles (Fishler et al., 2015; Elias-Kirma et al., 2020). Moreover, recent advances in airway on-chip technologies have led to the development of models that mimic chronic lung injuries. Specifically, two studies have used on-chip models to replicate the effects of cigarette smoke-induced lung injury (Benam et al., 2016) and electronic cigarette or vaping product-associated lung injury (Kaiser et al., 2021). These studies demonstrate the relevance and potential of microfluidic technology in reproducing *in vivo* conditions and studying the mechanisms of chronic lung injuries in a controlled and precise manner. There are a few advanced lung-on-chip models for the lower airways that are currently available which can recapitulate crucial features of the native alveolar *in vivo* milieu like topography (Huang et al., 2021) and breathing motion (Huh et al., 2010; Stucki et al., 2018; Sengupta et al., 2022). However, adequate inhalation-based lung-on-chip models for the distal lung are largely missing (Artzy-Schnirman et al., 2021).

Occupational exposure to nanosized titanium dioxide (TiO2) and zinc oxide (ZnO) NPs has been reported to cause severe lung toxicity, inflammation, and lead to emphysema development *in vivo* in animal studies and in human volunteers (Chen et al., 2006; Gustafsson et al., 2011; Monsé et al., 2019; Abdulnasser et al., 2020). Lung cells exposed to these NPs have also resulted in toxicity and inflammatory cytokines production (Remzova et al., 2019; Freire et al., 2021). For toxic chemical inhalation applications, a compound used in humidifier disinfectant, polyhexamethylene guanidine (PHMG) was used. PHMG inhalation was recently established in several studies to induce serious lung toxicity and fibrosis development (Kim et al., 2015; Park J. et al., 2019). To negate the inflammation caused by PHMG induction, a corticosteroid, fluticasone propionate (FL) was used. FL is included within the treatment regimen for severe COPD and asthma cases (Molino et al., 2018; NHS-choices. uk). Therefore, to establish a realistic anti-inflammatory drug treatment course, FL was included in our studies after PHMG-induction.

We report here a next-generation inhalation *in vitro* platform (Cloud α AX12) that seamlessly integrates the cutting-edge breathing ^{AX}Lung-on-chip technology with a cloud-based aerosol exposure chamber (Figure 1) to assess relevant physiological outcomes after toxicant or drug inhalation. Homogeneous and consistent cloud generation and aerosol dose distribution on-chip were initially tested using fluorescent tracer molecules. Three proof-of-concept studies (Table 1) were carried out with this system to determine a) NPs-induced inflammation (TiO2 and ZnO) in ALI

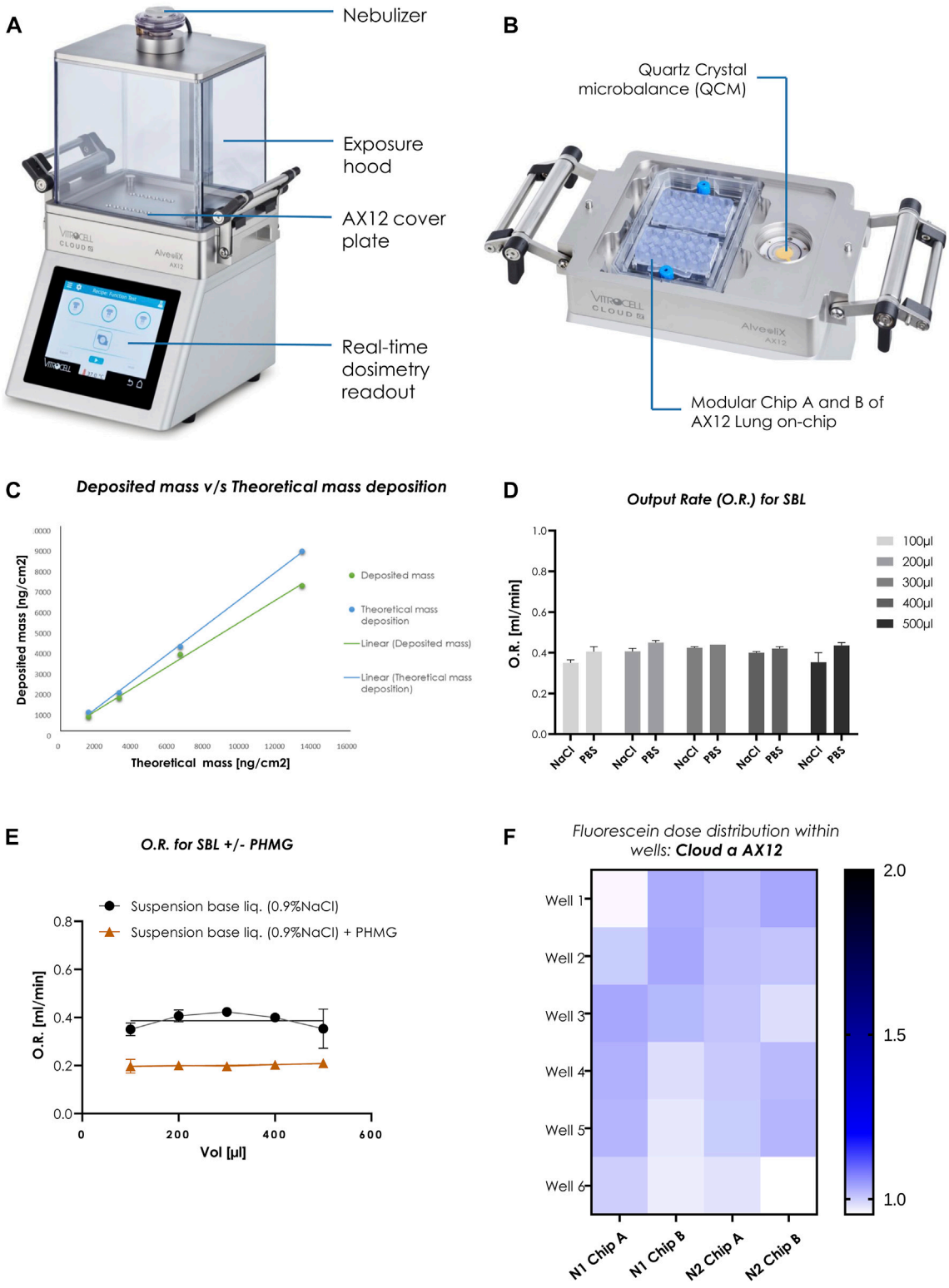

FIGURE 2
Homogenous dose distribution using the Cloud α AX12 **(A)** Design of the Cloud α AX12 comprised of a stainless-steel base module maintained at 37°C containing the AX12 plate placed on top covered by a steel plate. The holes on the steel base-plate are aligned to the wells within the AX12 plate. The QCM 6 placed inside the polycarbonate removable exposure hood quantify real-time cell delivered dose and are recorded and analyzed with the Vitrocell software. The nebulizer on top relies on a piezoelectric vibrating mesh to form a consistent aerosol cloud from the solubilized substance nebulized. **(B)** Detailed closer inspection of the orientation and placement for the AX12 plate and the QCM 6 sensor. **(C)** Comparison between deposited mass as measured from the QCM 6 readings (in green) and theoretically calculated (in blue). **(D)** O.R. (mL/min) was measured for different volumes (100–500 µL) for two SBLs (0.9% NaCl in distilled water and 1% PBS in distilled water) (n = 3). Data shown as mean ± SEM. **(E)** PHMG compound was dissolved in NaCl suspension base liquid as a reference. O.R. was measured for SBL without and with compound dilution using the Cloud α AX12 (n = 3). **(F)** Dose distribution measured from fluorescence signals [A.U.] of nebulized Fluorescein deposited on-chip. Signals from each well depicted in color scheme (white to blue; low fluorescence signal to high) from two individual rounds in AX12 plates (N = 2; n = 12).

and ALI + CS co-cultures on-chip, b) inhaled chemical inflammation and cytotoxicity triggered by PHMG, and c) inhaled corticosteroid treatment (FL) to reduce PHMG-induced inflammation. Given the unmet need for bio-relevant aerosol exposure setup for the alveolar space, the Cloud α AX12 represents a valuable tool for inhalation toxicology and drug safety and efficacy testing.

Methods

^{AX}Lung-on-chip

As described previously in Stucki et al., 2018 and Sengupta et al., 2022, the ^{AX}Lung-on-chip system (AlveoliX AG, Switzerland) comprises of the Lung-on-Chip (AX12) consumable along with two electro-pneumatic devices (^{AX}Exchanger and ^{AX}Breather), and the interface platform (^{AX}Dock) (Figure 1B). Cell seeding and medium exchanges were performed as recommended by the manufacturer (AlveoliX AG). To initiate the breathing mechanism, AX12 plate is positioned within the AXDock within the incubator. Then, three-dimensional (3D) CS (8% linear strain, 0.2 Hz) is initiated through a touchscreen control on the AXBreather, which deflects the microdiaphragm by generating negative cyclic pressure. CS and non-CS conditions are possible to run simultaneously on one AX12 plate, as the two chips are controlled independently.

Operation of the cloud α AX12

The Cloud α AX12 was used to perform the nebulization of chemicals and NPs on cells cultured inside the AX12, consumable of the ^{AX}Lung-on-chip.

The Cloud α AX12 uses a liquid aerosol nebulizer (Aerogen, Ireland) to produce cloud aerosol from solutions or suspensions. The nebulizer relies on a vibrating mesh technology (VMT) to form the aerosol (Figure 2A). Hereby, the nebulizer generates a high-frequency mechanical vibration from a piezoelectric element. This vibration is then transmitted to the mesh, a thin perforated membrane in contact with the solution. The vibratory movement of the mesh then creates a micro-pumping action that expulses droplets through the apertures (normally 4–6 µm in diameter, but other size ranges are available) and generates the aerosol. In the exposure chamber of the Cloud α AX12, the generated aerosol settles according to the principles of cloud settling and single droplet sedimentation. The cloud gets equally diverted and forms a symmetric pattern of vortices, to establish a spatially uniform sedimentation near the bottom of the chamber (Lenz et al., 2009). A homogeneous deposition is a crucial parameter to receive reproducible and consistent exposures of cells cultured in the AX12 plate under ALI conditions (Figure 2B).

A quartz crystal microbalance (QCM 6, VITROCELL, Germany) is integrated into the Cloud α AX12 allowing precise measurement of the deposited mass at the bottom of the exposure chamber (Ding et al., 2020). The QCM 6 consists of a piezoelectric quartz crystal oscillating at its resonance frequency by an electric oscillator (Figure 2B). The typical deposition profile was recorded by the QCM 6 during each nebulization step (Supplementary Figure S1A). The deposition profile can be divided into three phases (as described before in Ding et al., 2020): Phase I) Nebulization Phase: the nebulizer is activated and a dense cloud rapidly forms in the exposure chamber. The first droplets are deposited on the QCM 6 surface, leading to an increase of the QCM 6 signal. Phase II) Deposition Phase: 300 µL of the liquid suspension is completely nebulized and the cloud gradually settles to the bottom of the exposure chamber resulting in a steep increase in the QCM 6 signal. Next, the deposition signal reaches a maximum and the evaporation rate starts to increase, significantly reducing the QCM 6 signal and causing a plateau phase in which the saturated air inside prevents evaporation and stops aerosol deposition. Phase III) Evaporation Phase: the exposure chamber is opened and the QCM 6 is allowed to dry completely. This causes an abrupt rise in the QCM 6 signal, which stabilizes to the "true" mass deposition on the QCM 6 surface after a few seconds. It is important to note that only at this stage the QCM 6 signal represents the true deposited mass. Since the deposition values are measured at the end of evaporation phase for the toxicants, it is crucial that the QCM 6 signal remains stable over time since a shift in the baseline would affect reproducibility. Therefore, the baseline signal of the QCM6 must be verified. After 5 min (mins) (300 s) of recording, the signal of the QCM 6 was consistent across three different experiments (average SD: 21.3 ng/cm2) (Supplementary Figure S1B).

Before each experiment the exposure chamber was cleaned with 70% EtOH and heated to 37°C. To remove residues from previous usage, the nebulizer was dismounted and thoroughly cleaned according to the user manual. To pre-condition the exposure chamber, 300 µL of the suspension base liquid (SBL) (either 1% PBS or 0.9%NaCl) was nebulized. After cleaning, the AX12 was placed inside the heated compartment at the bottom of the exposure chamber as shown in Figure 2B. The AX12 is protected by a cover to ensure that the aerosol is deposited only within the cell wells and not on the remaining surfaces of the chip. Before starting the nebulization with the test substance, the exposure chamber was closed, and the microbalance zeroed. The nebulization was initiated by a touchscreen control on the Cloud α AX12. After the initiation of the nebulization, the cloud settled for 5–6 min. Hence the QCM 6 cannot measure liquid mass, it is important that only solid deposits remain (Ding et al., 2020). Therefore, the exposure chamber was then opened to evaporate the remaining liquid from the QCM 6 surface. Since deposition measurements usually take 5–10 min it is crucial to check that the QCM 6 signal does not drift during this period (Supplementary Figure S1B).

Dose distribution measurements in cloud α AX12

To check consistent depositions in the cell wells, initial experiments were performed with a reference substance (fluorescein) measuring deposition with the QCM 6. Fluorescein is a water-soluble fluorescent tracer (fluorescein sodium salt, SIGMA, F6377-100G). To determine the accuracy of the QCM 6, different concentrations of fluorescein (25.00, 12.50, 6.25, 3.13, 1.56, and 0.78 mg/mL) were dissolved in saline solution (0.9% NaCl) and nebulized. The aerosol output rate (O.R.), in mL/min, was then calculated by measuring the time needed for the whole solution to pass through the mesh nebulizer.

Ideally, the entire nebulized suspension reaches the bottom of the exposure chamber where the cells are placed. This ratio is referred to as deposition factor (Eq. 1):

Deposition factor (f_{dep})

V_{neb} represents the nebulized liquid volume and V_{dep} refers to the liquid aerosol volume deposited at the bottom of the exposure chamber (base steel plate).

$$f_{dep} = \frac{V_{dep}}{V_{neb}} \quad (1)$$

300 µL from each fluorescein concentrations were nebulized consecutively. Additionally, 300 µL of pure PBS was nebulized as a control. The deposition factor was based on the fluorescein dose obtained from the QCM 6 (exposed area of the quartz crystal: 3.8 cm^2). According to the nebulization protocol, the QCM 6 surface was rinsed with 300 µL 1X PBS in order to collect residual fluorescein. The fluorescence intensity result was then measured by plate reader type, absorption, wavelength (excitation wavelength: 483 nm; emission wavelength: 525 nm) and extrapolated to the entire surface area of the exposure chamber (200.75 cm^2). Between each fluorescein nebulization, the nebulizer mesh was washed with 300 µL 1X PBS solution to avoid any bias in subsequent depositions. Finally, by comparing the fluorescence intensities between different exposed wells, the spatial uniformity of the aerosol deposition was assessed. For the evaluation of the theoretical mass deposition, the V_{neb} plays a role as described in Eq. 2:

Theoretical mass deposited (m)

V_{neb} represents the nebulized liquid volume, m signifies the expected mass deposited in µg and c is the initial concentration (in µg/mL) of the test substance added to the nebulizer.

$$m = c^{*}V_{neb} \quad (2)$$

Additional experiments were performed to check the stability of the QCM 6 signal over time. Since exposure experiments typically last 5–10 min, it is important to check whether the QCM 6 idle values do not drift. To this end, the QCM 6 was gently and thoroughly wiped with an ethanol wetted tissue and the exposure chamber was warmed to 37°C. Once the QCM 6 was dry, the chamber was closed, and the microbalance was reset to 0. No substances were nebulized in this experiment; only the values given by the microbalance were recorded for 9 min (Supplementary Figure S1A). The sequence of a nebulization experiment using Fluorescein followed. The exposure chamber was opened after 5 min, and 2 more mins were recorded to mimic the drying phase of the QCM 6. Between each run the QCM 6 and the chamber were cleaned with a tissue soaked in 70% EtOH like for a normal nebulization experiment.

Cell culture

The alveolar epithelial cell line (^{AX}iAECs) used in this study was procured from AlveoliX (Switzerland). It was derived from primary human alveolar epithelial cells (AECs) that were isolated from resected lung tissue, and subsequently immortalized through the application of InscreeneX's CI-Screen technology (described in Lipps et al., 2018). This cell line represents a valuable tool for *in vitro* toxicity studies, as it is derived from primary human cells and retains some of their characteristics. These cells were cultured according to manufacturer instruction as previously described and characterized (Sengupta et al., 2022).

Human primary alveolar type II cells (^{AX}hAEpCs) were procured from AlveoliX (Switzerland). These cells were freshly isolated from lung tissue resections obtained with patient's informed consent and ethical approval.

On AX12 plates, the ^{AX}iAECs were maintained in AX Alveolar Epithelial Barrier medium supplemented with 1% penicillin-streptomycin (Thermo Fischer Scientific, Switzerland) and the ^{AX}hAEpCs in AX Alveolar Epithelial Medium (AlveoliX, Switzerland). After closing the chips, wells were filled with the respective mediums using the initial feed option. For mono-culture studies ^{AX}iAECs and ^{AX}hAEpCs were seeded on the apical side of the membrane at a density of 4×10^5 cells per cm^2 in medium. ^{AX}iAECs or ^{AX}hAEpCs apical cell seeding is always considered as day 0 in all the studies.

Calu3 cells purchased from ATCC® (Germany) was used as a human bronchial epithelial cell line. These cells were maintained in DMEM F-12 (Gibco; 21127-022) medium supplemented with 1% L-Glutamate, 10% fetal calf serum and 1% penicillin-streptomycin. For mono-culture studies Calu3 cells were seeded on the apical side of the membrane at a density of 1.9×10^5 cells per cm^2 in medium.

The THP-1 monocytes (ATCC; TIB-202) are immortalized monocyte-like cell line, derived from the peripheral blood of an acute monocytic leukemia case. These cells were cultured in RPMI (21875-034, Gibco) medium supplemented with 10% fetal calf serum and 1% penicillin-streptomycin in flasks. THP-1 monocytes were differentiated into macrophage-like cells using 8 nM and 200 nM phorbol 12-myristate 13-acetate (PMA; Sigma) and incubated for 48 h h) following previously established protocol (Kletting et al., 2018). Following incubation, the differentiated THP-1 (d-THP1s) macrophages were allowed to rest in PMA-free medium for further 24 h prior to seeding on-chip. For co-culture (^{AX}iAECs/d-THP1s; 5:1 cell density ratio) experiments on-chip, the d-THP1s were added apically in equal parts of AX Alveolar Epithelial Barrier and RPMI medium.

Human Lung Microvascular Endothelial Cells (HLMVECs) purchased from PromoCell were expanded in flasks using AX Endothelial Medium. For the triple-cell culture model on-chip (^{AX}iAECs/d-THP1s/HLMVECs; 5:1:2 cell density ratio), equal parts of AX E2 Alveolar Barrier Medium with RPMI were used. The HLMVECs were seeded on the basolateral side of each membrane, followed by a 2 h incubation and then by apical ^{AX}iAECs seeding on day0. Cells were then maintained at 37°C, 5% CO_2, and the medium was replaced every 2 days.

All cell lines were routinely monitored for *mycoplasma* contamination using a *mycoplasma* detection kit (MycoStrip, InvivoGen).

TER measurement

To determine barrier formation, transbarrier electrical resistance (TER) measurements were taken every 2 days, starting 48 h after cell seeding as discussed previously (Sengupta et al., 2022). In brief, a

commercially available 96-well plate electrode (STX100MC96; World Precision Instruments) and an Epithelial Volt/Ohm Meter (EVOM3; World Precision Instruments) was used. TER was measured in mono, co-culture and triple-cell culture conditions for up to 25 days. Before taking a reading, the electrodes were carefully sterilized using 70% v/v ethanol for 5 min and then rinsing them in distilled water for another 5 min at room temperature (RT). The "TER measurement" option was initiated on the AX Exchanger while taking readings. For cells kept in ALI, pre-warmed 1X sterile PBS was added 15 min prior to the measurements and then later re-equilibrated after TER readings. The background TER (ohm) data was obtained from a porous membrane having no cells. For analysis, the background subtracted TER (ohm) values were multiplied by the surface area of each cell culture well (0.071 cm^2 on-chip) to obtain the final TER reading in ohm-cm^2.

Cloud α AX12 exposures

The Cloud α AX12 Exposure System (developed by Vitrocell GmbH. and AlveoliX AG.) was used for exposure of cell cultures to control nebulized aerosols at ALI. ZnO NPs (uncoated NM-110 from the European Commission's Joint Research Centre - JRC; Ding et al., 2020) and TiO2 NPs (NM-105, CAS 13463-67-7) were kindly provided by Vitrocell. All NPs were diluted in 0.9% NaCl solution with a final volume of 300 µL. Prior to nebulization all NP-suspensions were sonicated in an ultrasonic bath (VWR #142-0084) for 15 min at 37°C to prevent agglomeration. Next, 100 µg/mL of the initial concentration of ZnO NPs were added to the nebulizer. Unless specified otherwise, high concentration studies of TiO2 NP, employed 100 µg/mL as initial concentration. The actual dose deposited on cells was calculated from the QCM 6 readings as 0.21 µg/cm^2 for both ZnO and TiO2 NPs. For experiments with combination of NPs, 50 µg/mL of ZnO NPs and 50 µg/mL of TiO2 NPs initial concentration (final deposited concentration: 0.10 µg/cm^2 TiO2 and 0.10 µg/cm^2 ZnO) were added for nebulization. Exposure to NPs was performed always at day 21.

PHMG (Boc Sciences #CAS 89697-78-9) was diluted in 0.9% NaCl solution to a final volume of 300 µL to receive an initial concentration of 1.84 mg/mL. A final deposition of 2.7 µg/cm2 was measured on the cells. Fluticasone propionate (Fl; GlaxoSmithKline, #F9428) corticosteroid was diluted in 0.5% DMSO in sterile 1X PBS. Treatment experiments with Fl in 96-well plate were performed with initial concentrations ranging from 100 to 1000 nM (final deposition concentrations from 0.0747 to 0.747 µg/cm2). On-chip, 100 nM (0.0747 ng/cm2) and 500 nM (0.374 ng/cm2) Fl was nebulized 24 h after PHMG treatment.

All untreated cells were nebulized only with the vehicle control (0.9% NaCl solution). Control (CTRL) samples were maintained within the same AX12 plate (for example, Chip A nebulized with control solvent and chip B with test substance) to remove bias effects of handling.

qRT-PCR

Total RNA was isolated separately from apical and basal chamber and subsequently purified using the Direct-zol™ RNA Microprep kit (Zymo Research, Switzerland) using the manufacturer protocol. Purity and concentration of RNA was analyzed using a Nano-Drop Spectrophotometer (Thermo Fischer Scientific, Switzerland). Next, cDNA was transcribed using the Super Script III Reverse Transcriptase kit (Life Technologies, Switzerland). Finally, qRT-PCR reactions were performed in triplicates with SYBR® Select Master Mix (Thermo Scientific) in an ABI7500 Fast (Applied Biosystems) real-time PCR system. Target gene expression was normalized to housekeeping gene expression (HPRT). The primer sequences are provided in Supplementary Table S1.

Immunofluorescence staining and imaging

Cells on-chip were fixed using 4% paraformaldehyde in distilled PBS- (PBS without calcium and magnesium). "Medium exchange" function on the AX Exchanger was used to fix the cells within the basal chamber. Chips were unscrewed and opened using the ^{AX}Disassembly tool (AlveoliX, Switzerland) prior to staining and mounting.

Cells were first permeabilized using 0.1% Triton X-100 (Sigma-Aldrich, Germany) dissolved in PBS- for 15 min at RT and then blocking buffer (2% BSA in sterile PBS) was added. The cells were incubated for 1 h at RT with the blocking buffer. The primary antibodies used for the study are mouse anti-ZO-1 antibody (1: 100 dilution; C# 33-9100, Fisher T Scientific), rabbit anti-α-SMA antibody (1:200 dilution; #SAB5500002; Sigma-Aldrich). The primary antibodies were diluted in 2% BSA/PBS and incubated overnight at 4°C. Secondary antibodies were used as follows: donkey anti-mouse Alexa Fluor 488 (1:200 dilution; C# A21202, Invitrogen), donkey anti-rabbit Alexa Fluor 568 (1:200 dilution; C# A10042, Invitrogen), were diluted 1:2000 in 2% BSA/PBS and incubated 2 h at RT. Nuclei were stained with Hoechst (1:1000 dilution; 33342, Invitrogen). The actin cytoskeleton was visualized using the conjugated Alexa Fluor 647 phalloidin stain (1:300 dilution; C# PHDN1-A, Cytoskeleton, Inc.). Lastly, the stained membranes were sealed between two glass coverslips using a mounting medium (C# F6182, Sigma-Aldrich).

Images were obtained using a confocal laser scanning microscope (Zeiss LSM 710) using appropriate filter settings. Zen Blue software v2.1 (Zeiss) was used for fluorescent intensity calculation to obtain background-corrected mean fluorescence intensity (MFI) for each channel of interest. To obtain comparable results from different areas of interest on the membrane, identical settings for the optical and digital gain, area of focus, and laser intensity were maintained. Finally, the mean fluorescence intensity (MFI) of the test channel (red, αSMA and for Phalloidin) was normalized with the MFI of the nuclei channel in blue (stained with Hoechst).

LDH cytotoxicity assay

Collected supernatants from the cells on-chip were analyzed for Lactate Dehydrogenase (LDH) release. The LDH cytotoxicity detection kit (Roche, #1164479301) was used according to the manufacturer's protocol. Briefly, for each sample equal volumes of supernatant to LDH reaction buffer was prepared and then transferred into 96-well plates in triplicate. The respective cell culture medium was taken as the "blank" control. Healthy

untreated cells were considered as "negative" control for the assay, whereas cells treated with 1% Triton X-100 for 4 h were considered as the "positive" control for maximum LDH release. 30 min after incubation with the LDH reaction mixture at RT, absorbance at 490 nm and a reference wavelength at 600 nm was measured using a microplate reader (Tecan Reader M1000).

Cellular ROS assay

To measure reactive oxygen species (ROS) from NPs exposed cells, the DCFDA/H2DCFDA cellular ROS assay kit (Abcam; ab113851) was used according to the manufacturer's instructions. In summary, the cell culture medium was aspirated out from the wells and the cells were washed with 1X Buffer (provided in the kit). Next, 100 µL of DCFDA solution was added to each well and subsequently incubated for 4 h protected from light at RT. The DCFDA solution was then carefully aspirated out and replaced with 100 µL 1X Buffer. A blank or negative control (well with no cells) was included to normalize the background for subtraction. A positive maximal ROS control was prepared with Ter-butyl hydrogen peroxide (TBHP) at a concentration of 150 µM in 1X buffer. DCF on-chip was then finally detected at Ex/Em = 485/535 nm in a fluorescence microplate reader (Tecan Reader M1000).

Statistical analysis

All data are presented as mean ± standard error of the mean (SEM) unless specified otherwise. For AX12 plate experiments, "N" represents the experimental repetitions, and "n" represents the number of individual wells estimated for all experiments with mRNA and cell supernatants, two wells were pooled into 1 and referred to as n = 1. All statistical tests were performed using t-tests, one-way or two-way analysis of variance (ANOVA) with p values adjusted for multiple comparisons using Tukey's multiple comparisons test, $^{*}p < 0.0332$, $^{**}p < 0.0021$, $^{***}p < 0.0002$, $^{****}p < 0.0001$. GraphPad Prism v8.0 software was used for data analysis. The exact number of repeats performed for each experiment is indicated in the corresponding figure legends.

Results

The cloud α AX12 system

To estimate the QCM 6 precision in the Cloud α AX12, theoretically calculated mass deposition (using Eq. 2, in *Methods*) was compared with the measured QCM 6 signals (actual mass deposited) for fluorescein concentrations. Here an average difference of 15% was found, which indicated that the actual mass deposition determined from the QCM 6 signal was 85% (SD: 5%) of the theoretically estimated mass deposition (Figure 2C). Thereafter, the spatially uniform and homogeneous dose distribution in the wells of the AX12 plate were assessed using a fluorescein concentration of 15 µg/mL.

The nebulization volume and the choice of base liquid have a major effect on the toxicant deposition and on their distribution in the exposure chamber. Hence, we tested two SBL, namely, 1% PBS in distilled water (PBS) and 0.9% NaCl in distilled water (NaCl) with nebulization volume ranging from 100 to 500 µL. The output rate (O.R.) of the nebulizer for the SBL is a key parameter, ideally staying between 0.2 and 0.4 mL/min, ensuring uniform cloud formation, which is essential for the homogeneity of aerosol deposition. The O. R is significantly affected by the choice of SBL used and the solubility of the test compounds within the SBL. It is calculated by measuring the time needed for the liquid (volume nebulized) to pass through the mesh nebulizer. Our results confirmed that there were no significant differences in the O.R. of the two SBLs used (Figure 2D). Hence, 0.9% NaCl was chosen as the SBL for all the consecutive studies (Table 1). Consistency of O.R. was tested by using different solutions are mixed with test compounds, PHMG was mixed with NaCl solution. A drastic reduction from 0.4 (NaCl only) to 0.2 mL/min (NaCl with PHMG) in O.R. was observed (Figure 2E), which was expected due to the increased viscosity of the liquid suspension used for nebulization. However, the values were within the manufacturer recommended range. Lastly, the fluorescence intensities of nebulized fluorescein measured by a plate reader showed a variation of ±8.5% fluorescein deposition within the AX12 plate (Figure 2F), which is within an acceptable range (up to 15%) according to the manufacturer (Vitrocell).

Nanoparticles (NPs)-induced inflammation on-chip

Cyclic stretch combined with ALI increased sensitivity of lung epithelial barrier to NPs

For the first proof-of-concept study mimicking physiologically relevant environmental cues, TiO2 and ZnO NPs were used. We investigated the inflammatory potential of ZnO NPs (0.21 µg/cm^2) on bronchial (Calu3; Supplementary Figure S2A) and alveolar (^{AX}iAECs; Figure 3A) mono-cell culture on-chip. One of the most critical parameters for toxicity studies *in vitro* is the existence of a tight and functional lung epithelial barrier (Derk et al., 2015). Hence, the barrier integrity for Calu3 cells cultured on-chip in healthy conditions was investigated and found to be around 1000 to 3000 Ω-cm2 between Day D)7–14 under both ALI and ALI + CS conditions (Supplementary Figure S2B). Barrier disruption was assessed before (at 0 h) exposure and 6 h and 24 h after nebulization with ZnO NPs for Calu3 cells on-chip. We found that aerosolized ZnO NPs exerted significant barrier gaps in Calu3 cells (Supplementary Figure S2C) reducing the TER values 3-folds at 6 h and around 7-folds at 24 h after exposure under ALI + CS conditions. Furthermore, significant increase in cytotoxicity levels was observed under ALI + CS conditions at 24 h (Supplementary Figure S2D). ^{AX}iAECs monoculture on-chip showed similar barrier disruption upon exposure to ZnO NPs at 24 h (45% reduction) and 48 h (62% reduction) but only under ALI + CS conditions (Figure 3B). In addition, LDH release was found to be almost 2-times higher under ALI + CS condition than under ALI condition alone in ^{AX}iAECs on-chip (Figure 3C). qPCR studies (measured in Fold change; fc) revealed increased levels of inflammation-associated genes notably interleukin 2 (IL2; fc in Calu3 21.46; ^{AX}iAECs 1.60) and TNFα (fc in Calu3 17.98; ^{AX}iAECs 1.98) among others in both ^{AX}iAECs and Calu3 cells on-chip under ALI + CS conditions when exposed to ZnO NPs (Figures 3D, Supplementary Figure S2E). In favor of an active inflammation,

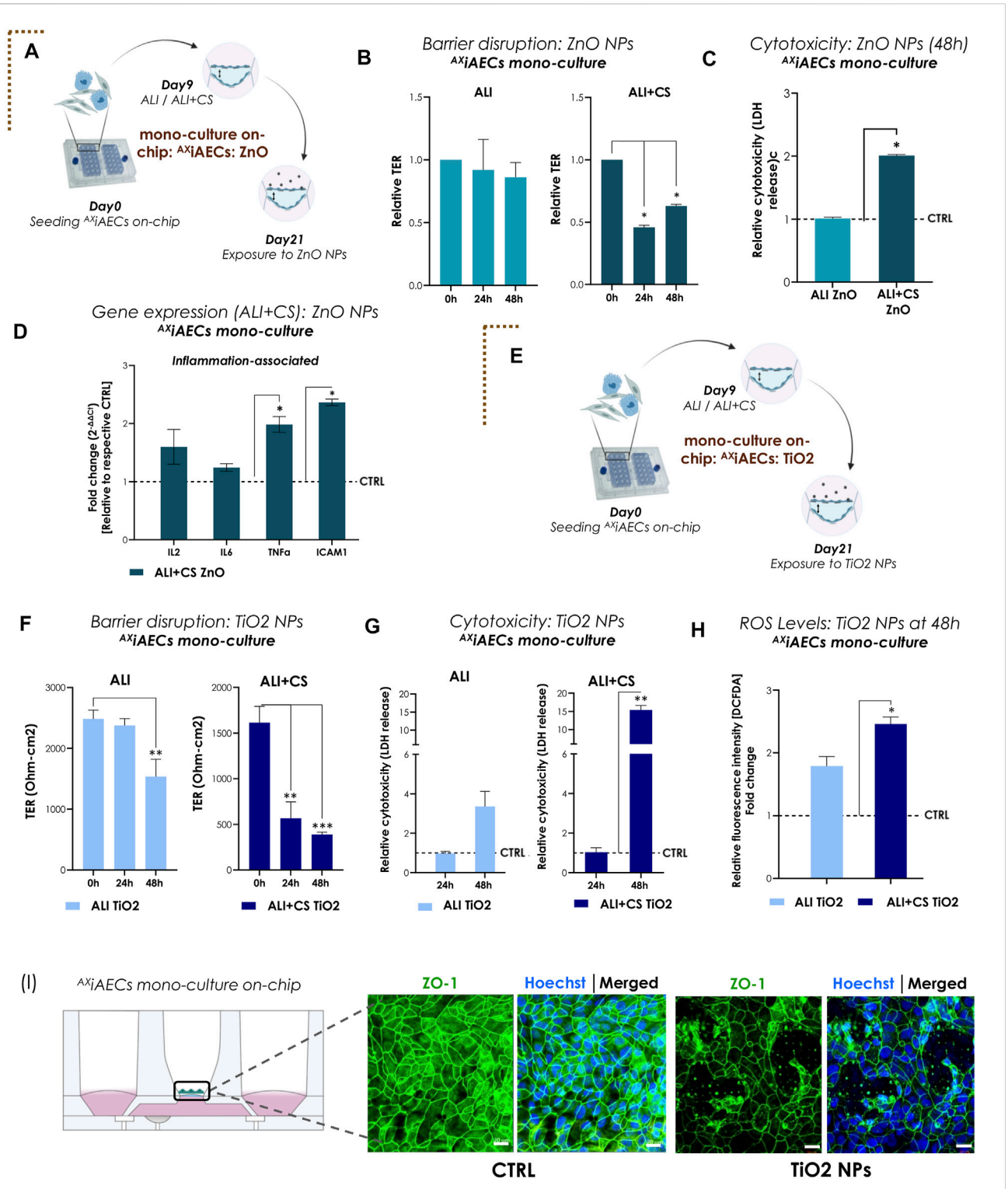

FIGURE 3
Nanoparticles (NPs)-induced inflammation and barrier disruption in AXiAECs mono-culture on-chip **(A)** The brown dotted corner bracket suggests the distinction between different trigger-induced models. On day 21 of the mono culture experiment, the AXiAECs were exposed to the ZnO NPs on-chip. Timeline and schematic provide further details of the experiment. **(B)** TER values (normalized to 0 h timepoint) for ALI and ALI + CS cell cultures exposed to ZnO NPs (n = 3/condition/timepoint). **(C)** Relative LDH release (NPs exposed with respect to Control; CTRL) shown for 48 h timepoint for ALI and ALI + CS cells (n = 4). **(D)** mRNA was isolated from CTRL and ZnO exposed cells (ALI + CS) at 48 h exposure timepoint. qPCR studies were performed with n = 4/conditions and exposure significance were measured in relation to CTRL expression levels. **(E)** Results for AXiAECs mono-cell culture model with TiO2 NPs is denoted by opening another brown dotted corner bracket. Timeline and schematic of TiO2 NPs nebulization on day 21 in monoculture (AXiAECs) on-chip. **(F)** Absolute TER values (Ohm-cm2) compared pre-TiO2 NPs exposure (at 0 h) with 24h and 48 h after exposure (N = 2; n = 6). **(G)** Significance for cytotoxicity was calculated relative to respective ALI or ALI+CS CTRL. Cytotoxicity was calculated from LDH release at 24h and 48 h after TiO2 NPs nebulization from both ALI and ALI + CS samples (N = 2; n = 4/time-point). **(H)** ROS generation was measured using the H2-DCFDA assay (N = 2; n = 4). Fluorescence intensity for exposed cells were normalized with respective healthy CTRL. **(I)** Representative immunofluorescence staining for alveolar barrier after 48 h of TiO2 NPs exposure. Cells were probed for tight junction, ZO1 (green) and nuclei with Hoechst (blue). Scale bar is 20 μm. Data are shown as mean ± SEM.

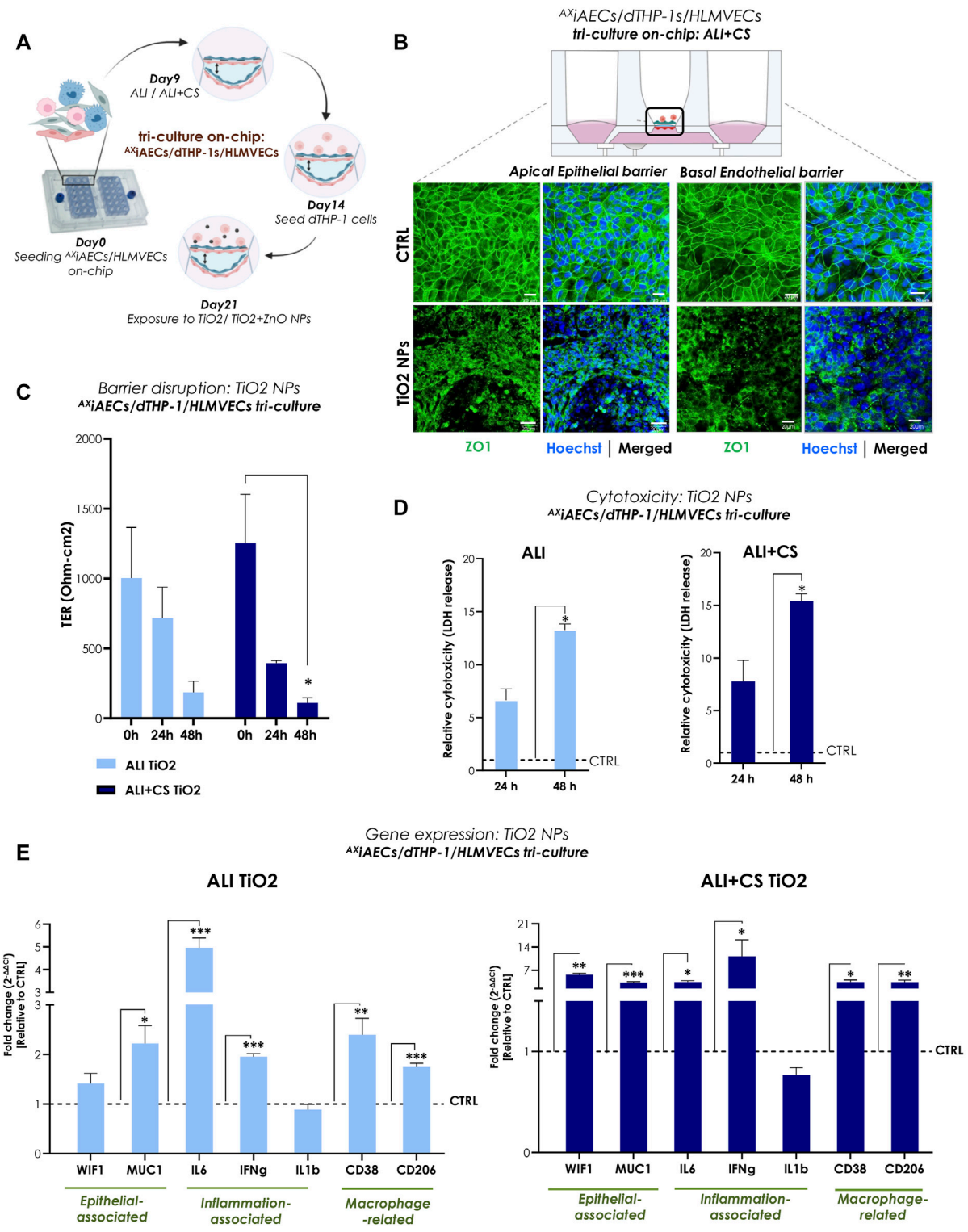

FIGURE 4
TiO2 NPs-induced inflammation and barrier disruption in triple-cell culture model on-chip **(A)** Overview of the timeline for cell seeding and NPs exposure on-chip. **(B)** Representative immunofluorescent (maximum projection intensity) images for alveolar apical and basal endothelial barrier stained with ZO1 (in green) and nuclei with Hoechst (in blue) under ALI + CS. Scale bar here is 20 μm. **(C)** TER (Ohm-cm2) measured before at 0 h and after TiO2 NPs exposure at 24 h and 48 h (N = 2; n = 6). **(D)** LDH release was measured from 24 h to 48 h samples in ALI and ALI + CS conditions (N = 2; n = 4/conditions/time-point). Significance was measured relative to the respective ALI or ALI+CS CTRL. **(E)** mRNA was harvested at 48 h time-point. Gene expression for epithelial, inflammation and macrophage related markers were measured in both ALI and ALI + CS conditions (N = 2, n = 4/conditions). Data are shown as mean ± SEM.

reduced expression of epithelial associated genes such as aquaporin 5 (AQP5), caveolin 1 (CAV1) in ^{AX}iAECs (Supplementary Figure S2G) and tight junction protein 1 (TJP1) and e-cadherin (ECAD) were observed in Calu3 cells (Supplementary Figure S2F) confirming a strong effect on their epithelial characteristics.

Next, ^{AX}iAECs on-chip were nebulized apically with TiO2 NPs (Figure 3E). Exposure to nebulized TiO2 NPs (0.21 μg/cm^2) demonstrated significant barrier damage in ^{AX}iAECs as revealed from their TER values after 48 h under ALI (38% decrease) and from 24 h under ALI + CS (24 h: 64%; 48 h: 75%) conditions (Figure 3F). Consistent with this, immunofluorescent stainings of ZO1 revealed substantial tight junction disruptions (Figure 3I) along with reduced proportion of actin filaments compared with healthy control cells (Supplementary Figure S1C). Nebulized high concentration of TiO2 NPs (0.21 μg/cm^2) showed increased cytotoxicity (15.3 folds) under ALI + CS cells from 48 h (Figure 3G), whereas low concentration of TiO2 NPs (0.021 μg/cm^2; 10-fold diluted) were unable to demonstrate any cytotoxic effect (Supplementary Figure S1D) either under ALI or ALI + CS conditions. Previous studies have shown that TiO2 NPs are a known trigger for the generation of reactive oxygen species (ROS) in lung cells and this increased ROS production plays a direct role in lung inflammation (Sayes et al., 2006; Horváth et al., 2018). Consistent with published literature, a high concentration of TiO2 NPs (0.21 μg/cm^2) nebulized with the Cloud α AX12 significantly increased ROS production in the alveolar cells after 48 h under ALI + CS conditions (Figure 3H). Further qPCR studies in ^{AX}iAECs revealed deregulation of inflammatory genes like interleukin 6 (IL6; fc: for ALI 1.13; ALI + CS 1.85), tumor necrosis factor α (TNFα; fc: for ALI 1.03; ALI + CS 2.25) and intercellular adhesion molecule 1 (ICAM1; fc: for ALI 0.95; ALI + CS 2.86) which displayed a strong trend towards increased activation when exposed to high concentration of TiO2 NPs (Supplementary Figure S1E).

In our alveolar and bronchial mono-cell culture model on-chip, ALI combined with CS conditions showed increased barrier sensitivity and thus increased inflammatory potential of NPs nebulized with the Cloud α AX12.

Higher inflammatory potential of TiO2 NPs under ALI + CS established using a triple-cell culture model on-chip

To reproduce a complex and physiologically relevant *in vitro* model of the alveolar-capillary barrier, a triple (tri)-cell culture was established on-chip with ^{AX}iAECs and differentiated THP1 (d-THP1) macrophages on the apical side of the cell-seeding membrane and HLMVEC endothelial cells on the basal side under ALI (Supplementary Figure S3A, B) and ALI + CS (Figures 4A, B). Interestingly, both the apically exposed alveolar cells and the basal indirectly exposed endothelial barriers revealed disrupted tight junction proteins when exposed to TiO2 NPs under ALI + CS state (Figure 4B). TER measurements before (0 h) and after exposure revealed significant decrease in barrier health at 48 h (80% reduction) under ALI + CS conditions (Figure 4C). In line, increased cytotoxicity from 48 h under both ALI (43% cytotoxicity) and ALI + CS (59% cytotoxicity) conditions (Figure 4D) was observed. Comprehensive gene expression analysis revealed activation of pro-inflammatory markers like IL6 (fc under ALI 4.95; ALI + CS 3.47) and interferon gamma (IFNg; fc under ALI 1.96; ALI + CS 11.14) under both ALI and ALI + CS states. Moreover, increased expression of Mucin1 (MUC; fc under ALI 2.21; ALI + CS 3.34) and Wnt inhibitory factor 1 (WIF1; fc under ALI + CS 5.65) along with deregulated levels of CD38 (fc under ALI 2.39; ALI + CS 3.47) and CD206 (fc under ALI 1.74; ALI + CS 3.41) suggest epithelial and macrophage activation respectively (Figure 4E).

In summary, exposure to TiO2 NPs (approximate *in vivo* dose correlation, see Supplementary Section S1) resulted in significantly reduced alveolar barrier integrity along with inflammation and cellular damage.

Nebulized NPs individual or in combination reproduced barrier gaps and inflammation in primary human alveolar cells on-chip

To recapitulate realistic occupational exposure of NPs in industrial spaces, we used equal parts of aerosolized TiO2 (0.10 μg/cm^2) and ZnO NPs (0.10 μg/cm^2) to test effect of NP combination. Primary human alveolar epithelial cells (^{AX}hAEpC) consisting of a pure AT2 cell population are still considered the "gold standard" for use as a distal lung cell model (Elbert et al., 1999). Therefore, to validate the Cloud α AX12, we utilized ^{AX}hAEpCs (Figure 5A). ^{AX}hAEpCs on-chip when exposed to nebulized TiO2 NPs alone and in combination with ZnO NPs demonstrated significant increase in barrier gaps under ALI + CS condition, as evidenced by reduced TER values at 6 h (TiO2: 67.4% decrease; TiO2+ZnO: 46.4% decrease) and 24 h (TiO2: 73.7% decrease; TiO2+ZnO: 69.1% decrease) after induction (Figure 5B). While no cytotoxic effects were observed in ALI conditions, significantly increased LDH release was seen under ALI + CS condition, with cells exposed to TiO2 NPs (Figure 5C). RNA was harvested from ALI + CS cells after 24 h exposure NPs exposure. Subsequent qPCR studies revealed deregulated epithelial-associated genes such as MUC1 (fc for TiO2 2.93; for TiO2+ZnO 4.21) and WIF1 (fc for TiO2 0.26) with increased inflammatory genes like IL6 (fc for TiO2+ZnO 5.1) and ICAM1 (fc for TiO2+ZnO 2.8) (Figure 5D).

^{AX}iAECs/dTHP-1/HLMVECs tri-cell culture on-chip were additionally exposed to mixed TiO2+ZnO NPs combination. Here, the NPs mixture were able to incite strong barrier disruption after 24 h (64.5% reduction) and 48 h (90.1% reduction) in ALI + CS (Supplementary Figure S2H) and elevated levels of inflammatory genes like interleukin 1b (IL1b; fc in ALI 2.62; in ALI + CS 3.60) and IFNg (fc in ALI 2.22; in ALI + CS 4.42) were observed under both CS and non-CS (ALI only) conditions (Supplementary Figure S2I).

Therefore, both primary ^{AX}hAEpCs and the cell-line models demonstrated similar patterns of inflammation and toxicity when exposed to TiO2 NPs alone or in combination (TiO2+ZnO NPs) using the Cloud α AX12 reinforcing the validity of our findings with diverse cellular models.

Toxic chemical "inhalation" on-chip

Nebulized PHMG induced cytotoxicity in alveolar triple-cell culture model on-chip

To investigate the effect of aerosolized PHMG, a humidifier disinfectant (Park J. et al., 2019), on a cellular level, both ^{AX}iAECs/

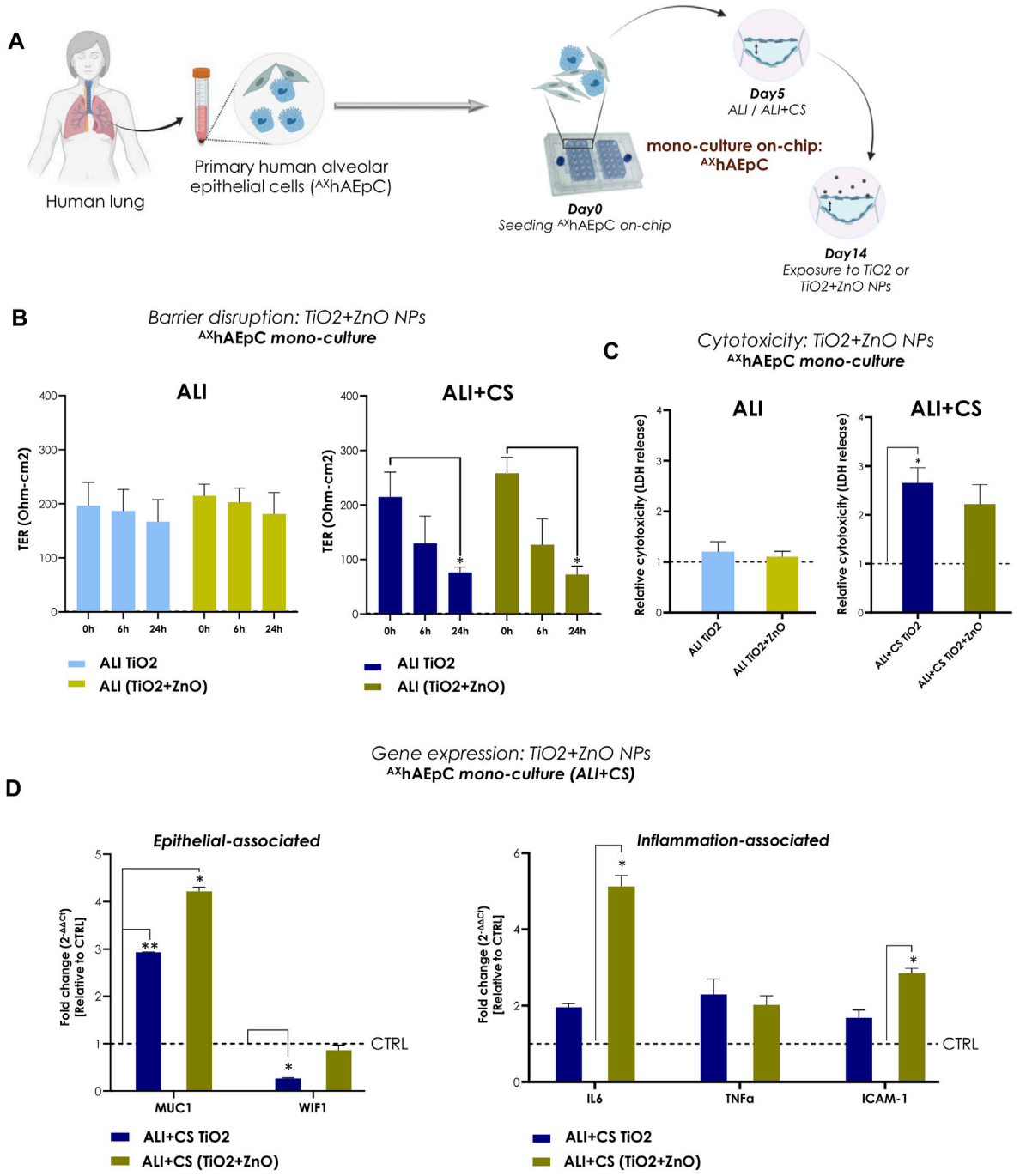

FIGURE 5
NPs-induced inflammation in primary human alveolar epithelial cells (AXhAEpC) on-chip **(A)** A schematic representation AXhAEpCs seeded in the AX12 plate. The timeline shows the cell culture and NP exposure process on-chip. **(B)** TER values (Ohm-cm2) were recorded before NPs nebulization (at 0 h) and at 6h and 24 h after TiO2 and TiO2+ZnO mixed NPs exposure (N = 2; n = 6). The significance of exposure at 6h and 24 h was measured compared with the values at 0 h. **(C)** The levels of LDH at 24 h were normalized using untreated control samples (ALI and ALI + CS) (N = 2, n = 4). **(D)** Gene expression was analyzed 24 h after NPs exposure using mRNA harvested from ALI + CS cell cultures. The fold change values were normalized to healthy controls (N = 2, n = 4). Data are shown as mean ± SEM.

d-THP1s co-culture and AXiAECs/d-THP1s/HLMVEC tri-cell culture model was utilized (Figures 6A, Supplementary Figure S5A). A significant reduction in TER (ohm-cm2) measurements was observed in the tri-cell culture starting as early as 4 h after nebulization and remained constant until 48 h under both ALI and ALI + CS cultured cells (Figure 6C). However, in the AXiAECs/d-THP1s co-culture model, barrier disruption was observed only at 24 h but remained constant until 48 h (Supplementary Figure S5B). In addition, Calu3 cells on-chip showed decreased barrier integrity from 24 h when exposed to PHMG under ALI + CS (Supplementary

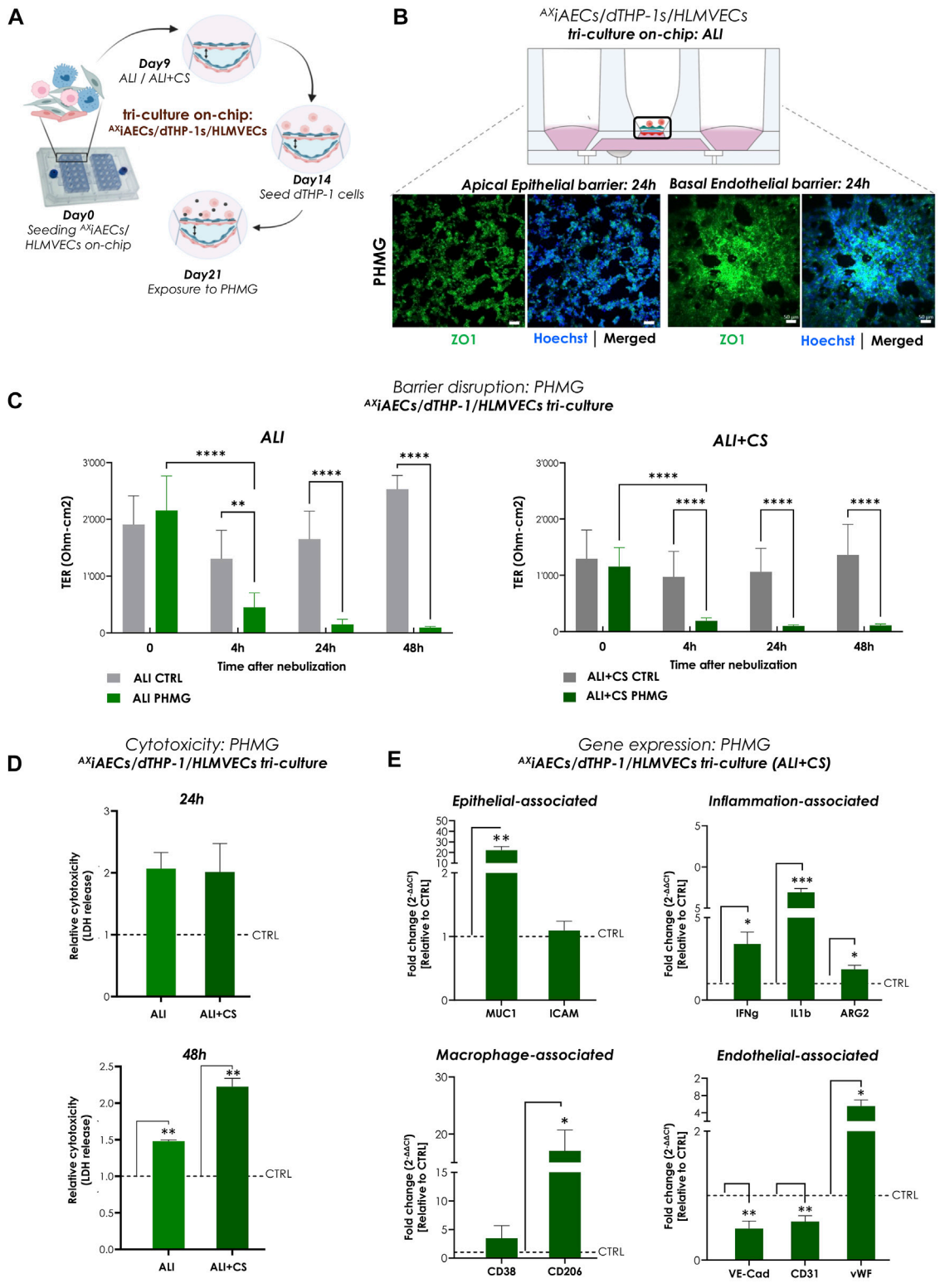

FIGURE 6
Aerosolized PHMG induced barrier disruption and cytotoxicity in triple-cell culture on-chip **(A)** Timeline and schematic of PHMG nebulization at day 21 in tri-cell culture (^{AX}iAECs/d-THP1/HLMVEC) model on-chip. **(B)** Representative immunofluorescence staining for apical alveolar and basal endothelial barrier after 24 h of PHMG exposure. Cells were analyzed for tight junction, ZO1 (green) and nuclei with Hoechst (blue). Scale bar is 50 μm. **(C)** TER values (Ohm-cm^2) were recorded before PHMG nebulization (at 0 h) and at 4 h, 24 h and 48 h after exposure (N = 3; n = 12). **(D)** Cytotoxicity was calculated from LDH release at 24 h and 48 h after PHMG nebulization from both ALI and ALI + CS conditions. LDH release was normalized with respective untreated controls. Data shown as mean ± SEM (N = 1; n = 3/condition/timepoint). **(E)** Gene expression after 48 h of exposure was assessed for cells in ALI + CS condition. Fold change values were normalized with respective untreated controls. Data presented as mean ± SEM (N = 3; n = 6).

Figure S4B). The presence of epithelial cells and macrophages on the apical side along with basal ECs was assessed with Imaris. $CD68^+$ expression confirmed the presence of differentiated THP1 (d-THP1) macrophages on the apical side (Supplementary Figure S3A, B). Consistent with the TER measurements, immunofluorescent stainings revealed drastic disruption of tight junction in both the apical alveolar and basal endothelial barriers under ALI (Figure 6B) and ALI + CS (Supplementary Figure S4A) in the tri-cell culture model. Moreover, increased CD163+ macrophages were observed upon PHMG exposure (Supplementary Figure S4A) under ALI + CS condition, confirming an ongoing inflammatory response (Skytthe et al., 2020). Furthermore, substantial LDH release was observed after 48 h under ALI and ALI + CS conditions the tri-cell culture (Figure 6D) confirming the cytotoxicity of PHMG (Song et al., 2019). Investigation of the gene expression profile after PHMG exposure in the co-culture revealed a significant increase in inflammatory markers such as arginase 2 (ARG2; fc: 1.81) and an increase M1-associated marker such as CD38 (fc: 1.76) (Supplementary Figure S5C). qPCR studies from the tri-cell culture, under ALI + CS cells revealed elevated levels of inflammatory genes like IFNg (fc: 3.39), IL1B (fc: 6.92) and ARG2 (fc: 1.86). In addition, the epithelial damage-related marker MUC1 (fc: 22.17) was found to be significantly elevated. Both M1-and M2-associated markers like CD38 (fc: 3.46) and CD206 (fc: 17.03) respectively showed increased levels upon PHMG induction. On the basal side, gene expression studies of endothelial cells identified decreased mRNA levels of VE-CAD (fc: 0.49) and Platelet endothelial cell adhesion molecule-1 (PECAM-1 or CD31; fc: 0.59), but increased levels of von Willebrand factor (vWF; fc: 5.54) (Figure 6E).

In summary, PHMG exposure in mono-culture, co-culture and tri-cell culture models on-chip resulted in drastic barrier disruption, increased cytotoxicity along with significant inflammation and cellular differentiation.

Aerosolized fluticasone (FL) corticosteroid reduces PHMG-induced EMT and inflammation

To evaluate the applicability of the Cloud α AX12 as a setup for testing the efficacy of inhaled drugs, we used the corticosteroid FL subsequently with the PHMG-induction on-chip. Initial testing was performed using 96- well plates in which FL was nebulized 24 h after PHMG induction on ^{AX}iAECs mono-culture (Figure 7A). Since, PHMG is known to induce epithelial-mesenchymal transition (EMT) in alveolar cells (Park Y. et al., 2019), protein expression of alpha smooth muscle actin (αSMA) as a mesenchymal cell marker was used as an indicator of EMT level. While PHMG exposure significantly increased αSMA levels, as expected, inhaled treatment with FL showed a dose-dependent reduction in αSMA protein expression combined with an improvement in cellular health (Figures 7B, C). To test this hypothesis on-chip, the ^{AX}iAECs/d-THP1s/HLMVEC tri-cell culture model was used. The FL treatment was carried out 24 h after PHMG exposure on day 22 (Figures 7D, Supplementary Figure S6A). FL exposure (Supplementary Figure S6A) was unable to recover the strong barrier damage inflicted by PHMG under both ALI (Supplementary Figure S6B) or ALI + CS (Supplementary Figure S6C) conditions. However, detailed qPCR studies indicated clear effects of the FL treatment under ALI + CS conditions. mRNA was isolated from cells, 24 h after FL treatment under ALI and ALI + CS conditions. Alveolar (TJP1) and endothelial (CD31) barrier-associated markers were increased after FL treatment, while the expression of alveolar damage marker (MUC1) and the inflammatory (ARG2, IL6 and IL8) gene levels (Figure 7E) were reduced. Moreover, treatment with aerosolized FL was able to significantly reduce the cytotoxic effect (55% decrease with 100 nM and 78% decrease with 500 nM) of PHMG under ALI + CS cells in a dose-dependent manner (Supplementary Figure S6D).

Briefly, the nebulized corticosteroid FL (approximate *in vivo* dose correlation, see Supplementary Section S1) provided significant anti-inflammatory effects that could be shown with the Cloud α AX12, demonstrating its potential for use in drug efficacy studies.

Discussion

We are constantly being exposed to a broad range of unidentified toxicants. Substances capable of penetrating deep into the distal part of the lungs leading to severe respiratory conditions such as ARDS, COPD and fibrosis (Adegunsoye & Rafeq, 2019). Due to the increasing incidence of these respiratory diseases, there is a growing demand for new inhaled targeted therapeutics for the lung. It is therefore of utmost importance to understand the response of the lung epithelial barrier to inhaled toxicants to develop effective treatments for such debilitating health conditions. Accordingly, we present here a new generation *in vitro* inhalation platform (Cloud α AX12) for the distal lung consisting of a cloud-based exposure chamber combined with a lung-on-chip technology (^{AX}Lung-on-chip). Exposure to aerosolized NPs (like TiO2, ZnO) and chemical (like PHMG) was shown to trigger an inflammation insult leading to epithelial barrier disruption and cytotoxicity on-chip. Our study reveals a clear effect of physiological levels of CS associated with ALI cell culture. In addition, the anti-inflammatory potential of inhaled FL treatment with the Cloud α AX12 platform, was demonstrated showing its applicability for aerosolized drug screening studies.

Although air-liquid exposure systems better model *in vivo* scenarios compared to instilled compound testing strategies, the interpretation and correlation with *in vivo* dosing remains a major challenge. Nevertheless, the integration of accurate QCM 6 in exposure systems for ALI culture studies have improved the accuracy and reduced the variability of the dose deposition. In our studies, we observed a ~8.5% variability which is consistent and in agreement with previous studies using earlier generations of the Vitrocell Cloud devices (Lenz et al., 2014; Ding et al., 2020). In contrast to earlier studies using ZnO and TiO2 NPs to study lung barrier toxicity (Y. H. Kim et al., 2010; Oliveira et al., 2019) carried out with concentrations ranging from 0.4 to 0.9 μg/cm^2 without CS inclusion (Ding et al., 2020), we observed significant cytotoxicity at even lower NPs concentrations (0.21 μg/cm^2) with nebulized TiO2 and ZnO NPs under ALI + CS. This suggests an effective aerosol to cell delivery of the Cloud α AX12 and the impact of physiological CS on the uptake of NPs. Moreover, an inter-laboratory study conducted in collaboration with 7 different

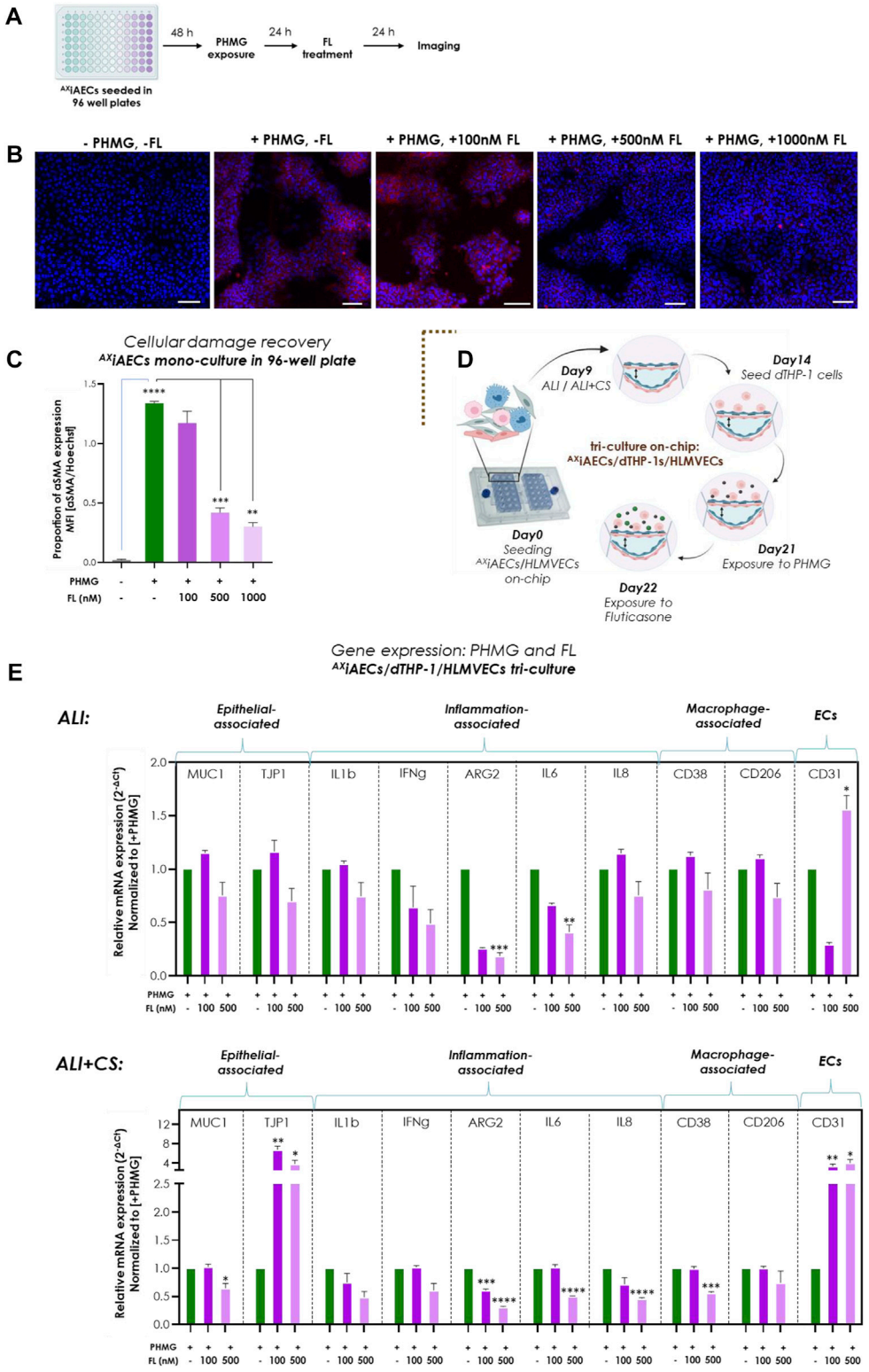

FIGURE 7
Inhaled Fluticasone reduced PHMG-induced inflammation and EMT **(A)** Schematic timeline of the PHMG exposure and subsequent FL treatment on AXiAECs mono-culture in 96- well plates. **(B)** Representative stainings of AXiAECs exposed to PHMG with/without FL treatment under ALI with αMA (in red) and Hoechst (in blue). Scale bar is 100 μm. **(C)** The mean fluorescent intensity (MFI) was calculated and the proprotion of αSMA expression was calculated by normalizing with the nuclei intensity. PHMG exposed cells (+PHMG, -FL) was compared with healthy untreated controls (-PHMG, -FL) to check inflammation by PHMG. Next, PHMG exposed cells (+PHMG, -FL) were compared with PHMG and FL treated cells (+PHMG, +100nM/500nM/1000 nM FL) to check anti-inflammatory effect of FL. Region of interest (ROI or n = 6/conditions). Data are shown as mean ± SEM. **(D)** Brown dotted brackets represent on-chip experiments. Timeline and schematic for PHMG and FL treatment in tri-cell culture (AXiAECs/d-THP1s/HLMVECs) on-chip. **(E)** Selected genes for epithelial cells, inflammation-associated, macrophage and endothelial cells were measured under both ALI and ALI + CS conditions on-chip. Significance associated with FL treated cells were estimated by comparing inflamed cells (+PHMG, -FL) with 100 nM (+PHMG, +100 nM FL) and 500 nM (+PHMG, +500 nM FL) FL nebulized cells (N = 2, n = 8). Data are shown as mean ± SEM normalized to PHMG induced but without subsequent FL (+PHMG -FL) treatment.

laboratory groups recently confirmed the homogenous dispersion of nanoparticles and consistent dose deposition profile using the VITROCELL® Cloud 12 system (Bannuscher et al., 2022). This study is a significant advancement in the standardization of *in vitro* toxicity studies using ALI culture conditions and advanced cloud exposure devices for regulatory purposes.

Although, there is still much debate and a lack of standardized protocols for correlating *in vivo* and *in vitro* dosing, especially for inhaled agents, our basic worst-case lifetime calculations indicate that the 100 µg/mL dose used in our studies correlate approximately with 18–60 h exposure for ZnO NPs and a 45–90 h exposure for TiO2 NPs for an adult human living in a highly polluted area (Supplementary Section S1). The difference in exposure time for ZnO and TiO2 is related to their differences in solubility and hydrophobicity profile (TiO2 is more hydrophobic than ZnO) which determine their deposition kinetics in the lung (J. Wang & Fan, 2014; IARC, 1989). The lack of standardized protocols may of course also explain the difference observed. It would therefore be important to understand the role of surface modifications of NPs and how that influence their uptake mechanism in the lungs. PHMG was chosen as a model for chemically induced toxicity because recent cases of severe lung toxicity and inflammation in Korea led to permanently ban PHMG as a component in humidifier disinfectants (Park D. et al., 2015). In addition, several compelling studies have shown that PHMG is a causative agent for lung toxicity, asthma, fibrosis and cancer using *in vivo* animal inhalation studies (S. R. Kim et al., 2015; S. H; Lee et al., 2021; Y. H; Lee & Seo, 2020). *In vitro* studies have shown increased cytotoxicity, ROS generation with EMT (S. Choi et al., 2022; Jeong et al., 2019; Park J. et al., 2019; Shin et al., 2018), which were confirmed on-chip in the present study.

To assess the applicability of the Cloud α AX12 model for simulating inflammation in the upper airway, we included bronchial Calu3 cells in our study. Calu3 cells are commonly used as a cellular model for the upper airway and have been previously shown to exhibit barrier disruption and decreased permeability when exposed to NPs (Banga et al., 2012; Dekali et al., 2014). Our results showed similar barrier disruption in Calu3 cells on-chip when exposed to nebulized NPs (ZnO and TiO2+ZnO NPs; Supplementary Figure S2). Furthermore, gene expression analysis of Calu3 cells exposed to nanoparticles on the chip provides strong evidence of an ongoing inflammatory response (Supplementary Figure S2E). Alveolar ^{AX}iAECs were used to model the distal region. Previous studies with those cells have shown lipopolysaccharide (LPS) induced inflammation and EMT mechanism induced by transforming growth factor β 1 (TGFβ1) (Sengupta et al., 2022). We further demonstrate here, that ^{AX}iAECs are very sensitive to nebulized NPs and chemicals and show signs of cellular damage, EMT, and a deregulated genetic profile. Furthermore, ^{AX}hAEpCs exposed to aerosolized NPs confirmed the results obtained with the ^{AX}iAECs model, with a disrupted barrier and a persistent inflammatory insult. Strikingly, increased MUC1 expression on NPs and PHMG trigger was observed in both ^{AX}hAEpCs and ^{AX}iAECs under dynamic CS conditions. MUC1 is a membrane associated mucin protein that is mainly released by AT2 cells and is present to a lesser extent in AT1 cells (Astarita et al., 2012). Previous research has shown that MUC1 or its partial released fragment, KL6 plays a role in anti-inflammatory reaction specially in diseases such as COPD and cancer (Ishikawa et al., 2011; Milara et al., 2018). Therefore, MUC1 was found in large amount during an active inflammatory phase, reflecting the results of our exposure. WIF1, another extracellular mediator of the Wnt signalling pathway, has recently been associated with clinical relevance in lung inflammation (J. Choi et al., 2020). A sub-population of AT2 cells expressing canonical AT2 markers like surfactant proteins A1, A2 and C (SP-C) among others were found to have increased expression of the WIF1 gene. This AT2 subpopulation and in particular the WIF1 gene have been found to be abundantly expressed during COPD and IPF suggesting their potential role in the pathogenesis of those diseases (Shi et al., 2017; Sauler et al., 2022). This is consistent with our data in which the WIF1 gene expression was increased upon exposure to TiO2 NPs (Figure 4E). This demonstrates the adequate potential of ^{AX}iAECs as a cell line model for lung barrier toxicity studies when primary alveolar epithelial cells are not available.

To include immune cells like macrophages in our system as an active player for alveolar inflammation, differentiated THP1 cells were used. d-THP1 cell line is classically used in co-culture studies for the lung to mimic a functional diffusion barrier (Herminghaus et al., 2022). Although, we have used PMA here for differentiation of the THP1 monocytes to activated d-THP1 macrophages according to previously established protocol (Kletting, 2017), several studies have pointed the upregulation of various unrelated genes which overrides the test-inducer associated inflammation (Park E. et al., 2007; Farcal et al., 2012). Future studies are therefore needed to optimize THP1 differentiation protocol to minimize undesirable leaky effects of PMA activation. To verify macrophage activation, CD68 surface protein marker was analyzed after PHMG induction. CD68$^+$ macrophages were verified in several studies to be upregulated during inflammation (Chistiakov et al., 2016; Klinge et al., 2020). Hence, increased expression of CD68 surface marker in our studies established the presence of activated macrophage population within the tri-cell culture model (Supplementary Figure S3). Activated CD68$^+$ THP1 macrophages were demonstrated to additionally have increased expression of M1-associated macrophage membrane associated protein, CD38 (Lam et al., 2019). Previous research findings have indicated the abundance of CD38 surface marker in THP1 cells during inflammation (Green et al., 2020; Yarbro et al., 2020) which goes in similar direction to what we demonstrated in our model on exposure to NPs (Figure 4E) and PHMG (Figure 7F). While the role of M2-associated macrophage marker CD206 in the lung is not completely established, few studies have shown a correlation of the presence of soluble CD206 forms with acute inflammation cases (Tsuchiya et al., 2019; Nielsen et al., 2020). Since CD206+ M2 macrophage-like cells could be activated through the IL4/IL13 axis (Genin et al., 2015), our hypothesis suggests that exposure to NPs and PHMG trigger an alternative activation of the THP1 cells in co-culture on-chip which might represent an onset for aberrant anti-inflammatory effort. However, further extensive profiling of the inflamed and activated THP1 subpopulations are required to have a conclusive statement.

Furthermore, in our tri-cell culture model, the basal side of the membrane was paved by ECs (HLMVEC). During inflammation, the apical alveolar exposure from a trigger is known to result in release of signaling factors that also activates the endothelial barrier and increase permeability and paracellular gap formations (Kuebler

et al., 2010; Bärnthaler et al., 2017). Therefore, in our studies we demonstrated disrupted endothelial barrier on NPs and PHMG exposure, whereas with FL treatment we observed an increase in CD31 (or Pecam) expression signifying an onset of the barrier recovery process. Moreover, increased vWF levels was observed on exposure to PHMG on-chip which is in line with current research findings confirming that elevated vWF amount is associated with inflammation and emphysema pathogenesis (Harrison et al., 2017; Langholm et al., 2020). It signifies that apical epithelial exposure of the NPs and toxic PHMG were able to induce a much deeper basal effect inciting endothelial activation and damage in our cellular models on-chip. FL treatment on-chip was able to reduce expression of inflammation and epithelial damage-associated genes, however it could not recover barrier damage induced by PHMG. One reason could be the small treatment window of 24 h which was not sufficient to recover major loss of barrier integrity by PHMG or booster doses of inhaled FL might be required to overcome such major damage (Kortekaas Krohn et al., 2019; Sibinovska et al., 2022).

Notably, we have found an immense effect of three-dimensional CS in our models. ALI along with CS culture conditions has a tremendous influence on the alveolar barrier and made it highly sensitive to the exposed NPs and PHMG. From our previous study (Sengupta et al., 2022) we had observed changes with the actin fibers on CS, which might hint towards a cytoskeletal rearrangement which facilitates better sensitivity to the exposed toxicants. Recent studies have shown convincing evidence that cell-ECM interactions play an important role for particle uptake kinetics and subsequent inflammation (Augustine et al., 2020; Engin et al., 2017; A; Lee et al., 2022). On the other side, abnormal ECM remodeling is a hallmark feature for COPD, asthma and fibrosis (Ito et al., 2019; Dekkers et al., 2021; Migulina et al., 2022). Therefore, it will be important to investigate the use of native lung-derived ECM hydrogels (Nizamoglu et al., 2022) along with CS in lung-on-chips to investigate inhalation toxicity. In another recent publication, authors demonstrated that under 2D linear strain, uptake of 100 nm particles was highly increased (Doryab et al., 2021) where endocytosis and cytoskeletal remodeling might play a prominent role (Freese et al., 2014; Augustine et al., 2020).

The presence of surfactant in the *in vivo* distal lung circuit for inhaled NPs is another crucial aspect to consider. Upon reaching the deep lung, NPs tend to initially interact with the lung surfactant film, which is a membrane-based lipid-protein complex secreted by alveolar cells. This film plays an important role as it insulates the respiratory ALI and can affect the toxicity of NPs (Olmeda et al., 2020). Based on the charge of NPs, they can either attach to the lipid heads or deplete the proportion of lipids. Therefore, in all cases there is an impact on the surface tension which greatly influences the interaction and translocation of NPs through the surfactant film (Radiom et al., 2020; Hidalgo et al., 2017; Bai et al., 2020). Thus, using *in vitro* ALI models with a thin layer of surfactant at the top is the recommended approach when studying toxicity of NPs (Schleh et al., 2013). Hence, it would be important for future studies to include pulmonary surfactant preparation containing saturated and unsaturated phospholipids and sufficient concentration of SP-B and SP-C proteins when performing toxicity studies using such lung-on-chip models (Pérez-Gil, 2022).

Moreover, current studies with tobacco smoke, which is known to be the major risk factor for COPD (cdc.gov) have indicated that CS plays a complex role in activating a mechano-inflammation response in cells on exposure to cigarette smoke and extract (Mondoñedo et al., 2020; Nossa et al., 2021). Hence, it will be interesting to examine the precise role of ALI and CS in toxicant uptake and reaction to cigarette smoke in future lung inhalation models.

Conclusion

Comprehensively, the Cloud α AX12 platform recapitulates critical parameters of inhalation toxicity in the lung epithelium such as deposition kinetics, reproducible cytotoxic and barrier disruption effects in cell models of varying complexities along with deregulated gene and protein regulation representative of an inflamed barrier. NPs like TiO2 and ZnO when exposed to cells on-chip induce an inflammatory cascade resulting in barrier damage and reduced cell viability in both alveolar and bronchial cell models. Also, aerosolized PHMG induced significant cytotoxic response including reduced barrier integrity, EMT and increased expression of inflammatory cytokines in mono, co- and tri-cell culture models on-chip. Moreover, we have demonstrated that nebulized FL corticosteroid was strongly able to diminish PHMG-induced toxic effects including EMT and inflammation. Therefore, with the Cloud α AX12 we could establish three different exposure models with varying multicellular complexities, where a crucial physiological impact of ALI and CS combined culture conditions could be conceived.

The Cloud α AX12 platform thereby allows for reproducible testing conditions along with simple user-friendly handling which is crucial for development of inhaled medicines and hazard assessment studies. Overall, our results strongly advocate in favor of this inhalation lung-on-chip model, and it will prove to be of high value for pre-clinical and precision medicine studies to serve as a suitable alternative for use of animal models in inhalation research.

Data availability statement

The original contributions presented in the study are included in the article/Supplementary Material, further inquiries can be directed to the corresponding author.

Author contributions

ArS, NH, and OG conceived and developed the overall pipeline of this study. AD and AH assisted with the technical validation of the Cloud α AX12. MJ, MS, WH, LD, AnS, TM, and PD performed cell culture experiments, assisted other authors with experiments and/or data management. ArS collected and analyzed the data. ArS wrote the manuscript. TM and PD provided inputs in their respective field of expertise. NH and OG contributed to the interpretation of the data and reviewed the manuscript. All authors provided feedback and approved the submitted version.

Acknowledgments

The Eurostars (project Nr. AIM4DOC) is greatly acknowledged for financial support. Part of the project was also funded by SNSF (grant number 185365). The authors would like to thank Yara-Maria Proust who conducted preliminary experiments with nanoparticle exposures on chip. Andreas O. Stucki was affiliated with the University of Bern at the conception of this study and is currently affiliated with PETA Science Consortium International e.V., Stuttgart, Germany. We are grateful to Paul Schumacher (Vitrocell) for reviewing parts of the manuscript. The authors also highly appreciate the support of Nuria Roldan and Aude Rapet (AlveoliX) in the AIM4DOC project.

Conflict of interest

OG, NH, and JS hold equity in AlveoliX AG. LM, AH, NH, and JS are employed by AlveoliX. OW and TK are employed by VITROCELL Systems GmbH.

The remaining authors declare that the research was conducted without any commercial or financial relationships that could be construed as a potential conflict of interest.

Publisher's note

All claims expressed in this article are solely those of the authors and do not necessarily represent those of their affiliated organizations, or those of the publisher, the editors and the reviewers. Any product that may be evaluated in this article, or claim that may be made by its manufacturer, is not guaranteed or endorsed by the publisher.

Supplementary material

The Supplementary Material for this article can be found online at: https://www.frontiersin.org/articles/10.3389/fphar.2023.1114739/full#supplementary-material

References

Abaci, H. E., and Shuler, M. L. (2015). Human-on-a-chip design strategies and principles for physiologically based pharmacokinetics/pharmacodynamics modeling. *Integr. Biol.* 7 (4), 383–391. doi:10.1039/c4ib00292j

Abdulnasser Harfoush, S., Hannig, M., Le, D. D., Heck, S., Leitner, M., Omlor, A. J., et al. (2020). High-dose intranasal application of titanium dioxide nanoparticles induces the systemic uptakes and allergic airway inflammation in asthmatic mice. *Respir. Res.* 21 (1), 168. doi:10.1186/s12931-020-01386-0

Adegunsoye, D., and Rafeq, S. (2019). *Toxic inhalational lung injury. Pulmonology Advisor*. Available at: https://www.pulmonologyadvisor.com/home/decision-support-in-medicine/pulmonary-medicine/toxic-inhalational-lung-injury/December 2, 2022).

Adeola, F. O. (2021). Global impact of chemicals and toxic substances on human health and the environment. *Handb. Glob. Health*, 2227–2256. doi:10.1007/978-3-030-45009-0_96

Animal Wellness Action (2022). *Biden signs five animal protection measures into law*. Washington DC, USA: GlobeNewswire News Room. Available at: https://www.globenewswire.com/en/news-release/2022/12/30/2581290/0/en/Biden-Signs-Five-Animal-Protection-Measures-into-Law.html.

Antonio, C., Guido, J., Khamir, M., Peng, G., and Andrzej, P. (2016). *Ddl.*

Artzy-Schnirman, A., Arber Raviv, S., Doppelt Flikshtain, O., Shklover, J., Korin, N., Gross, A., et al. (2021). Advanced human-relevant *in vitro* pulmonary platforms for respiratory therapeutics. *Adv. Drug Deliv. Rev.* 176, 113901. doi:10.1016/j.addr.2021.113901

Artzy-Schnirman, A., Zidan, H., Elias-Kirma, S., Ben-Porat, L., Tenenbaum-Katan, J., Carius, P., et al. (2019). Capturing the onset of bacterial pulmonary infection in acini-on-chips. *Adv. Biosyst.* 3 (9), 1900026. doi:10.1002/adbi.201900026

Assad, N., Sood, A., Campen, M. J., and Zychowski, K. E. (2018). Metal-induced pulmonary fibrosis. *Curr. Environ. Health Rep.* 5 (4), 486–498. doi:10.1007/s40572-018-0219-7

Astarita, J. L., Acton, S. E., and Turley, S. J. (2012). Podoplanin: Emerging Functions in development, the immune system, and cancer. *Front. Immunol.* 3, 283. doi:10.3389/fimmu.2012.00283

Augustine, R., Hasan, A., Primavera, R., Wilson, R. J., Thakor, A. S., and Kevadiya, B. D. (2020). Cellular uptake and retention of nanoparticles: Insights on particle properties and interaction with cellular components. *Mater. Today Commun.* 25, 101692. doi:10.1016/j.mtcomm.2020.101692

Banga, A., Witzmann, F. A., Petrache, H. I., and Blazer-Yost, B. L. (2012). Functional effects of nanoparticle exposure on calu-3 airway epithelial cells. *Cell. Physiology Biochem.* 29 (1-2), 197–212. doi:10.1159/000337601

Bannuscher, A., Schmid, O., Drasler, B., Rohrbasser, A., Braakhuis, H. M., Meldrum, K., et al. (2022). An inter-laboratory effort to harmonize the cell-delivered *in vitro* dose of aerosolized materials. *NanoImpact* 28, 100439.

Barnes, P. J., Bonini, S., Seeger, W., Belvisi, M. G., Ward, B., and Holmes, A. (2015). Barriers to new drug development in respiratory disease. *Eur. Respir. J.* 45 (5), 1197–1207. doi:10.1183/09031936.00007915

Bärnthaler, T., Maric, J., Platzer, W., Konya, V., Theiler, A., Hasenöhrl, C., et al. (2017). The role of PGE2 in alveolar epithelial and lung microvascular endothelial crosstalk. *Sci. Rep.* 7 (1), 7923. doi:10.1038/s41598-017-08228-y

Baumgartner, K. B., Samet, J. M., Coultas, D. B., Stidley, C. A., Hunt, W. C., Colby, T. V., et al. (2000). Occupational and environmental risk factors for idiopathic pulmonary fibrosis: A multicenter case-control study. Collaborating centers. *Am. J. Epidemiol.* 152 (4), 307–315. doi:10.1093/aje/152.4.307

Benam, K. H., Novak, R., Nawroth, J., Hirano-Kobayashi, M., Ferrante, T. C., Choe, Y., et al. (2016). Matched-comparative modeling of normal and diseased human airway responses using a microengineered breathing lung chip. *Cell. Syst.* 3 (5), 456–466.e4. doi:10.1016/j.cels.2016.10.003

Bliss, B., Tran, K. I., Sioutas, C., and Campbell, A. (2018). Ambient ultrafine particles activate human monocytes: Effect of dose, differentiation state and age of donors. *Environ. Res.* 161, 314–320. doi:10.1016/j.envres.2017.11.019

Bur, M., Rothen-Rutishauser, B., Huwer, H., and Lehr, C.-M. (2009). A novel cell compatible impingement system to study *in vitro* drug absorption from dry powder aerosol formulations. *Eur. J. Pharm. Biopharm.* 72 (2), 350–357. doi:10.1016/j.ejpb.2008.07.019

Carlier, F. M., De Fays, C., and Pilette, C. (2021). Epithelial barrier dysfunction in chronic respiratory diseases. *Front. Physiology* 12, 691227. doi:10.3389/fphys.2021.691227

Centers for Disease Control and Prevention (2022). *Smoking and COPD*. Office on Smoking and Health, USA: Centers for Disease Control and Prevention. Available at: https://www.cdc.gov/tobacco/campaign/tips/diseases/copd.html (Retrieved December 2, 2022).

Chen, H. W., Su, S. F., Chien, C. T., Lin, W. H., Yu, S. L., Chou, C. C., et al. (2006). Titanium dioxide nanoparticles induce emphysema-like lung injury in mice. *FASEB J.* 20 (13), 2393–2395. doi:10.1096/fj.06-6485fje

Chistiakov, D. A., Killingsworth, M. C., Myasoedova, V. A., Orekhov, A. N., and Bobryshev, Y. V. (2016). CD68/macrosialin: Not just a histochemical marker. *Lab. Investig.* 97 (1), 4–13. doi:10.1038/labinvest.2016.116

Choi, J., Park, J.-E., Tsagkogeorga, G., Yanagita, M., Koo, B.-K., Han, N., et al. (2020). Inflammatory signals induce AT2 cell-derived damage-associated transient progenitors that mediate alveolar regeneration. *Cell. Stem Cell.* 27 (3), 366–382.e7. doi:10.1016/j.stem.2020.06.020

Choi, S., Choi, S., Choi, Y., Cho, N., Kim, S.-Y., Lee, C. H., et al. (2022). Polyhexamethylene guanidine phosphate increases stress granule formation in human 3D lung organoids under respiratory syncytial virus infection. *Ecotoxicol. Environ. Saf.* 229, 113094. doi:10.1016/j.ecoenv.2021.113094

Cidem, A., Bradbury, P., Traini, D., and Ong, H. X. (2020). Modifying and integrating *in vitro* and *ex vivo* respiratory models for inhalation drug screening. *Front. Bioeng. Biotechnol.* 8, 581995. doi:10.3389/fbioe.2020.581995

Clippinger, A. J., Allen, D., Jarabek, A. M., Corvaro, M., Gaça, M., Gehen, S., et al. (2018). Alternative approaches for acute inhalation toxicity testing to address global regulatory and non-regulatory data requirements: An international workshop report. *Vitro* 48, 53–70. doi:10.1016/j.tiv.2017.12.011

Cooney, D. J., and Hickey, A. J. (2011). Cellular response to the deposition of diesel exhaust particle aerosols onto human lung cells grown at the air–liquid interface by inertial impaction. *Toxicol. Vitro* 25 (8), 1953–1965. doi:10.1016/j.tiv.2011.06.019

Dekali, S., Gamez, C., Kortulewski, T., Blazy, K., Rat, P., and Lacroix, G. (2014). Assessment of an *in vitro* model of pulmonary barrier to study the translocation of nanoparticles. *Toxicol. Rep.* 1, 157–171. doi:10.1016/j.toxrep.2014.03.003

Dekkers, B. G. J., Saad, S. I., van Spelde, L. J., and Burgess, J. K. (2021). Basement membranes in obstructive pulmonary diseases. *Matrix Biol. Plus* 12, 100092. doi:10.1016/j.mbplus.2021.100092

Derk, R., Davidson, D. C., Manke, A., Stueckle, T. A., Rojanasakul, Y., and Wang, L. (2015). Potential *in vitro* model for testing the effect of exposure to nanoparticles on the lung alveolar epithelial barrier. *Sens. Bio-Sensing Res.* 3, 38–45. doi:10.1016/j.sbsr.2014.12.002

Desai, L. P., Chapman, K. E., and Waters, C. M. (2008). Mechanical stretch decreases migration of alveolar epithelial cells through mechanisms involving Rac1 and TIAM1. *Am. J. Physiology-Lung Cell. Mol. Physiology* 295 (5), L958–L965. doi:10.1152/ajplung.90218.2008

Ding, Y., Weindl, P., Lenz, A.-G., Mayer, P., Krebs, T., and Schmid, O. (2020). Quartz Crystal microbalances (QCM) are suitable for real-time dosimetry in nanotoxicological studies using VITROCELL®Cloud Cell Exposure Systems. *Part. Fibre Toxicol.* 17 (1), 44. doi:10.1186/s12989-020-00376-w

Doryab, A., Taskin, M. B., Stahlhut, P., Schröppel, A., Orak, S., Voss, C., et al. (2021). A bioinspired *in vitro* lung model to study particokinetics of nano-/microparticles under cyclic stretch and air-liquid interface conditions. *Front. Bioeng. Biotechnol.* 9, 616830. doi:10.3389/fbioe.2021.616830

Elbert, K. J., Schäfer, U. F., Schäfers, H. J., Kim, K. J., Lee, V. H., and Lehr, C. M. (1999). Monolayers of human alveolar epithelial cells in primary culture for pulmonary absorption and transport studies. *Pharm. Res.* 16 (5), 601–608. doi:10.1023/a:1018887501927

Elias-Kirma, S., Artzy-Schnirman, A., Das, P., Heller-Algazi, M., Korin, N., and Sznitman, J. (2020). *In situ*-like aerosol inhalation exposure for cytotoxicity assessment using airway-on-chips platforms. *Front. Bioeng. Biotechnol.* 8, 91. doi:10.3389/fbioe.2020.00091

Engin, A. B., Nikitovic, D., Neagu, M., Henrich-Noack, P., Docea, A. O., Shtilman, M. I., et al. (2017). Mechanistic understanding of nanoparticles' interactions with extracellular matrix: The cell and immune system. *Part. Fibre Toxicol.* 14 (1), 22. doi:10.1186/s12989-017-0199-z

EPAA (2022). *European commission*. Available at: https://webcast.ec.europa.eu/the-2022-annual-conference-of-the-european partnership-for-alternative-approaches-to-animal-testing-epaa-accelerating-the-transition-to-animal-free-sustainable (Retrieved November 23, 2022).

Erhardt, C., and Kim, K.-J. (2021). *Drug absorption studies:* In situ*,* in vitro *and in silico models*.

Farcal, L. R., Uboldi, C., Mehn, D., Giudetti, G., Nativo, P., Ponti, J., et al. (2012). Mechanisms of toxicity induced by sio2nanoparticles ofin vitrohuman alveolar barrier: Effects on cytokine production, oxidative stress induction, surfactant proteins a mrna expression and nanoparticles uptake. *Nanotoxicology* 7 (6), 1095–1110. doi:10.3109/17435390.2012.710658

Fishler, R., Hofemeier, P., Etzion, Y., Dubowski, Y., and Sznitman, J. (2015). Particle Dynamics and deposition in true-scale pulmonary acinar models. *Sci. Rep.* 5 (1), 14071. doi:10.1038/srep14071

Fizeşan, I., Chary, A., Cambier, S., Moschini, E., Serchi, T., Nelissen, I., et al. (2018). Responsiveness assessment of a 3D tetra-culture alveolar model exposed to diesel exhaust particulate matter. *Toxicol. Vitro* 53, 67–79. doi:10.1016/j.tiv.2018.07.019

Freese, C., Schreiner, D., Anspach, L., Bantz, C., Maskos, M., Unger, R. E., et al. (2014). *In vitro* investigation of silica nanoparticle uptake into human endothelial cells under physiological cyclic stretch. *Part. Fibre Toxicol.* 11 (1), 68. doi:10.1186/s12989-014-0068-y

Freire, K., Ordóñez Ramos, F., Soria, D. B., Pabón Gelves, E., and Di Virgilio, A. L. (2021). Cytotoxicity and DNA damage evaluation of tio2 and zno nanoparticles. uptake in lung cells in culture. *Toxicol. Res.* 10 (2), 192–202. doi:10.1093/toxres/tfaa112

Fröhlich, E., Bonstingl, G., Höfler, A., Meindl, C., Leitinger, G., Pieber, T. R., et al. (2013). Comparison of two *in vitro* systems to assess cellular effects of nanoparticles-containing aerosols. *Toxicol.* Vitro 27 (1), 409–417. doi:10.1016/j.tiv.2012.08.008

Fröhlich, E., Mercuri, A., Wu, S., and Salar-Behzadi, S. (2016). Measurements of deposition, lung surface area and lung fluid for simulation of inhaled compounds. *Front. Pharmacol.* 7, 181. doi:10.3389/fphar.2016.00181

Geiser, M., and Kreyling, W. G. (2010). Deposition and biokinetics of inhaled nanoparticles. *Part. Fibre Toxicol.* 7 (1), 2. doi:10.1186/1743-8977-7-2

Genin, M., Clement, F., Fattaccioli, A., Raes, M., and Michiels, C. (2015). M1 and M2 macrophages derived from THP-1 cells differentially modulate the response of cancer cells to etoposide. *BMC Cancer* 15 (1), 577. doi:10.1186/s12885-015-1546-9

Gina Main Report (2022). *Global initiative for asthma*. GINA, Fontana, USA: GINA. Retrieved November 18, 2022, Available at: https://ginasthma.org/gina-reports/.

Government Bill (2020). *Third reading - strengthening environmental protection for a healthier Canada act - parliament of Canada. Government bill (senate) S-5 (44-1) - third reading - strengthening environmental protection for a healthier Canada act - parliament of Canada. (n.d.).* (Senate) S-5 (44-1). Retrieved November 23, 2022, Available at: https://www.parl.ca/DocumentViewer/en/44-1/bill/S-5/third-reading.

Green, I. D., Pinello, N., Song, R., Lee, Q., Halstead, J. M., Kwok, C.-T., et al. (2020). Macrophage development and activation involve coordinated intron retention in key inflammatory regulators. *Nucleic Acids Res.* 48 (12), 6513–6529. doi:10.1093/nar/gkaa435

Gustafsson, Å., Lindstedt, E., Elfsmark, L. S., and Bucht, A. (2011). Lung exposure of titanium dioxide nanoparticles induces innate immune activation and long-lasting lymphocyte response in the dark agouti rat. *J. Immunotoxicol.* 8 (2), 111–121. doi:10.3109/1547691X.2010.546382

Hamilton, R. F., Thakur, S. A., and Holian, A. (2008). Silica binding and toxicity in alveolar macrophages. *Free Radic. Biol. Med.* 44 (7), 1246–1258. doi:10.1016/j.freeradbiomed.2007.12.027

Harrison, J. M., Quanstrom, L. M., Robinson, A. R., Wobeser, B., Anderson, S. L., and Singh, B. (2017). Expression of von Willebrand factor, pulmonary intravascular macrophages, and toll-like receptors in lungs of septic foals. *J. Veterinary Sci.* 18 (1), 17–23. doi:10.4142/jvs.2017.18.1.17

He, S., Gui, J., Xiong, K., Chen, M., Gao, H., and Fu, Y. (2022). A roadmap to pulmonary delivery strategies for the treatment of infectious lung diseases. *J. Nanobiotechnology* 20 (1), 101. doi:10.1186/s12951-022-01307-x

Herminghaus, A., Kozlov, A. V., Szabó, A., Hantos, Z., Gylstorff, S., Kuebart, A., et al. (2022). A barrier to defend - models of pulmonary barrier to study acute inflammatory diseases. *Front. Immunol.* 13, 895100. doi:10.3389/fimmu.2022.895100

Hess, A., Wang-Lauenstein, L., Braun, A., Kolle, S. N., Landsiedel, R., Liebsch, M., et al. (2016). Prevalidation of the *ex-vivo* model PCLS for prediction of respiratory toxicity. *Toxicol. Vitro* 32, 347–361. doi:10.1016/j.tiv.2016.01.006

Hobi, N., Ravasio, A., and Haller, T. (2012). Interfacial stress affects rat alveolar type II cell signaling and gene expression. *Am. J. Physiology-Lung Cell. Mol. Physiology* 303 (2), L117–L129. doi:10.1152/ajplung.00340.2011

Horváth, T., Papp, A., Igaz, N., Kovács, D., Kozma, G., Trenka, V., et al. (2018). Pulmonary impact of titanium dioxide nanorods: Examination of nanorod-exposed rat lungs and human alveolar cells. *Int. J. Nanomedicine* 13, 7061–7077. doi:10.2147/IJN.S179159

Huang, D., Liu, T., Liao, J., Maharjan, S., Xie, X., Pérez, M., et al. (2021). Reversed-engineered human alveolar lung-on-a-chip model. *Proc. Natl. Acad. Sci.* 118 (19), e2016146118. doi:10.1073/pnas.2016146118

Huh, D., Matthews, B. D., Mammoto, A., Montoya-Zavala, M., Hsin, H. Y., and Ingber, D. E. (2010). Reconstituting organ-level lung functions on a chip. *Science* 328 (5986), 1662–1668. doi:10.1126/science.1188302

IARC (1989). *Titanium dioxide 1. exposure data - world health organization*. Retrieved November 30, 2022, Available at: https://monographs.iarc.who.int/wp-content/uploads/2018/06/mono93-7.pdf.

Ishikawa, N., Mazur, W., Toljamo, T., Vuopala, K., Rönty, M., Horimasu, Y., et al. (2011). Ageing and long-term smoking affects KL-6 levels in the lung, induced sputum and plasma. *BMC Pulm. Med.* 11 (1), 22. doi:10.1186/1471-2466-11-22

Ito, J. T., Lourenço, J. D., Righetti, R. F., Tibério, I. F. L. C., Prado, C. M., and Lopes, F. D. T. Q. S. (2019). Extracellular matrix component remodeling in respiratory diseases: What has been found in clinical and experimental studies? *Cells* 8 (4), 342. doi:10.3390/cells8040342

Jeong, M. H., Kim, H. R., Park, Y. J., and Chung, K. H. (2019). Akt and notch pathways mediate polyhexamethylene guanidine phosphate-induced epithelial-mesenchymal transition via ZEB2. *Toxicol. Appl. Pharmacol.* 380, 114691. doi:10.1016/j.taap.2019.114691

Ji, J., Upadhyay, S., Xiong, X., Malmlöf, M., Sandström, T., Gerde, P., et al. (2018). Multi-cellular human bronchial models exposed to diesel exhaust particles: Assessment of inflammation, oxidative stress and macrophage polarization. *Part. Fibre Toxicol.* 15 (1), 19. doi:10.1186/s12989-018-0256-2

Joint Research Centre, Institute for Health and Consumer Protection, Institute for Reference Materials and MeasurementsSingh, C., Levin, M., and Friedrichs, S. (2012). *NM-series of representative manufactured nanomaterials: Zinc oxide NM-110, NM-111, NM-112, NM-113 characterisation and test item preparation*. Publications Office.

Kaiser, A. J., Salem, C., Alvarenga, B. J., Pagliaro, A., Smith, K. P., Valerio, L. G., et al. (2021). A robotic system for real-time analysis of inhaled submicron and microparticles. *IScience* 24 (10), 103091. doi:10.1016/j.isci.2021.103091

Kim, S. R., Lee, Y. C., Kim, D. I., Park, H. J., and Kim, S. H. (2015). *Inhaled PHMG can induce pulmonary fibrosis through mitochondrial ros generation. 1.5 diffuse parenchymal lung disease*.

Kim, Y. H., Fazlollahi, F., Kennedy, I. M., Yacobi, N. R., Hamm-Alvarez, S. F., Borok, Z., et al. (2010). Alveolar epithelial cell injury due to zinc oxide nanoparticle exposure. *Am. J. Respir. Crit. Care Med.* 182 (11), 1398–1409. doi:10.1164/rccm.201002-0185OC

Kletting, S., Barthold, S., Repnik, U., Griffiths, G., Loretz, B., Schneider-Daum, N., et al. (2018). Co-culture of human alveolar epithelial (haelvi) and macrophage (THP-1) cell lines. *ALTEX* 35 (2), 211–222.

Klinge, U., Dievernich, A., Tolba, R., Klosterhalfen, B., and Davies, L. (2020). cd68+ macrophages as crucial components of the foreign body reaction demonstrate an unconventional pattern of functional markers quantified by analysis with double fluorescence staining. *J. Biomed. Mater. Res. Part B Appl. Biomaterials* 108 (8), 3134–3146. doi:10.1002/jbm.b.34639

Kolanjiyil, A. V., Kleinstreuer, C., Kleinstreuer, N. C., Pham, W., and Sadikot, R. T. (2019). Mice-to-men comparison of inhaled drug-aerosol deposition and clearance. *Respir. Physiol. Neurobiol.* 260, 82–94. doi:10.1016/j.resp.2018.11.003

Kortekaas Krohn, I., Seys, S. F., Lund, G., Jonckheere, A. C., Dierckx de Casterlé, I., Ceuppens, J. L., et al. (2019). Nasal epithelial barrier dysfunction increases sensitization and mast cell degranulation in the absence of allergic inflammation. *Allergy* 75 (5), 1155–1164. doi:10.1111/all.14132

Kuebler, W. M., Yang, Y., Samapati, R., and Uhlig, S. (2010). Vascular barrier regulation by PAF, ceramide, caveolae, and no - an intricate signaling network with discrepant effects in the pulmonary and Systemic Vasculature. *Cell. Physiology Biochem.* 26 (1), 29–40. doi:10.1159/000315103

Kuroda, E., Ozasa, K., Temizoz, B., Ohata, K., Koo, C. X., Kanuma, T., et al. (2016). Inhaled fine particles induce alveolar macrophage death and interleukin-1α release to promote inducible bronchus-associated lymphoid tissue formation. *Immunity*, 45(6), 1299–1310.

Lam, J. H., Ng, H. H., Lim, C. J., Sim, X. N., Malavasi, F., Li, H., et al. (2019). Expression of CD38 on macrophages predicts improved prognosis in hepatocellular carcinoma. *Front. Immunol.* 10, 2093. doi:10.3389/fimmu.2019.02093

Langholm, L. L., Rønnow, S. R., Sand, J. M. B., Leeming, D. J., Tal-Singer, R., Miller, B. E., et al. (2020). Increased von Willebrand factor processing in COPD, reflecting lung epithelium damage, is associated with emphysema, exacerbations and elevated mortality risk. *Int. J. Chronic Obstr. Pulm. Dis.* 15, 543–552. doi:10.2147/COPD.S235673

Lee, A., Sousa de Almeida, M., Milinkovic, D., Septiadi, D., Taladriz-Blanco, P., Loussert-Fonta, C., et al. (2022). Substrate stiffness reduces particle uptake by epithelial cells and macrophages in a size-dependent manner through mechanoregulation. *Nanoscale* 14 (40), 15141–15155. doi:10.1039/d2nr03792k

Lee, S.-H., Ahn, J.-R., Go, H.-N., Lee, S.-Y., Park, M. J., Song, K. B., et al. (2021). Exposure to polyhexamethylene guanidine exacerbates bronchial hyperresponsiveness and lung inflammation in a mouse model of ovalbumin-induced asthma. *Allergy, Asthma Immunol. Res.* 13 (4), 655–664. doi:10.4168/aair.2021.13.4.655

Lee, S. Y., Kim, J. S., Lee, J. M., Kwon, S. S., Kim, K. H., Moon, H. S., et al. (2008). Inhaled corticosteroid prevents the thickening of airway smooth muscle in murine model of chronic asthma. *Pulm. Pharmacol. Ther.* 21 (1), 14–19. doi:10.1016/j.pupt.2006.10.009

Lee, Y.-H., and Seo, D.-S. (2020). Toxicity of humidifier disinfectant polyhexamethylene guanidine hydrochloride by two-week whole body-inhalation exposure in rats. *J. Toxicol. Pathology* 33 (4), 265–277. doi:10.1293/tox.2020-0043

Leibrock, L., Wagener, S., Singh, A. V., Laux, P., and Luch, A. (2019). Nanoparticle induced barrier function assessment at liquid–liquid and air–liquid interface in novel human lung epithelia cell lines. *Toxicol. Res.* 8 (6), 1016–1027. doi:10.1039/c9tx00179d

Lenz, A. G., Karg, E., Lentner, B., Dittrich, V., Brandenberger, C., Rothen-Rutishauser, B., et al. (2009). A dose-controlled system for air-liquid interface cell exposure and application to zinc oxide nanoparticles. *Part. Fibre Toxicol.* 6 (1), 32. doi:10.1186/1743-8977-6-32

Lenz, A., Stoeger, T., Cei, D., Schmidmeir, M., Semren, N., Burgstaller, G., et al. (2014). Efficient Bioactive delivery of Aerosolized drugs to human pulmonary epithelial cells cultured in air–liquid interface conditions. *Am. J. Respir. Cell. Mol. Biol.* 51 (4), 526–535. doi:10.1165/rcmb.2013-0479OC

Leroux, M. M., Hocquel, R., Bourge, K., Kokot, B., Kokot, H., Koklič, T., et al. (2022). Aerosol–cell exposure system applied to semi-adherent cells for aerosolization of lung surfactant and nanoparticles followed by high quality RNA extraction. *Nanomaterials* 12 (8), 1362. doi:10.3390/nano12081362

Lewis, D. J., Williams, T. C., and Beck, S. L. (2013). Foamy macrophage responses in the rat lung following exposure to inhaled pharmaceuticals: A simple, pragmatic approach for inhaled drug development. *J. Appl. Toxicol.* 34 (4), 319–331. doi:10.1002/jat.2950

Lock, J. Y., Carlson, T. L., and Carrier, R. L. (2018). Mucus models to evaluate the diffusion of drugs and particles. *Adv. Drug Deliv. Rev.* 124, 34–49. doi:10.1016/j.addr.2017.11.001

London, L., Coggon, D., Moretto, A., Westerholm, P., Wilks, M. F., and Colosio, C. (2010). The ethics of human volunteer studies involving experimental exposure to pesticides: Unanswered dilemmas. *Environ. Health* 9 (1), 50. doi:10.1186/1476-069X-9-50

Migulina, N., Tjin, G., Faiz, A., Borghuis, T., Metzlar, M., Dijk, E. M., et al. (2022). *Differential roles for Lysyl oxidase (like) family members in chronic obstructive pulmonary disease; from gene and protein expression to function*. B108. ORIGINS AND OUTCOMES OF COPD.

Milara, J., Morell, A., de Diego, A., Artigues, E., Morcillo, E., and Cortijo, J. (2018). Mucin 1 deficiency mediates corticosteroid insensitivity in asthma. *Allergy* 74 (1), 111–121. doi:10.1111/all.13546

Molino, A., Calabrese, G., and Maniscalco, M. (2018). Patient considerations in the treatment of COPD: Focus on the new combination inhaler fluticasone furoate/umeclidinium/vilanterol. *Patient Prefer. Adherence* 12, 993–1001. doi:10.2147/PPA.S152179

Mondoñedo, J. R., Bartolák-Suki, E., Bou Jawde, S., Nelson, K., Cao, K., Sonnenberg, A., et al. (2020). A high-throughput system for cyclic stretching of precision-cut lung slices during acute cigarette smoke extract exposure. *Front. Physiology* 11, 566. doi:10.3389/fphys.2020.00566

Monsé, C., Raulf, M., Hagemeyer, O., van Kampen, V., Kendzia, B., Gering, V., et al. (2019). Airway inflammation after inhalation of nano-sized zinc oxide particles in human volunteers. *BMC Pulm. Med.* 19 (1), 266. doi:10.1186/s12890-019-1026-0

Naidu, R., Biswas, B., Willett, I. R., Cribb, J., Kumar Singh, B., Paul Nathanail, C., et al. (2021). Chemical pollution: A growing peril and potential catastrophic risk to humanity. *Environ. Int.* 156, 106616. doi:10.1016/j.envint.2021.106616

NHS (2022). *NHS choices*. Available at: https://www.nhs.uk/medicines/fluticasone-inhalers/ (Retrieved November 30, 2022).

Nielsen, M. C., Hvidbjerg Gantzel, R., Clària, J., Trebicka, J., Møller, H. J., and Grønbæk, H. (2020). Macrophage activation markers, CD163 and CD206, in acute-on-chronic liver failure. *Cells* 9 (5), 1175. doi:10.3390/cells9051175

Nizamoglu, M., de Hilster, R. H. J., Zhao, F., Sharma, P. K., Borghuis, T., Harmsen, M. C., et al. (2022). *An* in vitro *model of fibrosis using crosslinked native extracellular matrix-derived hydrogels to modulate biomechanics without changing composition*.

Nossa, R., Costa, J., Cacopardo, L., and Ahluwalia, A. (2021). Breathing *in vitro*: Designs and applications of engineered lung models. *J. Tissue Eng.* 12, 204173142110086. doi:10.1177/20417314211008696

Nuwer, R. (2022). US agency seeks to phase out animal testing. *Nature*. doi:10.1038/d41586-022-03569-9

OECD (2022). Case study on the use of an integrated approach for testing and assessment (IATA) for new approach methodology (NAM) for refining inhalation risk assessment from point of contact toxicity of the pesticide, *Chlorothalonil*. *OECD Ser. Test. Assess. No* 367. Available at: https://www.oecd.org/officialdocuments/publicdisplaydocumentpdf/?cote=env/cbc/mono(2022)31doclanguage=en

Oliveira, V. R., Uriarte, J. J., Falcones, B., Jorba, I., Zin, W. A., Farré, R., et al. (2019). Biomechanical response of lung epithelial cells to iron oxide and titanium dioxide nanoparticles. *Front. Physiology* 10, 1047. doi:10.3389/fphys.2019.01047

Olmeda, B., Alonso, A., Pérez-Gil, J., and Perez-Gil, J. (2020). Lipid–protein and protein–protein interactions in the pulmonary surfactant system and their role in lung homeostasis. *Int. J. Mol. Sci.* 21 (10), 3708. doi:10.3390/ijms21103708

Park, D.-U., Choi, Y.-Y., Ahn, J.-J., Lim, H.-K., Kim, S.-K., Roh, H.-S., et al. (2015). Relationship between exposure to household humidifier disinfectants and risk of lung injury: A family-based study. *PLOS ONE* 10 (5), e0124610. doi:10.1371/journal.pone.0124610

Park, E. K., Jung, H. S., Yang, H. I., Yoo, M. C., Kim, C., and Kim, K. S. (2007). Optimized THP-1 differentiation is required for the detection of responses to weak stimuli. *Inflamm. Res.* 56 (1), 45–50. doi:10.1007/s00011-007-6115-5

Park, Y. J., Jeong, M. H., Bang, I. J., Kim, H. R., and Chung, K. H. (2019). Guanidine-based disinfectants, polyhexamethylene guanidine-phosphate (PHMG-P), polyhexamethylene biguanide (PHMB), and oligo(2-(2-ethoxy)ethoxyethyl guanidinium chloride (PGH) induced epithelial-mesenchymal transition in A549 alveolar epithelial cells. *Inhal. Toxicol.* 31 (4), 161–166. doi:10.1080/08958378.2019.1624896

Park, J. S., Park, Y. J., Kim, H. R., and Chung, K. H. (2019). Polyhexamethylene guanidine phosphate-induced ROS-mediated DNA damage caused cell cycle arrest and apoptosis in lung epithelial cells. *J. Toxicol. Sci.* 44 (6), 415–424. doi:10.2131/jts.44.415

Paur, H.-R., Cassee, F. R., Teeguarden, J., Fissan, H., Diabate, S., Aufderheide, M., et al. (2011). *In-vitro* cell exposure studies for the assessment of nanoparticle toxicity in the lung—A dialog between aerosol science and biology. *J. Aerosol Sci.* 42 (10), 668–692. doi:10.1016/j.jaerosci.2011.06.005

Pedrini, L. F., Escaliante, L. C., and Scalvi, L. V. (2021). Deposition of tio2 thin films by dip-coating technique from a two-phase solution method and application to photocatalysis. *Mater. Res.* 24 (1). doi:10.1590/1980-5373-mr-2021-0007

Peng, C., Yan, Y., Li, Z., Jiang, Y., and Cai, Y. (2020). Chronic obstructive pulmonary disease caused by inhalation of dust: A meta-analysis. *Medicine* 99 (34), e21908. doi:10.1097/MD.0000000000021908

Pérez-Gil, J. (2022). A recipe for a good clinical pulmonary surfactant. *Biomed. J.* 45 (4), 615–628. doi:10.1016/j.bj.2022.03.001

Petersen, E. J., Sharma, M., Clippinger, A. J., Gordon, J., Katz, A., Laux, P., et al. (2021). Use of cause-and-effect analysis to optimize the reliability of *in vitro* inhalation toxicity measurements using an air–liquid interface. *Chem. Res. Toxicol.* 34 (6), 1370–1385. doi:10.1021/acs.chemrestox.1c00080

Preclinical development for inhalation drugs (2022). *Charles River laboratories*. Available at: https://www.criver.com/sites/default/files/resources/PreclinicalDevelopmentforInhalationDrugs.pdf.

Ramanarayanan, T., Szarka, A., Flack, S., Hinderliter, P., Corley, R., Charlton, A., et al. (2022). Application of a new approach method (NAM) for inhalation risk assessment. *Regul. Toxicol. Pharmacol.* 133, 105216. doi:10.1016/j.yrtph.2022.105216

Remzova, M., Zouzelka, R., Brzicova, T., Vrbova, K., Pinkas, D., Rőssner, P., et al. (2019). Toxicity of tio2, zno, and SiO2 nanoparticles in human lung cells: Safe-by-design development of construction materials. *Nanomaterials* 9 (7), 968. doi:10.3390/nano9070968

Röhm, M., Carle, S., Maigler, F., Flamm, J., Kramer, V., Mavoungou, C., et al. (2017). A comprehensive screening platform for Aerosolizable protein formulations for intranasal and pulmonary drug delivery. *Int. J. Pharm.* 532 (1), 537–546. doi:10.1016/j.ijpharm.2017.09.027

Rothen-Rutishauser, B. M., Kiama, S. G., and Gehr, P. (2005). A three-dimensional cellular model of the human respiratory tract to study the interaction with particles. *Am. J. Respir. Cell. Mol. Biol.* 32 (4), 281–289. doi:10.1165/rcmb.2004-0187OC

Sanches Santos Rizzo Zuttion, M., Moore, S. K., Chen, P., Beppu, A. K., and Hook, J. L. (2022). New insights into the alveolar epithelium as a driver of acute respiratory distress syndrome. *Biomolecules* 12 (9), 1273. doi:10.3390/biom12091273

Sauler, M., McDonough, J. E., Adams, T. S., Kothapalli, N., Barnthaler, T., Werder, R. B., et al. (2022). Characterization of the COPD alveolar niche using single-cell RNA sequencing. *Nat. Commun.* 13 (1).

Sayes, C. M., Wahi, R., Kurian, P. A., Liu, Y., West, J. L., Ausman, K. D., et al. (2006). Correlating nanoscale titania structure with toxicity: A cytotoxicity and inflammatory response study with human dermal fibroblasts and human lung epithelial cells. *Toxicol. Sci.* 92 (1), 174–185. doi:10.1093/toxsci/kfj197

Schleh, C., Kreyling, W. G., and Lehr, C.-M. (2013). Pulmonary surfactant is indispensable in order to simulate the *in vivo* situation. *Part. Fibre Toxicol.* 10 (1), 6. doi:10.1186/1743-8977-10-6

Schreier, H., Gagne, L., Conary, J. T., and Laurian, G. (1998). Simulated lung transfection by nebulization of liposome cDNA complexes using a cascade impactor seeded with 2-CFSME0-cells. *J. Aerosol Med.* 11 (1), 1–13. doi:10.1089/jam.1998.11.1

Sehlmeyer, K., Ruwisch, J., Roldan, N., and Lopez-Rodriguez, E. (2020). Corrigendum: Alveolar dynamics and beyond - the importance of surfactant protein C and cholesterol in lung homeostasis and fibrosis. *Front. Physiology* 11, 943. doi:10.3389/fphys.2020.00943

Sengupta, A., Roldan, N., Kiener, M., Froment, L., Raggi, G., Imler, T., et al. (2022). A new immortalized human alveolar epithelial cell model to study lung injury and toxicity on a breathing lung-on-chip system. *Front. Toxicol.* 4, 840606. doi:10.3389/ftox.2022.840606

Shi, J., Li, F., Luo, M., Wei, J., and Liu, X. (2017). Distinct roles of wnt/β-catenin signaling in the pathogenesis of chronic obstructive pulmonary disease and idiopathic pulmonary fibrosis. *Mediat. Inflamm.* 2017, 3520581–3520596. doi:10.1155/2017/3520581

Shima, T., Kashiwagi, H., Ino, H., Tanaka, S., Fukuda, M., and Kobata, H. (2022). Acute respiratory distress syndrome due to inhalation of acryloyl chloride. *Acute Med. Surg.* 9 (1), e724. doi:10.1002/ams2.724

Shin, D. Y., Jeong, M. H., Bang, I. J., Kim, H. R., and Chung, K. H. (2018). MicroRNA regulatory networks reflective of polyhexamethylene guanidine phosphate-induced fibrosis in A549 human alveolar adenocarcinoma cells. *Toxicol. Lett.* 287, 49–58. doi:10.1016/j.toxlet.2018.01.010

Sibinovska, N., Žakelj, S., Trontelj, J., and Kristan, K. (2022). Applicability of RPMI 2650 and Calu-3 cell models for evaluation of nasal formulations. *Pharmaceutics* 14 (2), 369. doi:10.3390/pharmaceutics14020369

Skytthe, M. K., Graversen, J. H., and Moestrup, S. K. (2020). Targeting of CD163+ macrophages in inflammatory and malignant diseases. *Int. J. Mol. Sci.* 21 (15), 5497. doi:10.3390/ijms21155497

Sokol, K., Sur, S., and Ameredes, B. T. (2013). Inhaled environmental allergens and toxicants as determinants of the asthma phenotype. *Heterogeneity Asthma* 795, 43–73. doi:10.1007/978-1-4614-8603-9_4

Song, J., Jung, K. J., Yoon, S., Lee, K., and Kim, B. (2019). Polyhexamethyleneguanidine phosphate induces cytotoxicity through disruption of membrane integrity. *Toxicology* 414, 35–44. doi:10.1016/j.tox.2019.01.001

Stewart, C. E., Torr, E. E., Mohd Jamili, N. H., Bosquillon, C., and Sayers, I. (2012). Evaluation of differentiated human bronchial epithelial cell culture systems for asthma research. *J. Allergy* 2012, 943982–944011. doi:10.1155/2012/943982

Stucki, A. O., Barton-Maclaren, T. S., Bhuller, Y., Henriquez, J. E., Henry, T. R., Hirn, C., et al. (2022). Use of new approach methodologies (NAMS) to meet regulatory requirements for the assessment of Industrial Chemicals and pesticides for effects on human health. *Front. Toxicol.* 4, 964553. doi:10.3389/ftox.2022.964553

Stucki, A. O., Stucki, J. D., Hall, S. R., Felder, M., Mermoud, Y., Schmid, R. A., et al. (2015). A lung-on-a-chip array with an integrated bio-inspired respiration mechanism. *Lab a Chip* 15 (5), 1302–1310. doi:10.1039/c4lc01252f

Stucki, J. D., Hobi, N., Galimov, A., Stucki, A. O., Schneider-Daum, N., Lehr, C.-M., et al. (2018). Medium throughput breathing human primary cell alveolus-on-chip model. *Sci. Rep.* 8 (1), 14359. doi:10.1038/s41598-018-32523-x

Thorsson, L., Edsbäcker, S., Källén, A., and Löfdahl, C.-G. (2001). Pharmacokinetics and systemic activity of fluticasone via Diskus® and PMDI, and of budesonide via turbuhaler®. *Br. J. Clin. Pharmacol.*, 52(5), 529–538. doi:10.1046/j.0306-5251.2001.01493.x

Tollstadius, B. F., Silva, A. C., Pedralli, B. C., and Valadares, M. C. (2019). Carbendazim induces death in alveolar epithelial cells: A comparison between submerged and at the air-liquid interface cell culture. *Toxicol. Vitro* 58, 78–85. doi:10.1016/j.tiv.2019.03.004

Tsuchiya, K., Suzuki, Y., Yoshimura, K., Yasui, H., Karayama, M., Hozumi, H., et al. (2019). Author correction: Macrophage mannose receptor CD206 predicts prognosis in community-acquired pneumonia. *Sci. Rep.* 9 (1), 3324. doi:10.1038/s41598-020-58958-9

van der Zalm, A. J., Barroso, J., Browne, P., Casey, W., Gordon, J., Henry, T. R., et al. (2022). A framework for establishing scientific confidence in new approach methodologies. *Archives Toxicol.* 96 (11), 2865–2879. doi:10.1007/s00204-022-03365-4

Van Eeden, S., Tan, W., Suwa, T., Mukae, H., Terashi, a, T., Fujii, T., et al. (2001). Cytokines involved in the systemic inflammatory response induced by exposure to particulate matter air pollutants (PM10). *Am. J. Respir. Crit. Care Med.* 164 (5), 826–830. doi:10.1164/ajrccm.164.5.2010160

Walenga, R. L., Babiskin, A. H., and Zhao, L. (2019). *In silico* methods for development of generic drug-device combination orally inhaled drug products. *CPT Pharmacometrics Syst. Pharmacol.* 8 (6), 359–370. doi:10.1002/psp4.12413

Wang, H., He, L., Liu, B., Feng, Y., Zhou, H., Zhang, Z., et al. (2018). Establishment and comparison of air-liquid interface culture systems for primary and immortalized swine tracheal epithelial cells. *BMC Cell. Biol.* 19 (1), 10. doi:10.1186/s12860-018-0162-3

Wang, J., and Fan, Y. (2014). Lung injury induced by tio2 nanoparticles depends on their structural features: Size, shape, crystal phases, and surface coating. *Int. J. Mol. Sci.* 15 (12), 22258–22278. doi:10.3390/ijms151222258

Wu, J., Wang, Y., Liu, G., Jia, Y., Yang, J., Shi, J., et al. (2018). Characterization of air-liquid interface culture of A549 alveolar epithelial cells. *Braz. J. Med. Biol. Res.* 51 (2), e6950. doi:10.1590/1414-431X20176950

Wu, J., Yan, Z., Schwartz, D. E., Yu, J., Malik, A. B., and Hu, G. (2013). Activation of NLRP3 inflammasome in alveolar macrophages contributes to mechanical stretch-induced lung inflammation and injury. *J. Immunol.* 190 (7), 3590–3599. doi:10.4049/jimmunol.1200860

Yarbro, J. R., Emmons, R. S., and Pence, B. D. (2020). Macrophage immunometabolism and inflammaging: Roles of mitochondrial dysfunction, cellular senescence, CD38, and Nad. *Immunometabolism* 2 (3), e200026. doi:10.20900/immunometab20200026

Zamprogno, P., Wüthrich, S., Achenbach, S., Thoma, G., Stucki, J. D., Hobi, N., et al. (2021). Second-generation lung-on-a-chip with an array of stretchable alveoli made with a biological membrane. *Commun. Biol.* 4 (1), 168. doi:10.1038/s42003-021-01695-0

Zhao, J., Li, M., Wang, Z., Chen, J., Zhao, J., Xu, Y., et al. (2019). Role of PM2.5 in the development and progression of COPD and its mechanisms. *Respir. Res.* 20 (1), 120. doi:10.1186/s12931-019-1081-3

frontiers | Frontiers in Pharmacology

TYPE Perspective
PUBLISHED 09 March 2023
DOI 10.3389/fphar.2023.1154193

OPEN ACCESS

EDITED BY
Xu Wang,
Shandong University, China

REVIEWED BY
Siva Subramanian,
Yeungnam University, Republic of Korea

*CORRESPONDENCE
Janette K. Burgess,
✉ j.k.burgess@umcg.nl

SPECIALTY SECTION
This article was submitted to Respiratory Pharmacology, a section of the journal Frontiers in Pharmacology

RECEIVED 30 January 2023
ACCEPTED 28 February 2023
PUBLISHED 09 March 2023

CITATION
Nizamoglu M and Burgess JK (2023), Current possibilities and future opportunities provided by three-dimensional lung ECM-derived hydrogels.
Front. Pharmacol. 14:1154193.
doi: 10.3389/fphar.2023.1154193

Current possibilities and future opportunities provided by three-dimensional lung ECM-derived hydrogels

Mehmet Nizamoglu[1,2] and Janette K. Burgess[1,2,3]*

[1]University of Groningen, University Medical Center Groningen, Department of Pathology and Medical Biology, Groningen, Netherlands, [2]University of Groningen, University Medical Center Groningen, Groningen Research Institute for Asthma and COPD (GRIAC), Groningen, Netherlands, [3]University of Groningen, University Medical Center Groningen, W.J. Kolff Institute for Biomedical Engineering and Materials Science-FB41, Groningen, Netherlands

Disruption of the complex interplay between cells and extracellular matrix (ECM), the scaffold that provides support, biochemical and biomechanical cues, is emerging as a key element underlying lung diseases. We readily acknowledge that the lung is a flexible, relatively soft tissue that is three dimensional (3D) in structure, hence a need exists to develop *in vitro* model systems that reflect these properties. Lung ECM-derived hydrogels have recently emerged as a model system that mimics native lung physiology; they contain most of the plethora of biochemical components in native lung, as well as reflecting the biomechanics of native tissue. Research investigating the contribution of cell:matrix interactions to acute and chronic lung diseases has begun adopting these models but has yet to harness their full potential. This perspective article provides insight about the latest advances in the development, modification, characterization and utilization of lung ECM-derived hydrogels. We highlight some opportunities for expanding research incorporating lung ECM-derived hydrogels and potential improvements for the current approaches. Expanding the capabilities of investigations using lung ECM-derived hydrogels is positioned at a cross roads of disciplines, the path to new and innovative strategies for unravelling disease underlying mechanisms will benefit greatly from interdisciplinary approaches. While challenges need to be addressed before the maximum potential can be unlocked, with the rapid pace at which this field is evolving, we are close to a future where faster, more efficient and safer drug development targeting the disrupted 3D microenvironment is possible using lung ECM-derived hydrogels.

KEYWORDS

extracellular matrix, fibrosis, *in vitro* models, collagen, chronic lung disease, biomechanics

1 Introduction

The human body is a complex, dynamic environment, consisting of many different cell types that reside in or traverse through defined microenvironments, which is tightly regulated to maintain a healthy state. When elements within this system become disrupted, this can lead to the development of disease. In the lung, disruption of the complex interplay between cells and the extracellular matrix (ECM), the scaffold that

provides support and biochemical and biomechanical cues, is emerging as a key element for deciphering the mechanism underlying diseases.

Why should we think about 3D in *in vitro* model systems?

When we think about the lung *in vivo*, we readily acknowledge that it is a flexible, relatively soft tissue that is three dimensional (3D) in structure. However, in general, when we work with model systems *in vitro*, to try to elucidate processes that underlie homeostasis and disease, we mostly work with two dimensional (2D) systems. In the lung cells are surrounded by a specialised ECM, that is appropriate for their location. Mesenchymal cells are located within a 3D ECM structure, while epithelial and endothelial cells are usually attached to a basement membrane on their basal side and their apical side is subjected to flow of epithelial lining fluid or blood respectively. The stiffness of the lung tissue, in health is usually between 1–5 kilo-pascals (kPa), and in fibrotic disease this can increase up to 100 kPa although the pattern of stiffness can be very heterogeneous (Booth et al., 2012; de Hilster et al., 2020). 2D systems are frequently based on a tissue culture plastic or glass surface, with a stiffness in the gigapascal range, and all cells are grown with polarity. While a lot has been gained from working in 2D systems there is now an opportunity to move forward with our models to establish cells in an environment that reflects the physiological conditions in the lung.

The literature builds a strong body of evidence that the microenvironment in which a cell resides dictates its responses. From simple single ECM component studies (Hirst et al., 2000; Freyer et al., 2001; Bonacci et al., 2003; Parameswaran et al., 2004; Nguyen et al., 2005; Peng et al., 2005; Bonacci et al., 2006; Dekkers et al., 2007; Reddel et al., 2013; Morris et al., 2014), through to more complex cell deposited ECM studies (Johnson et al., 2004; Chan et al., 2006; Harkness et al., 2017), the influence of the ECM components on lung cell proliferation, migration, factor output and response to treatment is evident. However, this information has been collated from cells exposed to ECM components in 2D. It is recognised that cells in a 3D environment have differential responses compared to those in 2D (Duval et al., 2017; Jensen and Teng, 2020). Therefore, developing systems where the influence of the ECM and the microenvironment in 3D can be explored will represent a next step forward for understanding disease underlying mechanisms in the lung.

Hydrogels from synthetic vs. natural materials

When considering the possibilities for generating 3D microenvironments in which lung cells can prosper there are many different options available. Within the tissue engineering field much work has concentrated on the development of polymers from which soft or stiff hydrogels can be cast or 3D printed (Tibbitt and Anseth, 2009; Melchels et al., 2012; Hospodiuk et al., 2017; Gungor-Ozkerim et al., 2018). These synthetic polymers [including polyacrylamide (Marinkovic et al., 2013) and dextran (Matera et al., 2020)] offer many opportunities for tuning biomechanical and structural properties of the microenvironment but are generally inhospitable environments for cells, requiring the addition of cell binding epitopes, such as RGD motifs, to enable cellular attachment (Lutolf and Hubbell, 2005; Reddy et al., 2021; Caracena et al., 2022). Alternatively, natural ECM components have also been used to generate single component hydrogels that readily support cell attachment, but are more limited in the possibilities for tuning their biomechanical properties. Examples of such hydrogels include collagen type I, fibrin, gelatin (methacrylate) and hyaluronan (Bourke et al., 2011; Tjin et al., 2017; Sun et al., 2020; Martinez-Garcia et al., 2021b; Hui et al., 2021; Blokland et al., 2022; Loebel et al., 2022; Martinez-Garcia et al., 2022). Such hydrogels provide the 3D environment for cells, modelling the dimensionality and possibly the biomechanical mimicry of the *in vivo* situation, but they are not reflective of the complexity of the ECM components within the tissue microenvironment. Hydrogels developed from the solubilized basement membrane matrix secreted by Engelbreth-Holm-Swarm (EHS) mouse sarcoma cells (marketed as Matrigel or Geltrex) have been used for more than 35 years to support cell growth for specific assays, particularly focussing on stem cell expansion assays (Kleinman et al., 1982; Kleinman and Martin, 2005; Benton et al., 2009; Hughes et al., 2010). However, not all cells thrive in such an environment and there are limited possibilities to manipulate the composition and biomechanical environment herein.

A recent advance for the lung field has been the development of hydrogels generated from ECM derived from decellularized lungs. Porcine lung ECM-derived hydrogels were initially reported (Pouliot et al., 2016), while human lung ECM-derived hydrogels have recently been established (de Hilster et al., 2020). This perspective article presents the latest advances in lung ECM-derived hydrogels with respect to their development, modification, characterization and utilization. Moreover, it explores opportunities and challenges for the field, highlighting where future research should focus to improve the comparability of data generated with different measurement systems using lung ECM-derived hydrogels. Finally, we discuss the multi-disciplinary nature of the research required to move these model systems forward.

2 The possibilities with lung ECM-derived hydrogels

2.1 Lung ECM-derived hydrogels for mimicking *in vivo* ECM biochemical composition

The ECM, including in the lung, is a complex structure of proteins, glycoproteins, matricellular proteins and many other regulatory proteins and enzymes that keep this dynamic structure in balance during tissue homeostasis (Hynes and Naba, 2012). Mimicking such a complex structure when generating an *in vitro* 3D environment in which to culture cells to study cell:matrix interactions is impossible when starting with individual

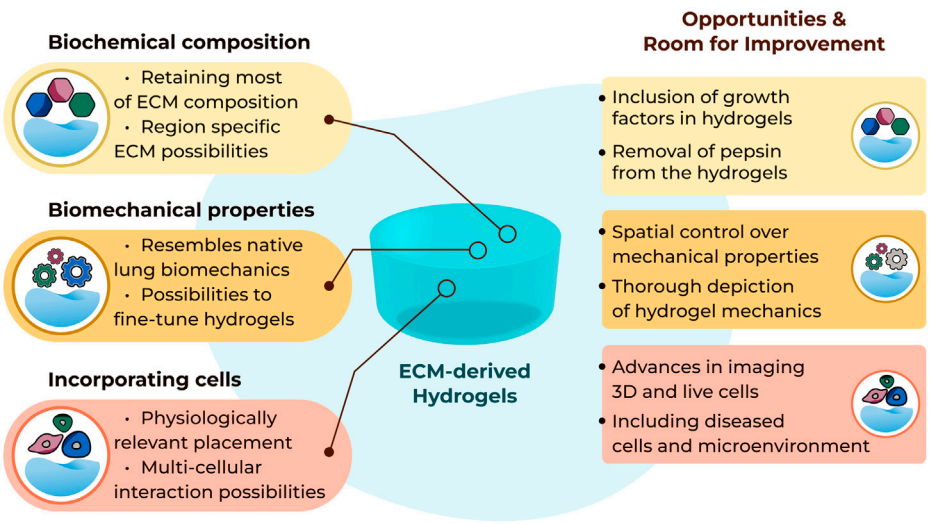

FIGURE 1
Summary of current possibilities and future opportunities with three-dimensional lung ECM-derived hydrogels.

components. Sourcing the ECM from decellularized lungs has provided an opportunity to develop hydrogels that reflect a major proportion of the elements within this complex mixture. The process of decellularization requires treating the tissue with a range of detergents and/or salt solutions (Booth et al., 2012; Wagner et al., 2014; Dabaghi et al., 2021) that do remove some of the elements that are part of the matrisome, particularly growth factors bound to the ECM and some glycoproteins, but the major structural fibres are retained during this process.

Early proteomic studies (Booth et al., 2012; Uhl et al., 2018) illustrated the retention of many components of the lung matrisome in decellularised scaffolds from control and diseased lung samples. A recent study from the team in the Weiss lab (Hoffman et al., 2023), has elegantly shown that the components of the ECM are specific for different compartments within the lung (airways, alveolus, blood vessels), and that these change during chronic lung disease. These decellularized scaffolds from lung tissues have now been used as a source of ECM for the generation of hydrogels. The processing of the scaffolds to generate the solution that will gel when brought to physiological conditions is not thought to lead to further loss of ECM components, making this an ideal method for developing a 3D *in vitro* model system in which cells can be cultured in the presence of this complex mixture of the lung ECM microenvironment.

It remains to be seen if the absence of the elements of the matrisome that are lost during the decellularisation process impose a limitation in the interpretation of data generated when cells are seeded in such hydrogels (Figure 1). The absence of growth factors anchored in the ECM scaffolds, and therefore the ECM-derived hydrogels, after the decellularization process may be considered a limitation, although it is evident that the growth factor retentive properties of the ECM are retained as growth factors supplied in growth media or as part of the secretome from other cells are rapidly absorbed and then subsequently released from the ECM hydrogels (van Dongen et al., 2019). In addition, ECM-derived hydrogels are a source of extracellular vesicles (Ulldemolins et al., 2022), adding another aspect to the regulatory processes induced by these cell support structures.

2.2 Lung ECM-derived hydrogels for mimicking tissue biomechanical environments

The structural environment provided for cells by lung ECM-derived hydrogels is another advantage when aiming to develop *in vivo* mimicking model systems. Although the adoption of the method for generating lung ECM-derived hydrogels was only recently reported (Pouliot et al., 2016; de Hilster et al., 2020), the field is advancing rapidly with innovative approaches exploring how different properties can be measured and modified. Among these properties, mechanical properties and topography are two important characteristics of the hydrogels.

When considering mechanical properties of the hydrogels stiffness, Young's modulus, viscosity or viscoelastic stress relaxation are the usual parameters measured (Vedadghavami et al., 2017). To date, a number of different strategies for measuring mechanical properties of lung ECM-derived hydrogels have been described, although it is important to highlight the challenge when it comes to comparing different studies performed using different measurement approaches for the mechanical properties (Polio et al., 2018). **Rheometry** is one of the most commonly applied methods for measuring mechanical properties of hydrogels (Stojkov et al., 2021). So far, characterization using rheometry has been applied to measure storage (G') and loss (G") moduli of porcine (Pouliot et al., 2016) and human lung ECM-derived hydrogels (Dabaghi et al., 2021). In addition, viscosity and Young's modulus of porcine-sourced lung hydrogels were reported using parallel

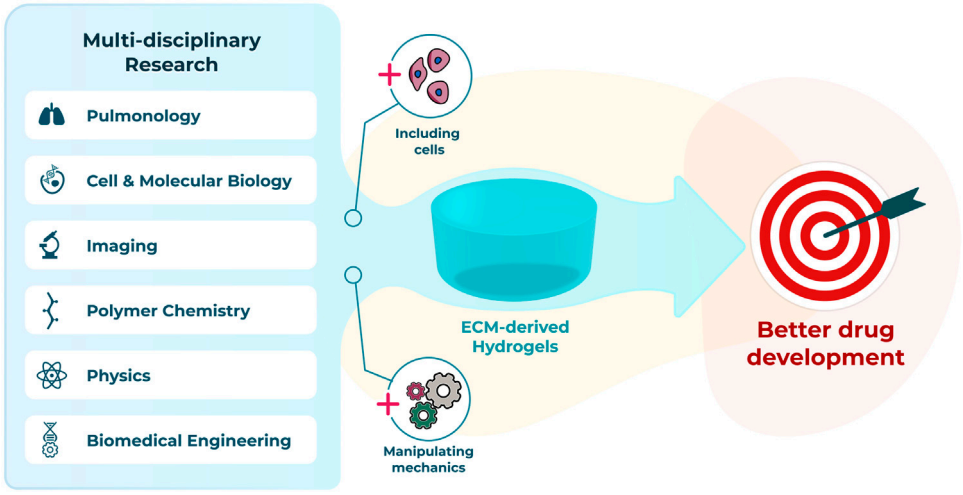

FIGURE 2
Interdisciplinary advances to progress towards a better preclinical model using hydrogels.

plate rheometry (Falcones et al., 2021). Other studies have utilized this method on alginate-porcine ECM (De Santis et al., 2021), poly(ethylene glycol) (PEG)-murine ECM (Saleh et al., 2022), and PEG-porcine ECM (Petrou et al., 2020) hybrid hydrogels. **Low-Load compression testing (LLCT)** is another compression-based method (Sharma et al., 2011) that has been used with lung ECM-derived hydrogels. Stiffness and viscoelastic stress relaxation capacity of human non-disease control, chronic obstructive pulmonary disease (COPD) and idiopathic pulmonary fibrosis (IPF) lung ECM-derived hydrogels have been reported; moreover, the mechanical properties of the hydrogels derived from these diseased lungs resembled such properties of the native tissues from which the ECMs were sourced (de Hilster et al., 2020). Similarly, LLCT-measured stiffness and stress relaxation parameters of both native and chemically crosslinked porcine lung ECM-derived hydrogels were also reported (Martinez-Garcia et al., 2021a; Nizamoglu et al., 2022a). Lastly, **atomic force microscopy (AFM)**, which is a more micro-level mechanical measurement based on indentation, was recently used to characterize Young's modulus values of porcine lung ECM hydrogels (Falcones et al., 2021).

Measuring the mechanical properties is not only useful for diseased environment characterization, but also for verification of the success of methodologies designed to alter such properties. While it is clear that the use of different concentrations of the starting ECM material (powder) (Pouliot et al., 2016) and adjusting the pepsin digestion duration (the essential step in generation of a pre-gel ECM-derived substrate) (Pouliot et al., 2020) influences the mechanical properties, one of the initial attempts to specifically modulate the mechanical properties of lung ECM-derived hydrogels was treating the porcine lung ECM with genipin to increase the stiffness (Link et al., 2017). This approach has been extended with thiol-functionalization (Petrou et al., 2020; Saleh et al., 2022), alginate-reinforcing (De Santis et al., 2021) or fibre crosslinking (Nizamoglu et al., 2022a) to allow greater control over mechanical parameters in the lung ECM-derived hydrogels.

The concepts of altering the mechanical properties, measuring and reporting these changes triggered in the lung ECM-derived hydrogels have been evolving as more novel tools are developed (Figure 1). However, mechanical characterization of lung ECM-derived hydrogels is far from completed. As of today, tensile testing or fatigue testing on such hydrogels have yet to be performed, although using polyacrylamide-ECM hybrid hydrogels these properties were characterized in an early study (Sava et al., 2017). A thorough mechanical and cross-platform characterization of lung ECM-derived hydrogels has not been reported yet. Providing (the comparison of) such characterizations would help the field regarding the interpretation and comparison of different studies using different methods to measure similar parameters. As the field is new, establishing different methods and discussing their advantages and limitations will be important for being able to understand the emerging knowledge about ECM mechanical properties and the functional impacts of these microenvironment parameters.

Another important property which goes hand-in-hand with mechanics is topography, reflecting the fibrous landscape within the ECM-derived hydrogels. In chronic lung diseases like COPD or lung fibrosis, the ECM topography is altered next to the mechanical properties of ECM (Abraham and Hogg, 2010; Tjin et al., 2014; Tjin et al., 2017; Burgess and Harmsen, 2022; Nizamoglu and Burgess, 2022). Using lung ECM sourced from diseased human lungs, for the generation of the hydrogels, would inherently convey (most of) the biochemical composition and resemble the mechanical properties; however, the native architecture of the lung ECM assembly is lost during the process of preparing ECM-derived hydrogels. Recently, preparing porcine lung ECM hydrogels with micropatterned surfaces was described as a method to prepare arrays for drug screening (Zhu et al., 2022). This study demonstrates the

preparation of spherical patterns on the hydrogel surface with different diameters, although the aspects of altering the hydrogel surface to guide cell fate, behaviour or differentiation remain unexplored. Alternatively, electrospinning could provide another opportunity to alter the structural organization of the fibres (Hasirci and Hasirci, 2018). While electrospun poly(L-lactic acid) (PLLA)/porcine lung ECM hybrid scaffolds have been previously established (Young et al., 2017), there is no report of electrospinning of pure decellularized lung ECM. Developing novel tools to modify the topography of the ECM fibres within the hydrogels and the regulation of the structural arrangements within these hydrogels requires more attention. Surface modifications on non-ECM-derived hydrogels is not a novel concept (Richbourg et al., 2019; Cai et al., 2020), yet little is known about applying such modifications to the locations within the hydrogels in different planes in order to mimic the architecture of the native lung tissue.

The details of measuring, reporting and altering the properties of lung ECM-derived hydrogels gain more importance as the field progresses. Unfortunately to date, attempts at modifying properties of lung ECM-derived hydrogels remain rather limited. While the latest studies have focused on altering mechanical properties at a global level, new and innovative methodologies that will allow us to initiate more targeted modifications in such properties are required. Especially considering the heterogeneity of lung tissue and its architecture, having more control over spatial distribution of alterations in mechanical properties would enhance the *in vivo* mimicking capacity of our models.

2.3 Lung ECM-derived hydrogels for mimicking cell:matrix interactions

The *in vivo* mimicry of the composition and mechanics of the cellular microenvironment present in the lung ECM-derived hydrogels creates an ideal setting for culturing cells within a 3D spatial location. As soon as cells are seeded in hydrogels they begin to remodel their microenvironment (Tjin et al., 2017; Martinez-Garcia et al., 2021b; Martinez-Garcia et al., 2022). Early reports of cells in lung ECM-derived hydrogels reflect findings in single component ECM hydrogels (Tjin et al., 2017), indicating that cells remodel the ECM in which they are embedded, and the nature of the ECM that they encounter directs these remodelling events (Nizamoglu et al., 2022b; Falcones et al., 2022). This fact makes the use of lung ECM-derived hydrogels sourced from diseased lungs an ideal model to understand cellular responses within such a diseased microenvironment and to provide greater knowledge of the influence of the microenvironment to treatment effects.

Initial studies using porcine lung ECM-derived hydrogels reported successful growth of human and rat mesenchymal stromal (stem) cells (MSCs) in 2016 (Pouliot et al., 2016). Link et al. (2017) then described successful culture of mouse MSCs, human alveolar epithelial cells (the cell line A549), human primary microvascular endothelial cells (HpuVECs), and human umbilical vein endothelial cells (HUVECs) in porcine lung ECM-derived hydrogels. The field is now rapidly expanding with additional cells types including murine fibroblasts (Petrou et al., 2020), rat lung MSCs (Falcones et al., 2021) and rat primary alveolar epithelial cells (Marhuenda et al., 2022b) being grown in porcine lung ECM-derived hydrogels. The use of human lung ECM-derived hydrogels is now also possible, with human fibroblasts and airway smooth muscle cells being grown both within and on top of these hydrogels (De Santis et al., 2021; Nizamoglu et al., 2022a; Nizamoglu et al., 2022b).

The field is now moving forward with the cellular systems that are being explored, taking advantage of the values of lung ECM-derived hydrogels. Multi-cellular culture systems are being developed to enable cellular cross-talk in a 3D microenvironment to be examined (Park et al., 2018), and lung ECM-derived hydrogels are being incorporated into other experimental systems (for example, lung on chip or stretching/mechanical force setups) to bring the cell microenvironment in those systems also (Park et al., 2021; Marhuenda et al., 2022a). The possibilities for 3D printing lung ECM-derived hydrogels are also being examined, suggesting greater scope for spatial arrangement of cells within their 3D microenvironment will be possible in the future (De Santis et al., 2021; Falcones et al., 2021).

While the 3D model systems made possible with the use of lung ECM-derived hydrogels are rapidly advancing, the readouts that can be used to investigate end points within these systems are presenting some limitations (Figure 1). Traditional imaging setups are excellent for capturing images in 2D but moving into the third dimension proves challenging to visualise. Lung ECM-derived hydrogels are not translucent, like many of the single ECM or synthetic hydrogels, and this opacity challenges the optical depth of field. The autofluorescence of the lung ECM generates a very noisy image when using many traditional fluorescent reporters. Finally, tracking cell behaviours over time in 3D is extremely difficult to automate when the cells continuously move out of the plane of focus. Advances in imaging and capturing information from cells when they are interacting within their microenvironment is urgently needed to facilitate the full capacity of lung ECM-derived hydrogels.

3 Discussion and future remarks

Studies in lung ECM-derived hydrogels will help to inform us of the optimal microenvironment for different cell types, as the cells continuously remodel their environment in, what appears to be, a programmed response. Whether there is temporal regulation of the remodelling, in particular in response to injury, is an outstanding question for the field. How these processes are altered in chronic lung diseases, and whether the progression of such processes can be reversed is knowledge that can be informed through the use of lung ECM-derived hydrogels. The approaches described above, including modulating mechanical properties of ECM-derived hydrogels without changing the ECM composition and the application of mechanical forces to cells within a 3D microenvironment, are attractive as they will facilitate research enabling the field to begin separating influences of the mechanical changes from those of the biochemical changes in the ECM in lung diseases. Such

elucidation may open the door for development of mechanosensitive therapeutic targets for lung diseases.

To fully leverage the advantages offered by lung ECM-derived hydrogels multi-disciplinary teams who bring together expertise from the diverse fields needed to advance such systems will be necessary (Figure 2). Innovative researchers from pulmonology, cell and molecular biology, polymer chemistry, biomedical engineering, imaging and physics backgrounds are all needed to maximise opportunities and ensure the current challenges quickly become advantages for this exciting, emerging area of lung disease research.

Data availability statement

The original contributions presented in the study are included in the article/Supplementary Material, further inquiries can be directed to the corresponding author.

Author contributions

MN and JKB conceptualized, drafted and edited the manuscript. MN prepared the figures. Both authors read and approved the submitted version.

Funding

MN and JKB receive unrestricted research funds from Boehringer Ingelheim. JKB also acknowledges support from the NWO (Aspasia 015.013.010).

Acknowledgments

Authors thank Albano Tosato for the assistance with figure preparation.

Conflict of interest

MN and JKB receive unrestricted research funds from Boehringer Ingelheim.

Publisher's note

References

Abraham, T., and Hogg, J. (2010). Extracellular matrix remodeling of lung alveolar walls in three dimensional space identified using second harmonic generation and multiphoton excitation fluorescence. *J. Struct. Biol.* 171 (2), 189–196. doi:10.1016/j.jsb.2010.04.006

Benton, G., George, J., Kleinman, H. K., and Arnaoutova, I. P. (2009). Advancing science and technology via 3D culture on basement membrane matrix. *J. Cell Physiol.* 221 (1), 18–25. doi:10.1002/jcp.21832

Blokland, K. E. C., Nizamoglu, M., Habibie, H., Borghuis, T., Schuliga, M., Melgert, B. N., et al. (2022). Substrate stiffness engineered to replicate disease conditions influence senescence and fibrotic responses in primary lung fibroblasts. *Front. Pharmacol.* 13, 989169. doi:10.3389/fphar.2022.989169

Bonacci, J. V., Harris, T., and Stewart, A. G. (2003). Impact of extracellular matrix and strain on proliferation of bovine airway smooth muscle. *Clin. Exp. Pharmacol. Physiol.* 30 (5-6), 324–328. doi:10.1046/j.1440-1681.2003.03838.x

Bonacci, J. V., Schuliga, M., Harris, T., and Stewart, A. G. (2006). Collagen impairs glucocorticoid actions in airway smooth muscle through integrin signalling. *Br. J. Pharmacol.* 149 (4), 365–373. doi:10.1038/sj.bjp.0706881

Booth, A. J., Hadley, R., Cornett, A. M., Dreffs, A. A., Matthes, S. A., Tsui, J. L., et al. (2012). Acellular normal and fibrotic human lung matrices as a culture system for *in vitro* investigation. *Am. J. Respir. Crit. Care Med.* 186 (9), 866–876. doi:10.1164/rccm.201204-0754OC

Bourke, J. E., Li, X., Foster, S. R., Wee, E., Dagher, H., Ziogas, J., et al. (2011). Collagen remodelling by airway smooth muscle is resistant to steroids and β_2-agonists. *Eur. Respir. J.* 37 (1), 173–182. doi:10.1183/09031936.00008109

Burgess, J. K., and Harmsen, M. C. (2022). Chronic lung diseases: Entangled in extracellular matrix. *Eur. Respir. Rev.* 31 (163), 210202. doi:10.1183/16000617.0202-2021

Cai, S. X., Wu, C. X., Yang, W. G., Liang, W. F., Yu, H. B., and Liu, L. Q. (2020). Recent advance in surface modification for regulating cell adhesion and behaviors. *Nanotechnol. Rev.* 9 (1), 971–989. doi:10.1515/ntrev-2020-0076

Caracena, T., Blomberg, R., Hewawasam, R. S., Fry, Z. E., Riches, D. W. H., and Magin, C. M. (2022). Alveolar epithelial cells and microenvironmental stiffness synergistically drive fibroblast activation in three-dimensional hydrogel lung models. *Biomater. Sci.* 10 (24), 7133–7148. doi:10.1039/d2bm00827k

Chan, V., Burgess, J. K., Ratoff, J. C., O'Connor, B. J., Greenough, A., Lee, T. H., et al. (2006). Extracellular matrix regulates enhanced eotaxin expression in asthmatic airway smooth muscle cells. *Am. J. Respir. Crit. Care Med.* 174 (4), 379–385. doi:10.1164/rccm.200509-1420OC

Dabaghi, M., Saraei, N., Carpio, M. B., Nanduri, V., Ungureanu, J., Babi, M., et al. (2021). A robust protocol for decellularized human lung bioink generation amenable to 2D and 3D lung cell culture. *Cells* 10 (6), 1538. doi:10.3390/cells10061538

de Hilster, R. H. J., Sharma, P. K., Jonker, M. R., White, E. S., Gercama, E. A., Roobeek, M., et al. (2020). Human lung extracellular matrix hydrogels resemble the stiffness and viscoelasticity of native lung tissue. *Am. J. Physiol. Lung Cell Mol. Physiol.* 318 (4), L698–L704. doi:10.1152/ajplung.00451.2019

De Santis, M. M., Alsafadi, H. N., Tas, S., Bolukbas, D. A., Prithiviraj, S., Da Silva, I. A. N., et al. (2021). Extracellular-matrix-reinforced bioinks for 3D bioprinting human tissue. *Adv. Mater.* 33 (3), e2005476. doi:10.1002/adma.202005476

Dekkers, B. G., Schaafsma, D., Nelemans, S. A., Zaagsma, J., and Meurs, H. (2007). Extracellular matrix proteins differentially regulate airway smooth muscle phenotype and function. *Am. J. Physiol. Lung Cell Mol. Physiol.* 292 (6), L1405–L1413. doi:10.1152/ajplung.00331.2006

Duval, K., Grover, H., Han, L. H., Mou, Y., Pegoraro, A. F., Fredberg, J., et al. (2017). Modeling physiological events in 2D vs. 3D cell culture. *Physiol. (Bethesda)* 32 (4), 266–277. doi:10.1152/physiol.00036.2016

Falcones, B., Sanz-Fraile, H., Marhuenda, E., Mendizabal, I., Cabrera-Aguilera, I., Malandain, N., et al. (2021). Bioprintable lung extracellular matrix hydrogel scaffolds for 3D culture of mesenchymal stromal cells. *Polymers* 13 (14), 2350. doi:10.3390/polym13142350

Falcones, B., Soderlund, Z., Ibanez-Fonseca, A., Almendros, I., Otero, J., Farre, R., et al. (2022). hLMSC secretome affects macrophage activity differentially depending on lung-mimetic environments. *Cells* 11 (12), 1866. doi:10.3390/cells11121866

Freyer, A. M., Johnson, S. R., and Hall, I. P. (2001). Effects of growth factors and extracellular matrix on survival of human airway smooth muscle cells. *Am. J. Respir. Cell Mol. Biol.* 25 (5), 569–576. doi:10.1165/ajrcmb.25.5.4605

Gungor-Ozkerim, P. S., Inci, I., Zhang, Y. S., Khademhosseini, A., and Dokmeci, M. R. (2018). Bioinks for 3D bioprinting: An overview. *Biomater. Sci.* 6 (5), 915–946. doi:10.1039/c7bm00765e

Harkness, L. M., Weckmann, M., Kopp, M., Becker, T., Ashton, A. W., and Burgess, J. K. (2017). Tumstatin regulates the angiogenic and inflammatory potential of airway smooth muscle extracellular matrix. *J. Cell Mol. Med.* 21, 3288–3297. doi:10.1111/jcmm.13232

Hasirci, V., and Hasirci, N. (2018). "Nano- and microarchitecture of biomaterial surfaces," in *Fundamentals of biomaterials*. Berlin, Germany: Springer New York, 303–329.

Hirst, S. J., Twort, C. H. C., and Lee, T. H. (2000). Differential effects of extracellular matrix proteins on human airway smooth muscle cell proliferation and phenotype. *Am. J. Respir. Cell Mol. Biol.* 23 (3), 335–344. doi:10.1165/ajrcmb.23.3.3990

Hoffman, E. T., Uhl, F. E., Asarian, L., Deng, B., Becker, C., Uriarte, J. J., et al. (2023). Regional and disease specific human lung extracellular matrix composition. *Biomaterials* 293, 121960. doi:10.1016/j.biomaterials.2022.121960

Hospodiuk, M., Dey, M., Sosnoski, D., and Ozbolat, I. T. (2017). The bioink: A comprehensive review on bioprintable materials. *Biotechnol. Adv.* 35 (2), 217–239. doi:10.1016/j.biotechadv.2016.12.006

Hughes, C. S., Postovit, L. M., and Lajoie, G. A. (2010). Matrigel: A complex protein mixture required for optimal growth of cell culture. *Proteomics* 10 (9), 1886–1890. doi:10.1002/pmic.200900758

Hui, E., Moretti, L., Barker, T. H., and Caliari, S. R. (2021). The combined influence of viscoelastic and adhesive cues on fibroblast spreading and focal adhesion organization. *Cell Mol. Bioeng.* 14 (5), 427–440. doi:10.1007/s12195-021-00672-1

Hynes, R. O., and Naba, A. (2012). Overview of the matrisome-an inventory of extracellular matrix constituents and functions. *Cold Spring Harb. Perspect. Biol.* 4 (1), a004903. doi:10.1101/cshperspect.a004903

Jensen, C., and Teng, Y. (2020). Is it time to start transitioning from 2D to 3D cell culture? *Front. Mol. Biosci.* 7, 33. doi:10.3389/fmolb.2020.00033

Johnson, P. R. A., Burgess, J. K., Underwood, P. A., Au, W., Poniris, M. H., Tamm, M., et al. (2004). Extracellular matrix proteins modulate asthmatic airway smooth muscle cell proliferation via an autocrine mechanism. *J. Allergy Clin. Immunol.* 113 (4), 690–696. doi:10.1016/j.jaci.2003.12.312

Kleinman, H. K., and Martin, G. R. (2005). Matrigel: Basement membrane matrix with biological activity. *Semin. Cancer Biol.* 15 (5), 378–386. doi:10.1016/j.semcancer.2005.05.004

Kleinman, H. K., Mcgarvey, M. L., Liotta, L. A., Robey, P. G., Tryggvason, K., and Martin, G. R. (1982). Isolation and characterization of type-iv procollagen, laminin, and heparan-sulfate proteoglycan from the ehs sarcoma. *Biochemistry* 21 (24), 6188–6193. doi:10.1021/bi00267a025

Link, P. A., Pouliot, R. A., Mikhaiel, N. S., Young, B. M., and Heise, R. L. (2017). Tunable hydrogels from pulmonary extracellular matrix for 3D cell culture. *J. Vis. Exp.* 119, 55094. doi:10.3791/55094

Loebel, C., Weiner, A. I., Eiken, M. K., Katzen, J. B., Morley, M. P., Bala, V., et al. (2022). Microstructured hydrogels to guide self-assembly and function of lung alveolospheres. *Adv. Mater.* 34 (28), e2202992. doi:10.1002/adma.202202992

Lutolf, M. P., and Hubbell, J. A. (2005). Synthetic biomaterials as instructive extracellular microenvironments for morphogenesis in tissue engineering. *Nat. Biotechnol.* 23 (1), 47–55. doi:10.1038/nbt1055

Marhuenda, E., Villarino, A., Narciso, M., Elowsson, L., Almendros, I., Westergren-Thorsson, G., et al. (2022a). Development of a physiomimetic model of acute respiratory distress syndrome by using ECM hydrogels and organ-on-a-chip devices. *Front. Pharmacol.* 13, 945134. doi:10.3389/fphar.2022.945134

Marhuenda, E., Villarino, A., Narciso, M. L., Camprubi-Rimblas, M., Farre, R., Gavara, N., et al. (2022b). Lung extracellular matrix hydrogels enhance preservation of type II phenotype in primary alveolar epithelial cells. *Int. J. Mol. Sci.* 23 (9), 4888. doi:10.3390/ijms23094888

Marinkovic, A., Liu, F., and Tschumperlin, D. J. (2013). Matrices of physiologic stiffness potently inactivate idiopathic pulmonary fibrosis fibroblasts. *Am. J. Respir. Cell Mol. Biol.* 48 (4), 422–430. doi:10.1165/rcmb.2012-0335OC

Martinez-Garcia, F. D., de Hilster, R. H. J., Sharma, P. K., Borghuis, T., Hylkema, M. N., Burgess, J. K., et al. (2021a). Architecture and composition dictate viscoelastic properties of organ-derived extracellular matrix hydrogels. *Polymers* 13 (18), 3113. doi:10.3390/polym13183113

Martinez-Garcia, F. D., Valk, M. M., Sharma, P. K., Burgess, J. K., and Harmsen, M. C. (2021b). Adipose tissue-derived stromal cells alter the mechanical stability and viscoelastic properties of gelatine methacryloyl hydrogels. *Int. J. Mol. Sci.* 22 (18), 10153. doi:10.3390/ijms221810153

Martinez-Garcia, F. D., van Dongen, J. A., Burgess, J. K., and Harmsen, M. C. (2022). Matrix metalloproteases from adipose tissue-derived stromal cells are spatiotemporally regulated by hydrogel mechanics in a 3D microenvironment. *Bioeng. (Basel)* 9 (8), 340. doi:10.3390/bioengineering9080340

Matera, D. L., DiLillo, K. M., Smith, M. R., Davidson, C. D., Parikh, R., Said, M., et al. (2020). Microengineered 3D pulmonary interstitial mimetics highlight a critical role for matrix degradation in myofibroblast differentiation. *Sci. Adv.* 6 (37), eabb5069. doi:10.1126/sciadv.abb5069

Melchels, F. P. W., Domingos, M. A. N., Klein, T. J., Malda, J., Bartolo, P. J., and Hutmacher, D. W. (2012). Additive manufacturing of tissues and organs. *Prog. Polym. Sci.* 37 (8), 1079–1104. doi:10.1016/j.progpolymsci.2011.11.007

Morris, G. E., Bridge, J. C., Eltboli, O. M., Lewis, M. P., Knox, A. J., Aylott, J. W., et al. (2014). Human airway smooth muscle maintain *in situ* cell orientation and phenotype when cultured on aligned electrospun scaffolds. *Am. J. Physiol. Lung Cell Mol. Physiol.* 307 (1), L38–L47. doi:10.1152/ajplung.00318.2013

Nguyen, T. T., Ward, J. P., and Hirst, S. J. (2005). beta1-Integrins mediate enhancement of airway smooth muscle proliferation by collagen and fibronectin. *Am. J. Respir. Crit. Care Med.* 171 (3), 217–223. doi:10.1164/rccm.200408-1046OC

Nizamoglu, M., and Burgess, J. K. (2022). The multi-faceted extracellular matrix: Unlocking its secrets for understanding the perpetuation of lung fibrosis. *Curr. Tissue Microenviron. Rep.* 2 (4), 53–71. doi:10.1007/s43152-021-00031-2

Nizamoglu, M., de Hilster, R. H. J., Zhao, F., Sharma, P. K., Borghuis, T., Harmsen, M. C., et al. (2022a). An *in vitro* model of fibrosis using crosslinked native extracellular matrix-derived hydrogels to modulate biomechanics without changing composition. *Acta Biomater.* 147, 50–62. doi:10.1016/j.actbio.2022.05.031

Nizamoglu, M., Koster, T., Thomas, M. J., Timens, W., Koss, C. K., El Kasmi, K. C., et al. (2022b). "3D fibrotic lung extracellular matrix hydrogels trigger pro-fibrotic responses in primary lung fibroblasts," in *D30 the injured lung: Mechanisms and therapeutic targets* (New York: American Thoracic Society), A5245–A5245. Available at: https://doi.org/10.1164/ajrccm-conference.2022.205.1_MeetingAbstracts.A5245

Parameswaran, K., Radford, K., Zuo, J., Janssen, L. J., O'Byrne, P. M., and Cox, P. G. (2004). Extracellular matrix regulates human airway smooth muscle cell migration. *Eur. Respir. J.* 24 (4), 545–551. doi:10.1183/09031936.04.00113103

Park, J., Wetzel, I., Dreau, D., and Cho, H. (2018). 3D miniaturization of human organs for drug discovery. *Adv. Healthc. Mater.* 7 (2), 1700551. doi:10.1002/adhm.201700551

Park, S., Kim, T. H., Kim, S. H., You, S., and Jung, Y. (2021). Three-dimensional vascularized lung cancer-on-a-chip with lung extracellular matrix hydrogels for *in vitro* screening. *Cancers (Basel)* 13 (16), 3930. doi:10.3390/cancers13163930

Peng, Q., Lai, D., Nguyen, T. T., Chan, V., Matsuda, T., and Hirst, S. J. (2005). Multiple beta 1 integrins mediate enhancement of human airway smooth muscle cytokine secretion by fibronectin and type I collagen. *J. Immunol.* 174 (4), 2258–2264. doi:10.4049/jimmunol.174.4.2258

Petrou, C. L., D'Ovidio, T. J., Bolukbas, D. A., Tas, S., Brown, R. D., Allawzi, A., et al. (2020). Clickable decellularized extracellular matrix as a new tool for building hybrid-hydrogels to model chronic fibrotic diseases *in vitro*. *J. Mater Chem. B* 8 (31), 6814–6826. doi:10.1039/d0tb00613k

Polio, S. R., Kundu, A. N., Dougan, C. E., Birch, N. P., Aurian-Blajeni, D. E., Schiffman, J. D., et al. (2018). Cross-platform mechanical characterization of lung tissue. *PLoS One* 13 (10), e0204765. doi:10.1371/journal.pone.0204765

Pouliot, R. A., Link, P. A., Mikhaiel, N. S., Schneck, M. B., Valentine, M. S., Kamga Gninzeko, F. J., et al. (2016). Development and characterization of a naturally derived lung extracellular matrix hydrogel. *J. Biomed. Mater. Res. A* 104 (8), 1922–1935. doi:10.1002/jbm.a.35726

Pouliot, R. A., Young, B. M., Link, P. A., Park, H. E., Kahn, A. R., Shankar, K., et al. (2020). Porcine lung-derived extracellular matrix hydrogel properties are dependent on pepsin digestion time. *Tissue Eng. Part C Methods* 26 (6), 332–346. doi:10.1089/ten.TEC.2020.0042

Reddel, C. J., Cultrone, D., Rnjak-Kovacina, J., Weiss, A. S., and Burgess, J. K. (2013). Tropoelastin modulates TGF-β1-induced expression of VEGF and CTGF in airway smooth muscle cells. *Matrix Biol.* 32 (7-8), 407–413. doi:10.1016/j.matbio.2013.04.003

Reddy, M. S. B., Ponnamma, D., Choudhary, R., and Sadasivuni, K. K. (2021). A comparative review of natural and synthetic biopolymer composite scaffolds. *Polymers* 13 (7), 1105. doi:10.3390/polym13071105

Richbourg, N. R., Peppas, N. A., and Sikavitsas, V. I. (2019). Tuning the biomimetic behavior of scaffolds for regenerative medicine through surface modifications. *J. Tissue Eng. Regen. Med.* 13 (8), 1275–1293. doi:10.1002/term.2859

Saleh, K. S., Hewawasam, R., Serbed, P., Blomberg, R., Noreldeen, S. E., Edelman, B., et al. (2022). Engineering hybrid-hydrogels comprised of healthy or diseased decellularized extracellular matrix to study pulmonary fibrosis. *Cell. Mol. Bioeng.* 15 (5), 505–519. doi:10.1007/s12195-022-00726-y

Sava, P., Ramanathan, A., Dobronyi, A., Peng, X., Sun, H., Ledesma-Mendoza, A., et al. (2017). Human pericytes adopt myofibroblast properties in the microenvironment of the IPF lung. *JCI Insight* 2 (24), e96352. doi:10.1172/jci.insight.96352

Sharma, P. K., Busscher, H. J., Terwee, T., Koopmans, S. A., and van Kooten, T. G. (2011). A comparative study on the viscoelastic properties of human and animal lenses. *Exp. Eye Res.* 93 (5), 681–688. doi:10.1016/j.exer.2011.08.009

Stojkov, G., Niyazov, Z., Picchioni, F., and Bose, R. K. (2021). Relationship between structure and rheology of hydrogels for various applications. *Gels* 7 (4), 255. doi:10.3390/gels7040255

Sun, Y. J., Hsu, C. H., Ling, T. Y., Liu, L., Lin, T. C., Jakfar, S., et al. (2020). The preparation of cell-containing microbubble scaffolds to mimic alveoli structure as a 3D drug-screening system for lung cancer. *Biofabrication* 12 (2), 025031. doi:10.1088/1758-5090/ab78ee

Tibbitt, M. W., and Anseth, K. S. (2009). Hydrogels as extracellular matrix mimics for 3D cell culture. *Biotechnol. Bioeng.* 103 (4), 655–663. doi:10.1002/bit.22361

Tjin, G., White, E. S., Faiz, A., Sicard, D., Tschumperlin, D. J., Mahar, A., et al. (2017). Lysyl oxidases regulate fibrillar collagen remodelling in idiopathic pulmonary fibrosis. *Dis. Models Mech.* 10 (11), 1301–1312. doi:10.1242/dmm.030114

Tjin, G., Xu, P., Kable, S. H., Kable, E. P., and Burgess, J. K. (2014). Quantification of collagen I in airway tissues using second harmonic generation. *J. Biomed. Opt.* 19 (3), 36005. doi:10.1117/1.JBO.19.3.036005

Uhl, F., Zvarova, B., Ahlers, B., Hood, C., Deng, B., Lam, Y., et al. (2018). Characterization of decellularized COPD lung matrices using mass spectrometry proteomics. *Eur. Respir. J.* 52 (62), LSC–1085. doi:10.1183/13993003.congress-2018.LSC-1085

Ulldemolins, A., Jurado, A., Herranz-Diez, C., Gavara, N., Otero, J., Farre, R., et al. (2022). Lung extracellular matrix hydrogels-derived vesicles contribute to epithelial lung repair. *Polymers* 14 (22), 4907. doi:10.3390/polym14224907

van Dongen, J. A., Getova, V., Brouwer, L. A., Liguori, G. R., Sharma, P. K., Stevens, H. P., et al. (2019). Adipose tissue-derived extracellular matrix hydrogels as a release platform for secreted paracrine factors. *J. Tissue Eng. Regen. Med.* 13 (6), 973–985. doi:10.1002/term.2843

Vedadghavami, A., Minooei, F., Mohammadi, M. H., Khetani, S., Kolahchi, A. R., Mashayekhan, S., et al. (2017). Manufacturing of hydrogel biomaterials with controlled mechanical properties for tissue engineering applications. *Acta Biomater.* 62, 42–63. doi:10.1016/j.actbio.2017.07.028

Wagner, D. E., Bonenfant, N. R., Parsons, C. S., Sokocevic, D., Brooks, E. M., Borg, Z. D., et al. (2014). Comparative decellularization and recellularization of normal versus emphysematous human lungs. *Biomaterials* 35 (10), 3281–3297. doi:10.1016/j.biomaterials.2013.12.103

Young, B. M., Shankar, K., Allen, B. P., Pouliot, R. A., Schneck, M. B., Mikhaiel, N. S., et al. (2017). Electrospun decellularized lung matrix scaffold for airway smooth muscle culture. *Acs Biomaterials Sci. Eng.* 3 (12), 3480–3492. doi:10.1021/acsbiomaterials.7b00384

Zhu, X., Li, Y., Yang, Y., He, Y., Gao, M., Peng, W., et al. (2022). Ordered micropattern arrays fabricated by lung-derived dECM hydrogels for chemotherapeutic drug screening. *Mater. Today Bio* 15, 100274. doi:10.1016/j.mtbio.2022.100274

frontiers | Frontiers in Pharmacology

TYPE Review
PUBLISHED 16 May 2023
DOI 10.3389/fphar.2023.1162889

OPEN ACCESS

EDITED BY
Didier Cataldo,
University of Liège, Belgium

REVIEWED BY
Ramaswamy Krishnan,
Beth Israel Deaconess Medical Center and Harvard Medical School, United States
Charlotte H. Dean,
Imperial College London, United Kingdom
Katherina Sewald,
Fraunhofer Institute for Toxicology and Experimental Medicine (FHG), Germany
Christian Martin,
University Hospital RWTH Aachen, Germany

*CORRESPONDENCE
Jane E. Bourke,
jane.bourke@monash.edu

RECEIVED 10 February 2023
ACCEPTED 19 April 2023
PUBLISHED 16 May 2023

CITATION
Lam M, Lamanna E, Organ L, Donovan C and Bourke JE (2023), Perspectives on precision cut lung slices—powerful tools for investigation of mechanisms and therapeutic targets in lung diseases. *Front. Pharmacol.* 14:1162889. doi: 10.3389/fphar.2023.1162889

Perspectives on precision cut lung slices—powerful tools for investigation of mechanisms and therapeutic targets in lung diseases

Maggie Lam[1,2,3], Emma Lamanna[1,4], Louise Organ[1], Chantal Donovan[5,6] and Jane E. Bourke[1,2]*

[1]Department of Pharmacology, Biomedicine Discovery Institute, Monash University, Clayton, VIC, Australia, [2]Centre for Innate Immunity and Infectious Diseases, Hudson Institute of Medical Research, Clayton, VIC, Australia, [3]Department of Molecular and Translational Sciences, Monash University, Clayton, VIC, Australia, [4]Institut Pasteur, Unit of Antibodies in Therapy and Pathology, INSERM UMR1222, Paris, France, [5]School of Life Sciences, Faculty of Science, University of Technology Sydney, Sydney, NSW, Australia, [6]Hunter Medical Research Institute and The University of Newcastle, Newcastle, NSW, Australia

Precision cut lung slices (PCLS) have emerged as powerful experimental tools for respiratory research. Pioneering studies using mouse PCLS to visualize intrapulmonary airway contractility have been extended to pulmonary arteries and for assessment of novel bronchodilators and vasodilators as therapeutics. Additional disease-relevant outcomes, including inflammatory, fibrotic, and regenerative responses, are now routinely measured in PCLS from multiple species, including humans. This review provides an overview of established and innovative uses of PCLS as an intermediary between cellular and organ-based studies and focuses on opportunities to increase their application to investigate mechanisms and therapeutic targets to oppose excessive airway contraction and fibrosis in lung diseases.

KEYWORDS

PCLS, airway, intrapulmonary artery, bronchodilator, vasodilator, fibrosis, standardisation

1 Introduction

Organotypic tissue slices from the lung have been extensively used for metabolic studies and toxicology assays (Freeman and O'Neil, 1984; Fisher et al., 1994; Yilmaz et al., 2019). However, the development of the precision cut lung slice (PCLS) technique, with improved methods for maintaining viability and function in prolonged culture, has resulted in numerous applications beyond these simple global measures of tissue activity and damage.

PCLS are a living tissue preparation, containing all resident cells, including smooth muscle cells, epithelial cells, and fibroblasts. These cells maintain their intercellular interactions and cell-to-matrix relationships within the complex structures of the lung. Pioneering work with PCLS involved the assessment of airway and artery contractility or ciliary activity *in situ* by research groups led by Martin (Martin et al., 1996) and Sanderson (Perez and Sanderson, 2005a; Perez and Sanderson, 2005b; Delmotte and Sanderson, 2006). Recent single-cell sequencing analyses have also confirmed the preservation of innate and adaptive immune cells in PCLS (Winters et al., 2021).

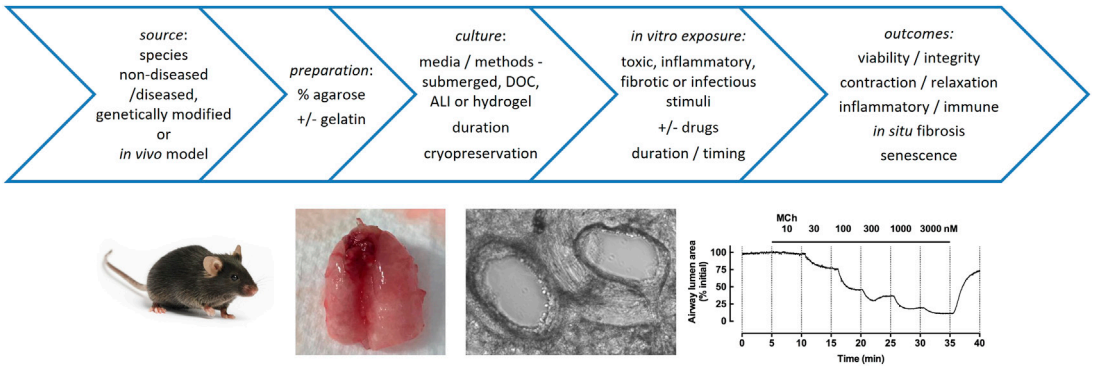

FIGURE 1
Factors in the preparation, culture and applications of PCLS. Top: Multiple precision cut lung slices can be prepared from non-diseased or diseased agarose-inflated whole lungs, lobes or resections from different species, and cultured under various disease-relevant conditions to test the effects of drugs on acute and chronic tissue responses, extending from airway reactivity to cytokine release to immune responses to infection to deposition of extracellular matrix. Bottom: PCLS have been widely used for assessment of airway contraction. Mouse lungs are shown after inflation of airways with agarose via the trachea and infusion of the pulmonary circulation with gelatin via the right ventricle; phase-contrast image of mouse PCLS shows patent adjacent airway and artery (~250 µm diameter); trace shows reversible airway contraction to methacholine (MCh) in mouse PCLS, with MCh administered at increasing concentrations at 5 min intervals, and contraction reaching near complete closure of the airway lumen (based on quantitation of images captured every 2 s, normalized to initial area).

PCLS are now widely used to measure integrated cellular responses initiated by inflammatory, fibrotic or infectious stimuli, and for studies of lung damage and regeneration. Importantly, multiple PCLS can be obtained from patient biobanks well as from animal models with established chronic disease, providing for higher throughout and improved translation potential, while minimizing the ethical implications of animal use for *in vivo* studies. Ongoing optimization of long-term culture and preservation methods and the emerging broader applications of PCLS, including their amenability to human omics studies, further emphasizes the unique potential of utilizing PCLS for both basic biology and drug discovery, bridging the gap between cell culture systems and *in vivo* systems.

There have been recent comprehensive reviews on PCLS, focusing on human disease and animal models of disease, including viral and bacterial infections (Liu et al., 2019; Alsafadi et al., 2020; Viana et al., 2022). In this review, we focus on the preparation and preservation of PCLS, measurements of airway and artery smooth muscle responsiveness, airway cilia activity and fibrosis, as well as assessment of dilator and anti-fibrotic treatments.

2 Preparation, culture and applications of PCLS

Multiple reviews and methodological papers have provided detailed overviews that address many of the factors that need to be considered in the preparation, culture and use of PCLS for various experimental outcomes (Sanderson, 2011; Liu et al., 2019; Alsafadi et al., 2020) (Figure 1). Multiple matched PCLS can be treated with disease-relevant stimuli *in vitro* to mimic the initiation of disease, either in the absence or presence of drugs. PCLS can also be prepared from animal models of disease, from genetically-modified mice or from lung tissue from human subjects where disease is already established, before *ex vivo* drug treatments are applied. As such, both preventative and therapeutic strategies can potentially be tested in PCLS.

2.1 Preparation

In the preparation of PCLS for all applications, lungs are inflated using an appropriate volume of liquefied low-melting point agarose solution in physiological buffer, prepared as a 0.5%–3% w/v solution depending on the tissue source. It is important that the agarose concentration used remains consistent within an experiment and is stated in the methods to allow for comparisons between studies performed in different laboratories. The concentration of agarose is important as too low a percentage or alternative mediums that are soft do not allow for sufficient inherent recoil capacity to mediate airway relaxation after contraction (Sanderson, 2011). Agarose is retained within the alveoli after preparation of PCLS, and although this does not prevent airway contraction, it is likely to alter the parenchymal stiffness within a PCLS and should be considered when assessing lung mechanics (Ma et al., 2013).

The lungs are then cooled to below 25°C to set the agarose and stiffen the parenchyma prior to slicing. Inflated lungs can then be sliced with "precision" using a vibratome/compresstome to obtain multiple PCLS with a consistency that was not achievable with the earliest hand-cut lung slices (Placke and Fisher, 1987; Dandurand et al., 1993). PCLS thicknesses vary depending on application, with slices typically ranging from 150 to 300 µm for optimal imaging of contractile responses, or up to 500 µm, if being fixed and sectioned for staining or to obtain sufficient yield of RNA (Sanderson, 2011; Alsafadi et al., 2017; Niehof et al., 2017; Stegmayr et al., 2021).

The instillation of agarose through to the parenchyma can occur via the trachea for relatively small species, such as rodents (Dandurand et al., 1993; Martin et al., 1996), while individual

lobes of larger species, such as sheep or human, can be inflated via the bronchi (Wohlsen et al., 2003; Lambermont et al., 2014). Although human surgical resection samples are more readily available than intact lung lobes, preparation of PCLS from these samples may be more challenging. If the distal airways that terminate in alveoli are not intact, agarose delivered via a segmental airway may leak. For these samples, multiple small airways are cannulated to deliver agarose, while others are clamped to limit leakage (Ressmeyer et al., 2010; Gerckens et al., 2019). Alternatively, agarose can be injected directly into the alveolar tissue with a fine gauge needle to inflate localized regions for slicing (Sturton et al., 2008; Yilmaz et al., 2019).

For airway contraction studies of human and mouse PCLS, a standardized approach of agarose inflation, ideally followed by a bolus of air, is required to obtain PCLS with patent intact airways. The presence of beating cilia lining the airways provides a visible marker consistent with airway viability prior to assessment of contractile responses (Bai and Ai, 2022; Koziol-White, 2022). It should be noted that the preparation of guinea pig PCLS requires the addition of the bronchodilator isoprenaline to both the agarose solution and the initial incubation medium to avoid *post-mortem* airway contraction (Ressmeyer et al., 2006).

Even though intrapulmonary arteries are commonly located adjacent to airways, the preparation of PCLS with patent arteries is challenging. The arteries tend to collapse during agarose inflation, as they are less securely tethered and tear away from surrounding connective tissue. To overcome this artefact, warm gelatin can be perfused via the heart through the pulmonary circulation to provide support for the arteries during the subsequent agarose inflation of the airways. The gelatin dissolves in cultured PCLS to allow subsequent visualization of artery contraction responses *in situ* (Perez and Sanderson, 2005a; Bai and Ai, 2022).

2.2 Culture conditions

Protocols for the preparation and subsequent culture of PCLS vary in terms of media conditions and duration, depending on the outcomes of interest (Figure 1). PCLS are subjected to wash protocols to remove cell debris and mediators released during slicing, then maintained in culture, irrespective of the outcome to be measured. Immersion of PCLS in media remains the most convenient and widely used tissue culture method, although the use of particular types of media and supplements to maintain viability and specific functionalities has not always been clearly justified (Sanderson, 2011). While PCLS contain resident structural and immune cells, they lack a circulating blood supply. While this provides for a more controlled environment to assess PCLS responses, it may also be considered a limitation e.g., for studies assessing effects of *in vitro* exposure to allergens or infectious agents. The development of integrated platforms that supply circulating blood-borne cells and other factors and measure their influence on contractile and secretory responses of PCLS will be another step supporting the clinical relevance of this already innovative methodology. Novel approaches to optimize PCLS culture and extend longevity using different media supplements, culture methods (dynamic organ roller culture (DOC), air-liquid interface (ALI) culture and hydrogels) and cryopreservation are detailed later.

2.3 Applications and considerations

PCLS are used to investigate multiple disease-relevant processes in addition to airway and artery reactivity.

Human PCLS with parenchyma only, prepared by coring of agarose-inflated lung, are increasingly used in a model of *in vitro* fibrogenesis. This protocol involves a 5-day treatment with a fibrotic cocktail (FC), comprising transforming growth factor-β (TGF-β), tumor necrosis factor-α (TNF-α), platelet-derived growth factor-AB (PDGF-AB) and lysophosphatidic acid (LPA) (Alsafadi et al., 2017). The interested reader is directed to detailed protocols and an extensive troubleshooting guide for the preparation of mouse, sheep and human PCLS used for infection studies, outlining approaches for measuring viability, viral load and iinflammatory responses (Rosales Gerpe et al., 2018; Sewald and Danov, 2022).

A recent methods chapter on mouse PCLS culture provides an excellent overview of both preparation and protocols for numerous useful experimental outputs including imaging for contractility studies, collagen and elastin imaging, mean linear intercept (MLI) measurement of alveolar airspace size, immunofluorescent staining and preparation of decellularized PCLS (Wu et al., 2019). A separate study in rabbit PCLS supports their use for some histomorphometric results such as tissue density and alveolar septal thickness, but suggests that MLI and septal may be confounded by agar infusion (Ragionieri et al., 2023).

In addition, two recently published methods have addressed the challenge of obtaining high-quality RNA from PCLS due to the presence of agarose. Recent methodology advances have also allowed PCLS to be utilized for genetic manipulation and adenovirus transfection (Rosales Gerpe et al., 2018; Ruigrok et al., 2018). Improved isolation of RNA suitable for RTqPCR and RNA microarray analysis has been achieved using a magnetic bead-based isolation approach from PCLS containing 1.5% agarose prepared from human, rat, mice, marmoset and rhesus macaque lungs (Niehof et al., 2017). This protocol for RNA isolation from PCLS has been modified to enable miRNA readouts (Niehof et al. 2021). An alternative protocol obtaining high RNA yields and purity from mouse, pig and human PCLS containing higher agarose concentrations of 3% has been validated for RNA-seq (Stegmayr et al., 2021).

Whether standardization of these various protocols for culture, treatment and measurement of outcomes is required to facilitate prolonged PCLS viability and reproducibility of outcomes is a subject of continued discussion among researchers in the field (Patel et al., 2021; Liu et al., 2022; Preuß et al., 2022). Nevertheless, it is clear that significant insights can be gained using PCLS prepared from experimental animals and humans, extending beyond than cell-based studies. Their scalability compared to *in vivo* studies has led to PCLS becoming more widely adopted as an experimental tool. Of note, a PubMed search for the term "precision cut lung slices" was associated with fewer than 20 publications during the 1990s, increasing to over 400 publications since 2010.

3 Investigations of smooth muscle responses and cilia activity in PCLS

Because of the contributions of intrapulmonary airways and arteries to airflow and pulmonary artery pressure respectively, it has

been critical to characterize mechanisms regulating their reactivity in health and disease. Traditional organ bath and myography approaches to measure changes in force are limited to readily dissected rings of trachea and bronchi, or main pulmonary arteries and first or second order branches. In contrast, PCLS provide access to relatively inaccessible small airways and arteries (typically 50–500 μm diameter), allowing contraction and relaxation to be visualized under phase contrast while the interdependency of smooth muscle and the surrounding parenchyma is maintained (Sanderson, 2011). While assessment of cilia function is routinely performed using epithelial cells isolated from the large cartilaginous airways, PCLS offer the opportunity for direct measurement of cilia beat frequency (CBF) *in situ* in the disease-relevant small airways, providing a more physiological setting to assess their critical role in airway protection.

3.1 Airways

One of the most valuable applications of PCLS has been to define the pharmacology and physiology of small airways. Pioneering studies established differential responses to specific contractile agonists with airway size within species, and to different agonists (acetylcholine (ACh), histamine, endothelin-1 (ET-1), serotonin (5-HT) and the thromboxane mimetic U46619) between species including mice, sheep, horses, non-human primates and humans (Martin et al., 1996; Held et al., 1999; Martin et al., 2000; Bergner and Sanderson, 2002; Bergner and Sanderson, 2003; Bai and Sanderson, 2006a; Ressmeyer et al., 2006; Vietmeier et al., 2007; Bai et al., 2009; Bai and Sanderson, 2009; Seehase et al., 2011; Lambermont et al., 2014).

Mechanistic insights into contractile signaling pathways have also been obtained using PCLS. Under confocal microscopy, agonist-induced increases in Ca^{2+} oscillations, occurring via release/uptake from intracellular stores within individual smooth muscle cells, can be visualized in PCLS loaded with Ca^{2+}-sensitive fluorescent dyes (Perez and Sanderson, 2005a; Perez and Sanderson, 2005b). The critical role of inositol 1,4,5 trisphosphate (IP_3) in Ca^{2+} release has been confirmed using flash photolysis of caged IP_3 to activate IP_3 receptors leading to airway contraction (Bai et al., 2009). PCLS have also been used to explore the contributions of a parallel pathway, termed Ca^{2+} sensitivity, to sustained airway contraction. Using a pharmacological approach, the application of caffeine and ryanodine to PCLS clamps free intracellular Ca^{2+}. Contraction can then occur in the absence of Ca^{2+} oscillations, due to increased Ca^{2+} sensitivity through protein kinase C (PKC) and Rho-activated kinase (ROCK) pathways (Bai and Sanderson, 2006b). These elegant approaches were developed and applied by the late Mike Sanderson, who trained many early career investigators still using PCLS to advance respiratory research.

More recently, a novel platform called tissue traction microscopy (TTM) has been applied to PCLS prepared from agarose-inflated lungs in the standard way then adhered to an adhesive and compliant silicone substrate. TTM provides spatial measurements of contractile force generated by airway smooth muscle within PCLS. Compared with the conventional measurements of changes in airway lumen area, this specialized approach resulted in increased sensitivity and less variability in responses to bronchoconstrictor stimuli in both porcine and human PCLS, and potentially addresses one of the limitations of PCLS by allowing the effects of cyclic stretch to be determined (Ram-Mohan et al., 2020). The wider application of TTM is likely to yield novel insights into the regulation of intrapulmonary airway contractility and responsiveness to dilator drugs.

The assessment of altered airway responses in PCLS in the context of acute infection and chronic lung diseases (asthma, COPD and IPF) is described later. These extensive studies have provided insights into mechanisms underlying altered reactivity to endogenous constrictors and impaired responsiveness to dilators in clinical use, as well as the assessment of assessing alternative therapeutics.

3.2 Arteries

Pharmacological assessment of intrapulmonary arteries in PCLS remains comparatively limited compared to airways, and has yet to be widely applied to PCLS prepared from models of pulmonary hypertension (PH). Nevertheless, studies using mouse, rat, guinea pig and human PCLS have established ET-1 as the most potent vasoconstrictor compared to 5-HT, potassium chloride (KCl), adrenaline, noradrenaline, phenylephrine and U46619 (Shi et al., 1998; Held et al., 1999; Moreno et al., 2006; Ressmeyer et al., 2006; Faro et al., 2007; Perez-Zoghbi and Sanderson, 2007; Rieg et al., 2011). Using the approaches applied for assessment of Ca^{2+} signaling in airways, Perez demonstrated that contraction of vascular smooth muscle cells in intrapulmonary arteries in mouse PCLS to 5-HT and ET-1 is also regulated by the frequency of Ca^{2+} oscillations and by Ca^{2+} sensitization (Perez and Sanderson, 2005a; Perez-Zoghbi and Sanderson, 2007). Physiological responses to hypoxia have also been established in PCLS. Sustained hypoxic vasoconstriction of intra-acinar arteries (20–150 μm diameter) has been established and linked to hypoxia-induced ROS production (Paddenberg et al., 2006; Paddenberg et al., 2014).

Several studies have applied disease models to PCLS for assessment of intrapulmonary arteries. PCLS prepared from non-smoker lung tissue before exposure to cigarette smoke extract (CSE) for 24 h, showed increased expression of ET-1 receptors, ET_A and ET_B, and ET-1-induced artery contraction (Milara et al., 2012). Similarly, PCLS prepared from guinea pigs after 2 weeks of daily exposure to cigarette smoke showed increased vasoconstrictor sensitivity to ET-1, along with impaired endothelial-dependent NO production and ACh-mediated relaxation compared with controls (Wright and Churg, 2008).

A single study using PCLS prepared from control subjects and patients with either idiopathic pulmonary fibrosis (IPF) or IPF and PH (IPF + PH) has implicated Janus kinase type 2 (JAK2) as a novel target to oppose contraction of intrapulmonary arteries (Milara et al., 2018). This extensive study demonstrated that the JAK2 inhibitor JSI-124 reduced basal tone, relaxed pulmonary arteries pre-contracted with 5-HT and inhibited the development of 5-HT induced contraction, with the latter protocol consistent with the prophylactic use of dilators in *p*H. Pharmacological approaches suggested that relaxation was mediated by activation

of large conductance calcium-activated potassium channel (BKCa) reducing intracellular Ca^{2+}. Of note, the responses to JSI-124 were reduced in IPF and IPP + PH PCLS compared to controls, suggesting that JAK2, a non-receptor tyrosine kinase activated by a broad spectrum of vasoactive mediators, might be upregulated in disease (Milara et al., 2018). Further studies are required to identify additional targets regulating vascular responses in PCLS from relevant disease models, and to use PCLS to compare responsiveness to both current and novel vasodilator treatments for PH.

3.3 Cilia

Measurement of cilia beat frequency (CBF) using differential interference contrast microscopy and high-speed video recording can provide key insights into mucociliary function in the distal lung. The presence of actively beating cilia activity visualized in PCLS may also be an indicator of airway viability, although these functions may be maintained or lost independently.

Measurements of CBF has shown that it occurs at a faster rate within mouse lung slices than in tracheal rings. Unlike the larger airways, CBF was not increased by extracellular ATP despite increased intracellular Ca^{2+} in the ciliated cells, suggesting constant vigilance for the immediate clearance of foreign material reaching the distal lung (Delmotte and Sanderson, 2006).

While not a major focus of this review, the pathological consequences of reduced CBF have also been explored using PCLS. Short-term *in vitro* treatment of mice PCLS with 2% NaCl was used to cause reversible ciliostasis, resulting in an increased viral yield with subsequent swine influenza virus infection, demonstrating reduced protection when cilia function was compromised (Kurosawa et al., 1995). In addition, while *in vivo* studies have shown variable effects of cigarette smoke and alcohol on CBF, co-exposure of mice PCLS *in vitro* resulted in decreased cilia beating, consistent with the significant decrease in bacterial clearance from the lung observed in an *in vivo* rodent model (Vander Top et al., 2005; Wyatt et al., 2012). Exposure of mouse PCLS to e-cigarette condensates prepared from menthol- and nicotine-containing e-fluids resulted in generalized oxidative stress and cytotoxicity as well as structural and functional consequences on airways, with impaired MCh-induced contractile responses and epithelial damage associated with reduced CBF (Herbert et al., 2023).

4 Investigations of airway reactivity and fibrosis in PCLS

Increased airway contraction, loss of bronchodilator sensitivity and fibrosis are common features of many chronic lung diseases. Short-term exposure of PCLS to disease-relevant conditions has the potential to both directly and indirectly influence airway reactivity and dilator responsiveness, and *in vitro* models of fibrogenesis in PCLS are now established. While access to human lung tissue with established disease may be limited, PCLS from *in vivo* models can be prepared to assess therapeutic interventions targeting excessive contraction and established fibrosis for clinical translation. The focus of this section of the review is to highlight knowledge gains from these studies and their impact in identifying therapeutic targets or novel treatments opposing airway contraction and fibrosis.

4.1 Assessment of contraction and dilator responsiveness in PCLS

β_2-adrenoceptor agonists, either alone or in combination with anti-inflammatory steroids, remain the most common treatment for acute asthma exacerbations caused by excessive bronchoconstriction. The effects of these dilator drugs on the signaling pathways leading to airway contraction have been established in human PCLS, with activation of adenylate cyclase/cAMP/PKA pathways to oppose contractile agonist-induced Ca^{2+} oscillations and increased Ca^{2+} sensitivity (Bai et al., 2006a; Delmotte and Sanderson, 2008; Delmotte et al., 2010) (Table 1).

The capacity of β_2-adrenoceptor agonists to dilate maximally contracted airways is limited by functional antagonism, even in healthy airways. Efficacy may be further compromised in severe disease, when airways hyperresponsiveness (AHR) is present and repeated use of high doses of dilator therapy can lead to receptor desensitization and loss of sensitivity. Other factors such as smoking and infections are also known to reduce dilator responsiveness by increasing airway inflammation and downregulating β_2-adrenoceptor expression.

These factors that limit effective dilator responses can be modelled in PCLS, providing a suitable platform for relatively high through-put assessment of potential alternative therapies. As the level of precontraction of airways in PCLS is increased e.g. with higher concentrations of a cholinergic agonist such as MCh, the relaxation response to a β_2-adrenoceptor agonist such as salbutamol declines. Overnight treatment of PCLS with high concentrations of β_2-adrenoceptor agonists also abolishes their dilator response (Cooper et al., 2011; An et al., 2012; Bourke et al., 2014; Donovan et al., 2015a; Koziol-White et al., 2020).

To date, relatively few studies have assessed airway contraction and dilator responses in PCLS from *in vitro* or *in vivo* experimental models. In terms of contractile responses, *in vitro* exposure of human PCLS to IL-13, but not to poly I:C, increased contraction to MCh, despite the viral mimetic causing the release of inflammatory cytokines predicted to alter airway reactivity (Cooper et al., 2009). MCh-induced contraction was also unaffected in PCLS from a mouse model chronic allergen challenge, despite established *in vivo* AHR to MCh (Donovan et al., 2013). However, contraction to MCh was altered in PCLS prepared after *in vivo* exposure to cigarette smoke either alone or in combination with flu infection (Donovan et al., 2015b; Donovan et al., 2016). Notably, the dilator potency and efficacy of salbutamol was also markedly reduced in PCLS from *in vivo* cigarette smoke models with and without infection, and shown to be associated with decreased β_2-adrenoceptor mRNA expression (Donovan et al., 2016).

The effects of numerous other drugs activating adenylate cyclase/cAMP/PKA and guanylate cyclase/cGMP/PKG and other signaling pathways have identified diverse mechanisms leading to airway relaxation (Table 1). While some of the drugs tested are

TABLE 1 Summary of studies assessing the efficacy and mechanisms of action of bronchodilator agents in PCLS.

Drug class	Bronchodilator	Pre-contraction	Species	References
β-adrenoceptor agonist	Isoprenaline (non-selective)	MCh CCh	Mouse, Rat Human	Bai and Sanderson (2006a), Bai and Sanderson (2006b), Ghosh et al. (2016), Lam et al. (2016)
	Salbutamol (SABA)	MCh	Mouse	Delmotte and Sanderson (2008)
	Formoterol (LABA)	MCh CCh, Histamine	Mouse Human	Delmotte and Sanderson (2010), Cooper et al. (2011)
	Salmeterol (LABA)	CCh	Human	Cooper et al. (2011)
	Indacaterol (ultra-LABA)	5-HT, CCh	Rat, Human	Sturton et al. (2008)
Prostaglandin	PGE_2	MCh	Mouse	FitzPatrick et al. (2014)
cAMP mimetic	8-Br-cAMP	MCh	Mouse	Bai and Sanderson (2006a), Bai and Sanderson (2006b)
Adenylate cyclase activator	Forskolin	MCh	Mouse	Bai and Sanderson (2006a), Bai and Sanderson (2006b)
Nitric oxide donor	NOC-5	5-HT	Mouse	{Perez-Zoghbi et al. (2010) #10}
Guanylate cyclase activator	BAY 41–2,272, BAY 60–2,770	CCh	Mouse, Human	Ghosh et al. (2016), Koziol-White et al. (2020)
Phosphodiesterase inhibitor	IBMX, caffeine (non-selective)	MCh	Mouse	Bai and Sanderson (2006a), Bai and Sanderson (2006b)
	CC3 (PDE4)	MCh	Rat	Martin et al. (2002)
	Osthole (PDE4D)[a]	ACh	Mouse	Wang et al. (2020)
Protein kinase C inhibitor	GF-109203X	MCh	Mouse	Bai and Sanderson (2006a), Bai and Sanderson (2006b)
Rho kinase inhibitor	Y-27632	MCh	Mouse	Bai and Sanderson (2006a), Bai and Sanderson (2006b)
PPARγ agonist	Rosiglitazone, Ciglitazone[1,a] Rosiglitazone[1a]	MCh, 5-HT, ET-1 MCh	Mouse Rat	Bourke et al. (2014), Donovan et al. (2014), Donovan et al. (2015a), Lam et al. (2016)
Bitter taste receptor (TAS2R) agonist	Chloroquine[a] Chloroquine, Quinine[a]	CCh MCh	Human Mouse	Deshpande et al. (2010), An et al. (2012) Donovan et al., 2014; Tan and Sanderson, (2014); Rosner et al. (2014)
FFA4 agonist	TUG-891, TUG-1197	CCh	Mouse, Human	Prihandoko et al. (2020)
RXFP1 receptor	Relaxin[b]	MCh, ET-1	Rat	Lam et al. (2016)
GABA PAM	SH-053–2′F-R-CH_3, MIDD0301	MCh	Mouse	Gallos et al., 2015; Yocum et al., 2019
CaSR NAM	NPS2143	ACh	Mouse	Yarova et al., 2015; Diao et al., 2021

ACh, Acetylcholine; 8-Br-cAMP, 8-bromo-adenosine 3′,5′-cyclic monophosphate; CaSR, calcium sensing receptor; CCh, Carbachol; ET-1, Endothelin-1; FFA4 Free fatty acid receptor four; GABA, Gamma-aminobutyric acid; 5-HT, serotonin; LABA, Long-acting β-adrenoceptor agonist; MCh, Methacholine; NAM, negative allosteric modulator; NO, nitric oxide; PAM, positive allosteric modulator; PPARγ, Peroxisome proliferator activated receptor γ; RXFP1 Relaxin family peptide receptor one; SABA, Short-acting β-adrenoceptor agonist; sGC, soluble Guanylate cyclase; TAS2R taste receptor type 2 efficacy:[1] in PCLS, from disease model.

[a]Under conditions of reduced responsiveness to β-agonists.

[b]Potentiated response to β-agonists.

purely experimental tools, positive findings with several drug classes have created considerable interest in their potential as novel therapies.

Recent findings with drugs that interact with soluble guanylate cyclase (sGC) in airway smooth muscle in PCLS are notable, as an increase cGMP would provide an alternative intracellular pathway to the cAMP-dependent relaxation activated by β_2-adrenoceptor agonists (Ghosh et al., 2016; Koziol-White et al., 2020; Lam and Bourke, 2020). sGC stimulator and activator drugs, BAY 41–2,272 and BAY 60–2,270, had similar efficacy and potency to the long-acting β_2-adrenoceptor agonist formoterol in human PCLS, with no cross-talk to the adenylate cyclase pathway. Notably, these drugs remained efficacious under conditions of β_2-adrenoceptor desensitization when relaxation to formoterol was abolished (Koziol-White et al., 2020).

Theophylline, a non-selective inhibition of phosphodiesterase (PDE), is a well-established bronchodilator, more selective inhibitors may be required minimize off-target effects. The mRNA transcripts of all PDE4D isoforms have been detected in the lung (Richter et al., 2005). Of interest, the PDE4D inhibitor osthole relaxed preconstricted airways in mouse PCLS, irrespective of β_2-adrenoceptor desensitization, by binding to enzyme's catalytic site to prevent cAMP binding and hydrolysis. Identification of osthole binding sites on PDE4D will guide further development of bronchodilators that may not cause the tachyphylaxis seen with β_2-adrenoceptor agonists (Wang et al., 2020).

TABLE 2 Summary of culture conditions for validation of long-term responsiveness of PCLS.

PCLS	Culture conditions	Outcomes	References
Human 600 μm	Media: DMEM/F12 with L-glutamine, HEPES, serum-free	Viability, inflammation LPS-induced cytokine response decreased over time	Temann et al., 2017
	Supplements: 7.5% $NaHCO_3$, pen/strep/gentamicin/fungizone, ITS-X		
	Media changed daily, for 14 days		
Rat 250–300 μm	Media: MEM with L-glutamine, HEPES	Viability for 29 days, not improved by FBS	Nußbaum et al., 2022
	Supplements: amino acids and vitamins, pen/strep ± 10% FBS	Contractility maintained for 13–25 days depending on mediator, but reduced relaxation	
	Media changed daily, for 29 days		
Mouse 150 μm	Media: DMEM/F12, serum-free	Contractility improved with insulin, increased contraction with IL-13 maintained	Li et al., 2020
	Supplements: 0.1, 0.5, 1, or 10 μg/ml insulin; antibiotic/antimycotic		
	Media changed every 48 h, for 14 days		
Human 500 μm	Media/Supps (all): antibiotic/antimycotic, L-glutamine, HEPES Hydrocortisone (acclimation only)	Viability, histology, inflammation	Patel et al. (2021)
	Media/Supps:E-199, insulin / Media/Supps: DMEM/F12, HEPES / Media/Supps: RPMI-1640, insulin, HEPES, retinyl acetate, 0.05% FBS	Variable but maintained viability, protein content, cytokine response to LPS or Poly I:C	
	Method: submerged or DOC or ALI		
	Media changed 3 times per week, for up to 4 weeks		
Sheep 300 μm	Maintenance media: DMEM with high glucose	Viability and viral infection	Rosales Gerpe et al., 2018
	Supplements: pen/strep/gentamicin/amphotericin B	3 days acclimatization in culture then >95% vector transduction or virus infection	
	8-Br-cAMP, IBMX, dexamethasone	Live-dead stain or resazurin, >90% viable over 4 weeks	
	Infection media: as above +10% FBS + L-glutamine or keratinocyte factor or hepatocyte factor; Media changed every 48 h, for up to 4 weeks		
Human 400–600 μm	Media: DMEM/F12 Supplements: 0.1% FBS, pen/strep	Fibrosis early fibrosis-like changes– fibrotic genes by 24h, ECM deposition, alveolar epithelial reprogramming	Alsafadi et al., 2017
	Fibrotic cocktail (FC)		
	5 ng/ml TGF-β1, 5 uM PDGF-AB, 10 ng/ml TNF-α, 5 uM LPA		
	Media with FC replenished at 48 h, cultured up to 5 days		
Human 250 μm	Media: DMEM/F-12 Supplements: pen/strep amphotericin B	Viability, fibrosis	Khan et al., 2021
	Fibrotic stimulus: 10 ng/ml human TGF-β1, 25 μM MMP inhibitor	Viable and metabolically active; Mesenchymal, epithelial, endothelial and immune cell types surviving for 14 days; conditioned media—induced ECM proteins	
	Media with stimulus replenished at 18 h, then every 72 h for 14 days		
Mice	Hydrogel—encapsulated in PEGNB with PEG-dithiol cross-linker	Viability, tissue integrity	Bailey et al., 2020
	Media: DMEM/F12. Supplements: 0.1% FCS pen/strep, amphotericin B	Viability, PCLS architecture cellular phenotype and vimentin expression > non-encapsulated PCLS	
	Media changed every 48 h, for 21 days		
Human 200–300 μm	Media: DMEM/F-12 Supplements: pen/strep	Viability, tissue integrity and transcriptome	Preuß et al., 2022
	Media changed regularly, up to 4 weeks	Progressive loss of vascular, cilia then alveolar integrity over 2 weeks; epithelium preserved for 4 weeks	

ALI, air–liquid interface; 8-Br-cAMP, 8-bromo-adenosine 3′,5′-cyclic monophosphate; DMEM, Dulbecco's Modified Eagle Medium; DMSO, dimethyl sulphoxide; FBS, foetal bovine serum; DOC, dynamic organ roller culture; ECM, extracellular matrix; 3-IBMX, isobutyl-1-methylxanthine; LPA, lysophosphatidic acid; MMP, matrix metalloproteinase (MMP); O/N overnight; PDGF-AB, Platelet-derived growth factor-AB; TGF-β, transforming growth factor-β; TNF-α, tumor necrosis factor-α

Several other receptors in addition to β_2-adrenoceptors have been investigated as targets to limit excessive airway contraction (Table 2). Peroxisome Proliferator Activated Receptor γ (PPARγ), Taste Receptor type 2 (TAS2R), Free Fatty Acid Receptor 4 (FFA4), Relaxin Family Peptide Receptor 1 (RXFP1), Gamma-AminoButyric Acid A Receptor ($GABA_AR$) and Calcium Sensing Receptor (CaSR) are all expressed on airway smooth muscle cells in the lung.

Apart from CaSR, activation of these receptors using a range of drug-like agonists promotes airway relaxation in PCLS from various species, although their downstream signaling pathways have yet to

be fully defined. For synthetic FFA4 agonists, relaxation is mediated at least in part by the release of PGE_2 that subsequently acts on EP_2 prostanoid receptors (Prihandoko et al., 2020). Direct comparisons of rosiglitazone (RGZ, PPARγ agonist) and chloroquine (TAS2R agonist) with β_2-adrenoceptor agonists in PCLS studies have shown that dilator responses to both RGZ and chloroquine are maintained in mouse models of allergic airways disease and under conditions of β_2-adrenoceptor desensitization in mouse and human PCLS respectively (An et al., 2012; Bourke et al., 2014; Donovan et al., 2014; Sharma et al., 2017), Relaxin (RXFP1 agonist) has additive effects with isoprenaline (non-selective β_2-adrenoceptor agonist) in rat PCLS (Lam et al., 2016). In considering potential for clinical translation, MIDD0301, a positive allosteric modulator (PAM) of $GABA_AR$, elicits airway relaxation, but has limited brain distribution, thus eliminating the potential for sedation (Yocum et al., 2019). Activation of CaSR by endogenous ligands such as spermine, or by calcium itself, promotes contraction, so negative allosteric modulators (NAMs) such as NPS2413 that inhibit contraction offer potential therapeutic benefit (Yarova et al., 2015; Diao et al., 2021).

Many of these dilators have other beneficial effects in the lung, independent of their direct effects on airway smooth muscle. Chronic *in vivo* administration of these drugs in models of allergic airways disease that mimic key features of asthma has been shown to reduce airway inflammation, remodeling and/or the development of AHR (Ward et al., 2006; Yarova et al., 2015; Sharma et al., 2017; Prihandoko et al., 2020). To support their clinical translation for asthma, further studies using human PCLS with increased sensitivity to contractile agonists, either from *in vitro* inflammatory models, or from patients with asthma, are required to provide the most relevant setting for validation of these novel dilators compared to current therapies.

4.2 Assessment of fibrosis in PCLS

There is increasing interest in the application of PCLS for investigation of disease mechanisms and treatments for idiopathic pulmonary fibrosis (IPF). Current clinical management involves treatment with nintedanib and pirfenidone, antifibrotic drugs that slow disease progression, but do not reverse established fibrosis.

As previously described, disease-relevant stimuli (TGF-β combined with other components to make a "fibrotic cocktail", FC) can be applied to PCLS to induce fibrogenesis, resulting in accumulation of ECM proteins implicated in long-term fibrosis in the IPF lung. Both low μM concentrations of nintedanib and mM concentrations of pirfenidone reduced expression of extracellular matrix proteins collagen one and fibronectin (COL1A1, FN1) when drugs were added to human PCLS that had been pre-treated with FC for 48 h followed by co-treatment with drugs (Lehmann et al., 2018). These findings in non-diseased PCLS provide evidence of efficacy in preventing the onset and early stages of fibrosis. Although the access to explanted diseased lungs is relatively limited, preparation of PCLS from the healthy margins of smaller surgical resections and the optimization of long-term culture conditions to establish fibrosis may provide opportunities to test interventions to reverse the newly laid down ECM.

To assess whether therapeutic interventions have the potential to reverse established fibrosis requires preparation of PCLS from the gold standard mouse bleomycin model of IPF or from either resections or explanted lungs from patients with established IPF. Validation of feasibility for this approach for screening anti-fibrotic drugs was first obtained using PCLS from an *in vivo* bleomycin model, which showed decreased hydroxyproline levels over 5 days of treatment with caffeine (Tatler et al., 2016).

More recently, it has been confirmed that PCLS from both bleomycin-treated rodents and human retain characteristics of fibrotic disease consistent with or IPF when cultured for up to 5 days, allowing potential reversal of fibrosis to be assessed. Relatively higher expression of fibrosis-related genes for COL1A1, FN1, *a*-smooth muscle actin (ACTA2), and proteins involved in ECM turnover, matrix metalloproteinase 12 and tissue inhibitor of metalloproteinases (MMP12, TIMP1) was shown in PCLS from mice with prior *in vivo* exposure to bleomycin (Lehmann et al., 2018; Cedilak et al., 2019). Similar levels of fibrosis-relevant proteins including *a*-SMA, collagen I and fibronectin were also present in matched PCLS from IPF patients compared over 5 days in culture (Wei et al., 2021).

Several studies have now modeled the clinical scenario in IPF, by testing the effects of nintedanib or pirfenidone on PCLS from bleomycin models or IPF patients (Mercer et al., 2016; Ahangari et al., 2022). In PCLS from the mouse bleomycin model, 3 days of *in vitro* treatment with the ALK5 inhibitor SB525334 or nintedanib resulted in differential inhibition of the expression of fibrosis-related genes, with both drugs decreasing COL1A1, FN1, but only SB525334 inhibiting ACTA2 (Cedilak et al., 2019).

Another study has used PCLS prepared from lungs of bleomycin-treated rats and patient donors with PF, measuring drug effects on levels of specific neoepitope biomarkers of type I, III and VI collagen formation or degradation in conditioned media (Hesse et al., 2022). Differential effects of nintedanib and pirfenidone were seen between species and treatments. Both PRO-C3 and C3M, neoepitopes associated with formation and degradation of type III collagen respectively, were decreased in nintedanib-treated human PCLS, while treatment of rat PCLS led to a reduction in C3M only. Pirfenidone had a marginal effect on PRO-C3 in human PCLS only, and there were no other notable effects of either nintedanib or pirfenidone on the biomarkers for other forms of collagen.

In terms of identification of novel agents for IPF treatment, a small molecule electrophilic nitroalkene, nitro-oleic acid (NO2-OA), reversed key indices of fibrosis in mice PCLS prepared 14 days post-bleomycin (Koudelka et al., 2022). Positive findings showed reductions in COL1A1 and FN1 gene expression, and other markers of myofibroblast differentiation, proliferation and collagen deposition. Inhibition of PGE_2 metabolism with the 15-PGDH inhibitor SW033291 was also shown to reduce collagen production in PCLS from IPF patients, consistent with the previously reported anti-fibrotic effects of PGE_2 (Bärnthaler et al., 2020). Neither of these studies made direct comparisons with pirfenidone or nintedanib.

Epigallocatechin gallate (EGCG), an inhibitor of lysyl oxidase-like2 (LOX2) and TGFβ1 signaling, induced collagen I turnover in IPF PCLS (Wei et al., 2021). EGCG decreased collagen I production

TABLE 3 Summary of cold storage and cryopreservation studies using PCLS.

PCLS	Culture conditions		Timing and outcomes of functional assays	References
Rat 250–300 μm	Cold storage: DMEM/F12 ± high potassium chloride (solution 1) or		Viability, contraction, response to LPS	Tigges et al. (2021)
	chloride-poor, lactobionate-rich analog (solution 2)		Solution 1 superior to solution 2 or standard DMEM/F-12 No contractility in DMEM/F12 alone after 14 days Gradual reduction in cytokine response in all conditions with time	
	3–28 days at 4°C *For contraction, LPS-induced cytokine release*			
	Media: warmed DMEM/F-12			
Mouse 250 μm	Cryopreservation: 10% DMSO in DMEM/F12		Contractility	Rosner et al. (2014)
	single PCLS/cryovial frozen at -80°C		Tested immediately post thaw	
	liquid N_2 for storage up to 3 months		Airway contraction maintained after cryopreservation and storage	
	Thaw: rapidly in 37°C water bath			
	For contraction			
	Media: DMEM/F-12			
	Supplements: kanamycin/pen/strep/amphotericin B			
	Media changed once an hour for 4 h then daily			
Mice, rats	Cryopreservation: 10% DMSO in DMEM/F12		Viability, response to toxin	Watson et al., 2016
	single PCLS/cryovial, frozen at -80°C		Immediately post thaw or up to 3 days later	
	For tox study		Decreased viability and metabolic activity	
	Media: DMEM/Ham's F-12		Similar toxin-induced changes in cell viability, mitochondrial integrity, and glutathione activity	
	Supplements: kanamycin/pen/strep/amphotericin B			
Human 250 μm	Overnight incubation DMEM/F12/antibiotics		Viability, immune cell function, contractility	Bai and Ai (2022)
	Cryopreservation: 10% DMSO in DMEM/F12		Immediately post thaw or up to 6 days later	
	3 PCLS/cryovial in 100% isopropyl alcohol, then frozen O//N		Contraction and relaxation, calcium signaling maintained	
	-80°C liquid N_2 for long-term storage			
	Thaw: rapidly in 37°C water bath		Cell viability, immune cell functions maintained	
	For contraction	*For lymphocyte activation*		
	Media: DMEM/F-12	Media: RPMI		
	Supplements: pen/strep	Supplements: 10% FBS, pen/strep/antimycotics		
		Media changed every 48 h		

DMEM, Dulbecco's Modified Eagle Medium; DMSO, dimethyl sulphoxide; FBS, foetal bovine serum; DOC, dynamic organ roller culture; 3-IBMX, isobutyl-1-methylxanthine; LPA, lysophosphatidic acid; MMP, matrix metalloproteinase (MMP); O/N overnight; PDGF-AB, Platelet-derived growth factor-AB; TGF-β, transforming growth factor-β; TNF-α, tumor necrosis factor-α

and crosslinking and increased its degradation via upregulation of MMP1 and downregulation of TIMP1, while neither nintedanib nor pirfenidone regulated these disease-relevant outcomes (Wei et al., 2021).

Overall, PCLS are being increasingly used as a relatively high-throughput screen for anti-fibrotic drugs for IPF and other interstitial lung diseases. To date, these studies have used PCLS prepared from parenchymal tissue, precluding the measurement of potential collagen deposition around the airways or arteries. Given the unmet need for drugs that reverse rather than retard fibrosis in asthma and COPD as well as IPF, further developments in this area that support broader clinical translation are eagerly anticipated.

5 Future directions

So what are the major challenges still to be overcome limiting the wider use of PCLS? Due to loss of viability in culture, the majority of PCLS studies have been performed within days of preparation. This limits their application for *in vitro* modeling of complex disease mechanisms or chronic toxicity and compromises the assessment of drugs to reverse established pathological changes. While short culture periods are sufficient for many studies, conditions need to be optimized to limit potential loss of viability and functional capacity over longer periods. Another limitation is that it is not always possible to utilize the large number of PCLS that can be generated from a single lung, whether from an animal model or from a precious clinical

sample. A number of studies have addressed these challenges, validating the effects of specific culture conditions and methods on PCLS viability, structure and diverse functions, and assessing the potential for successful cryopreservation (Tables 2, 3).

5.1 Media supplementation

With daily media changes, PCLS have been reported to maintain normal metabolic activity and overall structural integrity in serum-free media for at least 14 days in serum-free media, although the cytokine response to lipopolysaccharide (LPS) was markedly reduced over time compared to the response in fresh PCLS (Temann et al., 2017). Loss of contractile responses typically occurring within several days in culture, so that only short-term culture of PCLS in serum-free media is widely used when functionality of smooth muscle cells is required. Recently, the addition of insulin has been shown to preserve airway contractile responses in mouse PCLS for up to 2 weeks (Li et al., 2020).

Longer-term viability remains a challenge. A recent study cultivated more than 1,500 human PCLS from 16 different donors under standardized, serum-free conditions for up to 28 days. While viability of PCLS was well preserved, transcriptome analysis revealed a significantly increased immune response and significantly decreased metabolic activity within the first 24 h after PCLS generation. A continuous loss of cells was observed over time, occurring at different rates in the different anatomical compartments. The significant loss of vascular integrity within days extended to a gradually decrease in ciliary beat in the small airways after 1 week. Alveolar integrity was preserved for about 2 weeks, while bronchial epithelium was well preserved for 4 weeks (Preuß et al., 2022).

Media supplement requirements for long term *ex vivo* infection studies in sheep PCLS have been detailed, with PCLS maintained in DMEM containing antibiotics and already supplemented with 10% serum and glutamine. The selective addition of recombinant human keratinocyte factor or hepatocyte factor, present only during the infection period of the protocol, supports propagation of the virus of interest before the PCLS are returned to maintenance media, remaining viable for up to 4 weeks (Rosales Gerpe et al., 2018).

5.2 Culture methods

A recent study has systematically compared the standard protocol of human PCLS submerged in media with dynamic organ roller culture (DOC) or air-liquid interface (ALI) culture. PCLS could be maintained for up to 28 days in different combinations of each culture method with three different types of media. In general, PCLS showed similar histological features, viability and secretory responses to pro-inflammatory bacterial and viral mimetics LPS and poly I:C, irrespective of media or method (Patel et al., 2021). These findings require confirmation, since the overall numbers of PCLS tested in this study was relatively small.

Poly (ethylene glycol)-based hydrogel platforms have recently been evaluated as an alternative culture method for PCLS (Bailey et al., 2020). When encapsulated, PCLS maintained architecture, viability, cellular phenotype (as measured by SFTPC) and vimentin expression. These results suggest that the extended culture times required to study chronic lung diseases *ex vivo* could be possible using PCLS in hydrogels, validation of *in vitro* disease models or measurement of key disease-relevant outcomes has yet to be presented.

5.3 Cryopreservation and cold storage

Cryopreservation is used to preserve the structure and function of intact living cells and tissues. Using the conventional cryopreservative dimethyl sulfoxide (DMSO), PCLS have been frozen, stored and thawed for study of airway reactivity at extended time points (Table 3). Previous studies in mouse PCLS have shown that cryopreservation of slices for up to 2 weeks did not alter airway contraction to MCh or relaxation to the dilator, chloroquine (Rosner et al., 2014). In human freeze-thawed PCLS, airways had similar responses to MCh, histamine, formoterol as never-frozen PCLS, and inhibition of histamine-induced Ca^{2+} oscillations by the bitter taste agonist quinine could be visualized (Bai et al., 2016). Immune functions were also maintained after cryopreservation, shown as phagocytic activity and proliferation of lymphocytes supporting the broad use of cryopreserved PCLS for immunological studies in addition to physiological and pharmacological studies.

In a separate toxicology study, the viability and metabolic activity of cryopreserved PCLS from rats and mice was lower upon thawing than never-frozen PCLS (Watson et al., 2016). However, the expected changes in cell viability, mitochondrial integrity, and glutathione activity when exposed to toxin zinc chloride were maintained, and correlated with lung injury markers in lavage fluid from rats intratracheally instilled with zinc chloride. These findings support the feasibility of also using cryopreserved PCLS for predictive toxicology (Watson et al., 2016).

An alternative method to optimize PCLS utilization without cryopreservation evaluated long-term hypothermic (cold) storage at 4°C, in either DMEM/F-12 or two different preservation solutions (Tigges et al., 2021). After 14 days of cold storage, a range of parameters were better preserved after storage in potassium and chloride-rich tissue preservation solution (solution 1) and a chloride-poor, lactobionate-rich version (solution 2) compared with DMEM/F-12. PCLS stored in solution one responded substantially longer to inflammatory stimulation with LPS, resulting in higher TNF-α levels in conditioned media than in PCLS stored in DMEM/F-12 or solution 2. Notably, bronchoconstriction to ACh was observed after 14 days in both optimized solutions, but not DMEM/F-12 alone (Tigges et al., 2021). This approach may reduce logistical challenges in shipment of PCLS between laboratories and provide opportunities for stockpiling of PCLS samples.

5.4 Not just airways, not just fibrosis

Given the diversity of diseases affecting the lung, there are many new and emerging applications for PCLS beyond the scope of this

brief review. PCLS can be used to study local immune response and tissue factors influencing infectivity, as well allow integrated assessment of antiviral and anti-inflammatory agents (Liu et al., 2015). There is likely to be an increased focus on the use of PCLS to study lung infection, with emerging knowledge of populations of cells present, and the ongoing impact of the COVID-19 pandemic.

PCLS are providing new approaches to study both lung development and aging. Mice PCLS have been used to study the initiation of alveologenesis (Pieretti et al., 2014), with more recent advances in time-lapse imaging and live cell staining demonstrating that cell migration is a key to long-term alveologenesis during postnatal lung development (PMID: 30862802) (Akram et al., 2019). Increases in airway but not vascular reactivity have been demonstrated in mice PCLS a double-hit *in vivo* model of bronchopulmonary dysplasia (BPD) (Royce et al., 2016; Bui et al., 2019). More recently, PCLS from preterm rabbits were used in an *in vitro* model of BPD, in which septal defects and other structural abnormalities could be induced by hyperoxia (Ragionieri et al., 2023). While recognizing that further refinement may be required to mimic the influence of cyclical stretch from ventilation on development, further studies using PCLS from BPD and other early life models may provide novel insights into pathways involved in septation and identify potential therapeutic targets to enhance alveolarization.

As shown from their application in fibrosis studies, PCLS provide a translational model to study aberrant ECM remodeling and its influence on diverse cellular functions. The range of pathological conditions influenced by the ECM extends to aging (Blokand et al., 2020), but only limited studies have used PCLS to study senescence. Methods for determination of senescent myofibroblasts in PCLS have recently been validated (Cruz et al., 2021) and irradiated PCLS developed as an *ex vivo* model of cellular senescence (Narvaez et al., 2022). This will provide opportunities to study aging-related mechanisms, including bidirectional interactions between the ECM and senescent cells within PCLS.

6 Conclusion

PCLS are clearly established as a multifaceted and powerful tool to assess mechanisms contributing to multiple disease-relevant outcomes in the distal lung. Defining the optimum conditions for experimentation is critical, but will vary depending on whether only acute outcomes are being assessed or whether there is a need to establish a disease phenotype *ex vivo*. In general, DMEM/F12 is the medium of choice for PCLS studies, with frequent media changes appearing to support viability and function, and specific supplements added to maintain contractility and to support infection. The encapsulation of PCLS may extend survival for assessment of synthetic responses (cytokine release, ECM production), but functional assessment of contractility or cilia function, which requires airway, arteries and beating cilia to be visualized *in situ*, remains challenging in encapsulated PCLS. Irrespective of their intended use, PCLS offer the potential for relatively high throughput with fewer ethical implications than *in vivo* animal studies. It is critical for both preparation and culture conditions to be reported in detail to enable researchers to reproduce and extend research findings across the diverse applications of PCLS.

Exciting opportunities lie in the application of PCLS exposed to *in vitro* culture conditions to maintain viability and mimic the disease environment, from *in vivo* disease models, and from human diseased lung tissue. Now well established for assessment of novel bronchodilators and anti-fibrotics, further development of the PCLS technique will only enhance its utility to screen both preventative and treatment modalities as a bridge to clinical translation.

Author contributions

JB conceptualized the review. ML, EL, LO, CD and, JB wrote the article. All authors have read and approved the final manuscript. All authors listed have made a substantial, direct, and intellectual contribution to the work and approved it for publication. All authors contributed to the article and approved the submitted version.

Funding

This review was supported in part by National Health and Medical Research Council (NHMRC) of Australia Project Grants (GNT1165690 and GNT1187755) to JB.

Conflict of interest

The authors declare that the research was conducted in the absence of any commercial or financial relationships that could be construed as a potential conflict of interest.

Publisher's note

References

Ahangari, F., Becker, C., Foster, D. G., Chioccioli, M., Nelson, M., Beke, K., et al. (2022). Saracatinib, a selective src kinase inhibitor, blocks fibrotic responses in preclinical models of pulmonary fibrosis. *Am. J. Respir. Crit. Care Med.* 206 (12), 1463–1479. PMID: 35998281; PMCID: PMC9757097. doi:10.1164/rccm.202010-3832OC

Akram, K. M., Yates, L. L., Mongey, R., Rothery, S., Gaboriau, D. C. A., Sanderson, J., et al. (2019). Live imaging of alveologenesis in precision-cut lung slices reveals dynamic epithelial cell behaviour. *Nat. Commun.* 10 (1), 1178. PMID: 30862802; PMCID: PMC6414680. doi:10.1038/s41467-019-09067-3

Alsafadi, H. N., Staab-Weijnitz, C. A., Lehmann, M., Lindner, M., Peschel, B., Königshoff, M., et al. (2017). An *ex vivo* model to induce early fibrosis-like changes in human precision-cut lung slices. *Am. J. Physiol. Lung Cell Mol. Physiol.* 312 (6), L896–L902. doi:10.1152/ajplung.00084.2017

Alsafadi, H. N., Uhl, F. E., Pineda, R. H., Bailey, K. E., Rojas, M., Wagner, D. E., et al. (2020). Applications and approaches for three-dimensional precision-cut lung slices. Disease modeling and drug discovery. *Am. J. Respir. Cell Mol. Biol.* 62 (6), 681–691. PMID: 31991090; PMCID: PMC7401444. doi:10.1165/rcmb.2019-0276TR

An, S. S., Wang, W. C., Koziol-White, C. J., Ahn, K., Lee, D. Y., Kurten, R. C., et al. (2012). TAS2R activation promotes airway smooth muscle relaxation despite β(2)-adrenergic receptor tachyphylaxis. *Am. J. Physiol. Lung Cell Mol. Physiol.* 303 (4), L304–L311. Epub 2012 Jun 8. PMID: 22683571; PMCID: PMC3423830. doi:10.1152/ajplung.00126.2012

Bai, Y., and Ai, X. (2022). Utilizing the precision-cut lung slice to study the contractile regulation of airway and intrapulmonary arterial smooth muscle. *J. Vis. Exp.*, 183. doi:10.3791/63932-v

Bai, Y., Edelmann, M., and Sanderson, M. J. (2009). The contribution of inositol 1,4,5-trisphosphate and ryanodine receptors to agonist-induced Ca(2+) signaling of airway smooth muscle cells. *Am. J. Physiol. Lung Cell Mol. Physiol.* 297 (2), L347–L361. Epub 2009 May 22. PMID: 19465516; PMCID: PMC2742787. doi:10.1152/ajplung.90559.2008

Bai, Y., Krishnamoorthy, N., Patel, K. R., Rosas, I., Sanderson, M. J., and Ai, X. (2016). Cryopreserved human precision-cut lung slices as a bioassay for live tissue banking. A viability study of bronchodilation with bitter-taste receptor agonists. *Am. J. Respir. Cell Mol. Biol.* 54 (5), 656–663. PMID: 26550921; PMCID: PMC4942196. doi:10.1165/rcmb.2015-0290MA

Bai, Y., and Sanderson, M. J. (2006b). Airway smooth muscle relaxation results from a reduction in the frequency of Ca2+ oscillations induced by a cAMP-mediated inhibition of the IP3 receptor. *Respir. Res.* 7 (1), 34. PMID: 16504084; PMCID: PMC1459146. doi:10.1186/1465-9921-7-34

Bai, Y., and Sanderson, M. J. (2006a). Modulation of the Ca2+ sensitivity of airway smooth muscle cells in murine lung slices. *Am. J. Physiol. Lung Cell Mol. Physiol.* 291 (2), L208–L221. Epub 2006 Feb 3. PMID: 16461427. doi:10.1152/ajplung.00494.2005

Bai, Y., and Sanderson, M. J. (2009). The contribution of Ca2+ signaling and Ca2+ sensitivity to the regulation of airway smooth muscle contraction is different in rats and mice. *Am. J. Physiol. Lung Cell Mol. Physiol.* 296 (6), L947–L958. Epub 2009 Apr 3. PMID: 19346434; PMCID: PMC2692797. doi:10.1152/ajplung.90288.2008

Bailey, K. E., Pino, C., Lennon, M. L., Lyons, A., Jacot, J. G., Lammers, S. R., et al. (2020). Embedding of precision-cut lung slices in engineered hydrogel biomaterials supports extended *ex vivo* culture. *Am. J. Respir. Cell Mol. Biol.* 62 (1), 14–22. PMID: 31513744; PMCID: PMC6938134. doi:10.1165/rcmb.2019-0232MA

Bärnthaler, T., Theiler, A., Zabini, D., Trautmann, S., Stacher-Priehse, E., Lanz, I., et al. (2020). Inhibiting eicosanoid degradation exerts antifibrotic effects in a pulmonary fibrosis mouse model and human tissue. *J. Allergy Clin. Immunol.* 145 (3), 818–833. Epub 2019 Dec 5. PMID: 31812575. doi:10.1016/j.jaci.2019.11.032

Bergner, A., and Sanderson, M. J. (2002). Acetylcholine-induced calcium signaling and contraction of airway smooth muscle cells in lung slices. *J. Gen. Physiol.* 119 (2), 187–198. PMID: 11815668; PMCID: PMC2233801. doi:10.1085/jgp.119.2.187

Bergner, A., and Sanderson, M. J. (2003). Airway contractility and smooth muscle Ca(2+) signaling in lung slices from different mouse strains. *J. Appl. Physiol. (1985)* 95 (3), 1325–1332. Epub 2003 May 30. PMID: 12777405. doi:10.1152/japplphysiol.00272.2003

Blokland, K. E. C., Pouwels, S. D., Schuliga, M., Knight, D. A., and Burgess, J. K. (2020). Regulation of cellular senescence by extracellular matrix during chronic fibrotic diseases. *Clin. Sci. (Lond).* 134 (20), 2681–2706. PMID: 33084883; PMCID: PMC7578566. doi:10.1042/CS20190893

Bourke, J. E., Bai, Y., Donovan, C., Esposito, J. G., Tan, X., and Sanderson, M. J. (2014). Novel small airway bronchodilator responses to rosiglitazone in mouse lung slices. *Am. J. Respir. Cell Mol. Biol.* 50 (4), 748–756. PMID: 24188042; PMCID: PMC4068922. doi:10.1165/rcmb.2013-0247OC

Bui, C. B., Kolodziej, M., Lamanna, E., Elgass, K., Sehgal, A., Rudloff, I., et al. (2019). Interleukin-1 receptor antagonist protects newborn mice against pulmonary hypertension. *Front. Immunol.* 10, 1480. PMID: 31354700; PMCID: PMC6637286. doi:10.3389/fimmu.2019.01480

Cedilak, M., Banjanac, M., Belamarić, D., Paravić Radičević, A., Faraho, I., Ilić, K., et al. (2019). Precision-cut lung slices from bleomycin treated animals as a model for testing potential therapies for idiopathic pulmonary fibrosis. *Pulm. Pharmacol. Ther.* 55, 75–83. Epub 2019 Feb 15. PMID: 30776489. doi:10.1016/j.pupt.2019.02.005

Cooper, P. R., Kurten, R. C., Zhang, J., Nicholls, D. J., Dainty, I. A., and Panettieri, R. A. (2011). Formoterol and salmeterol induce a similar degree of β2-adrenoceptor tolerance in human small airways but via different mechanisms. *Br. J. Pharmacol.* 163 (3), 521–532. Epub 2011 Jun. PMID: 21306583; PMCID: PMC3101615. doi:10.1111/j.1476-5381.2011.01257.x

Cooper, P. R., Lamb, R., Day, N. D., Branigan, P. J., Kajekar, R., San Mateo, L., et al. (2009). TLR3 activation stimulates cytokine secretion without altering agonist-induced human small airway contraction or relaxation. *Am. J. Physiol. Lung Cell Mol. Physiol.* 297 (3), L530–L537. Epub 2009 Jun 19. PMID: 19542247. doi:10.1152/ajplung.00133.2009

Cruz, T., Mora, A. L., and Rojas, M. (2021). Determination of senescent myofibroblasts in precision-cut lung slices. *Methods Mol. Biol.* 2299, 139–145. PMID: 34028740; PMCID: PMC8650767. doi:10.1007/978-1-0716-1382-5_10

Dandurand, R. J., Wang, C. G., Phillips, N. C., and Eidelman, D. H. (1993). Responsiveness of individual airways to methacholine in adult rat lung explants. *J. Appl. Physiol. (1985)* 75 (1), 364–372. doi:10.1152/jappl.1993.75.1.364

Delmotte, P., Ressmeyer, A. R., Bai, Y., and Sanderson, M. J. (2010). Mechanisms of airway smooth muscle relaxation induced by beta2-adrenergic agonists. *Front. Biosci. Landmark Ed.* 15 (2), 750–764. doi:10.2741/3644

Delmotte, P., and Sanderson, M. J. (2006). Ciliary beat frequency is maintained at a maximal rate in the small airways of mouse lung slices. *Am. J. Respir. Cell Mol. Biol.* 35 (1), 110–117. Epub 2006 Feb 16. PMID: 16484686; PMCID: PMC2658692. doi:10.1165/rcmb.2005-0417OC

Delmotte, P., and Sanderson, M. J. (2008). Effects of albuterol isomers on the contraction and Ca2+ signaling of small airways in mouse lung slices. *Am. J. Respir. Cell Mol. Biol.* 38 (5), 524–531. Epub 2007 Dec 6. PMID: 18063837; PMCID: PMC2335335. doi:10.1165/rcmb.2007-0214OC

Delmotte, P., and Sanderson, M. J. (2010). Effects of formoterol on contraction and Ca2+ signaling of mouse airway smooth muscle cells. *Am. J. Respir. Cell Mol. Biol.* 42 (3), 373–381. Epub 2009 Jun 5. PMID: 19502388; PMCID: PMC2830407. doi:10.1165/rcmb.2008-0403OC

Deshpande, D. A., Wang, W. C., McIlmoyle, E. L., Robinett, K. S., Schillinger, R. M., An, S. S., et al. (2010). Bitter taste receptors on airway smooth muscle bronchodilate by localized calcium signaling and reverse obstruction. *Nat. Med.* 16 (11), 1299–1304. Epub 2010 Oct 24. PMID: 20972434; PMCID: PMC3066567. doi:10.1038/nm.2237

Diao, J., Lam, M., Gregory, K., Leach, K., and Bourke, J. .E. (2021). Biased negative allosteric modulators of the calcium-sensing receptor differentially oppose airway contraction in mouse precision cut lung slices. *Am. J. Respir. Crit. Care Med.* 203, A4516.

Donovan, C., Bailey, S. .R., Tran, J., Haitsma, G., Ibrahim, Z. .A., Foster, S. .R., et al. (2015a). Rosiglitazone elicits *in vitro* relaxation in airways and precision cut lung slices from a mouse model of chronic allergic airways disease. *Am. J. Physiol. Lung Cell Mol. Physiol.* 309 (10), L1219–L1228. Epub 2015 Sep 18. PMID: 26386117. doi:10.1152/ajplung.00156.2015

Donovan, C., Royce, S. G., Vlahos, R., and Bourke, J. E. (2015b). Lipopolysaccharide does not alter small airway reactivity in mouse lung slices. *PLoS One* 10 (3), e0122069. PMID: 25822969; PMCID: PMC4379153. doi:10.1371/journal.pone.0122069

Donovan, C., Royce, S. G., Esposito, J., Tran, J., Ibrahim, Z. A., Tang, M. L., et al. (2013). Differential effects of allergen challenge on large and small airway reactivity in mice. *PLoS One* 8 (9), e74101. PMID: 24040180; PMCID: PMC3765301. doi:10.1371/journal.pone.0074101

Donovan, C., Seow, H. J., Bourke, J. E., and Vlahos, R. (2016). Influenza A virus infection and cigarette smoke impair bronchodilator responsiveness to β-adrenoceptor agonists in mouse lung. *Clin. Sci. (Lond)* 130 (10), 829–837. Epub 2016 Apr 10. PMID: 27128803; PMCID: PMC5233570. doi:10.1042/CS20160093

Donovan, C., Simoons, M., Esposito, J., Ni Cheong, J., Fitzpatrick, M., and Bourke, J. E. (2014). Rosiglitazone is a superior bronchodilator compared to chloroquine and β-adrenoceptor agonists in mouse lung slices. *Respir. Res.* 15 (1), 29. PMID: 24621080; PMCID: PMC3995634. doi:10.1186/1465-9921-15-29

Faro, R., Moreno, L., Hislop, A. A., Sturton, G., and Mitchell, J. A. (2007). Pulmonary endothelium dependent vasodilation emerges after birth in mice. *Eur. J. Pharmacol.* 567 (3), 240–244. Epub 2007 Mar 30. PMID: 17540365. doi:10.1016/j.ejphar.2007.03.030

Fisher, R. L., Smith, M. S., Hasal, S. J., Hasal, K. S., Gandolfi, A. J., and Brendel, K. (1994). The use of human lung slices in toxicology. *Hum. Exp. Toxicol.* 13 (7), 466–471. doi:10.1177/096032719401300703

FitzPatrick, M., Donovan, C., and Bourke, J. E. (2014). Prostaglandin E2 elicits greater bronchodilation than salbutamol in mouse intrapulmonary airways in lung slices. *Pulm. Pharmacol. Ther.* 28 (1), 68–76. Epub 2013 Nov 28. PMID: 24291048. doi:10.1016/j.pupt.2013.11.005

Freeman, B. A., and O'Neil, J. J. (1984). Tissue slices in the study of lung metabolism and toxicology. *Environ. Health Perspect.* 56, 51–60. PMID: 6383802; PMCID: PMC1568205. doi:10.1289/ehp.845651

Gallos, G., Yocum, G. T., Siviski, M. E., Yim, P. D., Fu, X. W., Poe, M. M., et al. (2015). Selective targeting of the α5-subunit of GABAA receptors relaxes airway smooth muscle and inhibits cellular calcium handling. *Am. J. Physiol. Lung Cell Mol. Physiol.* 308 (9), L931–L942. Epub 2015 Feb 6. PMID: 25659897; PMCID: PMC4421780. doi:10.1152/ajplung.00107.2014

Gerckens, M., Alsafadi, H. N., Wagner, D. E., Lindner, M., Burgstaller, G., and Königshoff, M. (2019). Generation of human 3D lung tissue cultures (3D-LTCs) for disease modeling. *J. Vis. Exp.* 12, 144. doi:10.3791/58437

Ghosh, A., Koziol-White, C. J., Asosingh, K., Cheng, G., Ruple, L., Groneberg, D., et al. (2016). Soluble guanylate cyclase as an alternative target for bronchodilator therapy in asthma. *Proc. Natl. Acad. Sci. U. S. A.* 113 (17), E2355–E2362. Epub 2016 Apr 11. PMID: 27071111; PMCID: PMC4855555. doi:10.1073/pnas.1524398113

Held, H. D., Martin, C., and Uhlig, S. (1999). Characterization of airway and vascular responses in murine lungs. *Br. J. Pharmacol.* 126 (5), 1191–1199. PMID: 10205008; PMCID: PMC1565872. doi:10.1038/sj.bjp.0702394

Herbert, J., Kelty, J., Laskin, J., Laskin, D., and Gow, A. (2023). Menthol flavoring in E-cigarette condensate causes pulmonary dysfunction and cytotoxicity in precision cut lung slices. *Am. J. Physiol. Lung Cell Mol. Physiol.* 324, L345–L357. Epub ahead of print. PMID: 36692165. doi:10.1152/ajplung.00222.2022

Hesse, C., Beneke, V., Konzok, S., Diefenbach, C., Bülow Sand, J. M., Rønnow, S. R., et al. (2022). Nintedanib modulates type III collagen turnover in viable precision-cut lung slices from bleomycin-treated rats and patients with pulmonary fibrosis. *Respir. Res.* 23 (1), 201. PMID: 35927669; PMCID: PMC9351157. doi:10.1186/s12931-022-02116-4

Khan, M. M., Poeckel, D., Halavatyi, A., Zukowska-Kasprzyk, J., Stein, F., Vappiani, J., et al. (2021). An integrated multiomic and quantitative label-free microscopy-based approach to study pro-fibrotic signalling in *ex vivo* human precision-cut lung slices. *Eur. Respir. J.* 58 (1), 2000221. PMID: 33361096; PMCID: PMC8318569. doi:10.1183/13993003.00221-2020

Koudelka, A., Cechova, V., Rojas, M., Mitash, N., Bondonese, A., St Croix, C., et al. (2022). Fatty acid nitroalkene reversal of established lung fibrosis. *Redox Biol.* 50, 102226. Epub 2021 Dec 29. PMID: 35150970; PMCID: PMC8844680. doi:10.1016/j.redox.2021.102226

Koziol-White, C. (2022). Human precision-cut lung slices: Generation of and measurement of contractility and relaxation of small airways. *Methods Mol. Biol.* 2506, 111–117. PMID: 35771467.10.2174/1872312812666181022114622. PMID: 30345935. doi:10.1007/978-1-0716-2364-0_8

Koziol-White, C. J., Ghosh, A., Sandner, P., Erzurum, S. E., Stuehr, D. J., and Panettieri, R. A., Jr (2020). Soluble guanylate cyclase agonists induce bronchodilation in human small airways. *Am. J. Respir. Cell Mol. Biol.* 62 (1), 43–48. PMID: 31340135; PMCID: PMC6938135. doi:10.1165/rcmb.2019-0001OC

Kurosawa, H., Wang, C. G., Dandurand, R. J., King, M., and Eidelman, D. H. (1995). Mucociliary function in the mouse measured in explanted lung tissue. *J. Appl. Physiol. (1985)* 79 (1), 41–46. doi:10.1152/jappl.1995.79.1.41

Lam, M., and Bourke, J. E. (2020). A new pathway to airway relaxation: Targeting the "other" cyclase in asthma. *Am. J. Respir. Cell Mol. Biol.* 62 (1), 3–4. PMID: 31414885; PMCID: PMC6938138. doi:10.1165/rcmb.2019-0274ED

Lam, M., Royce, S. G., Donovan, C., Jelinic, M., Parry, L. .J., Samuel, C. S., et al. (2016). Serelaxin elicits bronchodilation and enhances β-adrenoceptor-mediated airway relaxation. *Front. Pharmacol.* 7, 406. PMID: 27833558; PMCID: PMC5081476. doi:10.3389/fphar.2016.00406

Lambermont, V. A., Schlepütz, M., Dassow, C., König, P., Zimmermann, L. J., Uhlig, S., et al. (2014). Comparison of airway responses in sheep of different age in precision-cut lung slices (PCLS). *PLoS One* 9 (9), e97610. PMID: 25229890; PMCID: PMC4167544. doi:10.1371/journal.pone.0097610

Lehmann, M., Buhl, L., Alsafadi, H. N., Klee, S., Hermann, S., Mutze, K., et al. (2018). Differential effects of Nintedanib and Pirfenidone on lung alveolar epithelial cell function in *ex vivo* murine and human lung tissue cultures of pulmonary fibrosis. *Respir. Res.* 19 (1), 175. PMID: 30219058; PMCID: PMC6138909. doi:10.1186/s12931-018-0876-y

Li, G., Cohen, J. A., Martines, C., Ram-Mohan, S., Brain, J. .D., Krishnan, R., et al. (2020). Preserving airway smooth muscle contraction in precision-cut lung slices. *Sci. Rep.* 10 (1), 6480. PMID: 32296115; PMCID: PMC7160136. doi:10.1038/s41598-020-63225-y

Liu, R., An, L., Liu, G., Li, X., Tang, W., and Chen, X. (2015). Mouse lung slices: An *ex vivo* model for the evaluation of antiviral and anti-inflammatory agents against influenza viruses. *Antivir. Res.* 120, 101–111. Epub 2015 May 27. PMID: 26022197; PMCID: PMC7125926. doi:10.1016/j.antiviral.2015.05.008

Liu, G., Betts, C., Cunoosamy, D. M., Åberg, P. M., Hornberg, J. J., Sivars, K. B., et al. (2019). Use of precision cut lung slices as a translational model for the study of lung biology. *Respir. Res.* 20 (1), 162. Epub 2019 Jul 19. PMID: 31324219; PMCID: PMC6642541. doi:10.1186/s12931-019-1131-x

Liu, Y., Wu, P., Wang, Y., Liu, Y., Yang, H., Zhou, G., et al. (2022). Application of precision-cut lung slices as an *in vitro* model for research of inflammatory respiratory diseases. *Bioeng. (Basel)* 9 (12), 767. PMID: 36550973; PMCID: PMC9774555. doi:10.3390/bioengineering9120767

Ma, B., Sanderson, M., and Bates, J. H. (2013). Airway-parenchymal interdependence in the lung slice. *Respir. Physiol. Neurobiol.* 185 (2), 211–216. Epub 2012 Nov 2. PMID: 23128069; PMCID: PMC3529993. doi:10.1016/j.resp.2012.10.015

Martin, C., Göggel, R., Dal Piaz, V., Vergelli, C., Giovannoni, P., Ernst, M., et al. (2002). Airway relaxant and anti-inflammatory properties of a PDE4 inhibitor with low affinity for the high-affinity rolipram binding site. *Naunyn Schmiedeb. Arch. Pharmacol.* 365 (4), 284–289. Epub 2002 Feb 27. PMID: 11919652. doi:10.1007/s00210-001-0525-7

Martin, C., Uhlig, S., and Ullrich, V. (1996). Videomicroscopy of methacholine-induced contraction of individual airways in precision-cut lung slices. *Eur. Respir. J.* 9 (12), 2479–2487. doi:10.1183/09031936.96.09122479

Martin, C., Ullrich, V., and Uhlig, S. (2000). Effects of the thromboxane receptor agonist U46619 and endothelin-1 on large and small airways. *Eur. Respir. J.* 16 (2), 316–323. doi:10.1034/j.1399-3003.2000.16b21.x

Mercer, P. F., Woodcock, H. V., Eley, J. D., Platé, M., Sulikowski, M. G., Durrenberger, P. F., et al. (2016). Exploration of a potent PI3 kinase/mTOR inhibitor as a novel anti-fibrotic agent in IPF. *Thorax* 71 (8), 701–711. Epub 2016 Apr 21. PMID: 27103349; PMCID: PMC4975851. doi:10.1136/thoraxjnl-2015-207429

Milara, J., Ballester, B., Morell, A., Ortiz, J. L., Escrivá, J., Fernández, E., et al. (2018). JAK2 mediates lung fibrosis, pulmonary vascular remodelling and hypertension in idiopathic pulmonary fibrosis: An experimental study. *Thorax* 73 (6), 519–529. Epub 2018 Feb 10. PMID: 29440315. doi:10.1136/thoraxjnl-2017-210728

Milara, J., Gabarda, E., Juan, G., Ortiz, J. L., Guijarro, R., Martorell, M., et al. (2012). Bosentan inhibits cigarette smoke-induced endothelin receptor expression in pulmonary arteries. *Eur. Respir. J.* 39 (4), 927–938. Epub 2011 Aug 4. PMID: 21828025. doi:10.1183/09031936.00021411

Moreno, L., Perez-Vizcaino, F., Harrington, L., Faro, R., Sturton, G., Barnes, P. J., et al. (2006). Pharmacology of airways and vessels in lung slices *in situ*: Role of endogenous dilator hormones. *Respir. Res.* 7 (1), 111. PMID: 16923180; PMCID: PMC1592489. doi:10.1186/1465-9921-7-111

Narvaez, M. C. M., Hu, Q., Ansari, M., Angelidis, I., Stoleriu, G., Hilgendorff, A., et al. (2022). An *ex vivo* model of cellular senescence and inflammaging in precision-cut lung slices. *ERJ Open Res.* 8, 162. doi:10.1183/23120541.LSC-2022.162

Niehof, M., Hildebrandt, T., Danov, O., Arndt, K., Koschmann, J., Dahlmann, F., et al. (2017). RNA isolation from precision-cut lung slices (PCLS) from different species. *BMC Res. Notes* 10 (1), 121. PMID: 28274266; PMCID: PMC5343379. doi:10.1186/s13104-017-2447-6

Niehof, M., Reamon-Buettner, S. M., Danov, O., Hansen, T., and Sewald, K. (2021). A modified protocol for successful miRNA profiling in human precision-cut lung slices (PCLS). *BMC Res. Notes* 14 (1), 255. PMID: 34215333; PMCID: PMC8252208. doi:10.1186/s13104-021-05674-w

Nußbaum, S. M., Krabbe, J., Böll, S., Babendreyer, A., and Martin, C. (2022). Functional changes in long-term incubated rat precision-cut lung slices. *Respir. Res.* 23 (1), 261. PMID: 36127699; PMCID: PMC9490993. doi:10.1186/s12931-022-02169-5

Paddenberg, R., König, P., Faulhammer, P., Goldenberg, A., Pfeil, U., and Kummer, W. (2006). Hypoxic vasoconstriction of partial muscular intra-acinar pulmonary arteries in murine precision cut lung slices. *Respir. Res.* 7 (1), 93. PMID: 16808843; PMCID: PMC1524949. doi:10.1186/1465-9921-7-93

Paddenberg, R., Mermer, P., Goldenberg, A., and Kummer, W. (2014). Videomorphometric analysis of hypoxic pulmonary vasoconstriction of intra-pulmonary arteries using murine precision cut lung slices. *J. Vis. Exp.* 14 (83), e50970. PMID: 24458260; PMCID: PMC4089409. doi:10.3791/50970

Patel, V., Amin, K., Allen, D., Ukishima, L., Wahab, A., Grodi, C., et al. (2021). Comparison of long-term human precision-cut lung slice culture methodology and response to challenge: An argument for standardisation. *Altern. Lab. Anim.* 49 (5), 209–222. PMID: 34836458. doi:10.1177/02611929211061884

Perez, J. F., and Sanderson, M. J. (2005a). The contraction of smooth muscle cells of intrapulmonary arterioles is determined by the frequency of Ca2+ oscillations induced by 5-HT and KCl. *J. Gen. Physiol.* 125 (6), 555–567. PMID: 15928402; PMCID: PMC2234075. doi:10.1085/jgp.200409217

Perez, J. F., and Sanderson, M. J. (2005b). The frequency of calcium oscillations induced by 5-HT, ACH, and KCl determine the contraction of smooth muscle cells of intrapulmonary bronchioles. *J. Gen. Physiol.* 125 (6), 535–553. PMID: 15928401; PMCID: PMC2234076. doi:10.1085/jgp.200409216

Perez-Zoghbi, J. F., Bai, Y., and Sanderson, M. J. (2010). Nitric oxide induces airway smooth muscle cell relaxation by decreasing the frequency of agonist-induced Ca2+ oscillations. *J. Gen. Physiol.* 135 (3), 247–259. PMID: 20176853; PMCID: PMC2828908. doi:10.1085/jgp.200910365

Perez-Zoghbi, J. F., and Sanderson, M. .J. (2007). Endothelin-induced contraction of bronchiole and pulmonary arteriole smooth muscle cells is regulated by intracellular Ca2+ oscillations and Ca2+ sensitization. *Am. J. Physiol. Lung Cell Mol. Physiol.* 293 (4), L1000–L1011. Epub 2007 Jul 6. PMID: 17616645. doi:10.1152/ajplung.00184.2007

Pieretti, A. .C., Ahmed, A. M., Roberts, J. D., Jr, and Kelleher, C. .M. (2014). A novel *in vitro* model to study alveologenesis. *Am. J. Respir. Cell Mol. Biol.* 50 (2), 459–469. PMID: 24066869; PMCID: PMC3930945. doi:10.1165/rcmb.2013-0056OC

Placke, M. E., and Fisher, G. L. (1987). Adult peripheral lung organ culture-a model for respiratory tract toxicology. *Toxicol. Appl. Pharmacol.* 90 (2), 284–298. doi:10.1016/0041-008x(87)90336-x

Preuß, E. .B., Schubert, S., Werlein, C., Stark, H., Braubach, P., Höfer, A., et al. (2022). The challenge of long-term cultivation of human precision-cut lung slices. *Am. J. Pathol.* 192 (2), 239–253. Epub 2021 Nov 10. PMID: 34767811; PMCID: PMC8891143. doi:10.1016/j.ajpath.2021.10.020

Prihandoko, R., Kaur, D., Wiegman, C. .H., Alvarez-Curto, E., Donovan, C., Chachi, L., et al. (2020). Pathophysiological regulation of lung function by the free fatty acid receptor FFA4. *Sci. Transl. Med.* 12 (557), eaaw9009. PMID: 32817367. doi:10.1126/scitranslmed.aaw9009

Ragionieri, L., Scalera, E., Zoboli, M., Ciccimarra, R., Petracco, G., Gazza, F., et al. (2023). Preterm rabbit-derived precision cut lung slices as alternative model of bronchopulmonary dysplasia in preclinical study: A morphological fine-tuning approach. *Ann. Anat.* 246, 152039. Epub 2022 Nov 24. PMID: 36436720. doi:10.1016/j.aanat.2022.152039

Ram-Mohan, S., Bai, Y., Schaible, N., Ehrlicher, A. J., Cook, D. P., Suki, B., et al. (2020). Tissue traction microscopy to quantify muscle contraction within precision-cut lung slices. *Am. J. Physiol. Lung Cell Mol. Physiol.* 318 (2), L323–L330. Epub 2019 Nov 27. PMID: 31774304; PMCID: PMC7052683. doi:10.1152/ajplung.00297.2019

Ressmeyer, A. R., Bai, Y., Delmotte, P., Uy, K. F., Thistlethwaite, P., Fraire, A., et al. (2010). Human airway contraction and formoterol-induced relaxation is determined by Ca2+ oscillations and Ca2+ sensitivity. *Am. J. Respir. Cell Mol. Biol.* 43 (2), 179–191. Epub 2009 Sep 18. PMID: 19767449; PMCID: PMC2937231. doi:10.1165/rcmb.2009-0222OC

Ressmeyer, A. R., Larsson, A. K., Vollmer, E., Dahlèn, S. E., Uhlig, S., and Martin, C. (2006). Characterisation of Guinea pig precision-cut lung slices: Comparison with human tissues. *Eur. Respir. J.* 28 (3), 603–611. Epub 2006 May 31. PMID: 16737991. doi:10.1183/09031936.06.00004206

Richter, W., Jin, S. L., and Conti, M. (2005). Splice variants of the cyclic nucleotide phosphodiesterase PDE4D are differentially expressed and regulated in rat tissue. *Biochem. J.* 388 (3), 803–811. PMID: 15717866; PMCID: PMC1183459. doi:10.1042/BJ20050030

Rieg, A. D., Rossaint, R., Uhlig, S., and Martin, C. (2011). Cardiovascular agents affect the tone of pulmonary arteries and veins in precision-cut lung slices. *PLoS One* 6 (12), e29698. Epub 2011 Dec 27. PMID: 22216346; PMCID: PMC3246495. doi:10.1371/journal.pone.0029698

Rosales Gerpe, M. C., van Vloten, J. P., Santry, L. A., de Jong, J., Mould, R. C., Pelin, A., et al. (2018). Use of precision-cut lung slices as an *ex vivo* tool for evaluating viruses and viral vectors for gene and oncolytic therapy. *Mol. Ther. Methods Clin. Dev.* 10, 245–256. PMID: 30112421; PMCID: PMC6092314. doi:10.1016/j.omtm.2018.07.010

Rosner, S. R., Ram-Mohan, S., Paez-Cortez, J. R., Lavoie, T. L., Dowell, M. L., Yuan, L., et al. (2014). Airway contractility in the precision-cut lung slice after cryopreservation. *Am. J. Respir. Cell Mol. Biol.* 50 (5), 876–81. PMID: 24313705; PMCID: PMC4068941. doi:10.1165/rcmb.2013-0166MA

Royce, S. G., Nold, M. F., Bui, C., Donovan, C., Lam, M., Lamanna, E., et al. (2016). Airway remodeling and hyperreactivity in a model of bronchopulmonary dysplasia and their modulation by IL-1 receptor antagonist. *Am. J. Respir. Cell Mol. Biol.* 55 (6), 858–868. PMID: 27482635. doi:10.1165/rcmb.2016-0031OC

Ruigrok, M. J. R., Xian, J. L., Frijlink, H. W., Melgert, B. N., Hinrichs, W. L. J., and Olinga, P. (2018). siRNA-mediated protein knockdown in precision-cut lung slices. *Eur. J. Pharm. Biopharm.* 133, 339–348. Epub 2018 Nov 7. PMID: 30414498. doi:10.1016/j.ejpb.2018.11.005

Sanderson, M. J. (2011). Exploring lung physiology in health and disease with lung slices. *Pulm. Pharmacol. Ther.* 24 (5), 452–465. Epub 2011 May 12. PMID: 21600999; PMCID: PMC3168687. doi:10.1016/j.pupt.2011.05.001

Seehase, S., Schlepütz, M., Switalla, S., Mätz-Rensing, K., Kaup, F. J., Zöller, M., et al. (2011). Bronchoconstriction in nonhuman primates: A species comparison. *J. Appl. Physiol. (1985)* 111 (3), 791–798. Epub 2011 Jun 23. PMID: 21700889. doi:10.1152/japplphysiol.00162.2011

Sewald, K., and Danov, O. (2022). Infection of human precision-cut lung slices with the influenza virus. *Methods Mol. Biol.* 2506, 119–134. PMID: 35771468. doi:10.1007/978-1-0716-2364-0_9

Sharma, P., Yi, R., Nayak, A. P., Wang, N., Tang, F., Knight, M. J., et al. (2017). Bitter taste receptor agonists mitigate features of allergic asthma in mice. *Sci. Rep.* 7, 46166. PMID: 28397820; PMCID: PMC5387415. doi:10.1038/srep46166

Shi, W., Wang, C. G., Dandurand, R. J., Eidelman, D. H., and Michel, R. P. (1998). Differential responses of pulmonary arteries and veins to histamine and 5-HT in lung explants of Guinea-pigs. *Br. J. Pharmacol.* 123 (8), 1525–1532. PMID: 9605557; PMCID: PMC1565318. doi:10.1038/sj.bjp.0701759

Stegmayr, J., Alsafadi, H. N., Langwiński, W., Niroomand, A., Lindstedt, S., Leigh, N. D., et al. (2021). Isolation of high-yield and -quality RNA from human precision-cut lung slices for RNA-sequencing and computational integration with larger patient cohorts. *Am. J. Physiol. Lung Cell Mol. Physiol.* 320 (2), L232–L240. Epub 2020 Oct 28. PMID: 33112185. doi:10.1152/ajplung.00401.2020

Sturton, R. G., Trifilieff, A., Nicholson, A. G., and Barnes, P. J. (2008). Pharmacological characterization of indacaterol, a novel once daily inhaled 2 adrenoceptor agonist, on small airways in human and rat precision-cut lung slices. *J. Pharmacol. Exp. Ther.* 324 (1), 270–275. Epub 2007 Oct 4. PMID: 17916760. doi:10.1124/jpet.107.129296

Tan, X., and Sanderson, M. J. (2014). Bitter tasting compounds dilate airways by inhibiting airway smooth muscle calcium oscillations and calcium sensitivity. *Br. J. Pharmacol.* 171 (3), 646–662. PMID: 24117140; PMCID: PMC3969078. doi:10.1111/bph.12460

Tatler, A. L., Barnes, J., Habgood, A., Goodwin, A., McAnulty, R. J., and Jenkins, G. (2016). Caffeine inhibits TGFβ activation in epithelial cells, interrupts fibroblast responses to TGFβ, and reduces established fibrosis in *ex vivo* precision-cut lung slices. *Thorax* 71 (6), 565–567. Epub 2016 Feb 24. PMID: 26911575; PMCID: PMC4893128. doi:10.1136/thoraxjnl-2015-208215

Temann, A., Golovina, T., Neuhaus, V., Thompson, C., Chichester, J. A., Braun, A., et al. (2017). Evaluation of inflammatory and immune responses in long-term cultured human precision-cut lung slices. *Hum. Vaccin Immunother.* 13 (2), 351–358. PMID: 27929748; PMCID: PMC5328235. doi:10.1080/21645515.2017.1264794

Tigges, J., Eggerbauer, F., Worek, F., Thiermann, H., Rauen, U., and Wille, T. (2021). Optimization of long-term cold storage of rat precision-cut lung slices with a tissue preservation solution. *Am. J. Physiol. Lung Cell Mol. Physiol.* 321 (6), L1023–L1035. Epub 2021 Oct 13. PMID: 34643087. doi:10.1152/ajplung.00076.2021

Vander Top, E. A., Wyatt, T. A., and Gentry-Nielsen, M. J. (2005). Smoke exposure exacerbates an ethanol-induced defect in mucociliary clearance of Streptococcus pneumoniae. *Alcohol Clin. Exp. Res.* 29 (5), 882–887. PMID: 15897734; PMCID: PMC1224709. doi:10.1097/01.alc.0000164364.35682.86

Viana, F., O'Kane, C. M., and Schroeder, G. N. (2022). Precision-cut lung slices: A powerful *ex vivo* model to investigate respiratory infectious diseases. *Mol. Microbiol.* 117 (3), 578–588. Epub 2021 Oct 31. PMID: 34570407; PMCID: PMC9298270. doi:10.1111/mmi.14817

Vietmeier, J., Niedorf, F., Bäumer, W., Martin, C., Deegen, E., Ohnesorge, B., et al. (2007). Reactivity of equine airways-a study on precision-cut lung slices. *Vet. Res. Commun.* 31 (5), 611–619. Epub 2007 Jan 24. PMID: 17252319. doi:10.1007/s11259-007-3501-y

Wang, S., Xie, Y., Huo, Y. W., Li, Y., Abel, P. W., Jiang, H., et al. (2020). Airway relaxation mechanisms and structural basis of osthole for improving lung function in asthma. *Sci. Signal* 13 (659), eaax0273. PMID: 33234690; PMCID: PMC8720283. doi:10.1126/scisignal.aax0273

Ward, J. E., Fernandes, D. J., Taylor, C. C., Bonacci, J. .V., Quan, L., and Stewart, A. G. (2006). The PPARgamma ligand, rosiglitazone, reduces airways hyperresponsiveness in a murine model of allergen-induced inflammation. *Pulm. Pharmacol. Ther.* 19 (1), 39–46. Epub 2005 Apr 25. PMID: 16286236. doi:10.1016/j.pupt.2005.02.005

Watson, C. Y., Damiani, F., Ram-Mohan, S., Rodrigues, S., de Moura Queiroz, P., Donaghey, T. C., et al. (2016). Screening for chemical toxicity using cryopreserved precision cut lung slices. *Toxicol. Sci.* 150 (1), 225–233. Epub 2015 Dec 29. PMID: 26719368; PMCID: PMC5009619. doi:10.1093/toxsci/kfv320

Wei, Y., Dong, W., Jackson, J., Ho, T. C., Le Saux, C. J., Brumwell, A., et al. (2021). Blocking LOXL2 and TGFβ1 signalling induces collagen I turnover in precision-cut lung slices derived from patients with idiopathic pulmonary fibrosis. *Thorax* 76 (7), 729–732. Epub 2021 Jan 20. PMID: 33472968; PMCID: PMC8222054. doi:10.1136/thoraxjnl-2020-215745

Winters, N. I., Taylor, C. J., Jetter, C. S., Camarata, J. E., Gutierrez, A. J., Bui, L. T., et al. (2021). Single-cell transcriptomic assessment of cellular phenotype stability in human precision-cut lung slices. Available at: https://www.biorxiv.org/content/10.1101/2021.08.19.457016v1 (Accessed August 19, 2021)

Wohlsen, A., Martin, C., Vollmer, E., Branscheid, D., Magnussen, H., Becker, W. M., et al. (2003). The early allergic response in small airways of human precision-cut lung slices. *Eur. Respir. J.* 21 (6), 1024–1032. doi:10.1183/09031936.03.00027502

Wright, J. L., and Churg, A. (2008). Short-term exposure to cigarette smoke induces endothelial dysfunction in small intrapulmonary arteries: Analysis using Guinea pig precision cut lung slices. *J. Appl. Physiol. (1985)* 104 (5), 1462–1469. Epub 2008 Mar 20. PMID: 18356485. doi:10.1152/japplphysiol.00520.2007

Wu, X., van Dijk, E. M., Bos, I. S. T., Kistemaker, L. E. M., and Gosens, R. (2019). Mouse lung tissue slice culture. *Methods Mol. Biol.* 1940, 297–311. PMID: 30788834. doi:10.1007/978-1-4939-9086-3_21

Wyatt, T. A., Sisson, J. H., Allen-Gipson, D. S., McCaskill, M. L., Boten, J. A., DeVasure, J. M., et al. (2012). Co-exposure to cigarette smoke and alcohol decreases airway epithelial cell cilia beating in a protein kinase Cε-dependent manner. *Am. J. Pathol.* 181 (2), 431–440. Epub 2012 Jun 5. PMID: 22677421; PMCID: PMC3409441. doi:10.1016/j.ajpath.2012.04.022

Yarova, P. L., Stewart, A. L., Sathish, V., Britt, R. D., Jr, Thompson, M. A., Lowe, A. P. P., et al. (2015). Calcium-sensing receptor antagonists abrogate airway hyperresponsiveness and inflammation in allergic asthma. *Sci. Transl. Med.* 7 (284), 284ra60. Epub 2015 Apr 22. PMID: 25904744; PMCID: PMC4725057. Fyarova. doi:10.1126/scitranslmed.aaa0282

Yilmaz, Y., Williams, G., Walles, M., Manevski, N., Krähenbühl, S., and Camenisch, G. (2019). Comparison of rat and human pulmonary metabolism using precision-cut lung slices (PCLS). *Drug Metab. Lett.* 13 (1), 53–63. doi:10.2174/1872312812666181022114622

Yocum, G. T., Perez-Zoghbi, J. F., Danielsson, J., Kuforiji, A. S., Zhang, Y., Li, G., et al. (2019). A novel $GABA_A$ receptor ligand MIDD0301 with limited blood-brain barrier penetration relaxes airway smooth muscle *ex vivo* and *in vivo*. *Am. J. Physiol. Lung Cell Mol. Physiol.* 316 (2), L385–L390. Epub 2018 Nov 29. PMID: 30489155; PMCID: PMC6397346. doi:10.1152/ajplung.00356.2018

frontiers | Frontiers in Pharmacology

TYPE Original Research
PUBLISHED 05 September 2023
DOI 10.3389/fphar.2023.1192798

OPEN ACCESS

EDITED BY
Corrado Pelaia,
Magna Græcia University, Italy

REVIEWED BY
Cheng-Yu Wu,
Cardio Pulmonary Institute (CPI), Germany
Jin-Ah Park,
Harvard University, United States

*CORRESPONDENCE
Rebecca L. Heise,
rlheise@vcu.edu

RECEIVED 23 March 2023
ACCEPTED 09 August 2023
PUBLISHED 05 September 2023

CITATION
Link PA, Farkas L and Heise RL (2023), Using extracellular matrix derived from sugen-chronic hypoxia lung tissue to study pulmonary arterial hypertension. *Front. Pharmacol.* 14:1192798. doi: 10.3389/fphar.2023.1192798

Using extracellular matrix derived from sugen-chronic hypoxia lung tissue to study pulmonary arterial hypertension

Patrick A. Link[1], Laszlo Farkas[2] and Rebecca L. Heise[1]*

[1]Department of Biomedical Engineering, Virginia Commonwealth University, Richmond, VA, United States, [2]Division of Pulmonary, Critical Care and Sleep Medicine, Department of Internal Medicine, Davis Heart and Lung Research Institute, College of Medicine, The Ohio State University Wexner Medical Center, Columbus, OH, United States

Pulmonary arterial hypertension has characteristic changes to the mechanical environment, extracellular matrix, and cellular proliferation. In order to develop a culture system to investigate extracellular matrix (ECM) compositional-dependent changes in pulmonary arterial hypertension, we decellularized and characterized protein and lipid profiles from healthy and Sugen-Chronic Hypoxia rat lungs. Significant changes in lipid profiles were observed in intact Sugen-Hypoxia lungs compared with healthy controls. Decellularized lung matrix retained lipids in measurable quantities in both healthy and Sugen-Chronic Hypoxia samples. Proteomics revealed significantly changed proteins associated with pulmonary arterial hypertension in the decellularized Sugen-Chronic Hypoxia lung ECM. We then investigated the potential role of healthy vs. Sugen-Chronic Hypoxia ECM with controlled substrate stiffness to determine if the ECM composition regulated endothelial cell morphology and phenotype. CD117+ rat lung endothelial cell clones were plated on the variable stiffness gels and cellular proliferation, morphology, and gene expression were quantified. Sugen-Chronic Hypoxia ECM on healthy stiffness gels produced significant changes in cellular gene expression levels of Bmp2, Col1α1, Col3α1 and Fn1. The signaling and cell morphology observed at low substrate stiffness suggests early changes to the ECM composition can initiate processes associated with disease progression. These data suggest that Sugen-Chronic Hypoxia ECM can be used to investigate cell-ECM interactions relevant to pulmonary arterial hypertension.

KEYWORDS

pulmonary arterial hypertension, substrate stiffness, ECM, angiogenesis, decellularization

1 Introduction

In Pulmonary Arterial Hypertension (PAH), many factors contribute to the progressive and irreversible nature of the disease including altered mechanical environment, increased extracellular matrix (ECM) deposition, apoptosis, proliferation, and cellular contraction (Stenmark et al., 2016; Karki and Birukova, 2018; Wang et al., 2019). Many groups have shown a role for ECM on disease progression in other lung diseases (Loessner et al., 2010; Booth et al., 2012; Sokocevic et al., 2013; Scarritt et al., 2014; Wagner et al., 2014; Sava et al., 2017). One strategy to study the contribution of the ECM to hypertensive disease progression used decellularized rat lungs seeded with naïve mesenchymal stem cells to show a

persistence of the hypertensive phenotype in rat models (Scarritt et al., 2014). However, this study did not identify the contribution of the ECM versus the mechanical environment alone to the persistence of the hypertensive hallmarks.

Extracellular matrix (ECM) is all the macromolecules present outside of the cell. These molecules can be lipids, proteins, glycoproteins, and polysaccharides. The ECM provides structural support for cells, allowing cells to attach, preventing cell movement, or providing a track to promote migration. The ECM is also a primary source of signal initiation. ECM can bind and release growth factors, transmit mechanical signaling forces through integrins, or begin signaling pathways using fragments of broken down ECM (Lu et al., 2012). Macromolecules, like fibronectin, collagen, tenascin-c, and sphingosine-1 phosphate generally increase in PAH (Bu et al., 2008; Jia et al., 2017). In PAH, the changes in ECM lead to changes in the structural micro-niches. Such structural changes often come with characteristic changes to the mechanical properties: more collagen leads generally to increased stiffness. However, groups have not decoupled the experiments to determine if compositional make-up can alter cellular phenotype independent of mechanical changes.

Elucidating the composition-induced effects on cellular behavior in lung diseases like PAH are critically important. To date, no one knows whether ECM composition alone is capable of inducing cellular disfunction in PAH. However, cytokines and hormone have half-lives on the order of minutes to hours, whereas proteins have half-lives on the order of days (Rahman and Sadygov, 2017). Furthermore, most ECM studies consider only the structural components of the ECM like collagen or elastin rather than other bound signaling components within the matrix like sphingolipids. Sphingolipids are known to play both pro- and anti-inflammatory roles in atherosclerosis (Piccoli et al., 2023) and PAH (Chen et al., 2014). Both structural and signaling components of ECM arecritical to consider when studying to disease progression. As an initial model for investigating diseased ECM–cell interactions in PAH, we test ECM composition independent of substrate stiffness to identify the role each plays in progressing endothelial cell disease phenotype. We hypothesize that incorporating diseased ECM composition from Sugen-Chronic Hypoxia (Su/CHx) rats into mechanical experiments is capable of producing the endothelial cell phenotype of disease.

2 Materials and methods

2.1 Decellularizing lung tissue

We decellularized lung tissue based on the same procedure described in (Link et al., 2017). We obtained healthy and Su/CHx left lung lobes from rats from a prior study (Bhagwani et al., 2019). We carefully dissected away large airways and vessels and then minced the distal lung tissue into small pieces to maximize the surface area for decellularization while minimizing the diffusion distance. We rinsed the tissue three times with PBS between each step. We submerged the lung tissue in 0.1% Triton X-100 solution for 24 h at 4°C, followed by 2% sodium deoxycholate for 24 h at 4°C. We drew the sodium deoxycholate out of the tissue by submerging the tissue in filtered NaCl solution for 1 h at 4°C. We removed the NaCl from the tissue with three rinses of ultrapure water (UPW). Then to remove the DNA, we submerged the tissue in filtered DNase solution for 1 h at 4°C, followed by three rinses with 1x PBS.

After decellularization, we lyophilized and cryomilled the tissue, to form a powder. We acid digested 10 mg of the powder in 1 mL of 0.01 M HCl with 1 mg of pepsin, under constant agitation, at room temperature for 4 h. We neutralized the acid with 0.1 M NaOH at a 1:10 ratio, and stored the solution at −80°C.

2.2 Protein differences in diseased ECM

After decellularization, before lyophilization, we took intact and decellularized tissues for quantitative mass spectrometry. We placed approximately 10 mg of tissue with PBS into a BeadBug tissue homogenizer. The tissue was homogenized three times for 30 s each time, vortexing in between homogenization. 100 mM ammonium bicarbonate containing a Rapigest concentration of 0.1%, 5 mL of 10 mM dithiothreitol in 0.1 M ammonium bicarbonate were added at room temperature for 0.5 h. Then 5 mL 50 mM iodoacetamide in 0.1 M ammonium bicarbonate was added at room temperature for 0.5 h. The samples were digested with 1 mg trypsin twice overnight and then quenched with 5% (v:v) glacial acetic acid. Each sample was analyzed in triplicate.

The samples were analyzed by a Waters Synapt G2Si mass spectrometer system with a nanospray ion source interfaced to a Waters M-Class C18 reversed-phase capillary column. Peptides were eluted using acetonitrile/0.1% formic acid gradient, with lockspray compound at a ow rate of 0.4 mL/min at 3.5 kV.

The data were analyzed by database searching using the PLGS search algorithm against the NCBIs rat database. Relative quantification was performed using the Progenesis program.

2.3 Sphingolipid differences in diseased ECM

To quantify differences in lipid content we used intact tissue and decellularized tissue. For the decellularized tissue, after decellularization, before lyophilization, we took intact and decellularized tissues for quantitative mass spectrometry. We placed approximately 10 mg of snap frozen tissue from each lung sample into a cryogrinder. Lipid levels were evaluated in the lung tissue by reverse-phase high-performance liquid chromatography separation, negative-ion electrospray ionization, and tandem mass spectrometry analysis, as previously described (Hait et al., 2009).

2.4 Cell culture and ECM stiffness experiments

Healthy and diseased ECM covalently bonded to 1 kilopascal (kPa) and 20 kPa polyacrylamide gels (PAGs) overnight. This established two expected environments 1 kPa +healthy ECM and

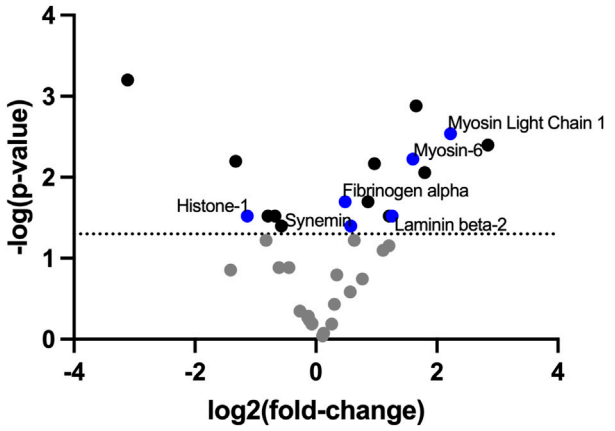

FIGURE 1
ECM decellularized from Su/CHx maintains significant differences compared to healthy tissue. Fold change presented as Su/CHx over healthy. Data points are averaged from three independent biological replicates (n = 3) in each group.

20 kPa +Su/CHx ECM, and two unusual environments 1 kPa +Su/CHx ECM and 20 kPa +healthy ECM. To determine if the results could be due to ECM protein adherence to the PAG, we quantified protein adsorption using a BCA (Pierce) assay.

CD117+ endothelial cell (EC) clones were isolated and cultured as previously published (Farkas et al., 2019). We added 20,000 CD117+ EC/cm^2 (Bhagwani et al., 2019; Farkas et al., 2019) to the PAGs and allowed them to attach for 24 h. After 24 h, we changed the media until the timepoint indicated. To quantify proliferation, we used cell counting kit-8 (CCK-8; Dojindo) according to manufacturer's directions.

2.5 Phenotype shifts measured through qPCR mRNA quantification

In brief, mRNA was isolated using a Qiagen mRNeasy kit protocol. Before converting to cDNA using iScript (BioRad) we balanced the mRNA to 25 ng/mL. Then we combined 4 mL cDNA with a mastermix consisting of individual forward and reverse primers (Supplementary Table S1), and SYBR green in a PCR plate. We covered the plate, placed it on a plate shaker for 2 min and centrifuged at 1,200 RPM for 2 min. To run qPCR, we placed the plate on a CFX Connect Real-Time System (BioRad) for thermocycling. We set the cycles to 95°C for 15 s, 58°C for 30 s, and then 72°C for 15 s to promote denaturing, primer annealing, and extension, respectively.

2.6 Statistics

Statistical analyses are reported in the figure captions. We determined statistical significance at p <0.05, using GraphPad Prism version 10.0.0 for Windows, GraphPad Software, Boston, Massachusetts USA, www.graphpad.com. All experiments were performed in n ≥3 experiments with technical replicates unless otherwise noted in the figure caption. Data presented mean ± SEM.

3 Results

3.1 Compositional differences in diseased ECM

To identify the ECM compositional changes which occur in PAH, we performed mass spectrometry on decellularized healthy and Su/CHx lung tissue. Many proteins and lipids differences found through mass spectrometry of PAH lungs were also present in our Su/CHx tissue (Figure 1; Supplementary Table S2). In similar fold changes to our results, Myosin light chain, Myosin-6, Laminin Beta-2, Synemin, Fibrinogen α, Histone-1 have been shown upregulated in PAH as well (Suntharalingam et al., 2008; Huang et al., 2018). In comparing intact tissue to decellularized Su/CHx tissue, we found increased the presence of Laminin C and Protein RGD, and further increased the presence of Myosin-6 and Keratin-78, but decreased the presence of β-actin, which was increased in the intact Su/CHx tissue (Supplementary Table S3). Combined these intracellular and extracellular protein changes may provide clues to ECM compositional changes which continue to progress cellular disease phenotype.

Decellularization is meant to remove lipids, specifically cellular membranes from tissue. However, lipids have been shown to play a role in PAH. S1P-induced a TGF-ß-like fibrosis but could be limited by Dihydrosphingosine-1 phosphate (Bu et al., 2008). Lipid analysis of intact healthy and Su/CHx tissues shows increased sphingosine, dihydrosphingosine, sphingosine-1 phosphate (S1P), dihydrosphingosine-1 phosphate (dHS1P), and ceramides with minimal changes to other lipids (Figure 2A). As expected, decellularization removes many of those lipids (Figure 2B), but the overall trend of differences was similar in decellularized Su/CHx vs. healthy lungs.

3.2 Decellularized protein solution as an *in vitro* coating

We first wanted to make sure that inherent differences between collagen, healthy ECM, and Su/CHx ECM did not have baseline differences as a coating, which could possibly affect cellular attachment and therefore cell behavior. To accomplish this, we first quantified how much protein adsorbed to the PAG. We added ECM to non-tissue treated plates overnight, rinsed twice with PBS, and then performed a BCA analysis on the adsorbed protein (Figure 3A). There was no significant difference in adsorbed protein between collagen, healthy ECM, and Su/CHx ECM coatings. We used a concentration of 0.05 mg/mL for all protein coatings because 0.05 mg/mL was shown to be the optimal concentration for cell attachment and proliferation (Zhang et al., 2009). Coating tissue culture plastic (TCP) and PAGs with 0.05 mg/mL protein produced similar coating efficacy compared to collagen on the same surface (Figure 3B).

3.3 CD117+ EC response to diseased ECM

3.3.1 Cell proliferation and morphology on different ECMs

To determine if our results could be due to proliferation, we plated CD117+ ECs on different ECMs on tissue culture plastic

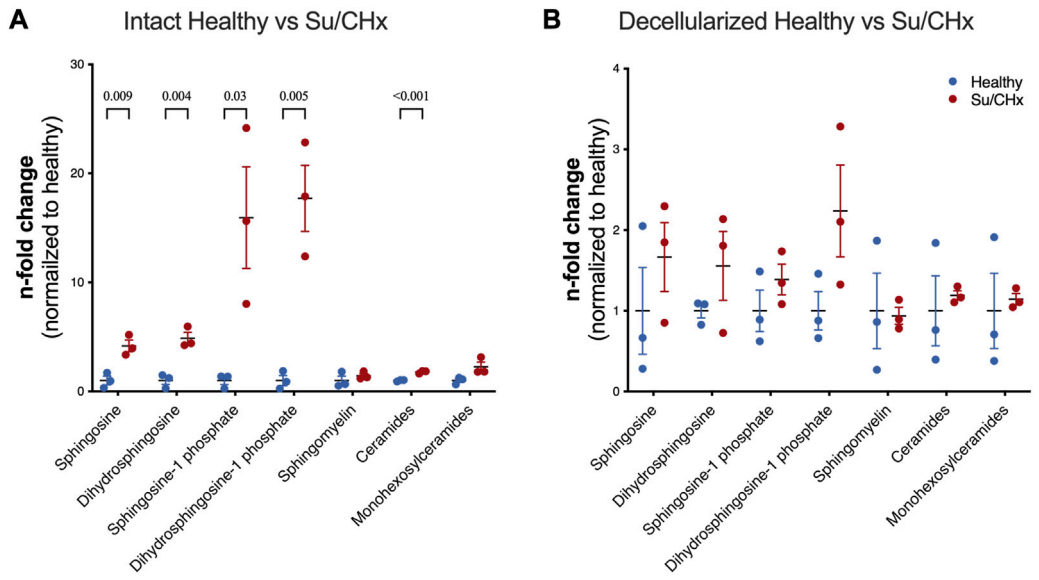

FIGURE 2
Lipids are increased in Su/CHx lung tissue. Differences between healthy and diseased lungs. Subspecies of sphingomyelins, ceramides, and monohexosylceramides have been normalized individually. **(A)** Lipid differences between intact healthy and intact Su/CHx lungs. **(B)** Lipid differences are decreased, but largely retained after decellularization. $N = 3$ from unpaired t-test, p-values line indicates $p < 0.01$, between groups as indicated. Data presented are individual biological replicates (points), mean, and SEM.

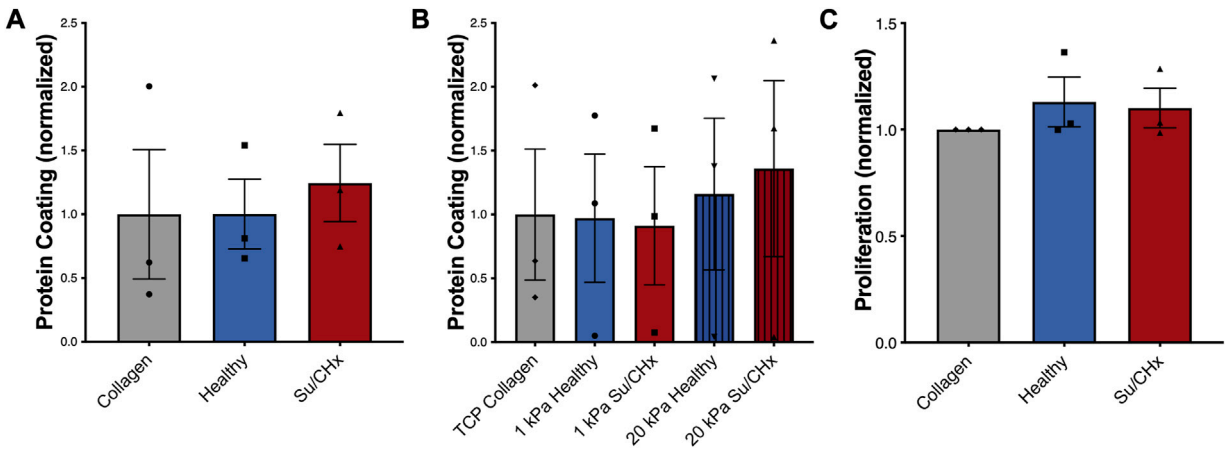

FIGURE 3
Su/CHx ECM does not affect CD117+ ECs proliferation. **(A)** Adsorption of heterogenous ECM protein is similar to collagen coating on TCP. $n = 3$; **(B)** Adsorption of heterogenous ECM protein is slightly increased on 20 kPa PAGs, though no statistically significant changes are observed. ECM coating measured through BCA. $n = 3$; **(C)** CD117+ ECs plated on TCP coated with collagen, healthy matrix, and Su/CHx matrix have statistically similar proliferation (Measured by CCK-8) after 24 h. $N = 3$ bars display mean ± SEM.

and on 1 or 20 kPa poly-acrylamide gels coated with the various ECMs. On TCP, cell proliferation was not significantly different between ECM groups (Figure 3C). Similarly, on different stiffnesses, increased stiffness produced a slight increase in proliferation, but there were no significant differences (Supplementary Figure S1A). The Su/CHx tissue produced a slight decrease in proliferation on both 1 and 20 kPa PAGs, but the differences were not significant.

Cellular morphology demonstrated changes with diseased ECM (Figure 4A). At early timepoints cells attached and appeared to form networks, indicative of vessels. The density of vessels appeared to be greatest in the 1 kPa healthy condition but were not quantified. 72 h after plating, CD117+ ECs plated on Su/CHx ECM were clustering, indicative of both phenotypic changes (Neagu et al., 2010) and vessel instability (Li et al., 2012). These effects may be transitive because most vessels

10.3389/fphar.2023.1192798

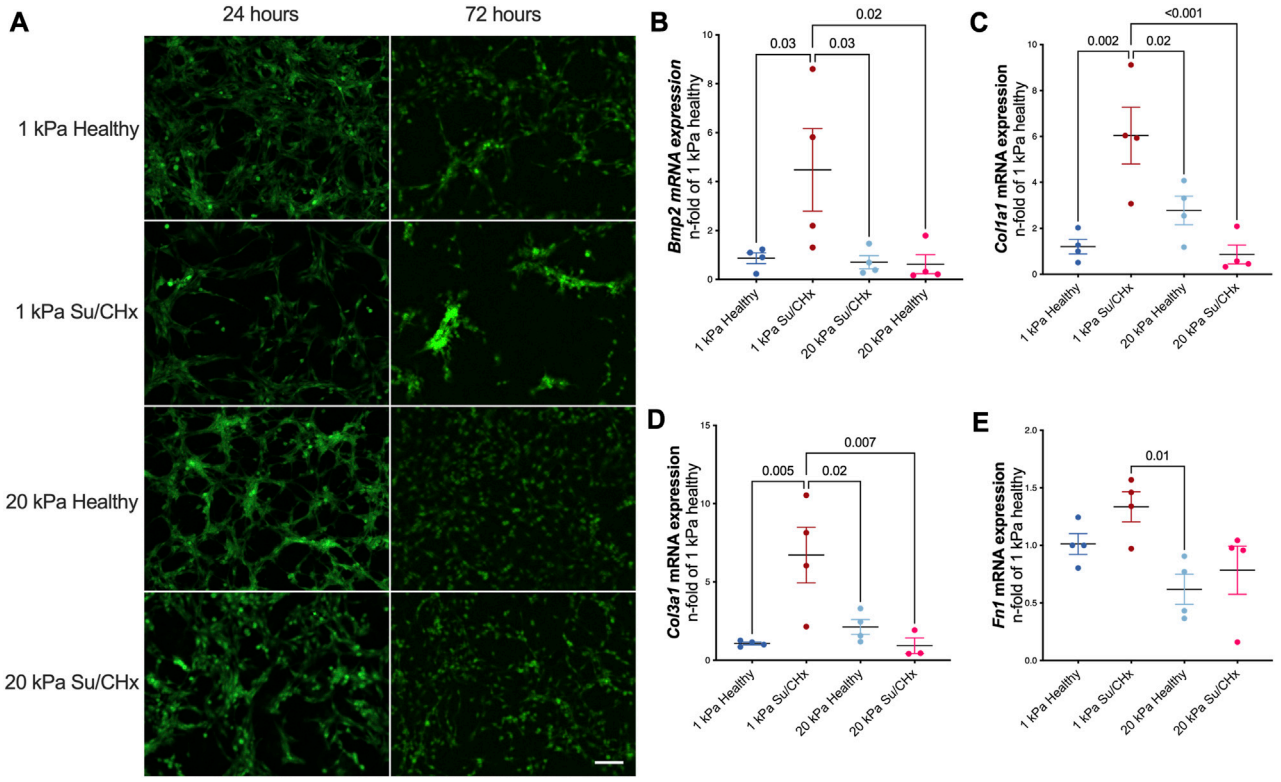

FIGURE 4
Diseased ECM changes tube formation and phenotype. **(A)** GFP positive CD117+ EC were plated on PAG hydrogels coated with healthy and diseased ECM. After 24 h tubules exist in all conditions. After 72 h, tubules are still present on 1 kPa healthy, cells cluster on 1 kPa Su/CHx. 20 kPa with both ECMs have increased proliferation though it appears there may be some tubulogenesis in the 20 kPa Su/CHx group. Scale 100 μm. **(B–E)** CD117+ ECs were added to ECM coated PAGs for 48 h. Changes are normalized to 1 kPa healthy for each gene. **(B)** *Bmp2*|Bone Morphogenic Protein-2; **(C)** *Col1a1*|Collagen type I α1; **(D)** *Col3a1*|Collagen type III α1; **(E)** *Fn1*|Fibronectin 1. Points indicate averaged technical replicates from n = 4 independent experiments. Statistical analysis was performed using a One-Way ANOVA with a Dunnett's *post hoc* test. Data presented are mean ± SEM.

need support cells for stability (Newman et al., 2011; Chatterjee and Naik, 2012). However, CD117+ ECs have been shown to form functional vasculature from a single cell (Fang et al., 2012). On 20 kPa substrates, cells appeared to lose the networked appearance and become more like a monolayer.

3.3.2 Su/CHx ECM alters CD117+ EC phenotype

ECM from Su/CHx lung tissue changes CD117+ ECs phenotype, primarily on healthy substrate stiffnesses. *Bmp2*, *Col1a1*, *Col3a1*, and *Fn1* mRNAs increased after 48 h on 1 kPa Su/CHx ECM (Figures 4B–E). *Bmp2* is expected to increase on softer substrates (Gilde et al., 2016), but we found similar expression levels when plated on healthy ECM of different stiffnesses and increased more on Su/CHx ECM. *Col1a1* and *Col3a1* increases initially on softer substrates with Su/CHx ECM and paradoxically decreases on 20 kPa Su/CHx substrates. We expect that signaling from the Su/CHx matrix indicates to cells that the substrate must be stiffer, increasing collagen production. However, on stiffer substrates, there is already signaling confirming the stiffness and with increased collagen content in the Su/CHx ECM, therefore the 20 kPa Su/CHx ECM group downregulates production of collagen.

4 Discussion

The aim of this study was to investigate whether the composition of the extracellular matrix (ECM) influences cell fate. To achieve this, we decellularized lungs from healthy and pulmonary arterial hypertension (PAH) rat models and digested the matrix to form an ECM coating solution. We then coated healthy and diseased ECM on healthy (1 kPa) and diseased (20 kPa) polyacrylamide substrates and observed the effects on CD117+ clonotype endothelial cells. We found that 24 h after plating, tube formation was similar in all conditions, but only healthy ECM on healthy stiffness retained the appearance of tube formation 72 h after plating. Supplementary Figure S1B shows quantification of the 72 h timepoint. We also observed changes in gene expression 48 h after plating, including pro-angiogenic BMP2 and ECM markers Col1α1 and Col3α1, which may indicate a dysregulated phenotype associated with aberrant angiogenesis in PAH.

Understanding the contribution of ECM composition is crucial since both substrate stiffness and decellularized lung matrix, which combines stiffness and diseased composition, have been shown to influence the disease state (Scarritt et al., 2014; Stenmark et al.,

2016). In addition, individual lipids and ECM proteins have been implicated in the progression and resolution of PAH (Orr et al., 2006; Bu et al., 2008; Gairhe et al., 2016). Our work identified changes in many lipids between intact healthy and diseased tissues, and trends were largely retained upon decellularization, albeit likely considerably decreased after decellularization. We observed trends of increased sphingosine, sphingosine 1 phosphate, dihydrosphingosine 1, and ceramides being retained in ECM at increased levels from Su/CHx ECM that likely altered the cell behavior. Sphingosine 1 phosphate is important in maintaining endothelial cell-cell junctions (Maceyka and Spiegel, 2014) and promoting angiogenesis (Williams et al., 2015; Weigel et al., 2023). Ceramides can also promote barrier dysfunction and apoptosis in endothelium (McVey et al., 2021). Our findings point toward the importance of these lipids in cell-ECM signaling.

The protein changes we identified between decellularized and healthy ECM were largely consistent with other reports of proteomics changes in PAH (Suntharalingam et al., 2008; Huang et al., 2018). Notably, extracellular proteins found in significantly different quantities in the decellularized tissues include Fibrinogen α and Laminin-ß2, both of which have been shown to play a role in PAH or processes associated with PAH. Fibrinogen concentration is associated with PAH and linked to disease severity and decreased barrier integrity (Lominadze et al., 2010; Hennigs et al., 2014). We have previously shown integrin β5, capable of binding to the RGD sequences of ECM proteins, to have a variable role in PAH (Blanchard et al., 2022), which may be explained through different ECM protein signals. Laminin changes occur in vascular remodeling, and altered laminin content may indicate vascular instability (Lugassy et al., 1999). However, many of the identified proteins are intracellular proteins that could act as damage-associated molecular patterns (DAMPs), eliciting an immunogenic response, causing the cellular phenotype shifts we see. We expect a general increase in DAMPs in decellularized tissue, but balancing decellularization methodology to remove cell debris yet retain as much of the native ECM and composition as possible has been shown to be desirable (Badylak, 2014). By retaining the composition, we can begin to investigate the effects of composition on cell phenotypes.

CD117+ endothelial cells have been implicated in the progression of PAH, as demonstrated by previous studies (Farkas et al., 2014; Farkas et al., 2019; Bhagwani et al., 2020). We have previously shown a susceptibility of CD117+ ECs to Endothelial-to-mesenchymal transition (Bhagwani et al., 2020). In this study, we observed that CD117+ ECs expressed higher levels of Col1α1 and Col3α1 in response to diseased ECM on healthy stiffness, suggesting that early changes to the ECM composition may contribute to the aberrant angiogenesis found in PAH. Previous research has shown that hypoxia can increase Col1α1 and Col3α1 expression in cell culture after 7 days (Zhang et al., 2018), and our data supports the notion that these changes may result from early alterations to the ECM composition. Additionally, our previous work has shown that CD117+ ECs expressing high levels of BMP2 form occlusive lesions when exposed to hypoxia (Bhagwani et al., 2019). Therefore, the findings presented in this study may provide insight into an early mechanism for the aberrant angiogenesis observed in PAH.

Our study has some limitations, such as the 2D nature of the experiments, which may not reliably test composition and stiffness on a monolayer. The proliferation of the cells needs to be further examined to take into account the attachment and analysis of the clonality of the CD117+ ECs. The efficacy of chunk decellularization depends on detergent contact time and piece size, so smaller pieces and longer periods in contact with detergents may improve decellularization. However, we believe that our approach retains a good approximation of the ECM composition after decellularization that provides basis for using this method in further study.

In conclusion, we showed that ECM compositional differences in cellular fragments, structural ECM, and lipid families are retained in decellularized lung ECM from Su/CHx rats compared with healthy controls. We also demonstrated the feasibility of examining the ECM composition separated from the substrate stiffness by utilizing decellularized matrix from diseased and healthy rats coated onto stiffness-controlled polyacrylamide gels. Our work furthers the field by presenting methodology and relevant endothelial cell phenotype response to compositional changes in a common rat model of PAH. Future studies could investigate the role of single sphingolipids or individual ECM proteins in cellular signaling events in PAH, as well as test human cells, human PAH-derived ECM and stiffness changes to better understand the role of ECM composition independent of organization and innate stiffness.

Data availability statement

The original contributions presented in the study are included in the article/Supplementary Material, further inquiries can be directed to the corresponding author.

Ethics statement

The animal study was approved by Virginia Commonwealth University IACUC. The study was conducted in accordance with the local legislation and institutional requirements.

Author contributions

PL performed experiments, analyzed data, drafted paper. LF provided cell clones and lungs for ECM isolation and helped drafting the manuscript. RH designed the study, analyzed data, drafted paper, and provided funding. All authors contributed to the article and approved the submitted version.

Funding

Parts of this work was funded by the NIH/NHLBI HL146250-02 (RH). Parts of the work pertaining to isolation and

characterization of CD117$^+$ rat lung EC clones were supported by NIH/NHLBI grant HL123044 (LF). The opinions expressed in this manuscript do not necessarily represent the opinions of the National Institutes of Health.

Acknowledgments

We would like to thank the VCU Chemical and Proteomic Mass Spectrometry Core Facility for performing our protein quantification mass specrometry. We would also like to thank the VCU Lipidomics Core Facility for conducting mass specrometry of the lipid composition.

Conflict of interest

The authors declare that the research was conducted in the absence of any commercial or financial relationships that could be construed as a potential conflict of interest.

Publisher's note

Supplementary material

The Supplementary Material for this article can be found online at: https://www.frontiersin.org/articles/10.3389/fphar.2023.1192798/full#supplementary-material

SUPPLEMENTAL FIGURE S1
(A) Su/CHx ECM does not affect CD117+ ECs proliferation on PAGs. CD117+ ECs plated on collagen, healthy matrix, and Su/CHx matrix have similar proliferation on different stiffnesses after 24 h. *n*=2. **(B)** Percent vessel coverage from an angiogenesis assay conducted following 72 h cultured on the varied conditions. Vessel percentage significantly decreases with Su/CHx ECM or increased stiffness. *n*=3.

References

Badylak, S. F. (2014). Decellularized allogeneic and xenogeneic tissue as a bioscaffold for regenerative medicine: factors that influence the host response. *Ann. Biomed. Eng.* 42, 1517–1527. doi:10.1007/s10439-013-0963-7

Bhagwani, A. R., Farkas, D., Harmon, B., Authelet, K. J., Cool, C. D., Kolb, M., et al. (2020). Clonally selected primitive endothelial cells promote occlusive pulmonary arteriopathy and severe pulmonary hypertension in rats exposed to chronic hypoxia. *Sci. Rep.* 10, 1136. doi:10.1038/s41598-020-58083-7

Bhagwani, A. R., Hultman, S., Farkas, D., Moncayo, R., Dandamudi, K., Zadu, A. K., et al. (2019). Endothelial cells are a source of nestin expression in pulmonary arterial hypertension. *PLoS One* 14, e0213890. doi:10.1371/journal.pone.0213890

Blanchard, N., Link, P. A., Farkas, D., Harmon, B., Hudson, J., Bogamuwa, S., et al. (2022). Dichotomous role of integrin-β5 in lung endothelial cells. *Pulm. Circ.* 12, e12156. doi:10.1002/pul2.12156

Booth, A. J., Hadley, R., Cornett, A. M., Dreffs, A. A., Matthes, S. A., Tsui, J. L., et al. (2012). Acellular normal and fibrotic human lung matrices as a culture system for *in vitro* investigation. *Am. J. Respir. Crit. Care Med.* 186, 866–876. doi:10.1164/rccm.201204-0754OC

Bu, S., Kapanadze, B., Hsu, T., and Trojanowska, M. (2008). Opposite effects of dihydrosphingosine 1-phosphate and sphingosine 1-phosphate on transforming growth factor-beta/Smad signaling are mediated through the PTEN/PPM1A-dependent pathway. *J. Biol. Chem.* 283, 19593–19602. doi:10.1074/jbc.M802417200

Chatterjee, S., and Naik, U. P. (2012). Pericyte-endothelial cell interaction: a survival mechanism for the tumor vasculature. *Cell adhesion Migr.* 6, 157–159. doi:10.4161/cam.20252

Chen, J., Tang, H., Sysol, J. R., Moreno-Vinasco, L., Shioura, K. M., Chen, T., et al. (2014). The sphingosine kinase 1/sphingosine-1-phosphate pathway in pulmonary arterial hypertension. *Am. J. Respir. Crit. Care Med.* 190, 1032–1043. doi:10.1164/rccm.201401-0121OC

Fang, S., Wei, J., Pentinmikko, N., Leinonen, H., and Salven, P. (2012). Generation of functional blood vessels from a single c-kit+ adult vascular endothelial stem cell. *PLoS Biol.* 10, e1001407. doi:10.1371/journal.pbio.1001407

Farkas, D., Kraskauskas, D., Drake, J. I., Alhussaini, A. A., Kraskauskiene, V., Bogaard, H. J., et al. (2014). CXCR4 inhibition ameliorates severe obliterative pulmonary hypertension and accumulation of C-Kit+ cells in rats. *PLOS ONE* 9 (2), 199. doi:10.1371/journal.pone.0089810

Farkas, D., Thompson, A. A. R., Bhagwani, A. R., Hultman, S., Ji, H., Kotha, N., et al. (2019). Toll-like receptor 3 is a therapeutic target for pulmonary hypertension. *Am. J. Respir. Crit. Care Med.* 199, 199–210. doi:10.1164/rccm.201707-1370OC

Gairhe, S., Joshi, S. R., Bastola, M. M., McLendon, J. M., Oka, M., Fagan, K. A., et al. (2016). Sphingosine-1-phosphate is involved in the occlusive arteriopathy of pulmonary arterial hypertension. *Pulm. Circ.* 6, 369–380. doi:10.1086/687766

Gilde, F., Fourel, L., Guillot, R., Pignot-Paintrand, I., Okada, T., Fitzpatrick, V., et al. (2016). Stiffness-dependent cellular internalization of matrix-bound BMP-2 and its relation to Smad and non-Smad signaling. *Acta biomater.* 46, 55–67. doi:10.1016/j.actbio.2016.09.014

Hait, N. C., Allegood, J., Maceyka, M., Strub, G. M., Harikumar, K. B., Singh, S. K., et al. (2009). Regulation of histone acetylation in the nucleus by sphingosine-1-phosphate. *Science* 325, 1254–1257. doi:10.1126/science.1176709

Hennigs, J. K., Baumann, H. J., Lüneburg, N., Quast, G., Harbaum, L., Heyckendorf, J., et al. (2014). Fibrinogen plasma concentration is an independent marker of haemodynamic impairment in chronic thromboembolic pulmonary hypertension. *Sci. Rep.* 4, 4808. doi:10.1038/srep04808

Huang, L., Li, L., Hu, E., Chen, G., Meng, X., Xiong, C., et al. (2018). Potential biomarkers and targets in reversibility of pulmonary arterial hypertension secondary to congenital heart disease: an explorative study. *Pulm. Circ.* 8, 2045893218755987. doi:10.1177/2045893218755987

Jia, D., He, Y., Zhu, Q., Liu, H., Zuo, C., Chen, G., et al. (2017). RAGE-mediated extracellular matrix proteins accumulation exacerbates HySu-induced pulmonary hypertension. *Cardiovasc. Res.* 113, 586–597. doi:10.1093/cvr/cvx051

Karki, P., and Birukova, A. A. (2018). Substrate stiffness-dependent exacerbation of endothelial permeability and inflammation: mechanisms and potential implications in ALI and PH (2017 grover conference series). *Pulm. Circ.* 8, 2045894018773044. doi:10.1177/2045894018773044

Li, G.-G., Zhu, Y.-T., Xie, H.-T., Chen, S.-Y., and Tseng, S. C. G. (2012). Mesenchymal stem cells derived from human limbal niche cells. *Investigative Ophthalmol. Vis. Sci.* 53, 5686–5697. doi:10.1167/iovs.12-10300

Link, P. A., Pouliot, R. A., Mikhaiel, N. S., Young, B. M., and Heise, R. L. (2017). Tunable hydrogels from pulmonary extracellular matrix for 3D cell culture. *J. Vis. Exp. JoVE* ~ 2017, e55094. doi:10.3791/55094

Loessner, D., Stok, K. S., Lutolf, M. P., Hutmacher, D. W., Clements, J. a., and Rizzi, S. C. (2010). Bioengineered 3D platform to explore cell-ECM interactions and drug resistance of epithelial ovarian cancer cells. *Biomaterials* 31, 8494–8506. doi:10.1016/j.biomaterials.2010.07.064

Lominadze, D., Dean, W. L., Tyagi, S. C., and Roberts, A. M. (2010). Mechanisms of fibrinogen-induced microvascular dysfunction during cardiovascular disease. *Acta physiol. Oxf. Engl.* 198, 1–13. doi:10.1111/j.1748-1716.2009.02037.x

Lu, P., Weaver, V. M., and Werb, Z. (2012). The extracellular matrix: a dynamic niche in cancer progression. *J. Cell Biol.* 196, 395–406. doi:10.1083/jcb.201102147

Lugassy, C., Shahsafaei, A., Bonitz, P., Busam, K. J., and Barnhill, R. L. (1999). Tumor microvessels in melanoma express the beta-2 chain of laminin. Implications for melanoma metastasis. *J. Cutan. Pathology* 26, 222–226. doi:10.1111/j.1600-0560.1999.tb01834.x

Maceyka, M., and Spiegel, S. (2014). Sphingolipid metabolites in inflammatory disease. *Nature* 510, 58–67. doi:10.1038/nature13475

McVey, M. J., Weidenfeld, S., Maishan, M., Spring, C., Kim, M., Tabuchi, A., et al. (2021). Platelet extracellular vesicles mediate transfusion-related acute lung injury by imbalancing the sphingolipid rheostat. *Blood* 137, 690–701. doi:10.1182/blood.2020005985

Neagu, A., Mironov, V., Kosztin, I., Barz, B., Neagu, M., Moreno-Rodriguez, R. A., et al. (2010). Computational modeling of epithelial--mesenchymal transformations. *Biosystems* 100, 23–30. doi:10.1016/j.biosystems.2009.12.004

Newman, A. C., Nakatsu, M. N., Chou, W., Gershon, P. D., and Hughes, C. C. W. (2011). The requirement for fibroblasts in angiogenesis: fibroblast-derived matrix proteins are essential for endothelial cell lumen formation. *Mol. Biol. Cell* 22, 3791–3800. doi:10.1091/mbc.E11-05-0393

Orr, A. W., Ginsberg, M. H., Shattil, S. J., Deckmyn, H., and Schwartz, M. A. (2006). Matrix-specific suppression of integrin activation in shear stress signaling. *MBoC* 17, 4686–4697. doi:10.1091/mbc.e06-04-0289

Piccoli, M., Cirillo, F., Ghiroldi, A., Rota, P., Coviello, S., Tarantino, A., et al. (2023). Sphingolipids and atherosclerosis: the dual role of ceramide and sphingosine-1-phosphate. *Antioxidants* 12, 143. doi:10.3390/antiox12010143

Rahman, M., and Sadygov, R. G. (2017). Predicting the protein half-life in tissue from its cellular properties. *PLOS ONE* 12, e0180428. doi:10.1371/journal.pone.0180428

Sava, P., Ramanathan, A., Dobronyi, A., Peng, X., Sun, H., Ledesma-Mendoza, A., et al. (2017). Human pericytes adopt myofibroblast properties in the microenvironment of the IPF lung. *JCI Insight* 2, e96352. doi:10.1172/jci.insight.96352

Scarritt, M. E., Bonvillain, R. W., Burkett, B. J., Wang, G., Glotser, E. Y., Zhang, Q., et al. (2014). Hypertensive rat lungs retain hallmarks of vascular disease upon decellularization but support the growth of mesenchymal stem cells. *Tissue Eng. Part A* 20, 1426–1443. doi:10.1089/ten.TEA.2013.0438

Sokocevic, D., Bonenfant, N. R., Wagner, D. E., Borg, Z. D., Lathrop, M. J., Lam, Y. W., et al. (2013). The effect of age and emphysematous and fibrotic injury on the re-cellularization of de-cellularized lungs. *Biomaterials* 34, 3256–3269. doi:10.1016/j.biomaterials.2013.01.028

Stenmark, K. R., Frid, M., and Perros, F. (2016). Endothelial-to-Mesenchymal transition: an evolving paradigm and a promising therapeutic target in PAH. *Circulation* 133, 1734–1737. doi:10.1161/CIRCULATIONAHA.116.022479

Suntharalingam, J., Goldsmith, K., van Marion, V., Long, L., Treacy, C. M., Dudbridge, F., et al. (2008). Fibrinogen Aalpha Thr312Ala polymorphism is associated with chronic thromboembolic pulmonary hypertension. *Eur. Respir. J.* 31, 736–741. doi:10.1183/09031936.00055107

Wagner, D. E., Bonenfant, N. R., Parsons, C. S., Sokocevic, D., Brooks, E. M., Borg, Z. D., et al. (2014). Comparative decellularization and recellularization of normal versus emphysematous human lungs. *Biomaterials* 35, 3281–3297. doi:10.1016/j.biomaterials.2013.12.103

Wang, W., Lollis, E. M., Bordeleau, F., and Reinhart-King, C. A. (2019). Matrix stiffness regulates vascular integrity through focal adhesion kinase activity. *FASEB J.* 33, 1199–1208. doi:10.1096/fj.201800841R

Weigel, C., Bellaci, J., and Spiegel, S. (2023). Sphingosine-1-phosphate and its receptors in vascular endothelial and lymphatic barrier function. *J. Biol. Chem.* 299, 104775. doi:10.1016/j.jbc.2023.104775

Williams, P. A., Stilhano, R. S., To, V. P., Tran, L., Wong, K., and Silva, E. A. (2015). Hypoxia augments outgrowth endothelial cell (OEC) sprouting and directed migration in response to sphingosine-1-phosphate (S1P). *PLoS One* 10, e0123437. doi:10.1371/journal.pone.0123437

Zhang, B., Niu, W., Dong, H., Liu, M., Luo, Y., and Li, Z. (2018). Hypoxia induces endothelial-mesenchymal transition in pulmonary vascular remodeling. *Int. J. Mol. Med.* 42, 270–278. doi:10.3892/ijmm.2018.3584

Zhang, Y., He, Y., Bharadwaj, S., Hammam, N., Carnagey, K., Myers, R., et al. (2009). Tissue-specific extracellular matrix coatings for the promotion of cell proliferation and maintenance of cell phenotype. *Biomaterials* 30, 4021–4028. doi:10.1016/j.biomaterials.2009.04.005

Frontiers in Pharmacology

Explores the interactions between chemicals and living beings

The most cited journal in its field, which advances access to pharmacological discoveries to prevent and treat human disease.

Discover the latest Research Topics

See more →

Frontiers

Avenue du Tribunal-Fédéral 34
1005 Lausanne, Switzerland
frontiersin.org

Contact us

+41 (0)21 510 17 00
frontiersin.org/about/contact